Institute of Electrical Engineering & Electrotechnologies
Lublin University of Technology

Polish Academy of Sciences Branch in Lublin

Centre of Excellence for the Application
of Superconducting and Plasma Technologies in Power Engineering

Proceedings of

the 7th International Conference

ELMECO-7

ELECTROMAGNETIC DEVICES AND PROCESSES
IN ENVIRONMENT PROTECTION

joint with

10th Seminar "Applications of Superconductors"

AoS-10

September 28 – 30, 2011

Nałęczów, Poland

Institute of Electrical Engineering & Electrotechnologies
Lublin University of Technology

Polish Academy of Sciences Branch in Lublin

Centre of Excellence for the Application
of Superconducting and Plasma Technologies in Power Engineering

Proceedings
of

the 7th International Conference

ELMECO-7

ELECTROMAGNETIC DEVICES AND PROCESSES
IN ENVIRONMENT PROTECTION

joint with

10th Seminar "Applications of Superconductors"

AoS-10

September 28 – 30, 2011

Nałęczów, Poland

Institute of Electrical Engineering and Electrotechnologies
Lublin University of Technology
38a Nadbystrzycka St. 20-618 Lublin

Tel./fax: 48 81 53 84 289, 48 81 53 84 643
E-mail: we.ipee@pollub.pl
http://ipee.pollub.pl/elmeco_aos

7th International Conference
ELMECO-7
ELECTROMAGNETIC DEVICES AND PROCESSES
IN ENVIRONMENT PROTECTION

joint with

10th Seminar "Applications of Superconductors"
AoS-10

September 28 – 30, 2011
Nałęczów, Poland

Organized by:

Institute of Electrical Engineering and Electrotechnologies
Lublin University of Technology

Polish Academy of Sciences Branch in Lublin

Centre of Excellence for the Application of Superconducting and Plasma Technologies in Power Engineering

Conference venue:
Conference Centre ENERGETYK
10 Paderewskiego St., 24 - 140 Nałęczów
tel. (48-81) 50 14 604

Scientific Committee

Kazimierz Adamiak	(University of Western Ontario, Canada)
Shin-ichi Aoqui	(Sojo University, Japan)
Krystyna Cedzyńska	(Technical University of Łódź, Poland)
Antoni Cieśla	(AGH University of Science and Technology, Cracow, Poland)
Marian Ciszek	(Polish Academy of Science, Wrocław, Poland)
Vladimir Datskov	(Joint Institute for Nuclear Research, Dubna, Russia)
Kenji Ebihara	(Kumamoto University, Japan)
Bartek A. Głowacki	(University of Cambridge, UK)
Bogusław Grzesik	(Silesian University of Technology, Gliwice, Poland)
Tadeusz Janowski	(Lublin University of Technology, Poland)
Ulrich Kogelschatz	(ABB, Switzerland)
Zbigniew Kołaciński	(Technical University of Łódź, Poland)
Jan Leszczyński	(Technical University of Łódź, Poland)
Bolesław Mazurek	(Electrotechnical Institute, Wrocław, Poland)
Jerzy Mizeraczyk	(Institute of Fluid Flow Machinery, PAS, Gdańsk, Poland)
Anthony J. Moses	(Wolfson Centre for Magnetics Techn., Cardiff Univ., UK)
Andrzej Nafalski	(University of South Australia, Adelaida)
Ryszard Pałka	(West Pomeranian University of Technology,Szczecin,Poland)
Krzysztof Schmidt-Szałowski	(Warsaw University of Technology, Poland)
Andrzej Siemko	(CERN, Geneva, Switzerland)
Jacek Sosnowski	(Electrotechnical Institute, Warsaw, Poland)
Petro G. Stakhiv	(Technical University of Lviv, Ukraine)
Henryka D. Stryczewska	(Lublin University of Technology, Poland)
Bronisław Susła	(Poznań University of Technology, Poland)
Jan Sykulski	(University of Southampton, UK)
Andrzej Wac-Włodarczyk	(Lublin University of Technology, Poland)
Chobei Yamabe	(Saga University, Japan)
Sotoshi Yamada	(Kanazawa University, Japan)
Kazimierz Zakrzewski	(Technical University of Łódź, Poland)
Andrzej Zaleski	(Polish Academy of Science, Wrocław, Poland

Organizing Committee

Tadeusz Janowski - **Chairman**
Henryka Danuta Stryczewska
Andrzej Wac-Włodarczyk
Paweł Surdacki
Beata Kondratowicz-Kucewicz
Grzegorz Wojtasiewicz
Renata Jaroszyńska - **Secretary**

ISBN: 978-83-62889-14-3

The proceedings have been published based on papers delivered by authors

PROGRAMME

Wednesday, 28 Sept.	Thursday, 29 Sept.	Friday, 30 Sept.
11:00-15:00 **Jubilee Session of 50th Anniversary of PSTAEE in Lublin**	08:00 – 09:00 **Breakfast**	08:00 – 09:00 **Breakfast**
	08:30 – 09:30 **Registration**	09:00 - 10:15 **Poster session P2** (with coffee)
	09:30 - 11:00 **Oral session O1**	10:15 - 12:15 **Oral session O3**
	11:00 - 11:30 **Coffee break**	12:15 – 12:30 **Closing session**
	11:30 – 12:45 **Oral session O2**	12:45 – 14:00 **Lunch**
	13:00 – 14:30 **Lunch**	
	14:30 - 15:45 **Poster session P1** (with coffee)	
17:00 – 19:00 **Registration Conference Centre "ENERGETYK" in Nałęczów**	16:00 – 18:30 **Guided sightseeing in Nałęczów**	
19:00 – 22:00 **Barbecue**	19:00 **Conference Dinner**	

Wednesday, 28 Sept. 2011

17:00 – 19:00 **Registration - Conference Centre "ENERGETYK" in Nałęczów**
19:00 – 22:00 **Barbecue**

Thursday, 29 Sept. 2011

08:00 – 09:00 **Breakfast**
08:30 – 09:30 **Registration**

09:30 -11:00 **Oral session O1**
(Chairpersons: Henryka D. Stryczewska, Kenji Ebihara)

1. **Bogusław Grzesik**, Mariusz Stępień
   Magnetic refrigeration
2. S.V. Gudkov, V.M. Drobin, D.E. Donets, **Evgeny D. Donets**, E.E. Donets, E. Kulikov, H. Malinowski, V.V. Salnikov and V.B. Shutov,
   Cryogenic and superconducting technologies in electron string ion sources of multicharged ions
3. **Monika Lewandowska**, Maurizio Bagnasco
   Conceptual design and analysis of a cryogenic system for a new test facility for high temperature superconductor current leads (HTS CLs)

11:00-11:30 **Coffee break**

11:30 – 12:45 **Oral session O2**
(Chairmen: Bronisław Susła, Toshiyuki Nakamiya)

1. **Mariusz Stępień**, Bogusław Grzesik
   FEM modelling of quench propagation in BSCCO tape
2. **Mariusz Woźniak**, Simon C. Hopkins, Bartłomiej A. Głowacki
   Characterisation of a MgB_2 wire using different current pulse shapes in pulsed magnetic field
3. **Agnieszka Łękawa-Raus**, Marek Burda, Lukasz Kurzepa, Xiaoyu Peng, Krzysztof K. Koziol
   Carbon nanotube fibre for electrical wiring applications

13:00 – 14:30 **Lunch**

14:30-15:45 **Poster session P1** (with coffee)
(Chairmen: Kenji Ebihara, Zbigniew Kołaciński)

1. Shinichi Aoqui, Ikuya Muramoto, Hiroharu Kawasaki, Tamiko Ohshima, Fumiaki Mitsugi, Toshiyuki Kawasaki, Tetsuro Baba, Yukio Takeuchi
   Optical study on the mechanisms for two and three phase gliding arc discharge
2. Fumiaki Mitsugi, Tomoaki Ikegami, Shin-ichi Aoqui, Yui Tashima, Hiroharu Kawasaki, Toshiyuki Nakamiya, Yoshito Sonoda, Henryka Stryczewska
   Application of optical wave microphone to gliding arc discharge
3. Tetsuro Baba, Yukio Takeuchi, Henryka Danuta Stryczewska, Shin-ichi Aoqui
   A study of simple power supply system with 6 electrodes configuration on gliding arc discharge
4. Yoichiro Iwasaki, Toshiyuki Nakamiya, Ryosuke Kozai, Fumiaki Mitsugi, Tomoaki Ikegami
   Automatic image analysis of laser annealing effects on characteristics of carbon nanotubes
5. Artur Berendt, Janusz Podliński, Jerzy Mizeraczyk
   Multi-DBD plasma actuator for flow separation control around NACA0012 and NACA0015 airfoil models
6. Janusz Podliński, Artur Berendt, Jerzy Mizeraczyk
   EHD secondary flow in the ESP with spiked electrodes
7. Anna Niewulis, Janusz Podliński, Jerzy Mizeraczyk
   EHD flow measured by 2D PIV in a narrow electrostatic precipitator with longitudinally-to-flow wire electrode
8. Michał Sobański, Artur Berendt, Mariusz Jasiński, Jerzy Mizeraczyk
   Optymalizacja mikrofalowego generatora plazmy o strukturze współosiowej zasilanego falowodem
9. Dariusz Czylkowski, Mariusz Jasiński, Jerzy Mizeraczyk
   Novel low power microwave plasma sources at atmospheric pressure
10. Jerzy Mizeraczyk, Bartosz Hrycak, Mariusz Jasiński, Mirosław Dors
    Low-temperature microwave microplasma for bio-decontamination
11. Bartosz Hrycak, Mariusz Jasiński, Dariusz Czylkowski, Marek Kocik, Mateusz Tański, Jerzy Mizeraczyk
    Tuning characteristics of cylindrical microwave plasma source operated with argon, nitrogen and methane at atmospheric pressure
12. Marek Kocik , Mateusz Tański, Jerzy Mizeraczyk
    3D structure of positive corona streamer reconstruction using stereo photography and computer algorothms
13. Mateusz Tański, Robert Barbucha, Marek Kocik, Jerzy Mizeraczyk
    Diagnostics of the laser generated plasma plume dynamics using time-resolved imaging
14. Jarosław Diatczyk, Tomasz Giżewski, Lucyna Kapka, Grzegorz Komarzyniec, Joanna Pawłat, Henryka Danuta Stryczewska
    Generation of non-equilibrium low-temperature plasma in the array of gliding arc plasma reactors
15. Jarosław Diatczyk, Julia Diatczyk ,Grzegorz Komarzyniec, Joanna Pawłat, Krzysztof Pawłowski, Henryka Danuta Stryczewska
    Problem zanieczyszczeń siloksanowych w instalacjach biogazowych
16. Grzegorz Komarzyniec, Henryka Danuta Stryczewska, Jarosław Diatczyk
    Supply system of water treatment installation from PV panels
17. Grzegorz Komarzyniec, Henryka Danuta Stryczewska, Jarosław Diatczyk
    Plasma deposition of ceramic layers directly onto the surfaces of the joints of osteoarthritis
18. Justyna Jaroszyńska-Wolińska, P. A. F. Herbert
    Decomposition of BTX by plasma generated ozone
19. Małgorzata Kalczewska Adhesive properties of the plasma treated PI/Cu laminate surface
20. Janusz Piechna, Witold Selerowicz, Teresa Opalińska, Małgorzata Kalczewska
    Reactants streams mixing in a chemical reactor employing of gliding discharge principles
21. Janusz Piechna, Witold Selerowicz, Teresa Opalińska, Bogdan Ulejczyk, Małgorzata Kalczewska
    Theoretical and experimental parameters of gliding discharge movement with a stream of reactants flowing through the discharge zone in a plasma reactor for a waste treatment device
22. Grzegorz Raniszewski, Zbigniew Kołaciński, Łukasz Szymański
    Plasma arc for utilization of soils
23. Zbigniew Kołacinski, Łukasz Szymanski, Grzegorz Raniszewski
    A rotating arc plasma reactor

24. Olena Solomenko, V. Chernyak, O. Nedybaliuk
Reforming of ethanol in plasma-liquid system tornado type with the addition of CO_2
25. Jacek Majewski
Methods for measuring ozone concentration in ozone-treated water
26. Paweł A. Mazurek
Methods to improve the electromagnetic compatibility of plasma reactor
27. Andrzej Wac-Włodarczyk, Andrzej Kaczor
Zaburzenia elektromagnetyczne na liniach zasilających reaktor plazmowy typu Glidarc
28. Mario Janda, Zdenko Machala, Deanna Lacoste, Karol Hensel, Christophe Laux
Discharge propagation in capillary tubes assisted by bias electric field
29. Karol Hensel, Pierre Le Delliou, Pierre Tardiveau, Stephane Pasquiers
Self-pulsing DC driven discharges in preheated air aimed for plasma assisted combustion
30. Matej Klas, Michal Stano, Štefan Matejčík
Electrical diagnostics of microdischarges in helium
31. Hyun-Ha Kim
Interaction of nonthermal plasma and catalyst at ambient temperature

16:00 – 18:30 **Guided sightseeing in Nałęczów**

19:00 **Conference Dinner**

Friday, 30 Sept.

08:00 – 09:00 **Breakfast**

09:00-10:15 **Poster session P2** (with coffee)
(Chairmen: Ryszard Pałka, Bogusław Grzesik)

1. Katarzyna Juda, Mariusz Woźniak, Mariusz Mosiadz, Simon C. Hopkins, Bartłomiej A. Głowacki, Tadeusz Janowski
Superconducting properties of YBCO coated conductors produced by inkjet printing
2. Dariusz Czerwiński, Leszek Jaroszyński, Janusz Kozak, Michał Majka,
Equivalent electromagnetic model for current leads made of HTS tapes
3. Leszek Jaroszyński, Dariusz Czerwiński
Numerical analysis of YBCO coated conductors
4. Tadeusz Janowski, Joanna Kozieł, Tomasz Giżewski, Dariusz Czerwiński
Modelowanie powrotnej charakterystyki rozgałęzionej taśmy nadprzewodnikowej HTS 2G
5. Michał Majka, Janusz Kozak, Tadeusz Janowski, Sławomir Kozak
Badania eksperymentalne i analiza skuteczności działania bezrdzeniowego indukcyjnego nadprzewodnikowego ogranicznika prądu
6. Janusz Kozak , Michał Majka, Tadeusz Janowski, Sławomir Kozak
Budowa i badania nadprzewodnikowego bezrdzeniowego indukcyjnego ogranicznika prądu średniego napięcia
7. Beata Kondratowicz-Kucewicz, Sławomir Kozak
Rozkład pola magnetycznego i energia nadprzewodnikowego zasobnika w różnej konfiguracji cewek
8. Tadeusz Janowski, Grzegorz Wojtasiewicz
Transformatory nadprzewodnikowe odporne na zwarcia i ograniczające prądy zwarcia
9. Ryszard Pałka
Synteza pola magnetycznego w nadprzewodnikowym ograniczniku prądowym
10. Anup Patel, Ryszard Pałka, Bartłomiej A. Głowacki
New bulk – bulk superconducting bearing concept using additional permanent magnets
11. Paweł Surdacki
Wpływ impulsu zaburzającego na parametry zanikania nadprzewodzenia w przewodzie nadprzewodnikowym MgB_2/Cu
12. Paweł Surdacki
Wpływ prądu i temperatury pracy na parametry zanikania nadprzewodzenia w przewodzie nadprzewodnikowym YBCO
13. Leszek Woźny, Anna Kisiel, Roman F. Szeloch, Eugeniusz Prociów
Electrical electrodes of Ni-Me (Me=Ag, Mo, Cu) on $YBa_2Cu_3O_x$ surface
14. Anna Kisiel, Małgorzata Mielcarek, Jan Ziaja
The influence of technological parameters on photovoltaic properties of TiO_2
15. K. Chybczyńska, M. Wróblewski, M. Wawrzyniak, Bronisław Susła
Conductance quantization in Nb-Ti alloys and BiPbSrCaCuO superconducting tapes nanocontacts
16. Michał Łanczont
Modelowanie rezystancyjnego nadprzewodnikowego ogranicznika prądu w środowisku SCILAB

17. Michał Łanczont
    Perspektywy zastosowanie technologii nadprzewodnikowej w budowie urządzenia georadarowego
18. Oleksandra Hotra, Piotr Bylicki
    Using the test method for optimization the Peltier device for achievement superconducting transition temperatures
19. Mariusz Mazurek, Elżbieta Jartych, Dariusz Oleszak
    Mössbauer studies of $Bi_5Ti_3FeO_{15}$ electroceramic prepared by mechanical activation
20. Elżbieta Jartych, Dariusz Oleszak, Mariusz Mazurek
    Hyperfine interactions in multiferroic mechanically activated $BiFeO_3$ compound
21. Joanna Michałowska-Samonek, Arkadiusz Miaskowski, Andrzej Wac-Włodarczyk
    Analysis electromagnetic field distribution and specific absorption rate in breast models
22. Arkadiusz Miaskowski, Andrzej Wac-Włodarczyk, Grażyna Olchowik
    Low frequency FDTD algorithm and its application to inductive hyperthermia
23. Piotr Gas
    Temperature distribution in human tissue during interstitial microwave hyperthermia
24. Eugeniusz Kurgan
    Comparison of different methods of force calculation in dielectrophoresis
25. Tomasz Giżewski, Andrzej Wac-Włodarczyk, Ryszard Goleman, Dariusz Czerwiński
    Analiza nieparametrycznych metod automatycznej klasyfikacji obiektów wielowymiarowych w aplikacji do nieniszczącej detekcji uszkodzeń
26. Andrzej Wac-Włodarczyk, Mateusz Wąsek
    Zastosowanie kamer termograficznych w bezinwazyjnej diagnostyce medycznej
27. Tadeusz Janowski, Mariusz Holuk
    Promoting renewable energy sources to supply home power plants
28. Eiji Sakai, Hiroshi Sakamoto
    Wireless rapid charger of super capacitor
29. Sławomir Wiak, Agnieszka Pyć, Marcin Pyć
    Electrical machines in the military more electric aircraft and their impact on the environment
30. Wojciech Jarzyna, Michał Augustyniak
    PD and LQR controllers applied to vibration damping of an active composite beam
31. Andrzej Kotyra, Waldemar Wójcik, Krzysztof Jagiełło, Konrad Gromaszek, Tomasz Ławicki, Piotr Popiel
    Biomass-coal combustion characterization using image processing
32. Andrzej Smolarz, Konrad Gromaszek, Waldemar Wójcik, Piotr Popiel
    Diagnostics of industrial pulverized coal burner using optical methods and artificial intelligence
33. Waldemar Wójcik, Sławomir Cięszczyk, Tomasz Ławicki, Arkadiusz Miaskowski
    Application of curvelet transform in the processing of data from ground penetrating radar
34. Paweł Komada, Sławomir Cięszczyk, Waldemar Wójcik
    Influence of gas concentration inhomogeneity on measurement accuracy in absorption spectroscopy

10:15 – 12:15 **Oral session O3**

(Chairpersons: Shin-ichi Aoqui, Henryka D. Stryczewska)

1. **Kenji Ebihara**, Henryka Danuta Stryczewska, Fumiaki Mitsugi, Tomoaki Ikegami, Takamasa Sakai, Joanna Pawlat, S. Teii
   Recent development of ozone treatment for agricultural soil sterilization and biomedical prevention
2. **Toshiyuki Nakamiya**, Fumiaki Mitsugi, Ryota Ide , Tomoaki Ikegami, Yoichiro Iwasaki, Ryoichi Tsuda, Yoshito Sonoda
   Tomographic visualization of discharge sound fields using optical wave microphone
3. **Zbigniew Kołaciński**, Łukasz Szymanski, Grzegorz Raniszewski, Sławomir Wiak
   Plasma synthesis of carbon nanotubes for electric and electronic devices
4. Valeriy Chernyak, **Sergij Olszewski**, Evgen Martysh, Oleg Nedybaluyk, Vitalij Yukhymenko, Sergij Sidoruk, Iryna Prysyazhnevich, **Olena Solomenko**
   Plasma assisted distruction of organic moleculs in dynamic plasma–liquid systems
5. **Mirosław Dors**, Tomasz Izdebski, Bartosz Hrycak, Jerzy Mizeraczyk
   Microwave plasma module for destruction of oil slicks
6. **Joanna Pawłat**
   Atmospheric pressure plasma jet for sterilization purposes

12:15 – 12:30 **Conference Closing**

(Chairpersons: Henryka D. Stryczewska, Tadeusz Janowski)

12:45 – 14:00 **Lunch**

OPTICAL STUDY ON THE MECHANISMS FOR TWO AND THREE PHASE GLIDING ARC DISCHARGE

Shinichi AOQUI[1], Ikuya MURAMOTO[1], Hiroharu KAWASAKI[2], Tamiko OHSHIMA[2], Fumiaki MITSUGI[3], Toshiyuki KAWASAKI[4], Tetsuro BABA[5], Yukio TAKEUCHI[5]

Sojo University (1), Sasebo College of Technology (2), Kumamoto University (3), Nippon Bunri University (4), VIC Co. Ltd(5)

***Abstract**. Mechanisms of a gliding arc discharge have been studied using monochromater and high speed camera. Two-dimensional images of two phase gliding arc discharge show shapes of a string, and they glides from upstream to the downstream along with electrodes by gas flow. Gliding speed strongly depends on gas flow rate and discharge condition. Some of the "string-like" arc discharge changes their shape, and some part of the discharge "re-connect" in the discharge area especially on the upstream region*

Keywords: Gliding arc discharge, *Two-dimensional images, re-connection*.

Introduction

Gliding arc (GA) discharge is one of the electric discharge plasma which can be generated to open air space[1-3]. GA forms "plane plasma" in the two dimensional space between electrodes. GA generated using the direct current and the exchange power supply were applied to decomposition of the quality of an air pollutant. Recently, the method which used the high frequency pulse power supply was also proposed, and they are applied to surface treatments, such as resin, glass, metal. On GA discharge, many studies had been accomplished, but, as for the most, there were many experiential elements about the constitution of the electric discharge part such as shape, geometry and materials of electrode, power supply system, plasma ignition and so on. In this paper, two dimensional photographs of the gliding arc discharge were taken by high speed camera, and optical emission spectroscopic measurements were applied for the GA discharge in the atmospheric pressure in the several discharge conditions, such as gas, gas flow rate, discharge power. As the results, a basic process of a GA discharge were studied.

Experimental

The electrodes of arc discharge were iron and gases used for the experiment were argon, oxygen, and carbon dioxide. However, the atmosphere gases were mixed these gases since the electric discharge domain is not sealed. Gas flow rate was controlled from 10 l/min to 50 l/min by the pressure regulator and the digital flow instrument. Discharge voltage was controlled by the voltage slide regulator, and increased by using the high voltage transformer, and then high voltage was applied to the electrodes. Discharge voltage was measured using the high-voltage probe, and discharge current was measured using the clamp current probe. Applied voltage to the voltage slide regulator were 40V, 60V and 80V, and net discharge voltage between electrode for gliding arc were 4.9kV, 7.2kV, and 9.7kV, respectively. Two dimensional photographs of the gliding arc discharge were taken by two kinds of high speed cameras (Casio, High speed exilim EX-F1; shutter speed was 1200 flame per second), and super high speed camera (Photron, FASTCAM SA5; shutter speed was 54000 flame per second). Optical emission spectra were measured by the USB small multichannel spectroscope.

Results and discussions

The structure of gliding arc discharge

Fig. 1 shows the photographs of two phase, two electrodes gliding arc using high speed camera. In this experiment, 60 V in input discharge voltage, and Ar gas flow was 50 l/min. As the results, arc discharge occurs between the shortest gaps and emission intensity is very high, like white-color emission. The arc discharge did not moved without gas flow, and it seems to one dimensional structure like needle to needle electrodes arc discharge as shown in Fig 1(a). The arc discharge glides from upstream to the downstream along with electrodes by Ar gas flow. The discharge spreads in two dimensions to the electrode and gas flow directions as shown in Figs. 1(b)-1(d). There were a lot of dischrage passes in the same flame of 0.83 ms gate time. We also observed two phase, two electrodes gliding arc discharge, not shown here. From the top view of them, discharge occurs between next electrodes and move to the side gap, like "delta" shape, at the early phase of discharge. However, the shape changes like "star" with the discharge glide to the downstream.

Fig. 2 shows the photographs of gliding arc using super high speed camera. In this experiment, shutter speed was 54000 flame per second, 60 V in input discharge voltage, and Ar gas flow was 50 l/min. As the results, shapes of arc discharge in the downstream region looks like "rope" or "string", and they seem to be twisted. Part of them looks like "re-connection".

Optical emission spectroscopy

Emission spectra at the downstream area and that at the upstream area in the same gliding discharge are shown in Fig. 1. In the upstream area N_2 molecular spectra, CO emission and O I emission peaks can be observed. On the other hand, there is only N_2 second positive band in the the spectrum and any other peaks are disappeared. As the results, an upstream area is a positive column of the main arc discharge around the shortest gaps area. Almost all discharge power were consumed at the place and they can be controlled by discharge power. In the downstream domain, plasma behaves "plasma jet" or "plasma plume" which exists across between electrodes that depend on the gas flow.

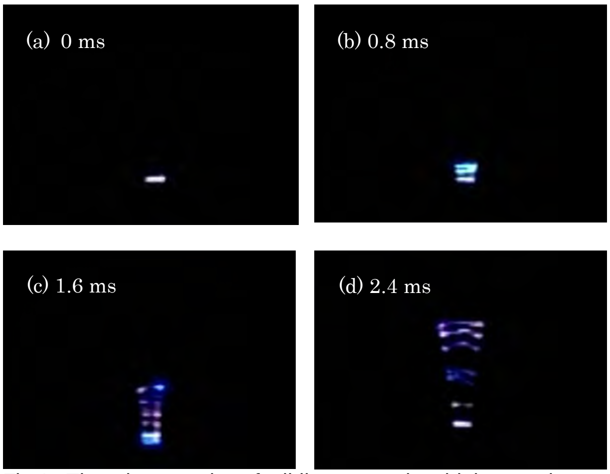

Fig.1. The photographs of gliding arc using high speed camera. (1200 fps, ISO1600, 60 V in input discharge voltage).

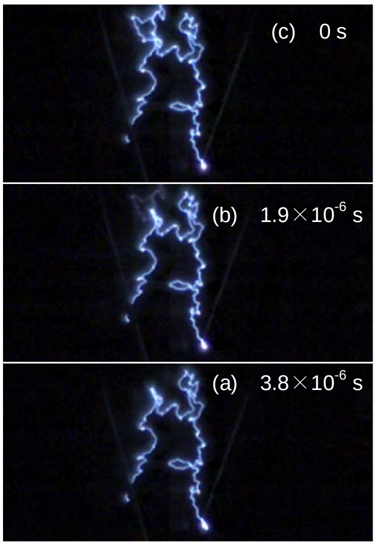

Fig.2. The photographs of gliding arc using super high speed camera. (54000 fps, 60 V in input discharge voltage)

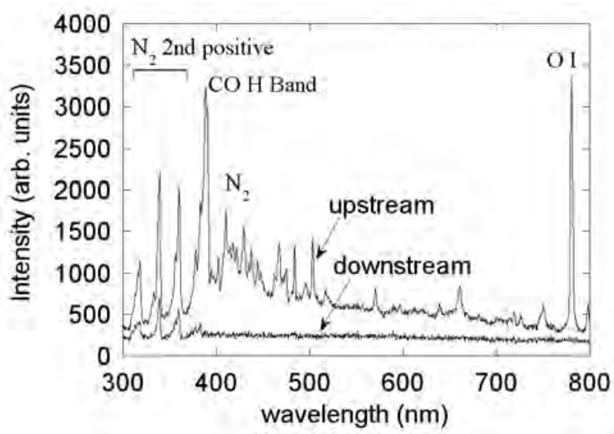

Fig.3. Emission spectra at the downstream area and that at the upstream area in the same gliding discharge.

CONCLUSION

Optical emission spectroscopic measurements for the gliding arc discharge in the atmospheric pressure suggests that two discharge domains exist in the upstream and downstream sides along with a gas flow. In the upstream discharge, emission spectra strongly depend on the gas, discharge power and gas flow rate. On the other hand, emission spectra in the downstream discharge domain is different from that in the upstream. In the spectra, there are no emission peaks other than N_2 second positive band.

REFERENCES

[1] A. Czemichowski: Gliding arc. Applications to engineering and environment control, Pure and Applied Chemistry, Vol.66 (1994), No.6, pp.1301-1310.
[2] A. Fridman, S. Nester, L. A. Kennedy, A. Saveliev, O. Mutaf-Yardimci, Gliding arc gas discharge, Progress in Energy and Combustion Science, Vol.25 (1999) pp.211-231.
[3] H. Shiki, H. Saito, S. Oke, Y. Suda. H. Takikawa, S. Yamanaka, T. Okawa, Y. Nishimura, S. Hishida, E. Usuki, Influence of Series Inductance in Pulsed Gliding Arc Discharge, Vol. 16,(2008), No.2, pp.105-112.

***Authors**: Mr. Ikuya MURAMOTO, Division of Energy Electronics, Sojo Univ., Ikeda 4-22-1, Kumamoto, 860-0082, Japan, E-mail: g101d01@cc.sojo-u.ac.jp, prof. dr Shin-ichi AOQUI, Graduate School of Electrical & Electronics Eng., Sojo Univ., Ikeda 4-22-1, Kumamoto, E-mail: aoqui@cc.sojo-u.ac.jp, prof. dr Hiroharu Kawasaki, Sasebo College of Tech., 1-1, Okishin, Sasebo, Nagasaki, Japan, E-mail: h-kawasa@sasebo.ac.jp; dr Tamiko Ohshima, Sasebo College of Tech., 1-1, Okishin, Sasebo, Nagasaki, Japan, E-mail: oshima@sasebo.ac.jp, dr Fumiaki MITSUGI, Faculty of Eng. Kumamoto Univ., Kurokami 2-39-1, Kumamoto mitsugi@cs.kumamoto-u.ac.jp, dr Toshiyuki KAWASAKI, Faculty of Eng. Nippon Bunri Univ., kawasaki@nbu.ac.jp, Tetsuro BABA, VIC Co. Ltd., baba@vic-int.co.jp, Yukio TAKEUCHI, VIC Co. Ltd., takeuchiy@vic-int.co.jp.*

Conference ELMECO–7
ELECTROMAGNETIC DEVICES AND PROCESSES IN ENVIRONMENT PROTECTION
joint with 10th Seminar AoS-10 APPLICATIONS OF SUPERCONDUCTORS
28–30.09.2011, Nałęczów, Poland

A STUDY OF SIMPLE POWER SUPPLY SYSTEM WITH 6 ELECTRODES CONFIGURATION ON GLIDING ARC DISCHARGE

Tetsuro BABA[1], Yukio TAKEUCHI[1], Henryka Danuta STRYCZEWSKA[2], Shin-ichi AOQUI[3]

VIC International Inc.(1), Lublin University of Technology (2), Sojo University (3)

Abstract. *We report the trial manufacture equipment of 6 phases gliding arc discharge and analyzed I-V characteristic.About the power supply, exclusive equipment was not used, and general-purpose equipment were combined and made.*
We investigated current voltage characteristic of gliding arc discharge.

Keywords : gliding arc, non-thermal equilibrium plasma, 6 phases alternating current discharge, gaseous processing

Introduction

The processing of exhausted industry hazardous gas is a top priority environmental protection matter now. In recent years a plasma technique has been used for purification of the exhaust pollution.

Inductively Coupled Plasma (ICP) is suitable technique for a decomposition of a neutral gas therefore, it is used widely. Because the temperature is high (5000 K-20000 K) in the plasma with ICP equipment, organic matter almost completely decomposes. And also equipment is simple normally.

However, large electric power is required to maintain the plasma which is near to thermal equilibrium with atmospheric pressure on ICP. On the other hand, Gliding Arc discharge generating non-thermal equilibrium plasma can generate atmospheric pressure plasma with small input electric power much more in comparison with ICP [1-3]. But, because gliding arc is non-thermal equilibrium, a volume of plasma is not large, and a large quantity of gaseous processing is not easy. Furthermore, the basic of plasma process is unknown enough. Therefore a system which combined a catalyzer with discharge has been proposed with many reactors on gliding arc [4].

In this study, it was carried out from the viewpoint of fundamental electric circuit system of a plasma generation and enhancement of the plasma volume with 3 and 6 phases electrode of gliding arc[5]. Particularly simple power supply system was proposed with 6 phases alternating current.

Experiment

Fig.1 shows the experimental setup. Gliding arc discharge strongly depends on an arrangement of electrode and power supply system. In this study, six pieces of knife edge-shaped electrodes made by pure iron were located at an angle of 60 degrees. The electrode distance was adjustable from 0 to 10 mm. Pure Ar gas was introduced by the electrodes lower part and gas flow was controlled by a flowmeter. Two three-phase circuit power transformers of maximum voltage 6.6kV were used. Generally an exclusive transformer is used to supply electrode with high voltage alternating current more than a three-phase circuit. However, it is difficult for the high voltage multi-phase transformer to maintain isolation of a winding wire between every phase. In addition, the price of that type is expensive, too. Therefore we examined a reverse connection of a three-phase circuit power transformer for power line use that was low-priced with high performance. In our study, as for one transformer (HV Trans 2), the phase was reversed for an inversion transformer to realize 6 phases. Therefore 6 generated phases were not phase differences of 60 degrees. A high voltage trigger electrode for an initial ignition was not used to avoid an unnecessary current path for explication of gliding arc plasma phenomenon.

A current and a voltage of each electrode were measured by digital oscilloscope with a high voltage probe and a current probe, respectively. The discharge was observed using a normal camera and high-speed camera.

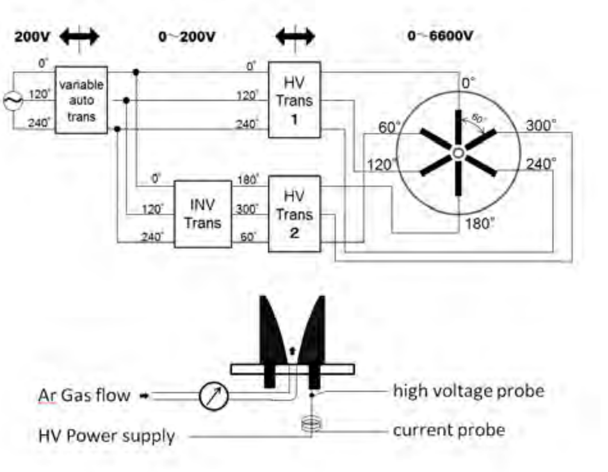

Fig.1 Experimental setup

Result

Fig.2 shows photography of the electrode with discharge.

Fig.3 shows a voltage waveform. Because there was not initial ignition electrode, a discharge did not start up to 3300V but after the ignition, the discharge was maintained at 2000V or less. The gas flow rate was 10L/min. The angular degree of each phase was according to setting before a discharge breakdown. After the discharge breakdown, the voltage waveform which was similar to two-phase or three-phase the gliding arc discharge was shown. With enhancement of the applied voltage (3, 4.5, 6 KV), the overall length of current paths of discharge extended. The current path of sub-m sec order was observed with a high-speed camera.

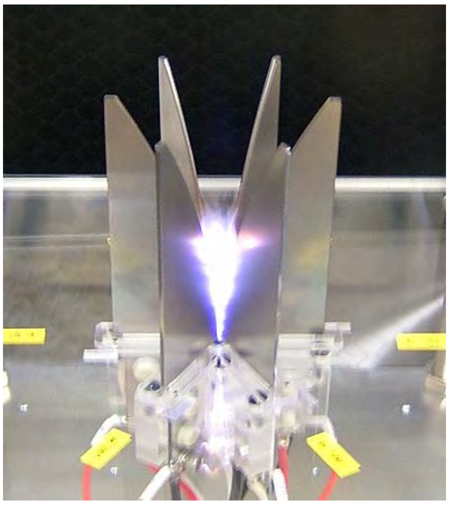

Fig.2 Electrode photograph

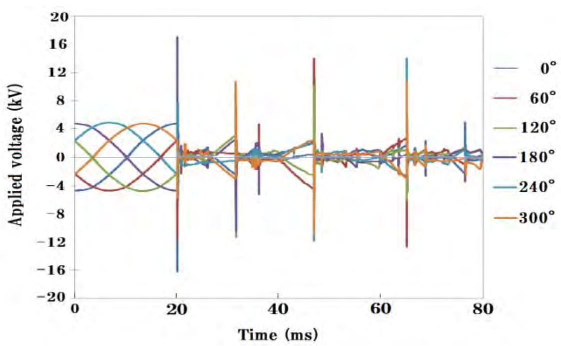

Fig.3 Voltage characteristic of gliding arc discharge border of discharge before and after.

Fig. 4 shows current voltage characteristic (I-V characteristic) in a case Ar gas flow rate was changed. A current flowed with a sharp break of the terminal voltage of each phase.

In addition, with the enhancement of the gas flow rates, the overall length of current paths of discharge extended.

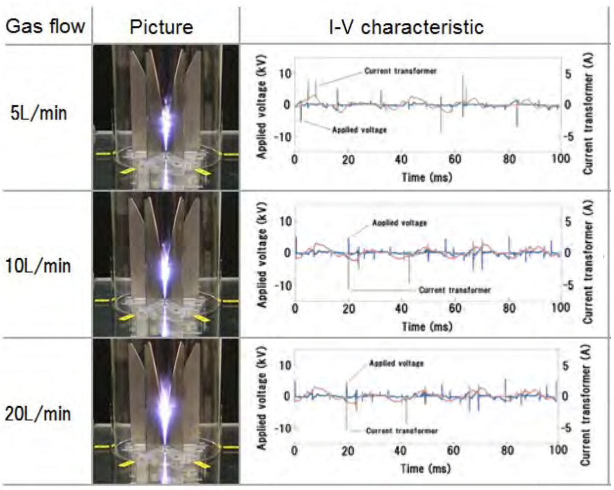

Fig.4 I-V characteristic of gliding arc discharge

Conclusion

A fundamental confirmation of the electrical discharge and fundamental electrical property were measured. That proposed that general-purpose equipment were combined and made for 6 phases gliding arc discharge by 6 phases power supply.

An enough discharge volume was secured without used 6 phases transformer with complex structure.

REFERENCES

[1] R.McAdams, J. Phys. D: Appl. Phys. 34, 2810 (2001)
[2] J. S.Chang, T. Myint, A. Chakrabarti, A. Miziolek, Jpn. J. Appl. Phys. 36, 5018 (1997)
[3] K. Krawczyk, B. Ulejczyk, Plasma Chemistry and Plasma Processing, 24, 2, 155 (2004)
[4] K. S-Szalowski, K. Krawczyk, M.Mlotek, Plasma Process. Polym, 4, 728 (2007)
[5] J. Diatczyk, G. Komarzyniec, and H. D. Stryczewska, I.J.PEST, vol. 5, no. 1, 12, (2011)

***Authors**: Tetsuro Baba, and Yukio Takeuchi, VIC International Inc., Nagaoka 2-1-2, Nishitama-gun Mizuho city, Tokyo 190-1232, Japan, E-mail:baba@vic-int.co.jp. ; Prof. Henryka Stryczewska, Institute of Electrical and Electrotechnologies, Lublin University of Technology, 38A Nadbystrzycka St. 20-618, Lublin, Poland, E-mail: h.stryczewska@pollub.pl; Prof. Shin-ichi Aoqui, Sojo University, Ikeda 4-22-1, Kumamoto city, Kumamoto 860-0082, Japan, E-mail: aoqui@cis.sojo-u.ac.*

Conference ELMECO–7
ELECTROMAGNETIC DEVICES AND PROCESSES IN ENVIRONMENT PROTECTION
joint with 10th Seminar AoS-10 APPLICATIONS OF SUPERCONDUCTORS
28–30.09.2011, Nałęczów, Poland

MULTI-DBD PLASMA ACTUATOR FOR FLOW SEPARATION CONTROL AROUND NACA0012 AND NACA0015 AIRFOIL MODELS

Artur BERENDT[1], Janusz PODLIŃSKI[1], Jerzy MIZERACZYK[1, 2]

Plasma and Laser Engineering, The Szewalski Institute of Fluid Flow Machinery, Polish Academy of Sciences (1),

Department of Marine Electronics, Gdynia Maritime University (2)

Abstract. *In this paper application of innovative multi-DBD plasma actuator for flow separation control is presented. The influence of the airflow generated by this actuator on the flow around NACA0012 and NACA0015 airfoil models was investigated. The results obtained from 2D PIV measurements showed that the multi-DBD actuator with floating interelectrode is attractive for leading and trailing edge separation control.*

Streszczenie. *W niniejszej pracy zaprezentowano innowacyjny aktuator plazmowy z elektrodą o potencjale pływającym. Aktuator ten zastosowano do aktywnej kontroli przepływu wokół elementów aerodynamicznych. Rezultaty badań wskazują, że badany aktuator umożliwia kontrolę oderwania warstwy przyściennej wokół modeli skrzydła NACA0012 i NACA0015.*

Keywords: plasma, airflow control, surface dielectric barrier discharge, DBD.
Słowa kluczowe: plazma, kontrola przepływu, powierzchniowe wyładowanie barierowe, DBD.

Introduction

Nowadays, the importance of an air transport in the world economy is constantly growing. Unfortunately, the heavy air traffic is the source of pollutions which are harmful for a human health and an environment. Thus, the great research effort is directed to make aircrafts more human and environment friendly. This objective can be achieve e.g. by improving aircraft aerodynamic. Unfortunately, using the conventional technologies, further improvements of the aircraft aerodynamic is severely limited. Thus, the new solutions like usage of dielectric barrier discharge (DBD) plasma actuators for active airflow control around aerodynamic elements are under development.

The DBD actuators are devices using plasma generated by the surface dielectric barrier discharge for active airflow control [1-3]. The DBD establishes when a voltage is applied to electrodes which are asymmetrically set on the top and bottom sides of a dielectric material. The plasma generated by the DBD actuator induces electrohydrodynamic (EHD) flow that allow to control flow around aerodynamic elements. Using DBD actuators it is possible to increase the lift of the airfoil or to decrease its aerodynamic drag, to control the boundary layer flow separation or laminar-turbulent flow transition. DBD plasma actuators are also used for reducing noise generated by the turbulent airflow around the aircraft.

Currently, researches on DBD plasma actuators for flow control are popular and are performed in many laboratories all over the world. Although, the published experiments results showed that DBD plasma actuators are capable of modifying airflow around aerodynamic elements they are still not used for practical applications. The main reason of this is relatively low airflow velocity generated by the DBD actuator (for single-DBD actuator generated airflow do not exceed 5 - 6 m/s) which is not adequate for efficient control of the flow around aircraft wing. Thus, indispensable are new investigations that will allow us to better know the properties of surface dielectric barrier discharge and mechanism of inducing EHD flow.

In this paper we present the innovative multi-DBD actuator with floating interelectrode for flow separation control. The results of the flow separation control experiments with NACA0012 and NACA0015 airfoil models are showed. Performed investigations showed that our multi-DBD actuator has very good parameters and could be attractive for aerodynamic applications.

Experimental set-up

Multi-DBD actuator with floating interelectrode

The investigated multi-DBD actuator with floating interelectrode is presented in Fig. 1 (more detailed description of the multi-DBD actuator with floating interelectrodes could be find in [4]). To fit the actuator on the NACA airfoil model flexible dielectric material (3 layers of a 45 Kapton tape) was used. All electrodes used in this actuator were made of a 50 μm-thick copper tape. The smooth HV electrode was 6 mm wide, while the saw-like grounded electrode and the floating interelectrode were 3 mm wide. The floating interelectrode consisted of a series of separated saw teeth (Fig. 2). The described above multi-DBD actuator was used in our investigations of flow separation control on NACA0012 and NACA0015 airfoil models.

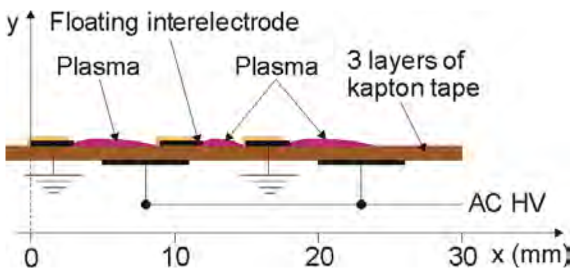

Fig. 1 Schematic side view of the multi-DBD actuator with saw-like floating interelectrode for flow separation control

Fig. 2 Schematic top view of the saw-like floating interelectrode consisted of a series of separated saw teeth

Airfoil models

Two airfoil models with fixed multi-DBD actuator were prepared. In both cases investigated airfoil model was 200 mm wide in chord and 595 mm wide in spanwise direction. The first airfoil model was NACA0012 and was used for the leading edge flow separation control experiments. The first DBD generated by the multi-DBD actuator was started at position x/C = 4% (x – distance from the leading edge, C – chord length).

The second airfoil model was NACA0015 and was used for trailing edge separation control. In this case the first DBD generated by the multi-DBD actuator was started at position x/C = 52%.

Experimental apparatus

The experimental apparatus for flow separation control investigations is presented in Fig. 3. It consisted of an AC power supply and a 2D particle image velocimetry (PIV) equipment for measurements of the velocity fields [4].

The sinusoidal high voltage (frequency 1.5 kHz) applied to multi-DBD actuator was generated by a function generator Trek model PM04015A.

The experiments were carried out in an ambient air at atmospheric pressure. A test section of the wind tunnel was 600 mm wide and 480 mm high. A free stream velocity in the wind tunnel during measurements was 10 m/s, 15 m/s or 20 m/s and the turbulence level was below 0.1%.

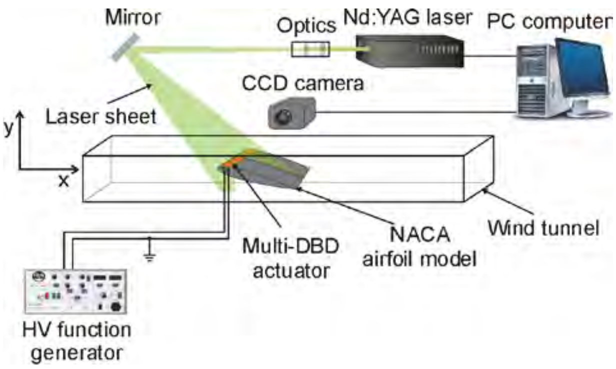

Fig. 3 Experimental set-up for flow separation control measurements

Results

The leading edge (NACA0012) and trailing edge (NACA0015) flow separation control experiments were performed. The examples of obtained time-averaged contour velocity maps for leading edge flow separation control investigations with multi-DBD actuator turned off and turned on are presented in Figs. 4 and 5, respectively. In this case the free stream velocity was V_0 = 15 m/s (Re = $2x10^5$) and an angle of attack was 11^o. The high voltage applied to multi-DBD actuator was 15 kV_{pp}. As it is seen, when the multi-DBD actuator was off airflow separated near the leading edge of the airfoil and a large vortex existed, while airflow reattachment occur when the multi-DBD actuator was turned on. Similar effect of actuation was observed for trailing edge flow separation experiments.

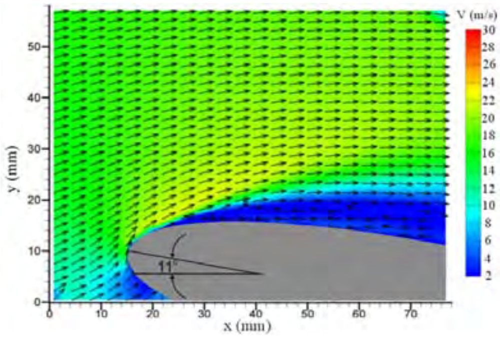

Fig. 4 Time-averaged contour velocity map of the airflow above the NACA0012 airfoil model. Free stream velocity V_0 = 15 m/s; angle of attack 11^o. Plasma OFF – separated airflow.

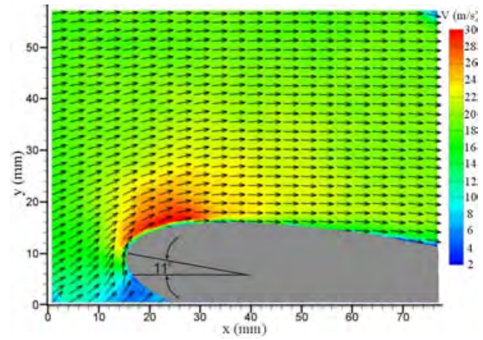

Fig. 5 Time-averaged contour velocity map of the airflow NACA0012 airfoil model. Free stream velocity V_0 = 15 m/s; angle of attack 11^o. Plasma ON – airflow reattached. The applied sine-wave voltage was 15 kV_{pp} and the frequency was 1.5 kHz.

Conclusions

The multi-DBD plasma actuator with floating interelectrode was investigated. The 2D PIV measurements of the flow around NACA0012 and NACA0015 airfoil models were performed. The obtained contour velocity maps shows that this kind of actuator is useful for controlling the leading and trailing edge flow separation. Such a result bring us to a conclusion that the multi-DBD actuator with floating interelectrode is attractive for aerodynamic applications.

REFERENCES

[1] Roth J. R, Sherman D. M., and Wilkinson S. P., Boundary layer flow control with a one atmosphere uniform glow discharge surface, *AIAA Meeting*, Reno, USA, #98-0328, 1998

[2] Moreau E., Airflow control by non-thermal plasma actuators, *J. Phys. D: Appl. Phys.* 40, 3 (2007)

[3] Touchard G., Plasma actuators for aeronautics applications - State of art review, *I. J. PEST*, 2, 1, 2008

[4] Berendt A., Podlinski J., Mizeraczyk J., Elongated DBD with floating interelectrodes for actuators, *EPJ AP*, 2011 (in print)

Authors: M.Sc. Artur Berendt aberendt@imp.gda.pl and Dr. Janusz Podliński janusz@imp.gda.pl, *Centre for Plasma and Laser Engineering, The Szewalski Institute of Fluid Flow Machinery, Polish Academy of Sciences, Fiszera 14, 80-952 Gdańsk; Prof. Jerzy Mizeraczyk jmiz@imp.gda.pl, Centre for Plasma and Laser Engineering, The Szewalski Institute of Fluid Flow Machinery, Polish Academy of Sciences, Fiszera 14, 80-952 Gdańsk and Department of Marine Electronics, Gdynia Maritime University, Morska 81-87, 81-225 Gdynia*

CONDUCTANCE QUANTIZATION IN Nb-Ti ALLOYS AND BiPbSrCaCuO SUPERCONDUCTING TAPES NANOCONTACTS

K. Chybczyńska[a] , M. Wróblewski[a,c], M. Wawrzyniak[b] , B. Susła[a]

[a]Institute of Physics, Poznan University of Technology
Nieszawska 13a, 60-965 Poznan, Poland
[b]Faculty of Electronics and Telecommunications
Poznan University of Technology, Piotrowo 3, 60-965 Poznan, Poland
[c]Institute of Molecular Physics, Polish Academy of Sciences, M. Smoluchowskiego 17, 60-179 Poland
Corresponding.bronislaw.susla@put.poznan.pl

***Abstract**. The paper present experimental results on the conductance quantization of heterojunction between Nb-Ti tip and a Nb-Ti wires and also between BiPbSrCaCuO tip and BiPbSrCaCuO tapes. The conductance stepwise behavior of the nanowires was directly observed with a storage oscilloscope. These data have been statistically analyzed by plotting histograms for more than 3 thousand conductance curves..*

***Keywords**: Nb-Ti alloys, nadprzewodnikowe ograniczniki prądu, BiPbSrCaCuO superconducting tapes.*

Over two decades ago it was discovered [1, 2] that the conductance of a ballistic point contact is quantized in units of the conductance quantum, $G_o=2e^2/h = (12.9\ k\Omega)^{-1}$. The origin of this phenomenon is the quantization of transverse momentum in the constriction. Each of the N opened channels degenerates transverse modes at the Fermi energy E_F in such quantum point contact and contributes $2e^2/h$ to the conductance. The appearance of these interesting and potentially useful effects in practical devices is related to the size scale. With smaller devices the effect will be important at higher temperature. When the wire width is reduced to the nanometer size or the Fermi wavelength (λ_F) scale, the conductance between electrodes is quantized. Electronic transport changes from diffusive to ballistic, that is, without scattering, as shown schematically in Fig. 1.

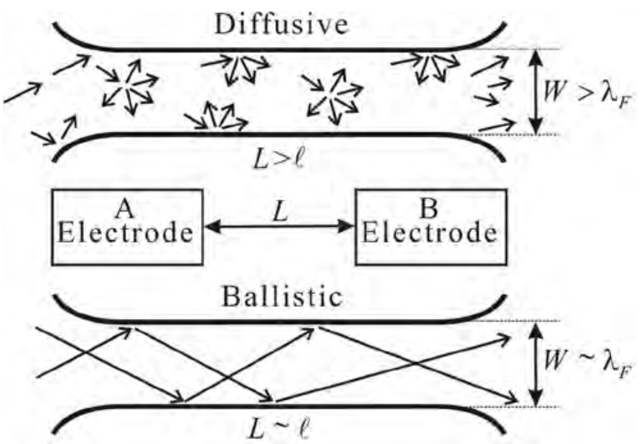

Fig. 1. Diffusive (a) and ballistic (b) transport of electrons in one-dimensional wires.

Quantum point contacts have been used in a wide variety of investigations, including transport through quantum dots, the quantum Hall effect, magnetic focusing and the Aharonov-Bohm effect [3].

The experimental setup is presented in Fig.2. Nanowires are formed between electrodes A and B of the studied materials. The experiments are performed at room temperature and in air.

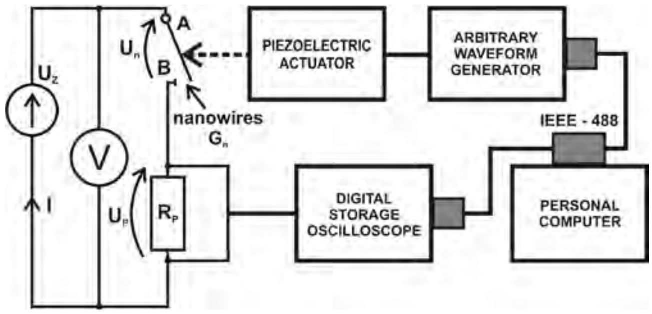

Fig. 2. Schematic diagram of the experimental setup used in investigations of conductance quantization.

We present experimental results on the conductance quantization of heterojunction between Nb-Ti tip and a Nb-Ti wires and also between BiPbSrCaCuO tip and BiPbSrCaCuO tapes. The conductance stepwise behavior of the nanowires was directly observed with a storage oscilloscope. Our data have been statistically analyzed by plotting histograms for more than 3 thousand conductance curves.

We show that conductance quantization phenomena can be observed at room temperature in materials used commercially in superconducting magnets. The important is that this kind of behavior happens in all cases on small enough size scale, and this kind of striking features is not governed by diffusion. This means that the devices, whose operation is based on diffusion models, will work differently.

Acknowledgements:
This work was supported in part by Poznan University of Technology under DS 62-176/11.

REFERENCES:

[1.] B.J. van Wees, H. van Houten, C.W. J. Beenakker, J.G. Williamson, L.P. Kouwenhoven, D. van der Marel, and C.T. Foxon, Phys. Rev. Lett. **60**, 848 (1988)
[2.] J.I. Pascual, J. Mendez, J. Gomez-Herrero, A.M. Baro, N. Garcia, Phys. Rev. Lett. **71,** 1852 (1993).
[3.] C.W.J. Beenakker and H.van Houten, Solid State Phys. **44**, 1 (1991)

***Authors**:*
***K. Chybczyńska**, **B. Susła** Institute of Physics, Poznan University of Technology,,Nieszawska 13a, 60-965 Poznan, Poland; **M. Wróblewski**, Institute of Physics, Poznan University of Technology,,Nieszawska 13a, 60-965 Poznan, Polan & Institute of Molecular Physics, Polish Academy of Sciences, M. Smoluchowskiego 17, 60-179 Poland, **M. Wawrzyniak**,Faculty of Electronics and Telecommunications, Poznan University of Technology, Piotrowo 3, 60-965 Poznan, Poland*
Corresponding.bronislaw.susla@put.poznan.pl

PLASMA ASSISTED DISTRUCTION OF ORGANIC MOLECULS IN DYNAMIC PLASMA–LIQUID SYSTEMS

Valeriy CHERNYAK, Sergij OLSZEWSKI, Evgen MARTYSH, Oleg NEDYBALYUK, Vitalij YUKHYMENKO, Sergij SIDORUK, Iryna PRYSYAZHNEVICH, Olena SOLOMENKO

Taras Shevchenko National Universityof Kyiv, Radio Physics Faculty

Abstract. *The processes of organic compound (phenol and cation-active surfactants) destruction in water solutions, which occur under the influence of plasma treatment was investigated in different dynamic plasma-liquid systems (PLS). The breakdown products of phenol and cation-active surfactants detected with absorption spectroscopy. The most effective system for phenol plasmolytic destruction in water solutions are the secondary discharge with a liquid electrode at atmospheric pressure and PLS*, based on the impulse discharge in the gas channel with liquid wall.

Keywords: dynamic plasma-liquid system, plasma-chemical processing, ultrasonic nebulization.

Introduction

Water is a valuable natural resource. With metabolic processes forming the base of human living, water plays an exclusive role in every aspect. The everyday human need for it is known to all. At the UN World Economic Forum (January 2008) held in Switzerland), has been claimed that the population of more than half of the world population will experience a shortage of clean water by 2025, and 75% by 2050. Methods based on plasma-chemical processes in the liquid-gas environments for water treatment and purification of highly polluted wastewater are among the most promising. Unlike the regenerative methods which remove the impurities from the water into the solid (adsorption), gas (desorption) or non-aqueous liquid (extraction) phase, the destructive method (technology of water and industrial waste plasma-chemical processing) is based on changing the chemical structure of molecules and impurities.

The problem of complete cleaning for the industrial wastewaters from organic high active and toxic substances (HATS) is important enough and simultaneously difficult to decide. However this problem can not be considered as decided. Apparently, plasmachemical technologies are represented by most perspective, as allow to achieve high velocity of substances destruction at the expense of high-energy concentration. However, it is necessary to take into account, that toxic substances are, frequently, the complex high-molecular compounds. Therefore destruction of HATS results in occurrence not only products of disintegration, but also wide spectrum more complex compounds [1]. The chemical reactions both in plasmachemical systems can proceed with participation of the electronic-exited particles, which practically are not investigated today. It is specified that high probability of unknown earlier substances occurrence at the data technologies. Therefore now the transition starts to complex technologies on a basis of plasmachemical processes.

Discharge systems for plasma stimulation of physical and chemical processes, peculiarities of oxidation and reduction reactions and the applicability issues, caused by contact between plasma and the liquid solution, were studied in the present work.

Experimental technique

The process of organic compound destruction in water solutions, which occurs under the influence of plasma, was investigated in different plasma-liquid systems (PLS).

The organic solutions in distillated water was treated by plasma of secondary discharge stimulated by transverse arc at atmospheric pressure [2, 3] of DC discharge in the gas channel with liquid wall and the additional excitation of ultrasonic field in liquid [4]. Pulse discharge in gas channel with liquid wall [5] and the discharge in reverse-vortex gas flow of “tornado” type with “liquid” electrode [6].

The studies were with various plasma-forming gases: dry air (mode A), water vapor (WV), a mixture of air and aerosol solution, which is handled by (S).

Experimental results

Examples of experimental results that were obtained by emission spectroscopic method in UV region ((200 - 400 nm) are shown in Fig. 1. The flow of plasma gas was stable - 0,13 $l \cdot s^{-1}$.

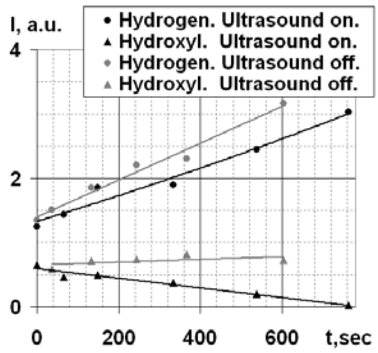

Fig. 1. Dependences of the relative intensity of the hydroxyl molecular band – trigonal points and hydrogen – round points in the emission spectra of DGCLW plasma on the distilled water treatment time. The black lines correspond to ultrasound in liquid is present. The grey lines – to ultrasound is absent. All spectral components are normalized on intensity of respective atomic lines of copper (electrodes material).

As follows from the analysis of aggregated data that there is always a strong absorption at λ (wavelength) < 250 nm for the spectra of hydrogen peroxide H_2O_2 and formic acid HCOOH. These compounds are formed during the plasma chemical processing regardless of the type of orifice gas, electrode material and polarity of the “liquid electrode”. During the plasma chemical processing, it was noted that there is a significant disruption of copper and graphite electrodes. “Liquid electrode” with a positive polarity is the most bright example. Bands of nitrogen compounds, typical for the absorption spectra are: NO_3^- (broad band with maximum 300 nm) and NO_2^- (broad band with maximum 355 nm). So, investigated discharges produce very powerful oxidizing species and can essentially change the acidity of our samples. The quantitative responses presented at Fig.2.

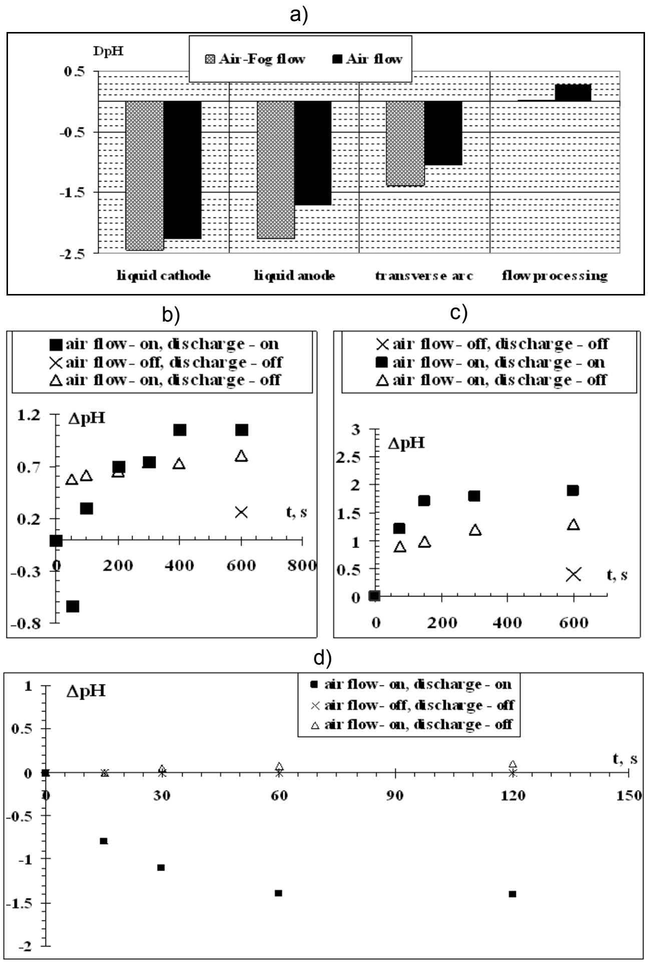

Fig. 2. Variation of pH value from air flow with and without plasma treatment. a - PLS with secondary di scharge; b, c - with DC and Pulse discharges in the gas channel with liquid wall; d - with the discharge in reverse-vortex gas flow of “tornado” type with liquid electrode.

Examples of experimental results that were obtained by spectrophotometric method in UV region ((200 - 400 nm) are shown in Fig. 3. In here set out results of plasma assisted destructions of phenol molecules in water solution 0,0003 mol/l. Solutions were treatment by plasma of secondary discharge stimulated by transverse arc with air flow and air-droplet flow. The air-droplet flow was generated by ultrasonic nebulization of initial solution. The total discharge power was ~ 800 W. The flow of plasma gas was stable - 0,13 l·s^{-1}.

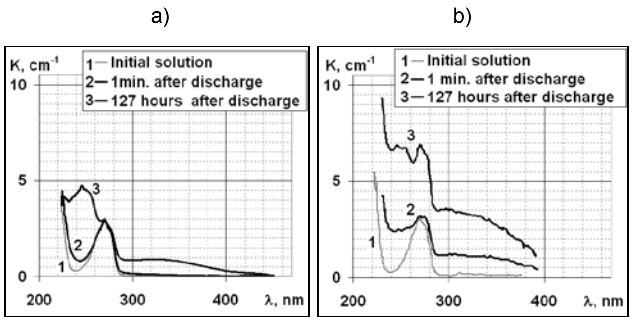

Fig. 3. Evolution of phenol-water solutions after plasma assisted destruction of phenol molecules. Chart -a) correspond to secondary discharge stimulated by transverse arc with air flow; chart -b) – with air-droplet flow. The plasma exposition time is 30 sec. The total discharge power ~ 800 W. The grey curve #1 correspond to initial solution, the black #2 – to processing solution in 60 sec after plasma treatment and the black #3 – to processing solution in 127 hours after plasma treatment.

Conclusions

It has been established that the water processing by plasma leads to destruction of toxic phenylic compounds in water solutions.

Analysing the received experimental data, it is possible to conclude that the cleaning of water occurs basically at the expense of oxidizing destruction of phenylic compounds. It is a result of hydrogen peroxide influence, nitric and nitrogenous acids, which are formed in water under influence of plasma secondary discharge, and also of others chemically active particles.

Plasma-chemical factors, which cause the compound destruction:

a) forming the active particles, which activate cascade chemical reactions with molecules of phenylic compounds (free radicals and active oxygen);

b) changing of water structure under plasma-radiolysis and as a consequence - displacement of equilibrium to destruction of molecules of phenylic compounds.

REFERENCES

[1] Bystritskij, V., Wood, T., Yankelevich, Y., Chaunan, S., Wessel, F. (1998) Abstr. 12th Intern.Conf. on High-Power Particle Beams, Haifa, Israel

[2] Prysiazhnevych, I., Chernyak, V., Olszewski, S., Yukhymenko, V. Chem. Listy 102, (2008),.s1403–s1407.

[3] Prysyazhnevich, I., Chernyak, V., Skalný, J.D., Matejčik, Š., Yukhymenko, V., Olszewsky, S., Naumov, V. “Sources of Nonequilibrium Plasma at Atmospheric Pressure”//UJP (2008) Vol. 53, N5, p. 472-476

[4] Olszewski, S., Solomenko, Ol., Yukhymenko, V., Chernyak, V. Abst. III Central European Symposium on Plasma Chemistry, August 23 – 27 (2009), Kyiv, Ukrane, - pp. 100-101.

[5] Sidoruk, S., Chernyak, V., Olszewski, S. Abst. III Central European Symposium on Plasma Chemistry, August 23 - 27, (2009) Kyiv, Ukrane, - pp. 92-93.

[6] Chernyak, V., Olszewski, S., Nedybaliuk, O., Sidoruk, S., Yukhymenko, V., Prysiazhnevych, I., Shchedrin, A., Levko, D., Naumov, V., Demchina, V., Kudryavzev, V. Proc. of the Tenth International Conference on Combustion and Energy Utilization (10th ICCEU), 4-8 May (2010), Mugla, Turkey.- pp. 295-300

Authors:
Valeriy Chernyak, Sergij Olszewski, Evgen Martysh, Oleg Nedybalyuk, Vitalij Yukhymenko, Sergij Sidoruk, Iryna Prysyazhnevich, Olena Solomenko: Taras Shevchenko National Universityof Kyiv, Radio Physics Faculty, Prospect Acad. Glushkova 2/5, Kyiv 03022, Ukraine, phone/fax:+380 44 526058/+380 44 5213590 e-mail: solaristics@gmail.com

Conference ELMECO–7
ELECTROMAGNETIC DEVICES AND PROCESSES IN ENVIRONMENT PROTECTION
joint with 10th Seminar AoS-10 APPLICATIONS OF SUPERCONDUCTORS
28–30.09.2011, Nałęczów, Poland

EQUIVALENT ELECTROMAGNETIC MODEL FOR CURRENT LEADS MADE OF HTS TAPES

Dariusz CZERWIŃSKI[1], Leszek JAROSZYŃSKI[1]
Janusz KOZAK[2], Michał MAJKA[2]

Lublin University of Technology (1), Electrotechnical Institute (2)

***Abstract**. An equivalent electromagnetic model that describes the behaviour of a current lead build of HTS tapes has been proposed. Electromagnetic filed analysis of HTS lead using FEM environment was made. The model is based on the physical structure and behaviour of HTS tapes. It was possible to calculate the magnetic filed distribution in the lead. Obtained results can be very useful in the analysis of quench states of the superconducting current leads.*

***Streszczenie.** W niniejszym opracowaniu został przedstawiony elektromagnetyczny model przepustów prądowych wykonanych z taśm nadprzewodnikowych HTS drugiej generacji. Model opiera się na fizycznej strukturze i zachowaniu taśmy HTS. Dzięki temu było możliwe obliczenie rozkładu pola elektromagnetycznego w przepuście. Uzyskane wyniki mogą być bardzo przydatne w analizie stanów przejściowych przepustów HTS.*

Keywords: HTS tape model, superconducting tapes analysis, quench state
Słowa kluczowe: model taśmy HTS, analiza taśm HTS drugiej generacji, stany przejściowe

Introduction

The development of the HTS tape manufacturing technologies leads to evolution of many superconducting devices. It is possible to build the current lead based on the high temperature superconducting tapes (Fig. 1). For this kind of current leads it is very important to keep the heat sources on the very low level (even 1 Joule).

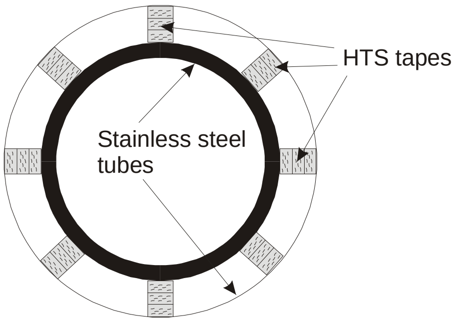

Fig. 1. Current lead build of HTS tapes

In this paper the authors showed the researches of the electromagnetic model of second generation superconducting tapes.

Tapes made of High Temperature Superconductors

Discovery of the HTS materials was the first step in development of new generation superconducting applications. Many of HTS materials are superconductors and carry significant current above the boiling point of liquid nitrogen at 77.4 K.

High performance high temperature superconductor wire underlies the worldwide opportunity to revolutionize the electric power grid, transportation, materials processing and many other industries, with a new generation of high efficiency, compact and environmentally friendly electrical equipment. Rapid progress in commercializing these many applications has been enabled by an HTS wire known as first generation (1G) [1].

This wire is a composite structure consisting of number of filaments of HTS material embedded in a silver alloy matrix. First generation HTS wire is characterized usually by low critical current, therefore many companies are making researches on improved performance of HTS wires.

Second generation wire has quite different architecture compared with first generation wire. The 2G HTS wire comprises multiple coatings on a base material or substrate. This architecture is designed to achieve the highest degree of alignment possible of the atoms in the superconductor material. The reason of such construction is reaching the highest possible electrical current.

Second generation (2G) HTS wire consists of a tape-shaped base, or substrate, upon which a thin coating of superconductor compound, usually $YBa_2Cu_3O_7$ (“YBCO”), is deposited or grown such that the crystalline lattice of the YBCO in the final product is highly aligned, creating a coating that is virtually a single crystal. The superconductor coating in this coated conductor wire architecture typically has a thickness on the order of one micron (Fig. 2) [1-5].

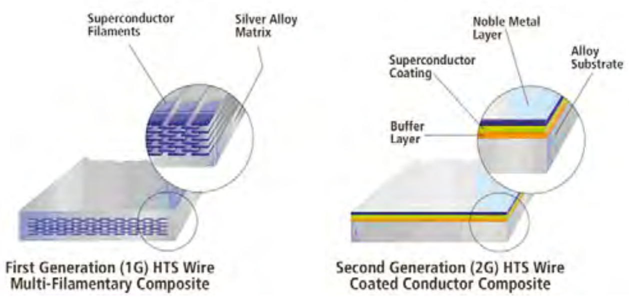

Fig. 2. First generation (1G) versus second generation (2G) HTS tape [1]

Another important aspect in HTS wire is the value of the critical current in external magnetic filed. When the magnetic flux increases the critical current decreases rapidly, even 10 times in some cases. To counteract this disadvantage the HTS wires are produced with special defects, so called pinning centres. Pinning can be achieved by introducing defects into the HTS material on a nanometer scale, comparable to the diameter of the flux lines passing through the HTS surface. While tubular defects can match the flux line geometry most optimally, a more practical approach is to find ways to introduce a high density of very fine particles called nanoparticles or nanodots. Particles of yttrium oxide (Y_2O_3) and yttrium cuprate ($Y_2Cu_2O_5$) are dispersed throughout wire's YBCO superconductor layer (Fig. 3). The effect of the dispersion is that nanodots become pinning centres of magnetic vortices associated with current flow in the superconductor. As the result the improvement of current carrying capability of the HTS wire can be observed.

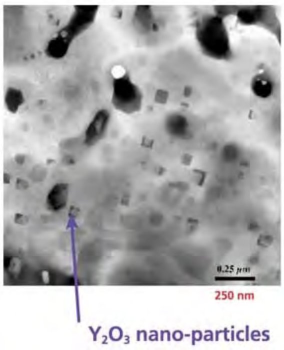

Fig. 3. Transmission electron micrograph of yttria nanodots in the YCBO matrix [2]

The AMSC is the company with the most experience in the production of 2G HTS tapes. The wire manufacturing process has been based on long, 40 millimeter wide strips of superconductor material that are produced in a high-speed, continuous reel-to-reel deposition process.

This process is similar to the low-cost production of motion picture film in which celluloid strips are coated with a liquid emulsion. The wires are laminated on both sides with copper, stainless-steel, or brass metals to provide strength, durability and certain electrical characteristics needed in applications. Finally the tape is formed into standard wires with a width of 4.4, 4.8 or 12 mm. [2]

Electromagnetic Model of the Second Generation High Temperature Superconductor Tape

Modelling of the second generation HTS wire is a difficult task, because of the large disparity of thickness to width of the tape. The width of the tape is at least 30 times bigger then thickness. The first step of the simulation was the construction of the 2G HTS tape FEM model (Fig. 4).

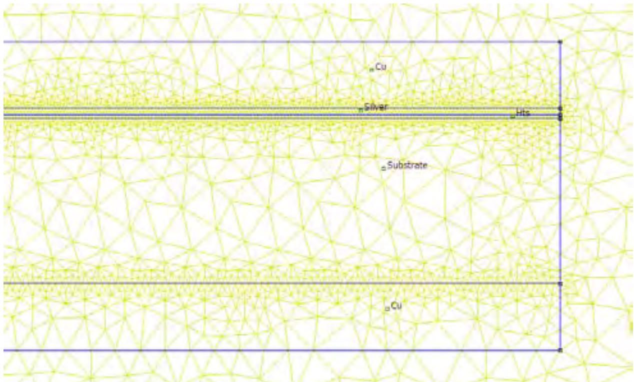

Fig. 4. FEM model of the second generation HTS tape

Model is based on the SCS3050 tape produced by the SuperPower company. Model consists of: thin layer of (RE)BCO superconductor (thickness 1 μm), substrate made of hastelloy (50 μm), silver overlayer (2 μm) and copper stabilizers (20 μm each). Width of the tape is 3 mm.

Building the mesh it is very important to obtain good quality elements in HTS layer, this will get the correct results. The value of the current is 50 A and it is less then critical current for this tape equal I_c=60 A. The tape was modelled in superconducting state. After the solution the flux distribution was obtained (Fig. 5).

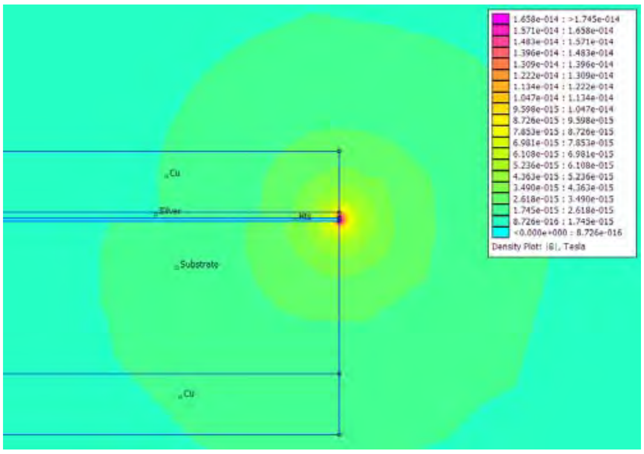

Fig.5. Distribution of the flux density in the model (self field)

One can notice that the ends of the strips are inhomogeneities in the distribution of magnetic flux.

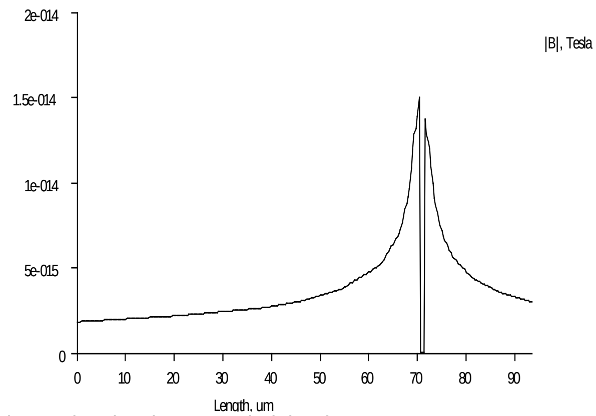

Fig. 6. Flux density versus height of tape

The flux highest values were obtained in hastelloy substrate, silver overlayer and copper stabilizers.

REFERENCES

[1] American Superconductor Corporation, http://www.amsuper.com/, 2011
[2] SuperPower®2G HTS Wire Specifications, http://www.superpower-inc.com/, 2011
[3] Seong-Woo Yim, Sung-Hun Lim, Hye-Rim Kim Si-Dole Hwang, Kohji Kishiro, Electrical Behavior of Bi-2223/Ag Tapes Under Applied Alternating Over-Currents, IEEE Transactions on Applied Superconductivity, vol. 15, No. 2, June 2005
[4] Y.S. Cha, Semi-Empirical Correlation for Quench Time of Inductively Coupled Fault Current Limiter, IEEE Transactions on Applied Superconductivity, vol. 15, No. 2, June 2005
[5] T. J. Arndt, A. Aubele, H. Krauth, M. Munz, B. Sailer, Progress in preparation of technical HTS tapes of type Bi-2223/Ag alloy of industrial lengths, IEEE Transactions on Applied Superconductivity, vol. 15, No. 2, June 2005

***Authors**: dr inż. Dariusz Czerwiński, dr inż. Leszek Jaroszyński, Politechnika Lubelska, Instytut Podstaw Elektrotechniki i Elektrotechnologii, ul. Nadbystrzycka 38A, 20-618 Lublin, e-mail: d.czerwinski@pollub.pl*
dr inż. Janusz Kozak, dr inż. Michał Majka, Instytut Elektrotechniki, ul. Pożaryskiego 28, 04-703 Warszawa

Conference ELMECO–7
ELECTROMAGNETIC DEVICES AND PROCESSES IN ENVIRONMENT PROTECTION
joint with 10th Seminar AoS-10 APPLICATIONS OF SUPERCONDUCTORS
28–30.09.2011, Nałęczów, Poland

NOVEL LOW POWER MICROWAVE PLASMA SOURCES AT ATMOSPHERIC PRESSURE

Dariusz CZYLKOWSKI[1], Mariusz JASIŃSKI[1], Jerzy MIZERACZYK[1,2]

The Szewalski Institute of Fluid Flow Machinery, Gdańsk (1), Gdynia Maritime University (2)

***Abstract**. The aim of this paper is to present the results of our experimental investigations concerning novel low power microwave plasma sources. Such devices are of high interest from industry point of view, namely for plastic or metal surface treatment. Proposed by us plasma sources are small, simple and low cost. Plasma generated by them is of regular shape. They can be operated at atmospheric pressure, at standard frequency of 2.45 GHZ and microwave power lower than 500 W.*

***Streszczenie.** Celem pracy jest zaprezentować wyniki naszych prac eksperymentalnych nad nowymi mikrofalowymi źródłami plazmy małej mocy. Takie urządzenia cieszą się zainteresowaniem przemysłu w celu zastosowań w obróbce plastikowych i metalowych powierzchni. Zaproponowane przez nas źródła plazmy małej mocy są małe, proste I tanie. Pracują pod ciśnieniem atmosferycznym I standardowej częstotliwości 2,45 GHz.*

Keywords: atmospheric pressure discharge, microwave plasma sources, surface treatment.
Słowa kluczowe: wyładowanie pod ciśnieniem atmosferycznym, mikrofalowe źródła plazmy, obróbka powierzchni.

Introduction

To meet industry expectations of having small and low cost source of plasma for surface treatment we started an experimental investigations concerning this problem. Except above-named properties generated plasma should be regular in shape. Currently, devices provided plasmas in the form of flame [1] or column [2] are well known. In this paper we presents results of our work and we propose a few novel low power microwave plasma sources. These are: waveguide slit plasma generator, multijet microwave plasma generator and microwave plasma sheet generator. All of them are operated at atmospheric pressure, at standard frequency of 2.45 GHz and microwave power not exceeding 500 W.

Waveguide slit plasma generator

The new waveguide slit plasma generator is based on the WR 430 standard rectangular waveguide. Its photo is presented in the figure 1. It has the form of the wedge waveguide tipped with a slit of dimensions 1×54,6 mm. From microwave power input side the generator is terminated with a teflon plate which prevent flowing of the gas to the waveguide circuit.

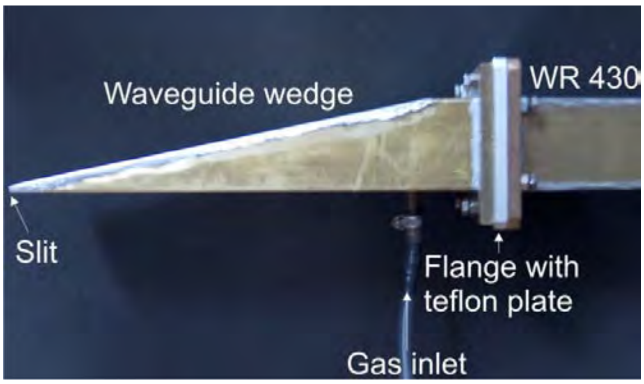

Fig.1. The photo of the waveguide slit plasma generator.

Generated in the waveguide slit plasma due to the gas flow leaves the waveguide region. For initiation the discharge the P_A absorbed microwave power, as low as 50 W, is required. Protruded plasma gives the possibility of contact with treatment material. Depending on the absorbed microwave power P_A the plasma has the form of separate or confluent spots (see figure 2). For assuring better efficiency of microwave power transfer to the plasma the three stub tuner can be used.

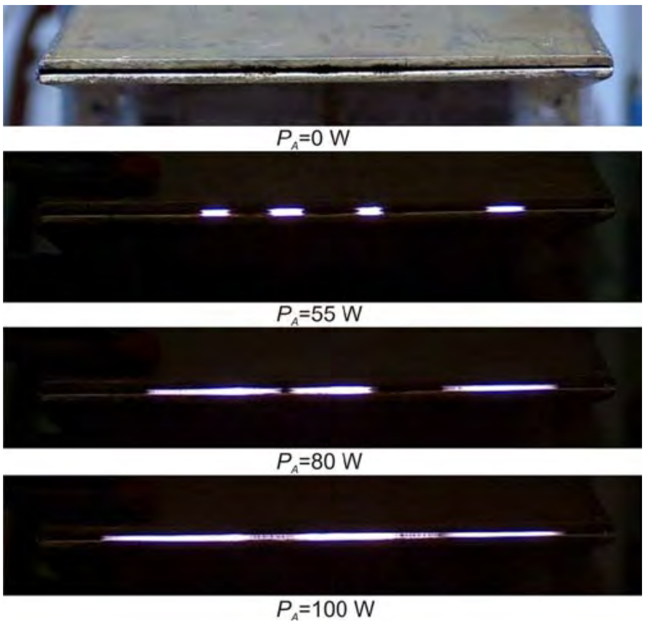

Fig.2. Waveguide slit argon plasma for different values of absorbed microwave power P_A. Gas flow rate Q=25 l/min.

Multijet microwave plasma generator

The idea of the multijet plasma generator is based on the surface wave sustained discharge in dielectric tubes [4]. Similarly like in [5] we accommodate a few quartz discharge tubes in one launching gap of the Surfaguide [6]. We coupled six single tubes together, with a low loss dielectric glue, in a single file. The inner and outer diameters of each tube are 1 and 5 mm, respectively. Such small tube inner diameter prevents plasma filamentation. Ensuring appropriate gas flow rate the plasma exits out of the tubes. On the figure 3 the photo of the six microwave plasma jets, for absorbed microwave power P_A=500 W, and argon total flow rate Q=15 l/min, can be seen. Changing the gas flow rate and position of the tubes within the waveguide the length of the plasma jets can be modified.

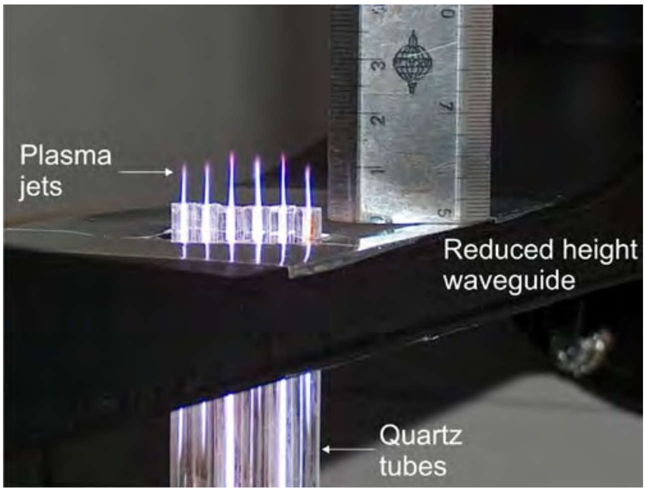

Fig.3. Six microwave plasma jets. Absorbed microwave power P_A=500 W, argon flow rate Q=15 l/min.

Microwave plasma sheet generator

The main advantage of presented here plasma source is a shape of generated plasma, namely sheet shape. It is convenient from surface treatment point of view, thus attractive for industry. The plasma is generated inside a quartz box through which the working gas flows. Because of the gas flow the plasma goes out of a box permitting the processing of the material's surface (see fig.4).

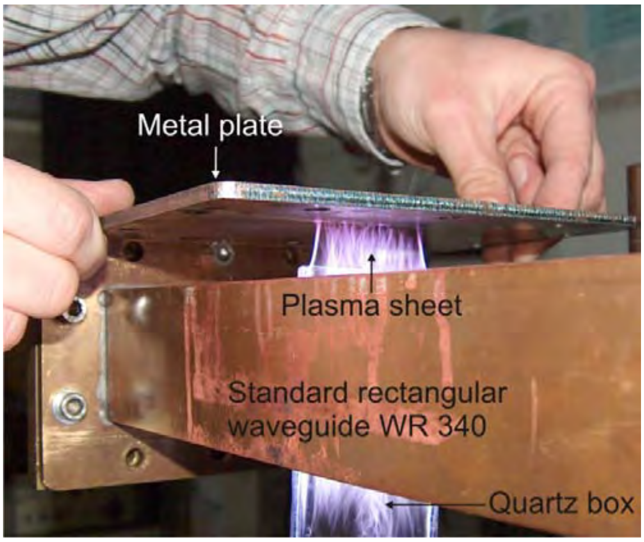

Fig.4. Plasma sheet, fed through waveguide, during metal plate treatment. Microwave power P_i=250 W, argon flow rate Q=25 l/min.

The exemplary dimensions of the generated plasma sheet could be 50 mm of width and 1 mm of thickness for absorbed microwave power P_A=200 W and argon flow rate Q=5 l/min. Depending on the microwave power and gas flow rate the gas temperature of the generated plasma varies from 400ºC to 800ºC. Presented here plasma sheet generator can be supplied from a waveguide, from a wedge waveguide or a stripline (see fig.5).

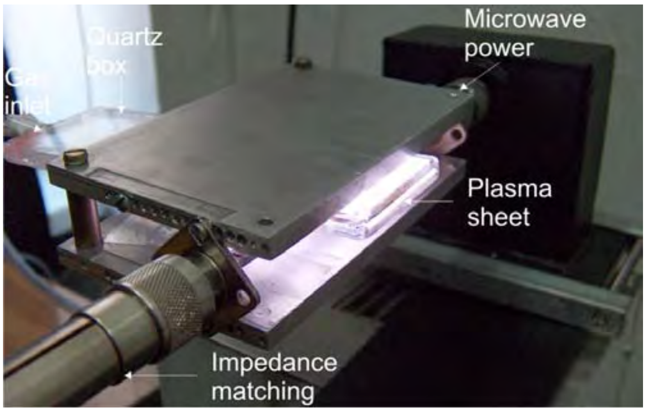

Fig.5. Stripline based device for generation og the microwave plasma sheet. Microwave power P_i=300 W, argon flow rate Q=5 l/min.

Conclusions

The undisputed advantages of presented in this paper microwave devices are as follows. They are of small dimensions (a few centimetres) and simple in design thus cheap in production. They can be operated at atmospheric pressure what eliminates an expensive vacuum apparatus. Standard microwave frequency of 2.45 GHz and microwave power not exceeding 1000 W allows to use cheap commercial magnetrons such as that installed in microwave oven. Sustaining the plasma in quartz tubes or box prevent contaminations from metallic electrode. Plasma generated in presented devices is of regular shape mainly has a form of a plasma sheet. Assuming, we conclude that presented in this paper devices makes them attractive for industry in surface treatment of various materials.

This research was supported by The Szewalski Institute of Fluid-Flow Machinery, Polish Academy of Sciences under the program IMP PAN O3Z1T1.

REFERENCES

[1] Moisan M., Zakrzewski Z., Rostaing J.C., Waveguide-based single and multiple nozzle plasma torches: the TIAGO concept, *Plasma Sources Sci. Technol.*, 10 (2001), 387-395
[2] Nowakowska H., Czylkowski D., Zakrzewski Z., Surface wave sustained discharge in argon: two-temperature collisional-radiative model and experimental verification, *J. Optoelectron. Adv. Mater.*, 7 (2005), 2427-2437
[3] Jasiński M., Goch M., Mizeraczyk M., Plasma device for treatment of material surfaces, *Patent Application*, No. P 383703
[4] Moisan M., Beaudry C., Leprince P., A new device for the production of long plasma columns at a high electron density, *Phys. Lett.*, 50A (1974), 125-126
[5] Moisan M., Zakrzewski Z., Etemadi R., Rostaing J.C., Multitube surface-wave discharges for increased gas throughput at atmospheric pressure, *J. Appl. Phys.*, 83 (1998), 5691-5701
[6] Moisan M., Zakrzewski Z., Pantel R., Leprince P.: A waveguide-based launcher to sustain long plasma columns through the propagation of an electromagnetic surface wave, *IEEE Trans. Plasma Sci.*, PS-12 (1984), 203-214

***Authors**: mgr inż. Dariusz Czylkowski, dr inż. Mariusz Jasiński, The Szewalski Institute of Fluid-Flow Machinery, Polish Academy of Sciences, ul. Fiszera 14, 80-952 Gdańsk, E-mail: dczylkowski@imp.gda.pl, mj@imp.gda.pl;*
prof. dr hab. inż. Jerzy Mizeraczyk, The Szewalski Institute of Fluid-Flow Machinery, Polish Academy of Sciences, ul. Fiszera 14, 80-952 Gdańsk and Gdynia Maritime University, Faculty of Marine Electrical Engineering, Morska 81-87, 81-225 Gdynia, E-mail: jmiz@imp.gda.pl

GENERATION OF NON-EQUILIBRIUM LOW-TEMPERATURE PLASMA IN THE ARRAY OF GLIDING ARC PLASMA REACTORS

Jarosław DIATCZYK[1], Tomasz GIŻEWSKI[1], Lucyna KAPKA[2], Grzegorz KOMARZYNIEC[1], Joanna PAWŁAT[1], Henryka Danuta STRYCZEWSKA[1]

[1]Lublin University of Technology, [2]Maria Curie-Skłodowska University in Lublin, [3]Institute of Rural Health

***Abstract**. The gliding arc array is the new idea of applying non-thermal and non-equilibrium plasmas for very large volume. The main problem is the properly designed power supply system for the GA array. Authors based on their previously experience in power supply systems plan to propose power supply that provide simultaneous ignition and discharge sustaining for all reactors in the grid.*

***Streszczenie.** Matryca reaktorów ze ślizgającym się wyładowaniem łukowym jest nowym rozwiązaniem, pozwalającym generować nierównowagową niskotemperaturową plazmę w dużej objętości. Głównym zadaniem jest zaprojektowanie odpowiedniego systemu zasilania matrycy reaktórów. Autorzy w oparciu o ich wcześniej doświadczenie w projektowaniu układów zasilania urządzeń wyładowczych planują zaproponować układ zasilania, który zapewni jednoczesny zapłon i podtrzymanie wyładowania we wszystkich reaktorach w matryce.*

Keywords: plasma reactors, non-equilibrium plasma.
Słowa kluczowe: reaktor plazmowy, nierównowagowa plazma.

Introduction

Nowadays atmospheric pressure low temperature plasmas are applied in many industrial processes. They are: treatment of flue gases emitted by industrial processes of combustion, painting and varnishing, wastes utilization, deodorization, disinfection and sterilization, material processing and new material manufacturing for application in microelectronics and nanotechnologies. Non-thermal and non-equilibrium plasma based methods allow treatment of organic materials, like rubber, fabrics, bio-materials and they are ecologically justified alternative for chemical ones.

Researches in the field of industrial application of plasma chemical methods are now concentrated on obtaining controllable plasma parameters and chemical reactions in large volume of treated gases. The gliding arc array is the new idea of applying non-thermal and non-equilibrium plasmas for very large volume [1].

Repeatability of the plasma-chemical process depends on stability of plasma parameters, which influence the proper chemical reaction path. The main parameters: are the chemical composition of the plasma gas, its pressure, flow rate, geometry of plasma reactor and electrical parameters of power system, i.e. value and form of supply voltage, power, and frequency.

Array of plasma reactors

Arc discharge can be the source of non-thermal and non-equilibrium plasma at some conditions of power supply system, reactor electrodes' geometry and gas flow rate. The gliding arc discharge plasma is the example of this kind of low temperature plasma that can be generated in multi-electrode reactors at atmospheric pressure. Gliding arc reactor considerably differs from other non-thermal plasma sources. Plasma generated in the gliding arc reactor is in non-equilibrium state: the temperature of "hot electrons" is much higher then gas temperature [2].

The array of gliding arc plasma reactors generate non-equilibrium plasma in very large volume. This kind of source of high energy electrons without heating the plasma gas in the whole volume of plasma reactor chamber is essential for typical plasma chemistry applications.

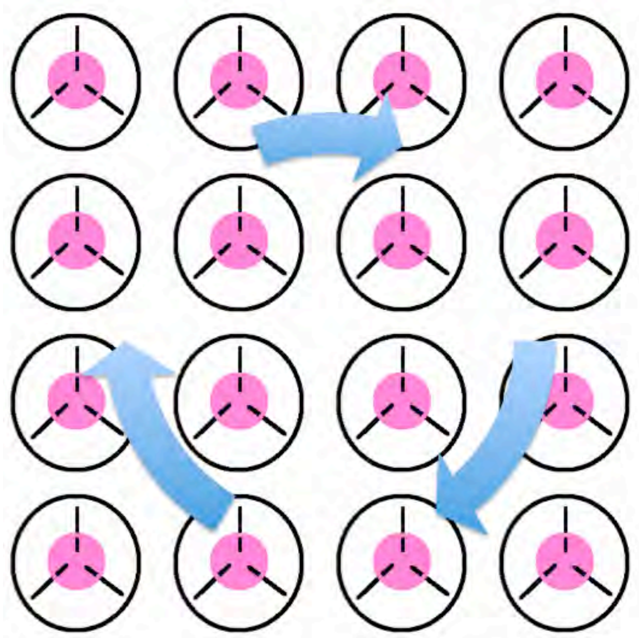

Fig.1. Proposition of arrangement of 16 gliding arc plasma reactors in matrix (arrows mean example flow of processing gas).

Creating array of plasma reactors involves necessity to solve several scientific problems:

- minimizing of gliding arc discharge reactor;
- designing of proper high frequency power supply system;
- elaborating of distribution and mixing system for process gases;
- diagnostics of plasma generated in the array of plasma reactors.

The array of gliding arc plasma reactors, as an electrical energy receiver, requests properly designed power supply system. Such power supply must provide simultaneous ignition and discharge sustaining for all reactors in the grid. The Institute of Electrical Engineering and Electrotechnologies at the Lublin University of Technology has long-time experience in this area. Authors have been developed three-phase power system for simultaneous supplying up to three plasma reactors (fig. 2).

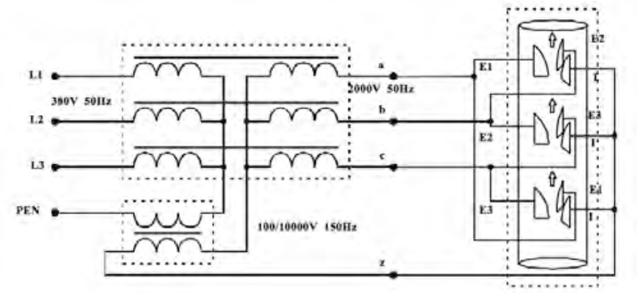

Fig.2. Power system for supplying three plasma reactors [3].

The main advantage of such array will be non-equilibrium generation of low-temperature plasma at atmospheric pressure. And so we do not need complicated and expensive vacuum systems. Construction of the array of minimized plasma reactors could produce discharges on a much larger volume compared to a conventional reactor with the gliding arc discharge [4].

Conclusion

A measurable effect of research will be:

- obtaining knowledge in field of methods of producing non-thermal non-equilibrium plasma in large volumes of treated gas and elaborating of plasma reactors array designing rules;
- implementation array of gliding arc plasma reactors, working at atmospheric pressure; power supply system for array of plasma reactors;
- elaborating of diagnostic methods (GC) of non-thermal non-equilibrium plasma generated in array of gliding arc plasma reactors;
- assessment of possibility to use practically non-thermal and non-equilibrium plasma generated in array of gliding arc plasma reactors.

Collected and elaborated research results will be useful in further research on designing of reactors of non-thermal non-equilibrium plasma and their power supply systems, especially in designing efficient power systems, with good regulating and exploiting features, for industrial scale applications.

Planned researches will allow broadening scope of industrial uses of gliding arc plasma reactors (e.g. surface modification, bio-medical applications and so on).

REFERENCES

[1] Stryczewska H. D., Diatczyk J., Pawłat J., Temperature Distribution in the Gliding Arc Discharge Chamber, *J. Adv. Oxid. Technol. Vol. 14, No. 2, 2011, 276-281*

[2] Diatczyk J., Komarzyniec G., Stryczewska H. D., Plazma nietermiczna – warunki generacji, wybrane zastosowania, *rozdział w monografii: Technologie nadprzewodnikowe i plazmowe w energetyce, Lublin 2009, 137-171*

[3] Stryczewska H. D., Technologie plazmowe w energetyce i inżynierii środowiska, *Wydawnictwo Politechniki Lubelskiej*, Lublin, 2009

[4] Diatczyk J., Stryczewska H. D., Komarzyniec G., Diagnostyka nierównowagi termodynamicznej plazmy ślizgającego się wyładowania łukowego, *Przegląd Elektrotechniczny, nr 5, 2010, 298-300*

***Authors**: Jarosław Diatczyk PhD Eng., Tomasz Giżewski PhD Eng., Grzegorz Komarzyniec PhD Eng., Joanna Pawłat PhD Eng., prof. Henryka Danuta Stryczewska PhD Eng. DSc, Lublin University of Technology, Institute of Electrical Engineering and Electrotechnology, ul. Nadbystrzycka 38a, 20-618 Lublin, E-mail: j.diatczyk@pollub.pl.*

Lucyna Kapka PhD, Institute of Rural Health, ul. Jaczewskiego 2, 20-090 Lublin.

Conference ELMECO–7
ELECTROMAGNETIC DEVICES AND PROCESSES IN ENVIRONMENT PROTECTION
joint with 10th Seminar AoS-10 APPLICATIONS OF SUPERCONDUCTORS
28–30.09.2011, Nałęczów, Poland

PROBLEM ZANIECZYSZCZEŃ SILOKSANOWYCH W INSTALACJACH BIOGAZOWYCH

Jarosław DIATCZYK[1], Julia DIATCZYK[2,3] ,Grzegorz KOMARZYNIEC[1], Joanna PAWŁAT[1], Krzysztof PAWŁOWSKI[4], Henryka Danuta STRYCZEWSKA[1]

[1]Lublin University of Technology, [2]Maria Curie-Skłodowska University in Lublin, [3]Institute of Rural Health, [4]ATUS Sp. z o.o.

***Abstract**. Biogas is an energy carrier produced from organic matter (biomass) in the process of anaerobic digestion. The preferred way of using this fuel is primarily the production of electricity, which in a simple way can be converted to any form of energy. Biogas purification requires the use of processes of siloxanes and sulfur compounds. An important element of the biogas treatment installation is appropriate detection of siloxane concentration.*

***Streszczenie.** Biogaz jest nośnikiem energii wytwarzanym z substancji organicznej (biomasy) w procesie fermentacji beztlenowej. Preferowana droga wykorzystania tego paliwa jest przede wszystkim produkcja energii elektrycznej, która w prosty sposób, z wysoką sprawnością może być zamieniana na dowolną postać energii. Biogaz wymaga zastosowania procesów oczyszczania z siloksanów i zwiazków siarki. Istotnym elementem instalcji oczyszczania biogazu jest właściwa detekcja zawartości siloksanów.*

Keywords: siloxanes, biogas, generators, boilers.
Słowa kluczowe: siloksany, biogas, generatory, kotły.

Wstęp

Racjonalne gospodarowanie energią ma kluczowe znaczenie dla przyszłości ludzkości. Wzrost liczebności populacji ludzkiej, stałe dążenie do poprawy poziomu życia, migracja ludności do miast, wzrost produkcji rolnej oraz działalność przemysłowa i transport powodują spotęgowane oddziaływanie na ecosystem [1].

Zapotrzebowanie na energię będzie wzrastać i tylko prawidłowe systemowe rozwiązania będą mogły ograniczyć negatywne skutki aktywności ludzkiej na otaczające środowisko. Ważnym jest racjonalne wytwarzanie podstawowych dóbr w procesach o relatywnie wyższej sprawności i mniejszej generacji zagrożeń dla środowiska. W tym kontekście uzasadnionym jest proces przekształcania sektora energetycznego, zdominowanego przez konwencjonalne technologię oparte głównie na spalaniu paliw kopalnianych, poprzez doskonalenie procesów wytwarzania energii elektrycznej i cieplnej w skojarzeniu oraz rozpowszechnienie technologii opartych na odnawialnych źródłach energii; docelowo zmierzając do popularyzacji technologii wykorzystujących wodór jako zasadniczy nośnik energii.

Dyrektywa Parlamentu Europejskiego i Rady Europy 2009/28/WE z dnia 23 kwietnia 2009 r. w sprawie promowania stosowania energii ze źródeł odnawialnych, określa i ustanawia wspólne ramy dla promowania energii ze źródeł odnawialnych oraz obowiązkowe krajowe cele ogólne w odniesieniu do całkowitego udziału energii ze źródeł odnawialnych w końcowym zużyciu energii brutto i w odniesieniu do udziału energii ze źródeł odnawialnych w transporcie [2].

W Polsce, a szczególnie na Lubelszczyźnie, duże nadzieje pokładane są w wykorzystaniu biogazu I biopaliw do produkcji energii elektrycznej, cieplnej lub obu jednocześnie (CHP).

Implementacja instalacji biogazowych rodzi różnorodne pozytywne skutki ekologiczne. Do niewątpliwych korzyści należą m. in. ograniczenie niekontrowanej emisji gazów cieplarnianych, dzięki zagospodarowaniu odpadów do produkcji paliwa oraz redukcja emisji zanieczyszczeń, dzięki wykorzystaniu do produkcji energii biogazu zamiast paliw kopalnych.

Biogaz

Biogaz jest nośnikiem energii wytwarzanym z substancji organicznej (biomasy) w procesie fermentacji beztlenowej. Fizycznie, biogaz stanowi roztwór gazowy składający się głównie z metanu i dwutlenku węgla oraz śladowych zanieczyszczeń, takich jak: para wodna, siarkowodór, siloksany, związki aromatyczne, tlen, azot, fluorowce (chlorki, fluorki, i inne) [3].

Skład jakościowy i udziały poszczególnych składników zależą od rodzaju surowca poddawanego procesowi biodegradacji oraz od sposobu realizacji tego procesu. Powyższe zanieczyszczenia usuwane są zazwyczaj z biogazu przed jego energetycznym wykorzystaniem.

Rys.1. Pozyskiwanie energii z biogazu [Dresser, 2010].

Zasadniczo można wyróżnić trzy typy instalacji wykorzystujących proces fermentacji beztlenowej do produkcji biogazu: biogazownie rolnicze, fermentacje osadów ściekowych w biologicznych oczyszczalniach ścieków oraz ujęcia biogazów na składowiskach odpadów. Proces realizowany jest najczęściej w ogrzewanych zamkniętych wydzielonych komorach fermentacyjnych (WKF) z mieszaniem osadu [4].

Wpływ zanieczyszczeń

Preferowaną drogą wykorzystania paliwa jest przede wszystkim produkcja energii elektrycznej, która w prosty sposób, z wysoką sprawnością może być zamieniana na dowolną postać energii.

Najczęściej obecnie stosowanym sposobem utylizacji biogazu są tłokowe silniki spalinowe, w których energia elektryczna jest wytwarzana ze sprawnością mniejszą niż 40%. Intensywnie są rozwijane, choć wciąż jeszcze bardzo drogie inwestycyjnie, ogniwa paliwowe, które dzięki bezpośredniej konwersji energii chemicznej paliwa do energii elektrycznej cechują się bardzo wysoką sprawnością wytwarzania elektryczności, na poziomie 50%.

Największym zagrożeniem dla prawidłowej pracy silników spalinowych są występujące w biogazie związki krzemu – siloksany, wysoka zawartość których prowadzi do obniżenia sprawności I uszkodzeń mechanicznych.

Z powodu relatywnie wysokiego poziomu zanieczyszczeń gaz składowiskowy powinien zostać poddany oczyszczeniu uwzględniając następujące etapy:

Etap I. Oczyszczenie wstępne polegające na usunięciu stałych i ciężkich składników oraz osuszeniu gazu.

Etap II. Oczyszczenie zaawansowane:

- odsiarczanie,
- usunięcie organicznych związków krzemu (siloksanów),
- usunięcie innych gazowych zanieczyszczeń (węglowodorów, amoniaku).

Usuwanie siloksanów

Siloksany to grupa związków organicznych wytworzonych przez człowieka, w których składzie znajduję się krzem, tlen i grupy metylowe. Siloksany stosowane są przy produkcji środków higieny osobistej i ochrony zdrowia, obecne są także w produktach przemysłowych. Na składowisku siloksany o niskiej masie cząsteczkowej ulatniają się, przedostając się do biogazu.

Podczas spalania gazu zawierającego siloksany, w celu wytworzenia energii (np. w turbinach gazowych, kotłach i silnikach spalinowych), siloksany przekształcają się w dwutlenek krzemu (SiO_2), który może osadzać się na elementach urządzeń związanych z procesem spalania i/lub odprowadzania spalin. O zawartości siloksanów w gazie składowiskowym świadczy obecność białego proszku na częściach urządzeń związanych ze spalaniem, lekki nalot na różnego rodzaju wymiennikach ciepła oraz lekki nalot na katalizatorach znajdujących się za częścią związaną ze spalaniem [5].

Podstawowymi metodami stosowanymi do usuwania siloksanów są:

- absorpcja na węglu aktywnym,
- absorpcja w ciekłej mieszaninie węglowodorów,
- oziębianie gazu z jednoczesnym usuwaniem wody. Gaz może być schłodzony nawet do 10°C, co prowadzi do usunięcia 99% siloksanów.
- reaktory kolumnowe, z możliwością regeneracji warstwy adsorbcyjnej.

Obecnie, te zanieczyszczenia usuwane są głównie za pomocą filtrów z węglem aktywnym. Chociaż tą metodą można usunąć większość zanieczyszczeń, to koszt zarówno węgla aktywnego jak i jego regeneracji oraz utylizacji jest wysoki.

Podsumowanie

Silniki tłokowe są najbardziej popularną technologią stosowaną w przypadku energetycznego wykorzystania biogazu. Konstrukcja ich jest wrażliwa na osadzanie się związków krzemu – siloksanów.

Biogaz wymagá zastosowania procesów oczyszczania z siloksanów i zwiazków siarki. Konieczność oczyszczania i jego stopień uzalezniony jest od stężenia zanieczyszczeń i od wymagań stawianych przez producentów silników.

Istotnym elementem instalcji oczyszczania biogazu jest właściwa detekcja zawartości siloksanów. Odpowiednio zaprojektowane metody chromatografii gazowej (GC) pozwalają realizować monitoring zawartości siloksanów w czasie rzeczywistym.

Szerokie pole do dalszych badań pozostawiają obecnie stosowane metody usuwania siloksanów (głównie absorpcja na węglu aktywnym). Autorzy widzą możliwości wykorzystania nierównowagowej niskotempraturowej plazmy generowanej przy ciśnieniu atmosferycznym do usuwania zanieczyszczeń gazowych (w tym związków siarki).

REFERENCES

[1] Piątek R., Produkcja i energetyczne wykorzystanie biogazu – przykłady nowoczesnych technologii, *Materiały pokonferencyjne, Konferencja Naukowo-Techniczna Odnawialne źródła energii w województwie śląskim. Zasoby, techniki i technologie oraz systemy wykorzystania OŹE*, Katowice, 2005

[2] *Dyrektywa Parlamentu Europejskiego i Rady Europy 2009/28/WE* z dnia 23 kwietnia 2009 r., adres internetowy: http://eur-lex.europa.eu/LexUriServ/

[3] Trogisch S. Baaske W. E. (eds.), Biogas powered fuel cells. Case studies for their implementation, *Publisher Trauner Verlag. Linz 2004*

[4] Miksch K. Biotechnologia środowiskowa. Część I, *Biblioteka Fundacji Ekologicznej SILESIA, tom IX, Katowice 1995*

[5] Wheless E., Pierce J., Siloxanes in landfill and Pigester Gas Update, SCS 2004

***Authors**: Jarosław Diatczyk PhD Eng., Grzegorz Komarzyniec PhD Eng., Joanna Pawłat PhD Eng., prof. Henryka Danuta Stryczewska PhD Eng. DSc, Lublin University of Technology, Institute of Electrical Engineering and Electrotechnology, ul. Nadbystrzycka 38a, 20-618 Lublin, E-mail: j.diatczyk@pollub.pl.*

Julia Diatczyk MSc, Institute of Rural Health, ul. Jaczewskiego 2, 20-090 Lublin.

Krzysztof Pawłowski MSc Eng., ATUT Sp. z o.o., ul. Bolesława Prusa 8, 20-064 Lublin

MICROWAVE PLASMA MODULE FOR DESTRUCTION OF OIL SLICKS

Mirosław DORS[1], Tomasz IZDEBSKI[1], Bartosz HRYCAK[1], Jerzy MIZERACZYK[1,2]

The Szewalski Institute of Fluid Flow Machinery Gdańsk (1), Gdynia Maritime University (2)

Keywords: plasma, microwave discharges, slicks.

Słowa kluczowe: plazma, wyładowania mikrofalowe, plamy ropy.

Introduction

During the last decade shipping has steadily increased, reflecting intensifying co-operation and economic prosperity around the Baltic Sea region. An average of 2,000 ships are at sea each day, including 200 tankers carrying oil or other potentially harmful products. It is estimated that the transportation of goods by sea will double by 2017 in the Baltic region. General cargo and container traffic is expected to triple, and oil transportation may increase by 40%. The expansion and construction of oil terminals on the shores of the Gulf of Finland and regional economic growth may lead to even higher increases in shipping. Increasing maritime transportation threatens fragile ecosystems and the livelihoods of many people who depend on the sea. Increased shipping is accompanied with increased operation in Baltic Sea ports. As a result frequency of small leakages of oil and bilge water become higher, most of all in the port and docs area. Since the only available way of destruction of such waste is incineration, pollution of air in the Baltic Sea region with combustion products increases. Moreover, incineration is energetically inefficient and expensive. In this work we present a new mobile device as a tool for removal and destruction of all kind of pollutions discharges from ships and operating installations. Using mobile devices which could destroy oil and oil-kind slicks directly on the sea surface would much decrease both energy consumption and air pollution.

Concept of the plasma device

The concept of the entire device is based on the module construction. All modules will be fixed on the platform equipped with floats. The following main modules has been developed (Fig. 1):

- power supply module – which provides proper voltage and current to all electrical components of the device, including pumps, valves, rotors, high voltage sections of plasma modules,
- first plasma module – the role of which is using microwave plasma for conversion of oil slick polluting sea surface to gaseous hydrocarbons,
- second plasma module – it has to decompose gaseous hydrocarbons transported from the first plasma section into harmless products,
- third plasma module (optional) – which should clean the output if the second plasma unit could not provide completely unpolluted exhaust gas.

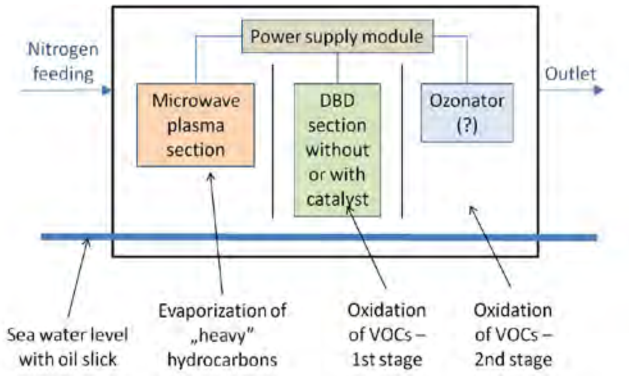

Fig.1. Concept of plasma device for oil slicks removal on the surface of seawater.

On the platform, besides above mentioned modules, also other element of the device will be installed, such us high pressure flask with nitrogen delivering gas to plasma modules, and drum separator for oil-water separation (Fig. 2).

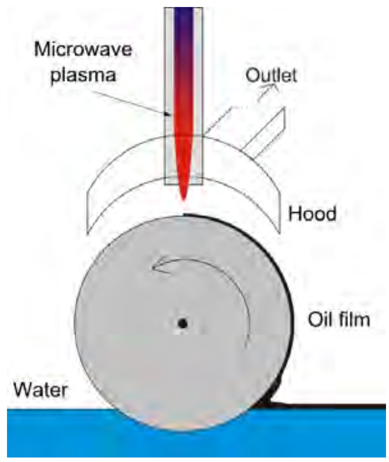

Fig.2. Oil-water separator with oleophilic foil.

Microwave plasma module

This paper presents only microwave plasma module, which is the first step in destruction of oil slick. Preliminary tests with other electrical discharges forming plasma and kerosene as a simulator of oil slick showed that corona discharge, spark discharge and dielectric barrier discharge

(DBD) transform the kerosene slick into aerosol only without any evaporation. The conclusion is that electrons accelerated and gaining high energy in corona, spark and DBD has not enough power neither to heat up the liquid hydrocarbon nor to brake bonds in their molecules producing volatile hydrocarbons. The same conclusions concerns oxidizing species such as ozone and oxygen atoms produced by above discharges. Their oxidizing potential is too low to convert liquid hydrocarbons into gaseous.

The only possible solution that could be then concerned is high temperature plasma such as arc plasma. In our laboratory a microwave plasma torch, similar to arc, was used for evaporation of kerosene from the oleophilic metal plate. The advantage of microwave plasma is that in contrast to arc plasma it does not have contact with discharge electrode and does not make erosion of the electrode which could pollute water with metals. The microwave plasma torch was generated in a quartz tube in the system presented in Fig. 3 using nitrogen as a plasma generating gas flowing with a rate of 10 L/min.

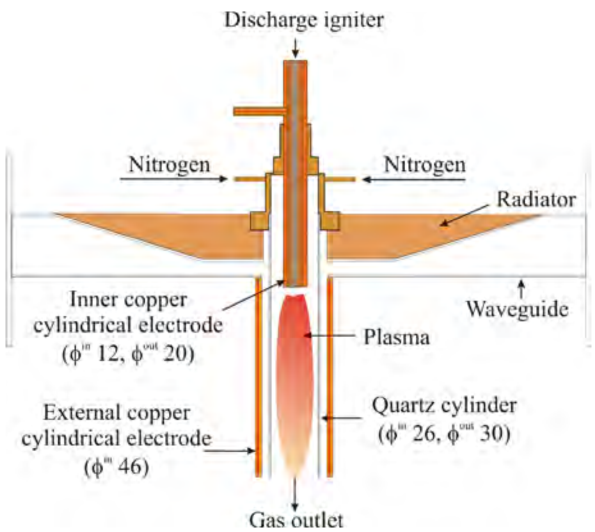

Fig.3. Microwave plasma source (MPS) for oil destruction.

The main parts of the microwave plasma module are: a microwave generator (magnetron), a microwave plasma source (MPS), a microwave supplying and measuring system and a nitrogen gas supplying system. The microwave power (2.45 GHz, 1 kW) was supplied from the magnetron to the MPS via a rectangular waveguide (WR-430) having a reduced-height section.

Nitrogen is introduced into the plasma by the four gas ducts creating the swirl flow in the cylinder. The swirl concentrated near the quartz cylinder wall and stabilized plasma generation. The swirl held the discharge at the centre of the cylinder and thus protected the cylinder wall from overheating.

The diameter of the copper shielding cylinder is 46 mm, so microwave at a frequency of 2.45 GHz cannot be guided along the copper shielding cylinder (operation below the cutoff frequency). This causes lower losses of microwave energy, i.e. higher microwave power is delivered to the unit volume of the plasma. Moreover, the copper shielding cylinder placed coaxially around the quartz discharge cylinder protects the personnel and instrumentation from the electromagnetic radiation.

The plasma is directed towards the kerosene separated from the water and forming a thin layer on the oleophilic surface of the drum separator (Fig. 4). As a result immediate evaporation of kerosene with partial oxidation is observed. Gaseous products of evaporation were analyzed by FTIR spectrophotometer and identified as:

- oxygen: ca. 13%,
- nitrogen: ca. 87%,
- water vapour: ca. 1.5%,
- kerosene: ca. 200 ppm,
- products of kerosene oxidation: CO - ca. 200 ppm, CO_2 - ca. 1000 ppm.

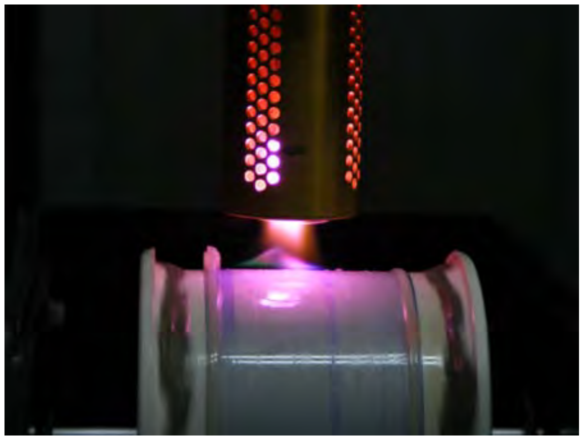

Fig.4. Microwave plasma destroying oil separated from water.

Products of the kerosene evaporation and partial oxidation are sucked from the plasma region to the second plasma module. There, DBD reactor is used to complete oxidation of hydrocarbons.

In our laboratory only microwave plasma module and oil-water separator has been built. Power supply module is constructed by a group from the West Pomeranian University of Technology in Szczecin, Poland, whereas the second plasma module is developed by a group from the Leibniz Institute for Plasma Science and Technology in Greifswald, Germany, in co-operation with the Lappeenranta University of Technology in Mikkeli, Finland.

This work is supported by the Baltic Sea Region Programme under the PlasTEP project .

***Authors**: dr hab. inż. Mirosław Dors, mgr inż. Tomasz Izdebski, mgr inż. Bartosz Hrycak, The Szewalski Institute of Fluid-Flow Machinery, Polish Academy of Sciences, ul. Fiszera 14, 80-952 Gdańsk, E-mail: mdors@imp.gda.pl;*
prof. dr hab. inż. Jerzy Mizeraczyk, The Szewalski Institute of Fluid-Flow Machinery, Polish Academy of Sciences, ul. Fiszera 14, 80-952 Gdańsk and Gdynia Maritime University, Faculty of Marine Electrical Engineering, Morska 81-87, 81-225 Gdynia, E-mail: jmiz@imp.gda.pl.

RECENT DEVELOPMENT OF OZONE TREATMENT FOR AGRICULTURAL SOIL STERILIZATION AND BIOMEDICAL PREVENTION

Kenji EBIHARA[1,2], Henryka Danuta STRYCZEWSKA[3], Fumiaki MITSUGI[2], Tomoaki IKEGAMI[2], Takamasa SAKAI[2], Joanna PAWLAT[3], S.TEII[4]

Environment and Energy Laboratory(1), Kumamoto University(2), Lublin University of Technology(3), Lunghwa University of Science and Technology(4)

Abstract
We have studied gaseous ozone sterilization for soil and biomedical prevention for infectious diseases and living safety. Experimental results obtained under ozone generation apparatuses, ozone sterilization system, and AFM measurement were shown. Urgent application of these information to environmental technologies required at the disaster area suffered from the earthquake, tsunami and nuclear power plant station accident was discussed.

Keywords: ozone, soil sterilization, biomedical prevention

Introduction

In Japan we have suffered great disasters form 2011 Tohoku earthquake and tsunami. Following the earthquake and tsunami, the critical damage due to the accidents of the Fukushima Daiichi nuclear power plant station results in severe radiation leaks which cause a long-term health and environmental hazards.

The number of the evacuees has once passed 300,000 (83,000 in Sep.) in Tohoku region and 113,000 residents within 30km of the nuclear plant are evacuated. These disasters resulted in shortages of food, water, shelter, medicine and fuel for survivors. Many shelters are not medically sufficiently equipped and are poor sanitary. Urgent actions for recovery and reconstruction from these disasters have been promoted in the improvement of municipal infrastructure, temporary housing, supplement budget, etc. Under the present situation of human life and environment crisis at the suffered area, it is just time for us to create new technologies aiming at great urgency process in severe circumstance of food, living, medical and sanitary conditions. We now face innumerable problems such as air purification and disinfection of emergency medical treatment at shelters and temporary housing, purification of drinking water, soil salinization, tsunami debris and radioactive waste materials.

In addition, an outbreak of the highly contagious foot –and –mouth disease (FMD) occurred in Miyazaki Prefecture in southwestern part of Kyusyu Island, affecting cattle, pigs, goats and other cloven-hoofed animals. Over 290,000 livestock were sacrificed and the financial loss has been calculated at approximately ¥235 Billion ($3Billion).

Ozone (O_3) is the strongest commercially available disinfectant and also is very effective at destroying bacteria, viruses and odors. It had a very short half-life in water and soil, and decomposes in simple diatomic oxygen or forms oxide matters.

We have studied the application of gaseous ozone to soil sterilization and the biological effect of gas phase ozone on the DNA genome contained in bacteria and viruses[1-10]. We have proposed the gaseous ozone sterilization system for agricultural soil which ensures a secure agricultural production. The reaction of the soil components with ozone causes complicated and rapid change in physical, chemical and biological properties.

The pH value defined by pH=-log$_{10}$ [H^+] is useful index to estimate soil properties treated by ozone. In-situ measurement of pH value during ozone treatment showed that the pH linearly decreased with time at the initial process phase which is due to formation of H^+ ions (decomposition of OH^- ions) [9,10].

The agricultural field trials for plant growth proved that the ozone sterilization system developed is effective to sterilize the agricultural soil [8,10].

Atomic force microscopy (AFM) has become one of the most widely used technique of biochemical study in understanding of nano-size structure of the DNA samples. We employed the AFM technology to investigate the biochemical effect on ozone treatment on the DNA. AFM images showed that the molecular structure of the λ-E.Coli DNA collapsed completely using high dense ozone with 5% concentration in oxygen gas [7-10].

We have also designed and developed ozone sterilization system to be used to disinfect large area of agricultural land. The dielectric barrier discharge generated in the coaxial type geometry of a screw type electrode provided high ozone concentration over 100g/m^3 in oxygen. Additionally, we studied ozone diffusion length in the soil to estimate the appropriate arrangement for ozone gas drip tubes put in the soil [2,4].

Our experimental results can be used to be applied to develop a new environmental technology related to air purification at the shelters and temporary houses, emergency medical treatment, disposal of tsunami debris and improvement of saline and radioactive waste soil.

In this paper, we would like to review recent our research which will be useful to solve above issues needed at the disaster area suffered from the earthquake, tsunami and nuclear power plant station accident. We report here ozone generation systems which can provide large volume ozone with high concentration, sterilization systems, soil properties in the process of ozone treatment, biological phenomena and DNA visualization.

Experimental

<u>Ozone generation system</u> [4-8]

The dielectric barrier discharge was used to produce highly concentrated ozone available for sterilization of bacteria, virus and nematodes in the soil. A pulsed electric power was generated by high frequency oscillator (10-30kHz) .

<u>Ozone sterilization system</u>[1-10]

Generated ozone was directly injected into the agricultural soil. Fig.1 shows the outline of ozone treatment system for large scale agricultural field (US Patent 5624635). The ozone supplier is moved over the field by a trailer or a vehicle. We have developed an ozone injection system with 12 channel electrode injectors .In-situ measurements of the pH and the electrical conductivity were carried out using pH/Nitricion and pF/EC meter.

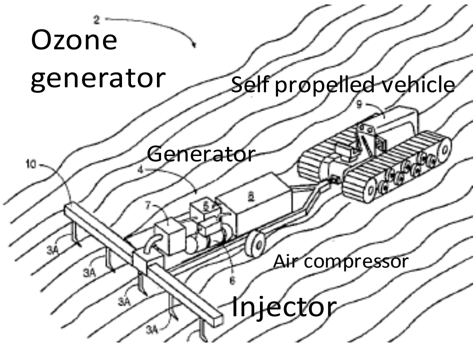

Fig.1. Field sterilization (US Pt.5624635)

<u>DNA visualization</u> [5-10]

AFM(SPI3800N) was applied to observe nano-size structure of the non-conducting mode. Ozone was bubbled into the micro centrifuge tube containing the DNA solution. The ozone treated DNA solution was dropped on the substrate and was dried.

Results and Discussion

Fig.2 shows temporal change of pH value of the soil at various conditions. Most of pH vales rapidly decrease in the initial phases. Viruses of FMD were eliminated under the conditions such as pH less than 6.5 or larger than 11.

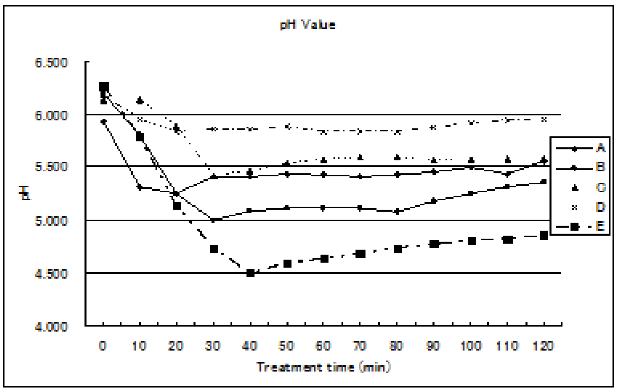

Fig.2 pH value as a function of time.

Sterilization conditions are listed below:

Sample Number		A	B	C	D	E(2ch)
Ozone Concentration	g/m3	100	100	100	40	100
Treatment time	min	60	60	60	60	60
Flow rate	lite/min	2	2	3	2	2x2chan.
Distance	mm	30	30	30	30	30
O3Dosage	g	12	12	18	4.8	24

Fig.3.shows AFM image of DNA (white thread) conjugated with antibody (white spot). Other AFM images in our experiment showed that the DNA structures were broken by ozone treatment.

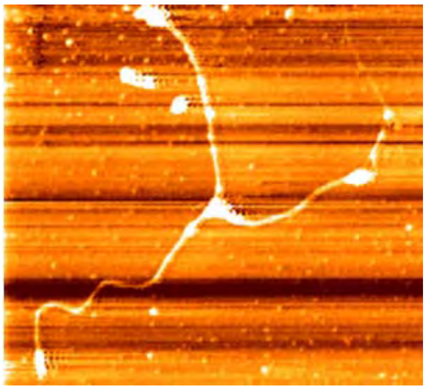

Fig.3. AFM images of DNA and Antibody

Conclusion

We shows soil properties treated by high dense ozone and biological characteristics of the λ-E.Coli DNA in the ozonized solution. Application of these research to environmental technologies for urgency medical and sanitary treatment at disaster area hit by the earthquake, tsunami and nuclear power plant accidents is under consideration.

References

[1.] Ebihara,K., Takayama,M.,Ikegami, T., Ogata,K. Stryczewska,H.D., Gyoutoku,Y., and Sakai,T ,J.Adv. Oxid. Technol. Vol.9,No.2,pp.170-173,2006.

[2.] Takayama, M., Ebihara,K., Stryczewska,H.D., Ikegami,T., Gyoutoku,Y., Kubo,K., Tachibana,M. , Thin Solid Films, 506-507, pp.396-399,2006.

[3.] Ebihara,K., Takayama,M., Ikegami,T., Stryczewska,H.D., Gyoutoku,Y., Yokoyama,T., Gunjikake,N., Tachibana,M., Sakai,T , Proceedings of 17th International Symposium on Plasma Chemistry, Toronto, Canada,August 7th-12th,CD(1201).,2005.

[4.] Ebihara,K., Takayama,M., Strycewska,H.D., Ikegami,T., Gyoutoku,Y., Tachibana,M., IEEJ Transaction (in Japanese), 125, No.10, pp.963-969,2006.

[5.] Ebihara, Kenji., The Workshop on the Applications of Plasma to Green Environmental Technology ,Taoyuan, Taiwan, December 11-12,2006: Proceedings, pp.86-90,2006.

[6.] Ebihara,K.,Sugimoto,S.,Ikegamo,T.,Mitsugi,F.,Stryczewska, H.D., 6th International Conference on Electromagnetic Devices and Processes in Environment Protection (ELMECO-6), Nateczow, Poland, June 24-28,2008.

[7.] Ebihara,K.,Ikegami T.,Mitsugi, F.,Ikegami, T., Stryczewska,D.H.,Goutoku, Y., Proceedings of the applications of plasma to bio-medical Engineering, December 15-17, Lunghwa University of Science and Technology, Taoyuan,Taiwan,2008.

[8.] Ebihara,K., Mitsugi,F.,Ikegami Tomoaki,Ikegami Takashi, D.H.Stryczewska, 6th Asia-Pacific International Symposium on Basic and Application of Plasma Technology, Dec.14-16,Hsinchu, Taiwan, X07,pp.7,2009.

[9.] Ebihara,K.,Mitsugi,F.,Ikegami,Tomoaki , Sakai,T., Ikegami,Takashi, Stryczewska,H.D.,The 16th International Conference on Advanced Oxidation Technologies for Treatment of Water, Air and Soil, San Diego, California, Nov.15-18,2010,pp.104-105.

[10.] Ebihara,K., Stryczewska,H., Ikegami,T., Mitsugi F., Pawlat,J. Electrical Review, R.87 NR7/2011, pp.148-152,2011.

Authors: Professor Emeritus Dr. Kenji Ebihara, E-mail:k-shrimp@road.ocn.ne.jp,
Professor Dr hab.inz. Henryka Danutra Stryczewska,
Lublin University of Technology E-mail: h.stryczewska@pollub.pl.

TEMPERATURE DISTRIBUTION IN HUMAN TISSUE DURING INTERSTITIAL MICROWAVE HYPERTHERMIA

Piotr GAS

AGH University of Science and Technology

***Abstract**. A model which is an example of local interstitial microwave hyperthermia is presented. A microwave coaxial-slot antenna placed in the liver tissue is the heat source. For simplification, a two-dimensional model is adopted. The presented issue is therefore a coupling of the electromagnetic field and the temperature field. Using the finite element method, the wave equation for TM wave case and bioheat equation under steady-state condition have been solved. At the end the obtained simulation results are presented.*

***Streszczenie.** W pracy przedstawiono model będący przykładem zastosowania miejscowej hipertermii śródmiąższowej. Źródłem ciepła jest współosiowa antena mikrofalowa z szczeliną powietrzną umieszczona w wątrobie. Dla uproszczenia przyjęto model dwuwymiarowy. Przedstawiony problem stanowi sprzężenie pola elektromagnetycznego i pola temperatury. Posługując się metodą elementów skończonych rozwiązano równanie falowe dla przypadku fali TM, a następnie biologiczne równanie ciepła. Na końcu przedstawiono uzyskane wyniki symulacji.*

Keywords: interstitial microwave hyperthermia, TM waves, bioheat equation, finite element method (FEM).
Słowa kluczowe: śródmiąższowa hipertermia mikrofalowa, fale TM, biologiczne równanie ciepła, metoda elementów skończonych (MES).

Introduction

Hyperthermia is a method of therapy in which the pathological tissues are exposed to high temperatures exceeding 40°C. There are many techniques for hyperthermia treatment but interstitial hyperthermia seems to be the most effective one, because it delivers the heat directly at the site of the tumor and minimally affects the surrounding normal tissues the. For interstitial hyperthermia high frequency needle electrodes, microwave antennas, ultrasound transducers, laser fibre optic conductors, or ferromagnetic rods, seeds or fluids are injected or implanted into the tumor. With these applicators a heat can be applied high enough to induce thermonecrosis in tumors at the distance of 1 to 2 cm around the heat source. This technique is suitable for tumors less than 5 cm in diameter. Moreover, interstitial hyperthermia has reached positive clinical results in combination with radiotherapy and chemotherapy. This method is now gaining new fields of applications, for instance in the treatment of liver, breast, kidney, bone and lung tumors. [1].

Main equations and model geometry

Let us consider the coaxial – slot antenna as shown in Figures 1 and 2. Due to the axial symmetry the cylindrical coordinates r, z, ϕ are used. The antenna consists of an inner conductor, dielectric, outer conductor and plastic catheter. There are also two symmetric air slots in the external conductor. Each of them has the size $d = 1$ mm. Antenna dimensions are taken from [3]. In the presented model transverse magnetic (TM) waves are used and there are no electromagnetic field variations in the azimuthal direction. A magnetic field $\mathbf{H}$ has only the ϕ - component and an electric field $\mathbf{E}$ propagates in r-z plane. Therefore, it can be written

(1) $$\mathbf{H}(r,z,t) = H_{\phi}(r,z)\mathbf{e}_{\phi}\, e^{j\omega t}$$

(2) $$\mathbf{E}(r,z,t) = \left[E_r(r,z)\mathbf{e}_r + E_z(r,z)\mathbf{e}_z\right] e^{j\omega t}$$

In the axial-symmetric mode, the wave equation takes the form of scalar equation as follows

(3) $$\nabla \times \left[\left(\varepsilon_r - j\frac{\sigma}{\omega\varepsilon_0}\right)^{-1} \nabla \times H_{\phi}\right] - \mu_r k_0^{\,2} H_{\phi} = 0$$

where ε_r and μ_r are the relative permittivity and the relative permeability of the medium respectively, ε_0 is the permittivity of vacuum, σ is the electrical conductivity of the medium and k_0 is the wave number in vacuum.

For all metallic surfaces, the PEC (perfect electric conductor) boundary conditions are set as

(4) $$\mathbf{n} \times \mathbf{E} = 0$$

External boundaries of the computational domain, which do not represent a physical boundary (except the boundary at the z symmetry axis where E_{ϕ} = 0) have the so-called matched boundary conditions. They make the boundary totally non-reflecting and assume the form

(5) $$\mathbf{n} \times \sqrt{\varepsilon}\mathbf{E} - \sqrt{\mu}H_{\phi} = -2\sqrt{\mu}H_{\phi}$$

where $\boldsymbol{H}_{\phi}$ is an input field incident on the antenna given by

(6) $$H_{\phi} = \frac{1}{r}\sqrt{\frac{ZP_{AV}}{\pi r \ln(r_2 / r_1)}}$$

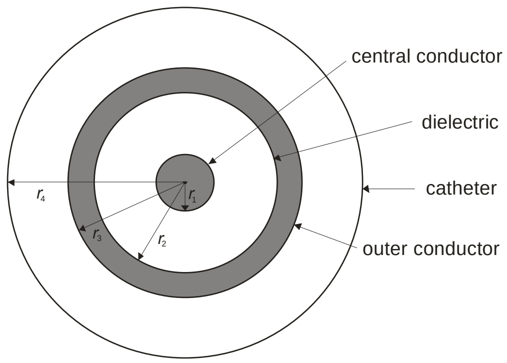

Fig.1. Cross section of the antenna with geometrical dimensions

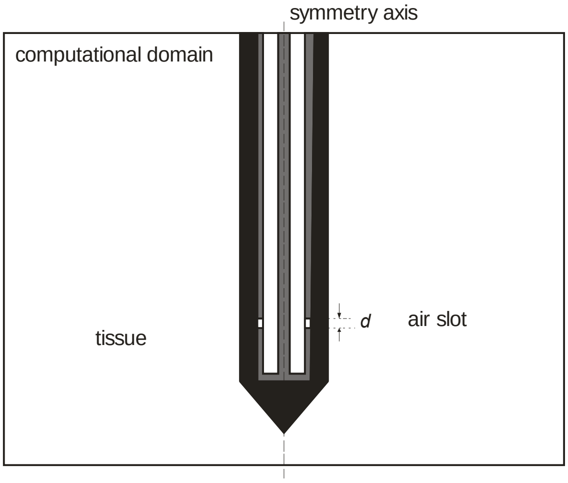

Fig.2. Schematic view of the part of the coaxial antenna with the air slots located in the human tissue

In equation (6) Z signifies the wave impedance of the dielectric, P_{AV} is the time-average power flow in it, while r_1 and r_2 are the dielectric's inner and outer radii, respectively. The seed point is modelled using a port boundary condition with the power level set to $P_{\text{in}} = 5\text{W}$ at the low-reflection external boundary of the coaxial dielectric cable.

The second basic equation used in the presented simulation is the so-called bioheat equation given by Pennes in the mid-twentieth century [2]. It describes the phenomenon of transport and heat transfer in biological tissues. In steady-state analysis it is expressed by

(7) $$\nabla\left(-k\nabla T\right) = \rho_b C_b \omega_b (T_b - T) + Q_{ext} + Q_{met}$$

where T is body temperature [K], k – tissue thermal conductivity [W/(m^2 K)], T_b – blood vessel temperature [K], ρ_b – blood density [kg/m^3], ω_b – blood perfusion rate [1/s], C_b – blood specific heat [J/(kg K)]. The described model takes into account both the metabolic heat generation rate Q_{met} [W/m^3] as well as the external heat sources Q_{ext} [W/m^3], which is responsible for the changing of the temperature inside the exposed body according to the following equation

(8) $$Q_{ext} = 0.5\,\sigma\mathbf{E}\cdot\mathbf{E}^* = 0.5\,\sigma\left|\mathbf{E}\right|^2$$

The boundary condition explaining heat exchange on the surface of the human tissue uses insulation and is given as

(9) $$\mathbf{n}\cdot\left(k\nabla T\right) = 0$$

Simulations results

In the analyzed model, the liver tissue and antenna are considered as homogeneous media with averaged material parameters. The antenna operates at the frequency $f = 2.45\text{ GHz}$. Moreover, blood parameters are given in Table 1 and the metabolic heat generation rate of the tissue is set as $Q_{met} = 300[\text{W/m}^3]$. The other parameters of the model are taken from [3].

Table 1. Physical parameters of blood taken in the bioheat equation

Tissue	ρ_b [kg/m^3]	C_b [J/(kg·K)]	T_b [K]	ω_b [1/s]
Blood	1020	3640	310.15	0.004

Equations (3) and (7) with appropriate boundary conditions were solved using the finite element method. The simulation results are summarized in Figures 3 – 4. Fig. 3 represents the distribution of isotherms in the analyzed model.

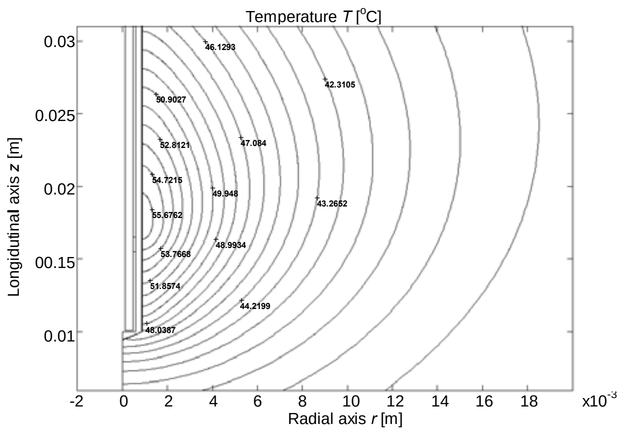

Fig.3. Isothermal lines inside the computational domain

Temperature distribution along a path crossing the tissue area at the height of the air slot is presented in Fig. 4.

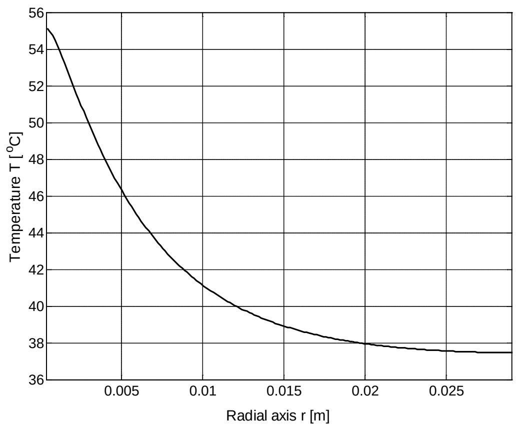

Fig.4. Temperature distribution along the path at the height of the air slot (z = 0.0165 m)

Conclusions

Numerical methods are often used for dosimetric calculations for a number of important bioelectromagnetic issues. The thermal analysis of the presented problem using the FEM allows the estimation of the temperature distribution in the specified area. The demonstrated plots show that the temperature decreases rapidly with the distance from the microwave applicator. Therapeutic values of temperature (above 40°C) are just 1 cm from it. This range can be easily extended by increasing the antenna input power. It is worth noting that interstitial hyperthermia has reached positive clinical results in combination with radiotherapy and chemotherapy. This method is now gaining new fields of applications, e.g., in the treatment of liver, breast, kidney, bone and lung tumors.

REFERENCES

[1] Baronzio G.F., Hager E.D., *Hyperthermia in Cancer Treatment: A Primer*, Landes Bioscience and Springer Science + Business Media, New York 2006.
[2] Pennes H.H.: Analysis of tissue and arterial blood temperatures in resting forearm, *J. Appl. Physiol.*, 1, 93, 1948.
[3] Saito K., Taniguchi T., Yoshimura H., and Ito K., Estimation of SAR Distribution of a Tip-Split Array Applicator for Microwave Coagulation Therapy Using the Finite Element Method, *IEICE Trans. Electronics*, vol. E84-C, 7, pp. 948–954, July 2001.

***Authors**: mgr inż. Piotr Gas, AGH University of Science and Technology, Department of Electrical and Power Control Engineering, al. Mickiewicza 30, 30-059 Kraków, Poland, E-mail: piotr.gas@agh.edu.pl.*

Conference ELMECO–7
ELECTROMAGNETIC DEVICES AND PROCESSES IN ENVIRONMENT PROTECTION
joint with 10th Seminar AoS-10 APPLICATIONS OF SUPERCONDUCTORS
28–30.09.2011, Nałęczów, Poland

ANALIZA NIEPARAMETRYCZNYCH METOD AUTOMATYCZNEJ KLASYFIKACJI OBIEKTÓW WIELOWYMIAROWYCH W APLIKACJI DO NIENISZCZĄCEJ DETEKCJI USZKODZEŃ

Tomasz GIZEWSKI[1], Andrzej WAC-WŁODARCZYK[1], Ryszard GOLEMAN[1] Dariusz CZERWIŃSKI[1]

Lublin University of Technology (1)

***Abstract**. The article presents the discussion on nonparametric classification methods in relation to the numerical model of a physical object. The main theme is the analysis of algorithms in applications to non-destructive testing of ferromagnetic materials. The particular attention was given to model parameterization as a significant factor in minimizing the cost of the learning process.*

***Streszczenie.** Artykuł przedstawia problematykę nieparametrycznych metod klasyfikacji w odniesieniu do numerycznego modelu obiektu fizycznego. Głównym tematem jest analiza skuteczności algorytmów pod kątem zastosowań w nieniszczącej detekcji uszkodzeń. Szczególną uwagę zwrócono na parametryzację modelu, jako czynnika istotnego przy minimalizacji kosztów procesu uczenia.*

Keywords: non-destructive testing, nonparametric classifier, multidimensional model.
Słowa kluczowe: badania nieniszczące, klasyfikatory nieparametryczne, model wielowymiarowy.

Wprowadzenie

Budowa automatów klasyfikujących obiekty wielowymiarowe wymaga analizy naturalnych systemów rozpoznawania wzorców. W wybranych aplikacjach, takich jak mowa i widzenie, projekcja rzeczywistości jest spowodowana wpływami nabytej wiedzy, której formowanie w naturze jak i w przypadku automatów nazywamy procesem uczenia [6].

Każdy proces rozpoznawania obiektu wymaga podjęcia szeregu działań wstępnych, których zadaniem jest przetworzenie grupy danych. W przypadku obrazów graficznych, dla których z założenia przyjmuje się wzorcowe zdjęcia, wyselekcjonowano fizyczne, typowe różnice między wybranymi obiektami - długość, szerokość, liczba cech szczególnych. Występuje potrzeba zdefiniowania funkcji, której zadaniem jest analiza cech, czyli określenie funkcji celu w klasyfikatorach automatycznych.

Badania nieniszczące są działaniami pomiarowymi, których ocena należy do trudniejszych procesów kontrolnych w technice. Stąd też idea artykułu koncentruje się na badaniach obiektów z automatycznym klasyfikatorem.

Zastosowanie klasyfikatorów do oceny stanu obiektu, opisanego wielowymiarową przestrzenią parametrów, jest przedmiotem badań w wielu dziedzinach nauki. W niniejszym artykule podjęto tematykę zastosowania i oceny klasyfikatorów nieparametrycznych. Aplikację związano z funkcją gęstości powstałą z analizy danych histerezy dynamicznej [15].

Proces akwizycji danych

Istotną cechą danych wiążących postrzeganie obiektu jest szereg zakłóceń lub zmian wynikających z warunków i sposobów pomiaru [7, 8]. Badany prototyp systemu, przeznaczony jest do wykonywania bardzo konkretnego zadania. Składowe elementy takiego rozwiązania służą kolejno do:

- rejestracji danych oraz przetworzenia uporządkowanego zbioru danych,
- segmentacji, oddzielenia od siebie powtarzających się obiektów podobnych,
- identyfikacji, czyli ekstrakcji cech szczególnych z danych pomiarowych,
- klasyfikacji, która przyporządkowuje informacje do bazy wiedzy na podstawie kryterium podobieństwa [9, 10].

Analizy automatycznie ocenianych zbiorów danych uwzględniają średnie poziomy typowych zakłóceń. Przeprowadzają rozpoznanie progowych wartości danych dla obiektów podobnych.

W procesie programowania klasyfikatora ważne jest określenie własności procesu pomiarowego z jego zakłóceniami i specyfiką dynamiki układu [11].

Istotnym aspektem konstrukcji automatycznych klasyfikatorów jest zdefiniowanie maksymalnego poziomu błędu. W przypadku każdego systemu automatycznego często nie ma możliwości określenia funkcji jednoznacznie przyporządkowującej do danej klasy obiektów i naturalną staje się błędna interpretacja danych. Dlatego też w konstrukcjach algorytmów klasyfikujących proponowane jest ustalenie granicy decyzji [8, 9].

Istotą projektowania automatycznych klasyfikatorów są techniki tworzenia wzorców, nawet, gdy nie—mamy wystarczającej porcji danych uczących. Zagadnienie to zawsze wymaga znajomości dziedziny problemu. Jeżeli model podstawowy można przypisać porcji danych, ~~to~~ wtedy badany obiekt da się przyporządkować ~~można~~ do wybranej klasy.

Systemy rozpoznawania wzorców (także i klasyfikacji) powinny analizować wzór danych wejściowych, na podstawie syntezy danych wejściowych wzorca [3, 8, 10].

Nieparametryczne techniki klasyfikacji

Istotnym procesem wybranych metod identyfikacji jest wyznaczanie funkcji gęstości prawdopodobieństwa na podstawie danych uczących. Rozpoznawanie podobieństwa do wzorców, na podstawie zbiorów klasyfikujących, w technikach nieparametrycznych nie wymaga określenia funkcji gęstości. Często spotyka się brak zgodności rozkładów gęstości podobieństwa z typowymi postaciami parametrycznymi.

Techniki klasyfikacji nieparametrycznej mogą być stosowane dla dowolnej dystrybucji. Nie wymagają określania postaci funkcji gęstości prawdopodobieństwa.

Praca podejmuje dyskusję nad kilkoma rozwiązaniami technik nieparametrycznych. Zasada działania pierwszej polega na wstępnym szacowaniu funkcji gęstości $p(x|\omega_k)$ na podstawie próbki wzorców. Druga charakteryzuje procedurę bezpośredniego szacowania prawdopodobieństwa $P(\omega_k|x)$.

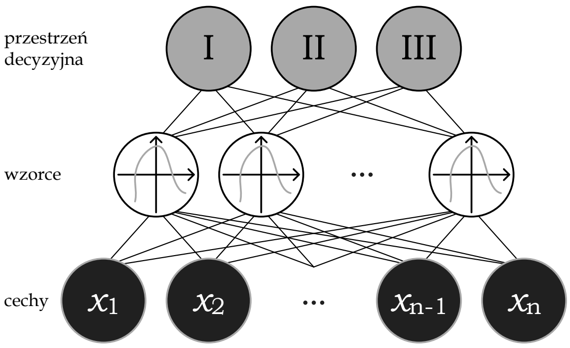

Rys. 1. schemat probabilistycznej sieci neuronowej

Za szczególną metodę uznano klasyfikację probabilistycznymi sieciami neuronowymi (Probabilistic Neural Networks) [2, 5].
Probabilistyczny model automatu klasyfikującego przedstawiono w postaci wielowarstwowego perceptronu o jednej warstwie ukrytej rys. 1. Warstwę wejściową sieci stanowią wybrane odpowiednio cechy wzorca. Zależą one od własności funkcji gęstości przypisanej danej wadzie materiałowej [14, 15]. Warstwę ukrytą stanowią wzorce, odpowiadające danej klasie, a warstwa wyjściowa odwzorowuje przestrzeń decyzyjną.
Zadania klasyfikacji nieparametrycznej, prowadzą ku dyskusji nad cechami głównymi wprowadzanymi do warstwy wejściowej algorytmu neuronowego.

Model- funkcja gęstości
Cechy główne zjawiska bądź urządzenia wiążą postrzeganie obiektu poprzez jego model. Zwykle najlepszą reprezentacją jest równanie opisane zbiorem szczegółowych parametrów. W użytecznym ujęciu klasyfikacji lub modelowania, parametr jest numerycznym lub ogólnie abstrakcyjnym atrybutem, opisującym istotne dla analizy właściwości obiektu.
Poddanie procesowi automatycznej klasyfikacji obiektów wymusza przyjęcie wielowymiarowych funkcji gęstości. Ich dobór uzależnia efektywność jak i koszt związany z procedurą uczącą. Proponowanym przez autorów rozwiązaniem jest zastosowanie funkcji statycznej, zidentyfikowanej na podstawie badań defektoskopowych, opisujących różnicową wartość napięcia nierównowagi mostka w układzie zmiennoprądowym [14, 15]. Oszacowanie kształtu funkcji wagi $\mu(\alpha, \beta)$, polega na wyznaczeniu rodziny odwracalnych krzywych magnesowania pierwszego stopnia. Na postawie tych wartości, do identyfikacji szukanej powierzchni dostępne są różne algorytmy.

Pierwszym jest algorytm podany przez I. Mayergoyza i służy do wyznaczania funkcji gęstości modelu Preisacha na podstawie danych eksperymentalnych. Procedura wymaga wymuszenia zmian amplitudy wartości wymuszającej do uzyskania stanu ujemnego nasycenia. Następnie wymagany jest jej przyrost tylko do odpowiednio pomniejszanych granic [12]. Taka zmiana napięcia wejściowego umożliwia pozyskanie narastającej część pętli histerezy. Kolejne krzywe powstają poprzez ponowne doprowadzenie układu do stanu ujemnego nasycenia, po czym następuje monotoniczny wzrost amplitudy w taki sposób, aby uzyskać odpowiednio pomniejszoną wartość indukcji [12].

□ Drugi z algorytmów wymaga kolekcji typowych rodziny pętli histerezy magnetycznej, dla ustalonych przebiegów przemagnesowania. Wyznaczenie ich łączy się z koniecznością badań przy coraz większych amplitudach wymuszenia, przy stałej częstotliwości. Trzeci algorytm „pochodny", analogiczny do pierwszego, wymaga jedynie określenia innego kształtu napięcia zasilającego. Podobnie jak w algorytmie I. Mayergoyza, badaniom podlegają pewne krzywe, wyznaczone na podstawie przebiegu rozmagnesowującego. W pierwszej fazie materiał doprowadzony zostaje do stanu nasycenia. W celu eliminacji efektu pamięci zalecane jest poddanie materiału kilkukrotnemu przemagnesowaniu o największej dobranej amplitudzie.
Dobór funkcji gęstości ma znaczący wpływ na efektywność badanego procesu automatycznej klasyfikacji.

REFERENCES

[1] Tendero A, Tixier C., Tristant P., Desmaison P, Leprince P, Atmospheric pressure plasmas: A review, Spectrochimica Acta Part B 61 (2006) pp. 2–30.
[1] Honkela T., Duch W., Girolami M., Kaski S., Artificial Neural Networks and Machines Learning-ICANN 2011, Springer 2011.
[2] Principe J. C., Information Theoretic Learning, Springer 2010.
[3] Hung-Chih Chiang Moses R.L., Potter L.C., Model-based classification of radar images, IEEE Transactions on Information Theory, Vol. 46, pp. 1842 - 1854, 2002.
[4] El-Helw A.M., Moniri M., Chibelushi C.C., Error-resilient pattern classification using a combination of spreading and coding gains, IET Image Processing, Vol. 1, 2007.
[5] Parekh R., Yang J., Honavar V., Constructive neural-network learning algorithms for pattern classification, IEEE Transactions on Neural Networks, Vol. 11, pp. 436-451, 2002.
[6] Stąpor K., Automatyczna klasyfikacja obiektów. Akademicka Oficyna Wydawnicza EXIT, Warszawa 2005.
[7] Kukiełka L., Podstawy badań inżynierskich, Wydawnictwo Naukowe PWN, Warszawa 2002.
[8] Seo S., Bode M., Obermayer K., Soft nearest prototype classification, IEEE Trans. on Neural Networks, Vol. 14, pp. 390 - 398, 2003.
[9] Hemion G., The Classification of Knots and 3-Dimensional Spaces, Oxford University Press 1992.
[10] Cichosz P., Systemy uczące się. Wydawnictwo Naukowo-Techniczne, Warszawa 2000.
[11] Weinberger S., The Topological Classification of Stratified Spaces, Lectures in Mathematics, University of Chicago 1995.
[12] Mayergoyz I. D., Mathematical Models of Hysteresis, Springer-Verlag, Berlin 2002.
[13] Henze O., Rucker W.M., Identification procedures of Preisach model, IEEE Trans. Magn., Vol. 38, pp. 833 – 836, 2002.
[14] Wac-Włodarczyk A., Goleman R., Giżewski T.: The experimental identification of the Preisach differential surface in the arrangement of AC bridge, Przegląd Elektrotechniczny, 12/2010.
[15] Wac-Włodarczyk A., Goleman R., Giżewski T.: The methodology of magnetic materials classification, Przegląd Elektrotechniczny 03/2011.

***Autorzy**:*
dr inż. Tomasz Giżewski, Politechnika Lubelska, Instytut Podstaw Elektrotechniki i Elektrotechnologii, ul. Nadbystrzycka 38a, 20-618 Lublin, E-mail: t.gizewski@pollub.pl.
dr hab. inż Andrzej Wac-Włodarczyk, prof. PL, Politechnika Lubelska, Instytut Podstaw Elektrotechniki i Elektrotechnologii, ul. Nadbystrzycka 38a, 20-618 Lublin, E-mail: a.wac-wlodarczyk@pollub.pl.
dr inż. Ryszard Goleman, Politechnika Lubelska, Instytut Podstaw Elektrotechniki i Elektrotechnologii, ul. Nadbystrzycka 38a, 20-618 Lublin, E-mail: r.goleman@pollub.pl.
dr inż. Dariusz Czerwiński, Politechnika Lubelska, Instytut Podstaw Elektrotechniki i Elektrotechnologii, ul. Nadbystrzycka 38a, 20-618 Lublin, E-mail:d.czerwinski@pollub.pl.

MAGNETIC REFRIGERATION

Bogusław GRZESIK, Mariusz STĘPIEŃ

Silesian University of Technology

Abstract*. The basic information about magnetic refrigeration is the subject of the paper. The information is devoted for the future FEM analysis of the refrigerator.*

Streszczenie. *Podano podstawowe informacje o magnetycznym chłodzeniu. Informacje te przeznaczone są do przyszłych badań ukierunkowanych na analizę metodą elementów skończonych systemu chłodzącego tego typu.*

Keywords: magnetic refrigeration, vapour compression, rare earth materials, .
Słowa kluczowe: chłodzenie magnetyczne, sprężanie parowe, materiały ziem rzadkich

Introduction

Magnetic refrigeration is the contemporary technology that allows for more efficient cooling, used e.g. in household friges. Magnetic refrigeration is based on magnetocaloric effect. The phenomenon was discovered by Warburg (1881) [1] and independently by P. Weiss, A. Piccard (1918) [2]. The second step was by done by P. Debye (1926) [3] and W.F. Giauque (1927) [4] who gave the theoretical explanation of magnetocaloric phenomena. Then the research on it was undertaken by many scientific teams, e.g. [9]. The intensive research work is carried the following reports are the only small number of examples [6], [7], [9]. The main efforts are concentrated on magnetocaloric materials [6] and magnets. An introductory presentation of magnetocaloric refrigeration is the aim of the paper. It will be used to FEM analyses and experimental research. The research is motivated by environmental and efficiency arguments. Such refrigerators are more friendly for environment and are more efficient in comparison with the ones based on vapour-compression process.

Vapour-compression refrigeration

The vapour-compression refrigeration can bi illustrated by Fig. 1 where Freon gas is used as the coolant. It contains four essential parts. A compressor is the one. The expansion valve is the second one. The thermally insulated compartment where low temperature is kept is the third part of it. The last one is the radiator (hot heat exchanger) which transfers the heat to the outside environment. The compressor increases the pressure of the coolant gas. After that the compressed gas having high temperature flows to the hot heat exchanger. The heat Q is transferred in there to the outside environment in there. It results in condensation of high pressure gas to the liquid. Next the coolant - Freon, being at high pressure is flowing from outside radiator the to expansion valve and then to the insulated compartment (cold heat exchanger). The temperature of the coolant is there at low pressure (because of expansion). At the same time the coolant is lower in the temperature than the surrounding air. It causes transfer of the heat Q to the coolant. Absorption of the heat causes endothermic vaporisation of the coolant. It closes cooling cycle. The vapour-compression process can be described by T-s (temperature-entropy) diagram of refrigeration cycle [8]

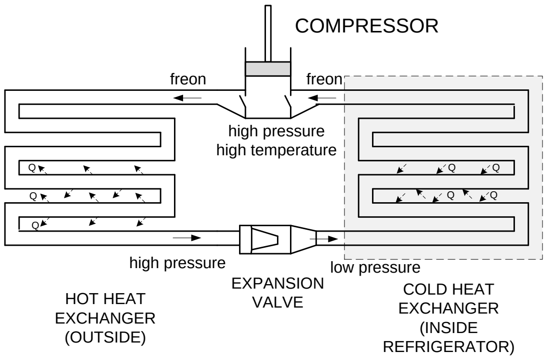

Fig.1. Schematic diagram of the compression-expansion refrigerator [5]

Magnetic refrigeration

Magnetic refrigeration looks similar to the compression-expansion. A magnetocaloric material (MCM) operates like coolant. The change of its internal energy takes place by means of change of outside magnetic field. Brief explanation of magnetocaloric refrigerator can be obtained using Fig. 2 [6].

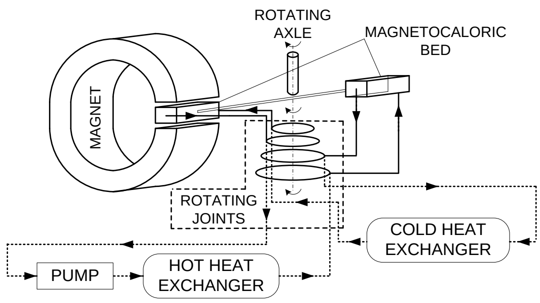

Fig.2. Schematic diagram of the magnetocaloric refrigerator [6]

It contains two magnetocaloric beds (MCB) through them the cooling liquid is flowing to the stationary part. The MCB rotate around rotating axle changing position of MCB in relation to magnet. When MCB is inside magnet it warms up since energy is taken of the MCB changing its magnetic portion of entropy. Before it riches the opposite position is. When the MCB is outside magnet it is cooled by means of heat exchange being transferred to the spins of the MCB.

After that the heat is transferred to the MCB, that is outside the magnet, to the cold heat exchanger. The hot heat exchanger and cold heat exchanger are connected to the MCB via system of four pipes that includes rotating joints. The described process can be illustrated as is done in Fig. 3 and Fig. 4.

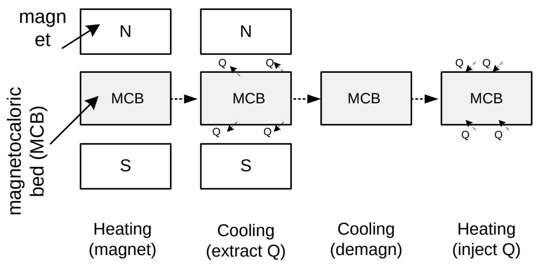

Fig.3. Magnetic refrigeration cycle [9]

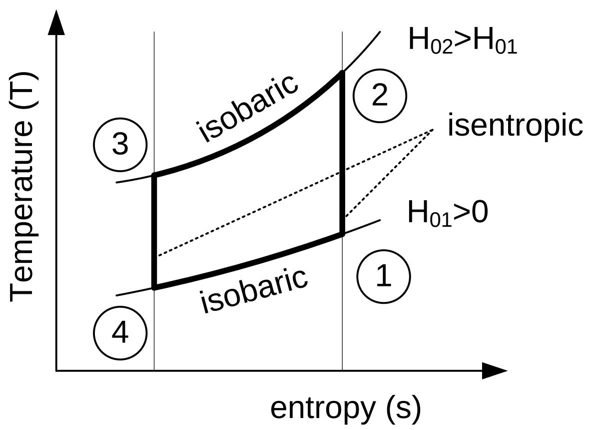

Fig.4. Bryton cycle of magnetocaloric process

Conclusions

Presented short information about magnetic refrigeration has to be developed in to be useful for FEM analysis.

REFERENCES

[1] Warburg E., Magnetische Untersuchungen über einige Wirkungen der Koerzitivkraft. *Ann. Phys.* 13, 141 -164, 1881.

[2] Weiss P., Piccard A., Pike G.E., Sur un nouveau phénomene magnétocalorique, *Compt. Rend. Ac. Sc.,* 166, 352, 1918.

[3] Debye P., Einige Bemerkungen zur Magnetisierung bei tiefer Temperatur, *Ann Phys.* 81, 1154 -1160, 1926

[4] Giauque W. F., A proposed method of producing temperatures considerably below 1° absolute. *J. Amer. Chem. Soc.* 49, 1864 -1870, 1927.

[5] Casiday R,. Frey R., Phase changes and Refrigeration, *http://www.chemistry.wustl.edu/~courses/genchem/LabTutorials/Thermochem/Fridge.html*

[6] Tegus O. et al, MnFe(P,As) and related materials for magnetic refrigeration *http://icmp.imr.ac.cn/ss07/PPT/deBoer/deboer16.pdf*

[7] Podmiljsak B., The magnetocaloric effect, Seminar for the lecture of materials, *Josef Stefan Institute, Lubljana, http://www.ijs.si/~kutnjak/reprints/Magnetocaloric.pdf*

[8] 6.5 Simple Vapor Compression Refrigeration System, *http://nptel.iitm.ac.in/courses/IIT -MADRAS/Applied_Thermodynamics/Module_6/6_Simple_Vapor_Compression_RS.pdf*

[9] Egolf P. W. et al, An introduction go magnetic refrigeratrion, *http://www.centrogalileo.it/nuovapa/Articoli%20tecnici/INGLESE%20CONVEGNO/XII%20Convegno%20English/II%20SESSIONE/Egolf%201_eng.pdf*

***Authors**: dr hab. inż. Bogusław Grzesik, prof. Pol. Śl., dr inż. Mariusz Stępień, Politechnika Śląska, Katedra Energoelektroniki, Napędu Elektrycznego i Robotyki, ul. Krzywoustego 2, 44-100 Gliwice,* Boguslaw.Grzesik@polsl.pl Mariusz.Stepien@polsl.pl,

CRYOGENIC AND SUPERCONDUCTING TECHNOLOGIES IN ELECTRON STRING ION SOURCES OF MULTICHARGED IONS

S.V. GUDKOV, V.M. DROBIN, D.E. DONETS, E.D. DONETS, E.E. DONETS, E. KULIKOV, H. MALINOWSKI, V.V. SALNIKOV and V.B. SHUTOV

Joint Institute for Nuclear Research, Dubna, 141980, Russia

Keywords: electron string ion sources , multicharged ions

Electron String Ion Source (ESIS) is the relatively novel type of ion sources, which is under development in JINR since 1994 (see most recent [1-2] and refs therein), when the electron string phenomenon was first observed with use of Krion-2 Electron Beam Ion Source (EBIS), working in reflex mode of operation with magnetic field 3.3 Tesla. Electron beam ion sources (EBIS) realized in pioneer works in JINR are used widely in leading accelerator centers for production of highly charged ions including bare nuclei of heavy elements.

Electron beam/string ions sources operation is based on magnetically compressed electron beam with electron energy in a range 3 ÷ 100 KeV and electron current density in range 200 ÷2000 A/cm^2; ionization of working elements is due to electron impact in electron beam/string. The necessary vacuum conditions in ionization drift tube space is about 10^{-12} Torr in order to get multicharged ions of heavy elements like Au55+ and higher. Natural way to provide such conditions is using of superconducting solenoids with magnetic field of few Tesla for beam magnetic compression and confinement; at the same time, drift tube structure (surrounding ionization/beam region of ion source) maintaining at the liquid helium temperature provides the required vacuum conditions without and external pumping during ionization.

In order to increase ion yield one needs to increase magnetic field. Technology of SC solenoids manufacturing was elaborated and tested during last few years. Few test solenoids of 20 cm length and of 5 cm bore diameter were produced and tested recently. The results: 7.4 - 7.8 Tesla maximal magnetic field (at transition point) were obtained and reproduced few times. Full-size SC solenoid with length 120 cm and bore diameter 5 cm is under manufacturing at the present time; it is expected to get 6 ÷ 6.5 Tesla magnetic field in its working range with current up to 110 A.

Safety system of SC solenoids are very important for their stable and long-life operation. Experimental results of the elaborated safety systems testing under solenoids transition into the normal (nonsuperconducting) state will be discussed. This results have both practical and academic meaning.

Further expected applications of ESIS-type ion sources will be discussed in brief. One possible application will be emphasized: newly proposed "non-accelarator" method of cancer radiotherapy [3] with use of 60÷80 KeV X-rays irradiating the incorporated into the tumor gold nanoparticles.

Referces

[1] D.E. Donets et al., "Production of highly charged ion beams Kr^{32+}, Xe^{44+} and Au^{54+} with ESIS Krion-2 and corresponding basic and applied studies", 2010 JINST **5** C09001; http://iopscience.iop.org/1748-0221/5/09/C09001.

[2] D.E. Donets et al., "Production and ion-ion cooling of highly charged ions in Electron String Ion Source", Rev. Sci. Instrum. **80** (2009) 063304.

[3] A.P. Kavanagh et al., «Radiation from K-shell filling in highly charged ions: a drive for resonant combination cancer therapy ?», 2007 J. Phys.: Conf. Ser. 58 439. http://iopscience.iop.org/1742-6596/58/1/101.

Authors: *.V. Gudkov, V.M. Drobin, D.E. Donets, E.D. Donets, E.E. Donets, E. Kulikov, H. Malinowski, V.V. Salnikov and V.B. Shutov , Joint Institute for Nuclear Research, Dubna, 141980, Russia*

DISCHARGE PROPAGATION IN CAPILLARY TUBES ASSISTED BY BIAS ELECTRIC FIELD

Karol HENSEL[1], Pierre Le DELLIOU[2], Pierre TARDIVEAU[2], Stephane PASQUIERS[2]

Comenius University, Bratislava, Slovakia (1), Université Paris-Sud, Orsay, France (2)

***Abstract**. The paper presents experimental results on the discharge generated in capillary tubes by pulsed power assisted by additional bias electric field. The electric field applied in addition to the pulsed voltage affected the discharge propagation inside the capillaries. The results on discharge development and velocity as functions of capillary tube diameter and amplitude of the bias field as analyzed by fast imaging camera are presented.*

Keywords: pulsed discharge, capillary tubes, streamer velocity, fast camera imaging

Introduction

Automotive catalytic converters have been developed and used for the abatement of exhaust gases for almost forty years. Despite their high efficiency, legislation limits for automobile emissions require new technologies in order to meet the current emission standards. The major problems of the automotive catalysts are their low activity at low temperatures and weak performance in non-stiochiometric conditions. Several techniques have been applied to overcome these problems, e.g. hydrocarbon adsorbing traps, closely coupled catalysts, as well as efforts to develop new catalysts. Another potential solution is to generate non-thermal plasma inside the automobile catalytic converters. The plasma contains various charged and neutral reactive species which may effectively activate the catalyst and initiate various heterogeneous chemical reactions even at room temperature. Atmospheric plasmas are often used in various applications, including environmental and biomedical treatment and surface modifications. The plasma can be generated by various types of electric discharges either in large volumes but also in small constricted spaces, pores and cavities alike those in automotive catalytic converters.

The present study is focused on the discharge generation in glass capillary tubes which simulate the long capillaries of honeycomb shaped automotive catalytic converter. In past we have performed several tests and generated stable plasma inside bunch of capillary tubes by using combination of AC and DC power supplies. We addressed the effects of the amplitude of the applied voltages; length, diameter and number of capillary tubes as well as gas used mixtures on the discharge properties and stability [1,2].

The paper presents experimental results on discharge generated in a single capillary tube generated by pulsed power supply and assisted by bias electric field. The electric field applied in addition to the pulsed voltage affected the discharge propagation inside the glass capillary tubes. The results on propagation and velocity of the discharge front as affected by the amplitude of the bias field diameter of capillary tubes are presented.

Experimental setup

The experimental set-up is roughly depicted in Figure 1. The reactor consisted of 30 mm long glass capillary tube with inner diameter of 0.2 mum or 1 mm. Tungsten wire of 50 μm diameter was plugged into the tube from a bottom. The top end of the capillary tube was set inside packed bed reactor (a quartz tube wrapped by aluminium tape with a rod in centre) filled with TiO_2 pellets. The tungsten wire was powered by a pulsed power, while packed pellet bed was operated by AC power. The packed pellet reactor was used to generate auxiliary discharge that by the application of the pulsed power to the rod may spread though the capillary tube [2]. The imaging system consisted of high speed ICCD camera (4-Picos Stanford Computer Optics cameras) synchronized with the voltage pulse was used to record a single event in capillary tube. By changing of the camera delay and gate opening we were able to follow the dynamics of the discharge and measure discharge propagation velocity inside the tube.

Fig.1. Schematic of the experimental set-up.

Experimental results

The propagation of the discharge generated inside the capillary tube has been monitored along 20 mm (visible part) of the capillary tube. The positive pulse (amplitude +15 kV, duration 20 ns) has been applied to the tip of tungsten wire (anode). Figure 2 shows the propagation of the discharge front as a distance from the anode in time for tube of 1 mm diameter.

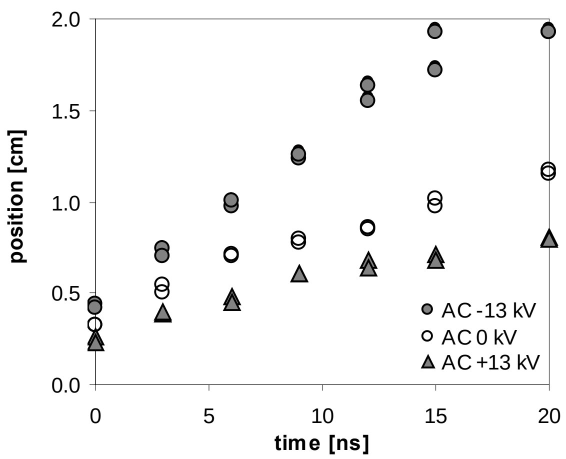

Fig.2. Distance of the discharge front from anode as function of time and bias electric field [1 mm diameter, pulsed voltage +15 kV].

Without auxiliary discharge (AC 0 kV) the discharge front moved almost linearly with time. The instant velocity of the front was found approximately constant, however slightly decreasing from $7.5*10^7$ cm/s (measured during 1st ns) to $3.4*10^7$ cm/s (during 20th ns). Application of the negative bias electric field (-13 kV) to the rod of the pellet bed reactor resulted gave an increase to the average velocity of the discharge front. Compared to previous case, the instant velocity increased to 10^8 cm/s (the 1st ns), and $7.5*10^7$ cm/s (in 20th ns). On the other hand the discharge front propagation slowed down if positive bias was applied to the rod. Comparison of the results obtained for 1 mm and 0.2 mm diameter capillary tubes showed that discharge instant and average velocities increased with the decreasing tube diameter. In the present study, the average velocities were found 4.3 and $9.97*10^7$ cm/s for 1 and 0.2 mm diameter tube, respectively. These results are in agreement with those of Jánský et al. [3]. More data addressing the effect of the bias field and capillary tube diameter including high speed camera images will be presented during the symposium.

.

Acknowledgements: Effort sponsored by Slovak grant agency VEGA 1/0711/09.

REFERENCES

[1] Hensel K., *J. Eur. Phys. J. D 54* (2009), 141-148

[2] S. Sato, K. Hensel, H. Hayashi, K. Takashima, A. Mizuno: *J. Electrostat.* 67 (2009), 77-83

[3] Jánsky J., Le Delliou P., Tholin F., et al., *J. Phys. D. Appl. Phys.* 44 (2011), Art. No. 225201

***Authors**: Karol Hensel, PhD., Division of Environmental Physics, Faculty of Mathematics, Physics and Informatics, Comenius University in Bratislava, Mlynska dolina F2, 84248 Bratislava, Slovakia, E-mail: hensel@fmph.uniba.sk; Pierre Le Delliou, Pierre Tardiveau, PhD., Stephane Pasquiers, PhD., University Paris-Sud, Laboatioire de Physique des Gaz et des Plasma, UMR 8578 CNRS, 91405 Orsay, France, E-mail: pierre.tardiveau@u-psud.fr.*

Conference ELMECO–7
ELECTROMAGNETIC DEVICES AND PROCESSES IN ENVIRONMENT PROTECTION
joint with 10th Seminar AoS-10 APPLICATIONS OF SUPERCONDUCTORS
28–30.09.2011, Nałęczów, Poland

USING THE TEST METHOD FOR OPTIMIZATION THE PELTIER DEVICE FOR ACHIEVEMENT SUPERCONDUCTING TRANSITION TEMPERATURES

Oleksandra HOTRA (1), Piotr BYLICKI (1)

Lublin University of Technology, Electrical Engineering and Computer Science Faculty (1)

***Abstract**: A new method for determining electric and thermal characteristics of Peltier devices is analyzed with the aim of optimization of Peltier devices. Obtained results give the possibility to optimize thermoelectric cooler systems such as Peltier cascades to reach most efficient operating state and to achieve the lowest possible temperature. In optimized by proposed method four stage Peltier cooling cascade the achieved temperature could be near to the superconducting transition temperature of $HgBa_2CaCu_2O_{6+\delta}$. Peltier device is not damaged during the test process and still can be used.*

***Streszczenie:** W artykule przeanalizowano nową metodę wyznaczania elektrycznych oraz termicznych parametrów ogniw Peltiera celem wykorzystania jej wyników do optymalizacji elementów Peltiera. Otrzymane wyniki dają możliwość optymalizowania chłodziarek termoelektrycznych takich jak kaskadowe elementy Peltiera w celu osiągnięcia najbardziej efektywnego punktu pracy i osiągnięcie najniższej możliwej temperatury. W czterostopniowej chłodziarce termoelektrycznej zoptymalizowanej przy użyciu proponowanej metody otrzymana temperatura może być bardzo bliska temperaturze nadprzewodnictwa $HgBa_2CaCu_2O_{6+\delta}$. Badany element Peltiera nie ulega uszkodzeniu podczas wyznaczania parametrów i może być dalej używany.*

Keywords: *thermoelectric coolers, thermoelectric properties, Peltier device, test method of Peltier device, superconductor temperature*
Słowa kluczowe: *chłodziarki termoelektryczne, moduł termoelektryczny, charakterystyki ogniw Peltiera*

Introduction

Thermoelectric modules are widely used in military equipment, aeronautics and industry. They owe their popularity to simple construction without any mechanical elements, that increases the reliability. Peltier cooling devices have special place in superconductor electronics. Superconducting microelectronic circuits are largely miniaturized and only a small cooling power of the order of milliwatts is needed. In multi-stage thermoelectric coolers the temperature as low as 149 K can be reached [1,2]. This temperature approaches the superconducting transition temperature of 124 K which can be achieved in thin films of $HgBa_2CaCu_2O_{6+\delta}$ However, the designing of high performance cooling systems or thermoelectric generators is very difficult because the characteristics of modules provided by manufactures do not fit the required cooling levels [9]. The optimization of cooling 0or generating systems, based on ΔT_{max}, I_{max} or Q_{max} , is hard to realize.

In this article, the new concept for testing method of the Peltier devices [3] is analyzed. The proposed method allows determining Peltier device characteristics, including thermal and thermoelectric material characteristics and electric resistance without affecting the device structures, unlike classic methods do [4-8]. The accuracy of different versions of the method was analyzed and the most accurate version was chosen. The results obtained from the proposed method give the possibility to optimize the thermoelectric cooler systems towards the most efficient operating state.

Method

In the experimental setup, the thermoelectric module is placed between a heat source (1) and a cooler (5), that causes heat flux through the tested element. The temperatures T_{h0} and T_{c0}, the heat flux Q_0, the electromotive force E_0 and the current I_0 (generated immediately after the circuit is shortened) are measured when the thermoelement approaches a thermally stable state. After the measurements are conducted, the circuit is shorted and I_0 is measured with an ammeter of the lowest available resistance. When the Peltier device reaches a new thermally stable state, the temperatures T_{hz} and T_{cz}, the current I_z , the heat flux Q_z and the voltage E_z (generated immediately after the circuit is opened) are measured.

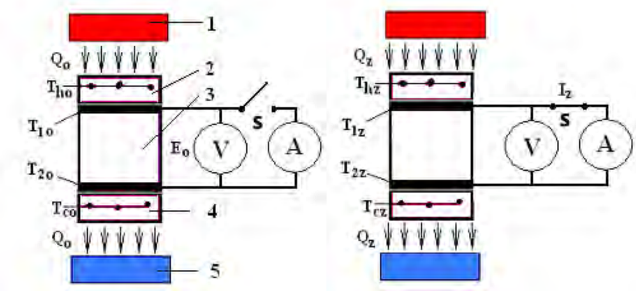

Fig. 1. The test system for Peltier device: 1 - electric heater; 2, 4 - heat conducting and temperature equalizing plates; 3- the Peltier device under test; 5 – cooler; V – voltmeter; A-ammeter; K-switch

The basic principle of the proposed method is that the heat fluxes through the surfaces at temperatures T_h and T_c are equal when no external electric load is inserted into the circuit. There are two states of the Peltier device which meet abovementioned condition: when the electrical circuit, fed from the device, is shorted, and when it is opened.

For a single thermoelectric element of Peltier device, the heat equation can be written as follows:

$$Q_{h,c} = \frac{(T_1 - T_2)}{\psi_p} + AIT_{1,2} \mp \frac{1}{2} RI^2 , \tag{1}$$

where $Q_{h,c}$ are the heat fluxes on the hot and cold sides respectively, T_1 and T_2 are the temperatures at the contact points between thermoelectric material and copper connectors, Ψ_p is the thermal resistance of thermoelectric material, A is the real electromotive force, I is the current, R is the electric resistance of the Peltier device (the true electric resistance of the thermoelectric material added to the electric resistance of the contact layer R_c).

When the circuit is short, and assuming that mutual dependence of heat fluxes can be applied and written down using average values of thermoelectric material properties, the following set of equations can be written:

(2)
$$\begin{cases} Q_z = (T_{hz} - T_{1z}) / \psi_t \\ Q_z = (T_{1z} - T_{2z}) / \psi_p + I_z \cdot A \cdot T_{1z} - I_z^2 R / 2 \\ Q_z = (T_{1z} - T_{2z}) / \psi_p + I_z \cdot A \cdot T_{2z} + I_z^2 R / 2 \\ Q_z = (T_{2z} - T_{cz}) / \psi_t \\ I_z = E_z / R \\ E_z = A \cdot (T_{1z} - T_{2z}) \end{cases}$$

where Ψ_t is the total thermal resistance of copper connections, contact surfaces adjacent to the structure of a heating or cooling system at the level of temperature measurement points T_h or T_c. Taking into account that, $\overline{T}_z$=(T_{hz}+T_{cz})/2=(T_{1z}+T_{2z})/2 for heat fluxes in the contact point between the thermoelectric material and the copper connection layer, the following formula can be written:

(3)
$$Q_z = \frac{E_z Q_0}{E_0} + I_z A \overline{T}_z \cdot$$

From the aforementioned equations, one can obtain:

(4)
$$A = \left(\frac{Q_z}{I_z} - \frac{Q_0}{E_0 / R} \right) \frac{1}{\overline{T}_z},$$

Equation (4) shows that it is possible to conduct the experiment in several ways. The te sts can be performed:
- at a constant average value of temperature during the experiment - *that makes possible eliminating the inaccuracy resulting from thermal dependencies of constructional materials and the temperature*
- at equal heat fluxes $Q_0 = Q_z$ - *that gives possibility to make experiment faster*
- at equal currents $I_z = I_0$.

In order to compare the accuracy of abovementioned variants, they are analyzed using the maximum approximation error formula:

(5)
$$\Delta_A = \sqrt{\left(\frac{\partial A}{\partial Q_0} \cdot \Delta_{Q_0}\right)^2 + \left(\frac{\partial A}{\partial Q_Z} \cdot \Delta_{Q_z}\right)^2 + \left(\frac{\partial A}{\partial I_Z} \cdot \Delta_{I_Z}\right)^2 + \left(\frac{\partial A}{\partial I_0} \cdot \Delta_{I_0}\right)^2 + \left(\frac{\partial A}{\partial T_H} \cdot \Delta_{T_H}\right)^2 + \left(\frac{\partial A}{\partial T_C} \cdot \Delta_{T_C}\right)^2}$$

The derivatives for each term of equation (5) and for each variant of the experiment are given in Table 1.

Table 1. Expressions for derivatives coefficients

	$\frac{\partial A}{\partial Q_Z}$	$\frac{\partial A}{\partial Q_0}$	$\frac{\partial A}{\partial I_Z}$	$\frac{\partial A}{\partial I_0}$	$\frac{\partial A}{\partial T_H}$	$\frac{\partial A}{\partial T_C}$
$\overline{T} = const$	$\frac{1}{\overline{T} I_z}$	$-\frac{1}{\overline{T} I_0}$	$-\frac{Q_z}{\overline{T} I_z^2}$	$\frac{Q_0}{\overline{T} I_0^2}$	$-\left(\frac{Q_z}{I_z} - \frac{Q_0}{I_0}\right)\frac{1}{\overline{T}^2}$	
Q_0=Q_z	$\frac{1}{\overline{T}}\left(\frac{1}{I_Z} - \frac{1}{I_0}\right)$		$-\frac{Q}{\overline{T} I_z^2}$	$\frac{Q}{\overline{T} I_0^2}$	$\frac{Q}{\overline{T}^2}\left(\frac{1}{I_z} - \frac{1}{I_0}\right)$	
I_z=I_o	$\frac{1}{\overline{T} I}$	$-\frac{1}{\overline{T} I}$	$-\frac{Q_z - Q_o}{\overline{T} I^2}$		$-\frac{Q_z - Q_o}{\overline{T}^2 I}$	

After substitution the experimental data into relationships from Table 1, the values of derivative coefficients can be obtained.

Table 2. Values of derivative coefficients

	$\frac{\partial A}{\partial Q_Z}$	$\frac{\partial A}{\partial Q_0}$	$\frac{\partial A}{\partial I_Z}$	$\frac{\partial A}{\partial I_0}$	$\frac{\partial A}{\partial T_H}$	$\frac{\partial A}{\partial T_C}$
$\overline{T} = const$	0,29	-0,24	-14,89	8,52	-0,09	
Q_z=Q_o	0,05		-14,89	9,89	0,05	
I_z=I_o	0,29	-0,29	-0,14		-0,04	

Let the accuracy of the research setup equipment is as follows: ΔT = +/- 0,5 ^{o}C, ΔQ = +/- 0,5 W, ΔI = +/- 0,1 A.
From equation (5) and the coefficients given in Table 2, the accuracy for each variant of the method can be expressed as: ΔA = 1,72% (for T_s=const), ΔA = 1,78% (for Q_z=Q_0), and ΔA = 0,20%. (for I_z=I_0)

From the obtained results It can be seen that the experiment be about 0,2%; that gives very good support for precise optimization.

Conclusions

The proposed method allows determining Peltier device parameters, and it is possible to determine the total thermal resistance of copper connections, contact surfaces with structure of a heating or cooling system and thermal resistance of semiconductor material. This feature gives the possibility to obtain the true electromotive force (A) based on the temperatures T_1 and T_2. The analysis shows that the accuracy of each variant of experiment is different. The most accurate is the variant for I_o=I_z which gives ΔA about 0,2%.. For a four-stage Peltier cooling cascade optimized by this method, it could be possible to achieve the temperature as low as 124 K which is sufficient for superconducting transition of thin films of $HgBa_2CaCu_2O_{6+\delta}$.

REFERENCES

[1] Huebener R.P., Tsuei C.C., Prospects for Peltier cooling of superconduction electronics, *Cryogenics* 38 (1998) 325-328

[2] Huebener R.P., Metzger T., Modelling and cooling behaviour of Peltier cascades, *Cryogenics* 39 (1999) 235-239

[3] Lozbin V., Bylicki P., Cuba V., New method of determining electric and thermal characteristics of Peltier device, *7th International Conference NEET 2011* [in review]

[4] Rowe D. M., Thermoelectrics Handbook – Macro to Nano edited by D.M. Rowe, PhD., D.Sc.,2006

[5] Ahiska R., New Method for Investigation of Dynamic Parameters of Thermoelectric Modules, *Turk J Elec Engin*, vol. 15, no 1, 2007

[6] Greber, G., Erk, S., Grigull, U., Principles of Heat Exchange. Translation from the German edited by Prof. A. A. Gukhman. M., ИЛ, 1958.

[7] Chirkin V. S., Thermal Conductivity of Industrial Materials, Fd. 2 [in Russian], Mashgiz, Moscow,1962

[8] Ciylan B., Yılmaz S., Design of a thermoelectric module test system using a novel test method, *International Journal of Thermal Sciences* 46 (2007) 717–725

[9] Huang B.J, Chin C.J., Duang C.L., A design method of thermoelectric cooler, *International Journal of Refrigeration* 23 (2000) 208-218

***Authors**: dr hab. inż. Oleksandra Hotra, prof. PL, Lublin University of Technology, Electrical Engineering and Computer Science Faculty 20-618 Lublin, Poland E-mail: o.hotra@pollub.pl; mgr inż. Piotr Bylicki, Lublin University of Technology, Electrical Engineering and Computer Science Faculty 20-618 Lublin, Poland e-mail: piotrbylicki@wp.pl*

Conference ELMECO–7
ELECTROMAGNETIC DEVICES AND PROCESSES IN ENVIRONMENT PROTECTION
joint with 10th Seminar AoS-10 APPLICATIONS OF SUPERCONDUCTORS
28–30.09.2011, Nałęczów, Poland

TUNING CHARACTERISTICS OF CYLINDRICAL MICROWAVE PLASMA SOURCE OPERATED WITH ARGON, NITROGEN AND METHANE AT ATMOSPHERIC PRESSURE

Bartosz HRYCAK[1], Mariusz JASIŃSKI[1], Dariusz CZYLKOWSKI[1], Marek KOCIK[1], Mateusz TAŃSKI[1], Jerzy MIZERACZYK[1, 2]

The Szewalski Institute of Fluid Flow Machinery Gdańsk (1), Gdynia Maritime University (2)

***Abstract**. The cylindrical microwave plasma source (MPS) is a device used to produce high temperature plasma at atmospheric pressure and high working gases flow rates. In our experiment the plasma was generated with 2.45 GHz microwaves at powers between 600 W to 5600 W and argon, nitrogen and methane as the working gases. At optimal positions of movable plunger, the use of argon, nitrogen and methane as the working gases caused, that 15 %, 0 % and 17 % of the incident power was reflected, respectively. The MPS can be used in gas processing applications.*

***Streszczenie.** Prezentowany cylindryczny mikrofalowy generator plazmy jest urządzeniem wytwarzającym plazmę o wysokiej temperaturze pod ciśnieniem atmosferycznym, przy wysokich przepływach gazów. Plazma wzbudzana jest mikrofalami o częstotliwości 2,45 GHz i mocy od 600 W do 5600 W. Jako gazu roboczego użyto argonu, azotu oraz metanu. Odpowiednio dla argonu, azotu oraz metanu przy optymalnym położeniu ruchomego zwarcia odbita moc wynosiła 15%, 0% oraz 17% mocy padającej. Generator plazmy może być używany m.in. do obróbki gazów.*

Keywords: plasma sources, microwave discharges, tuning characteristics, gas processing.
Słowa kluczowe: generatory plazmy, wyładowania mikrofalowe, charakterystyki strojenia, obróbka gazów.

Introduction

Recently, microwave plasma sources (MPSs) operated at atmospheric pressure have been developed [1-3]. Such devices were used in spectroscopy, technological processes like surface treatment, carbon nanotubes synthesis and sterilization. They also found applications in the processing of various gases. Destruction of Freon HFC-134a [4] and production of hydrogen via methane conversion [5] in microwave atmospheric pressure plasmas were reported lately.

This paper presents results of experimental investigations with a new, cylindrical, 2.45 GHz microwave plasma source operated at atmospheric pressure gases at high gas flow rates.

Microwave plasma source MPS

The sketch of the cylindrical microwave plasma generator is shown in Fig. 1. The generator was based on a standard WR 430 rectangular waveguide with a section of reduced-height, preceded and followed by tapered sections. The plasma flame was generated inside a quartz tube which penetrated microwave plasma generator through circular gaps on the axis of the waveguide wide wall and protruded below bottom waveguide wall. On the outside of the waveguide the quartz tube was surrounded by cylindrical metal shield with gap for visualization. The inner and outer diameters of the quartz discharge tube were 26 mm and 30 mm, respectively. The working gases created swirl flows inside the tube. The discharge was initiated using the rod entered to the discharge area to increase local electric field. In case of methane the discharge was initiated in nitrogen or argon and then gases were changed.

Experimental setup

The diagram of the experimental setup is presented in Fig. 2. The main parts of the experimental setup were: microwave generator (2.45 GHz and maximal power of

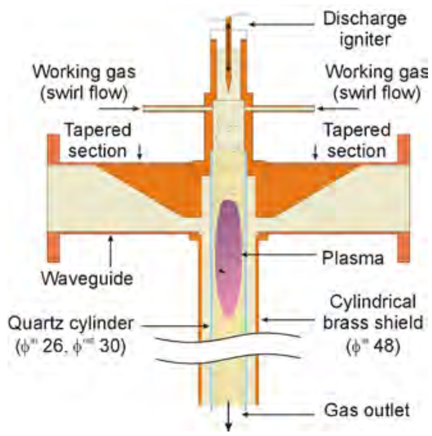

Fig.1. The sketch of cylindrical microwave plasma source

6 kW) secured with water insulator, rectangular waveguide (WR 430) as a feeding line, directional coupler equipped with heads and dual channel power meter, cylindrical MPS terminated with movable plunger, ensuring the short at the

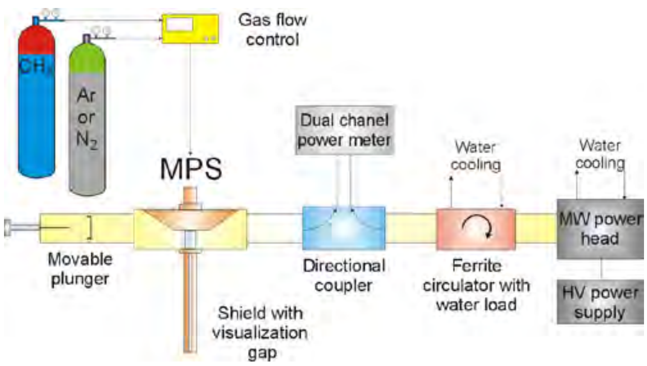

Fig.2. Experimental setup

end of microwave line and gas supplying and measuring system.

The microwave power P_A absorbed by the plasma was determined from (P_I - P_R), where P_I and P_R are the incident and reflected microwave powers, respectively. The tuning characteristics are defined as the dependence of the reflected coefficient P_R / P_I as a function of the distance $\boldsymbol{l}$ between the plasma axis and the movable short. This function is recurrent, with period $\lambda_g/2$, where λ_g is the waveguide wavelength (147.7 mm for WR 430 waveguide).

During experiments argon and nitrogen swirl flow rates were 50 l/min and 200 l/min and methane swirl flow rates were 88 l/min and 175 l/min. The absorbed microwave power level was varied from 600 W up to 5600 W.

Results

Minimal microwave absorbed powers for sustaining plasmas were about 600 W in argon and nitrogen and 1500 W in methane. Fig. 3 shows the photos of argon and nitrogen plasmas.

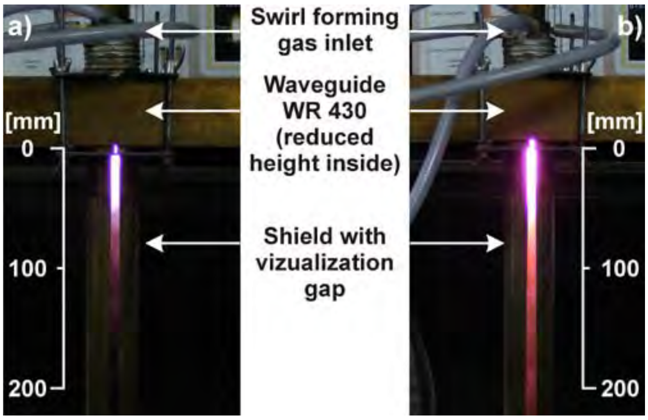

Fig.3. Microwave argon (a) and nitrogen (b) plasmas. Gas flow rate Q - 200 l/min, microwave absorbed power P_{abs} – 2000 W.

The use of argon as the working gas caused, that the tuning characteristics were the widest. Fig. 4 presents the normalised tuning characteristics of the cylindrical MPS operated in argon and nitrogen at atmospheric pressure for different microwave incident powers at flow rate of 200 l/min. These characteristics were almost independent of discharge conditions. The narrowest tuning characteristics were observed, when methane was used as the working gas. Practically, only one position ($\boldsymbol{l}$ ≈ 270 mm) of the movable plunger ensured sustaining of the discharge. Fig. 5 shows the fraction of the incident power reflected at the MPS input P_R / P_I for two different flow rates at fixed position of movable plunger ($\boldsymbol{l}$ ≈ 270 mm).

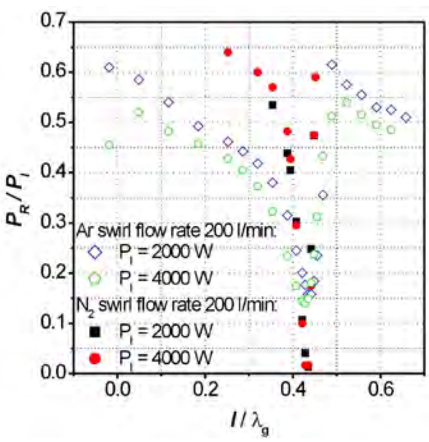

Fig.4. Normalised tuning characteristics of the cylindrical microwave plasma generator operated in argon and nitrogen at atmospheric pressure. Gas flow rate 200 l/min, microwave incident power: 2000 W and 4000 W. $\boldsymbol{l}$ – distance between the plasma axis and movable plunger, λ_g – waveguide wavelength (147.7 mm).

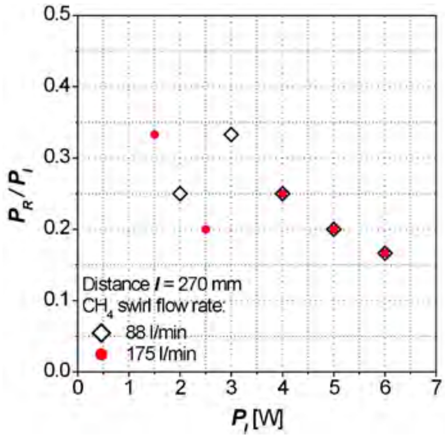

Fig.5. The fraction of the incident power reflected at the MPS input for different conditions at fixed position of movable plunger ($\boldsymbol{l}$ ≈ 270 mm).

Conclusions

This paper concerns the tuning characteristics of the cylindrical microwave plasma source operated with argon, nitrogen and methane at atmospheric pressure. Investigations of the tuning characteristics showed that at optimal positions of movable plunger, the use of argon, nitrogen and methane as the working gases caused, that 15 %, 0 % and 17 % of the incident power was reflected, respectively.

Stable operation at wide range of parameters, as well as good impedance matching, allows the concluding that MPS can be very attractive tool for different gas processing at high flow rates.

This research was supported by the The National Centre for Research and Development (NCBiR) under the programme NR14-0091-10/2010.

REFERENCES

[1] Tendero C.,Tixier C., Tristant P., Desmaison J., Leprince P., Atmospheric pressure plasmas: A review, *Spectrochimica Acta Part B*, 61 (2006), 2

[2] Moisan M., Zakrzewski Z., Rostaing J.-C., Waveguide-Based Single and Multiple Nozzle Plasma Torches: the TIAGO Concept, *Plasma Sources Sci. Technol.*, 10 (2001),387-394

[3] Uhm H.S., Hong Y.C., Shin D.H., A Microwave Plasma Torch and its Applications, *Plasma Sources Sci. Technol.*, 15 (2006), S26-S34

[4] Jasiński M., Dors M., Mizeraczyk J., Destruction of Freon HFC-134a Using a Nozzleless Microwave Plasma Source, *Plasma Chemistry and Plasma Processing*, 29 (2009), 363-372

[5] Jasiński M., Dors M., Mizeraczyk J., Applications of Atmospheric Pressure Microwave Plasma Source for Production of Hydrogen via Methane Reforming, *The European Physical Journal D*, 54 (2009), 179-183

***Authors**: mgr inż. Bartosz Hrycak, dr inż. Mariusz Jasiński, The Szewalski Institute of Fluid-Flow Machinery, Polish Academy of Sciences, ul. Fiszera 14, 80-952 Gdańsk, E-mail: bhrycak@imp.gda.pl; mj@imp.gda.pl;*
prof. dr hab. inż. Jerzy Mizeraczyk, The Szewalski Institute of Fluid-Flow Machinery, Polish Academy of Sciences, ul. Fiszera 14, 80-952 Gdańsk and Gdynia Maritime University, Faculty of Marine Electrical Engineering, Morska 81-87, 81-225 Gdynia, E-mail: jmiz@imp.gda.pl.

Conference ELMECO–7
ELECTROMAGNETIC DEVICES AND PROCESSES IN ENVIRONMENT PROTECTION
joint with 10th Seminar AoS-10 APPLICATIONS OF SUPERCONDUCTORS
28–30.09.2011, Nałęczów, Poland

AUTOMATIC IMAGE ANALYSIS OF LASER ANNEALING EFFECTS ON CHARACTERISTICS OF CARBON NANOTUBES

Yoichiro IWASAKI[1], Toshiyuki NAKAMIYA[1], Ryosuke KOZAI[1], Fumiaki MITSUGI[2], Tomoaki IKEGAMI[2]

Tokai University (1), Kumamoto University (2)

***Abstract**. Carbon nanotubes (CNTs) have several excellent properties, and wide application fields are expected as a nanomaterial. The diameters of the tubes greatly influence the physical properties of CNTs. Therefore, it is important to measure the diameters of the tubes. This paper proposes an image processing algorithm to measure the diameters of CNTs to automate the measurement work. We measured the diameters of CNTs before and after laser annealing by use of our algorithm, and demonstrated the changes of statistical values of the diameters.*

Keywords: carbon nanotubes, image processing, diameter measurement of CNTs, laser anneal

Introduction

Carbon nanotubes (CNTs) have several excellent properties, and wide application fields are expected as a nanomaterial. Therefore, numerous researches on CNTs have been done. We also research CNTs [1, 2].

It is very important to evaluate uniformity of the diameters of CNTs in order to increase the uniformity of the characteristics of CNTs. The diameters of CNTs are generally measured manually using the image taken by a scanning electron microscopy (SEM) or a transmission electron microscopy (TEM). Such human visual works are extremely inefficient.

In this paper, we propose a diameter measurement algorithm using image processing for wide areas of CNTs electron microscopy images [3]. Proposed algorithm provides the numerous values of diameters detected by horizontal and vertical scans for the binary images. The diameter measurement was carried out for the CNTs SEM images. We confirmed that the mean value of the diameters measured by using our algorithm approximated that of human visual work.

We measured the diameters of the CNTs before and after laser annealing by using our algorithm, and demonstrated the changes of statistical values of the diameters.

Proposed algorithm to measure the diameters of CNTs

Fig. 1 shows a CNTs image taken by a SEM.

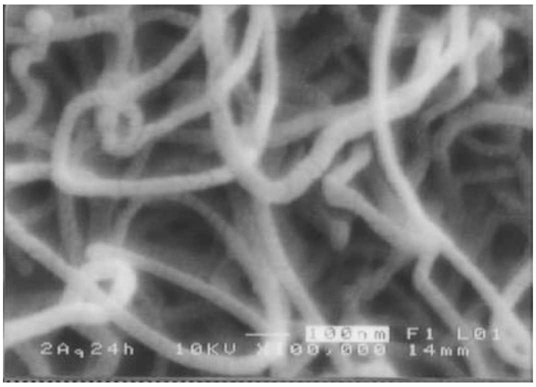

Fig. 1. A CNTs image taken by a SEM

The proposed algorithm is mainly composed from the image processing and the measurement of the diameters of the CNTs.

At first, the captured CNTs image is treated the noise reduction and binarization by the image processing. The gray levels of captured image are reversed, and the image is converted to 8-bit grayscale image. The histogram equalization is carried out to emphasize the contrast. Then, the noise is reduced by the median filter. After that, the automatic binarization is performed using Otsu's method [4]. We have confirmed that the Otsu's method is effective for the binarization of CNTs images. The closing and opening operations are followed to remove the binarization noise.

After the binarization of the CNTs image, the measurement of diameters of the CNTs is performed. In this algorithm, x (horizontal) and y (vertical) direction scans are executed to search CNTs, and measure the diameters.

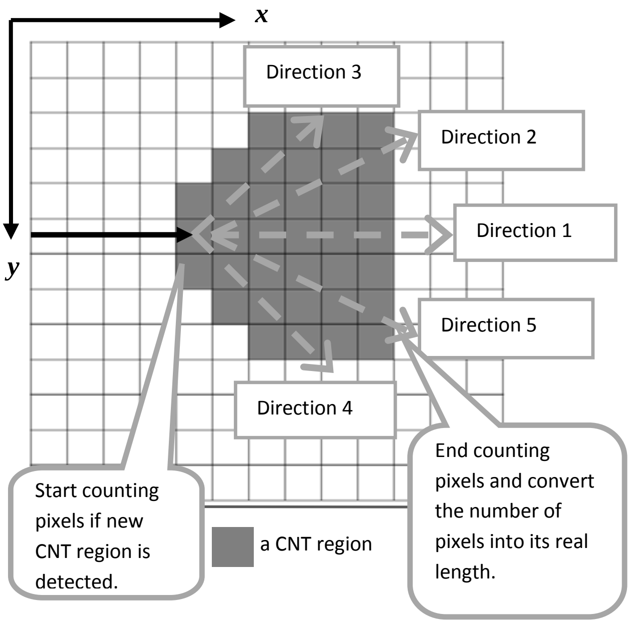

Fig. 2. x (horizontal) direction scan

At first, the y axis is fixed, and x-direction scan starts. If the pixel value at x is 0 (black) and the pixel value at the x-1 is 255 (white), the program recognizes that the x position is the edge of a CNT, and starts counting black pixels in 5 directions of 0, 25, 45, 315, 335 degrees shown in Fig. 2. The numbers of counted black pixels are converted into their real lengths, and the minimum length in the 5 measured lengths is regarded as the diameter. The color of the pixels regarded as the diameter is changed. This process is repeated by increasing y positions.

After x-direction scan, the scan direction is changed, and y-direction scan is executed like the horizontal scan. In vertical scan, 5 directions of 225, 245, 270, 295, 315 degrees are used.

The distribution of diameters is assumed as a normal distribution, and the range considered as diameters is decided based on inferential statistics because our algorithm detects also another parts other than diameter regions.

Finally, the output image which indicates the detected diameters is shown as Fig. 3.

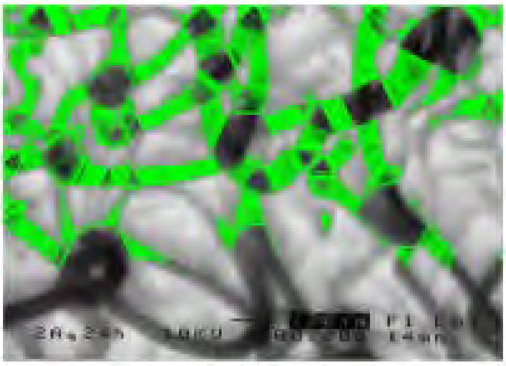

Fig. 3. The diameter detection result for the CNTs image shown in Fig. 1

Experimental results

The measurement result for the CNTs image shown in Fig. 1 is described below.

In x-direction scan, 11,615 diameters were detected and their mean value was 35nm. In y-direction scan, 16,974 diameters were detected and their mean value was 34nm. We could confirm that both scan results were close to each other. Moreover, we measured 100 diameters by human visual work, and the mean value of the 100 diameters was 36nm. The results using our algorithm approximated to the result by human visual work. Therefore, the accuracy and effectiveness of our algorithm have been verified.

Laser anneal experiments and their results

The pulse laser light was irradiated to CNTs with the experimental apparatus shown in Fig. 4, and the CNTs were laser annealed. Table 1 shows the irradiation conditions.

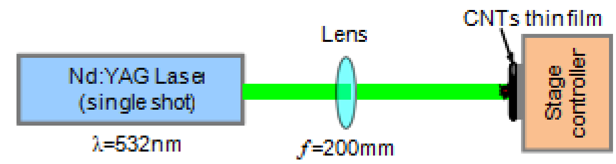

Fig. 4. Laser anneal apparatus

Table 1. Irradiation conditions

Laser energy density	33.82-247.51 mJ/cm^2
Irradiation frequency	1 shot
Gas	N_2, Air

We measured the diameters of CNTs before and after laser annealing by use of our algorithm

Tables 2 and 3 show the diameter measurement results of CNTs before and after laser annealing in N_2 and air atmospheres, respectively. The tendency that the diameters of CNTs grew by the laser energy density larger was seen from the results.

Table 2. Laser anneal experiments in N_2

Laser energy density	Before annealing	146.78 mJ/cm^2	188.51 mJ/cm^2	247.51 mJ/cm^2
Number of detection in both x and y direction scans	52,204	57,418	47,107	41,642
Standard deviation of diameters	9.61 nm	11.27 nm	11.61 nm	17.05 nm
Mean value of diameters	24.3 nm	23.8 nm	27.2 nm	32.1 nm

Table 3. Laser anneal experiments in air

Laser energy density	Before annealing	33.82 mJ/cm^2	151.10 mJ/cm^2	217.29 mJ/cm^2
Number of detection in both x and y direction scans	52,204	59,098	52,003	48,975
Standard deviation of diameters	9.61 nm	9.81 nm	11.70 nm	19.97 nm
Mean value of diameters	24.3 nm	26.4 nm	24.2 nm	36.2 nm

Conclusion

In this paper, we proposed an image processing algorithm to measure the diameters of CNTs to automate the measurement work. We measured the diameters of the CNTs before and after laser annealing by use of our algorithm, and demonstrated the changes of statistical values of the diameters.

REFERENCES

[1] Nakamiya T. *et al.*, Pulsed laser heating process of multi-walled carbon nanotubes film, *Diamond and Related Materials*, 17 (2008), 1458-1461

[2] Nakamiya T. *et al.*, Effect of a pulsed Nd:YAG laser irradiation on multi-walled carbon nanotubes film, *Thin Solid Films*, 517 (2009), 3854-3858

[3] Iwasaki Y. *et al.*, An Automatic Measurement Algorithm for the Diameters of Carbon Nanotubes by Using Image Processing, *Technological Developments in Networking, Education and Automation*, Springer (2010), 275-280

[4] Otsu N., A Threshold Selection Method from Gray-Level Histograms, *IEEE Transactions on Systems, Man, and Cybernetics*, 9 (1979), No. 1, 62-66

***Authors**: Prof. Dr. Yoichiro Iwasaki, Graduate School of Industrial Engineering, Tokai University, 9-1-1 Toroku, Kumamoto 862-8652, Japan, E-mail: iwasaki@tokai.ac.jp; Prof. Dr. Toshiyuki Nakamiya, Graduate School of Industrial Engineering, Tokai University, 9-1-1 Toroku, Kumamoto 862-8652, Japan, E-mail: nakamiya@tokai.ac.jp; Mr. Ryosuke Kozai, Graduate School of Industrial Engineering, Tokai University, 9-1-1 Toroku, Kumamoto 862-8652, Japan, E-mail: 0bijm002@mail.tokai-u.jp; Dr. Fumiaki Mitsugi, Graduate School of Science and Technology, Kumamoto University, 2-39-1 Kurokami, Kumamoto 860-8555, Japan, E-mail: mitsugi@cs.kumamoto-u.ac.jp; Prof. Dr. Tomoaki Ikegami, Graduate School of Science and Technology, Kumamoto University, 2-39-1 Kurokami, Kumamoto 860-8555, Japan, E-mail: ikegami@cs.kumamoto-u.ac.jp.*

SELF-PULSING DC DRIVEN DISCHARGES IN PREHEATED AIR AIMED FOR PLASMA ASSISTED COMBUSTION

Mario JANDA[1], Zdenko MACHALA[1], Deanna LACOSTE[2], Karol HENSEL[1], Christophe LAUX[2]

Comenius University Bratislava (1), Ecole Centrale Paris (2)

***Abstract**. We studied electrical and optical properties of DC driven self-pulsing discharges with kHz repetition frequency and short current pulse duration (~ns) in atmospheric pressure air preheated up to 1000 K. The goal was to find a low cost repetitively pulsed discharge operating at high temperatures usable for stabilization of lean flames. The utilization of obtained discharge regimes for the plasma assisted combustion is the next step in this research.*

Keywords: self-pulsing discharges, preheated air, plasma assisted combustion

Introduction

Nanosecond repetitively pulsed (NRD) discharge operating at frequency above 10 kHz was shown to be able to stabilize lean flames, while consuming only ~70 W [1]. Using lean combustion mixtures leads to decrease of NO generation thanks to lower combustion temperature. The plasma assisted combustion has therefore significant environmental benefits. However, the disadvantage of NRP discharge could be relatively expensive high voltage (HV) high frequency pulse generators. We therefore plan to test for stabilization of lean flames another type of repetitively pulsed discharge named transient spark (TS) [2]. Despite the pulsed character, TS is driven by a simpler and cheaper DC HV power supply, and it already proved to be usable for several environmental and bio-medical applications [3]. However, for purposes of plasma assisted combustion, we first had to test and optimize the behaviour of TS in preheated air, since we studied it only at laboratory temperature till now.

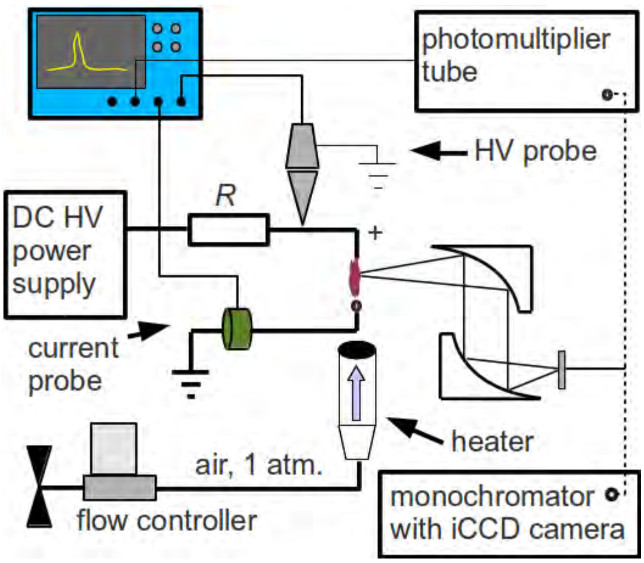

Fig.1. Schematic of the experimental set-up.

Experimental set-up

Experiments were carried out in atmospheric pressure air preheated with controlled ohmic heater to 300–973 K, with an axial flow with velocity 2 m/s. The distance between the stainless steel needle electrodes (point-to-plain configuration with anode at the top) was 5 mm. A positive polarity DC HV power supply HCL 14-20000 connected via a series resistor (R = 10 MΩ) was used to generate a discharge. The discharge voltage was measured by a HV probe LeCroy PMK-14kVAC and the discharge current was measured using a Pearson Electronics 2877 (1V/A) current probe linked to a 350 MHz digitizing oscilloscope LeCroy Waverunner 434 (maximum 2GS/s).

The UV-VIS spectra were obtained using a monochromator (Acton SpectraPro 2500i) fitted with an intensified CCD camera (Princeton Instruments PI-MAX). For time-resolved optical emission measurements, a photomultiplier tube (PMT) module with a 1.4-ns rise time (Hamamatsu H9305-3) was used. Besides the total emission, we monitored emission of N_2 2nd positive system by inserting a bandpass interference filter transparent at 337 nm (3nm width) into the optical path. The experimental set-up is depicted on Fig. 1.

Results and Discussion

Our previous studies of TS at input gas temperature (T_g) 300 K showed that it is initiated by a streamer, which creates a relatively conductive plasma bridge between the electrodes. After this, during the streamer-to-spark transition phase, the temperature inside this channel grows due to the joule heating. A transition to the short (~ns) high current (~A) spark pulse occurs at ~1000 K [4]. During the spark, the discharge voltage U drops almost to zero and the whole energy accumulated in the internal capacity C of used electrical circuit (~10-40 pF) is delivered to the gap. This small value of C is responsible for short duration of TS current pulses and therefore also for characteristics of generated plasma, which remains non-thermal. After the conductivity of plasma generated by TS decreases enough, charging of C and a growth of U start again. As U exceeds certain threshold value, we observe streamer corona discharge. Further increase of U above certain threshold value U_{TS} leads to the generation of 'stronger' streamers, capable to initiate another TS pulse. TS discharge is thus based on charging and discharging of C, with a typical frequency f from given approximately by:

(1) $$f \approx \frac{1}{RC\ln\left(\frac{U_o}{U_o - U_{TS}}\right)}$$

where U_o is the onset voltage delivered by power supply.

The growth of f up to ~10 kHz can thus be controlled by the increase of U_o. At higher f, new discharge regime appears – pulse-less high pressure glow discharge (GD) [4] with a constant current starting from ~2 mA. However, due to large external resistor R and U_o limited to maximum 20 kV, the GD regime was not stable in our experiments. The discharge randomly switched between GD and high frequency TS regimes.

When we increase input gas temperature to 400 K and higher, we observed new phenomenon. Even the first streamers, which appear at $U_{STR} \approx 3$ kV (this is well below U_{TS}) are followed by instantaneous partial drop of the voltage to a certain minimal value U_{min}. However, this voltage is drop is not so drastic as in case of TS. It is rather gradual and it takes several μs to reach U_{min}. After this partial discharging event, C is charged again till U_{STR} is reached. As a result, streamer pulses appear with a relatively regular frequency f_{STR}, which is given by a modified version of Eq. 1, where U_{min} is also considered:

$$f_{STR} \approx \frac{1}{RC\ln\left(\frac{U_o - U_{\min}}{U_o - U_{STR}}\right)} \quad (2)$$

We thus obtained a new self-pulsing discharge regime preliminarily named 'repetitive streamer' (RS) discharge. This regime actually initially inhibits the appearance of TS, because U_{TS} cannot be reached due to relatively significant voltage drop after the streamers. However, we observed that U_{min} tends to decrease and the voltage drop accelerates with increasing T_g and increasing f_{STR}. And as U_{min} approaches ~200 V, we again observed much narrower and higher current pulses attributable to TS discharge. Although, compared to TS pulses at T_g = 300 K, at higher T_g there is no streamer-to-spark transition time, and fast discharging with spark current pulse starts almost instantaneously after the streamer.

At higher T_g, a stable TS discharge was observed only at 1000 K. At lower temperatures, we mostly observed only unstable TS, i. e. the discharge randomly switched between RS and TS regimes, generating current pulses of two types (see Fig. 2 for illustration of RS and TS current pulses obtained both at 900 K). We even observed a situation when discharged randomly switched between all three possible regimes, including GD. A chart describing achievable discharge regimes depending on T_g and U_o is depicted in Fig. 3.

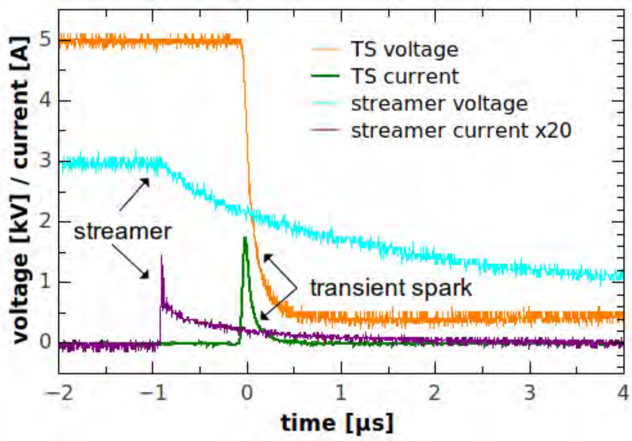

Fig.2. Typical waveforms of streamer regime (current multiplied by 20), compared to current pulse of unstable TS regime, T_g = 900 K.

Optical characteristics of different discharge regimes also changes. In TS, one can see two peaks of the total emission: the first one is produced by the streamer, and the second one by the short spark. The emission during the 'streamer' peak can be mostly attributed to the N_2(C) species, whereas the 'spark' peak is mostly due to the excited atomic species. Compared to TS, the emission from N_2(C) does not change much in RS discharge regime, but the emission of excited atomic species almost completely disappears. In RS regime we also did observe any gas heating as it was in case of TS at T_g = 300 K. No gas heating was observed also in case of TS discharge regime at T_g = 1000 K.

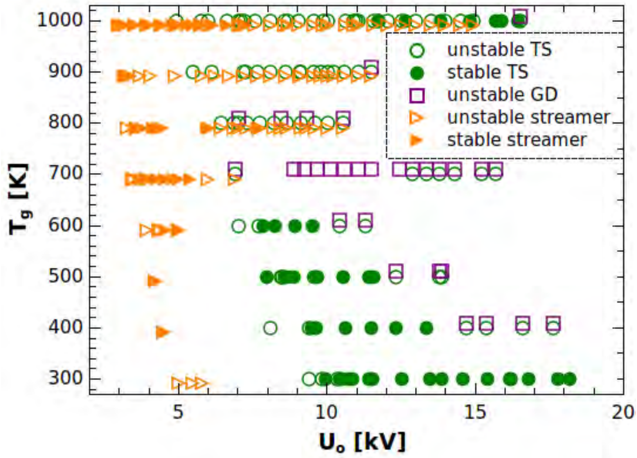

Fig.3. Discharge regimes as function of applied voltage U_o and input gas temperature T_g.

Conclusions

We succeeded to generate high frequency self-pulsing discharges using simple electrical set-up containing a DC power supply in pre-heated up to 1000 K. However, changes of input gas temperature significantly influenced discharge regimes we were able to generate. Properties of generated plasma and amount of produced reactive species might significantly differ from regime to regime, as can be deduced from optical measurements. It is therefore necessary to perform further research to identify the best possible application for observed discharge regimes. As a first step, we will try transient spark for the stabilization of lean flames.

Acknowledgements: Effort sponsored by Slovak Research and Development Agency APVV SK-FR-0038-09, and Slovak grant agency VEGA 1/0668/11 and 1/0711/09.

REFERENCES

[1] Pilla G. et al., *IEEE Trans. Plasma Sci.*, 34 (2006) 2471
[2] Janda M. et al., *Plasma Sources Sci. Technol.*, 20 (2011) Art. No. 035015
[3] Machala Z. at al., *J. Mol. Spectrosc.*, 243 (2007) 194
[4] Machala Z. at al., *J. Advanced Oxid. Technol.*, 7 (2004) 133

***Authors**: Mario Janda, PhD., Zdenko Machala, PhD., Karol Hensel PhD., Division of Environmental Physics, Faculty of Mathematics, Physics and Informatics, Comenius University in Bratislava, Mlynska dolina F2, 84248 Bratislava, Slovakia, E-mail: janda@fmph.uniba.sk; Deanna Lacoste, PhD., Prof. Christophe O. Laux, PhD., Laboratoire EM2C CNRS-UPR 288, Ecole Centrale Paris, Grand Voie des Vignes, 92290 Chatenay-Malabry, France, E-mail: laux@em2c.ecp.fr.*

Conference ELMECO–7
ELECTROMAGNETIC DEVICES AND PROCESSES IN ENVIRONMENT PROTECTION
joint with 10th Seminar AoS-10 APPLICATIONS OF SUPERCONDUCTORS
28–30.09.2011, Nałęczów, Poland

PROMOTING RENEWABLE ENERGY SOURCES TO SUPPLY HOME POWER PLANTS

Tadeusz JANOWSKI[1], Mariusz HOLUK[2]

Lublin University of Technology (1), The State School of Higher Education in Chełm (2)

***Abstract**. The purpose of this article is promoting renewable energy sources connected with micro combined heat and power systems in lubelskie province. The special attention was focused in micro-cogeneration systems on Stirling engine. The premise of concerning the possibility of biomass in micro combined heat and power system in agricultural farms in the following years.*

***Streszczenie.** Celem artykułu jest promowanie odnawialnych źródeł energii związanych z układami skojarzonego wytwarzania ciepła I energii elektrycznej w województwie lubelskim. Przedstawiono układy mikrokogeneracyjne wykorzystujące silnik Stirlinga. Omówiono przesłanki możliwości wykorzystania biomasy w kogeneracji energii elektrycznej I ciepła w gospodarstwach rolnych w najbliższych latach.*

Keywords: Micro-cogeneration, renewable energy sources, Stirling engine.

Słowa kluczowe: Mikrokogeneracja, odnawialne źródła energii, silnik Stirlinga. (Promowanie odnawialnych źródeł energii poprzez elektrociepłownie domowe).

Introduction

Renewable sources of energy appear promising in reducing emissions and slowing down world's energy consumption. New technologies offer the promise of clean, abundant energy gathered from self-renewing resources such as the sun, wind, earth and plants. The article will review the possibilities of biomass application in microcogeneration devices and let specify the profitability of microCHPH application (Eng. Micro Combined Heat and Power for the Home) with Stirling engine in agricultural farms.

Micro combined heat and power plants are promising, innovative and commercial solution to produce both, heat and electric power in decentralised power plants. Using biomass as a fuel for these power plants confers advantages in terms of clean energy.

The exploitation of renewable sources of energy in cogeneration is crucial issue, in accordance with the present tendencies of stable development in power industry.

The reduced resources of primary energy, dangers caused by greenhouse gases emission, low efficiency of transmission heat energy systems, requirements of high quality of electric energy by advanced industrial and computer technologies [4]. They require searching other ways of producing, transmission and the using of electric and heat energy. One of the solution is the idea of generating electric energy and heat directly in a flat, especially in a detached house called "Power plant for Home or Micro Combined Heat and Power for the Home".

The high efficiency (about 90%) of domestic microCHPH ensures the less exploitation of natural gas resources and at the same time it places in the tendencies of stable development. The basic source of renewable energy in Poland is biomass in solid form, biogas and biofuels.

Producing heat from biomass is practised in our climate from old times and it is taken control, however the heat conversion in electric energy is developed in big power stations and in heat and power stations.

In domestic micro heat and power stations (microCHPH) using biomass to convert the heat in mechanical energy the most predisposed is engine with external consuming like Stirling engine because: it is quiet and can be put in a flat and can be powered by any renewable fuel (biogas, liquid biofuels, wood, straw, briquettes), as well as non renewable (natural gas, oil derivatives fuel, coal or peat).

The experimental research carried out concerning the biomass application by microCHPH system application it is the problem that has not been taken up in Poland yet.

Methodology

Searching of new solutions for electric power warranty and heating small objects caused the technologies development connected with associated production of heat and electric energy on the basis of sources of small power with renewable sources usage [1].

Combined Heat and Power (CHP) is the simultaneous production of heat and power from primary fuel (gas, oil, coal). In any electricity generating plant using a thermal process, both heat and power are produced. Combined Heat and Power is industrial processes or to heat buildings and generally produces electrical power near the point of demand, substantially avoiding the electrical distribution losses.

The idea of microCHPH system operation consists in simultaneously production of two or more types of usable energy from one source of primary energy and using waste heat from devices producing electric energy. The diagram presents the way this system works in picture 1.

The electricity and the teat are produced at the location they will be consumed, thus avoiding the electrical and thermal distribution losses associated with centralized plant. Equally importantly, the heat will be produced at the time it is required by the individual household, unlike large scale communal CHP schemes which are unable to respond to the thermal demands of individual homes. In fact, microCHPH works very much like the gas boiler in a central heating system and heats the home in just the same way. However, at the same time it generates electricity, most of which is used in that home. The remainder is exported to the grid. It is not usually practical to provide all of the homes electricity from the microCHPH unit all the time. Instead, peak electrical needs are met by importing some power from the grid. Although the home may produce the same total amount of electricity over the course of a year as it consumes. It will import at some time and export at others [2].

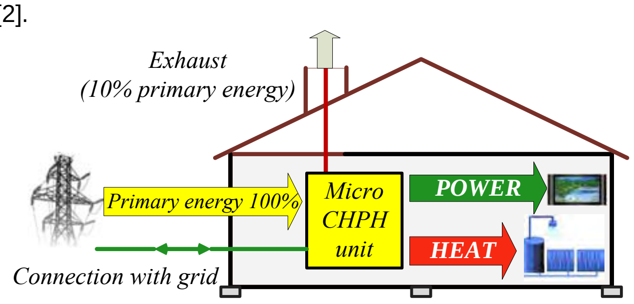

Fig. 1. The system of microCHPH

Among the latest solutions the small power systems (microCHPH) are proposed below 10 kW heat power and electric power 1 – 5 kW dedicated to separate household. The idea of operation such „micro heat and power station at home" consists in placing the source of electric energy as well as heat energy inside the powered building, which eliminates the total loss of heat and transmission costs.

In micro CHP system the primary energy embodied in natural or liquid gas, fuel oil, biomass and others is transformed into electric and heating energy. Efficiency of the system is around 90%. Electric energy is produced in a turbine of 10-45% efficiency. The heat, which is a result of fuel combustion, is recovered in a heat exchanging system and constitutes 45-80 % of primary energy. It heats mains water and water in the central heating.

Discussion and conclusions

The article verify the promotion renewable energy sources, the possibilities of different forms of biomass application in microcogenertion devices and let specify the profitability of microCHPH in agricultural farms. Methodology of combined heat and power production is intended to prepare experimental system model.

It is an important scientific issue to conduct research regarding combined heat and power systems with the use of microcogeration unit with the Stirling engine fed by biomass, which can operate while burning different forms of primary energy. The analysis of microCHPH system fed by biomass in individual households has never been investigated on a larger scale before in Poland, which proves its innovation.

In EU politics new energy priorities have been applied which emphasize the use of energy from renewable sources and underscore high restrictions regarding the emission of pollution. When EU curtailments are taken into consideration, the projects involving the use of biomass in microcogeneration seem to be even more crucial. This will enable the development of biomass production for power engineering purposes. Promoting the solutions included in the project aims at fulfilling international and EU standards.

The subject becomes part of strategy accepted by Poland. It is in accordance with UE guidelines and with Regional Strategy of lubelskie voivodeship Innovation and with the voivodeship programme of development alternative sources of energy for lubelskie voivodeship realised which makes conditions to use renewable energies on the level up to 7,5% in 2010 and 14% in 2020, accepted in 2004.

The application of the solution proposed can bring tangible benefits for natural environment by: the reliability increase the powering of objects, waste usage (biomass), better development of refuse dump (biogas), better usage of renewable sources of primary energy, decreasing the emission of greenhouse gases.

The potential consumers of devices to producing electric energy for households from renewable sources are small households especially from rural areas with poor infrastructure connected with support in media, for example, gas or heat, and possessing the potential sources of fuels from renewable sources, for example, biomass. The application of technology proposed concerning obtaining the electric and heat energy in separate households can cause the reduction of households maintenance costs, and the increase of life quality of members of local communities.

Prospective users of devices producing the electric energy from renewable sources for individual households are agricultural farms and small possessions situated in countryside areas, where infrastructure concerning gas and heat supply is poorly developed but where there can be found renewable sources of energy.

The measuring station will undergo exploitation tests. The device efficiency will be specified as well as regulations of usage will be set when using the primary energy from renewable sources. The results will indicate the range of microcogeneration systems implementation in individual households and apartments. The experimental research will allow denoting profitability of biomass usage in domestic microcogeneration in lubelskie province.

Information gathered, results and experiments will be useful for further research regarding associated heat and electricity production.

REFERENCES

[1] Alhakeem S.A.M., Al.-Tai M.A., Utilisation of micro combined heat and power system using alternative fuels, IEEE Explore, UPEC 2007
[2] Harrisom J., Micro CHP the big Picture, 2010
[3] Janowski T., Holuk M., The microcogeneration system on Stirling engine, Proceedings of Elektrotechnical Institute , 249 (2011)
[4] Hradilek Z., Moldrik P., Chválek R., Electrical energy storage systems, Electrical Review, 2 (2011)

***Authors**: prof. dr hab. inż. Tadeusz Janowski, Lublin University of Technology, Faculty of Electrical Engineering and Komputer Science, 38A Nadbystrzycka Street, 20-618 Lublin, E-mail: t.janowski@pollub.pl; mgr inż. Mariusz Holuk, The State School of Higher Education in Chełm, The Institute of Technical Sciences, 54 Pocztowa Street, 22-100 Chełm, E-mail: mholuk@pwsz.chelm.pl.*

MODELOWANIE POWROTNEJ CHARAKTERYSTYKI ROZGAŁĘZIONEJ TAŚMY NADPRZEWODNIKOWEJ HTS 2G

Tadeusz JANOWSKI, Joanna KOZIEŁ, Tomasz GIŻEWSKI, Dariusz Czerwiński

Lublin University of Technology, Institute of Electrical Engineering and Electrotechnologies

Abtract. *The paper presents an modeling algorithm of the retrogressive branched characteristics of HTS superconductors for the simulation of dynamic circuits. The basis of the considerations is the typical macroscopic current-voltage characteristics of superconducting HTS tapes. Given the specificity and the need for analysis of the circuit model, the authors propose to apply the Preisach model with static characteristics simulated as a Gaussian function. Parameters of the Gaussian function are related to the typical observable physical properties of HTS tape. As a basis for discussion the current-voltage characteristics of HTS tapes SF12050 Super Power Inc. were proposed. HTS tapes were prepared for the circuit transient analysis of transformer type superconducting current limiter.*

Streszczenie. *Praca przedstawia algorytm modelowania powrotnej charakterystyki rozgałęzionej nadprzewodników HTS dla potrzeb dynamicznego modelowania obwodów. Podstawą rozważań jest typowa makroskopowa charakterystyka prądowo- napięciowa taśmy nadprzewodnikowej HTS. Uwzględniając specyfikę i potrzebę analiz obwodowych autorzy proponują zastosowanie modelu Preisacha z charakterystyką statyczną w postaci funkcji Gaussa. Parametry funkcji Gaussa autorzy uzależniają od typowych obserwowalnych właściwości fizycznych takich jak : prąd krytyczny. Jako podstawę dyskusji zaproponowano przebiegi charakterystyk prądowo- napięciowych taśmy HTS SF12050 firmy Super Power Inc., sporządzonych dla potrzeb obwodowej analizy stanów przejściowych nadprzewodnikowego ogranicznika prądu typu transformatorowego.*

Keywords: superconducting tapes HTS 2G, critical current, superconducting fault current limiter.
Słowa kluczowe: taśmy nadprzewodnikowe HTS 2G, prąd krytyczny, nadprzewodnikowy ogranicznik prądu.

Wstęp

Nadprzewodnikowy ogranicznik prądu typu transformatorowego działa analogicznie jak transformator z przełącznikiem wartości rezystancji (element nadprzewodnikowy) w obwodzie wtórnym. Analiza pracy urządzeń z elementami nadprzewodnikowymi przeprowadzana jest na dwa sposoby. Pierwszy, związany z (najczęściej numeryczną) analizą pola elektromagnetycznego, sprzężonego z obwodowym modelem urządzenia. Drugi rodzaj analizy to typowo obwodowa analiza stanów przejściowych, związana z charakterystykami makroskopowymi z jednym stopniem swobody. Obydwie metody ogranicza specyfika zjawisk dynamicznych stanów rezystywnego i nadprzewodnikowego.

Postać charakterystyki rozgałęzionej elementu nadprzewodnikowego

Analizy polowo-obwodowe ograniczone są możliwością prostego uwzględnienia nieliniowości materiałów nadprzewodzących. Jak wiadomo ich charakterystyki zależą od szeregu wartości oddziałujących: natężenie pola magnetycznego H, temperatury T oraz wartości natężenia prądu I.

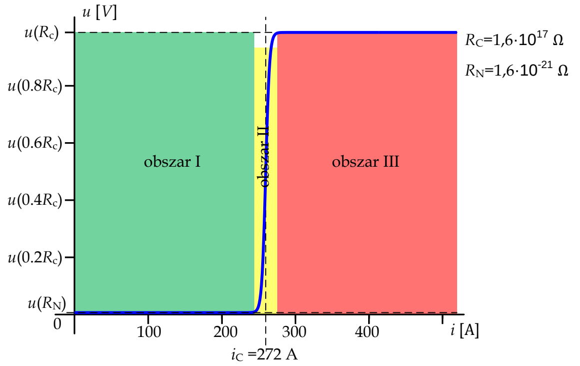

Rys. 1. Podstawowa charakterystyka zewnętrzna materiału nadprzewodnikowego HTS

Rozważanie stanów przejściowych, z możliwie dokładnym przybliżeniem wyniku w stosunku do wartości obserwowalnych eksperymentalnie, wymaga sformułowania równania stanu, uwzględniającego precyzyjną charakterystykę makroskopową elementu nadprzewodnikowego. Materiały nadprzewodnikowe rozważać można w trzech stanach pracy: nadprzewodzącym, rezystywnym i przejściowym (Rys.1). W pierwszym przypadku wykazują one blisko zerową rezystywność, co występuje jednak tylko w ściśle określonych warunkach. Podstawowe kryteria zewnętrzne nadprzewodnictwa [7]: temperatura krytyczna, gęstość prądu krytycznego oraz krytyczna wartość natężenia pola magnetycznego wyznaczają powierzchnię krytyczną poniżej której element znajduje się w stanie nadprzewodzącym (Rys. 2.).

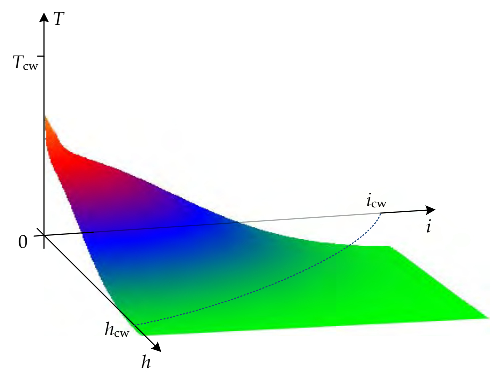

Rys.2. Względna powierzchnia krytyczna stanu nadprzewodnictwa

Rezystancja taśmy nadprzewodnikowej drugiej generacji

Struktura taśmy nadprzewodnikowej, poddawanej analizie składa się z siedmiu lub dziewięciu warstw [5]. Z punktu widzenia modelu makroskopowego, istotne są tylko warstwy przewodzące (HTS, srebro, hastelloy oraz opcjonalnie miedź)[6],[7]. Komponenty te w strukturze rozmieszczone są w taki sposób, że elektrycznie tworzą układ równolegle połączonych elementów. Badania obejmują temperatury w granicach kriogenicznych oraz duży zakres zmian wartości natężenia prądu. Charakterystyki elementów przewodzących konstrukcyjnych (srebro, hastelloy, miedź) wykazują nieliniowość. Jednakże zmiany te są na tyle nieistotne, że przyjęto ich liniową charakterystykę w funkcji prądu.

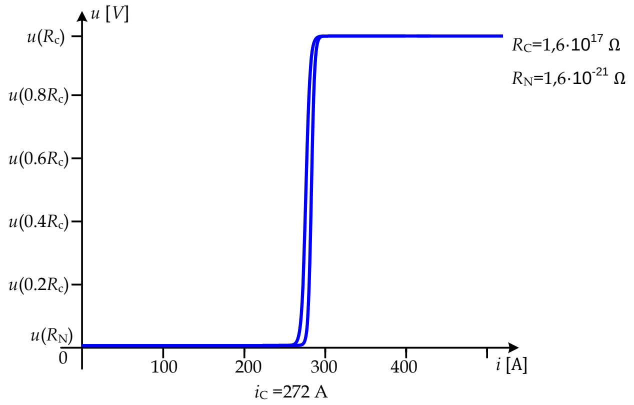

Rys.3. Rozgałęziona charakterystyka powrotna materiału nadprzewodnikowego

Fenomenologiczny opis modelu

Model Preisacha, jako makroskopowy model układu jest przedstawiany poprzez złożenie ważonych operatorów histerezowych $\gamma_{\alpha\beta}$, przyjmujących wartości -1 lub 1 w zadanych granicach narastającej lub opadającej wartości wymuszającej [2].

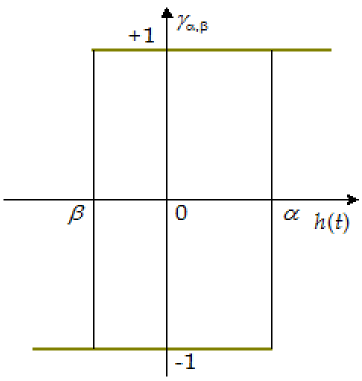

Rys .4. Elementarny operator histerezy

Matematycznie model Preisacha zdefiniowano w postaci odwzorowania w ograniczonej dziedzinie dwuwymiarowego zbioru liczb rzeczywistych. Jest to sumowanie dla każdego elementu dziedziny udziału każdego z operatorów histerezowych $\gamma_{\alpha\beta}$. Wartość tego elementu określa się poprzez przyporządkowanie każdemu z nich położenia współrzędnymi (α, β) oraz dobranie wartości funkcji gęstości $\mu(\alpha, \beta)$.

Każdy z pojedynczych elementarnych operatorów reaguje wartością odpowiedzi stosownie do wartości wejściowej. Suma ważona wszystkich wartości wyjściowych elementarnych operatorów, przemnożonych przez funkcję gęstości ustala całkowite wyjście układu. Zbiór wag $\mu(\alpha, \beta)$ kształtuje funkcję wagi, którą zdefiniowano jako opis względnego udziału elementarnego operatora do całkowitej histerezy [2].

Modelowanie charakterystyki powrotnej HTS

Analogie pomiędzy oddziaływaniem pola magnetycznego na poszczególne domeny magnetyczne, umieszczonego w nim materiału ferromagnetycznego a całościowym obiegiem histerezy, pozwoliły sformułować model opisujący względny udział poszczególnych podobszarów w rozgałęzionej charakterystyce zewnętrznej. Tego typu opis obiektu usprawiedliwia dynamiczne modelowanie urządzeń, których zasada działania związana jest z przejściem ze stanu nadprzewodnikowego do rezystywnego.

Na wykresie przedstawionym na Rysunku 5 zauważono, że jakościowo przebieg odzwierciedla z dużym stopniem zgodności charakterystykę z Rysunku 3. Informacja ta jest o tyle istotna, że przedstawiony model umożliwia dynamiczne modelowanie elementu nadprzewodnikowego oraz związanej z nim charakterystyki taśmy na podstawie funkcji wagi.

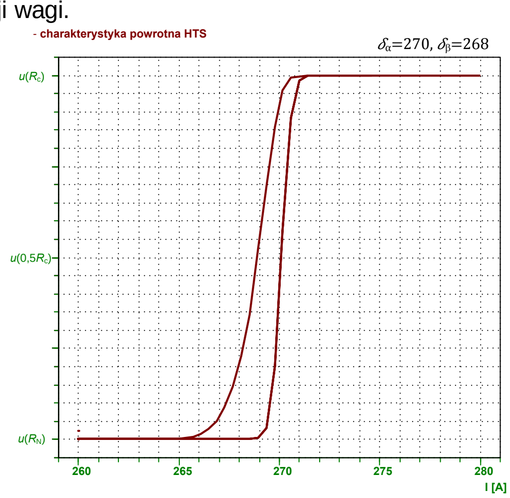

Rys.5. Charakterystyka powrotna modelowana dla materiału

Wnioski

Zastosowanie modelu Preisacha pozwala na wykorzystanie licznych jego własności, pozwalających ograniczać błąd modelowania dynamicznego. Wprawdzie jest to model statyczny, ale dzięki możliwości zachowania historii przebiegu wartości wejściowych w granicach występujących ekstremów oraz możliwości tworzenia charakterystyki w pełni rozgałęzionej, można opracować charakterystyki cząstkowe. Przeprowadzając modelowanie dla zmian dynamicznych istnieje możliwość ograniczenia błędu symulacji.

REFERENCES

1. Azzerboni B., Cardelli E., Finocchio G.: A comparative study of Preisach scalar hysteresis models. *Physica* B 343 (2004).
2. Giżewski T.: *Modelowanie obwodów magnetycznych przy zastosowaniu algorytmów sztucznych sieci neuronowych*, rozprawa doktorska prezentowana w Politechnice Lubelskiej, Lublin 2009.
3. Kozak S.: Modelowanie elektrycznych urządzeń nadprzewodnikowych, *Prace Instytutu Elektrotechniki,* Zeszyt 221, 2005.
4. Mayergoyz I. D.: *Mathematical Models of Hysteresis, Springer-Verlag,* Berlin 2002.
5. Yuan W.: *Second-Generation High-Temperature Superconducting Coils and Their Applications for Energy Storage,* Springer-Verlag London 2011.
6. Superpower Inc. Technical documents. http://www.superpower-inc.com.46
7. Kalsi S.S.: *Applications of high temperature superconductors to electric power equipment*, A JOHN WILEY & SONS, INC., PUBLICATION,IEEE PRESS, New Jersey 2011.

***Authors**: prof. dr hab. inż. Tadeusz Janowski, mgr inż. Joanna Kozieł, dr inż. Tomasz Giżewski, dr inż. Dariusz Czerwiński, Politechnika Lubelska, Wydział Elektrotechniki i Informatyki, Instytut Podstaw Elektrotechniki i Elektrotechnologii, ul. Nadbystrzycka 38A, 20-618 Lublin,*

Conference ELMECO–7
ELECTROMAGNETIC DEVICES AND PROCESSES IN ENVIRONMENT PROTECTION
joint with 10th Seminar AoS-10 APPLICATIONS OF SUPERCONDUCTORS
28–30.09.2011, Nałęczów, Poland

TRANSFORMATORY NADPRZEWODNIKOWE ODPORNE NA ZWARCIA I OGRANICZAJĄCE PRĄDY ZWARCIA

Tadeusz JANOWSKI [1], Grzegorz WOJTASIEWICZ [2]

Politechnika Lubelska (1), Instytut Elektrotechniki w Warszawie (2)

Abstract. The fault current limiting feature of SC transformer with HTS 2G windings provide protection and significantly reduce wear and tear for circuit breakers and other substation power equipment. An analysis result shows that YBCO 2G tapes enable to built superconducting transformers limiting the short circuit currents. **Fault current limitation in power network by superconducting transformers.**

Streszczenie. The fault current limiting feature of SC transformer with HTS 2G windings provide protection and significantly reduce wear and tear for circuit breakers and other substation power equipment. An analysis result shows that YBCO 2G tapes enable to built superconducting transformers limiting the short circuit currents. **Fault current limitation in power network by superconducting transformers.**

Keywords: superconducting transformer, 2nd generation HTS tape, fault current limitation.
Słowa kluczowe: transformator nadprzewodnikowy, taśma HTS 2G (2-giej generacji), ograniczanie prądów zwarcia

Wstęp

Pierwsze próby budowy transformatorów z rdzeniem ferromagnetycznym i bezrdzeniowych z uzwojeniami z nadprzewodnika Nb-Ti, w latach 70-tych ubiegłego stulecia, nie odniosły sukcesu. Badania nad transformatorami z nadprzewodnikowymi uzwojeniami HTS podjęto w latach 90 XX wieku, wykorzystując włókniste (matrycowe) przewody bizmutowe (Bi-2212 i Bi-2223), a w latach 2002 – 2007 powstało kilka prototypowych konstrukcji o mocach (1 ÷ 100) MVA. Przewody konstrukcji matrycowej były zbyt słabe mechanicznie, o dopuszczalnych naprężeniach niższych od miedzi (75 ÷ 268) MPa i nie wytrzymywały naprężeń występujących przy gęstości prądu krytycznego.

Bardziej intensywne badania prowadzone w zakresie nadprzewodnikowych ograniczników prądu zwarcia (SFCL) doprowadziły do wyraźnego wzrostu rezystywności nadprzewodników w stanie nienadprzewodzącym przez domieszkowanie niklem i cerem, ale również do powstania taśm warstwowych 2G, w których nadprzewodnik stanowi 1% grubości taśmy a stabilizator i podłoże mają dużą rezystywność. Prąd przemienny płynący w stanie nadprzewodzącym warstwą nadprzewodnika indukuje małe straty w pozostałych warstwach, a po przekroczeniu gęstości prądu krytycznego płynie wszystkimi warstwami taśmy.

Do chłodzenia uzwojeń stosuje się techniki chłodzenia w kąpieli, z wykorzystaniem ciekłego azotu, lub chłodzenie kontaktowe. Z dotychczasowych badań i analiz wynika, że wydatki na chłodzenie uzwojeń transformatora nadprzewodnikowego pochłaniają około ¼ zysku z ograniczenia strat mocy w uzwojeniach (tab. 1).

Tabela 1. Porównanie strat mocy i sprawności transformatorów: konwencjonalnego i nadprzewodnikowego, o mocy 20 MVA [3]

Transformator 3-fazowy o mocy 20 MVA	Z uzwojeniami Cu	Z uzwojeniami HTS
straty ogółem, w tym:	100%	16%
straty w uzwojeniach	91%	3%
straty w rdzeniu	9%	5%
moc chłodzenia	-	8%
sprawność	99,4%	99,9%
masa rdzenia	100%	54%
- wartość w % względem wartości transformatora konwencjonalnego przyjętej za 100		

Nowe przewody nadprzewodnikowe HTS 2G wytwarzane na bazie itru (YBCO), o dużej rezystywności w stanie nienadprzewodzącym pozwalają budować transformatory odporne na zwarcia, ponieważ po przekroczeniu gęstości prądu krytycznego nadprzewodnika rezystancja uzwojeń gwałtownie wzrasta do wartości, która może ograniczyć prąd zwarcia nawet do wartości mniejszej od prądu znamionowego transformatora.

Uwzględniając powyższe do zalet transformatorów z uzwojeniami nadprzewodnikowymi można zaliczyć:

- ograniczenie strat mocy w uzwojeniach. Straty Joule'a, ze względu na zerową rezystancję nadprzewodnika w stanie nadprzewodzącym są wyeliminowane,
- odporność na zwarcia. Wartość prądu zwarcia nie może wzrosnąć ponad wartości prądu krytycznego uzwojenia nadprzewodnikowego transformatora,
- eliminacje olejowego układu chłodzenia. Są one przez to bezpieczne i przyjazne dla środowiska naturalnego i użytkowników.
- zmniejszenie masy i gabarytów transformatorów.

Odporność transformatora nadprzewodnikowego na zwarcia. Ograniczanie prądów zwarcia.

Odporność transformatora nadprzewodnikowego na zwarcia, będąca efektem samoograniczenia prądu zwarcia przez uzwojenia nadprzewodnikowe, jest najważniejszą korzyścią płynącą z zastąpienia uzwojeń konwencjonalnych uzwojeniami nadprzewodnikowymi. Poziom samoograniczenia prądu zwarcia zależy od charakterystyki pracy uzwojeń nadprzewodnikowych, ich budowy oraz parametrów zastosowanego przewodu nadprzewodnikowego HTS (2G). Odporność transformatora nadprzewodnikowego na zwarcia umożliwia małą wartość procentowego napięcia zwarcia, a tym samym obniża wahania napięć w sieci przy zmianach jej obciążenia.

Tabela 2. Procentowe napięcia zwarcia transformatorów z uzwojeniami konwencjonalnymi i nadprzewodnikowymi

	Procentowe napięcie zwarcia - u_z %	
Transformatory	Konwencjonalne	Nadprzewodnikowe
małej mocy	< 6	< 2 – 5
dużej mocy	10 – 15	< 6 – 10

W tabeli 2 porównano procentowe napięcia zwarcia transformatorów z uzwojeniami konwencjonalnymi oraz nadprzewodnikowymi, o takiej samej wysokości uzwojeń i takiej samej szczelinie między uzwojeniami δ.

Napięcie zwarcia transformatorów nadprzewodnikowych jest mniejsze od napięcia zwarcia transformatorów konwencjonalnych. Jest ono proporcjonalne do pola powierzchni trapezu z rys. 1. Ze względu na znacznie mniejszą grubość uzwojeń nadprzewodnikowych mniejsze jest pole powierzchni trapezu, a więc i mniejsze napięcie zwarcia, przy takiej samej szczelinie powietrznej δ. Można przyjąć, że napięcie zwarcia transformatora nadprzewodnikowego zależy tylko od szerokości szczeliny powietrznej, ponieważ uzwojenia transformatorów nadprzewodnikowych są bardzo cienkie ($a_{Cu} >> a_{HTS}$), rys 1).

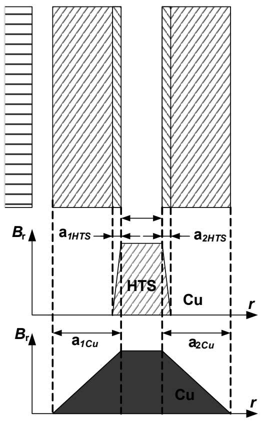

Rys. 1. Wpływ grubości uzwojeń transformatora na wartość napięcia zwarcia

Jednym z czynników decydującym o doborze wartości napięcia zwarcia transformatorów konwencjonalnych jest dopuszczalna wartość prądu zwarciowego. Ze względu na dynamiczne skutki zwarcia w transformatorach dużych mocy nie można dopuścić do dużych wartości prądów zwarciowych. W transformatorach z uzwojeniami nadprzewodnikowymi przekroczenie, w skutek zwarcia, wartości prądu krytycznego nadprzewodnika powoduje jego natychmiastowe przejście do stanu rezystywnego, co skutkuje samoograniczeniem prądu zwarciowego. Proces przejścia uzwojenia nadprzewodnikowego do stanu rezystywnego, oraz czas, po którym to przejście nastąpi, zależą od kształtu charakterystyki prądowo napięciowej uzwojenia nadprzewodnikowego (rys. 2)

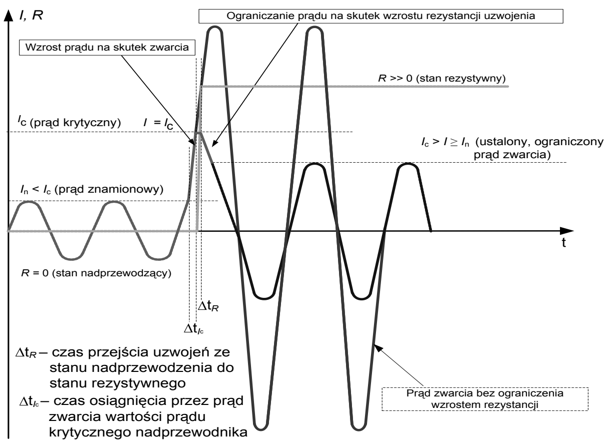

nadprzewodnikowym transformatora

W stanie nadprzewodzącym rezystancja uzwojenia R jest równa zeru, a prąd znamionowy I_n mniejszy od prądu krytycznego nadprzewodnika I_c. Po wystąpieniu zwarcia prąd uzwojenia zaczyna wzrastać, i w czasie t_1 osiąga wartość prądu krytycznego nadprzewodnika I_c. Zaczyna się stan przejściowy, trwający do czasu t_2, kiedy to następuje całkowite przejście uzwojenia nadprzewodnikowego do stanu rezystywnego. Rezystancja uzwojenia R osiąga wartość $R >> 0$, podczas gdy wartość prądu zwarcia zostaje ograniczona do wartości $I \geq I_n$, w zależności od rezystancji uzwojeń nadprzewodnikowych w stanie rezystywnym. W czasie trwania stanu przejściowego (Δt) prąd zwarcia osiąga maksymalną wartość równą wartości prądu krytycznego nadprzewodnika, $I_{zw} = I_c$, po czym zaczyna maleć, w skutek wzrostu rezystancji uzwojenia. Czas trwania stanu przejściowego pracy uzwojenia nadprzewodnikowego, Δt, jest znacznie krótszy od ¼ czasu trwania okresu prądu zwarcia i nie przekracza 1 ms [4].

Można stwierdzić, że przy poprawnie zaprojektowanych i zbudowanych uzwojeniach nadprzewodnikowych oraz odpowiednim doborze gęstości prądu znamionowego uzwojeń transformatora nie musimy ograniczać prądu zwarciowego napięciem zwarcia. W transformatorach nadprzewodnikowych szerokość szczeliny powietrznej wynika jedynie ze względów izolacyjnych, podczas gdy w transformatorach konwencjonalnych, ze względów izolacyjnych oraz konieczności ograniczenia prądów zwarciowych. Biorąc pod uwagę tylko względy izolacyjne szczelina pomiędzy uzwojeniami nadprzewodnikowymi może być mniejsza niż pomiędzy uzwojeniami miedzianymi, ponieważ ciekły azot ma większą wytrzymałość na przebicia niż olej transformatorowy [5].

Po przejściu transformatora nadprzewodnikowego do stanu rezystywnego wzrost rezystancji uzwojeń, w zależności od rezystywności użytej taśmy nadprzewodnikowej, powoduje kilka do kilkuset krotny wzrost impedancji transformatora, w stosunku do jego impedancji w stanie nadprzewodzącym.

Obecnie istnieją techniczne możliwości produkcji przewodów nadprzewodnikowych HTS 2G o wymaganych wartościach rezystywności i wytrzymałości mechanicznej. Pozwala to na sformułowanie wymagań technicznych dla przewodów nadprzewodnikowych potrzebnych do wykonania uzwojeń transformatora nadprzewodnikowego, ze względu na wymaganą wartość prądu zwarcia.

LITERATURA

[1] Lee Ch., Soek B.Y., Design of the 3 Phase 60 MVA HTS Transformer With YBCO Coated Conductor Winding, *IEEE Trans. On Applied Superconductivity*, Vol. 15, No 2, June 2005, pp. 1867-1870.

[2] Hayashi H., Okamoto H., Harimoto T., Imayoshi T., Tomioka A., Bouno T., Konno M., A study for designing YBCO power transformer, *Physica C* 463–465 (2007) 1233–1236

[3] Kajimo H., Hata H., Fujimoto H., Nagashima K., Kieda K., Hamada H., Samuki Y, Tomioka A., Umomori K., Yoshida S., Iwakuma M., Funaki K., Fabrication of Superconducting Traction Transformer for Railway Rolling Stock, *Journal of Physic: Conference Series* 43 (2006) 841- 844.

[4] Janowski T. *Nadprzewodnikowe ograniczniki prądu*, Liber 2002

***Autorzy**: prof. dr hab. Inż. Tadeusz Janowski Politechnika Lubelska, Nadbystrzycka 36a, 20-618 Lublin, E-mail: t.janowski@pollub.pl, .dr inż. Grzegorz Wojtasiewicz, Instytut Elektroenergetyki w Warszawie, Pracownia Technologii Nadprzewodnikowych w Lublinie, Nadbystrzycka 36a, 20-618 Lublin, E-mail: g.wojtasiewicz@iel.waw.pl.*

DECOMPOSITION OF BTX BY PLASMA GENERATED OZONE

J. Jaroszyńska-WOLIŃSKA[1] , P.A.F. HERBERT[2]

Lublin University of Technology , Poland(1), Plasma Ireland, 22 Summerhill North, Cork, Ireland (2)

***Abstract**. Dielectric Barrier Discharge plasma generated ozone is applied in the decomposition of Benzene, Toluene and Xylene pollutants in water. In BTX mixtures a reduction in hydrocarbon content of 88% was achieved..*

Introduction

Pollution by petroleum derivatives of ground waters is a significant issue. Biodegradation of such pollutants is comparatively slow and application of oxidizing methods appears to be the most efficient of the available artificial breakdown processes. The most hazardous petroleum-derivative pollutants are benzene, toluene, and xylene (BTX). Among oxidizers, ozone is highly efficient in neutralizing synthetic and natural organic compounds including those that influence taste and smell of water. In organic compound removal, ozone can act either as an oxidizer or cause decomposition via an ozonelysis process which causes uncoupling of double bonds in all organic compounds including aromatics very frequently found in waters. Both aromatic rings and side chains are subject to ozone action. Ozone can react with pollutant compounds either by direct reaction of molecular ozone or indirectly through reactions of free radicals that form in the process of ozone decomposition in water.

Experimental Setup

Model solutions saturated with benzene, toluene, xylene, and their mixtures were prepared by mixing 1 L of water with 1 mL of hydrocarbon. Such solutions were then exposed to ozone in both static and dynamic conditions. Ozone was plasma generated in a tubular reactor from oxygen substrate gas flowing at 600 mL/hour. The plasma type was the dielectric barrier discharge generated by a sinusoidal voltage of 5.9 kV across the discharge gap between the grounded cylindrical outer electrode and the high voltage inner electrode along the main axis of the cylinder around which inner electrode was wrapped polyethylene dielectric.

In dynamic conditions the ozone generated was bubbled through model solutions directly on leaving the reactor. In static conditions pure, de-ionised water was saturated with ozone from the reactor following which such water was added to model solutions. Sample analysis was carried out by extraction in methylene dichloride both before and after ozone application followed by gas chromatography using flame-ionization detection and the Chromax 2000 software. The effect of ozone on BTX was determined by comparison of spectral peaks with those of control samples.

Results AND conclusions

Figures 1 and 2 show the % decomposition of each model solution after static and dynamic oxidation respectively:

Following the application of plasma generated ozone to the individual model solutions in static conditions, benzene shows the least reduction at 12%, 32% of toluene undergoes decomposition and xylene's reduction is almost complete at 98% (Figure 1).

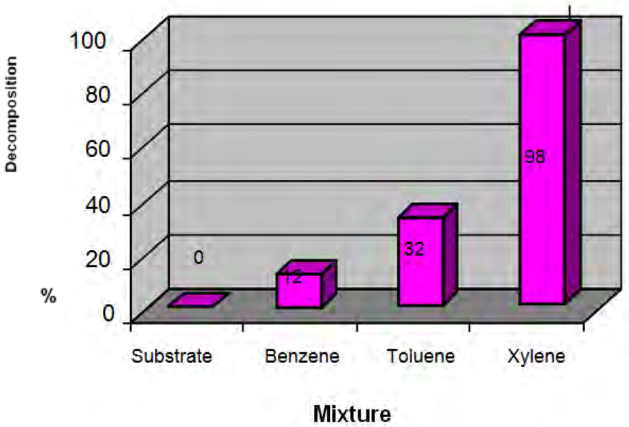

Figure 1: % Decomposition of each hydrocarbon model solution after static ozone oxidation

In dynamic conditions, benzene's reduction is 76%, toluene's 94% and xylene’s 99% (Figure 2).

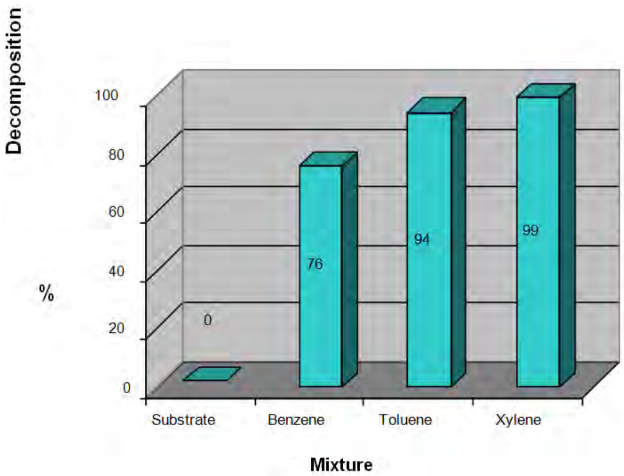

Figure 2: % Decomposition of each hydrocarbon model solution after dynamic ozone oxidation

The effect of ozone on mixtures of the hydrocarbon model solutions was investigated. In the case of a benzene-toluene-xylene mix, a reduction of total BTX content of only 3% was achieved by the static process (benzene 4%, toluene 3%, xylene 3%). However, in dynamic conditions a reduction in hydrocarbon content of 88% was seen (benzene 83%, toluene 92%, xylene 96%). In mixes of toluene and xylene only greater decomposition of both hydrocarbons was observed in dynamic conditions, namely 99% of toluene and 98% of xylene.

Conclusions:

1. Ozone generated by plasma reactor effectively removes volatile aromatic hydrocarbons (BTX) from the water phase in both static and dynamic processes although dynamic processes are much more effective;
2. In toluene-xylene contaminated water a high reduction rate of 98% has been observed;
3. The presence of benzene in a hydrocarbon mixture reduces efficiency to 88%;
4. Ozone is most effective in removing xylene and least effective against benzene.

***Authors**: dr hab. J. Jaroszyńska-Wolińska, Faculty of Civil Engineering and Architecture, Lublin University of Technology, Nadbystrzycka 40, 20-618 Lublin, Poland. Email: j.wolinska@gmail.com P.A.F. Herbert, Plasma Ireland, 22 Summerhill North, Cork, Ireland.*

Conference ELMECO–7
ELECTROMAGNETIC DEVICES AND PROCESSES IN ENVIRONMENT PROTECTION
joint with 10th Seminar AoS-10 APPLICATIONS OF SUPERCONDUCTORS
28–30.09.2011, Nałęczów, Poland

NUMERICAL ANALYSIS OF YBCO COATED CONDUCTORS

Leszek JAROSZYŃSKI, Dariusz CZERWIŃSKI

Lublin University of Technology

***Abstract**. Second generation high-Tc superconducting wire has a layered structure The ratio of thickness of superconducting layer to overall width of HTS tape can be as high as 1:10000. FEM computer simulation of such thin subdomains is difficult and very time-consuming. Creation of a finite element mesh of acceptable quality and execution of calculations in reasonable time are the main opposing problems In this paper, authors present possibilities of overcoming the difficulty of unfavourable geometric ratio of thin HTS layers.*

***Streszczenie.** Taśma nadprzewodnikowa drugiej generacji ma strukturę warstwową. Stosunek grubości do szerokości warstwy nadprzewodnika w takiej taśmie może osiągać wartość 1:10000. Symulacja numeryczna metodą elementów skończonych tak cienkich obszarów jest bardzo utrudniona. W artykule autorzy przedstawiają wybrane możliwości obejścia problemu niekorzystnej geometrii cienkiej warstwy nadprzewodnikowej.*

Keywords: YBCO coated conductors, FEM computer simulation.
Słowa kluczowe: nadprzewodniki cienkowarstwowe, symulacja numeryczna metodą elementów skończonych.

Introduction

Second generation (2G) high-T_c superconducting (HTS) wire has a layered structure. In most cases, a thin coating of superconductor compound, usually $YBa_2Cu_3O_7$ (YBCO), is applied or grown on a flat metallic substrate by means of chemical vapour deposition (CVD) or pulsed laser deposition (PLD). The superconductor coating in this coated conductor (CC) wire typically has the thickness of the order of one micron (Fig. 1).

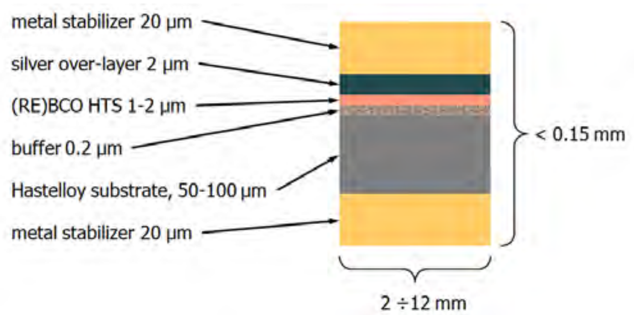

Fig. 1. Cross-section of 2G HTS tape (anisotropic scale)

Numerical simulation appears as an effective and relatively inexpensive tool of designing of novel electromagnetic devices. Unfortunately, a finite element method (FEM) simulation of superconducting coated conductors provokes a few major difficulties i.e. creation of a finite element mesh of acceptable quality and execution of calculations in reasonable time.

Computer simulation of high-T_c superconductors

Highly non-linear electrical behaviour of HTS can be described by equation (1) binding the resistivity and the current density.

$$\rho = \frac{E_c}{J_c}\left(\frac{|J|}{J_c}\right)^{n-1} \tag{1}$$

where: ρ – resistivity, E_c – constant (electric field intensity, 10^{-4} V/m), J_c, – critical current density, J – current density, n – constant exponent.

Maxwell equations can be written in a few forms depending on the chosen state variables. As proposed in [1], magnetic field strength can be calculated by solving equation (2).

$$\mu\frac{\partial \mathbf{H}}{\partial t} + \nabla\times(\rho\nabla\times\mathbf{H}) = 0 \tag{2}$$

where: μ – magnetic permeability, $\mathbf{H}$ – magnetic field vector.

This problem formulation permits for a convenient incorporation of the fundamental superconductor feature (1) in the numerical problem. Because of formula (3), which holds for two-dimensional problems: relation (1) is transformed into FEM solvable task.

$$J_z = \frac{\partial H_y}{\partial x} - \frac{\partial H_x}{\partial y} \tag{3}$$

where: J_z – perpendicular component of current density, H_x, H_y – in-plane magnetic field components.

The AC power losses (in W/m) in superconducting subdomain can be calculated using equation (4):

$$P = \frac{1}{T}\int_0^T \mathrm{d}t \int_S \mathbf{E}\cdot\mathbf{J}\,\mathrm{d}S \tag{4}$$

where: P – power losses, T – current period, $\mathbf{E}$ – electric field vector, S – superconductor subdomain cross-section.

Geometrical aspect ratio

Models with large geometric scale differences are always problematic to mesh. The ratio of thickness of superconducting layer to HTS tape width can be high as 1:10000. These extremely thin subdomains are very difficult to analyse using FEM computer simulation because of gigantic number of degrees of freedom (Fig. 2). Creation of a finite element mesh of acceptable quality and execution of calculations in reasonable time are the main opposing problems. There are three resolutions to these obstacles: thickness manipulation, mesh scaling and shell region usage.

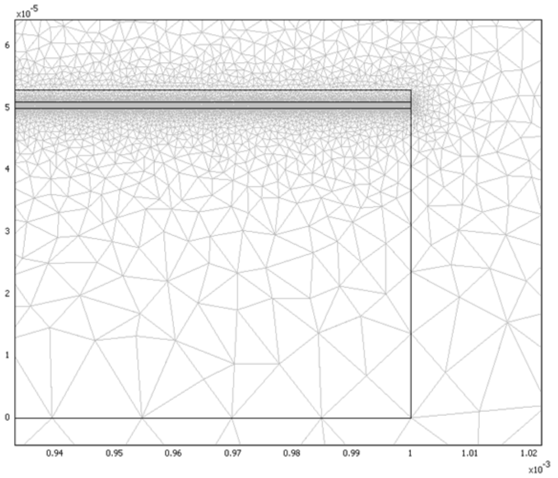

Fig. 2. Refined FEM mesh of 2G HTS tape with superconductor geometrical aspect ratio of 1:2000 (~180 000 vertices)

Subdomain thickness manipulation

Thin superconducting or resistive layers can be geometrically rescaled in order to obtain lower aspect ratio for meshing process [2, 3, 4]. The thickness of HTS and metal over-layers is multiplied by a factor of 10÷1000. In such situation, for approximation of the real solution, five physical parameters need also to be scaled: critical current density of superconducting subdomain, resistivity or electric field intensity, magnetic permeability, specific heat and heat transfer coefficient. This kind of manipulation shortens computation time meaningfully, maintaining realistic results of magneto-thermal modelling. Although, simulation results demand cautious interpretation because of the parameters manipulation.

Mesh mapping and multiscale mesh

One way to reduce meshing problem is to split the geometry into several regions and mesh them independently. Some FEM packages allow to use structured meshes, which density and basic element type is chosen independently for a particular subdomain. The connection of the different meshes into one single model is achieved by identity boundary conditions [5].

It is also possible to lower the number of degrees of freedom significantly and to accelerate calculation process using so-called “mesh mapping” (Fig. 3). This simple manipulation may give reliable results of AC losses estimation [6].

Integral equation or shell regions

In order to decrease the number of degrees of freedom and computation time, it is possible to substitute thin two-dimensional strips by a corresponding one-dimensional segments [7, 8]. It is also possible to replace three-dimensional thin strips with two-dimensional equivalents [9].

Contemporary FEM packages offer the ability to model thin layers with equation-based modelling using tangential derivative variables. Some of them poses specialized application modes, different ones require user to define problem in the weak form.

In case of 2G HTS tapes, current density distribution in the cross-section of 2D strip can be described by Brandt’s integral equation. It can be formulated as a partial differential equation (PDE) and solved by FEM software. To describe electromagnetic interactions of one-dimensional strips with other subdomains, it is necessary to couple integral equation with two-dimensional problem.

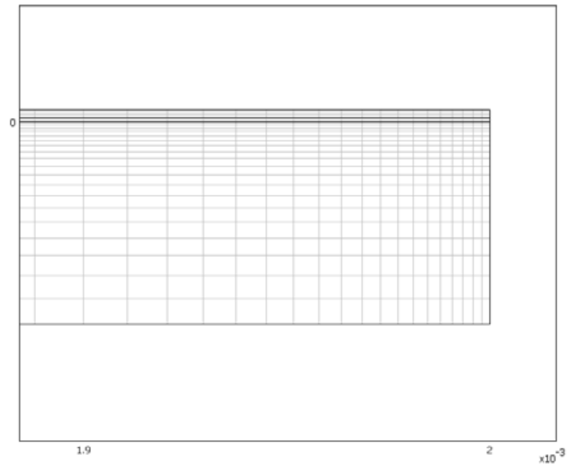

Fig. 3. Anisotropic mapped mesh of HTS tape

REFERENCES

[1] Brambilla R., Grilli F., Martini L., Development of an edge-element model for AC loss computation of high-temperature superconductors, *Supercond Sci Technol*, 20 (2007), 16-24

[2] Roy F., Dutoit B., Grilli F., Sirois F., Magneto-Thermal Modeling of Second-Generation HTS for Resistive Fault Current Limiter Design Purposes, *IEEE T Appl Supercon*, vol. 18 (2008), No. 1, 29-35

[3] Duron J., Grilli F., Antognazza L., Decroux M., Dutoit B., Fischer Ø., Finite-element modeling of YBCO fault current limiter with temperature dependent parameters, *Supercond Sci Tech*, 20 (2007), 338-344

[4] Duron J., Grilli F., Antognazza L., Decroux M., Stavrev S., Dutoit B., Fischer Ø., Finite-element modelling of superconductors in over-critical regime with temperature dependent resistivity, *J Phys Conf Ser*, 43 (2006), 1076-1080

[5] COMSOL Multiphysics simulation software, www.comsol.com

[6] Rodriguez-Zermeno V.M., Sørensen M.P., Pedersen N.F., Mijatovic N., Abrahamsen A.B., Fast 2D Simulation of Superconductors: a Multiscale Approach, *Proceedings of the COMSOL Conference*, Milan, 2009

[7] Stavrev S., Grilli F., Dutoit B., Ashworth S., Comparison of the AC losses of BSCCO and YBCO conductors by means of numerical analysis, *Supercond Sci Technol*, 18 (2005), 1300-1312

[8] Brambilla R., Grilli F., Martini L., Sirois F., Integral equations for the current density in thin conductors and their solution by the finite-element method, *Supercond Sci Tech*, 21 (2008), 105008

[9] Wan Kan Chan, Masson P.J., Luongo C., Schwartz J., Three-Dimensional Micrometer-Scale Modeling of Quenching in High-Aspect-Ratio $YBa_2Cu_3O_{7-\delta}$ Coated Conductor Tapes-Part I: Model Development and Validation, *IEEE T Appl Supercon*, vol. 20 (2010), No. 6, 2370 - 2380

***Authors**: dr inż. Leszek Jaroszyński, dr inż. Dariusz Czerwiński, Lublin University of Technology, Institute of Electrical Engineering and Electrotechnologies, ul. Nadbystrzycka 38A, 20-618 Lublin, e-mail: l.jaroszynski@pollub.pl*

HYPERFINE INTERACTIONS IN MULTIFERROIC MECHANICALLY ACTIVATED $BiFeO_3$ COMPOUND

Elżbieta JARTYCH[1], Dariusz OLESZAK[2], Mariusz MAZUREK[1]

Lublin University of Technology (1), Warsaw University of Technology (2)

***Abstract**. In this work the results of structural and magnetic investigations for multiferroic $BiFeO_3$ compound prepared by mechanical activation are presented. The structural analysis and hyperfine interactions investigations were performed by X-ray diffraction and Mössbauer spectroscopy, respectively.*

***Streszczenie.** W pracy przedstawiono wyniki badań strukturalnych i magnetycznych dla multiferroicznego związku $BiFeO_3$ otrzymanego w procesie aktywacji mechanicznej. Badania struktury i oddziaływań nadsubtelnych przeprowadzono odpowiednio metodami dyfrakcji promieniowania X oraz spektroskopii efektu Mössbauera.*

Keywords: bismuth ferrite, mechanical activation, hyperfine interactions, Mössbauer spectroscopy.
Słowa kluczowe: żelazian bizmutu, aktywacja mechaniczna, oddziaływania nadsubtelne, spektroskopia mössbauerowska.

Introduction

Bismuth ferrite $BiFeO_3$ (or BFO) is one of the most known multiferroics is which ferroelectric and antiferromagnetic ordering exist at room temperature. $BiFeO_3$ is reported to have a rhombohedrally distorted perovskite-like structure with space group *R3m* where the unit cell has parameters a = 5.58102(4) Å and c_{hex} = 13.8757(2) Å [1]. The multiferroic properties of BFO are as follows: ferroelectric Curie temperature T_C = 1100 K and antiferromagnetic Néel temperature T_N = 640 K [1]. The possessing of both ferroelectric and antiferromagnetic properties above an ambient temperature makes the BFO very attractive material from the application point of view. Recently, researches make every effort to synthesize BFO as pure phase in polycrystalline form. Among many preparation methods there are the conventional solid-state sintering, the rapid-liquid-phase sintering, sol-gel route and solid-state ionic titration technique. In most of cases the presence of impurity phases, mainly $Bi_2Fe_4O_9$ or $Bi_{25}FeO_{40}$ leads to poor ferroelectric behavior. Recently, the mechanical activation (MA) has been reported as an efficient method to prepare the pure phase of BFO as polycrystalline [2] or nanocrystalline material [3]. In this technique the mechanical treatment is performed in the suitable ball mill and necessary thermal processing completes the formation of the ceramic phase.

In this work mechanical activation was performed in two manners: (1) mixing and milling of stoichiometric amounts of Bi_2O_3 and Fe_2O_3 followed by thermal treatment and (2) separate milling of individual Bi_2O_3 and Fe_2O_3 powders, mixing, further milling and thermal processing. The structure of BFO samples was examined using X-ray diffraction (XRD). The main goal of the present study was to determine hyperfine interactions parameters in the BFO obtained by MA using Mössbauer spectroscopy (MS).

Experimental details

Mechanical activation of the stoichiometric amounts of the Fe_2O_3 and Bi_2O_3 oxides were performed into the stainless-steel vial of a Fritsch P5 Pulverisette planetary ball mill equipped with hardened steel balls. The ball-to-powder weight ratio was 10:1. In the first process (MA I) both oxides were milled together up to 100 h under an air atmosphere. After the MA process the mixture was annealed isothermally in a furnace at 973 K in air for 1 h. In the second MA process (MA II), stoichiometric amounts of the Fe_2O_3 and Bi_2O_3 oxides were milled separately up to 10 h in air and than the powders were mixed and milled together during 50 h in air. Thermal processing of the obtained mixtures was performed in two ways: (a) heating from the room temperature up to 993 K in a calorimeter (DSC) under an argon atmosphere with the rate of 20 $Kmin^{-1}$ and (b) isothermal annealing in a furnace at 973 K in air for 1 h. The crystalline structure of the mechanically activated samples was analyzed by the Rigaku MiniFlex II diffractometer with CuK_α radiation. MS studies were carried out at room temperature in standard transmission geometry using a source of ^{57}Co in a chromium matrix. A 25-μm-thick metallic iron foil was taken as a standard for calibration of a spectrometer.

Results and discussion

In Fig. 1 the XRD patterns of mechanically activated Fe_2O_3 and Bi_2O_3 oxides for various milling times are presented together with the pattern for annealed mixture. It may be seen that during milling process the diffraction peaks are broadened and shifted. After 100 h MA I the formation of the new crystalline phase may be observed, however it is not a pure BFO. To complete solid-state reaction the isothermal annealing process at 973 K was performed. Unfortunately, besides the main BFO phase the

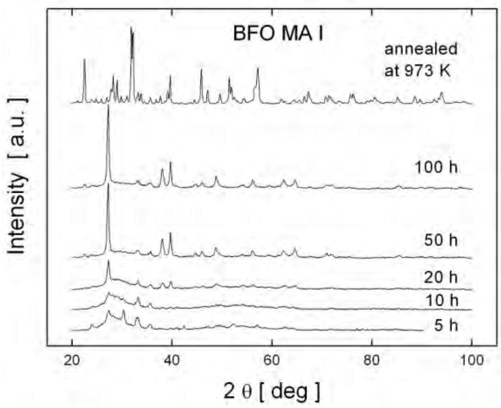

Fig.1. X-ray diffraction patterns of the Fe_2O_3 and Bi_2O_3 oxides mixture milled for different times and annealed at 973 K.

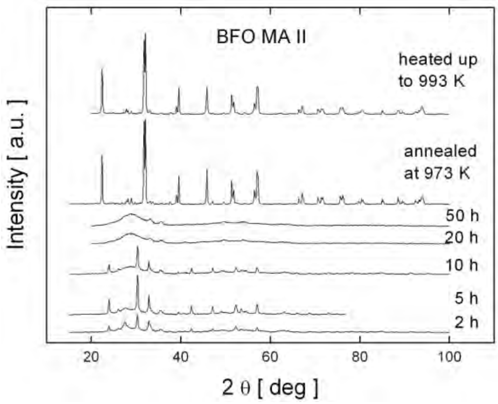

Fig.2. X-ray diffraction patterns of the initially milled Fe_2O_3 and Bi_2O_3 oxides, then mechanically activated during different times and subsequently annealed at 973 K and heated up to 993 K.

diffraction peaks coming from impurity $Bi_2Fe_4O_9$ phase are also visible. The estimated contribution of the desired BFO is about 70 % and the average crystallite sizes of this compound determined using Scherrer formula are 45 nm +/- 10 nm.

Fig. 2 presents XRD patterns of the initially milled Fe_2O_3 and Bi_2O_3 oxides up to nanometer level (~20 nm) and subsequently mechanically activated during 2-50 h. It may be noted that after 50 h MA II the mixture is amorphous. After thermal treatment the desired BFO phase is formed in 90 %, as roughly estimated from XRD patterns. About 10 % of material makes impurity phase $Bi_2Fe_4O_9$. After thermal processing the average crystallite sizes of $BiFeO_3$ phase are as follows: 70 nm +/- 25 nm for heated material and 72 nm +/- 24 nm for annealed sample.

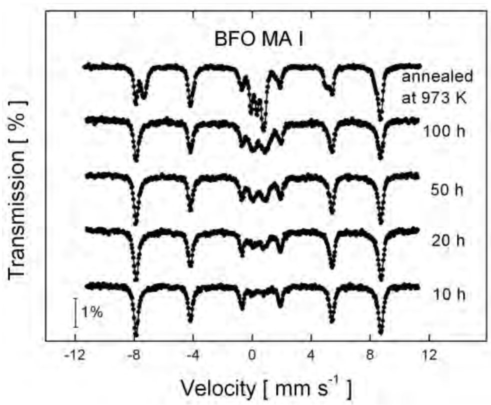

Fig.3. Room-temperature Mössbauer spectra of the Fe_2O_3 and Bi_2O_3 oxides milled for different times and annealed at 973 K.

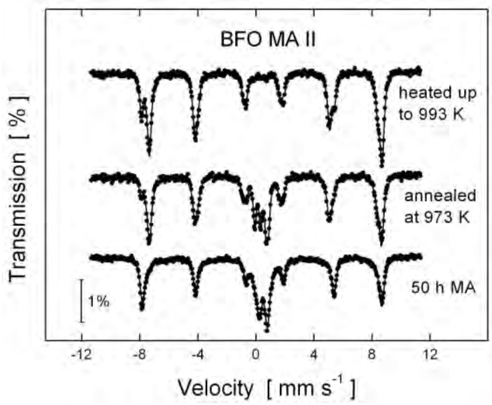

Fig.4. Room-temperature Mössbauer spectra of the initially milled Fe_2O_3 and Bi_2O_3 oxides, then mechanically activated during 50 h and subsequently annealed at 973 K and heated up to 993 K.

Detailed phase and structural analysis using Rietveld method performed for the sample milled for 50 h and annealed at 973 K allowed to determine the lattice parameters as follows ***a*** = 5. 5745(4) Å, ***c*** = 13.8588(6) Å. The obtained values agree well with the data base [4].

Mössbauer spectroscopy confirmed XRD results. Spectra for mixtures milled during MA I process for 10-100h are a superposition of one sextet and one doublet (Fig. 3). Both sextet and doublet may be attributed to the bismuth iron oxides with unknown chemical composition $Bi_xFe_yO_z$ with small amount of hematite Fe_2O_3. After isothermal annealing of the sample, in the Mössbauer spectrum sextets are clearly separated (top spectrum in Fig. 3). Besides two sextets attributed to the desired BFO compound, two doublets and sextet from hematite were fitted to the spectrum. The hyperfine interaction parameters of doublets are similar to those for $Bi_2Fe_4O_9$ and sillenite. In the case of the MA II process (Fig. 4) MS spectra were computer fitted using two doublets and three sextets. Two of three sextets may be attributed to the nanostructured BFO compound; however, small amount of hematite is still visible. As previously, paramagnetic doublets in the spectra are attributed to the impurity phases $Bi_2Fe_4O_9$ and sillenite. All the values of hyperfine interactions parameters are in good agreement with the literature data [1, 5-6].

Conclusions

Mechanical activation method allowed obtaining the desired BFO compound with small amount of impurities. The gradual heating in the calorimeter seems to be more effective method in terms of an amount of paramagnetic impurities. The values of the hyperfine magnetic fields for mechanically activated BFO are smaller than those for conventionally sintered samples. This is mainly due to the reduced grain sizes to the nanometer level as well as the residual strains introduced into the sample during mechanical milling process. Moreover, desired BFO phase was formed by mechanical activation and subsequently thermal processing at the temperature lower by 30-50 K as compared to the conventional sintering method.

REFERENCES

[1] Palewicz A., Szumiata T., Przeniosło R., Sosnowska I., Margiolaki I., Search for new modulations in the $BiFeO_3$ structure: SR diffraction and Mössbauer studies, Solid State Commun., 140 (2006), 359-363
[2] Maurya D., Thota H., Nalwa K.S., Garg A., $BiFeO_3$ ceramics synthesized by mechanical activation assisted versus conventional solid-state-reaction process: A comparative study, J. Alloys Comp., 477 (2009), 780-784
[3] Szafraniak I., Połomska M., Hilczer B., Pietraszko A., Kępiński L., Charactrization of $BiFeO_3$ nanopowder obtained by mechanochemical synthesis, J. Europ. Ceramic Soc., 27 (2007), 4399-4402
[4] ICSD collection codes: 15299, 20288, 20372, 20618, 22342, 28027, 28622, 75324, 51664, 97591, 109370, 154394.
[5] Blaauw C., van der Woude F., Magnetic and structural properties of $BiFeO_3$, J. Phys. C: Solid State Phys. 6(1973), 1422-1431
[6] Freitas V.F., Grande H.L.C., de Medeiros S.N., Santos I.A., Cotica L.F., Coelho A.A., Structural, microstructural and magnetic investigations in high-energy ball milled $BiFeO_3$ and $Bi_{0.95}Eu_{0.05}FeO_3$ powders, J. Alloys Comp., 461(2008), 48-52

***Authors**: Prof. Elżbieta Jartych, Lublin University of Technology, Department of Electronics, Nadbystrzycka str. 38a, 20-618 Lublin, E-mail: e.jartych@pollub.pl; Dr Dariusz Oleszak, Warsaw University of Technology, Faculty of Material Science and Engineering, Wołoska str. 141, 02-507 Warsaw, E-mail: doleszak@inmat.pw.edu.pl; MSc Mariusz Mazurek, Lublin University of Technology, Department of Electronics, Nadbystrzycka str. 38a, 20-618 Lublin, E-mail: mariusz.mazurek@pollub.pl*

Conference ELMECO–7
ELECTROMAGNETIC DEVICES AND PROCESSES IN ENVIRONMENT PROTECTION
joint with 10th Seminar AoS-10 APPLICATIONS OF SUPERCONDUCTORS
28–30.09.2011, Nałęczów, Poland

PD AND LQR CONTROLLERS APPLIED TO VIBRATION DAMPING OF AN ACTIVE COMPOSITE BEAM

Wojciech JARZYNA[1], Michał AUGUSTYNIAK[2]

Electrical Drive Systems and Electrical Machines Dep., Lublin Univ. of Technology (LUT) (1)
INDUSTER Sp. z o.o. Lublin, Poland, PhD student at LUT (2),

***Abstract**. Presented results describe an application of piezoelectric composite actuator for vibration reduction of cantilever beam. Operational characteristics of these composite systems are formed in closed loop control systems. The paper describes two kinds of systems. The first base on feedback control and PD regulator. The second one operates with state loop control with the gain tuned by LQR index. Better repeatability of results we obtained for the LQR controller, while the PD controller was very sensitive to changes in the position of strain gauge*

***Streszczenie.** Przedstawione wyniki opisują zastosowanie piezoelektrycznego układu kompozytowego do redukcji drgań belki wysięgnikowej. Charakterystyki pracy tego układu kompozytowego kształtowane są w układzie regulacji zamkniętej. W artykule opisano dwa układy regulacji. Pierwszy oparty jest na strukturze ujemnego sprzężenie zwrotnego z regulatorem PD. Drugi układ działa ze sprzężeniem od wektora stanu, a jego wzmocnienie strojone jest według wskaźnika LQR. Lepszą powtarzalność wyników uzyskano dla regulatora LQR, podczas gdy regulator LQ był bardzo czuły na zmiany położenia tensometru.*

Keywords: MFC piezoelectric actuator, active vibration damping, PD and LQR controllers
Słowa kluczowe: piezoelektryczny aktuator MFC, aktywne tłumienie drgań, regulatory PD i LQR.

Introduction

Mechanical vibrations reduction improves the operating quality of machines and increases their reliability. In order to receive reduced value of such vibrations, several methods are applied.

The basic and required task is to design the system in a way that its work does not take place near the own frequency of the system.

The second method base on designing passive mechanical dampers, which e.g. satisfy viscous smoothers or specially chosen construction materials which have increased wet friction.

The two mentioned methods do not solve all the problems with vibrations. Therefore, new techniques from the area of modern material engineering and control theory are applied. One of such materials are active actuator systems, which have light and flexible composite structure and may be included inside the material construction. This example structure is a piezoelectric Macro Fiber Composite (MFC) which operates with large deflections and generates big forces.

Embedding these composites into the structure of the device, results in the higher reliability and better air flow around elements. Therefore such construction can successfully be applied in aviation industry.

Results are presented within a range of research projects including study of possible applications of smart materials in aircrafts.

In this synopsis a construction of MFC piezoelectric actuators is described and the mission of control systems is precised. Moreover two types of control algorithms: PD and LQR are derivated. Also an example cantilever beam tests are done and their results are shortly discussed.

Structures and properties of Macro Fiber Composites

Piezoelectric elements are transducers which convert electric energy into mechanical one and mechanical energy into electrical one. For this reason, those systems perform two functions: one of the actuator displacement and second of strain sensors. In industrial applications they are used in the form of piezoelectric elements in crystalic form, referred to as monolithic elements of the PZT (Lead Zirconate Titanate) or a composite piezoelectric AFC (Active Fiber Composite) and MFC (Macro Fiber Composite) made of piezo-ceramic fibers.

For industrial applications in the aerospace industry, the elements of MFC are particularly interesting. In contrast to the homogeneous PZT systems, their structure is usually referred to as the matrix structure built from components of the orthotropic physical properties, which is closed by the outer epoxy plates. Polarizing electrodes located inside the MFC structure, produce an electric field which directly affect the generation of mechanical stress in the piezoelectric fibers. The use of such structure as a sensor assures that electric charge stored on the electrodes is proportional to the measured voltage and capacity of the element.

Application of PD controller

PD controller uses standard algorithms which are widely implemented through Single Input Single Output (SISO) feedback control systems. They are commonly known because of the usage of the simple form of algorithms and not complicated control structure.

Tested system of cantilever beam has one control loop conducting $x(t)$ signal measured by strain gauge. Then, this signal is compared to the $u(t)$ set point and receives control error which is the input value for PD controller (Fig.1). Applied power amplifier operates in the range of -500V up to +1500V. It supplies the MFC type piezoelectric actuator which is embedded onto the surface of vibrating beam. This structure allows also dumping oscillations as position control.

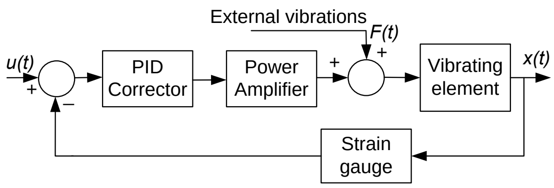

Fig.1. Feedback control with PD controller and oscillating disturbance force *F(t)*

Conducted tests are provided only for vibration dumping. Therefore, set point *u(t)* is assumed as equal to zero.

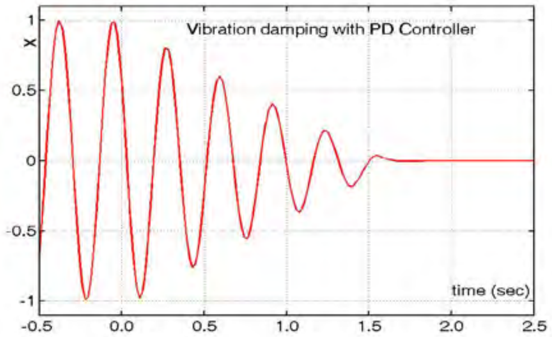

Fig.2. Vibration dumping with implemented PD feedback control extended in first lag inertia and amplifier with asymmetrical saturation -500V do +1500V.

During selection of the PD parameters we undertook a suppressing time as a main requirement of the control. Obtained results gave us almost aperiodic answer during simulation tests, when we omitted saturation effect. Taking into account a saturation effect, we received strongly damping oscillations (Fig.2).

However, the very good result has been obtained after many experiments with different strain gauge placement. Only with one certain placement, the system could damp oscillations. Even a small change of system conditions can cause generation of big oscillations and significant increase of the supply voltage.

The LQR Algorithm

An alternative solution to the PD controller is a regulator tuned according to LQR algorithm. Such regulator has a gain matrix in the state loop (Fig.3). Values of this gain matrix are tuned to minimize quadratic index (1) which depends on the state vector **x**(t) and input vector **u**(t).

(1) $$\mathbf{J} = \frac{1}{2}\int_0^\infty \left(\mathbf{x}^T(t)\mathbf{Q}\mathbf{x}(t) + \mathbf{u}^T(t)\mathbf{R}\mathbf{u}(t)\right)dt$$

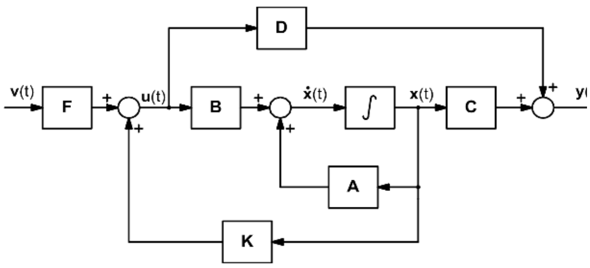

Fig.3. The state feedback control with the K gain matrix calculated from the Riccati equation.

The control index (1) is a compromise between quality of control and control costs. The control quality determines the first part of integrated expression. The second part of integrated expression minimizes energy consumption.

As the index function (1) fulfills conditions of the Riccati equation the weight of control matrix **Q** can be determined by output matrices $\mathbf{Q} = \mathbf{C}^*\mathbf{C}^T$ and matrices **K** and **R** are found out in Riccati equation procedure.

In consequence the results shown in Fig.4 characterizes damping comparable to PD controller but at smaller energy consumption.

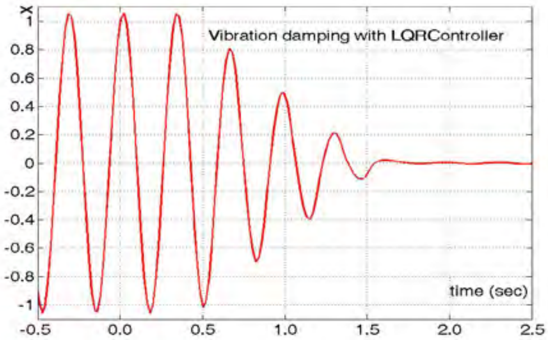

Fig.4. Vibration dumping with implemented LQR state feedback control and amplifier with asymmetrical saturation -500V do +1500V

Similarly to the previous tests with the PD controller presented In Fig 2, limitation/saturation of power amplifier causes longer time of control.

.

Conclusions

Active damping of cantilever beam with embedded piezoelectric composite actuator gives efficient results and have good dynamic characteristics. In the described synopsis there were tested damping features of composite beam actuated by external force having the frequency equal the own frequency of the beam.

During tests we implemented two control systems. The first control system SISO worked in feedback control with the PD controller. The second system operated in multivariable structure MIMO and was tuned according to LQR algorithm.

Comparing obtained results, we can see that the LQR has better characteristics. This type of regulator is not so sensitive on systems changes as much as PD controller. Therefore the LQR algorithms will be examined in the nearest future.

References

[1] Bocheński M., Warmiński J.: Badania doświadczalne drgań autoparametrycznego układu belkowego, *Przegląd Mechaniczny,* 2006, **12**, 32-34

[2] Byrski W.: *Obserwacja i sterowanie w systemach dynamicznych.* Wyd. AGH Kraków, 2007.

[3] Jarzyna W., Augustyniak M., Warmiński J., Bocheński M.: *Characteristics and Implementation of Piezoelectric. Structures in Active Composite Systems.* Electrical Review (Przegląd Elektrotechniczny). No 7/2010

[4] Vasques C.M.A., Dias Rodrigues J.: *Active vibration control of smart piezoelectric beams: Comparison of classical and optimal feedback control strategies.* Elsevier, Computers and Structures, vol.84, 2006.

Acknowledgments

Financial Support of the Structural Funds in the Operational Programme – Innovative Economy (IE OP) financed from the European Regional Development Fund – Project No POIG.0101.0200-015/08 is gratefully acknowledged

***Authors**: Dr hab. inż. Wojciech Jarzyna, Associate Prof at Lublin University of Technology, Electrical Drive Systems and Electrical Machines Department (EDS&EM), 38A Nadbystrzycka Street, 20-618 Lublin, Poland, E-mail w.jarzyna@pollub.pl; Mgr inż. Michał Augustyniak, PhD student at EDS&EM, Induster Sp. z o.o., Lublin, E-mail:* mich.augustyniak@ gmail.com;

Conference ELMECO–7
ELECTROMAGNETIC DEVICES AND PROCESSES IN ENVIRONMENT PROTECTION
joint with 10th Seminar AoS-10 APPLICATIONS OF SUPERCONDUCTORS
28–30.09.2011, Nałęczów, Poland

SUPERCONDUCTING PROPERTIES OF YBCO COATED CONDUCTORS PRODUCED BY INKJET PRINTING

Katarzyna L. JUDA[1], Mariusz WOŹNIAK[1], Mariusz MOSIADZ[1], Simon C. HOPKINS[1], Bartłomiej A. GŁOWACKI[1,2], Tadeusz JANOWSKI[3]

University of Cambridge (1), Institute of Power Engineering (2), Lublin University of Technology (3)

Abstract. *Current methods of producing $YBa_2Cu_3O_{7-\delta}$ coated conductors (YBCO CC) require expensive processing. A new technology combining chemical solution deposition (TFA-MOD) with inkjet printing, demonstrated successfully in this paper as confirmed by Hall probe magnetometry, shows considerable potential as a cost-effective replacement. The flexible control of ink stoichiometry and rheology, and the ease of introducing additions, offered by CSD inkjet printing has the potential to reduce the strong I_c anisotropy of YBCO CCs revealed by goniometric I_c measurements.*

Streszczenie. *Nowa technologia produkcji nadprzewodzących taśm $YBa_2Cu_3O_{7-\delta}$, łącząca szlak chemicznej depozycji roztworu za pomocą drukowania atramentowego, ma szansę zastąpić obecne kosztowne metody produkcji. Pomiar magnetometryczny czujnikiem Halla potwierdził nadprzewodnictwo próbki YBCO otrzymanej na szlaku chemicznym, który to umożliwia łatwą kontrolę stechiometrii i reologii inku, a także wprowadzanie dodatkowych komponentów, mających na celu redukcję silnej anizotropii I_c w filmach YBCO, ukazanej przez pomiar goniometryczny.*

Keywords: YBCO, sol-gel, Hall probe measurement, goniometric measurement
Słowa kluczowe: YBCO, sol-gel, pomiar czujnikiem Halla, pomiar goniometryczny

Introduction

A chemical solution deposition (CSD) method combining sol-gel synthesis, based on the trifluoroacetate metalorganic deposition (TFA-MOD) route, with inkjet printing, is a very promising technology for $YBa_2Cu_3O_{7-\delta}$ coated conductor (YBCO CC) fabrication, presenting clear opportunities for industrial application. The method enables the controllable deposition of liquid sol on the metallic substrate and does not require expensive equipment and vacuum conditions, which can significantly decrease manufacturing costs [1]. Because of the anisotropic properties of superconducting YBCO, the dependence of its superconducting properties on oxygen content, and the weak grain boundaries which impede critical current transport, the deposition and subsequent heat treatment of the YBCO ink must be optimised to obtain a crystallographically well textured and superconducting film.

Experimental

The YBCO sol was prepared using the trifluoroacetate (TFA) route, from $YBa_2Cu_3O_{6.9}$ powder (SSC Inc.). Anhydrous acetone was mixed with the YBCO powder in the ratio of 15 cm^3 to 3 g. Trifluoroacetic acid (TFAH) was added drop-wise to the YBCO powder at room temperature in the molar ratio of 13:1 (Reaction 1). The reaction was run for 72 h at 85 ºC in a N_2 atmosphere. Subsequently the resulting solution was heated under vacuum in a rotary evaporator at a temperature ranging between 65 and 80 ºC. This product was diluted to the appropriate concentration with anhydrous methanol, resulting in a green solution, and sealed in a vial under a nitrogen atmosphere.

(1) $$YBa_2Cu_3O_{7-\delta} + 13\ TFAH \rightarrow Y(TFA)_3 + 2\ Ba(TFA)_2 + 3\ Cu(TFA)_2 + 6.5\ H_2O$$

The prepared sol (ink) was deposited on a Ni-5%W rolling-assisted biaxially textured substrate (RABiTS) with a double $La_2Zr_2O_7$ (LZO) buffer layer and a single CeO_2 cap layer (Ni-5%W/2LZO/CeO_2) provided by Zenergy Power plc. (Germany). The ink was deposited on the substrate by means of drop on demand printing using an electromagnetic nozzle (a solenoid micro-valve modified from a Domino MacroJet printer) and other equipment schematically presented in Fig. 1. The printing parameters were adjusted to give complete and uniform coverage of the buffered substrate. The printing procedure was carried out in an inert atmosphere of pure N_2 at room temperature, with a relative humidity below 20%.

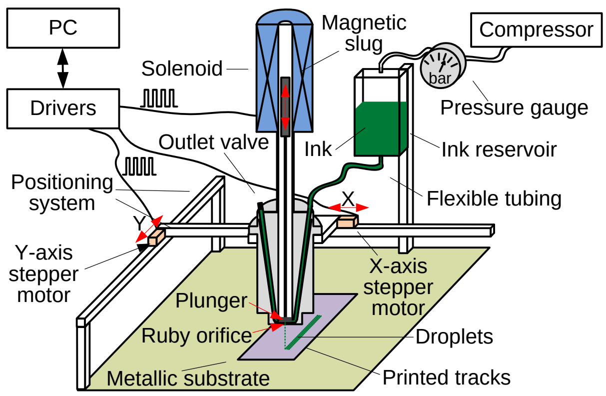

Fig.1. Schematic of the drop on demand inkjet printing system with electromagnetic nozzle. To print continuous tracks, the drivers are set to deliver pulses of current at a rate synchronised with the positioning system velocity.

Heat treatment of the samples was performed in a horizontal tube furnace with a valve controller. Pyrolysis was conducted in a wet O_2 atmosphere at 340 ºC; YBCO growth was in 200 ppm O_2 in an Ar atmosphere at 780 ºC; oxidation was in a dry O_2 atmosphere at 450 ºC. The flow rate was always 0.5 L/min. The temperature and humidity were controlled and measured during heat treatment.

The resulting YBCO films were zero field cooled to 77 K and magnetized with a field of 0.1 T applied perpendicular to the tape surface, and subsequently measured using a scanning Hall Probe system [2] to map the trapped magnetic field. The Hall probe active area was 0.1 × 0.1 mm, at a scan height of 0.2 mm and with a step size of 0.2 mm. The trapped field profile indicates the regions with critical current density, J_c, above 0.2 MA/cm^2.

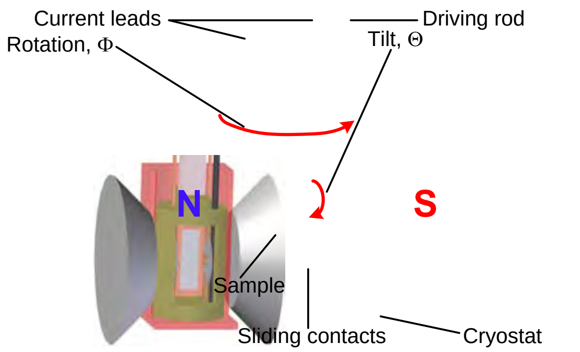

Fig. 2. Experimental set-up of a two-axis high current goniometer.

A high transport critical current measurement system has been developed based on a two-axis goniometer probe (Fig. 2) [3]. Tape samples 36 mm long were mounted on a rotating platform, with the length of the tape parallel to the current and a voltage contact separation of 6 mm. Measurements were performed in liquid nitrogen with an applied field of 0.6 T. The critical current was measured as a function of two-axis orientation, extracting critical current, I_c, and the n-value from automated power-law fits with a 1 μV/cm electric field criterion.

Results

It was found that the sample obtained by the CSD TFA-MOD sol-gel route by inkjet printing is superconducting (Fig. 3 a) with a trapped field of 2.10 mT. Although results for commercial MOCVD (metalorganic chemical vapour deposition) tape (SuperPower, Fig. 3 b) are higher, with a trapped field of 16.21 mT it is likely that the performance to price ratio will become more attractive after complete optimisation of the TFA-MOD process.

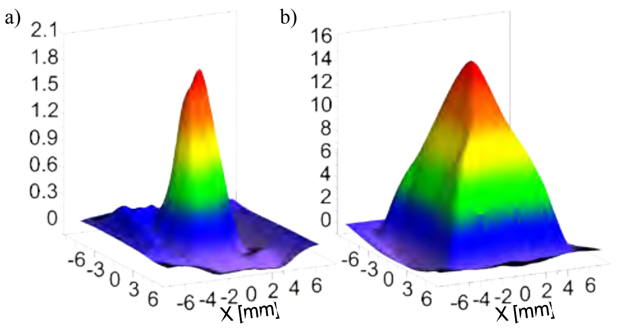

Fig. 3. Hall probe scans performed on YBCO tapes: a) obtained from the CSD metal TFA sol gel route by inkjet printing; b) commercially available, produced by MOCVD (SuperPower).

The angular dependence of I_c in the MOCVD sample from SuperPower is presented in Fig. 4. The peak I_c is shifted +6° from both +90° and -90°, suggesting a 6° angle between the c axis of the textured film and the normal to the substrate plane. The I_c is strongly dependent on rotation angle, and asymmetric about 0°, with a ratio of 2.4 between maximum and minimum I_c. In most applications, there is an off-axis (radial) field component and the maximum operating current is limited by this angular dependence. $I_c(\Phi)$ can be made much more isotropic, and the position and magnitude of the peaks controlled, by substitution (e.g. Gd) or the addition of other phases (e.g. $BaZrO_3$); and it has been demonstrated that this can be readily controlled in CSD routes [4]. The combination of this approach with inkjet printing is a key focus of ongoing research.

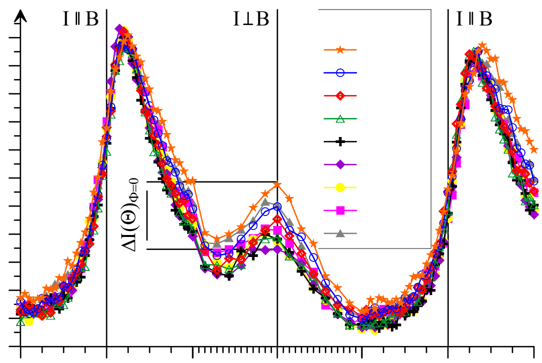

Fig. 4. The critical current dependence on rotation, Φ, at different tilts, Θ, at 77 K and 0.6 T. The spacing of minor tick marks on the rotation axis is 5°, and the range of rotation from -70° to 70° is shown at a reduced scale. The I_c peak is shifted +6° from ±90°, and minimum I_c occurs for a rotation angle of 70°.

Acknowledgments
This research was supported by the EU 7th Framework Programme project 'EFECTS'. M. Woźniak acknowledges with gratitude the financial support of Siemens Magnet Technology. M. Mosiadz would like to thank the EU 6th Framework Programme Marie Curie Actions project 'NESPA'.

REFERENCES

[1] Glowacki B. A., Mosiadz M., The role of sol gel processing in the development of high-temperature superconductors for AC applications, *J Sol-Gel Sci Techn*, 51 (2009) 335-347.
[2] Łękawa A., Głowacki B. A., Woźniak M., Hopkins S. C., Kozlowski G., Stryczewska H. D., Janowski T. Magnetic measurements of percolation in coated conductors as an analogue of deteriorating living neural networks, *Prz Elektrotech*, 85 (2009), nr 5, 194-197.
[3] Janowski T., Glowacki B. A., Wojtasiewicz G., Kozak S., Kozak J., Kondratowicz-Kucewicz B., Majka M., Wozniak M., Fault Current Limitation in Power Network by the Superconducting Transformers Made of 2G HTS, *IEEE T Appl Supercon*, 21 (2011) 1413-1416.
[4] Gutierrez J., Llordes A., Gazquez J., Gibert M., Roma N., Ricart S., Pomar A., Sandiumenge F., Mestres N., Puig T., Obradors X., Strong isotropic flux pinning in solution-derived $YBa_2Cu_3O_{7-x}$ nanocomposite superconductor films, *Nat Mater*, 6 (2007) 367-373.

***Authors**: mgr inż. Katarzyna L. Juda, e-mail: klj35@cam.ac.uk; mgr inż. Mariusz Woźniak, e-mail: mw477@cam.ac.uk; mgr inż. Mariusz Mosiadz, e-mail: mm701@cam.ac.uk; dr Simon C. Hopkins, e-mail: sch29@cam.ac.uk; prof. dr Bartłomiej A. Głowacki, e-mail: bag10@cam.ac.uk, University of Cambridge, Department of Materials Science and Metallurgy, Applied Superconductivity and Cryoscience Group, Pembroke Street, Cambridge CB2 3QZ, UK; prof. dr Bartłomiej A. Głowacki also from Institute of Power Engineering, Augustówka 6, 02-981 Warszawa, Poland; prof. dr hab. inż. Tadeusz Janowski, e-mail: t.janowski@pollub.pl, Lublin University of Technology, Institute of Electrical Engineering and Electrotechnologies, Nadbystrzycka 38A, 20-618 Lublin, Poland.*

Conference ELMECO–7
ELECTROMAGNETIC DEVICES AND PROCESSES IN ENVIRONMENT PROTECTION
joint with 10th Seminar AoS-10 APPLICATIONS OF SUPERCONDUCTORS
28–30.09.2011, Nałęczów, Poland

ADHESIVE PROPERTIES OF THE PLASMA TREATED PI/Cu LAMINATE SURFACE

Małgorzata KALCZEWSKA[1]
Tele and Radio Research Institute (1)

***Abstract**. A modification of polyimide surface in PI/Cu laminate by means of dielectric barrier discharge (DBD) generated in argon was made to enhance the adhesive strength of the laminate surface with a FR4 rigid board. A 90° peel test, which was used to check the improvement of the adhesive properties between the examined surfaces revealed that the adhesive strength increased from 0.24 to 0.33 kG/cm after the plasma treatment. The AFM research showed changes in the surface topography after the plasma processing.*

***Streszczenie.** Przeprowadzono modyfikację powierzchni laminatu PI/Cu przy użyciu plazmy generowanej w wyładowaniu barierowym w argonie pod ciśnieniem atmosferycznym w celu zwiększenia przyczepności laminatu do powierzchni sztywnej płyty FR4. W celu sprawdzenia właściwości adhezyjnych pomiędzy badanymi powierzchniami wykonano próby na odrywanie. Po obróbce plazmowej wytrzymałość na odrywanie wzrosła z 0.24 do 0.33 kG/cm. Badanie powierzchni metodą AFM pozwoliło zaobserwować zmiany topografii powierzchni po obróbce plazmowej.*

Keywords: polyimide, laminate, peel strength, dielectric barrier discharge, surface modification
Słowa kluczowe: poliimid, laminat, wytrzymałość na odrywanie, wyładowanie elektryczne z barierą dielektryka, modyfikacja powierzchni

Introduction

Rigid flex boards, schematically shown in Fig.1, consist of rigid parts typically made of FR4 laminate, connected to a flexible link made of polyimide-copper (PI/Cu) laminate [1].

Fig. 1. The example of a rigid flex circuit construction;
■ - polymer
▨ - copper
□ - adhesive
■ - FR4.

The polyimide layer is very smooth on the outside and has insufficient adhesion to the FR4 laminate, which is used to stiffen certain areas. For this reason, it is necessary to make incisions in these areas, in the protective polyimide layer. If there are many such incisions on the board or if they cover a large area of the board, it causes difficulties with packaging (before pressing). In addition, the mechanical strength of coupling areas decreases significantly in the presence of incisions.
Selective etching of the polyimide layer would increase the adhesion in particular areas, however it wouldn't influence the mechanical strength of the polyimide cover layer.
The aim of the study was to determine whether the method of DBD plasma treatment of the PI/Cu laminate can effectively improve the adhesive properties of the modified polyimide layer.
To examine the changes of adhesive properties on the treated surface, a 90° peel test was performed. The method was designed to examine a flexible adherence attached to a rigid substrate and it has been widely used [2]. To reveal the surface topography changes, we used the AFM research.

Experimental

The experimental setup was the same as that applied previously to the modification process of pure polyimide foil [3]. It consisted of: a working gas vessel, a mass flow controller, a plasma reactor that was used to carry out the surface etching process, a power supply device and an arrangement to measure the electric parameters of the discharge. The working gas (argon) flow rate was 0,2 Nl/h. The samples were exposed to plasma under the atmospheric pressure. The dielectric barrier discharge with a frequency of 50 kHz was generated between the surface of the polyimide protective layer of the laminate and the surface of a brass high-voltage electrode. The experiments were carried out for various discharge gaps (d): 0.40, 0.75 and 1.00 mm. The exposure time of each of the experiments was 15 minutes.

Results and discussion

The AFM research was carried out for the selected samples. The AFM micrographs are presented in Fig. 2.

a)

b)

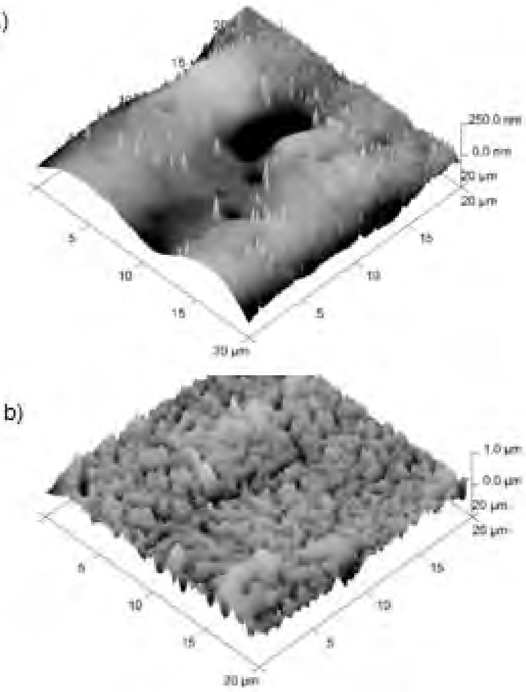

Fig. 2. The AFM micrographs of the laminate surface: a) untreated sample; b) sample treated in argon

The AFM micrographs show that after the plasma treatment the surface of the PI covered laminate was changed (Fig. 2). It has numerous regularly located hollows of similar size and a depth of several dozen nanometers. The difference between the maximal and the minimal hollow depths (R_{max}) amounted to over 200 nm over the whole profile of the sample.
It is a significant increase in comparison with the R_{max} value of the untreated sample (Fig. 2a), for which R_{max} was in the range of 50-100 nm. Irregularly located needle-like structures are visible on the surface of the raw material. The presented AFM micrographs (Fig. 2) show that the plasma treatment removed the structures characteristic for the raw material and formed a new regular image.
Our results are consistent with those obtained by W. J. Park and others [4] and S-J. Park and others [5]. They revealed that after the plasma treatment of the polyimide layer, the roughness of the surface increases [4, 5]. The plasma treatment leads to the generation of abundant active entities on the polymer surface and they can originate the formation of crosslinked aggregates on the surface. This phenomenon may cause the increase of the surface roughness [5] and we can suppose it leads to the increase of adhesive properties of the surface.
A subsequent part of the presented work consisted in revealing how the plasma surface modification affected the peel strength of the etched polyimide on the FR4 type laminate.
A sample of etched polyimide (DuPont Kapton) was pressed on the FR4 substrate. The pressing was carried out under conditions standard for the polyimide link: temperature 175°C, pressure 18 at., the total time of cycle 120 min.
The method we used in the investigation of adhesion of the copper to examine the adhesion of the polyimide samples to FR4 was as follows. Strips of samples of 5 mm width were torn perpendicularly off the substrate and the peel strength was measured by a dynamometer. The results are shown in Table 2.

Table 2. The peel strength for the samples treated in plasma.

sample	d [mm]	Q [kG/cm]
untreated	-	0.24
A	0.40	0.30
B	0.75	0.33
C	1.00	0.33

After the plasma treatment, the peel strength increased by about 25% at the discharge gap (d) of 0.40 mm (Table 2, sample A) and over 35%, for the wider discharge gaps (Table 2, sample B and C). The results prove a significant improvement in adhesion properties of plasma-treated surface compared to the untreated one.

The increase of the adhesive strength between the polyimide foil and Cu after the plasma treatment was examined also by Y. Takagia and others [6]. The adhesive strength between the examined surfaces increased nearly twice.
The obtained results of the 90° peel test are consistent with the AFM surface analysis. It is supposed that the improvement of the adhesive properties between the examined surfaces may be caused by two factors. First is the increase of the surface roughness that leads to an increase of the surface energy [5]. The other may be the chemical changes on the treated surface. It was revealed previously that on the treated PI surface the active oxygen species are formed [3] and they may be responsible for the better adhesion between the examined materials.

Conclusions

The plasma modification process of polyimide surface in PI/Cu laminate was performed. As a result of etching the properties of the etched surfaces have changed. The AFM method allowed to obtain images of the surface topography that clearly show the positive effect of the experiments. The images of the surface topography obtained with the AFM method clearly show that DBD plasma treatments increased the roughness of the treated surfaces.
The peel strength increased by more than 35% after the plasma treatment in comparison with the untreated sample. It suggests that the adhesion properties of the treated samples improved.
On the basis of the peel strength test results it is supposed that the plasma modification method of polyimide-copper laminate surface may be useful in the appropriate stage of the process of manufacturing the rigid flex boards.

Acknowledgement

This work was supported by the Polish State Committee for Scientific Research under the framework of Tele & Radio Research Institute Statutory Fund.

REFERENCES

[1] Fjelstad J., Flexible Circuit Technology, BR Publishing, Inc, 2006
[2] Song J.Y, Yu Jin, Analysis of the T-peel strength in a Cu/Cr/Polyimide system, *Acta Materialia*, 50 (2002), 3985–3994
[3] Kalczewska M., Opalińska T., Więch M., *Elektronika*, 7 (2010), 179-185
[4] Park W.J, Yoon S.G., Jung W.S., Yoon D.H., Surf. Coat. Technol., 201 (2007), 5017-5020
[5] Park S-J., Lee H-Y, *Colloid and Interface Science*, 285 (2005), 267-272
[6] Takagi Y., Gunjo Y., Toyoda H., Sugai H., *Vacuum*, 83 (2009) 501–505

***Authors**: mgr inż. Małgorzata Kalczewska, Instytut Tele- i Radiotechniczny, ul. Ratuszowa 11, 03-450 Warszawa, E-mail: malgorzata.kalczewska@itr.org.pl*

INTERACTION OF NONTHERMAL PLASMA AND CATALYST AT AMBIENT TEMPERATURE

Hyun-Ha KIM

National Institute of Advanced Industrial Science and Technology (AIST)

Abstract*. Understanding of the fundamental interaction between NTP and catalyst is of special important for the further optimization of the combined system. In this work, physical interaction of NTP with the active metal nanoparticles supported zeolites was investigated using a microscope-ICCD camera system, and electrical waveforms.*

Keywords: Nonthermal Plasma, Catalyst, Nanoparticle, ICCD Camera, Surface Streamer

Introduction

Combination of atmospheric-pressure nonthermal plasma (NTP) with catalyst is gathering attention due to its various synergistic effects. In the decomposition of volatile organic compounds (VOCs), for example, the combined system can achieve higher CO_2 selectivity (i.e. deep oxidation) and better carbon balance [1]. Since the early 1990s, technical feasibility of NTP alone process has been tested for the various types of VOCs using different plasma sources and reactors. Despite several interesting advantages of NTP, two important technical problems of large energy consumption and harmful byproduct have been raised to be solved before the industrial use. As an alternative to overcome the drawbacks of plasma alone process, the combination of nonthermal plasma with catalyst is currently gathering attentions.

Understanding of the fundamental interaction between NTP and catalyst is of special important for the further optimization of the combined system. Recently, the important physical interaction between NTP and metal nanoparticles supported on various zeolites (such as MS-13X, mordenite, HY) has been reported [2, 3]. In this work, physical interaction of NTP with the active metal nanoparticles supported zeolites was investigated using a microscope-ICCD camera system, and electrical waveforms.

Experimental

The microscope-ICCD camera observation system consists of an XY stage, optical microscope, image intensifier (Hamamatsu Photonics, C9016-03) and a charge coupled device (CCD) camera (Hamamatsu Photonics, C8484-05G). A small plane type dielectric barrier discharge (DBD) reactor packed with high-silica Y-type (HSY) zeolite was used in this study. The size of HSY pellet was 1.6 mm in diameter and 3-6 mm in length. The gap distance of the DBD reactor was 4 mm. This DBD reactor was energized with a Trek 20/20B or neon transformer, capable of delivering up to 20 kV_{max}. The observation area can be adjusted by changing the optical lens. Electrical characteristic was measured with a current transformer (Pearson Inc., Model 2877), a high voltage probe (Tektronix, P6015A) and an oscilloscope (Tektronix, TDS3032B).

Results and Discussion

Figure 1 shows the ICCD photographs on the plasma generation on HSY zeolite supported with 10 wt% Ag. AC high voltage with 50 Hz was applied to the 4 mm gap DBD reactor filled with the catalysts.

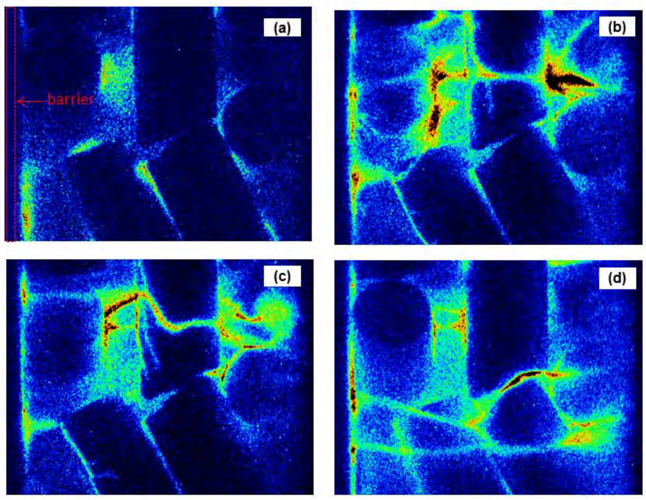

Fig. 1 ICCD camera images of discharge plasmas generated on the Ag/HSY Zeolite; (a) 16 kV_{max}, (b, c) 19 kV_{max}, (d) 21 kV_{max} . All at 50 Hz with exposure time of 4 ms.

At 16 kV, Fig. 1(a), discharge was observed vicinity of contact points of zeolite pellets, which is also referred to as partial discharge. This enhanced electric field reduces corona plasma onset voltage compared to the plasma reactor without catalyst packing. As increasing the applied voltage, plasma was observed not only at the contact points but also on the surface of the Ag/HSY zeolite.

The property of surface streamers was different from gas-phase streamer. First, in contrast to the gas-phase streamers, the propagation of the surface streamer is not always along the electric-field. They sometimes propagate in bent manner as shown in Fig. 1(c). The position of surface streamer randomly changed, and well-known memory effect was not observed. As was reported with the MS-13X, HY, and mordenite zeolites in [2], the supporting of Ag nanoparticles enhanced both the catalytic activity (enhancement factor, CO_2 selectivity and carbon balance) and the expansion of plasma area on the surface of catalyst. The expansion of plasma was confirmed by the increased number of current pulses.

Summary

The interaction of nonthermal plasma and zeolite catalyst was investigated. The packing of zeolite enhances the decomposition efficiency of VOC. It was also found that the zeolite catalyst changes the generation of plasma. The packing of zeolite reduces the plasma onset voltage by the enhanced electric field at the contact points of zeolites pellets. And the loading of Ag nanoparticles expanded plasma area over the wide area of zeolite surface. Interestingly, surface streamer was bending and curving during the propagation on the zeolite surface.

References

[1] H. H. Kim, A. Ogata, S. Futamura, *Appl. Catal. B: Environ.*. 79 (2008)., 356,

[2] H. H. Kim, J. H. Kim, A. Ogata, *J. Phys. D: Appl. Physics*. 42 (2009), 135210,

[3] H.H. Kim, A. Ogata, *Euro. Phys. Journal Appl. Phys.*, 55 (2011), 13806

***Authors**: Dr. Hyun-Ha KIM, National Institute of Advanced Industrial Science and Technology (AIST), 16-1 Onogawa, Tsukuba 305-8569, Japan E-mail: hyun-ha.kim@aist.go.jp;*

Conference ELMECO–7
ELECTROMAGNETIC DEVICES AND PROCESSES IN ENVIRONMENT PROTECTION
joint with 10th Seminar AoS-10 APPLICATIONS OF SUPERCONDUCTORS
28–30.09.2011, Nałęczów, Poland

THE INFLUENCE OF TECHNOLOGICAL; PARAMETERS ON PHOTOVOLTAIC PROPERTIES OF TiO_2

Anna KISIEL[1], Małgorzata MIELCAREK, Jan ZIAJA[1]

Wroclaw University of Technology (1)

***Abstract**. The aim of this study was to obtain structures of TiO_2 thin films with photovoltaic properties. The layers were produced by magnetron sputtering. The influence of basic process parameters (power, frequency and duration of sputtering) on the of photovoltaic properties was investigated. The results obtained showed that the power of magnetron sputtering and annealing temperature of samples is crucial for the proper formation of the crystalline structure and photovoltaic activity of titanium oxide films.*

***Streszczenie.** Celem pracy było otrzymanie cienkowarstwowych struktur TiO_2 o właściwościach fotowoltaicznych. Warstwy wytwarzane były metodą rozpylania magnetronowego. Wyniki badań wykazały, że moc rozpylania oraz temperatura wygrzewania próbek ma decydujący wpływ na powstanie odpowiedniej struktury krystalicznej i aktywność fotowoltaiczną warstw tlenku tytanu. (**Wpływ parametrów procesu technologicznego na właściwości fotowoltaiczne warstw TiO_2**).*

Keywords: titanium dioxide, photovoltaics, magnetron sputtering.
Słowa kluczowe: dwutelenek tytanu, fotowoltaika, rozpylanie magnetronowe.

Introduction

Production of electricity from renewable energy sources causes still increasing interest in the world. An important advantage of renewable energy sources is the fact that in contrast to the conventional sources, they are available around the world, although not everywhere in the same extent. Nowadays predominant source of energy is still oil next coal, methane and nuclear energy. Alternative energy sources are today only about 3% of the overall energy consumption, but in the future is expected significant growth in their participation.

Among unconventional sources of energy particularly important is solar energy. Technologies based on its use are developing extremely dynamic. Solar energy, possible to obtain, exceeds 1,000 times global demand, but major obstacle to its use are problems with energy storage [1].

Solar energy can be directly converted into electricity through the photovoltaic cells, which can be made of different materials. Among them is the most commonly used silicon, but cells made of it are complex and expensive. The high price is still one of the biggest drawbacks of photovoltaic systems. One of the solutions is selection of suitable material for application in photovoltaic cells. Such material should be characterised by low price, the high chemical stability, high photovoltaic activity and non-toxicity as well. Among the materials that meet most of these requirements is titanium dioxide. Therefore, TiO_2 has recently attracted enormous attention of many researchers. Unfortunately its range of light absorption is small. This can be improved by adding certain elements [2, 3], other compounds [4, 5], or by application of suitable method for its preparation [6, 7, 8].

In this work, titanium dioxide thin films were deposited on ITO substrate by magnetron sputtering method. This method was chosen because of its relatively easy way to control conditions of film deposition. In addition, this method allows the production of large-area coating.

Experimental

TiO_2 films were made by the magnetron sputtering method. The magnetron was equipped with a titanium target (99.9% purity) of a diameter 100 mm. The substrate-to-target distance was fixed. The films of titanium dioxide were deposited onto glass substrates with ITO layer in oxygen atmosphere, at the pressure $9.4\ 10^{-3}$ Tr.

Magnetron sputtering process was carried out for varied input power, time of deposition, and the frequency.

Usually thin TiO_2 films obtained at room temperature do not show crystalline phases, therefore annealing was also applied. This process was conducted in the temperature range 350 – 700°C for half an hour. Samples from the same series were annealed at constant temperature.

The crystal structure was investigated by X-ray diffraction both for annealed and non-annealed films.

Results

In the Figure 1 dependences of the photocurrent intensity on light wavelength for titanium dioxide films obtained at different sputtering power are shown.

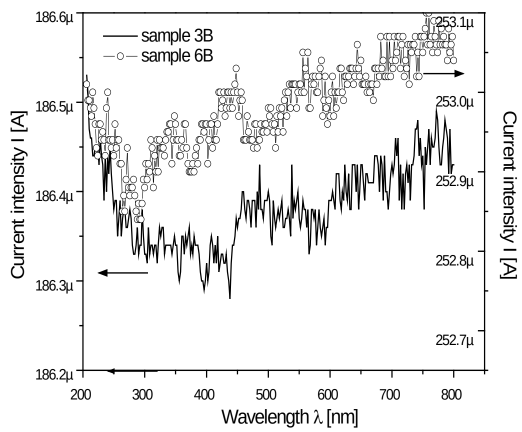

Fig.1. Photocurrent spectrum of TiO_2 thin films obtained with different sputtering power: 1 kW (sample 3B), 3 kW (sample 6B)

Figure 2 displays the relationship between current intensity and the wavelength for titanium dioxide thin films prepared with the same sputtering power and frequency, but for different time deposition.

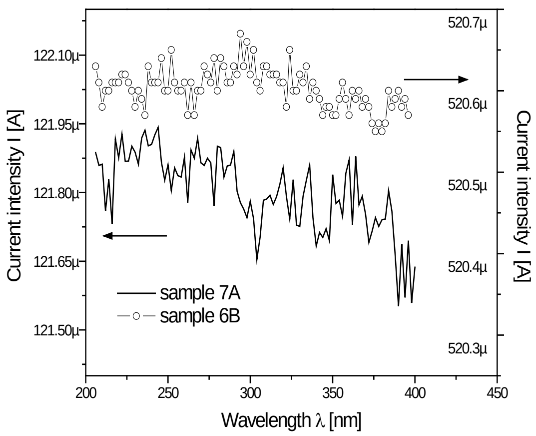

Fig. 2. Photocurrent spectrum of TiO_2 thin films prepared at different time deposition: 5 min (sample 7A), 10 min (sample 6B)

In the Figure 3 the current-voltage characteristics for one of the TiO_2 film after annealing at 550°C is presented.

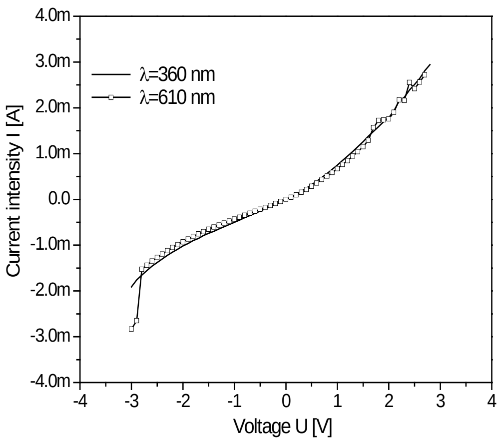

Fig. 3. Current - voltage characteristics for TiO_2 thin film measured at different wavelentgh (sputtering power 3 kW, time of deposition 5 min, frequency 4.3 kHz)

Conclusion

In the first stage of work thin films of titanium dioxide were manufactured. During technological process a few of its main parameters were varied. Sputtering power was changed in the range 1-3 kW, the frequency from 100 Hz to 4,3 kHz and time sputtering from 2.5 to 25 minutes. The selection of parameters of the sputtering process of TiO_2 thin films sought to obtain samples of good photovoltaic properties.

Another important step was to examine the structure of obtained films. Method used for this purpose was the X-ray diffraction. It allows primarily to determine the degree of order structure of the material. It also provides information about the content of each phase.

In the tested TiO_2 films there was no rutile crystalline phase. Probably annealing temperature was too low and there were no such arrangement of the structure.

TiO_2 thin films obtained at different technological parameters characterised by different photovoltaic properties. The layers obtained at lower sputtering power showed negligible photoelectric activity, regardless of the applied wavelength of the light.

Dependences of photocurrent intensity as a function of wavelength for titanium oxide films prepared at various time showed that the sample formed for 10 min. demonstrated more than three times higher current value, compared to that one which was prepared for 5 min (Fig. 2). These differences have been seen in the whole measured spectral range.

The results obtained indicate that the choice of relevant parameters of film formation is extremely important. It affects not only the quality of the obtained films - their proper adhesion to the substrate, cohesion, but primarily on the structure of the obtained titanium oxide. In the applied process of preparation of titanium oxide films was not possible to regulate the temperature of the substrate. The main parameter determining the formation of appropriate phases of TiO_2 and its photovoltaic activity was the sputtering power. Other conditions of film formation, such as frequency and time of deposition also play an important role, but their influence on the photovoltaic properties of titanium oxide films has not yet been studied adequately.

Following this study samples were obtained which differed significantly in photovoltaic activity. The best parameters showed a titanium oxide film obtained at maximum power sputtering (3 kW), frequency of 4.3 kHz and the sputtering time 5 min. This sample was annealed at temperature 550 °C.

This work was supported by the Polish Committee for Scientific Research under basic research of Institute of Electrical Engioneering Fundamentals, Wroclaw University of Technology, no. 341732.

REFERENCES

[1] Elliot D., Sustainable Energy. Opportunities and Limitations. PALGRAVE MACMILLAN, New York, 2007

[2] Sun H., Liu H., Ma J., Wang X., Wang B., Han L., Preparation and characterization of sulfur-doped TiO_2/Tiphotoelectrodes and their photoelectrocatalytic performance, *Journal of Hazardous Materials,* 156 (2008), 552-559

[3] Chatterjee S., Titania-germanium nanocomposite as a photovoltaic material, *Solar Energy*, 82 (2008), 95-99

[4] Chi Y., Fu G., Qi L., Shi K., Zhang H., Yu H.,Preparation and photo electric performance of ITO/TiO_2/CdS composite thin films, *Journal of Photochemistry and Photobiology A: Chemistry*, 195 (2008), 357–363

[5] Chatterje A., Islam M., Fabrication and characterization of TiO_2-epoxy nanocomposite, *Materials Science and Engineering A,* 487 (2008), 574-585

[6] Pavasupree S., Ngamsinlapasathian S., Nakajima M., Suzuki Y., Yoshikawa S., Synthesis, characterization, photocatalytic activity and dye-sensitizedsolar cell performance of nanorods/nanoparticles TiO_2 with mesoporous structure,, *Journal of Photochemistry and Photobiology A: Chemistry*,184 (2006), 163–169

[7] Yoo B., Kim K., Lee S., Kim W., Park N., ITO/ATO/TiO_2 triple-layered transparent conducting substrates for dye-sensitized solar cells, *Solar Energy Materials & Solar Cells*, 92 (2008), 873– 877

[8] Shi J., Liang J., Peng S., Xu W., Chen J. , Synthesis, characterization and electrochemical properties of a compact titanium dioxide layer, *Solid State Sciences,* 11(2009), 433–438

***Autorzy**: dr inż. Anna Kisiel, Politechnika Wrocławska, Instytut Podstaw Elektrotechniki i Elektrotechnologii, ul. Wybrzeże Wyspiańskiego 27, 50-370 Wrocław, E-mail: anna.kisiel@pwr.wroc.pl; dr inż. Jan Ziaja, Politechnika Wrocławska, Instytut Podstaw Elektrotechniki i Elektrotechnologii, ul. Wybrzeże Wyspiańskiego 27, 50-370 Wrocław, E-mail: jan.ziaja@pwr.wroc.pl*

ELECTRICAL DIAGNOSTICS OF MICRODISCHARGES IN HELIUM

Matej KLAS, Michal STANO, Štefan MATEJČÍK

Comenius University, Slovak Republic

Abstract*. In this paper we have investigated the validity of Paschen law for microdischarges generated in a system consisting of two plan-parallel tungsten electrodes at separations from 100 to 1µm in Helium. The DC breakdown and V/I characteristics were measured in pressure range from 985mbar to 30mbar. The results are presented in the form of Paschen curves. Our studies deliver new data on DC breakdown under these experimental conditions and on validity of the Paschen law in Helium.*

Keywords: Microdischarges, Paschen Law, Field emission

Introduction

The Paschen law states that the breakdown voltage of a gas is a function of the product *p.d* (operating pressure and the electrode spacing) [1]. The validity of the Paschen Law was confirmed for variety of DC discharge conditions (pressures, distances, electrode materials) [2, 3]. However, already in fifties of the 20 century, the departures from the Paschen law have been observed at high electric fields generated in small electrode gaps [4, 5]. These experiments shown, that when a sufficient high electric field is achieved the field emission and the ion-enhanced field emission affect the left branch of the Paschen curve. In spite of large number of publications devoted to the measurement of breakdown voltages at micro separation there exist only few studies in the literature for separation smaller than 300µm and in homogeneous electric field [6]. For this reason we built the new system to measure the DC breakdown from 500µm to 1µm separations between plan-parallel tungsten electrodes in homogeneous electric field.

Experimental apparatus

Schematic view of apparatus is shown in Fig. 1. Experimental apparatus consist of the plan-parallel discharge system located in the high-vacuum chamber and of positioning system to achieve precise centering and tilting of the electrodes. In this experiment highly polished tungsten electrodes were used. In order to prevent discharge to ignite at longer paths the electrodes were covered by dielectric glass cap. Electrical measurements were done using AD converter with 10kHz sampling frequency and 10 samples averaging.

Results and discussion

In the present experiments we have measured the breakdown voltage as a function of the He pressure and the electrode distance. The measured curves are presented in the form of a Paschen curve in the Fig. 2. Present data are compared with Paschen-curve of He of ordinary planar discharge tube published by Hartmann et al. [7]. The agreement between present data and the data of Hartmann et al. is satisfactory for measurement at fixed electrode separation (100µm) and variable pressure and also for measurement at atmospheric pressure with variable electrode gap down to the value *p.d* of 1Torr.cm. below this value the effects associated with high value of the electric field occur. It is clear from the Figure 2., that combination of small electrode distance and high reduced electric field leads to decrease of breakdown voltages. This departure from the theoretical Paschen curve is caused by the influence of high electric field and ion-enhanced field emission [8,9].

In figures 3-5 we present examples of Volt/ampere characteristics of discharge for 100µm and 10µm electrode separations. The breakdown curve for 100um shows no apparent departure from Paschen law and thus we consider it for a normal discharge. This is confirmed by the V/A characteristics in the Figures 3. and 4. At 10 µm electrode separation the breakdown curve shows departure from Paschen law and thus discharge generated at this electrode separation represents a different type of discharge due to important role of processes associated with high electric field (field emission of electrons from the surface and the ion enhanced field emission). The V/A characteristic for this discharge (Figure 5.) shows that the current is practically limited by the field emission of the electrons from the electrode.

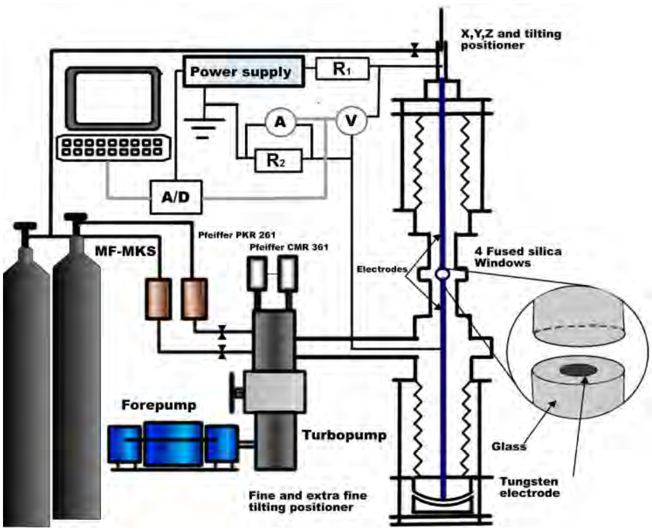

Fig. 1 Schematic view of experimental apparatus

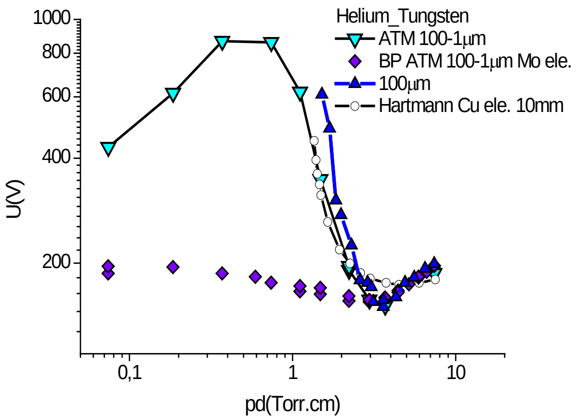

Fig. 2 Paschen curve for microdischarges in Helium

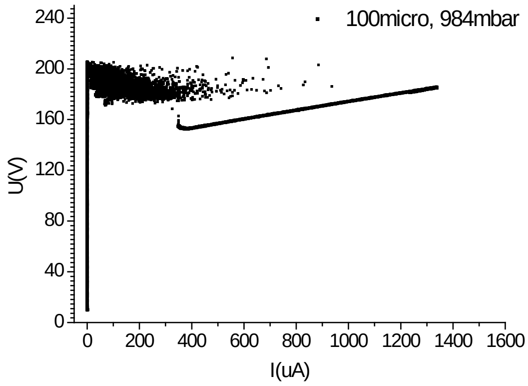

Fig. 3 V/I characteristics for 100μm on the right-hand side of the Paschen minimum

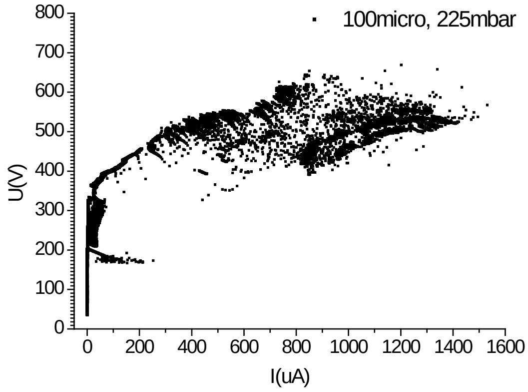

Fig. 4 V/I characteristics for 100μm on the left-hand side of the Paschen minimum

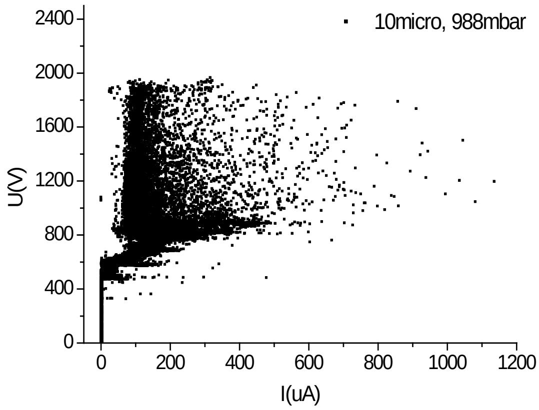

Fig. 5 V/I characteristics for 10μm at atmospheric pressure

Acknowledgements

This work has been supported by project Slovak grant agency VEGA, project Nr. 1/0379/11.

REFERENCES

[1] Paschen, Ann. *Phys. Chem*,(1889),69, 37
[2] Meek J M and Craggs J D, *Electrical breakdown of gases* Oxford University Press,1953
[3] Reizer Y.,*Gas discharge physics* Springer-*Verlag,.* Berlin Heidelberg, (1991)
[4] Boyle W. S. and Kisliuk, *P Phys. Review* 97(1955) 255
[5] Boyle W S and Germer L H , *J. Appl. Phys.* (1955)26, 571
[6] Dhariwal R.S, *Sci. Meas. Technology* Vol 147,5,2000
[7] Hartmann and Donko, PlasmaSourcesSci.Technol.,(2000) 9 183–190
[8] M. Klas *et al, EPL* ,(2011)**95** 35002
[9] Radmilovic-Radjenovic M.,*Contrib. Plasma Phys. 47*, (2007) No. 3, 165 – 172

***Authors**: RNDr. Matej Klas, Department of Experimental Physics, Comenius University, Mlynska dolina F2, 84245 Bratislava, Slovak Republic E-mail: matej.klas@gmail.com , prof. Dr. Štefan Matejčík, DrSc., Department of Experimental Physics, Comenius University, Mlynska dolina F2, 84245 Bratislava, Slovak Republic E-mail: Stefan.Matejcik@fmph.uniba.sk*

3D STRUCTURE OF POSITIVE CORONA STREAMER RECONSTRUCTION USING STEREO PHOTOGRAPHY AND COMPUTER ALGOROTHMS

Marek KOCIK [1], Mateusz TAŃSKI [1], Jerzy MIZERACZYK[1,2],

Szewalski Institute of Fluid-Flow Machinery (1), Gdynia Maritime University (2)

***Abstract**. 3D structure of corona streamer was measured using stereo photography method. To enhance and speed-up the image processing computer algorithms were developed for automatic reconstruction of 3D structure of streamers*

***Streszczenie.** W niniejszym artykule przedstawiono metodę rekonstrukcji struktury przestrzennej strimera wyładowania koronowego. Dzięki zastosowaniu opracowanych algorytmów komputerowych możliwe było zautomatyzowanie procesu odtwarzania struktury strimera z wykonanych metodą stereofotografii obrazów.*

Keywords: corona streamer, 3D reconstruction, stereo photography, local methods
Słowa kluczowe: strimery wyładowania koronowego, stereo fotografia, metody lokalne

Introduction

Positive streamers are widely used in the field of air pollution control such as NOx or SOx removal and VOCs decomposition based on plasma chemical reactions. Although the streamers have been studied for many years, they are still not fully understood due to their complex nature. One of such unexplored issue in streamer research is the breakup of single channels, called streamer branching. Streamer branching is commonly seen in experiments [1,2]. Multiple streamer branching actually determines the gas volume that is crossed by streamers and consecutively chemically activated for plasma processing purposes. However, up to now, only the conditions of the first branching event have been resolved in microscopic models. On the other hand, the distribution of branching lengths and angles is an ingredient of models for the complete branching tree on larger scales [3]. Therefore, there is a need for experimental data of streamer branching lengths and angles. For imaging of streamer discharges digital cameras (CCD cameras) or intensified cameras (ICCD) are used. The result of the imaging is two dimensional (2D) representations of what is actually a three-dimensional (3D) phenomenon. These 2D representations can be difficult in the interpretation and measurements of i.e. branching angles can lead to false conclusions. For this purpose, we have implemented a stereo photography method which makes it possible to image streamer discharges in 3D. The stereographical method we used is commonly used for imaging sparks [4], flames [5], dusty plasmas [6] and pulsed streamers [7]. However, in previous experiments (including our own research [8]) reconstruction of 3D structure was done manually what is difficult and time consuming. The limited number of images which are possible to obtain in that way reduce significantly the value of experimental data. To increase the statistics we decided to develop computer algorithms for automatic reconstruction of 3D structure of streamers.

Computer algorithms

To reconstruct the 3D streamer structure several numerical methods were applied and compared.

3D streamer reconstruction methods

We can divide 3D reconstruction methods into 2 groups: global and local approaches which is related to global and local error minimization. In the first approach the 3D discharge model is created and subsequently modified to stereo photography matching using particle simulations or evolutionary searching methods [9]. The comprehensive description of global methods used for 3D streamer reconstruction problem can be found in [10]. In the local approach broadly described in this article in the first step two 2D models are created separately for each of projection photography. In the second step 3D model is built based on 2D projection models. The first step can be divided into image preprocessing stage and lines (curves) + nodes detection which can be named as vectorization stage. The first step can be accomplished as full manual, semi automatic (interactive) or full automatic process. In the first case the user can draw lines and nodes by hand based on original images. In the second case the user can accept or correct the algorithmical suggestions. In the third case the process is the quickest but demands knowledge incorporation which is the most difficult challenge. The knowledge about physical phenomenon in the most simple approach can be represented by curve continuity and curvature limitation. In more advanced approach the learning based on manually obtained examples can be used to acquire human knowledge from manual and semi automatic methods to full automatic one.

Morphological method

The main advantages of morphology usage for image preprocessing stage is their generality, speed, and easy nodes detection. It seems that the simplest approach to image preprocessing is to use the well known image processing methods like morphological operations to obtain a skeleton of an image. The example sequence of operations with example parameter values and on example couple of images were showed in Fig. 1.

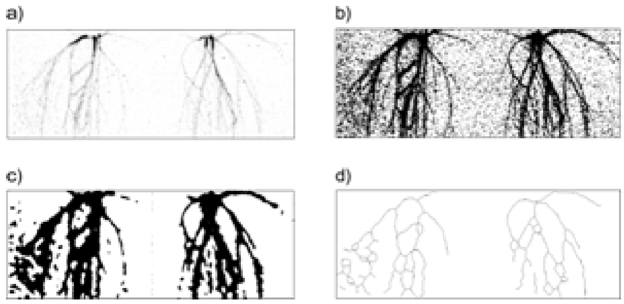

Fig. 1 Morphological operations: a) original images, b) after binarization, c) after closing, d) after skeletonization with short curves reduction.

The binarization operation (Fig. 1b) changes each image into monochromatic one using chosen threshold value. The morphological closing operation (Fig. 1c) at next step is used for empty areas closing and to cancel the noise spots which are placed rather out of streamer channels. The operation is composed with dilation and erosion and was repeated several times. In this example the dilation determined each pixel value as ,,1" if more than 3 pixel values from 3x3 adjacent pixels were equal to 1. The erosion worked in the same way but the threshold was equal 7. The skeletonization process (Fig. 1d) is used to obtain the net composed of thin curves which helps to find single curves and nodes. As can be seen in Fig. 1d the number of nodes and its vertical position are quite different in each projection which makes the 3D stream model reconstruction a difficult task. Other drawbacks of standard morphological operations in discharge 3D streamer reconstruction can be listed as following:

- limited number of node branches ,
- information loss related to binarization operation,
- branch leaving related to discontinuity of stream channel image,
- difficulties with distinguishing branching nodes from line crosses.

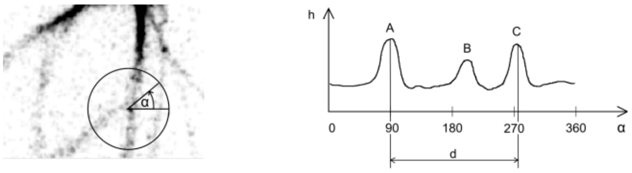

Fig. 2 Histogram-based nodes and lines detection : weighted pixel intensity related to direction angle diagram and diagram calculation area

Another approach to increase object detection quality is connected with direct expert knowledge incorporation by using dedicated image preprocessing methods prepared specially for streamer channel modelling. Histogram based object detection method is considered as an example of such approach..

Histogram based method

For each analysed pixel, histogram based on circular area is calculated. In a simple version each pixel which belongs to area was classified to one histogram bar related to particular angle. The weighted average pixel intensity value for each considered angle was calculated. The weight value is invertly proportional to distance between analysed pixel and considered pixel circular area e.g. when distance is higher the weight is lower. Fig. 2 presents example diagram after normalization and smoothing. Each branch can be detected as peak in the diagram, each straight line can be detected as two peaks shifted by the distance of about 180 degrees. Appearing of more than two peaks (see Fig. 2) suggests the node existence. The learning decision system can be used to classify histogram features using human expert decision.

Conclusions

Two methods of image preprocessing and object detection were presented as a local method component. Local methods help to overcome high computational complexity related to global ones by direct application of real streamer features during 2D models creation and simple nodes matching algorithm.

The morphological operations help to detect nodes and curves quickly but not so precisely. Histogram based method is specially prepared for 3D streamer model reconstruction. During initial experiments the histogram based method seemed to be more accurate but the way of knowledge incorporation makes this method less general than morphological. Moreover, the knowledge used for preparing algorithms may be uncertain or incomplete because physical phenomenon is under investigation.

REFERENCES

[1] R. Morrow, J.J. Lowke, "Streamer propagation in air", J. Phys. D: Appl. Phys., vol. 30, pp. 614–627, 1997.

[2] T. Ohkubo, S. Kanazawa, Y. Nomoto, M. Kocik, J. Mizeraczyk „Characteristics of DC Corona Streamers Induced by UV Laser Irradiation in Non-Thermal Plasma", J. Adv. Oxid. Tech., 8, 2, pp. 218-225, 2005.

[3] M. Akyuz, A. Larsson, V. Cooray, G. Strandberg, "3D simulations of streamer branching in air", J. Electrost. vol. 59, pp. 115-141, 2003.

[4] J. M. K. MacAlpine, D. H. Qiu, and Z. Y. Li, "An analysis of spark paths in air using 3-dimensional image processing", IEEE Trans. Dielectr. Electr. Insul., vol. 6, 331, 1999.

[5] W. B. Ng and Y. Zhang, "Stereoscopic Imaging and Reconstruction of the 3D Geometry of Flame Surface", Exp. Fluids, vol. 34, 484, 2003.

[6] E. Thomas, Jr, J. D. Williams, and J. Silver, "Application of stereoscopic particle image velocimetry to studies of transport in a dusty (complex) plasmas", Phys. Plasmas, vol. 11, L37, 2004.

[7] S. Nijdam, J. S. Moerman, T. M. P. Briels, E. M. van Veldhuizen, U. Ebert, "Stereo-photography of streamers in air", Appl. Phys. Lett., vol. 92, 101502, 2008.

[8] R. Ichiki, S. Kanazawa , S. Akamine, T. Ohkubo, M. Kocik, J. Mizeraczyk, „Reconstruction of 3-dimensional structure of streamer discharges", Annual Meeting of of the Institute of Electrostatics Japan, Tokyo City University, Tokyo, Japan, Sept.10, 2009

[9] D. Goldberg, Genetic Algorithms in Search, Optimization and Machine Learning, Addison-Wesley Inc., 1989.

[10] M. Kocik, M. Tański, J. Mizeraczyk, R. Ichiki, S. Kanazawa, J. Dembski, "Reconstruction of the 3D image of corona discharge streamer", 7th Conference of the French Society of Electrostatics SFE 2010, Montpellier, France, 30.08.-01.09.2010

***Authors**:*
dr Marek Kocik, Instytut Maszyn Przepływowych PAN, ul. Fiszera 14, 80-231 Gdańsk, E-mail: kocik@imp.gda.pl; mgr. inż. Mateusz Tański, Instytut Maszyn Przepływowych PAN, ul. Fiszera 14, 80-231 Gdańsk, E-mail: tanski@imp.gda.pl; prof. dr hab. inż. Jerzy Mizeraczyk, Instytut Maszyn Przepływowych PAN, ul. Fiszera 14, 80-231 Gdańsk, Akademia Morska, ul. ul. Morska 81-87, 81-225 Gdynia, E-mail: jmiz@imp.gda.pl;

Conference ELMECO–7
ELECTROMAGNETIC DEVICES AND PROCESSES IN ENVIRONMENT PROTECTION
joint with 10th Seminar AoS-10 APPLICATIONS OF SUPERCONDUCTORS
28–30.09.2011, Nałęczów, Poland

PLASMA SYNTHESIS OF CARBON NANOTUBES FOR ELECTRIC AND ELECTRONIC DEVICES

Zbigniew KOLACINSKI, Łukasz SZYMANSKI, Grzegorz RANISZEWSKI, Sławomir WIAK

Institute of Mechatronics and Information Systems
Technical University of Lodz

***Abstract**. In this paper the microwave plasma system for synthesis of carbon nanotubes is presented. The target of the system is the ability to produce carbon nanotubes in the form required to design a novel generation of electric and electronic devices.*

***Streszczenie.** W artykule przedstawiono mikrofalowy system plazmowy do syntezy nanorurek węglowych. Jako docelowe zastosowanie tego systemu przewiduje się wytwarzanie nanorurek węglowych w postaci wymaganej do projektowania nowej generacji urządzeń elektrycznych i elektronicznych.*

Keywords: microwave plasma, carbon nanotubes

Słowa kluczowe: plazma mikrofalowa, nanorurki węglowe

Introduction

The world demand for nanomaterials to be used in the new advanced products is annually growing with the rate over 60%. Energy sector, Electronics and Health Care seem to be the largest markets. Application of nanotechnology to the fields of Solar Energy and Energy Saving is a very much required commercial action of the current times. Day by day received and reviewed published research results allow to understand, to recognize and to discuss the most promising nanotechnology application to Solar Cells, Hydrogen Fuel Cells, Rechargeable Batteries and Supercapacitors.

Due to the ability of high Li-ions intercalation the carbon and metallic nanotubes can increase several times the battery power and capacity of energy. Considering supercapacitors the current research has shown, that the use of thin film electrodes with multi walled aligned nanotubes increases the specific power density to 30kW/kg. This makes the capacitor able to deliver high instant power when required (i.e. for accelerating a car).

Micro mechatronics is one of Mechatronics areas and has made remarkable progress recently, such as micro sensor and actuator for automotive technology, avionics technology, bio-medical technology, consumer electronics, and many others. There is a number of electric and electronic devices wasiting for this new nano material.
The paper describes a new carbon nanotubes (CNT's) synthesis plasma method that is not being hybridized with a CVD furnace. It allows producing CNT's in the powder form or making deposits on substrates such as silica, metals and on refractory insulators. This can be applied to some elctronic devices as heat sinks. Conditions required for CNT's synthesis in microwave plasma are specified. Also the process parameters and plasma jet temperature measurements are presented.

This paper is an offer to conduct joint research to employ substrates with oriented carbon nanotubes for the use in electronics, mechatronics and electrical engineering.

CNT's Synthesis

One of the main challenges to achieve optimal performance of the product is to develop a continuous synthesis process as possible and in the product form of uniform layer of carbon nanotubes deposited on the substrate. Currently, a method commonly used for this purpose is the method of CVD (Chemical Vapor Deposition). It consists of a furnace for heating in the pyrolysis process of carbon containing substances. In this furnace the catalytic synthesis of nanometer-scale diameter tubes of graphene structure takes place. Carbon atoms and molecules can be supplied with acetylene, benzene, ethylene, methane, propylene, carbon monoxide and other carbon-containing gases, as well as from the solid material (eg. ferrocene), which is lead to the evaporation or materials in liquid (eg. iron pentacarbonyl) that can be introduced into the plasma in the form of an aerosol. Catalysts are mainly iron, cobalt and nickel. Synthesis takes place in a noble gas flow at temperatures ranging from 500 to 1400 ° C.

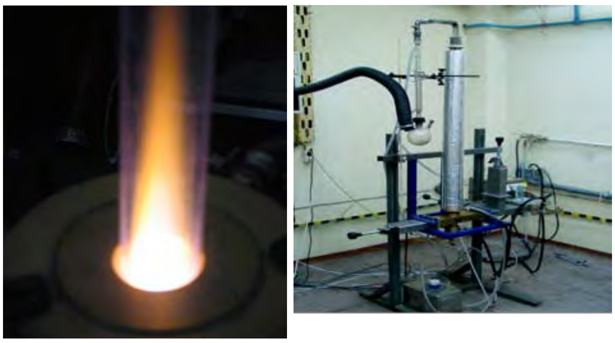

Fig. 1. The microwave plasma – left and the setup for synthesis of carbon nanotubes- right [2]

Literature report [1] suggests that microwave plasma may be used as an activator of the synthesis process of carbon nanotubes. It can be applied at the entrance to the furnace CVD. Then the tube furnace is used to ensure the conditions necessary for the synthesis process. However the microwave plasma takes also part in preparation (activation) of catalytic gas and mixing it with carbon carrying gas.

In order to the process optimizing the first studies were conducted in a hybrid system: microwave plasma plus a CVD tube furnace. Then the furnace was removed and the quartz tube was thermally insulated (Fig. 1 – right photo).

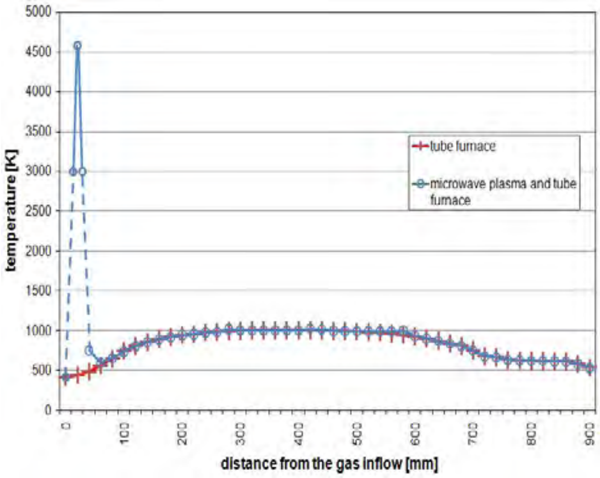

Fig. 2. Temperature distribution along the quartz tube axis for the tube furnace working alone and for the furnace with microwave plasma for the conditions as follows: the 1-st furnace zone (0-300mm) and the 2-nd one (300-600mm) were set on 1000K, the 3-rd furnace zone (600-900mm) was not heated, gas flows Ar =10 l/min, N_2 =10 l/min, microwave power set on 1680W.

Our studies have shown that microwave plasma may itself lead to the synthesis of carbon nanotubes without the use of CVD furnace. The vertical geometry of the quartz reactor tube causes symmetrical heating gas flowing at a positive impact on the homogeneity of the product, preventing the local overheating of the quartz tube.

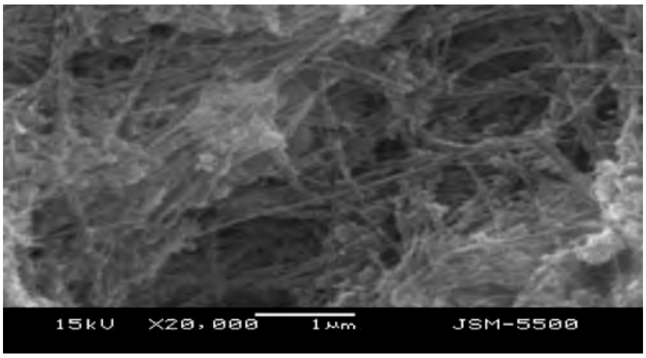

Fig. 3. SEM image of carbon nanotubes [3]

In order to compare the two systems the spectral measurements of plasma temperature and the thermocouple method, measuring the temperature distribution inside a quartz reactor along its axis were employed. The temperature distribution along the axis of the hybrid reactor is shown in Fig. 2. It should be noted that the edge of the furnace tube in zone 1 was cooled with water. For this reason, the gas temperature at the beginning of the axis (0) was relatively low (about 450 K). The measurement can see that the presence of plasma did not give a visible impact in the distribution of gas temperature in zone 2 and 3 of the furnace tube. Microwave plasma is used, in this case, for the activation of iron from iron pentacarbonyl.

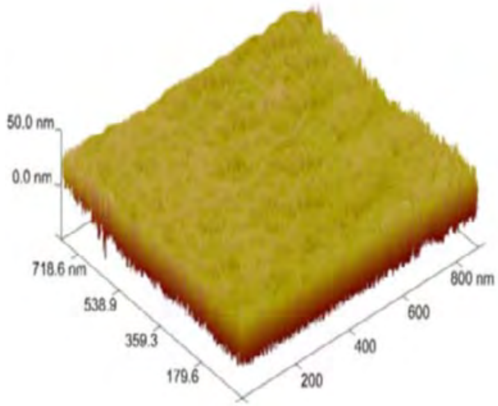

Fig. 4. AFM image of the slice vertically oriented carbon nanotubes obtained with microwave plasma [4]

In the second approach, which is the goal of our studies tube furnace was removed and in its place introduced thermal insulation (Fig. 1a). A series of spectral and thermocouple temperature measurements along quartz reactor axis for different process parameters were done. Presented in Fig. 2 the measurement results prove that the microwave power is sufficient for the synthesis reaction temperature. The samples of CNT's in the random orientation are presented in Fig.3 and AFM microscope image shows the vertically oriented CNT's carpet in Fig. 4.

CONCLUSION

This communication constitutes an offer to conduct joint research with regard to obtain substrates with oriented carbon nanotubes used in electrical engineering and electronics.

Acknowledgement

The presented here research results have been sponsored by the following grants of the Polish Ministry of Science and Higher Educations and the National Research and Development Centre: No. R01 011 03 "Development and demonstration of the system to produce carbon nanotubes in microwave plasma at atmospheric pressure" and No. R01-0016-10 "Plasma system for continuous synthesis of carbon nanotubes on a moving substrate".

References

[1] J. Han S. Uhm, Yong C. Hong and Dong H. Dhin: Microwave plasma torch and its applications, *Plasma Sources Sci. Technol*. 15 S26 (2006),

[2] Z. Kolacinski, L. Szymanski, G. Raniszewski, M. Druri: Hybrid Vertical Flow Reactor for Continuous CNTs Synthesis, 20th European Conf. on Diamond, Diamond-Like materials, Carbon Nanotubes and Nitrides, Athens, Conf. Mat. P.1.8.11, (2009),

[3] Z. Kolacinski, G. Raniszewski, L. Szymanski: CNTs synthesis carrier gas analysis, The 7th EU-Japan Joint Symposium on Plasma Processing, Liblice, Czech Republic, p.35 (2009),

[4] Z. Kolacinski, L. Szymanski, M. Druri, G. Raniszewski, S. Mitura, K. Cedzynska, W. Kaczorowski: Microwave plasma for CNTs deposit continuous fabrication at atmospheric pressure, Workshop on Progress in Bio- and Nanotechnology, Technical Univ. of Lodz, p.28 (2009),

***Authors**: prof. dr hab. inż. Zbigniew Kolacinski, E-mail: zbigniew.kolacinski@p.lodz.pl; dr inż. Łukasz Szymański, E-mail: lukasz.szymanski@p.lodz.pl, dr inż. Grzegorz Raniszewski, E-mail: grzegorz.raniszewski@p.lodz.pl, prof. dr hab. inż. Sławomir Wiak, E-mail: slawomir.wiak@p.lodz.pl Instytut Mechatroniki i Systemów Informatycznych, Politechnika Łódzka, ul. Stefanowskiego 18/22, 90-924 Łódź*

Conference ELMECO–7
ELECTROMAGNETIC DEVICES AND PROCESSES IN ENVIRONMENT PROTECTION
joint with 10th Seminar AoS-10 APPLICATIONS OF SUPERCONDUCTORS
28–30.09.2011, Nałęczów, Poland

A ROTATING ARC PLASMA REACTOR

Zbigniew KOLACINSKI, Łukasz SZYMANSKI, Grzegorz RANISZEWSKI

Institute of Mechatronics and Information Systems, Technical University of Lodz

***Abstract**. The main objective of this research was the demonstration of a stable rotating arc discharge generation to be applied for nanomaterials synthesis. The most important phenomenon which is obtained thanks to the rotating arc is an uniform jet of vapor delivered from the arc anode to the cathode for an effective material transfer.*

***Streszczenie.** Celem przedstawionych badań było wytworzenie stabilnego wirującego wyładowania łukowego dla zastosowania do łukowej syntezy nanomateriałów.. Wirowanie łuku w tych badaniach miało na celu wytworzenie intensywnego i równomiernego strumienia par przekazywanego z anody do katody w celu zapewnienia efektywnego przepływu masy materiału.*

Keywords: rotating arc, magnetic field.
Słowa kluczowe: łuk wirujący, pole magnetyczne.

Introduction

The rotating arc is formed as a result of interaction of arc current and applied axial magnetic field. The effect of this phenomenon are electrodynamics forces, which cause a deviation of the arc and finally it's spinning.

A magnetic wall is formed on boundary of two areas, if one area is a homogeneous magnetic field with a high induction and the second one is located in the plasma, but without any magnetic field there. Charged particles running from the plasma area are reflected from the boundary layer (Fig. 1) [1].

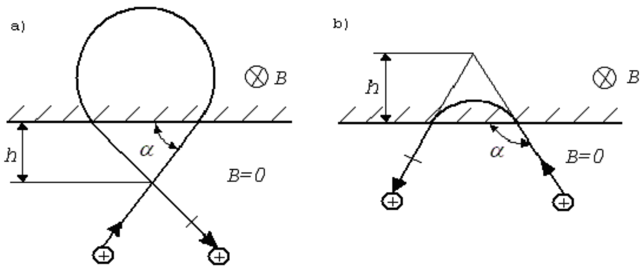

Fig.1. Magnetic wall: a) a reflection of the ion incident angle α <, the reflection of the ion incident at an angle α> [1].

Generation of a magnetic wall shown in Fig. 1. is not possible in practice, because the boundary between both of areas will not be always clear and magnetic field will not be fully homogeneous. This causes some instabilities in the formed plasma. It is also not possible to surround all sides of experimental environment by walls with the identical properties and this is reason of further instability of the plasma.

Moving charged particle undergoes action of force directed perpendicularly to direction of it's motion and direction of the magnetic field [1].

Force operating on the particle will be equal to:

$$F = m\frac{dv}{dt} = q(v \times B) \tag{1}$$

Force F operates perpendicularly to the plane in which are the vectors v and B. Its shift has the direction of movement of screw turning right from v to B vectors and module vBsin θ (where θ - the angle between vectors v and B) as it follows by definition of vector product. Force F does not perform any work, because of its perpendicular direction to the movement of particles, but it causes a centripetal acceleration, constantly changing direction of particles velocity, thus it causes curvature of particle course without changing its velocity module. The kinetic energy does not change.

The particle begins moving by a circle with a radius r_c at a constant speed (Fig. 2a) by a cyclotron orbit (Larmor) [1].

The angular velocity is equal to:

$$\omega = \frac{qB}{m} \tag{2}$$

where: - the component velocity of particle perpendicular to the vector B.

The particle will be moving along the screw course (Fig. 1b), when the initial velocity vector of particle will not be perpendicular to B.

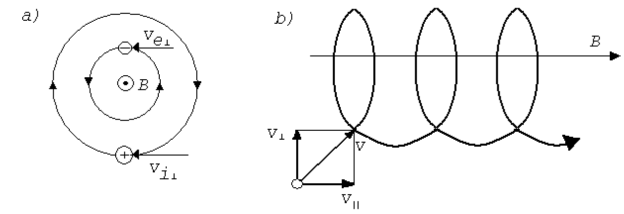

Fig. 2. The course of charged particulars in homogenous magnetic field [1]:
a) a component of velocity along magnetic field lines equal to 0
b) a component of velocity along magnetic field lines unequal to 0

Positive ions move in the opposite direction with a lower cyclotron frequency. Cyclotron radius of ions is larger than the electron cyclotron radius. Collisions with other particles precipitate analyzed particle from its path. It starts spinning the other course with changed radius, but with the same cyclotron frequency because of changing its speed after the collision [1]. Part of the described circle by a particle between successive collisions is called the Hall parameter.

It amounts to:

(3) $$\beta = \omega\tau = \omega\mu$$

where: β - parameter Hall, τ - time of the free course [s], μ - mobility particle [m2 * V-1 * s-1]

Formulas from (1) to (3) are taken from the literature [1].

Modelling

In the first stage of work computer model of the rotating arc generator was designed.

It was also simulating the process of burning of the arc in the system anode rod and cathode flat surface. Using the FLUENT package samples of simulation results are presented bellow.

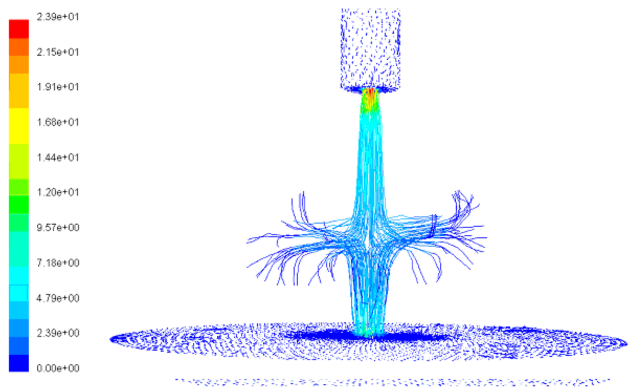

Fig.3. Velocity of particles [m/s]. Vapor disk created in the arc with a rod anode and flat cathode. The distance between electrodes was 2 mm

This parameter is very important for phenomena occurring in plasma, when it moves in a magnetic field. It is much larger for electrons, so it can be often ignored in the consideration for ions [1].

Experimental

Observations were carried out with the use of a high speed camera FASTCAM APX-RS 250K which allows registration at a rate of 250,000 frames per second at the minimum possible aperture 2 microns. Fig. 4. shows pictures taken in combination of rod anode with a flat cathode. The distance between electrodes was 2 mm. Pictures shown in Fig.4 were taken at a rate of 30,000 frames per second.

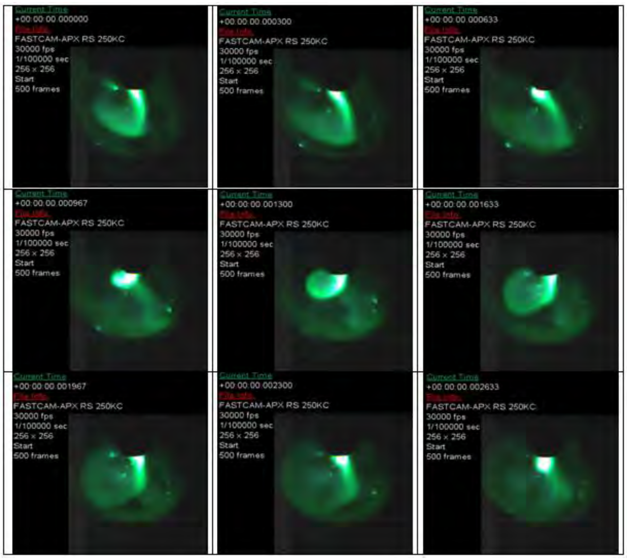

Fig. 4. Frames of film registrated by high speed camera. Photos taken at approximately 0.0003 seconds.

The spectroscopic measurements (not presented here) confirmed the much more uniform distribution of plasma temperature in the cathode region compared to the arc without magnetic rotation. As the arc discharge cross section plasma temperature is dropping down typically from 5000K in the centre of the arc channel to the ambient gas temperature a privilege region of nanotubes formation can be found. It is also determined on densities of carbon species decreasing in the radial direction due to the plasma expansion and on heat fluxes, which if are to high they may lead to overheating preventing formation of stable nanostructures.

REFERENCES

[1] Celiński Z., Plazma, Państwowe Wydawnictwo Naukowe, Warszawa 1980

Acknowledgement

The work here presented relates to the Polish Ministry of Science and High Education project No N N510 390138 on "Influence of External Magnetic Field on Arc Plasma Properties Related to Effective Synthesis of Carbon Nanotubes"

***Authors**: prof. dr hab. inż. Zbigniew Kolacinski, E-mail: zbigniew.kolacinski@p.lodz.pl; dr inż. Łukasz Szymański, E-mail: lukasz.szymanski@p.lodz.pl, dr inż. Grzegorz Raniszewski, E-mail: grzegorz.raniszewski@p.lodz.pl, Instytut Mechatroniki i Systemów Informatycznych, Politechnika Łódzka, ul. Stefanowskiego 18/22, 90-924 Łódź*

Conference ELMECO–7
ELECTROMAGNETIC DEVICES AND PROCESSES IN ENVIRONMENT PROTECTION
joint with 10th Seminar AoS-10 APPLICATIONS OF SUPERCONDUCTORS
28–30.09.2011, Nałęczów, Poland

INFLUENCE OF GAS CONCENTRATION INHOMOGENEITY ON MEASUREMENT ACCURACY IN ABSORPTION SPECTROSCOPY

Paweł KOMADA, Sławomir CIĘSZCZYK, Waldemar WÓJCIK

Lublin University of Technology

Abstract*. The article presents influence of a variable compound concentration along measurement path on results obtained by absorption spectroscopy. It is very important, especially for the case when long optical path are applied. The discussed measurement method is utilized e.g. in environment control of power boilers when biomass is co-combusted with coal.*

Streszczenie.
*Artykuł porusza problem wpływu na wynik pomiarów uzyskanych metodą spektroskopii absorpcyjnej występowania na ścieżce pomiarowej zmiennego stężenia badanego związku. Problem ten jest szczególnie istotny w przypadku wykonywania pomiarów dla długich ścieżek optycznych. Pomiary tego typu są wykonywane m.in. przy kontroli składu środowiska w kotłach energetycznych przy współspalaniu biomasy i węgla. (**Wpływ niejednorodności stężenia gazu na dokładność pomiarów w spektroskopii absorpcyjnej**)*

Keywords: absorption spectroscopy, gas concentration.
Słowa kluczowe: spektroskopia absorpcyjna, koncentracja gazów.

Introduction

Absorption spectroscopy is a measurement method that is widely used, among others in combustion process diagnosis [1, 2]. Its main advantage is lack of interaction with a environment to be controlled as well as high rate of obtaining measurement results. It is very important, especially in the case of controlling rapid processes such as combustion.

Coal combustion is still one of the commonest ways of electrical power production. More and more rigorous regulations concerning acceptable levels of combustion gases emissions as well as the required percentage of renewable energy have leaded to spread coal-biomass co-combustion technologies in existing power plants with different types of biomass.

Operating a combustion process is complicated for large number of factors affecting its course such as: the temperature inside a combustion chamber and its distribution, air-fuel ratio, fuel composition. For the mentioned above reasons, combustion of pulverized coal is relatively a complex process to run, especially when additions of biological origin are mixed with pulverized coal. Apart from problems connected with appropriate preparing of fuel mixture, e.g. difficulties with size reduction of wood waste, flame stability issues can occur and flame-out is possible.

A very important consequence of biomass-coal co-combustion in power boilers are changes in atmosphere composition. Research have shown [3] that atmosphere composition inside a power boiler greatly influences intensity of corrosion processes.

The proper operating of a combustion process requires an access to many various measurement signals, including signals of gas composition.

Problems arise when spectroscopic methods for gas composition measurement inside power boilers are applied. Usually, it is assumed that laser beam runs through measurement path of homogeneous environment. Such an assumption means that there is constant value of gas mixture concentration, constant pressure as well as temperature. It is suitable only in laboratory measurements, where samples are properly prepared and measurement path is short. Examining composition of a gas mixture inside a power boiler requires relatively long measurement path, that could be located e.g. across combustion chamber. The mentioned above parameters are not constant in the case being discussed. Therefore, it is necessary to take into account influence of measurement path inhomogeneity on measurement accuracy.

The atmosphere inside the power boiler

Gas mixture composition inside a power boiler is diversified considerably and depends mainly on chemical constitution of a fuel. Biomass co-combustion with coal leads to formation many gaseous products, that cannot be observed when only pulverized coal is burned.

Moreover, for the large size of a power boiler and the way combustion process is organized, atmospheric composition is different for given point of a combustion chamber as well as a flame. A proper utilization of fuel requires formation of a proper areas that differs in oxygen content Thus, contents of the other components is also different within a combustion chamber.

As it was pointed out in [3, 4], changes in composition of a mixture is relatively high. It results in distinguishing a special area within a combustion chamber called near-wall zone.

The main components of the combustion chamber atmosphere are: nitrogen, carbon monoxide and dioxide, water vapor, oxygen and both nitric and sulfur oxides. Their fraction in combustion chamber atmosphere depends on many factors. An example profile of CO concentration distribution in power boiler is shown in figure 1.

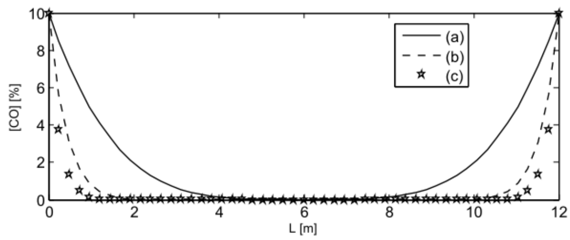

Fig.1. An example CO concentration distribution inside a power boiler

Simulation studies - assumptions

Due to presence of concentration inhomogeneity of atmospheric components inside a combustion chamber of a power boiler a question arises how it affect results of spectroscopic measurements. Thus, simulation research have been done in case of variable CO concentration distribution inside a combustion chamber.

The following assumptions have been made adopted:: the measurement path was 12 m length, total pressure (that equals 1 atm) was constant along the path and the temperature was 1073K. CO concentration profile was accepted as the approximation functions that are presented in figure 1, profile marked as (a) - polynomial of 4^{th} order (dashed line), (b) – polynomial of 14^{th} order (solid line), (c) – polynomial of 24^{th} order (star). The second profile corresponds to more homogeneous conditions as opposite to (a) profile, third – to more than a second.

It was assumed, that atmospheric composition is typical for combustion chamber of a power boiler. Its main components are carbon mono- and dioxide as well as water vapor with 10% of [CO_2] and [H_2O] while amount of CO varies according to the assumed profile - from 0% to 10%. The analysis has been done within the spectral range from 1,558μm to 1,570μm. Within the discussed spectral range, taking into consideration typical gas mixture that is present inside a combustion chamber, only CO, CO_2 and H_2O have enough strong absorption lines that makes quantitative analysis possible. The other gas mixture components have no an effect on a shape of absorption spectrum being analyzed for they have no or very weak absorption lines, that could be neglected [5]. In the presented simulation, in order to determine absorption spectrum of gas mixture, the HITRAN database has been used [6]. Change in shape of the considered CO absorption line (λ=1568,035nm) due to change of concentration is presented in fig. 2

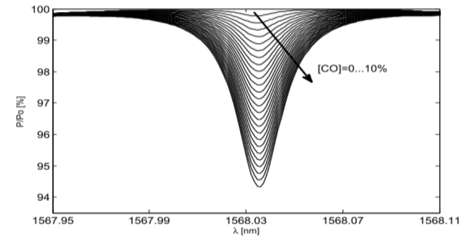

Fig.2. Changes of shape CO line corresponding to concentration rise from 0 % to 10%

Results

The results of the carried out analyses are shown in fig. 3-6. The first one presents comparison of spectra shape, that were obtained for the three concentration profiles with spectra corresponded to the maximum and the mean concentration values.

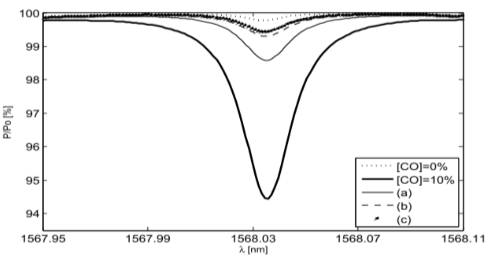

Fig.3. Transmission spectrum of a gas mixture for different profiles of CO concentration changes in the measurement path

Comparing the presented spectra one can notice their different shape. Measurement results will depend, among other things, on the spectroscopic method that is applied. If a direct method is utilized, where an absorption peak is analyzed, measuring error depends on concentration profile as it is depicted in table 1. Results for the method based on an area under the curve are also shown in table 1.

Table 1. Dependence of CO concentration error in a gas mixture due to inhomogeneous concentration along the measurement path

profile type	(a)	(b)	(c)
$[CO]_{avg.}$	2%	0,6%	0,2%
measured absorbance	0,1293	0,0625	0,0499
absorbance at $[CO]_{avg.}$	0,1212	0,0489	0,0386
error relative	6,68%	27,81%	29,27%
absorbance at $[CO]_{max}$	0,534	0,534	0,534
error relative	-75,79%	-88,30%	-90,66%
measured absorption peak	98,5814%	99,2981%	99,4333%
absorption peak at $[CO]_{avg.}$	98,6674%	99,444%	99,5555%
error relative	-0,09%	-0,15%	-0,12%
absorption peak at $[CO]_{max}$	94,3354	94,3354	94,3354
error relative	4,50%	5,26%	5,40%

Conclusions

The presented analysis shows influence of concentration changes of a given component on absorption spectrum of a gas mixture that is typical for combustion chamber of power boiler. Change in spectrum shape in the discussed conditions causes errors in determination of gas mixture contents.

The carried out simulations have shown, that in order to maintain measurement correctness it is necessary to take into account concentration profile of a given component along the measurement path. It was shown that when concentration profile is highly inhomogeneous (profile marked as (a)) greater misfit errors than in the homogeneous profile.

It should be remembered that in real conditions inhomogeneity is not only narrowed to concentration, but also temperature inhomogeneity should be taken into consideration. It makes the whole analysis even more complicated. Acquaintance of concentration profile as well as application of advanced analysis methods should ensure concentration determination of a given substrates, keeping a minimal error even in case of considerable medium inhomogeneity inside a power boiler.

REFERENCES

[1] Ebert V., et al., Simultaneous Diode-Laser-Based In-situ-Detection of Multiple Species and Temperature in a Gas-fired Power-Plant, *28th Int. Symposium on Combustion*, University of Edinburgh, Edinburgh, Scotland, (2000)

[2] Wójcik W., et al., Pomiar stężenia CO z wykorzystaniem metod TDLAS w bliskiej podczerwieni, *Przegląd Elektrotechniczny*, 3 (2008), 238-240

[3] Kruczek H., Przydatność pomiaru warstwy przyściennej do oceny stopnia zagrożenia korozją wysokotemperaturową (niskotlenową), *Energetyka*, 7 (2002), 419-427

[4] Kruczek H., Sikora A., Analiza pól temperaturowych komory paleniskowej kotła OP-650 na węgiel brunatny wraz z oceną stężeń gazowych składników spalin, *Diagnostyka jakości spalania w energetyce'98 - materiały konferencyjne* (1998), 139-150

[5] Wójcik W., et al., Pomiar stężenia CO z wykorzystaniem metod TDLAS w bliskiej podczerwieni, *Przegląd Elektrotechniczny*, 3 (2008), 238-240

[6] Rothman L.S., et al., HITRAN HAWKS and HITEMP: high-temperature molecular database, *Proceedings of SPIE*, 2471 (1995), 105-111

***Authors**: dr inż. Paweł Komada, dr inż. Sławomir Cięszczyk, prof. dr hab. inż. Waldemar Wójcik, Politechnika Lubelska, Katedra Elektroniki, ul. Nadbystrzycka 38a, 20-618 Lublin, E-mail: p.komada@pollub.pl*

SUPPLY SYSTEM OF WATER TREATMENT INSTALLATION FROM PV PANELS

Grzegorz KOMARZYNIEC, Henryka Danuta STRYCZEWSKA, Jarosław DIATCZYK

Lublin University Of Technology

Abstract*. This work presents a little household water ozonization installation, which is made of the following: ozonizer, oxygen generator, ozonization system, system of filters, ozone destructors, water pumps plus both monitoring and controlling systems. The system's total power is 2 kW. The whole system is designed in such a way as not to be dependant on the power supply from energy network. It was equipped with photovoltaic polycrystalline cells and the energy storage system which is made of gel accumulator batteries.*

Streszczenie. *W pracy przedstawiono system ozonowania wody składający się z: systemu generacji ozonu, sytemu kolumn kontaktowych wraz z filtrami I destruktorami ozonu oraz systemu konroli I regulacji. System jest zaprojektowany jako niezależny od zasilania z sieci energetycznej. Wyposażony został w polikrystaliczne ogniwa fotowoltaiczne oraz układ magazynowania energii w akumulatorach żelowych.*

Keywords: water ozonization installation, ozone generator, photovoltaic cells
Słowa kluczowe: instalacja ozonowania wody, generator ozonu, ogniwa fotowoltaiczne

Introduction

In the future, the noticeable climatic changes plus the natural environmental pollution may become the cause of the necessity to treat water of a very bad quality in order to satisfy the need for potable water.

The solution these problems are small water ozonation installations supplied with electric energy from renewable energy sources. The correctly selected system should cover about 95÷100% of electrical energy demand during summer [1].

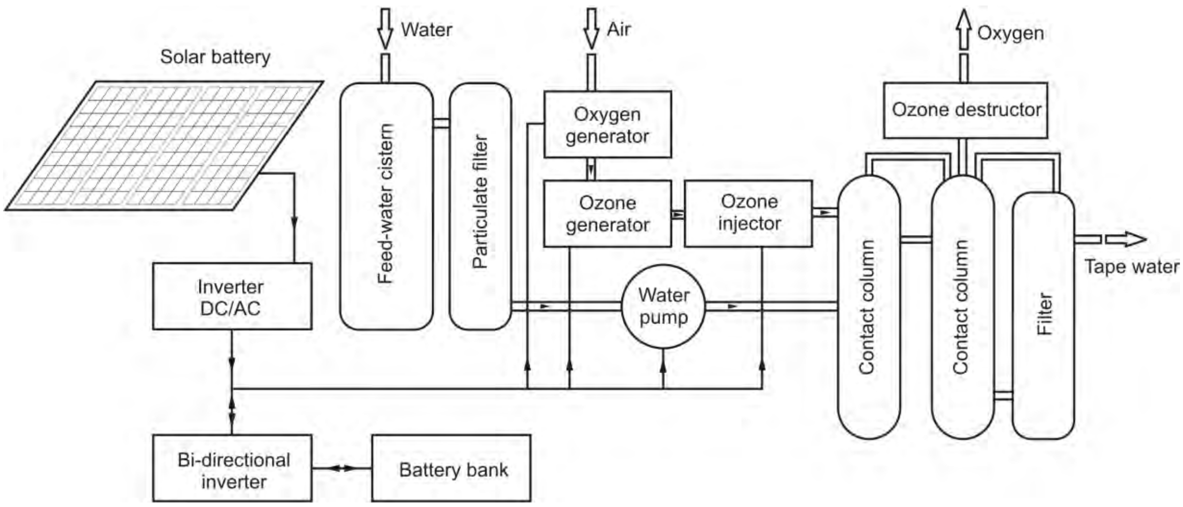

Fig. 1. Water ozonation system

Figure 1 depicts water ozonation installation. The system is made of three basic systems: electric energy power system, ozone production system and water treatment system [2].

This system is totally autonomous, excellent to be utilized on remote terrains, which are distant from electroenergetic network or in the places where the electroenergetic main is unstable and fallible.

Water treatment system

In the majority of ozonation systems ozone is added to water in the form of bubbles through diffuser. The effectiveness of such a process is low because of two reasons: (1). ozone is not evenly mixed with water, (2). ozone, when in large quantities, evaporates from water into ozone destructors, from where the unused oxygen is blown out into the atmosphere. The other problem of water ozonation installations is coloring water, which is the result of chemical reactions between ozone and ores that are in water.

These problems are completely eliminated by the use of Wofil contact columns. This solution enabled the increase of ozonation process' efficiency by almost 30 % without the increase of electrical energy consumption. It also resulted in reduction of amount of gas which is blown out into ozone destructors and in lower values of residual ozone after the contact container. The obtained water is disinfected and purified with vestigial amount of residual ozone.

Ozone production system

The ozone generation takes place with the usage of corona discharge. The basic part of ozone generator are flat titanium electrodes. The surface of one of electrodes has a ceramic barrier which protects the uniformity of electric discharge and prevents spark or arc discharges.

Table 1. The technical data of ozone generator

Max. ozone production	6 grams/hour
Max. ozone concentration	4% weight
Max. reactor pressure	0.4 bar
Feed gas flow range	3.3÷4.7 lpm
Power consumption	180 watts

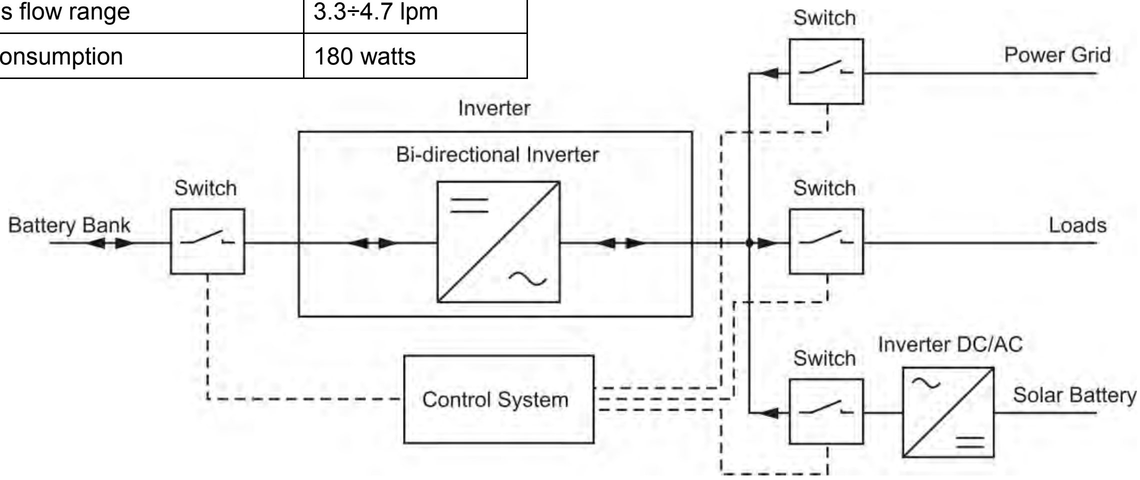

Fig. 2. Grid supplying water ozonation system with electric energy

The constant inflow of oxygen into the ozonier provides the oxygen generator. The molecular sieves of the ozone generator provides 93% pure oxygen and automatically regenerate themselves through the cyclic flow in contra-current of oxygen. This solution ensures practically unlimited durability of oxygen generator.

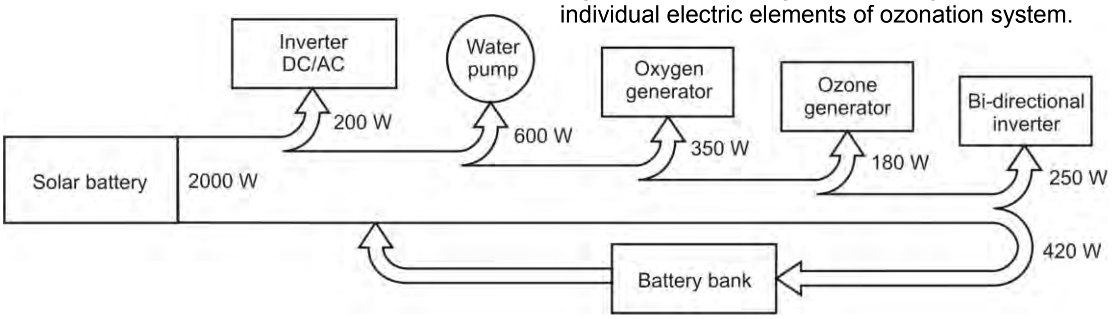

Fig. 3. Electric energy consumption in the system

The important issue is an electric power supply and connected with it problem of the co-operation between ozone generator and voltage source. It is caused by the capacitive character of ozone generator and non-linearity of phenomena which take place in it. The ozonizer is supplied with the separate high frequency supplier with pulse control and amplitude modulation. You can smoothly regulate the ozone concentration by changing the setpoint of the supplier.

Electric energy power system

The all water ozonation system devices are powered with 230V, 50 Hz. Figure 3 depicts a flow chart of electric grid which cooperates with water ozonation system.

The main element of circuits is bi-directional inwerter. It administers loads, the flow of energy and the work of accumulators. It constitutes a comfortable link of AC and DC units into one energy system. Inwerter creates 24 V grid of DC voltage and a typical grid of AC voltage 110 V 60 Hz or 230 V 50 Hz. Within these grids all pieces of equipment are integrated ranging from electric generators to energy receivers. Photovoltaic systems, air turbine, generators with diesel motors, water-power plants are connected together with load on the side of alternating voltage. The batteries of accumulators, fuel cells and DC receivers, however, are integrated on the side of DC voltage.

The connection solar batteries on the side of alternating voltage require application additional DC/AC inverter.

The advantage his solution is a possibility to install the solar batteries a long distance from the ozonation system. The application of DC/AC inverter eliminates the necessity of using an expansive DC wiring and causes a high level of adjustment.

The main problem in designing a system is the limited power value that could be received from photovoltaic cells. Figure 3 depicts a graph showing power consumption of individual electric elements of ozonation system.

Summary

The presented water ozonation instalation is a fully autonomic system with modular construction and it can be easily adjusted to individual needs. It may constitute a fitting of a detached house but also it can be deployed for purifying water in underdeveloped countries.

REFERENCES

[1] Stryczewska H. D., Komarzyniec G., Nalewaj K., The possibilities of using solar energy in water ozonation systems, *Przegląd Elektrotechniczny*, nr 5/2010, 333-332

[2] Komarzyniec G., Stryczewska H. D., Muszański R., Automomos Water Treatment Instalation Energized from PV Panels, *Journal of Advanced Oxidation Technologies*, vol. 13, nro 2, June 2010, 146-152

***Authors**:*
dr inż. Grzegorz Komarzyniec, E-mail: g.komarzyniec@pollub.pl; prof. dr hab. inż. Henryka Danuta Stryczewska, E-mail: h.stryczewska@pollub.pl; dr inż. Jarosław Diatczyk, E-mail: j.diatczyk@pollub.pl;Politechnika Lubelska, Instytut Podstaw Elektrotechniki i Elektrotechnologii, ul. Nadbystrzycka 38A, 20-618 Lublin

Conference ELMECO–7
ELECTROMAGNETIC DEVICES AND PROCESSES IN ENVIRONMENT PROTECTION
joint with 10th Seminar AoS-10 APPLICATIONS OF SUPERCONDUCTORS
28–30.09.2011, Nałęczów, Poland

PLASMA DEPOSITION OF CERAMIC LAYERS DIRECTLY ONTO THE SURFACES OF THE JOINTS OF OSTEOARTHRITIS

Grzegorz KOMARZYNIEC, Henryka Danuta STRYCZEWSKA, Jarosław DIATCZYK

Lublin University Of Technology

***Abstract**. The aim of the research is develop of plasma method of joints reconstruction, an alternative to endoprosthetics and capoplastics. The core of the procedure would be putting a layer of bio-ceramic material of low rubbing factor and low friction factor directly onto damaged joint tangent surfaces. This will allow remaining the natural position of shaft and femur letting the anatomic work of joint. In the plasma layers covering technique there will be no need for femur resection nor milling of the joint surface. The basic research problem is elaborating construction of plasma reactor and methodology for putting the bio-ceramic layers directly onto the joint surface.*

***Streszczenie.** W artykule przedstawiono problematykę związaną z badaniami nad opracowaniem nowej metody rekonstrukcji stawów objętych zmianami zwyrodnieniowymi , która będzie alternatywą dla endoprotetyki i kapolastyki. Podstawowym celem badawczym projektu jest opracowanie nisko inwazyjnej metody, wykorzystującej nietermiczną plazmę generowaną przy ciśnieniu atmosferycznym do nanoszenia warstw bioceramicznych bezpośrednio na zniszczone zmianami zwyrodnieniowymi stawy.*

Keywords: plasma reaktor, degenerative joint diseases, ceramic layers
Słowa kluczowe: reaktor plazmowy, choroba zwyrodnieniowa stawów, warstwy ceramiczne

Introduction

Degenerative joint diseases (lat. arthrosis deformans, osteoarthrosis, osteoarthritis) belong to group of the greatest social and health problems worldwide. That is why World Health Organization declared decade 2000-2010 the Bones and Joints Decade. Despite great progress in diagnostics and treatment methods development, problems connected to joints degeneration or deforming are still a huge medical problem.

Degenerative and deformation changes occur in 3 to 15 per cent of worldwide population, depending on given statistics. It is estimated that the disease in Poland occurs in about 2 million cases. It is thought that the disease concerns 25 to 30 per cent of people between 45 and 64 years, 60 per cent of people older than 65 and and more than 80 per cent people aged 75 and more. The disease is the most common cause for disability declaring.

The general and characteristic symptom of degenerative joint disease is pain. The pain leads to disabling of the joint functions with limiting of the joint mobility. The sum of pain and mobility disabling is always limiting of the movement ability of a patient, as well as their social functioning.

The aim of the research is develop of plasma method of joints reconstruction, an alternative to endoprosthetics and capoplastics. The basic research problem is elaborating construction of plasma reactor and methodology for putting the bio-ceramic layers directly onto the joint surface.

Endoprosthetics and capoplastics

The degenerative joint disease treatment ends in many cases with surgical procedure, called arthroplasty. For over 40 years arthroplasty has been a quickly developing domain in the field of orthopedics. Every year there have been hundreds thousands of procedures executed worldwide. Surgical treatment bases on implanting, with former removing of bone base, endoprosthesis made of metal alloys. Example endoprostheses are shown on Figure 1.

Endoprosthesis is an implant which function is to replace irreversibly damaged joints surfaces and to allow painless movement. It is made of metal elements (steal or titanium) and one polyethylene element and they allow together the joint to move [1, 2]. Endoprosthesis elements are set inside bone with special cement or they are screwed into the bone, or established wedge-like. Setting endoprostheses is connected to a huge interference into patient's bone structure and is an irreversible procedure - the joint, in case of failure of procedure, can not be replaced.

Fig.1. Endoprosthesis of knee joint and hip joint

Clinical result of orthopedic surgery depends among others on the correct fixing implants in patient's bones structure. Faulty implants fixing may lead to necessity of second operation, or it may cause harming important for life and health structures.

Prosthesis plastic is a domain of orthopedics which develops very dynamically. Nevertheless there are still problems with using out the artificial joint surface, loosening and organism's intolerance to implant. All these factors cause limitation in activity of patients after prosthesis plastic.

Method of plasma coatings putting

Method of plasmic ceramic layers putting is a widely used way of correcting rust preventive features and improving resistance to rubbing of materials used in rolling bearings, shaft pivots, reducers. In this process, the material which is the cover, usually in the form of powder, is injected into plasmic stream where it is heated and accelerated towards the surface where it is to be put. In the instance of hitting with the surface the plasma together with the transported ceramic material is rapidly cooled, created a protective layer, sticking to the surface. In the above uses the plasma covering process is well known theoretically and practically.

As far as the process of plasma covering directly onto the bone is concerned it is a very complicated issue in many ways, unknown in Poland and worldwide. It is a new issue for the interdisciplinary discourse in the field of bio-engineering.

temperature of plasma. Another important problem is protecting the surrounding tissues against penetrating by particles of ceramic material.

Advantages of ceramic layers are huge biological tolerance and chemical neutrality, which means they are safe for human organism, don't react with their fluids, don't rust nor get destructed. The issue of research is choice of material for the ceramic layer. Commonly used ceramic materials are fragile and not always closely stuck to the surface.

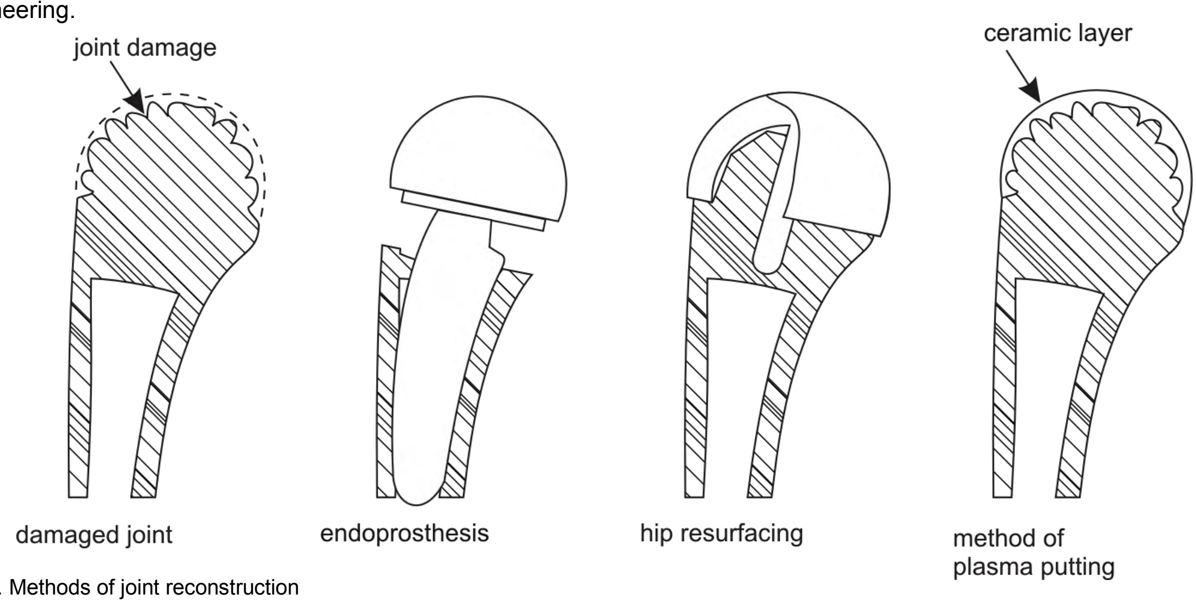

Fig. 2. Methods of joint reconstruction

The core of the procedure would be putting a layer of bio-ceramic material of low rubbing factor and low friction factor directly onto damaged joint tangent surfaces. This will allow remaining the natural position of shaft and femur letting the anatomic work of joint. In the plasma layers covering technique there will be no need for femur resection nor milling of the joint surface.

The procedure will consist in preparing the joints surface by clearing it and polishing any uneven spots, protruding from the natural joint silhouette. Next the ceramic shaping and strengthening layer will be put on joint. The layer of base is supposed to create a ground well connected to the bone surface, fill the gaps in joint surfaces and give the joint the right shape. After final shaping of joints, a thin hardening ceramic layer will be put, of appropriate durability and slide, to allow the proper work of the tangent surfaces of joints. The thickness of the layers (prosthesis) might be about a few micrometers.

Expected advantages of plasma bio-ceramic covering directly onto joints surfaces are:

- remaining of anatomic position of shaft and femur in the acetabulum,
- high durability of rubbing surfaces, allowing long term functioning,
- it is a procedure advancing the “classic” prosthesis plastic. If necessary, shaft and femur may be removed and implanted with a pin with metal head.

Complexity of the process of covering joints surfaces with ceramic layers is connected to multiplicity of factors which must be taken into account to assure the right structure and features of the layer. During plasma covering the particles heat up greatly and the material is melted partly, therefore there is a risk of bone overheating and breaking its structure. On the other hand, the micro-structure and nano-crystalline cover features depend on

During plasma ceramic layers putting directly onto the bone surface, the right mechanical and friction parameters may be obtained with the use of materials of nano-crystalline structure. The strength of bond of nano-ceramic covers is two times greater than that of traditional covers. Nano-ceramic covers are hugely resistant to shocks, and because they get out of shape together with their ground, they have no, even microscopic, fractures.

Summary

The final effect of the scientific research will be elaborating a new, low-invasive method of plasma treatment for the degenerative joint disease which a severe medical problem, one of the most important social and medical problems worldwide. A method will be developed in which treating degeneration diseases will mean rebuilding joints natural geometry without necessity of removing parts of bones.

REFERENCES

[1] A. A. Amis, Wongwit Senavongse, P. Darcy, Biomechanics of Patellofemoral Joint Prostheses, *Clinical orthopaedics and related research*, Number 436, pp. 20–29,

[2] S. Pramanik, A. K. Agarwal, K. N. Rai, Chronology of Total Hip Joint Replacement and Materials Development, *Trends Biomater. Artif. Organs*, Vol 19(1), pp 15-26 (2005),

***Authors**:*

dr inż. Grzegorz Komarzyniec, E-mail: g.komarzyniec@pollub.pl;

prof. dr hab. inż. Henryka Danuta Stryczewska, E-mail: h.stryczewska@pollub.pl;

dr inż. Jarosław Diatczyk, E-mail: j.diatczyk@pollub.pl;

Politechnika Lubelska,

Instytut Podstaw Elektrotechniki i Elektrotechnologii,

ul. Nadbystrzycka 38A, 20-618 Lublin

Conference ELMECO–7
ELECTROMAGNETIC DEVICES AND PROCESSES IN ENVIRONMENT PROTECTION
joint with 10th Seminar AoS-10 APPLICATIONS OF SUPERCONDUCTORS
28–30.09.2011, Nałęczów, Poland

ROZKŁAD POLA MAGNETYCZNEGO i ENERGIA NADPRZEWODNIKOWEGO ZASOBNIKA W RÓŻNEJ KONFIGURACJI CEWEK

Beata KONDRATOWICZ-KUCEWICZ, Sławomir KOZAK

Electrotechnical Institute in Warsaw

***Abstract**. Superconducting Bi-2223/Ag SMES winding was realised in Laboratory of Superconducting Technology in Lublin. This paper presents the experimental and numerical investigation results of the magnetic field distribution end stored energy in solenoidal and toroidal configuration of magnet*

***Streszczenie.** W Pracowni Technologii Nadprzewodnikowych w Lublinie zaprojektowano i zbudowano uzwojenie nadprzewodnikowe dla zasobnika energii wykorzystując taśmę nadprzewodnikową Bi-2223/Ag. W pracy przedstawiono wybrane wyniki badań i analizy numerycznej rozkładu pola magnetycznego i energii zgromadzonej w elektromagnesie nadprzewodnikowym zasobnika w konfiguracji solenoidalnej i cewkowo-toroidalnej.*

Keywords: HTS tape, superconducting SMES configuration, solenoid, toroid
Słowa kluczowe: Taśma HTS, konfiguracja nadprzewodnikowego zasobnika energii, solenoid, toroid

Wprowadzenie

Nadprzewodnikowe magnetyczne zasobniki energii (SMES) jako urządzenia do magazynowania energii wykorzystują stosunkowo prosty pomysł polegający na gromadzeniu energii w polu magnetycznym wytworzonym przez przepływ prądu w cewce nadprzewodzącej. Zmagazynowana energia, może być uwalniana z powrotem do podłączonego systemu zasilania przez rozładowanie cewki z uwzględnieniem systemu kondycjonowania energii, który przekształca prąd stały (DC) na zmienny (AC).

Chociaż zjawisko nadprzewodnictwa zostało odkryte w 1911 roku, to przez dziesięciolecia nie mogło znaleźć zastosowania w przemyśle ze względu na znaczne koszty eksploatacji i ekstremalne warunki eksploatacji. W 1969 roku zostały opracowane pierwsze magnetyczne zasobniki energii. Idea urządzenia polegała na ładowaniu elektromagnesu nadprzewodnikowego w okresie mniejszego zapotrzebowania na energię w systemie energetycznym i rozładowania w czasie szczytu.

Przed odkryciem i opracowaniem technologii wytwarzania nadprzewodników wysokotemperaturowych HTS, wszystkie projekty urządzeń SMES opierały się na nadprzewodnikach niskotemperaturowych LTS, które wymagają ciekłego helu jako czynnika chłodzącego. Nowsze projekty zasobników wykorzystujące nadprzewodniki HTS wykorzystują układy „suchego” chłodzenia za pomocą kriochłodziarek (cryocooler) lub chłodzenie „w kąpieli” za pomocą ciekłego azotu.

Tab.1 Zrealizowane projekty SMES na świecie

Nazwa	Rok	Energia	Materiał	Temp.[K]
Australian SMES	2005	2.48 kJ	BSSCO-2223	25
Korean HTS-SMES	2005	626 kJ	BSSCO-2223	20
Japan FBC coil	2004	270 kJ	NbTi	4.2
Israel SMES	2003	1.5 kJ	BSSCO-2223	64
Japanese UPS SMES	2007	100 kJ	NbTi	4.2
Japanese hybrid SMES	2007	14.9 kJ	BSSCO-2212	4.2
Japanese CIC SMES	2004	2.9 MJ	NbTi	4.2
Japanese SMES	2003	100 kJ	BSSCO-2212	20
Italian SMES	1999	2.6 MJ	NbTi	4.2
ACCEL SMES	2003	2 MJ	NbTi	4.2
French SMES	2008	814 kJ	BSSCO-2212	20

W naładowanej cewce prąd praktycznie płynie bez strat, które mogą być spowodowane jedynie przez rezystancję przepustów prądowych. Dla przepustów wykonanych z nadprzewodników niskotemperaturowych rezystancja ta jest szacowana jako 10^{-10} Ω. Energia może być więc „przechowywana” w uzwojeniu nadprzewodnikowym przez bardzo długi czas. Jeżeli cewka byłaby wykonana w technologii tradycyjnych z przewodów miedzianych to energia magnetyczna byłaby rozpraszana w postaci ciepła ze względu na rezystancje przewodu.

Uzwojenie nadprzewodnikowe dla SMES’a

W Pracowni Technologii Nadprzewodnikowych w Lublinie zaprojektowano i zbudowano uzwojenie nadprzewodnikowe dla zasobnika energii nawinięte taśmą nadprzewodnikową Bi-2223/Ag (Tab.2) (rys.1.).

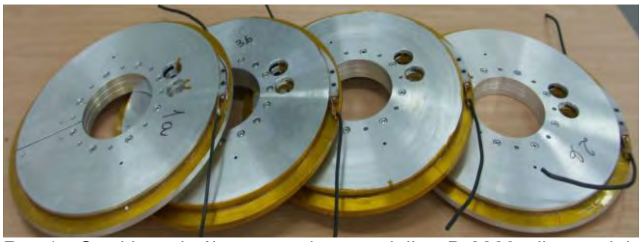

Rys.1. Cewki podwójne z nadprzewodnika B-2223 dla modelu SMES’a o konstrukcji cewkowo-toroidalnej.

Tab.2. Parametry taśmy Bi-2223 (America Superconductor) [4]

HTS High Strength Wire Stainless Steel Laminated		
Nadprzewodnik	Bi-2223 ($Bi_2Sr_2Ca_2Cu_3O_{10}$)	
Grubość	mm	0,31
Szerokość	mm	4,2
Min. średnica gięcia	mm	70
Prąd krytyczny	A	115
Temperatura krytyczna	K	77

Siedem podwójnych cewek (Rys.2) zostało wykorzystanych do budowy uzwojenia solenoidalnego. Konfiguracja taka została przebadana z wykorzystaniem konwertera elektronicznego umożliwiającego dwukierunkowy przepływ energii pomiędzy siecią elektryczna i elektromagnesem nadprzewodnikowym.

Rys.2 Podwójne uzwojenie krążkowe (dwucewka)

Zbudowane cewki podwójne mogą być też wykorzystane do budowy uzwojenia w konfiguracji toroidalnej z rdzeniem magnetycznym. Dwie rozpatrywane konfiguracje uzwojeń nadprzewodnikowych przedstawione są na rysunku 3.

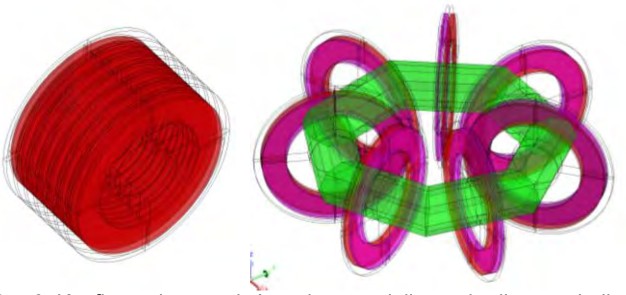

Rys.3 Konfiguracje uzwojeń nadprzewodnikowych dla zasobnika energii: a) układ solenoidalnym b) układ cewkowo-toroidalny.

Konstrukcja solenoidalna uzwojenia jest prostsza i łatwiejsza w realizacji. Charakteryzuje się też większą gęstością energii na jednostkę długości przewodu nadprzewodnikowego niż w układzie cewkowo-toroidalnym.

W rozwiązaniu cewkowo-toroidalnym konstrukcja uzwojenia nadprzewodnikowego jest bardziej złożona, ale strumień rozproszenia pola magnetycznego na zewnątrz uzwojenia jest znacznie ograniczony.

Rozkład indukcji pola magnetycznego wyznaczony numerycznie dla obu konfiguracji uzwojenia pokazano na rysunku 4 i 5.

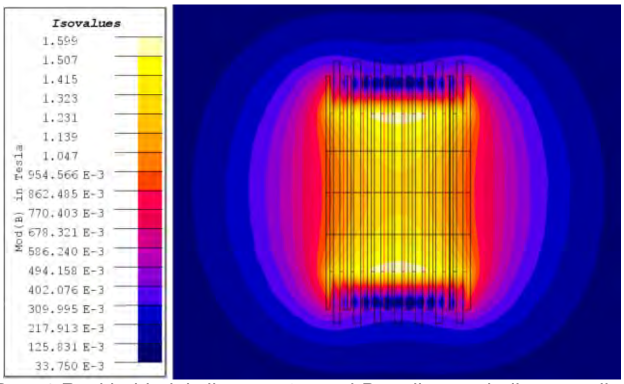

Rys. 4 Rozkład indukcji magnetycznej B w dla zasobnika energii w konfiguracji solenoidalnej.

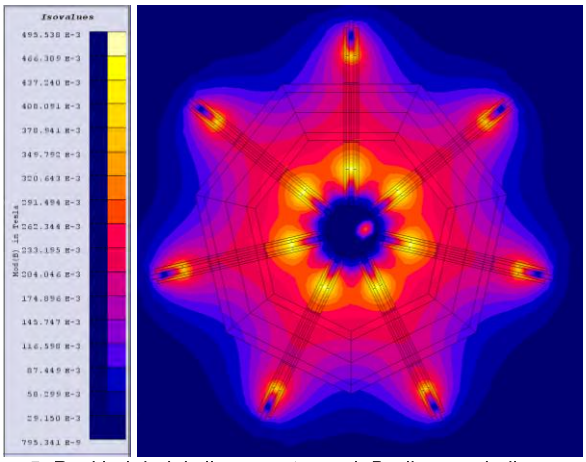

Rys. 5 Rozkład indukcji magnetycznej B dla zasobnika energii w konfiguracji cewkowo-toroidalnej

W układzie solenoidalnym elektrodynamiczne siły promieniowe rozciągają uzwojenie, a osiowe ściskają je. W układzie cewkowo - toroidalnym na poszczególne cewki składowe działają znaczne siły, które muszą być zrównoważone odpowiednimi elementami konstrukcyjnymi. Rozkład tych sił zależy od geometrii i konfiguracji uzwojeń. W konfiguracji toroidalnej siła dośrodkowa ściska toroid dążąc do zmniejszenia jego średnicy.

Energia zgromadzona w uzwojeniu nadprzewodnikowym

Ze względu na mały strumień rozproszenia w konfiguracji cewkowo toroidalnej energia zgromadzona w uzwojeniu może być większa niż w konfiguracji solenoidalnej.. Wpływ na wartość energii w uzwojeniu toroidalnym ma promień toroidu.

Tab.3. Wartości zgromadzonej energii w uzwojeniu solenoidalnym w zależności od temperatury pracy uzwojenia nadprzewodnikowego.

Temperatura, K	Prąd krytyczny, A	Energia, J
77	25	310
64	50	1250
35	180	16200
13	264	34800

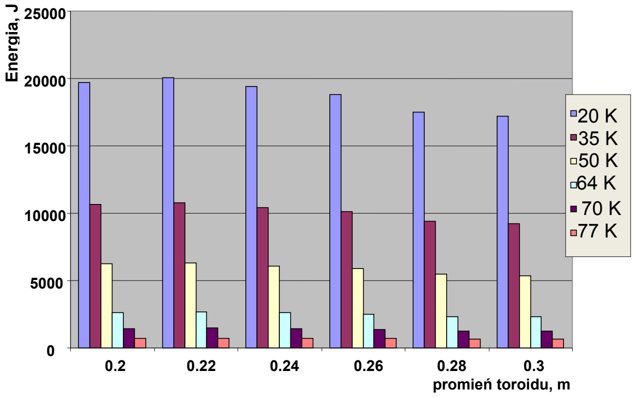

Rys. 6 Energia SMES-a w dla różnych promieni toroidu i dla różnych temperatur pracy przy uwzględnieniu zależności parametrów krytycznych taśmy nadprzewodnikowej od temperatury i kąta pomiędzy indukcją magnetyczna i taśmą

Podsumowanie

W pracy przedstawiono wybrane wyniki analizy rozkładu pola magnetycznego i energii zgromadzonej w elektromagnesie nadprzewodnikowym dla zasobnika energii. Dla układu toroidalnego strumień rozproszenia pola magnetycznego generowanego przez uzwojenie jest minimalny, więc energia zgromadzona w uzwojeniu może mieć większą wartość. Ponadto wartość energii jest uzależniona od promienia toroidu, co pokazano na rysunku 6. W obu konfiguracjach elektromagnesu wartość zgromadzonej energii można zwiększyć przez obniżenie temperatury pracy uzwojenia. Pozwala to osiągnąć lepsze dla uzwojenia parametry krytyczne, a tym samym większe wartości prądu i energii pola magnetycznego.

LITERATURA

[1] American Superconductor, http://www.amsuper.com/

[2] B. Kondratowicz-Kucewicz, G. Wojtasiewicz, Magnetyczne zasobniki energii z cewkowo toroidalnymi uzwojeniami HTS, Przegląd Elektrotechniczny, R. 85 Nr 5/2009.

Authors: *mgr inż. Beata Kondratowicz-Kucewicz, dr hab.inż.Sławomir Kozak prof. IEL, Instytut Elektrotechniki, Pracownia Technologii Nadprzewodnikowych w Lublinie, ul.Nadbystrzycka 38a, 20-618 Lublin, E-mail: b.kondratowicz-kucewicz@iel.waw.pl s.kozak@iel.waw.pl*

Conference ELMECO–7
ELECTROMAGNETIC DEVICES AND PROCESSES IN ENVIRONMENT PROTECTION
joint with 10th Seminar AoS-10 APPLICATIONS OF SUPERCONDUCTORS
28–30.09.2011, Nałęczów, Poland

BIOMASS-COAL COMBUSTION CHARACTERIZATION USING IMAGE PROCESSING

Andrzej KOTYRA[1], Waldemar WÓJCIK[1], Krzysztof JAGIEŁŁO[2], Konrad GROMASZEK[1], Tomasz ŁAWICKI[1], Piotr POPIEL[1]

Lublin University of Technology, Department of Electronics (1), Institute of Power Engineering, Thermal Division (2)

***Abstract**. The article presents application of visual system equipped with high speed video camera for combustion characterization of biomass-coal mixture. Combustion tests were made for different air-fuel ratios as well as different thermal power of test facility. Some flame image geometric parameters were examined as pointers of a current state of pending combustion process.*

***Streszczenie.** W artykule zaprezentowano zastosowanie systemu wizyjnego do charakteryzowania współspalania biomasy i węgla kamiennego. W tym celu przeprowadzono laboratoryjne testy spalania dla różnych obciążeń cieplnych stanowiska i stosunków paliowo-powietrze. Badano wybrane parametry geometryczne płomienia w celu oceny ich przydatności do określania stanu zachodzącego procesu spalania*

Keywords: flame, biomass co-combustion, image processing.
Słowa kluczowe: płomień, współspalanie biomasy, przetwarzanie obrazu.

Introduction

The use of renewable fuels as well as renewable energy sources are considered as the main ways of reducing greenhouse-gas emissions, especially CO_2. Co-combustion of coal and biomass is the easiest and cheapest way of using renewable energy source for the possibility of using existing combustion facilities. Thus, biomass-coal co-combustion can be quickly adapted in large-scale systems. Combustion process is stabilized by presence of coal in fuel mixture. Moreover, substituting biomass for coal reduces SO_2 emissions as well as NOx due to the low sulfur and low nitrogen contents of biomass [1].

On the other side, biomass-coal co-firing has also some drawbacks, especially decreased combustion efficiency and negative side-effects due to mineral components of biomass that can affect the boiler operation (increased slagging, corrosion). Another problems are connected with keeping constant physical and chemical parameter of biomass that affect [2].

For the combustion process of biomass-coal mixture is difficult to lead, a proper diagnostic system should be applied The quickest, but on the other hand difficult way of drawing information of a combustion process is to analyze its radiation features. Flame is a volumetric source of radiation, and reflects chemical reactions in a reaction zone. Thus, it is possible to assess combustion process through flame image.

Vision systems for combustion monitoring allow to determine various parameters of flame such as geometric (e.g. size, position), radiation properties (e.g. emission spectrum, irradiation distribution), flame flicker frequency, etc. Information obtained from vision combustion monitoring systems combined with information of exhaust gases composition and fuel chemical and physical properties could lead to optimize the combustion process. Vision-based combustion diagnostic systems work both in laboratory [3] and industrial scale [4].

Laboratory tests

Combustion tests were done in a 0.5 MW_{th} laboratory facility at the Institute of Power Engineering. It enables scaled down (10:1) combustion conditions of a full-scale swirl burner that was fired with pulverized fuel. The test stand of horizontal layout consists of cylindrical combustion chamber, 0.7 m in diameter and 2.5 m long. A model of low-NOx swirl burner about 0.1 m in diameter is mounted at the front wall. The stand is equipped with all necessary supply systems: primary and secondary air, biomass, coal, and oil. Biomass-coal mixture for combustion was prepared in advance and dumped into the coal feeder bunker. A two-worm dust conveyor supplies biomass-coal dust into primary air duct.

The combustion chamber has two lateral inspection openings on each side, that enabled image acquisition. A high-speed CMOS camera was placed close to burner outlet as shown in fig.1. To avoid influence of high temperature on camera work, it was equipped with a 0.7m boroscope transmitting flame images. Digital video acquisition system was capable to capture images with resolution of 800x800 pixels at 150 frames per second.

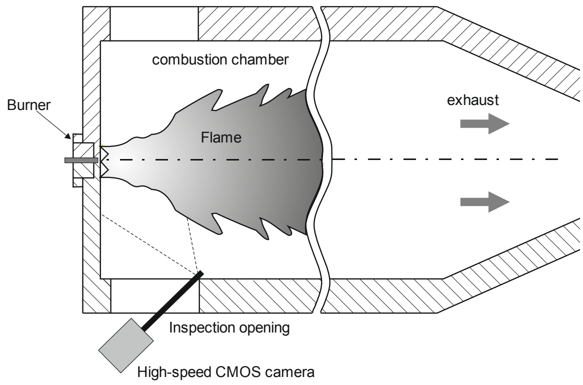

Fig. 1. Combustion chamber with camera mounting

A typical combustion test consisted of the following steps. First, the combustion chamber was warmed up by oil. When the temperature rose enough, the feeding device was started and the biomass-coal mixture was delivered to the burner, simultaneously with the oil. After reaching the proper temperature level, the oil was switched off. Primary

air is used mainly for delivering pulverized coal to burner nozzle, while secondary airs are used for regulation purposes.
Combustion testes were done for different combinations (variants) of the combustion facility: thermal power, excess air coefficient (λ) for known biomass content (0%, 10%, 20%, 30%) and angle of air-fuel mixture swirl. The mentioned above parameters were kept constant during combustion tests. The exact values of thermal power and excess air coefficient are collected in Table 1.

Table 1. The variants of biomass-coal combustion tests

Variant #	1	2	3	4	5	6	7	8	9
Power (kW)	250	250	250	300	300	300	400	400	400
λ	0.75	0.65	0.85	0.75	0.65	0.85	0.75	0.65	0.85

Flame images were captured for every variant of the combustion facility. The images were converted to 8-bit grayscale, thus pixel amplitude ranged from 0 to 255. For each frame out of the acquired image sequence flame area was determined on the basis of pixel amplitude. Such a assumption was possible to accept for the flame was the only luminous object within a combustion chamber. Next, some geometric properties of flame area were examined, such as for example: flame area, length of flame contour and coordinates of flame central point.

Experiment results

Flame area is defined as a sum of all the pixels contained within the flame region. Length of flame boundary is defined as a sum of all boundary pixels, assuming that the distance between two neighboring contour points parallel to the coordinate axes is rated 1, while the distance on the diagonal is rated $\sqrt{2}$.

Changes of flame area obtained for flames with 30% biomass added with swirl of 60° is presented in figure 2 and changes of flame area contour length is presented in figure 3.

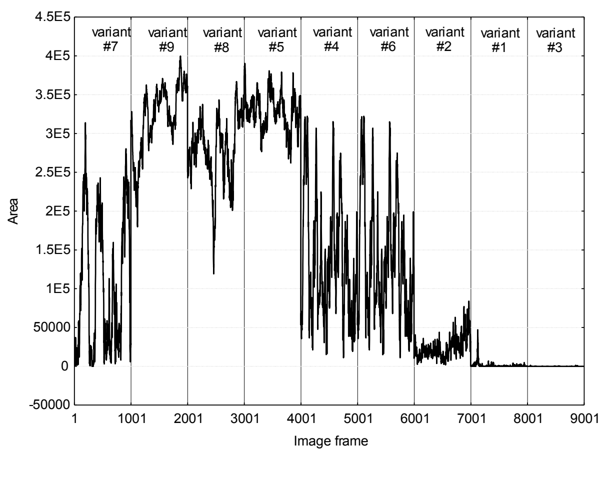

Fig. 2. Flame area obtained for different states of combustion process

It should be noted, that the discussed flame area parameters strongly depends on the way the flame area was defined. They differs within every combustion variants being analyzed. Generally magnitude of both flame area and its contour length depends on the thermal power of the combustion facility, especially for 250kW (variants 1, 2, and 3) the discussed parameters are relatively small.

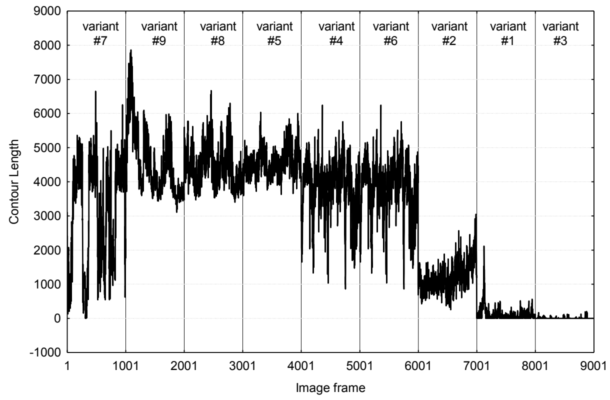

Fig. 3. Flame contour length obtained for different states of combustion process

Another important factor is variability of both flame area and flame contour length, that is greater for variants 7, 4 and 6, that were for different λ.

Conclusions

Biomass-coal co-combustion, especially with greater amount of biomass may proceed in improper way due to different densities of fuel components and possible stratification of the fuel within the duct. The presented flame area geometric features reflect temporary changes of heat that is emitted during combustion process but not the excess air coefficient.

REFERENCES

[1] Hein K.R.G., Bemtgen J.M., EU clean coal technology – co-combustion of coal and biomass, *Fuel Processing Technology*, (1998), 159-169
[2] Golec T., Współspalanie biomasy w kotłach energetycznych, *Energetyka i Ekologia* (2004), No. 7, 437-444
[3] Lu G., Gilbert G., Yan Y., Vision based monitoring and characterization of combustion flames. *Journal of Physics: Conference Series,* 15 (2005), 194–200
[4] Marques J.S., Jorge M.P., Visual inspection of a combustion process in a thermoelectric plant, *Signal Processing, vol. 80*, (2000), Elsevier, 1577-1589
[5] Kotyra A, Wójcik W., Wykorzystanie cech obrazu płomieniao oceny procesu spalania*, Pomiary Automatyka Kontrola,* nr 2, (2009), 117-120

Authors*: dr hab. inż. Andrzej Kotyra, Politechnika Lubelska, Katedra Elektroniki, ul. Nadbystrzycka 38a, 20-618 Lublin, E-mail: a.kotyra@pollub.pl; prof. dr hab. inż. Waldemar Wójcik, Politechnika Lubelska, Katedra Elektroniki, ul. Nadbystrzycka 38a, 20-618 Lublin, E-mail: waldemar.wojcik@pollub.pl; mgr inż. Krzysztof Jagiełło, Instytut Energetyki, Zakład Procesów Cieplnych, Augustówka 36, 02-981 Warszawa, E-mail: krzysztof.jagiello@ien.com.pl; dr inż. Konrad Gromaszek, Politechnika Lubelska, Katedra Elektroniki, ul. Nadbystrzycka 38a, 20-618 Lublin, E-mail: k.gromaszek@pollub.pl; mgr inż. Piotr Popiel, Politechnika Lubelska, Katedra Elektroniki, ul. Nadbystrzycka 38a, 20-618 Lublin, E-mail: p.popiel@pollub.pl; mgr inż. Tomasz Ławicki, Politechnika Lubelska, Katedra Elektroniki, ul. Nadbystrzycka 38a, 20-618 Lublin E-mail: t.lawicki@pollub.pl*

BUDOWA I BADANIA NADPRZEWODNIKOWEGO BEZRDZENIOWEGO INDUKCYJNEGO OGRANICZNIKA PRĄDU ŚREDNIEGO NAPIĘCIA

Janusz KOZAK[1] , Michał MAJKA[1], Tadeusz JANOWSKI[2], Sławomir KOZAK[1]

Instytut Elektrotechniki (1), Politechnika Lubelska (2)

Streszczenie. *W artykule opisano budowę i badania nadprzewodnikowego bezrdzeniowego indukcyjnego ogranicznika prądu średniego napięcia o prądzie znamionowym 600 A. Uzwojenia nadprzewodnikowe pierwotne i wtórne zbudowane są z taśmy drugiej generacji SF12050 i są sprzężone magnetycznie z pierwotnym uzwojeniem miedzianym. Ogranicznik chłodzony jest ciekłym azotem do temperatury 77 K. Przedstawiona konstrukcja bezrdzeniowa jest lekka, a przeprowadzone badania zwarciowe potwierdzają skuteczność ograniczania udarowego prądu zwarciowego.*

Abstract*. In this work, we report the design and tests results of coreless inductive SFCL with a 600 A rated current for MV distribution system. The primary and secondary windings made of 2G HTS tape SF12050 are magnetically coupled with the primary Cu winding The presented solution reduces the size and the weight of the device. Tests performed at high power test facility shows the effectiveness of short circuit current limiting.*

Słowa kluczowe: nadprzewodnikowy ogranicznik prądu, taśma nadprzewodnikowa, konstrukcja bezrdzeniowa.
Keywords: superconducting fault current limiter, superconducting tape, coreless structure.

Wstęp

Nadprzewodnikowe ograniczniki prądu są urządzeniami elektroenergetycznymi, które w ostatnich latach są w fazie intensywnych badań. W ośrodkach naukowych i firmach prywatnych powstało wiele prototypów tych urządzeń. Dostępność na rynku taśm nadprzewodnikowych drugiej generacji o znacznie lepszych parametrach w porównaniu do taśm pierwszej generacji spowodowała przyspieszenie prac nad nadprzewodnikowymi ogranicznikami prądu w celu zainstalowania prototypowych urządzeń w sieci elektroenergetycznej. Nadprzewodnikowe ograniczniki prądu dzięki specyficznym właściwościom wysokotemperaturowych nadprzewodników umożliwiają budowę urządzeń elektrycznych o parametrach nieosiągalnych przy użyciu materiałów konwencjonalnych [1]. Ograniczanie prądów zwarciowych przez nadprzewodnikowe ograniczniki prądu zapewnia ochronę urządzeń takich jak transformatory i wyłączniki oraz znacznie zmniejsza ich zużycie [2]. Gwałtowna zmiana impedancji ogranicznika po przekroczeniu wartości prądu krytycznego nadprzewodnika ogranicza udarowy prąd zwarciowy. Nadprzewodnikowy ogranicznik prądu typu indukcyjnego instalowany w systemie elektroenergetycznym składa się z miedzianego uzwojenia pierwotnego, rdzenia magnetycznego oraz umieszczonego w kriostacie zwartego wtórnego uzwojenia nadprzewodnikowego. Zaletami takiej konstrukcji jest brak konieczności stosowania przepustów prądowych w porównaniu do ograniczników rezystancyjnych. Dodatkowo pierwotne uzwojenie miedziane zapewnia ciągłość obwodu w przypadku uszkodzenia uzwojenia nadprzewodnikowego. Wadą tego rozwiązania jest ciężki rdzeń magnetyczny oraz spadek napięcia na ograniczniku podczas normalnej pracy spowodowany reaktancją rozproszenia zależną od odległości pomiędzy uzwojeniami pierwotnym i wtórnym. W Pracowni Technologii Nadprzewodnikowych Instytutu Elektrotechniki, gdzie od ponad 10 lat prowadzone są badania nad różnymi rozwiązaniami nadprzewodnikowych ograniczników prądu, zaprojektowano i przebadano bezrdzeniowy lekki nadprzewodnikowy ogranicznik prądu typu indukcyjnego zbudowany z taśmy drugiej generacji.

Budowa ogranicznika SFCL-SN

Zbudowany nadprzewodnikowy ogranicznik prądu ma lekką konstrukcją bezrdzeniową, ponadto pierwotne uzwojenie miedziane jest chłodzone ciekłym azotem, co dodatkowo redukuje masę urządzenia. Urządzenie składa się z czterech modułów połączonych szeregowo (Rys.1a). Każdy moduł ma trzy uzwojenia, pierwotne uzwojenie miedziane, równolegle podłączone do niego pierwotne uzwojenie nadprzewodnikowe i zwarte wtórne uzwojenie nadprzewodnikowe (Rys.1b). Siły promieniowe działające na uzwojenia ogranicznika podczas zwarcia zostały ograniczone poprzez specjalną konstrukcję uzwojeń nadprzewodnikowych. Uzwojenia nadprzewodnikowe pierwotne i wtórne nawinięte zostały jednocześnie.

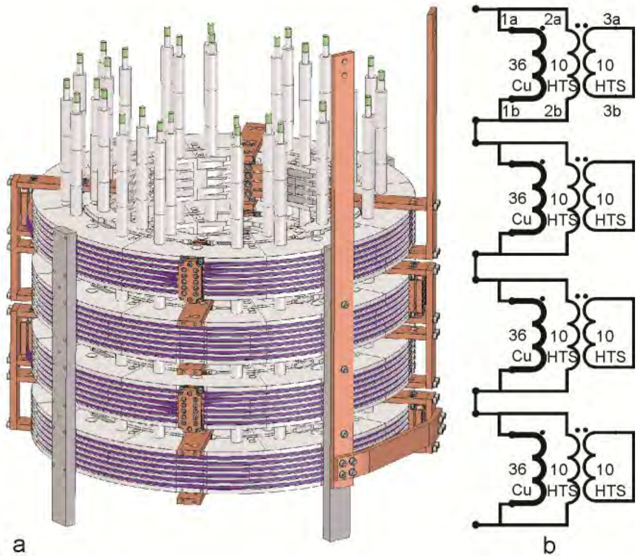

Rys. 1. a) Budowa nadprzewodnikowego bezrdzeniowego ogranicznika prądu typu indukcyjnego SFCL-SN wykonanego z taśmy nadprzewodnikowej drugiej generacji SF12050 2G tape, b) schemat połączeń modułów nadprzewodnikowego ogranicznika prądu SFCL-SN

Pomiędzy zwojami uzwojenia pierwotnego znajdują się zwoje uzwojenia wtórnego. Taka konstrukcja zapewnia dobre sprzężenie magnetyczne i małą reaktancję rozproszenia. Spadek napięcia na ograniczniku podczas normalnej pracy (I = 600 A) jest pomijalnie mały U < 1V. Ogranicznik składa się z czterech identycznych modułów. Każdy moduł ma dwa karkasy wykonane obróbką CNC z materiału POM-C. Na karkasie zewnętrznym uzwojenia miedzianego nawinięte jest 36 zwojów drutem miedzianym prostokątnym. Na karkasie wewnętrznym uzwojeń nadprzewodnikowych nawinięte są pierwotne i wtórne uzwojenia HTS, każde z uzwojeń HTS ma 10 zwojów [3].

Próba zwarciowa

Próba zwarciowa ogranicznika SFCL-SN wykonana została po schłodzeniu ogranicznika ciekłym azotem w układzie przedstawionym na rysunku 2. Bateria kondensatorów naładowana do napięcia 10 kV została rozładowana po zamknięciu załącznika zwarciowego ZZ, a po około 50 ms obwód został rozłączony wyłącznikiem W.

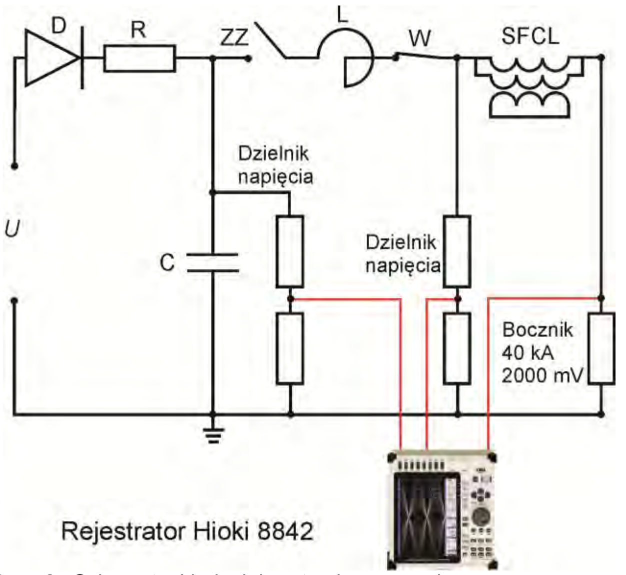

Rys. 2. Schemat układu laboratoryjnego z włączonym w szereg ogranicznikiem SFCL-SN

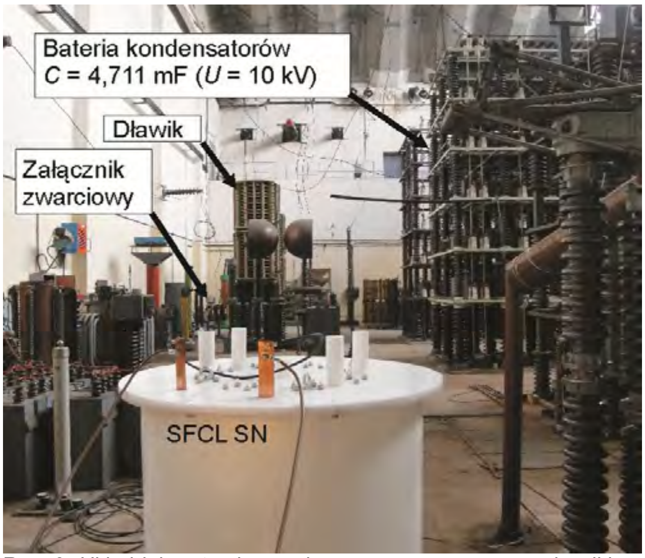

Rys. 3. Układ laboratoryjny z włączonym w szereg ogranicznikiem SFCL-SN

Z porównania przebiegów prądu zwarciowego w obwodzie z ogranicznikiem i bez ogranicznika widać, iż prąd spodziewany 15 kA ograniczony został do wartości 5 kA. Podczas próby zwarciowej w wyniku działania sił osiowych uszkodzony został karkas uzwojenia miedzianego. W wyniku uszkodzenia karkasu po około 12 ms od chwili zwarcia w obwodzie zwarły się miedziane bloki łączące poszczególne moduły ogranicznika.

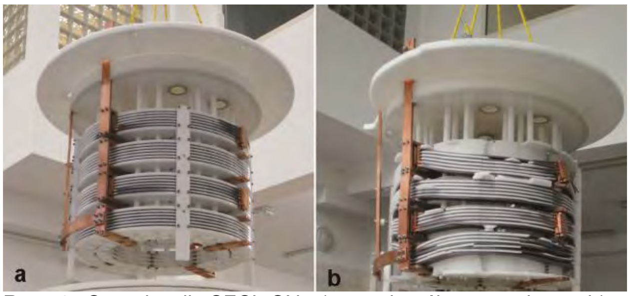

Rys. 4. Ogranicznik SFCL-SN a) przed próbą zwarciową, b) po próbie zwarciowej

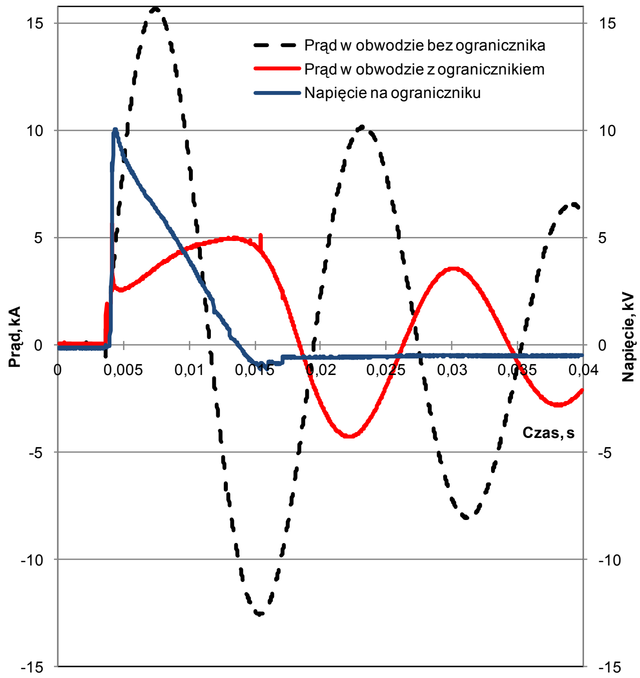

Rys. 5. Przebiegi prądu zwarciowego w obwodzie z ogranicznikiem i bez ogranicznika

Podsumowanie

Ogranicznik SFCL-SN, zgodnie z założeniami, ograniczył prąd udarowy z 15 kA do 5 kA. Zastosowany do budowy karkasu materiał POM-C w temperaturze 77 K okazał się nie odporny na działanie sił udarowych.

LITERATURA

[1] Kozak J., Majka M., Janowski T., Kozak S., Wojtasiewicz G., Kondratowicz-Kucewicz B., Test and performance analysis of coreless inductive HTS fault current limiter, *IEEE Trans. Appl. Supercon.*, 21, (2011), No. 3, 1303-1306
[2] Noe M., Steurer M., " High temperature superconductor fault current limiter: Concepts applications and development status, Supercond. Sci. Technol., 20, (2007) R15-R29
[3] Fault Current Limiter Application, SuperPower® 2G HTS Wire Spec Sheet, 3. (2009), www.superpower-inc.com

***Autorzy**: dr inż. Janusz Kozak, Instytut Elektrotechniki, ul. Nadbystrzycka 38a, 20-618 Lublin, E-mail: j.kozak@iel.waw.pl; dr inż. Michał Majka, E-mail: m.majka@iel.waw.pl; dr hab. inż. Sławomir Kozak, E-mail: s.kozak@iel.waw.pl, prof. dr hab. inż. Tadeusz Janowski, Politechnika Lubelska, ul. Nadbystrzycka 38a, 20-618 Lublin, E-mail: t.janowski@pollub.pl.*

Conference ELMECO–7
ELECTROMAGNETIC DEVICES AND PROCESSES IN ENVIRONMENT PROTECTION
joint with 10th Seminar AoS-10 APPLICATIONS OF SUPERCONDUCTORS
28–30.09.2011, Nałęczów, Poland

COMPARISON OF DIFFERENT METHODS FORCE CALCULATION IN DIELECTROPHORESIS

Eugeniusz KURGAN

AGH University of Science and Technology, Department of Electrical and Power Control Engineering

***Abstract**. In this article two different methods electric force computation in dielectrophoresis is presented. The first is based on equivalent dipole method, which is easy to use, but in some situations not accurate. The second one is based on Maxwell stress tensor and gives in all possible situations accurate results, but is much more cumbersome in implementation. These two methods will be compared with regard to computational accuracy in different practical combination of particle position and dimension and interdigitated electrode dimensions*

***Streszczenie.** W publikacji tej zostaną porównane dwie różne metody obliczania siły działającej na cząsteczkę w dielektroforezy. Pierwsza z nich jest oparta na metodzie równoważnego dipola elektrycznego, ale w pewnych sytuacjach jest niezbyt dokładna, natomiast druga z nich oparta jest na metodzie naprężeń Maxwella i jest znacznie bardziej dokładna, choć trudniejsza w implementacji. Te dwie metody zostaną porównane pod względem dokładności obliczeń względem różnych położeń i rozmiarów cząsteczki oraz rozmiarów komory z ciekłym elektrolitem.*

Keywords: dielectrophoresis, equivalent dipole method, Maxwell stress tensor, force calculation.
Słowa kluczowe: dielektroforeza, metoda równoważnego dipola, tensor naprężeń Maxwella, obliczanie sił.

Introduction

All materials from electrical point of view is composed of positive and negative charges which experience an electrostatic force when is placed in an electric field. In a uniform electric field, electrically neutral particles experience a dielectric polarization, but no net force. In a nonuniform electric field, however, forces acting on polarised charges are not balanced, and a motion called dielectrophoresis (DEP) occurs. There are actually two types of dielectrophoresis involving particles suspended in a medium: positive DEP – where the particles move toward the region of stronger electric field, and negative DEP – where the fluid surrounding the particles experience a stronger attractive force than the particles, which causes the suspended particles to be pushed toward the area of weaker electric field.

In comparison to electrophoresis, by which we understand particle motion due to the force resulting from coupling between an applied external electric field and a charge particle, dielectrophoresis has the disadvantage that the polarization forces acting on polarized particle are quite weak. In general, efficient particle manipulation in microelectrode arrangement requires taken into account other factors, such as viscous, buoyancy, and electrohydrodynamic forces. This constitutes complicated system of mathematically coupled different physical fields, which results in mutually coupled system partial differential equations. From practical point of view only numerical methods can give from practical point of view satisfactory results. Based on the measurement of electric and dielectric properties, a further study of selective segregation and purposeful manipulation of micro- or nanostructures of living organisms can be achieved. The phenomenon of dielectrophoresis (DEP) was first defined by Pohl [1] as the motion of neutral but polarizable particles subjected to nonuniform electric fields. DEP provides an increased measurement precision and sensitivity in the detection of cells with different dielectric properties, without any need for labeling them. Two different methods electric force computation in dielectrophoresis is presented. The first is based on equivalent dipole method, which is easy to use, but in some situations not accurate [2, 3]. The second one is based on Maxwell stress tensor and gives in all possible situations accurate results, but is much more cumbersome in implementation. These two methods will be compared with regard to computational accuracy in different practical combination of particle position and dimension and chamber dimension.

Equivalent dipol method

In this article authors calculate electric field and forces in interdigitated system of electrodes, as it is shown in Fig.1

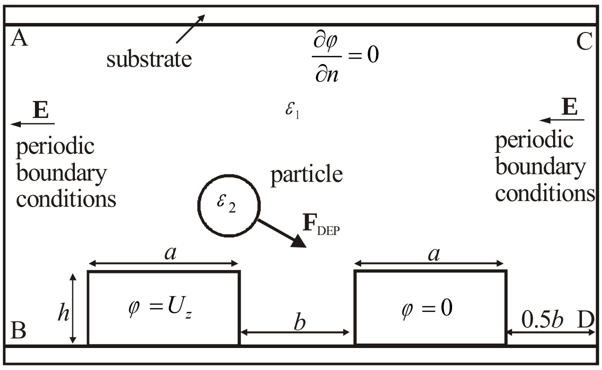

Fig.1. Schematic view of the two electrodes and suspension.

In our case the field is described by set of following well known equations:

(1) $$\nabla\cdot(\varepsilon\mathbf{E})=\rho_c \qquad \mathbf{E}=-\nabla\varphi$$

where $\mathbf{E}$ is the electric field, $\mathbf{J}$ is current density vector, φ is the electric potential. Boundary conditions on the computational problem boundary are Neuman's or Dirichlet's type. On the bottom and top insulating substrate current cannot flow into this boundary, so Neuman's conditions here apply. Periodic boundary conditions are present on the left and right sides A-B and C-D of the model boundary to simulate the presence of neighbouring electrodes. It is assumed that all computational cells are of the same type. Using typical fabrication procedures, the thickness of the deposited metal that forms the interdigitated electrodes is in most cases less than 1μm.

In static field, the force acting on small particle at equilibrium is given by

$$\mathbf{F} = (\mathbf{p} \cdot \nabla)\mathbf{E} \tag{2}$$

where $\mathbf{p}$ is the dipole moment and $\mathbf{E}$ external electric field strength. Assuming now, that small spherical particle has the volume $V = \pi r^2 L$ the total electophoretic force is given by

$$F = 2\pi r^3 \varepsilon_0 \varepsilon_1 \left(\frac{\varepsilon_2 - \varepsilon_1}{\varepsilon_2 - \varepsilon_1} \right) \nabla E^2 \tag{3}$$

The above equation tells us that the dielectrophoretic force depends on the relevant permittivities, which does not increase without limit as the permittivity of the particle increases.

Maxwell stress tensor approach

There exists also another method computation of the total force acting on particle, namely the Maxwell stress method. The DEP force acting on particle is obtained by integrating the Maxwell stress tensor $\mathbf{T}^{\mathrm{e}}$ as follows:

$$\mathbf{F}_{\mathrm{DEP}} = \oint_S \mathbf{T}^{\mathrm{e}} \cdot \mathbf{n} \mathrm{d}S \tag{4}$$

where S represents the surface enclosing the particle, **n** is the unit vector normal to the surface and the elements of the tensor are given by.

$$\mathbf{T}^{\mathrm{e}(i)} = \varepsilon_i \varepsilon_0 \left(\mathbf{E}_l^{(i)} \mathbf{E}_m^{(i)} - \frac{1}{2} \left(\mathbf{E}^{(i)} \right)^2 \delta_{l,m} \right) \tag{5}$$

where $\mathbf{E}_l^{(i)}$ is the i-th component of the electric field in medium i, ε_i is the permittivity of medium i, and, $\delta_{l,m}$ is the Dirac delta function. This tensor must be evaluated on both sides of the interface between body and the fluid. The net force $\mathbf{F}$ on the particle can be obtained by integrating the Maxwell stress tensor over a single surface that encloses it

$$\mathbf{F} = \varepsilon_1 \varepsilon_0 \oint_S \left[\mathbf{E}(\mathbf{E} \cdot \mathbf{n}) - \frac{1}{2} E^2 \cdot \mathbf{n} \right] \mathrm{d}S \tag{6}$$

where *S* is integration surface surrounded surface charge distribution on both sides particle-suspension boundary. More practically is to divide the whole integration surface on two parts on both sides of particle surface, integrate over them separately and next subtract one from another.

Simulation results

The finite element calculations was done for following geometrical dimensions: A–B = 60 μm, A–C = 160 μm, $a = 40$ μm, $b = 40$ μm, $h = 4$ μm. Spherical dielectric particle has radius $r = 4$ μm and relative permittivity $\varepsilon_2 = 80$. The fluid, where particle moves has permittivity $\varepsilon_1 = 4$. First electric potential φ was calculated (as in Fig.3) and next electric displacement **D** (Fig.4)

The total force acting on particle computed from (6) at point (6, 1.5) μm has the value

$$\mathbf{F}_{\mathrm{DEP}} = \left(0.26\mathbf{a}_x - 0.82\mathbf{a}_y \right) [\mu\mathrm{N/m}] \tag{7}$$

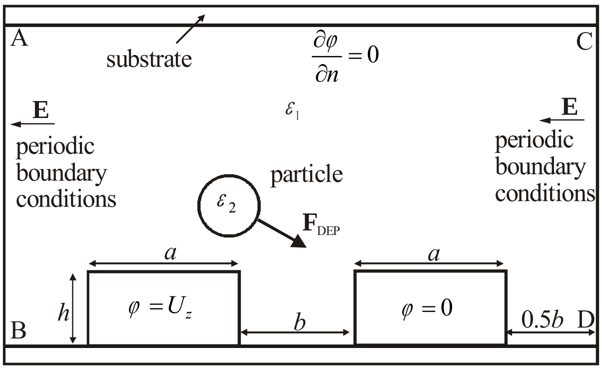

Fig.1. Cross section of the electrode arrangement with one pair of electrodes and moving biological particle is depicted.

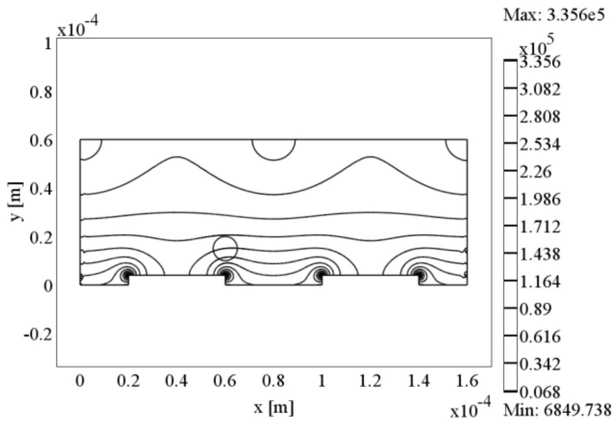

Fig.2. Equivalue lines of the modulus of the electric field strength **E**.

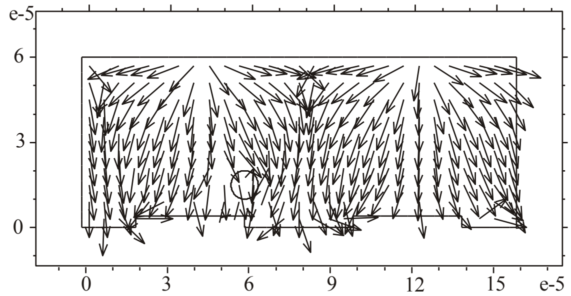

Fig.3. Distribution of force acting on two-dimensional cylindrical particle.

Generally difference between forces calculated by equivalent dipole method and Maxwell stress tensor is less then 5%. The differences are greater when we consider particles with greater dimensions and interdigitated electrodes with smaller dimensions.

REFERENCES

[1] Pohl H., *Dielectrophoresis*, Cambridge University Press, Cambridge, UK, 1978.

[2] Y. Huang, X.B. Wang, F.F. Becker, P.R.C. Gascoyne, Introducing dielectrophoresis as a new force field for field-flow fractionation, *Biophys. J.*,vol. 73, (1997), pp. 1118–1129

[3] J. Yang, Y. Huang, X.B. Wang, F.F. Becker, P.R.C. Gascoyne, Cell separation on microfabricated electrodes using dielectrophoretic/gravitational field-flow fractionation, *Anal. Chem.*, vol 71, (1999), pp. 911–918

***Authors**: Dr hab. inż. Eugeniusz Kurgan, prof. nz., Akademia Górniczo-Hutnicza, Katedra Elektrotechniki i Elektroenergetyki, al. Mickiewicza 30, 30-059 Kraków, E-mail: kurgan@agh.edu.pl.*

Conference ELMECO–7
ELECTROMAGNETIC DEVICES AND PROCESSES IN ENVIRONMENT PROTECTION
joint with 10th Seminar AoS-10 APPLICATIONS OF SUPERCONDUCTORS
28–30.09.2011, Nałęczów, Poland

PERSPEKTYWY ZASTOSOWANIE TECHNOLOGII NADPRZEWODNIKOWEJ W BUDOWIE URZĄDZENIA GEORADAROWEGO

Michał ŁANCZONT

Politechnika Lubelska, Instytut Podstaw Elektrotechniki i Elektrotechnologii

Streszczenie. *Dokument opisuje podstawowe rodzaje urządzeń georadarowych, ich zasadę działania. Prezentuje także założenia zastosowania nadprzewodników w celu poprawy parametrów układu antenowego urządzenia.*

Abstract*. The paper describes the basic kinds of georadar devices and their principle of working. It prezents also aim of improvement of parameters arrangement in antenna's achived by appling the superconducting technology.*

Słowa kluczowe: georadary, fale elektromegnetyczne, nadprzewodnictwo, squid.
Keywords: georadar devices, electromagnetic wave, superconductor, squid.

Wstęp

Technologia radarowa umożliwia lokalizowanie oddalonych obiektów za pomocą fal elektro-magnetycznych [1]. Powszechnie stosowane radary umożliwiają wykrywanie obiektów znajdujących się powietrzu lub na powierzchni wody. Opracowane są także konstrukcje radarów umożliwiających penetrację wnętrza ziemi, zwane georadarami. Umożliwiają one przeprowadzenie bezinwazyjnego badania przypowierzchniowych warstw ziemi, do kilkuset metrów. Technika ta umożliwia badanie struktury warstw litologicznych, wykrywania złóż surowców, dokładnej detekcji obiektów (zastosowanie w inżynierii lądowej lub archeologii).

Stosowane powszechne konstrukcje georadarów charakteryzują się stosunkową małą głębokością penetracji. Wydaje się że zastosowanie SQUID'ów w układzie anteny odbiorczej mogło by w sposób diametralny zwiększyć zasięg georadaru oraz poprawić dokładność uzyskiwanych obrazów georadarowych [3].

Zasada działania georadaru

Opracowano i powszechnie stosuje się trzy rodzaje georadarów:

1. z modulacją amplitudy AM,
2. z modulacją częstotliwości FM,
3. z kompensacją impulsu,

ponadto znane są jeszcze dwie konstrukcje:

1. system fali ciągłej – CW radar,
2. radar interferencyjny,

Jednakże są one znacznie rzadziej stosowane.

Zasada działania georadaru jest analogiczna do pracy zwykłego radaru. Antena nadawcza emituje fale elektromagnetyczną, która po natrafieniu na obiekt ulega odbiciu i powraca gdzie jest rejestrowana przez antenę odbiorczą. W przypadku georadaru specyfika środowiska pracy wpływa istotnie na budowę, rejestrację oraz interpretację wyników. Struktura ośrodka w którym propaguje fala elektro-magnetyczna charakteryzuje się bardzo dużym tłumieniem sygnału, ponadto względu na istniejące normy, ograniczona jest także moc sygnału sondującego, wysyłana przez georadar. Powoduje to że rejestrowana amplituda odbicia fali sondującej jest zazwyczaj bardzo mała. Istotnym problemem wtedy staje się oddzielenie tła (szumu) od sygnału niosącego informacje.

Najczęściej obecnie stosowanym typem georadaru jest radar impulsowy z modulacją amplitudy sygnałem. Emitowany impuls elektromagnetyczny charakteryzuje się mocą szczytową sygnału dochodzi do kilkuset watów oraz określoną częstotliwością, jak pokazano na rysunku 1.

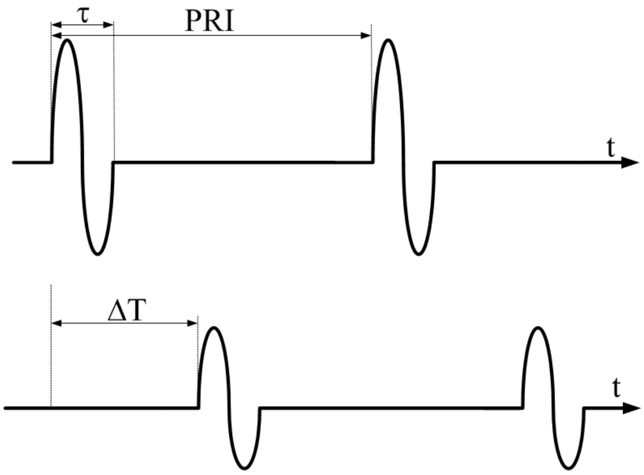

Rys.1. Sygnał sondujący i sygnał odpowiedzi. τ – szerokość impulsu, ΔT – czas odpowiedzi, PRI – interwał pomiędzy sygnałami sondującymi

Szerokość impulsu radarowego zazwyczaj mieści się w zakresie od 0,5 ns do kilkudziesięciu nanosekund. Im impuls jest węższy tym większa jest rozdzielczość radaru. Interwał pomiędzy impulsami jest wielokrotnie większy od szerokości impulsu, powoduje to że pomimo dużej wartości mocy szczytowej impulsu, wartość średnia mocy za okres jest stosunkowo niewielka (1).

(1)

$$P_{sr} = P_{imp} \cdot \frac{\tau}{PRI}$$

gdzie: P_{sr} – moc średnia za okres, P_{imp} – moc impulsu sondującego

W okresie pomiędzy emisją sygnałów sondujących rejestrowane są przez antenę odbiorczą sygnały odbite niosące informację o strukturze ośrodka. Szerokość okna czasowego, w którym rejestrowane są impulsy odbite, jest parametrem definiowanym przez użytkownika radaru. Szerokość okna nie może być większa od interwału pomiędzy kolejnymi impulsami sondującymi. Im większa jest szerokość okna pomiarowego tym rejestrowane są dane z większych głębokości. Jednocześnie jednak z im większej głębokości pochodzi zarejestrowany impuls tym jest on słabszy i trudniejsze może być odróżnienie go od szumu.

Równie interesującą, oraz charakteryzującą się wieloma zaletami konstrukcją, jest radar pracujący w systemie fali ciągłej modulowanej. Sygnał sondujący emitowany przez antenę nadawczą radaru charakteryzuje się zmienną częstotliwością opisaną przez sygnał piłokształtny, jak pokazano na rysunku 2.

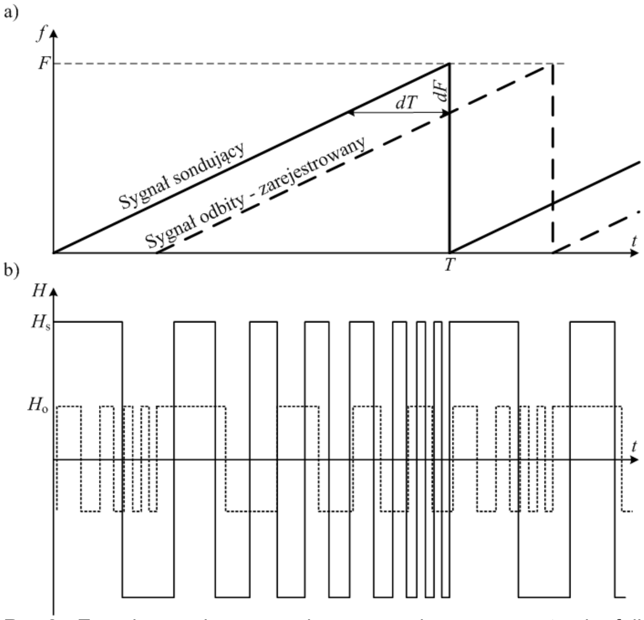

Rys.2. Zasada pomiaru w radarze pracującym w systemie fali ciągłej modulowanej: a) Zasada pomiaru czasu, b) sygnał sondujący i odbity. T – czas trwania pakietu sygnału sondującego, F – maksymalna częstotliwość sygnału sondującego, dT – czas pomiędzy emisją sygnału sondującego rejestracją sygnału odbitego, dF – różnica pomiędzy częstotliwością sygnału emitowanego a sygnału rejestrowanego

Radary tego typu jednocześnie emitują i rejestrują sygnał. Obydwa sygnały różnią się częstotliwością. Odległość od obiektu zaburzającego wyznaczana jest na podstawie różnicy częstotliwości pomiędzy sygnałami.
(2)

$$R = \frac{dF \cdot T \cdot \nu}{2 \cdot F}$$

gdzie: R – odległość do obiektu, ν - prędkość fali elektromagnetycznej w ośrodku.

Zastosowanie elementu nadprzewodnikowego

Zastosowanie nadprzewodnika w obwodzie anteny odbiorczej może zapewnić znaczący wzrost czułości urządzenia georadarowego, oraz zwiększyć głębokość penetracji. Wydaje się że efekt ten można osiągnąć w dwojaki sposób:

1. zastosowanie nadprzewodnikowego interferometru kwantowego – SQUID'u

Zastosowanie squid'u w obwodzie anteny odbiorczej, jak pokazano na rysunku 3, może zapewnić zdecydowany wzrost czułości układu odbiorczego georadaru. Wydaje się że w sposób znaczący powinna wzrosnąć głębokość penetracji, bez ingerencji w pozostałe elementy urządzenia.

2. wykonanie anteny radaru z materiału nadprzewodzącego

Znaczącym elementem wpływającym na skuteczność działania anteny jest jej rezystancja [2]. Dąży się do jej zminimalizowania. Zbudowanie anteny z materiału nadprzewodzącego, charakteryzującego się rezystancją bliską zeru, może zapewnić znaczący wzrost efektywności całego urządzenia.

Wnioski

Urządzenia georadarowe są przyrządami umożliwiającymi szybką i bezinwazyjną analizę przypowierzchniowych warstw ziemi. W zależności od parametrów sygnału próbkującego i budowy anten możliwe jest skanowanie na głębokość nawet kilkuset metrów.

Wydaje się że zastosowanie materiałów nadprzewodnikowych mogło by w znaczący sposób poprawić jakość (rozdzielczość i dokładność) uzyskanych obrazów georadarowych jak również zwiększyć głębokość penetracji.

LITERATURA

[1] Karnowski J., Zarys metody georadarowej, *AGH Uczelniane Wydawnictwo Naukowo-Dydaktyczne*, Kraków 2007
[2] Szóstak J., Fale i anteny, *Wydawnictwo Komunikacji i Łączności*, Warszawa 2006
[3] Jha A. R., Superconductor technology – Applications to microwave, electro-optics, electrical machines, and propulsion systems, *A Wiley-Interscience Publications, John Wiley & Sons, INC*, New York 1998

***Autorzy**: dr inż. Michał Łanczont, Politechnika Lubelska, Instytut Podstaw Elektrotechniki i Elektrotechnologii, ul. Nadbystrzycka 38A, 20-618 Lublin, E-mail: m.lanczont@pollub.pl;*

Conference ELMECO–7
ELECTROMAGNETIC DEVICES AND PROCESSES IN ENVIRONMENT PROTECTION
joint with 10th Seminar AoS-10 APPLICATIONS OF SUPERCONDUCTORS
28–30.09.2011, Nałęczów, Poland

MODELOWANIE REZYSTANCYJNEGO NADPRZEWODNIKOWEGO OGRANICZNIKA PRĄDU W ŚRODOWISKU SCILAB

Michał ŁANCZONT

Politechnika Lubelska, Instytut Podstaw Elektrotechniki i Elektrotechnologii

Streszczenie. *Artykuł opisuje projekt modelu numerycznego rezystancyjnego nadprzewodnikowego ogranicznika prądu. Przedstawiono założenia modelu matematycznego, charakterystykę modelowanego obiektu oraz wyniki symulacji.*

Abstract*. The paper describes basics of proposed numerical model of resistive superconducting fault current limiter. It was described the foundations of numerical model as well as present the results of simulation.*

Słowa kluczowe: numerical modeling, superconducting fault current limiter, SCILAB.
Keywords: modelowanie numeryczne, nadprzewodnikowe ograniczniki prądu, SCILAB.

Wstęp

Analiza urządzeń elektrycznych zawierających elementy wykonane z materiału nadprzewodnikowego jest procesem skomplikowanym wynikającym z nieliniowego charakteru nadprzewodnika. W odróżnieniu od materiałów konwencjonalnych rezystancja nadprzewodnika jest funkcją trzech parametrów, temperatury, natężenia prądu płynącego przez element oraz natężenia zewnętrznego pola magnetycznego (niewygenerowanego przez sam nadprzewodnik) w jakim pracuje.

W artykule zaprezentowano model matematyczny ogranicznika rezystancyjnego, uwzgledniający wpływ natężenia prądu i temperatury na rezystancje elementu nadprzewodnikowego ogranicznika. Zdefiniowano model numeryczny obwodu z ogranicznikiem rezystancyjnym, oraz zamieszczono wyniki symulacji numerycznych.

Nadprzewodnikowy rezystancyjny ogranicznik prądu

Rezystancyjne nadprzewodnikowe ograniczniki prądu zasadę działania opierają na nieliniowej charakterystyce rezystywności materiału nadprzewodnikowego w funkcji prądu płynącego przez ten materiał [3]. W okolicy pewnej wartości prądu, zwanej krytyczną, następuje gwałtowny wzrost rezystywności materiału [2], jak pokazano na rysunku 1.

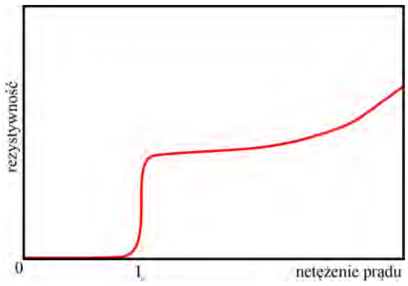

Rys.1. Charakterystyka zależności rezystywności materiału nadprzewodzącego od wartości natężenia prądu płynącego w tym materiale

Ograniczniki indukcyjne wykonuje się zazwyczaj w postaci uzwojenia bezindukcyjnego wykonanego z taśmy lub elementu konstrukcyjnego. W większości przypadków element nadprzewodnikowy ogranicznika bocznikowany jest rezystorem, jak pokazano na rysunku 2. Rozwiązanie to stosuje się w celu ochrony elementu nadprzewodnikowego przed termicznym uszkodzeniem do jakiego może doprowadzić przepływ dużego prądu zwarciowego.

W niektórych konstrukcjach obiektem bocznikującym jest element konstrukcyjny z którym powiązany jest nadprzewodnik, jak podłoże lub matryca. W tym wypadku jednak nadprzewodnik nie jest w pełni zabezpieczony przed uszkodzeniem termicznym ze względu na kontaktowe sprzężenie nadprzewodnika z bocznikiem.

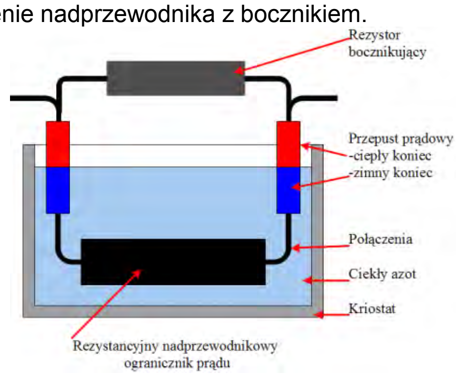

Rys.2. Schematyczny rysunek budowy rezystancyjnego nadprzewodnikowego ogranicznika prądu

Matematyczny model elementu nadprzewodnikowego

W ogranicznikach rezystancyjnych skokowa zmiana rezystancji ogranicznika następuje zazwyczaj pod wpływem prądu, w pewnych sytuacjach może jednak dojść do termicznego wymuszenia przejścia do stanu rezystywnego [1]. Zaproponowany model uwzględnia obydwie drogi utraty stanu nadprzewodzącego (1).

$$
(1)\quad \begin{cases} R_I = \dfrac{R}{e^{I_C(T_N)-|i_N|}+1} \\[2ex] R_T = R \cdot A\sinh\left(\dfrac{T_C}{T_0} \left(\dfrac{T_N - T_0}{T_C - T_0} \right)^3 \right) \end{cases}
$$

gdzie: I_C – wartość prądu krytycznego nadprzewodnika, i_N – wartość chwilowa prądu płynącego przez nadprzewodnik, T_C – temperatura krytyczna, T_0 – temperatura medium chłodzącego, T_N – temperatura nadprzewodnika, R – rezystancja nadprzewodnika w stanie rezystywnym

Charakterystyki obrazujące działanie modelu pokazano na rysunku 3.

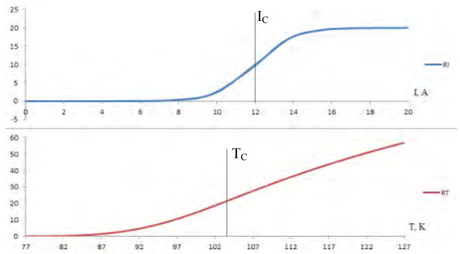

Rys.3. Charakterystyki rezystancji elementu nadprzewodnikowego w funkcji prądu i temperatury

Zależność prądowa rezystancji uwzględnia nieliniową funkcję wiążącą prąd i temperaturę krytyczną nadprzewodnika (2).

$$(2)\quad I_C = I_{C_0}\left[1-\left(\frac{T_N}{T_C}\right)^2\right]$$

Numeryczny model ogranicznika rezystancyjnego

W oparciu o zaproponowany model numeryczny elementu nadprzewodnikowego zbudowany został model numeryczny obwodu zwarciowego z rezystancyjnym nadprzewodnikowym ogranicznikiem prądu, jak pokazano na rysunku 4.

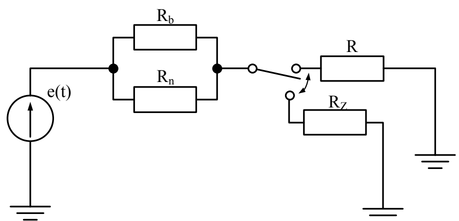

Rys.4. Schemat obwodu zwarciowego modelu numerycznego

Symulowany obwód ma charakter czysto rezystancyjny. Rezystancja R stanowi znamionową rezystancję badanego obwodu. Ogranicznik jest reprezentowany przez równoległe połączenie rezystora R_n opisującego element nadprzewodnikowy oraz R_b odpowiadający rezystorowi bocznikującemu. Badany obwód zasilany jest ze źródła napięcia przemiennego. Zwarcie symulowane jest poprzez przełączenie pomiędzy rezystancją znamionową obwodu a rezystancją zwarcia R_Z.

Symulacja

W środowisku SCILAB napisano program symulujący działanie ogranicznika rezystancyjnego. Zagadnienie opisane układem równań nieliniowych rozwiązywane jest za pomocą wbudowanej funkcji fsolve. Rozwiązanie analizowanego układu równań są wartości chwilowe prądów płynących w obwodzie oraz temperatury nadprzewodnika i bocznika (matrycy).

Czas symulacji ustalono na 0.1 s, krok symulacji na 10 μs, zaś czas trwania zwarcia ustawiono na 0.02 do 0.06 s (dziesięcio krotny spadek wartości rezystancji obciążenia).

Wybrane wyniki symulacji zaprezentowano na rysunkach 5-8.

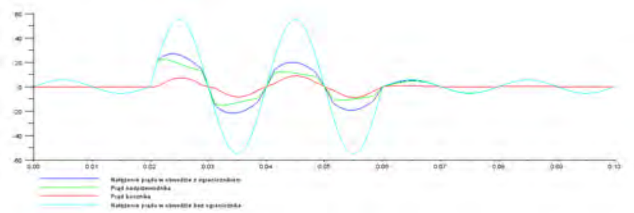
Rys.5. Przebiegi prądów płynących w obwodzie: a – prąd główny w obwodzie z ogranicznikiem, b – prąd płynący przez nadprzewodnik, c – prąd płynący przez bocznik, d – prąd płynący w obwodzie bez ogranicznika

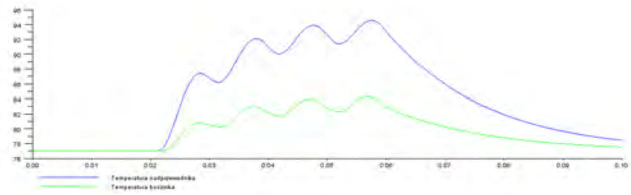
Rys.6. Przebieg zmian temperatury nadprzewodnika i bocznika

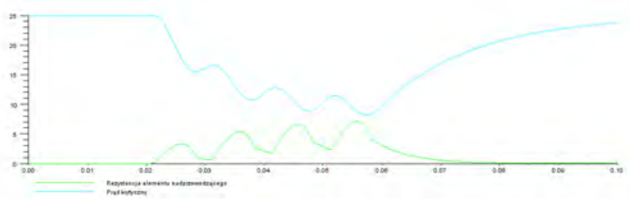
Rys.7. Przebiegi zmian rezystancji elementu nadprzewodzącego ogranicznika oraz wartości krytycznej prądu tego elementu

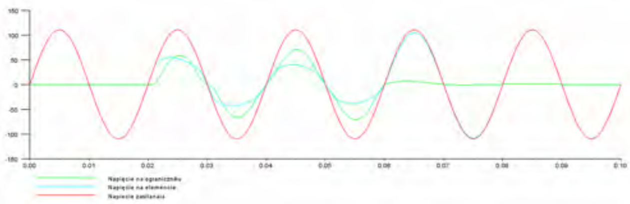
Rys 8. Przebiegi napięcia zasilającego oraz spadki napięcia na ograniczniku i obciążeniu

Wnioski

Zaproponowana metoda analizy urządzeń nadprzewodnikowych zaprezentowana na przykładzie modelu obwodu zwarciowego z rezystancyjnym nadprzewodnikowym ogranicznikiem prądu umożliwia na uzyskanie wyników zbieżnych z rzeczywistymi. Zaproponowany model uwzględnia wpływ prądu i temperatury na wartość rezystancji elementu nadprzewodzącego ogranicznika.

Model zbudowany w środowisku SCILAB umożliwia łatwą modyfikację i zastosowanie w modelowaniu innych urządzeń nadprzewodnikowych.

LITERATURA

[1] L. Jaroszyński, D. Czerwiński: Modelowanie numeryczne elementów nadprzewodnikowych, *VIII Seminarium Zastosowania Nadprzewodników*, p. 112-121, Nałęczów 2007

[2] M. Łanczont, T. Janowski: Analiza działania nadprzewodnikowych ograniczników prądu, Technologie nadprzewodnikowe i plazmowe w energetyce, *Lubelskie Towarzystwo Naukowe, ISBN: 978-83-61391-76-9*, Lublin 2009

[3] Jha A. R., Superconductor technology – Applications to microwave, electro-optics, electrical machines, and propulsion systems, *A Wiley-Interscience Publications, John Wiley & Sons, INC*, New York 1998

***Autorzy**: dr inż. Michał Łanczont, Politechnika Lubelska, Instytut Podstaw Elektrotechniki i Elektrotechnologii, ul. Nadbystrzycka 38A, 20-618 Lublin, E-mail: m.lanczont@pollub.pl;*

CARBON NANOTUBE FIBRE FOR ELECTRICAL WIRING APPLICATIONS

Agnieszka LEKAWA-RAUS[1], Marek BURDA[1,2], Lukasz KURZEPA[1], Xiaoyu PENG[1], Krzysztof K. KOZIOL[1]

University of Cambridge, UK (1),Silesian University of Technology, Poland (2)

***Abstract**. The need for new technological solutions allowing more efficient and greener utilization of electrical energy motivates the search for new materials with a potential to improve the performance of electrical devices and processes. In this paper, the development of carbon nanotube based electrical wires is presented. The successful application of electrical insulation and electrical contacts to macro-scale fibre made purely of carbon nanotubes is described.*

***Streszczenie.** Zapotrzebowanie na nowe rozwiązania technologiczne pozwalające na bardziej wydajne i bezpieczne dla środowiska użytkowanie energii elektrycznej motywuje do poszukiwania nowych materiałów, które mogłyby poprawić działanie urządzeń i sprawność procesów elektrycznych. Poniżej przedstawiono postępy w zakresie wytwarzania przewodów elektrycznych z nanorurek węglowych. Opisane zostały sposoby izolowania przewodów z nanorurek węglowych oraz wykonywania połączeń elektrycznych.*

Keywords: carbon nanotube fibre, CNT wire, electrical contacts, electrical insulation

Słowa kluczowe: włókno z nanorurek węglowych, przewody elektryczne z nanorurek węglowych, połączenia elektryczne, izolacja elektryczna

Introduction

Increasing awareness of the need for environmental sustainability directs research towards building new devices and finding novel engineering solutions allowing greener production, as well as more efficient and waste-free utilization of energy. Very often the current technology due to being based on old, conventional materials reaches its limits, which cannot be overcome anymore by new concepts and technological adjustments. Therefore the synthesis and applications of new materials become an issue of paramount importance, enabling solutions that contribute to retardation or decrease in degradation of the environment. The report of Ijima published in 1991 has initiated an extensive research on carbon nanotubes (CNTs) [1]. Carbon nanotubes being a rolled up single layer of graphene, i.e. flat hexagonal lattice of carbon atoms, are extremely light-weight material characterized by diverse electrical properties, superior mechanical and thermal properties as well as due to their nanosized symmetry and huge aspect ratios showing many peculiar phenomena like ballistic transport of electrons. Owing to these properties CNTs were recognised as a promising material for many engineering applications including electrical wiring. The merits of such wiring may be the considerable decrease of weight which entails the drop of fuel consumption in aircraft. The possible increase in electrical conductivity can decreases the energy losses and the improvement of mechanical properties will influence the reliability of electrical networks. Room temperature operation can save the additional energy of cooling systems. Carbon nanotubes were already successfully produced from CO_2, which gives hope for decreasing the amount of this problematic gas and use it as a renewable material [2].Finally, very low cost of production and maintenance may be one of the crucial advantages of carbon nanotube based technology. However, there are still many challenges to be overcome before their application into real electrical circuits.

Carbon nanotube fibre

The superior electrical properties of individual CNTs have inspired the development of diverse structured CNT based macro-materials of defined properties and shapes designed for various applications. Several groups have so far succeeded in developing different methods for manufacturing thick fibres with diameters within micron range made purely of CNTs. The fibres used in this work were produced by chemical vapour deposition (CVD) dry direct spinning process developed at the University of Cambridge. In this process the fibre is continuously drawn from carbon nanotube aerogel formed in the hot area of the reactor. Carbon nanotubes are produced from pyrolysis of hydrocarbons, e.g. methane as carbon precursor, metal catalyst and sulphur promoter. The CVD reactor is maintained in inert conditions using hydrogen. As the last step the fibre gets condensed radially during evaporation of acetone sprayed on the material directly after drawing it out from the reactor. Furthermore, it is also stretched using differential two roller winding system, particularly to increase the alignment of the nanotube bundles within the fibre. The schematic drawing of the direct spinning process is presented in Fig. 1.

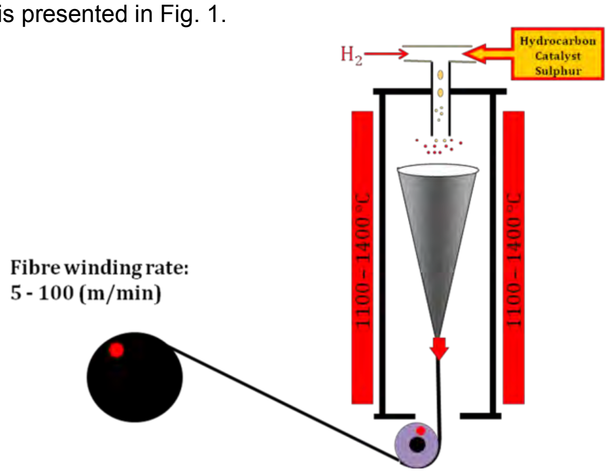

Fig. 1. Spinning of CNT fibre by CVD process developed at the University of Cambridge

Fig. 2 a-c presents the optical and scanning electronmicroscope images of individual CNT fibre.

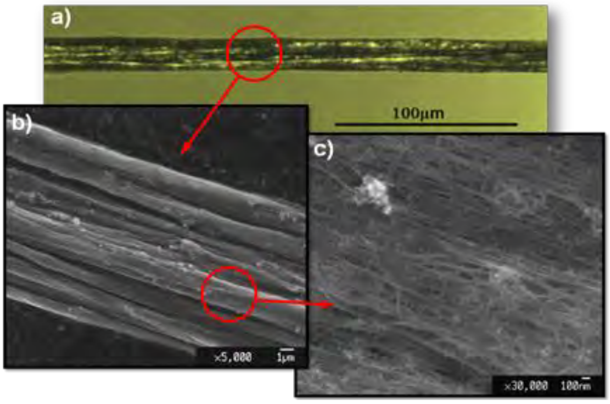

Fig. 2. a) Optical microscope and b), c) Scanning Electron Microscope images of CNT fibre.

Mechanically the fibre is stronger and stiffer than any conventional material used for electrical wiring, including steel. Strength and stiffness are compared as specific values i.e. divided by the material's density [3]. Specific values of electrical conductivity were calculated as conductance of a sample multiplied by its length and divided by linear density given in tex i.e. g/km [4]. Linear density may be experimentally measured gravimetrically or using a vibroscopic method often applied in textile industry for the evaluation of the linear density of yarns which cross-sectional area is difficult to estimate. For comparison the specific conductivity values may be calculated for all conventional materials as conductivity divided by volumetric density. Table 1 shows the comparison of specific conductivity values for different materials.

Table 1 Specific conductivities of conducting materials.

Material	***Specific conductivity ($S*m^{-1}g^{-1}m^{-3}$)***
Copper (electrolytic)	6.52
Aluminium	14.15
Silver	5.89
Steel/Iron	1.31
High performance carbon fibre (M60J) TORAY [3]	0.07
CNT yarn	0.4 - 1.3

The as made CNT fibre is at the moment comparable to steel, which is a very promising result indicating that further optimisation will easily improve its properties reaching the values for copper and beyond.

Turning CNT fibre into CNT wire

For most electrical engineering applications wires require low resistance contact to further conducting paths and where necessary insulation from other live parts of the circuit. Several methods of highly conductive electrical contacts were developed allowing easy joining of full cross-sectional area of a CNT fibre into standard conductors or to another CNT fibre. The continuous insulation of the CNT fibres was also provided including the isolation of individual fibres of up to 20μm in diameters. The choice of the insulating material is crucial to achieve highly flexible and thin layer on the surface of CNT fibre. Fig. 3 shows the scanning electron microscope image of cross-section of single CNT fibre insulated with highly flexible polymer coating.

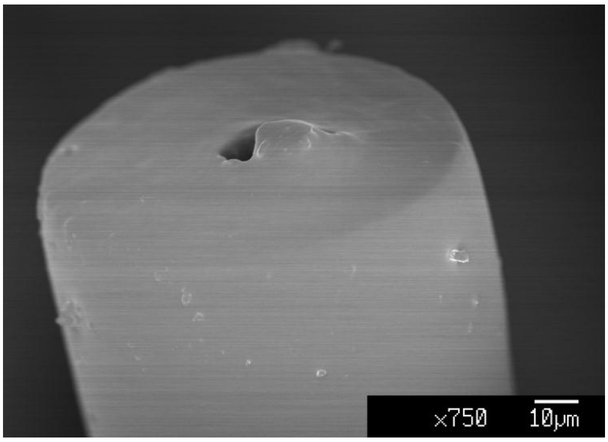

Fig. 3. Scanning electron microscope image of single CNT fibre insulated with highly flexible coating.

Summary

Carbon nanotubes are very promising material for the electrical engineering applications. Using CNTs as a building material for devices has the potential to allow the design of more environmentally friendly devices and processes. The mechanical properties of as made fibre are already better than any conventional wiring metal and electrically are on the level of steel. Electrical performance will be further improved by optimization of the CNT synthesis parameters. As small as 20μm in diameters CNT fibres were successfully electrically insulated and connected with low resistance electrical contacts. The CNT fibres show a potential to be applied as low cost and high performance next generation electrical wiring.

REFERENCES

[1] Iijima S., Helical microtubules of graphitic carbon, *Nature* 354 (1991) 56–58

[2] Simate G. S., Iyuke S. E., Ndlovu S., Yah C. S., Walubita L. F., *J. Nat. Gas Chem.* 19, (2010), 453–460

[3] Koziol K. K., Vilatela J., Moisala A., Motta M., Cunniff Ph., Sennett M., Windle A, High performance carbon nanotube fibre, *Science*, 318 (2007) 1892-1895

[4] Lekawa-Raus A.E., Koziol K.K., Windle A., Dependence of electric al resistance of carbon nanotube proto yarn on force, *Conference proceeding of NT10 11th International Conference on Science and Application of Nanotubes, 2010 Montreal, Canada*.

Authors: *Agnieszka Lekawa-Raus, PhD student of the University of Cambridge, E-mail: ael42@cam.ac.uk; Marek Burda PhD student of Silesian University of Technology E-mail: marek.burda@polsl.pl, Lukasz Kurzepa, research assistant, University of Cambridge, E-mail: lk345@cam.ac.uk, Xiaoyu Peng, PhD student of the University of Cambridge, E-mail: xp213@cam.ac.uk, Dr Eng. Krzysztof K. Koziol Department of Materials Science and Metallurgy, University of Cambridge, Pembroke Street, CB2 3QZ Cambridge, UK, E-mail: kk292@cam.ac.uk.*

Conference ELMECO–7
ELECTROMAGNETIC DEVICES AND PROCESSES IN ENVIRONMENT PROTECTION
joint with 10th Seminar AoS-10 APPLICATIONS OF SUPERCONDUCTORS
28–30.09.2011, Nałęczów, Poland

CONCEPTUAL DESIGN AND ANALYSIS OF A CRYOGENIC SYSTEM FOR A NEW TEST FACILITY FOR HIGH TEMPERATURE SUPERCONDUCTOR CURRENT LEADS (HTS CLs)

Monika LEWANDOWSKA[1], Maurizio BAGNASCO[2]

West Pomeranian University of Technology, Szczecin (1), was EPFL-CRPP, Villigen PSI (2)

***Abstract**. In view of the R&D program on HTS CL at EPFL-CRPP PSI Villigen it is foreseen to extend the capabilities of an existing facility (JORDI) in order to be able to perform tests of HTS CL in different conditions. The present work is focused on the conceptual design of the cryogenics needed for the facility upgrade considering the requirement of an as extended as possible range of operation. Two cooling options for the copper part of a CL are considered. The use of heat exchangers for the optimization of the cryogenic system is discussed and their size is assessed.*

***Streszczenie.** W związku z trwającymi w EPFL-CRPP PSI Villigen pracami B&R nad nadprzewodnikowymi krioprzepustami prądowymi (HTS CLs) przewiduje się uruchomienie tam stanowiska eksperymentalnego do prowadzenia testów HTS CLs w różnych warunkach. W pracy zaprezentowano projekt koncepcyjny układu kriogenicznego dostarczającego chłodziwo do tego stanowiska. Rozważono możliwość dwóch opcji chłodzenia części miedzianej HTS CLs. Przedyskutowano konieczność zastosowania wymienników ciepła w układzie kriogenicznym i oszacowano ich rozmiar.*

Keywords: HTS current leads, thermal-hydraulic analysis, cryogenic system, heat exchanger.
Słowa kluczowe: nadprzewodnikowe krioprzepusty prądowe, analiza cieplno-przepływowa, układ kriogeniczny, wymiennik ciepła.

Introduction

Current leads (CLs) transfer the operating current from a room temperature power supply to a superconducting cable at cryogenic temperature. Conventional CLs are made of metals, whereas advanced high-current CLs consist of a metallic heat exchanger(HEX) part connected with either a low-Tc superconductor or high-Tc superconductor (HTS) material. It has been shown that the use of HTS CLs leads to a reduction of the refrigeration power consumption typically by a factor 3 with respect to the optimally designed conventional metallic CLs [1]. Further improvement of this promising technology would be advantageous. In particular, the development of new cooling concepts for HTS CLs is needed, aimed at shifting the coolant inlet temperature towards higher values and further reduction of the refrigeration power consumption.

Experimental investigations of HTS CLs are foreseen at the EPFL-CRPP (Villigen PSI), which requires the extension of the capabilities of the existing JORDI facility in order to perform tests of HTS CL's in different cooling conditions. The present work is focused on the conceptual design and thermal-hydraulic analysis of the cryogenics needed for the facility upgrade considering the requirement of an as extended as possible range of operation. The designed cryogenic circuit should be capable to provide enough coolant for the most demanding planned test conditions. In our analysis we consider: (i) a variable helium mass flow rate at low temperature (LT) to obtain the required mass flow rate at a particular intermediate temperature (IT) from mixing the existing LT and room temperature (RT) lines, (ii) two cooling options for the HEX part of a CL, (iii) the use and sizing of heat exchangers in the cryogenic circuit.

Basic assumptions and description of the designed cryogenic circuit

The basic assumptions resulting from the limitations of the existing refrigerator and from the functional requirements are as follows:

1. The existing refrigerator is able to provide up to 4 g/s of LT high pressure (HP) helium (at 4.5 K and 10 bar).
2. The maximum current of the HTS CL is planned to be 18 kA, which results in the maximum heat load of about $\dot{Q}_{ce}$ = 5.2 W at the cold end of a HTS CL.
3. During operation the cold end of the HTS CL should be kept at maximum temperature of 5 K.
4. Two cooling options of HEX part of a CL, as specified in Fig. 1, should be possible.
5. The facility should be able to provide up to 2.5 g/s (Option 1) or 6 g/s (Option 2) of IT helium at 50 K to 80 K for cooling the HEX part of a CL.

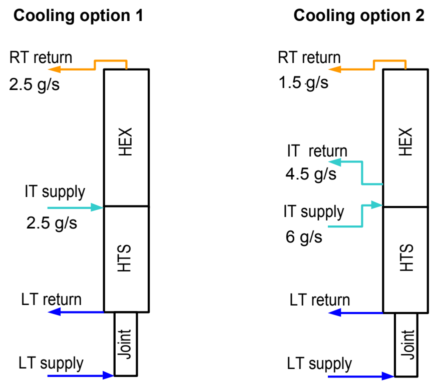

Fig. 1. Cooling options for HTS CL

The basic elements of the cooling system concept are presented schematically in Fig. 2. The vacuum-insulated transfer lines carry the LT HP helium from the remote refrigerator coldbox (point 0) to the test vacuum vessel. We propose to use a bath heat exchanger HX1 to pre-cool helium warmed-up in the transfer line prior to flowing to the cold end of a HTS CL. At the exit of the cold end of a HTS CL (point 3) helium is divided into two parts. One flow is expanded through the Joule-Thomson valve CV15 to provide the liquid helium to the bath in HX1. The LT low pressure helium gas leaving HX1 is fed back to the refrigerator. The second part is mixed with the warm helium at point M, through a mixing chamber to equalize pressures

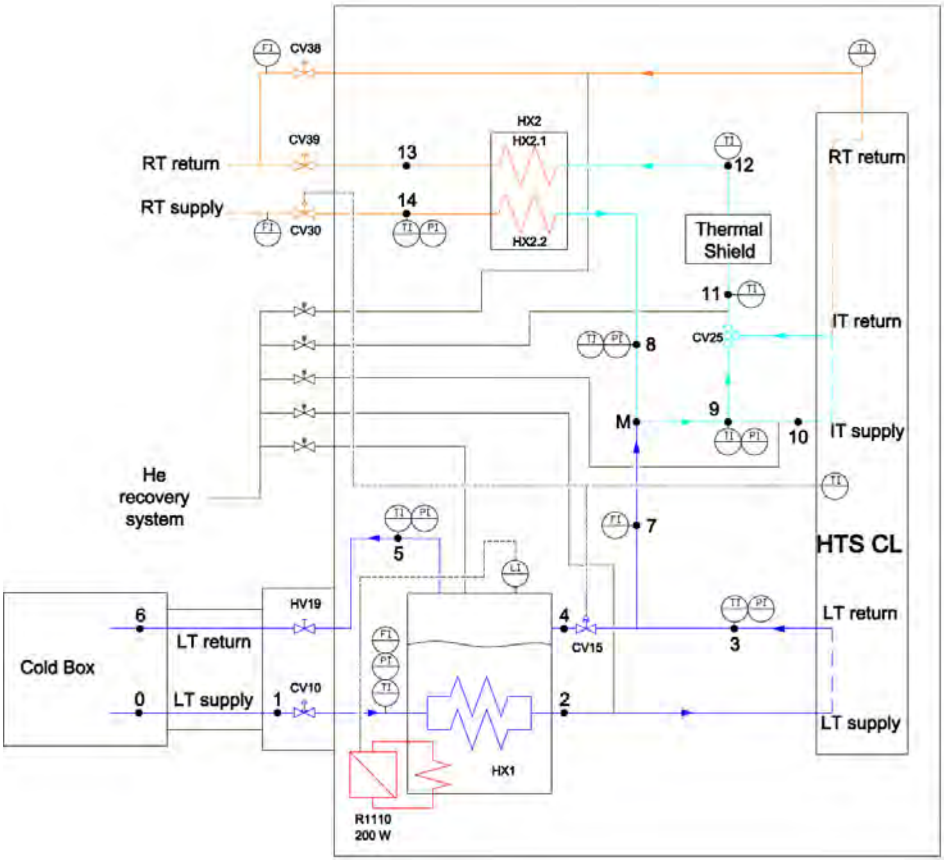

Fig. 2. Scheme of the cryogenic circuit for the HTS CL test facility

of the two branches of the circuit, to provide the IT helium for cooling the HEX part of a CL and the thermal shield. It results from the preliminary analysis that it is impossible to obtain the maximum mass flow rate of the IT helium required in the cooling option 2 by mixing the available LT helium with the RT helium, thus the use of a recuperator HX2 to pre-cool the RT helium is indispensable. The appropriate cooling option is chosen using the tri-flow on-off valve CV25. The RT helium exiting the warm end of the cooper part of a CL is sent directly to the compressor. The IT helium (at point 11) is used to cool the thermal shield and afterwards to pre-cool the room temperature helium stream in the heat exchanger HX2, prior to flowing to the compressor.

Thermal – hydraulic analysis of the cryogenic circuit

The analysis is performed for the total mass flow rate of the LT HP helium $\dot{m}_0$ = 3 to 4 g/s and for the most demanding functional requirements, i.e. assuming the maximum expected heat loads in the circuit as well as the minimum temperature (50 K) and the maximum mass flow rate of the IT helium supply to the HEX part of CL (at point 8), i.e. $\dot{m}_8$ =2.5 g/s and 6 g/s for the cooling option 1 and 2 , respectively. At each point of the cryogenic circuit, the helium mass flow rate as well as the state parameters p and T are determined using the mass and energy balance equations and the correlations mentioned below.

The convective heat transfer coefficient between the bulk of helium flowing in a pipe and the pipe surface is calculated using the standard Dittus-Boelter correlation for a forced turbulent flow [2]. For the heat transfer between the helium in the bath and the pipe surface we use the Churchill-Chu correlation for the free convection from a horizontal isothermal cylinder [3]. To assess the friction factor for flows in pipes we use the standard Blasius smooth tube correlation [2]. For the flow in the outer pipe in the heat exchanger HX2 we use the correlation for a turbulent flow in a concentric annular duct [2].

We assume that the heat exchanger HX1 consist of a spiral copper pipe immerged in a helium bath at temperature T_4 =4.27 K. Two possible options for HX1 are analyzed: (i) a single pipe and (ii) two pipes connected in parallel. The length of HX1 is assessed assuming that the helium temperature at its outlet (point 2) should not exceed 4.5 K. Two possible simple realizations of the counterflow recuperator HX2 are studied (i) a single pipe-in-tube and (ii) two pipe-in-tubes connected in parallel. The length of HX2 is assessed for various pipes diameters.

It results from our analysis that the proposed cryogenic circuit is capable to provide sufficient amount of coolant needed to perform tests of HTS CL's in the most demanding planned conditions.

REFERENCES

[1] Heller R., *et al*, Experimental Results of a 70 kA High Temperature Superconductor Current Lead Demonstrator for the ITER Magnet System, *IEEE Trans. Appl. Supercon.*, 15 (2005), 1496-1499
[2] Shah R.K., Sekulić D.P., *Fundamentals of Heat Exchanger Design*, Wiley, New Jersey (2003)
[3] Churchill S.W., Chu H.H.S., Correlating Equations for Laminar and Turbulent Free Convection from a Horizontal Cylinder, *Int. J. Heat Mass Transfer* 18 (1975), 1949-1053

***Authors**: Dr Monika Lewandowska, Institute of Physics, Faculty of Mechanical Engineering and Mechatronics, West Pomeranian University of Technology, Szczecin, Al. Piastów 48, 70-311 Szczecin, Poland, E-mail: monika.lewandowska@zut.edu.pl; Dr Maurizio Bagnasco, was EPFL/CRPP, Fusion Technology - Superconductivity Division, CH-5232 Villigen-PSI, Switzerland, E-mail: maurizio.bagnasco@gmail.com*

METHODS FOR MEASURING OZONE CONCENTRATION IN OZONE-TREATED WATER

Jacek MAJEWSKI[1]

Technical University of Lublin (1)

***Abstract**. The ozone measurements are gaining in importance as the area of environmental ozone applications to liquids and especially to water grows. Some four lub or five methods can be enumerated, and each of them has only limited area of applications. The comparison of the methods shows, that there still is a need for rugged, reliable, ozone-specific, direct measurement methods and sensors for measuring ozone concentration in ozonated water.*

***Streszczenie.** Przyrządy i metody do pomiaru stężenia ozonu w cieczach, a zwłaszcza w wodzie, nabierają coraz większego znaczenia w miarę rozszerzania się obszarów zastosowan ozonu w ochronie środowiska. Spośród czterech lub pięciu współcześnie stosowanych metod, każda wykazuje tylko ograniczony obszar przydatności. Niezbędne jest opracowanie nowych, selektywnych, wiarygodnych, bezpośrednich metod pomiaru.*

Keywords: water ozonation, dissolved ozone concentration measurement, water disinfection systems.
Słowa kluczowe: ozonacja wody, pomiary stężeń rozpuszczonego ozonu, układy do dezyfekcji wody.

Introduction

The global increase in pollution of surface fresh water as well as seawater is mainly caused by human industrial activity. This problem is even more urgent in highly populated areas of developed countries, since the environment becomes ecologically damaged – and this degradation is a factor enhancing e.g. the risk of water-spread epidemies [1]. On the other hand, consumers require from the manufacturers better quality of water and food for realizing healthy lifestyle. For these reasons, an intensive search for fast and efficient methods of water purification without residual taste, odour or toxic by-products is continued. The method of water ozonation seems to satisfy these requirements to highly promising degree.

Although ozone was discovered in 1839 (by C. F. Schonbein) and used for tap water treatment in Nice (1907) and St. Petersburg (1910) [3], the water ozonation process is still widely investigated; especially after 1982, when the US Food and Drug Administration (FDA) recognized safe status for ozone usage in bottled water, and later for liquid food and beverages processing (since 1997). The designing of optimal water ozonation system is a complex task because of unique features of gaseous ozone technology as chemical agent. Firstly, the ozone generators can operate only on either air (the output is 1-3% ozone) or pure oxygen (the output is ca. 6 % ozone) – if the corona-discharge or other high voltage-based generator is used (the main idea is similar to the natural generation of ozone by lighting during thunderstorms) [2]. The UV or VUV generators give not sufficient output (0.5% ozone or less).

Secondly, ozone is highly unstable gas and cannot be stored. The life time of a single ozone molecule in pure air is estimated as ca. 15 minutes and in distilled water ca. 20 minutes. This facilitates the problem of excess ozone utilization, but forces the installation of the ozone generator as integral part of the ozonation plant [4-5].

Thirdly, the solubility of ozone in water is rather low – it is approximately 10 times lower than solubility of chlorine (for this reason, chlorine is still used; although the ozone killing power of microorganisms is 400 times stronger than chlorine). Therefore, special chamber, called bubble columns (or contact tanks, or contactors) are necessary to allow diffusing the ozone gas into bulk water. The ozone (mixed with the air or oxygen from the generator) is injected into the water in fine gas bubbles, and the mass transfer occurs. The efficiency of this process is dependent on the water temperature and pH, but also on the injected gas pressure: higher pressures increase the solubility, according to Henry's law. Higher temperatures mean decrease in ozone solubility, but increase in reaction rates. Since the bubbles contain a few percents of ozone, and the solubility is low, the mass transfer and, in consequence, the reaction rates are moderate, even for such powerful oxidant as ozone (only fluoride exhibits higher oxidation potential than ozone) [6].

When the ozone is dissolved in water, there is a need of measuring the ozone concentration at the inlet. The required concentration level of the applied ozone depends on the kind of microorganisms or inorganic pollutants to be destroyed, and on the required reduction ratio (expressed in logarithmic scale). This level also depends on the designed treatment time; the disinfection standards take into account both factors (e.g. exposure to 4 ppm ozone concentration for 4 minutes is required) [7]. In practice, the applied ozone exhibits concentrations from 0.2 ppm to 10 ppm; only some processes in wafer technology require ultra-pure water treated with 30 ppm ozone.

The last question is the monitoring of the outflow water. Gaseous ozone over 20 % is explosive – but this never happens in industrial conditions. More dangerous are levels under 1 ppm: the long-term exposure of the personnel to 0.2 ppm is harmful for lungs and respiratory tract. Ca. 0.1 ppm ozone is present in the ambient air; in urban areas during the summer its concentration can reach ca. 0.2 ppm. For workspace, the US Occupational Safety and Health Administration (OSHA) limits the allowable ozone concentration to 0.1 ppm. For these reasons, the residual dissolved ozone in the exit water should be checked and maintained at 5-50 ppb; if necessary, it should be decomposed using UV radiation of ca. 250 nm wavelengths [8,9].

Methods for measuring dissolved ozone in water

The measurement methods can be categorized into direct or indirect, on-line or off-line, and ozone-specific or non-specific. The methods for measuring dissolved ozone level emerged from the methods aimed at gas concentration measurement (gaseous ozone and oxygen).

Chronologically, the first sensors for measuring aqueous ozone, the “redox” (or ORP) sensors emerged. Because of narrow measurement range (0-1ppm) and lack of selectivity to ozone, are used in places like swimming pools, where the overall oxidizing capacity of the water is important. The ORP sensors are inexpensive, and do not need temperature compensation. However, they must be calibrated *in situ*, to take into account the chemistry of local water. Nowadays, their use is limited to noncritical installations, rather as detectors.

The modern counterpart of ROP sensors are the electrochemical sensors, which are built in two versions: the “bare-metal electrodes” sensors, and the membrane sensors. in the case of the “bare-metal electrodes” sensors, the water flows through the galvanic cell and serves as electrolyte. The oxidant present in the water is reduced at the cathode, and the generated current is proportional to the oxidant concentration. The range is 0-2 ppm, but the accuracy is about 1 ppb, and the response time even ca. 5 sec. The design is rugged and reliable but as non-specific to ozone, requires assuring that the concentrations of oxidants other than ozone are negligible.

The membrane sensors are more selective to ozone, since the membrane allows diffusing through for mainly the ozone. Ozone reacts with the electrolyte solution to form an compound reduced by a polarizing voltage. The range is wide (0-200 ppm) and the accuracy is 1% of measured value. Response times are reported above 60 sec.; but tese sensors need frequent calibration against a reference method (UV or “indigo”).

There is a type of sensor based on removing the ozone from the water before measurement (so called “stripping”). The stripped ozone in air headspace can be measured using the UV method. However, this method is not reliable without calibration against the “indigo” method.

The indigo method was developed between 1979 and 1982 in Switzerland [10]. The blue indigo trisulfonate is bleached by the ozone taken into a glass ampul, which is compared with a blank sample spectrophotometrically in a digital colorimeter at the wavelength of 600 nm. The concentration of ozone is calculated from the difference in light absorption. The range is 0-1.5 ppm, and the accuracy is 1.5 %. This method is the most sensitive, selective, fast and accurate, but need skilful technicians and is expensive. As off-line method, the “indigo” method is used for calibrating the on-line sensors.

Throughout 1980’s the UV absorption method became popular, because of its selectivity to ozone, high accuracy (3%) and wide range (0-100 ppm). Higher concentrations are measured directly in water, whereas lower need the preliminary stripping the ozone from the water. The applied UV light has the wavelength from 253.7 to 260 nm. As other organic compounds can absorb the UV light as well as the ozone, the method is recommended for deionised, high-purity water. In laboratory conditions, this method is applied to calibrate on-line sensors, because of extremely linearity of the relationship between the ozone concentration and the absorbance.

Conclusions

For minimizing energy consumption, the ozone concentration should be tailored for a given application, and kept low; however, in applications where the short treatment time or very high water purity is essential, the concentrations can be increased considerably. Therefore, a wide spectrum of measurement ranges should be available, and the measuring device should be precisely chosen for each case. The off-line methods are more accurate, but time-consuming and useless for e.g. emergency shutdown circuits. The ozone non-specific methods can be applied if other oxidising agents (like chlorine) are filtered before the water reaches the ozone injection point. Because of the required safety and reliability level, the ozone measuring devices based on direct measurement methods of dissolved ozone (in water) should be developed; that implies improved sensor designs, rugged and easy in maintenance.

REFERENCES

[1] Izdebski T., Dors M., Mizeraczyk J., River Water Remediation Using Electrohydraulic Discharges or Ozonation, *IEEE Transactions on Plasma Science,* Vol. 39, No. 3, March 2011, 953-959

[2] Kuraica M. M. et al., Ozonized water generator based on coaxial dielectric-barrier-discharge in air, *Vacuum*, 73 (2004), 705-708

[3] Guzel-Seydim Z. B., Greene A. K., Seydim A. C., Use of ozone in the food industry, *Lebensmittel Wissenschaft und Technologie,* 37(2004), 453-460

[4] Cullen P. J. et al., Modelling approaches to ozone processing of liquid foods, *Trends in Food Science and Technology*, 20 (2009), 125-136

[5] Loboda O. A., Goncharuk V. V., Theoretical Research into Interaction of Water Clusters with Ozone, *Journal of Water Chemistry and Technology,* Vol. 31, No. 4, (2009), 213-219

[6] Tizaoui C. et al., A comparison of novel ozone-based systems and photocatalysis for the removal of water, *Desalination*, 227 (2008), 57-71

[7] Baba S., Satoh S., Yamabe C., Development of measurement equipment of half life of ozone, *Vacuum*, 65 (2002), 489-495

[8] Yershov B. G. et al., Kinetic Regularities of Ozone Decomposition in Water, *Journal of Water Chemistry and Technology,* Vol. 31, No. 6, (2009), 381-388

[9] Farines V. et al., Ozone transfer from gas to water in a co-current upflow packed bed reactor containing silica gel, *Chemical Engineering Journal*, 91 (2003), 67-73

[10] Bader H., Hoigné J., Determination of Ozone in Water by the Indigo Method: A Submitted Standard Method, *Ozone: Science and Engineering,* 4 (1982), 169-175

Author*: dr inż. Jacek Majewski, Politechnika Lubelska, Wydział Elektrotechniki i Informatyki, ul. Nadbystrzycka 38a, 20-618 Lublin, E-mail: j.majewski@pollub.pl;.*

Conference ELMECO–7
ELECTROMAGNETIC DEVICES AND PROCESSES IN ENVIRONMENT PROTECTION
joint with 10th Seminar AoS-10 APPLICATIONS OF SUPERCONDUCTORS
28–30.09.2011, Nałęczów, Poland

BADANIA EKSPERYMENTALNE I ANALIZA SKUTECZNOŚCI DZIAŁANIA BERDZENIOWEGO INDUKCYJNEGO NADPRZEWODNIKOWEGO OGRANICZNIKA PRĄDU

Michał MAJKA[1], Janusz KOZAK[1], Tadeusz JANOWSKI[2], Sławomir KOZAK[1]

Instytut Elektrotechniki (1), Politechnika Lubelska (2)

Streszczenie. *Nadprzewodnikowe ograniczniki prądu (SFCL) są przeznaczone do ochrony sieci elektroenergetycznej od zwarć wynikających z wyładowań atmosferycznych, zerwanych linii energetycznych i innych zakłóceń. Kilka konstrukcji bezrdzeniowych indukcyjnych ograniczników prądu opierających się na taśmie HTS drugiej generacji zostało przetestowane, opisane i porównane.*

Abstract. *Superconducting fault current limiters (SFCL) are designed to protect the electrical grid from faults that result from lightning strikes, downed power lines and other system disturbances. Several coreless constructions of inductive SFCLs based on HTS 2G tapes have been tested described and compared.*

Słowa kluczowe: nadprzewodnikowy indukcyjny ogranicznik prądu, taśma nadprzewodnikowa, nadprzewodnik wysokotemperaturowy.
Keywords: superconducting inductive fault current limiter, superconducting tape, high-temperature superconductor.

Wstęp

Indukcyjny ogranicznik prądu składa się z uzwojenia pierwotnego i magnetycznie sprzężonego z nim uzwojenia wtórnego, oraz z najczęściej występującego rdzenia magnetycznego. Uzwojenie pierwotne, wykonane jest zazwyczaj z miedzi i włączone jest bezpośrednio od obwodu chronionego. Uzwojenie wtórne ogranicznika wykonane jest z nadprzewodnika wysokotemperaturowego i stanowi zwój zwarty (lub zwarte zwoje). Ze względu na konieczność zapewnienia elementom nadprzewodnikowym temperatury pracy niższej od temperatury krytycznej uzwojenie nadprzewodnikowe umieszczane jest w kriostacie azotowym wypełnionym ciekłym azotem [1]. W ogranicznikach indukcyjnych można stosować rdzeń magnetyczny zamknięty, jednak zastosowanie takiego rdzenia w ograniczniku o dużej mocy wiąże się z dużymi gabarytami i masą rdzenia magnetycznego. Budowane są również ograniczniki z rdzeniem otwartym o parametrach zbliżonych do ograniczników z rdzeniem zamkniętym, ale o mniejszej masie. Najmniejszą i najlżejszą konstrukcją ogranicznika typu indukcyjnego jest wykonana i przebadana konstrukcja bezrdzeniowa w której całkowicie wyeliminowano rdzeń magnetyczny [2].

Badania eksperymentalne i analiza skuteczności działania bezrdzeniowego indukcyjnego nadprzewodnikowego ogranicznika prądu

Wykonany bezrdzeniowy indukcyjny ogranicznik prądu składa się z czterech uzwojeń nawiniętych na karkasie z ERTALONU (rys. 1). Ogranicznik składa się z jednego uzwojenia miedzianego nawiniętego izolowanym drutem miedzianym o przekroju 4 mm x 2 mm oraz trzech izolowanych folią poliimidową uzwojeń nadprzewodnikowych wykonanych z taśmy SF12050 firmy SuperPower. Parametry poszczególnych uzwojeń ogranicznika zamieszczono w tablicy 1. W prezentowanej konstrukcji bezrdzeniowej ogranicznika wszystkie uzwojenia chłodzone są w kąpieli ciekłego azotu. Zastosowanie chłodzenia uzwojenia miedzianego pozwala na znaczne zmniejszenie masy całego urządzenia, ponieważ do wykonania uzwojenia miedzianego możliwe jest użycie przewodu o mniejszym przekroju poprzecznym od wymaganego w temperaturze pokojowej.

Tablica 1. Parametry uzwojeń bezrdzeniowego indukcyjnego ogranicznika prądu wykonanego z taśmy SuperPower SF12050

Zaciski uzwojeń	**1-2**	**3-4**	**5-6**	**7-8**
materiał	Cu	SF12050	SF12050	SF12050
średnica wewnętrzna	120,0 mm	129,0 mm	131,0 mm	132,4 mm
średnica zewnętrzna	128,8 mm	130,8 mm	132,2 mm	133,0 mm
wysokość	130 mm	130 mm	130 mm	130 mm
liczba zwojów	60	60	40	20
I_c	-	270 A	270 A	270 A
R (297 K)	53,4 mΩ	13,39 Ω	9,04 Ω	4,53 Ω
R (77 K)	6,55 mΩ	12,7 μΩ	11,9 μΩ	10,4 μΩ

Rys. 1. Nadprzewodnikowy ogranicznik prądu z uzwojeniami wykonanymi z taśmy drugiej generacji SuperPower SF12050

Zamieszczone w tablicy 1 wartości rezystancji uzwojeń ogranicznika uwzględniają rezystancję miedzianych doprowadzeń prądowych oraz zastosowanych połączeń śrubowych. Uzwojenia ogranicznika podczas badań eksperymentalnych były łączone w różnych konfiguracjach izolowanymi przewodami miedzianymi o przekroju 16 mm^2. Rezystancja miedzianych przewodów połączeniowych przyjmowała wartości od 12 μΩ do 34 μΩ w temperaturze 77 K w zależności od długości użytego przewodu. Na rysunku 2 przedstawiono schematy badanych ograniczników bezrdzeniowych dla których przeprowadzono badania eksperymentalne.

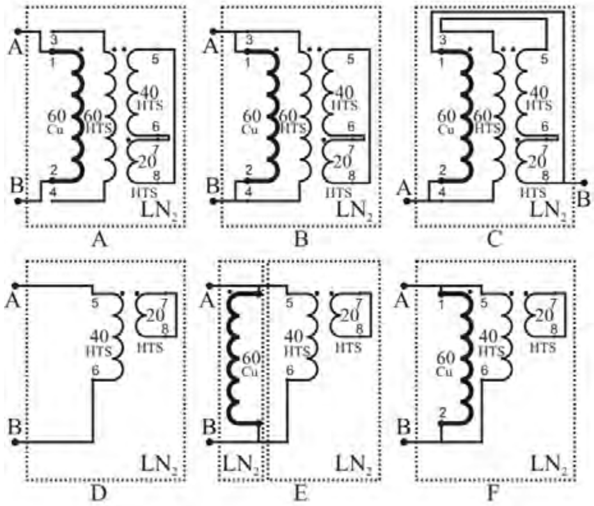

Rys. 2. Schematy badanych ograniczników wykonanych z taśmy drugiej generacji SuperPower SF12050

Ogranicznik o schemacie (A) ma konwencjonalne pierwotne uzwojenie miedziane o 60 zwojach oraz zwarte uzwojenie wtórne HTS o łącznie 60 zwojach. Schemat (B) przedstawia ogranicznik z pierwotnym uzwojeniem miedzianym o 60 zwojach połączonym równolegle z uzwojeniem nadprzewodnikowym w celu poprawy sprzężenia magnetycznego pomiędzy uzwojeniami i zmniejszenia gęstości prądu w uzwojeniu pierwotnym. Konstrukcja bifilarna ogranicznika (schemat C) została przetestowana pod kątem właściwości i skuteczności ograniczania prądu zwarciowego i porównana z ogranicznikami (A) i (B). Ogranicznik o schemacie (D) ma zarówno pierwotne jak i wtórne uzwojenie nadprzewodnikowe wykonane z taśmy HTS 2G. Właściwości ogranicznika (D) zostały porównane z ogranicznikiem (F), w którym uzwojenie pierwotne składa się z dwóch cewek miedzianej i nadprzewodnikowej połączonych równolegle. W ograniczniku o schemacie (F), uzwojenia pierwotne i wtórne były nawinięte współśrodkowo na wspólnym karkasie i sprzężone magnetycznie między sobą. Ogranicznik (F) został porównany z ogranicznikiem (E), w którym cewka miedziana uzwojenia pierwotnego był identyczna jak cewka uzwojenia pierwotnego ogranicznika (F), ale nie była sprzężona magnetycznie z uzwojeniami nadprzewodnikowymi. Wartość prądu znamionowego ograniczników (A), (B) i (C) wynosiła 131,7 A, ograniczników (D), (E) i (F) - 65,8 A.

Z porównania prądu zwarciowego szczytowego odniesionego do amplitudy prądu znamionowego (rys. 3) wynika że wszystkie badane konstrukcje ograniczników z uzwojeniami HTS 2G skutecznie ograniczają prąd zwarciowy szczytowy. Dla badanych konstrukcji ograniczników prąd zwarciowy szczytowy jest jedynie od 2,5 dla ogranicznika (B) do 5,5 dla ogranicznika (E) razy większy od amplitudy prądu znamionowego.

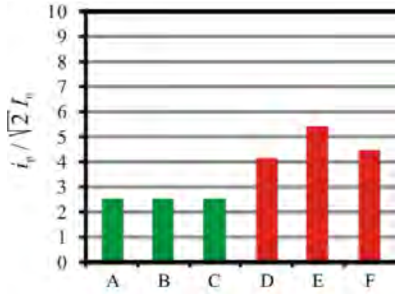

Rys. 3. Prąd zwarciowy szczytowy odniesiony do amplitudy prądu znamionowego dla badanych konfiguracji ograniczników

W stanie wyczekiwania spadek napięcia na ograniczniku spowodowany jest głównie reaktancją rozproszenia i rezystancją uzwojenia pierwotnego. Napięcie na ograniczniku w stanie wyczekiwania powinno być możliwe małe. Największy spadek napięcia spośród badanych konstrukcji ograniczników (rys. 4) wystąpił na ograniczniku (A) w którym uzwojeniem pierwotnym było uzwojenie miedziane o znacznej rezystancji. W tym przypadku napięcie na ograniczniku w stanie wyczekiwania dla prądu znamionowego przekracza 5% napięcia zasilającego U_s = 40 V. Najmniejsze napięcie spośród badanych konstrukcji wystąpiło na ogranicznikach (D), (E) i (F) w których uzwojenie pierwotne wykonano z taśmy HTS.

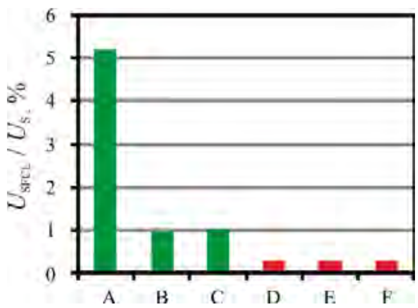

Rys. 4. Napięcie na ograniczniku w stanie wyczekiwania przy prądzie znamionowym jako procent napięcia zasilania

Podsumowanie

Analiza przebadanych rozwiązań bezrdzeniowych nadprzewodnikowych ograniczników prądu typu indukcyjnego pozwala stwierdzić, że ograniczniki z uzwojeniami nadprzewodnikowymi wykonanymi z taśmy HTS 2G skutecznie ograniczają prąd zwarciowy szczytowy. Konstrukcja bezrdzeniowa jest lekka, a chłodzenie miedzianego uzwojenia pierwotnego pozwala na zmniejszenie jego masy ponad 7 krotnie. Zastosowanie równoległego połączenia cewki miedzianej i cewki HTS jako uzwojenia pierwotnego zabezpiecza obwód zwarciowy przez otwarciem w przypadku uszkodzenia taśmy HTS.

LITERATURA

[1] Janowski T. i inni, Nadprzewodnikowe ograniczniki prądu, *Drukarnia Liber*, Lublin, (2002)
[2] Kozak J., Majka M., Janowski T., Kozak S., Wojtasiewicz G., Kondratowicz-Kucewicz B., Test and performance analysis of coreless inductive HTS fault current limiter, *IEEE Trans. Appl. Supercon.*, 21, (2011), 1303-1306

***Autorzy**: dr inż. Michał Majka, Instytut Elektrotechniki, Pracownia Technologii Nadprzewodnikowych, ul. Nadbystrzycka 38a, 20-618 Lublin, E-mail: m.majka@iel.waw.pl; dr inż. Janusz Kozak, Instytut Elektrotechniki, ul. Nadbystrzycka 38a, 20-618 Lublin, E-mail: j.kozak@soul-kozak.com; dr hab. inż. Sławomir Kozak, Instytut Elektrotechniki, ul. Nadbystrzycka 38a, 20-618 Lublin, E-mail: s.kozak@iel.waw.pl, prof. dr hab. inż. Tadeusz Janowski, Politechnika Lubelska, ul. Nadbystrzycka 38a, 20-618 Lublin, E-mail: t.janowski@pollub.pl.*

Conference ELMECO–7
ELECTROMAGNETIC DEVICES AND PROCESSES IN ENVIRONMENT PROTECTION
joint with 10th Seminar AoS-10 APPLICATIONS OF SUPERCONDUCTORS
28–30.09.2011, Nałęczów, Poland

MÖSSBAUER STUDIES OF $Bi_5Ti_3FeO_{15}$ ELECTROCERAMIC PREPARED BY MECHANICAL ACTIVATION

Mariusz MAZUREK[1], Elżbieta JARTYCH[1], Dariusz OLESZAK[2]

Lublin University of Technology (1), Warsaw University of Technology (2)

***Abstract**. The present work involves the structure analysis and the determination of hyperfine interactions parameters of multiferroic $Bi_5Ti_3FeO_{15}$ electroceramic, prepared by high-energy ball milling of polycrystalline precursors (mixture of the Bi_2O_3, TiO_2 and Fe_2O_3 simple oxides). This analysis was performed by X-ray diffraction and Mössbauer spectroscopy.*

***Streszczenie.** W pracy przedstawiono wyniki badań dla multiferroicznej elektroceramiki $Bi_5Ti_3FeO_{15}$ otrzymanej podczas procesu aktywacji mechanicznej (mielenie wysokoenergetyczne polikrystalicznych proszków Bi_2O_3, TiO_2 i Fe_2O_3). Badania struktury i oddziaływań nadsubtelnych przeprowadzono metodami dyfrakcji promieniowania X oraz spektroskopii efektu Mössbauera.*

Keywords: Aurivillius compounds, mechanical activation, hyperfine interactions, Mössbauer spectroscopy.
Słowa kluczowe: związki Aurivilliusa, aktywacja mechaniczna, oddziaływania nadsubtelne, spektroskopia mössbauerowska.

Introduction

Materials on the basis of bismuth ferrite $BiFeO_3$ are of substantial interest because of applications in magnetoelectric devices, i.e. as different types of memory elements of new generation [1]. Magnetoelectric effect has been predicted by P. Curie in 1894 on the basis of symmetry conditions. This effect concerns materials which can be polarized electrically by placing them in a magnetic field and magnetically by placing them in an electric field [2]. Bismuth iron titanate $Bi_5Ti_3FeO_{15}$ is an example of ferroelectromagnetic material, otherwise known as multifferroic, in which both ferroelectric and antiferromagnetic ordering exists simultaneously. Electroceramic $Bi_5Ti_3FeO_{15}$ is Aurivillius phase composed of four perovskite-like layers per slab interleaved with Bi_2O_2 layers; three oxygen-octahedra have Ti ion at the centre and one octahedron has Fe ion [3, 4].

The standard method for preparation of ceramics is a solid-state sintering. However, equally promising technology is a mechanical activation (MA). It is a high-energy ball milling process in which elemental precursors are repeatedly fragmented, flattened, welded and fractured. Such a preparation method may be used in an industrial scale.

The aim of this work was to investigate the hyperfine interactions in multiferroic Aurivillius phase $Bi_5Ti_3FeO_{15}$ prepared by MA. The investigations of the structure and magnetic properties of the samples were performed by using X-ray diffraction (XRD) and Mössbauer spectroscopy (MS).

Experimental details

$Bi_5Ti_3FeO_{15}$ ceramic powder was prepared by the high-energy ball milling in a Fritsch Pulverisette P5 planetary ball mill, using hardened steel medium (vial and balls). XRD measurements were carried out using a Philips PW 1830 diffractometer working in a continuous scanning mode with CuK_α radiation. The ball-to-powder weight ratio was 10:1. The total weight of the powders was 10 g. For selected times the milling process was interrupted and a small amount of the milled powders was taken out for further examinations.

Thermal treatment of the mechanically activated $Bi_5Ti_3FeO_{15}$ compound was performed in two ways: (1) heating from the room temperature up to 993 K in a calorimeter (Perkin Elmer DSC 7) under an argon atmosphere with the rate of 20 K per min and (2) isothermal annealing in a furnace at 973 K for 1 h in vacuum.

Mössbauer spectroscopy studies were carried out on POLON spectrometer in the transmission geometry at room temperature. The source ^{57}Co in a Cr matrix with an activity of about 10 mCi was used. Hyperfine interactions parameters of the investigated material were related to the α-Fe standard.

Results and discussion

Fig. 1 shows the XRD patterns of the powders mechanically activated for various milling times.

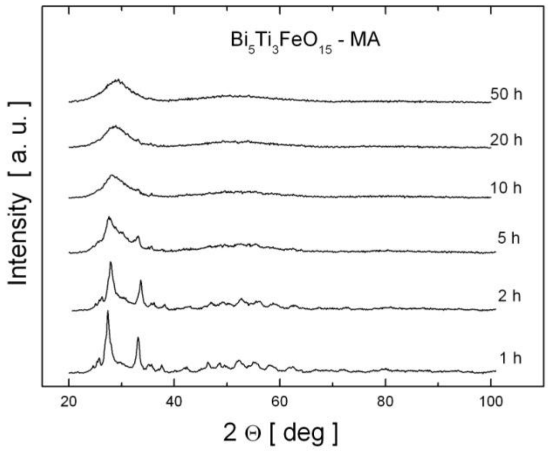

Fig.1. X-ray diffraction patterns of the oxides mixture milled for different times.

It may be seen that during milling the crystalline phases systematically transform into nanocrystalline and/or amorphous state. Only after thermal treatment the desired $Bi_5Ti_3FeO_{15}$ compound was formed what is proved by XRD patterns presented in Fig. 2 (the angular positions of diffraction peaks are marked according to database [5]). The crystallite sizes were analyzed using the Debye-Scherrer method. It was found that the average crystallite sizes of $Bi_5Ti_3FeO_{15}$ compound heated up to 993 K are about 30 nm while those of compound annealed at 973 K are 40 nm.

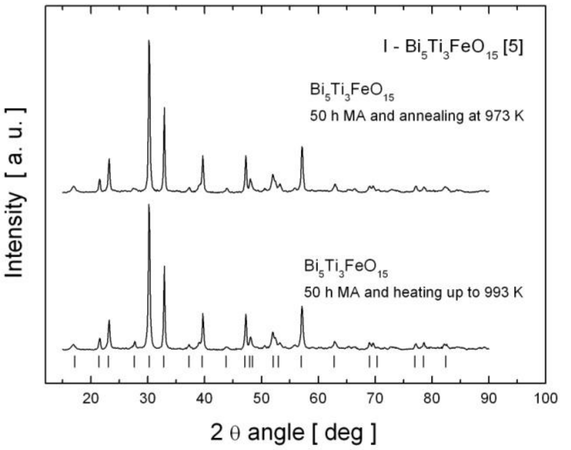

Fig.2. XRD patterns of $Bi_5Ti_3FeO_{15}$ compound after mechanical activation and heating up to 993 K and annealing at 973 K.

Mössbauer spectra of the oxides mixture after various milling times are presented in Fig. 3. It may be seen that spectra for 2 and 10 h consist of the six lines while in the spectrum for 50 h paramagnetic doublet in the centre may be observed besides the sextet. The numerical fitting of the spectra allowed determining the hyperfine interactions parameters which are listed in Table 1. The six-line component originates from the hematite and the paramagnetic doublet is attributed to the $Bi_5Ti_3FeO_{15}$ electroceramic.

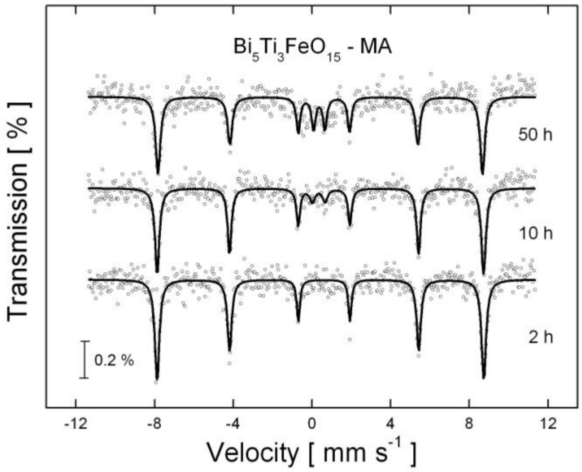

Fig.3. Room-temperature Mössbauer spectra of mechanically activated $Bi_5Ti_3FeO_{15}$ electroceramic after various milling times.

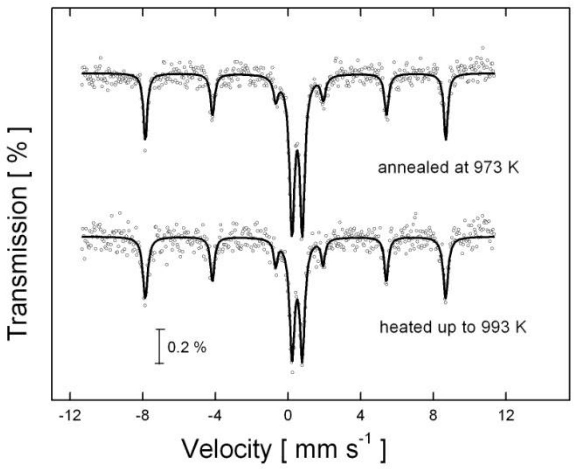

Fig.4. Room-temperature Mössbauer spectra of $Bi_5Ti_3FeO_{15}$ mechanically activated and annealed at 973 K and heated up to 993 K.

Fig.4 presents MS spectra for $Bi_5Ti_3FeO_{15}$ mechanically activated and thermally treated. It may be noted that besides the paramagnetic doublet sextet from the hematite still exists in the spectra. It means that not a whole amount of hematite reacted during thermal processing. On the other hand it is known that bismuth evaporates from the mixture during technological process. However, in spite of small preparation deficiency, it may be stated that mechanical activation allowed obtaining the desired $Bi_5Ti_3FeO_{15}$ electroceramic. The determined hyperfine interactions parameters for mechanically activated $Bi_5Ti_3FeO_{15}$ compound agree well with the data for conventionally sintered ceramic [6].

Table 1. Hyperfine interactions parameters of $Bi_5Ti_3FeO_{15}$ after MA and after thermal treatment; IS – isomer shift relative to α-iron, QS – quadrupole splitting of the doublet (D), Δ – quadrupole shift of the sextet (S), B_{hf} – hyperfine magnetic field.

	IS [mm/s]	QS [mm/s]	Δ [mm/s]	B_{hf} [T]	Remarks
50 h MA	0.23(2) 0.37(1)	0.29(2) –	– 0.10(1)	– 51.34(47)	D – $Bi_5Ti_3FeO_{15}$ S – hematite
Annealed at 973 K	0.36(1) 0.37(1)	0.28(1) –	– 0.11(1)	– 51.50(39)	D – $Bi_5Ti_3FeO_{15}$ S – hematite
Heated up to 993 K	0.36(1) 0.37(1)	0.28(1) –	– 0.11(1)	– 51.46(51)	D – $Bi_5Ti_3FeO_{15}$ S – hematite

Conclusions

Mechanical activation allows obtaining $Bi_5Ti_3FeO_{15}$ electroceramic; however, technological process must be improved. X-ray diffraction and Mössbauer spectroscopy as complementary techniques may be used to monitoring of technological process. Mechanical activation as well as solid-state sintering gives the possibility to produce single-phased compound. The heat treatment plays an important role in both cases. In the conventional solid-state route, the sintering at various temperatures under the pressure is the consecutive stage of the process. Mechanical activation seems to be a simpler method; however the final product of milling requires thermal treatment to complete the solid-state reaction. The values of hyperfine interaction parameters of $Bi_5Ti_3FeO_{15}$ electroceramic were determined firstly for mechanically activated samples, in accordance with the knowledge of the authors. The improvement of technological process will be the subject of further investigations.

REFERENCES

[1] Surowiak Z., Ferroelectric electroceramics (in Polish: Elektroceramika ferroelektryczna), Wydawnictwo Uniwersytetu Śląskiego, Katowice 2004

[2] Curie P., Oeuvres de Pierre Curie Gautheir-Villavs, J. Physique, 3e serie t. III (1894), reprinted (1908), 136-137

[3] Aurivillius B., Mixed Bismuth Oxides with Lauer Lattices: I, *Ark. Kemi.*, (1949), 463-471

[4] Subbaro E.C., A Family of Ferroelectric Bismuth Compounds, *J. Phys. Chem. Solids* 23 (1962), 665-676

[5] ICSD card number 88869

[6] Jartych E.,Mazurek M.,Lisińska-Czekaj A., Czekaj D., Hyperfine interactions in some Aurivillius $Bi_{m+1}Ti_3Fe_{m-3}O_{3m+3}$ compounds, *J. Magn. Magn. Mater.*, 322 (2010), 51-55

***Authors**: MSc Mariusz Mazurek, Lublin University of Technology, Department of Electronics, Nadbystrzycka str. 38a, 20-618 Lublin, E-mail: mariusz.mazurek@pollub.pl; Prof. Elżbieta Jartych, Lublin University of Technology, Department of Electronics, Nadbystrzycka str. 38a, 20-618 Lublin, E-mail: e.jartych@pollub.pl; Dr Dariusz Oleszak, Warsaw University of Technology, Faculty of Material Science and Engineering, Wołoska str. 141, 02-507 Warsaw, E-mail: doleszak@inmat.pw.edu.pl*

METHODS TO IMPROVE THE ELECTROMAGNETIC COMPATIBILITY OF PLASMA REACTOR

Paweł A. MAZUREK

Lublin University of Technology

***Abstract**. GlidArc - plasma reactor is the source of non-thermal and equilibrium plasma used to the utilization of gas dirts. The reactor is the source of radiated interference emissions around chamber of discharge and around of the power supply module. The reactor is also the source of conducted interferences propagating by the power supply module to the local power system. In this article author introduced the results of the investigations of interferences executed in the circuit of the ignition of the plasma reactor and EMC filter proposed.*

***Streszczenie.** Źródłem nietermicznej, nierównowagowej plazmy są reaktory plazmowe. Reaktor GlidArc jest źródłem zaburzeń zarówno w postaci pola elektromagnetycznego rozłożonego przestrzennie wokół komory wyładowczej i modułu zasilania jak i źródłem zaburzeń oddziaływujących poprzez tor zasilania na lokalny system energetyczny. W artykule przedstawiono wyniki badań zaburzeń przewodzonych wykonanych w torze zapłonu reaktora oraz zaproponowano układ filtrujący.*

Keywords: electromagnetic compatibility, electromagnetic interferences, plasma reactor, GlidArc.
Słowa kluczowe: kompatybilność elektromagnetyczna, zaburzenia elektromagnetyczne, reaktor plazmowy, GlidArc.

Introduction

One type of plasma reactor is a reactor with gliding arc discharge along the electrodes (GlidArc). Institute of Electrical Engineering and Electrotechnologies of Lublin University of Technology has a reactor (Fig. 1, 2). The quasi-arc discharge is a source of non-thermal plasma filling the space part of the discharge chamber. Plasma source and way to deliver energy to it is a forced flow of electric current in the gas. Plasma is ionized gas that conducts electricity, and this property is used in the manufacture of plasma arc. After the initiation of the electric arc is sustained by passing an electric current and can use it as a plasma source. Arcing is highly nonlinear and asymmetrical load associated with the dynamically changing phenomena of the transitional and short-circuit.

Plasma reactor

The source of plasma is an electric arc in the gas. The geometry of space (length, volume and location of the chamber) and the characteristics of the free arc plasma generated therein are constantly changing at random. It is hard to steer and control the parameters required in the processes of plasma [2,8].

Fig.1. Quasi-arc discharge in plasma reactor, Laboratory of Institute of Electrical Engineering and Electrotechnologies

By changing the geometry of the reactor, the composition of the working gas and power parameters can affect the electrical performance and thermal discharge in the discharge of the reactor chamber. Affecting the power of discharge, temperature plasma generated, the degree of ionization of gas, the chemical composition of the atmosphere can, in turn, shape the ongoing process of technological parameters of plasma [2,3,8].
Discharge ignition on the working electrode plasma reactor is initialized to jump from an additional electrical spark ignition electrode system (or one electrode). Depending on the type of power supply are used in two systems of ignition with single spark electrode, located centrally between the electrodes working, spark is generated directly to the working electrode, or with two ignition electrodes, placed symmetrically and between which is the main discharge of the skip on the electrode working (Fig. 1) [2,3,6,8]

Installation of the plasma reactor

Tests of the reactor installation was done in the place of its installation – in laboratory of Institute IPEE. In the institute there are several plasma reactor designs [1,7]. The research discussed in this paper has been design with few electrodes (three active - connected to power, and two ignition electrodes). The reactor works only for research. Factors working reactor at the time of his actions were nitrogen, argon, oxygen or air mixture. All factors were compressed in the cylinders and by special arrangement was directed into the space discharge. Any fumes from the combustion are removed through an exhaust system.

Fig.2. Installation of the plasma reactor in Institute

Evaluation of quality equipment from the standpoint of electromagnetic compatibility recommendations requires an appropriate conformity assessment procedure [5]. In the analysis of compatibility of the reactor can be used in the provisions relating to fixed installations. Treatment of the plasma reactor system as a result of the fixed nature of its work. Reactor systems are built industrial facilities dedicated to specific objects, in which there is already an autonomous pressure systems with active chemicals [6].

Conducted interferences 9kHz-30MHz

The analysis was conducted disturbances measured in the circuit of the reactor ignition electrodes, ranging from 150kHz to 30MHz. The main elements of the measurement system is measuring the receiver interference and a set of auxiliary equipment such as artificial networks, clamp measurement. ESCI3 (Rohde-Schwarz) used for research its complies with the requirements of CISPR 16.

The first tests were made on the supply side of the ignition module. To measure internerences the current probe EZ17 was used. Current probe, made in the system current transformer, to measure asymmetric currents flowing abnormalities in the ducts attached to the module. The advantage of this configuration is the introduction of the probe to the circuit without disconnecting the network, the disadvantage of lack of stabilization of the impedance of the supply network [6].

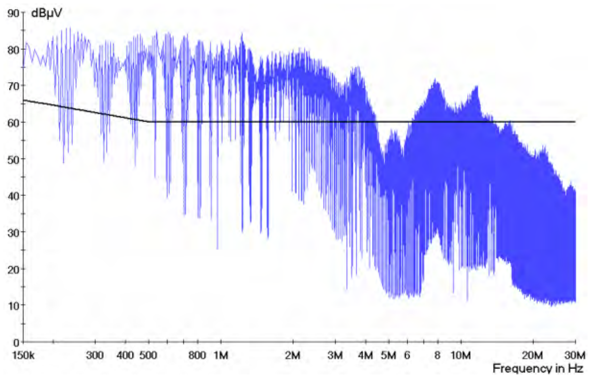

Fig.3. Interferences in modules of ignition system, detector AV, black Line – the EN61000-6-4 limit

The results are unambiguous. The nature of the measured disturbance is broadband characteristics. Nonlinear and asymmetric load, which is characterized by a plasma reactor results in exponentially on the random nature of the distribution of emissions. Limits disturbances measured AV detector for industrial equipment in the frequency range from 0.15 to 0.5 MHz are 66 dB, and in the range from 0.5 to 30 MHz is 60 dB. Thus, the results show a significant excess levels [4,5,6,9]. The next phase of the study concerned the determination of disturbances occurring in the ignition electrodes. And this spectrum disorders exceeds the permissible value (Fig. 5).

Fig. 4. Ferrites in ignition system

Existing problems are problematic for the restriction. While the current flowing through the electrode ignition circuit is not too large (3 - 4A), the existing high voltage (15kV) is an effective barrier for the interference filters.

The large change in the ignition system will change the working conditions and load, which affects the effectiveness of arc. Too weak discharge can not ignite, especially at higher supply air gases. Thus abandoned to install filters. Used to reduce distortions of ferrite components for ignition wires. The use of a single ferrite with a small volume of magnetic material (TR 16 × 8 × 13) not reduced interferences. Safe levels of disturbances were obtained only after installing four SFC 20-10-10 ferrites (Fig. 4).

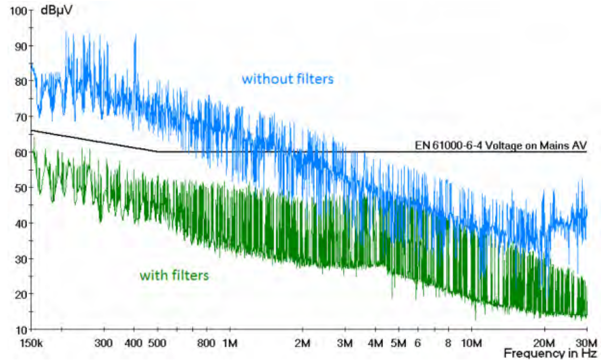

Fig.5. Interferences in ignition system, detector AV, blue- without filters, green – with filters and ferrities

Summary

The tests inform about the levels of disturbance generated by the plasma reactors GlidArc [4,5,6,9]. Research conducted emission (9kHz-30MHz) was carried out in two stages, the working electrode power supply circuit and the circuit ignition electrode. In both circuits had high levels of interference exceeding permissible levels. The proposed installation of plasma reactors absolutely must be equipped with systems reduce electromagnetic disturbances. In the case of disturbances conducted filtration improvement is possible by using cascading phase consisting of EMI filters, additionally supported by a specially selected ferrite chokes.

REFERENCES

[1] Janowski T., H. D. Stryczewska, A. Wac-Włodarczyk, Technologie nadprzewodnikowe i plazmowe w energetyce, Lubelskie Towarzystwo Naukowe, Lublin 2009

[2] Komarzyniec G.: Analiza pracy transformatora pięciokolumnowego w układzie zasilania łukowego reaktora plazmowego, rozprawa doktorska, Politechnika Lubelska 2008

[3] Mazurek P.A.: Rozkład emisji pola elektrycznego i magnetycznego wokół reaktora plazmowego typu Glidarc, *Przegląd Elektrotechniczny*, R. 86 NR 12/2010, 95-98

[4] Mazurek P.A.: Wprowadzenie do badań zaburzeń przewodzonych w instalacji reaktora plazmowego, *Elektro.info*, ISSN 1642-8722, 12/2010, str. 32-34

[5] Mazurek P. A.: Raport końcowy projektu badawczego NN510349936, Politechnika Lubelska, Instytut Podstaw Elektrotechniki i Elektrotechnologii

[6] Stryczewska H. D.: Technologie plazmowe w energetyce i inżynierii środowiska. Wydawnictwo Politechniki Lubelskiej, Lublin 2009

[7] Wac-Włodarczyk A., Stryczewska H. D., Mazurek P. A., Komarzyniec G.: Analiza zaburzeń elektromagnetycznych emitowanych przez urządzenia plazmowe, XXVIII IC-SPETO, Ustroń, 11–14.V.05, 183-186.

***Author**: dr inż. Paweł A. Mazurek, Politechnika Lubelska, Instytut Podstaw Elektrotechniki i Elektrotechnologii, ul. Nadbystrzycka 38a, 20-618 Lublin, E-m\i:l p.mazurek@pollub.pl*

LOW FREQUENCY FDTD ALGORITHM AND ITS APPLICATION TO INDUCTIVE HYPERTHERMIA

Arkadiusz Miaskowski[1], Andrzej Wac-Włodarczyk[2], Grażyna Olchowik[3]

University of Life Sciences in Lublin (1), Lublin University of Technology (2), Medical University of Lublin (3)

***Abstract**. The paper attempts to show the application of low frequency FDTD algorithm to the investigation of ACD and SAR distribution in female breast phantom and their dependence on frequency. Special attention has been given to the values of ACD and SAR in the skin layer because both of them play an important role in hyperthermia treatment when skin overheating occurs.*

***Streszczenie.** W artykule przedstawiono zastosowanie algorytmu niskoczęstotliwościowego FDTD do analizy gęstości prądów wirowych i SAR w modelu gruczołu piersiowego. Szczególną uwagę położono na wartość wspomnianych wielkości w warstwie skóry ze względu na efekt jej przegrzania, jaki ma miejsce podczas leczenia hipertermicznego.*

Keywords: hyperthermia, FDTD, eddy currents, SAR.
Słowa kluczowe: hipertermia, FDTD, gęstość prądów wirowych, SAR.

Introduction

The power of healing by heat generation has been known for a long time. It is known as an innovative form of cancer therapy among classical methods like chemotherapy, surgery and irradiation. In general, hyperthermia is based on the principle that temperatures higher than 42^0C may lead to apoptosis. Apart from clinical problems, theoretical and engineering tasks have to be solved. One of them is the proper design of hyperthermia applicator in order to avoid the skin overheating during treatment. In this paper the authors have not considered temperature distribution on the skin but investigated two factors that are responsible for heat generation in a human body i.e. current density (ACD) and Specific Absorption Rate (SAR).

Low frequency FDTD algorithm

The finite-difference time-domain technique is a well established numerical method for modeling very complicated, inhomogeneous electromagnetic problems at high frequencies [1]. However, bioelectromagnetic simulations at low frequencies using FDTD method require special consideration. Frequency scaling algorithm is often used at quasi-static frequencies, where the *E*-field and *H*-field are assumed to be uncoupled. Using this algorithm the actual simulation is performed at a higher frequency *(f*)* (with the quasi-static approximation being still valid) and the induced fields are scaled to the frequency of interest *(f)* after the higher frequency FDTD-simulation is finished [2]. Assuming that the electric field in the air (E_{air}) is normal to the body surface, one can write:

(1) $$j\omega\varepsilon_0\hat{n}E_{air}(\omega) = (\sigma + j\omega\varepsilon)\hat{n}E_{tissue}(\omega)$$

From (1) it can be concluded that:

(2) $$E_{tissue}(f) = \frac{\omega(\sigma^* + j\omega^*\varepsilon^*)}{\omega^*(\sigma + j\omega\varepsilon)}E_{tissue}(f^*) \cong \frac{f\sigma^*}{f^*\sigma}E^*_{tissue}(f^*)$$

Assuming that $\sigma + j\omega\varepsilon \cong \sigma$ for both *f* and *f** and σ^* and σ are close enough, the equation (2) can be simplified to:

(3) $$E_{tissue}(f) = \frac{f}{f^*}E^*_{tissue}(f^*)$$

In our case the actual FDTD calculations were performed at the frequency f^* = 10 MHz and afterwards the induced electric field E^* at the frequency f^* was scaled to the frequency of question, i.e. *f* =150 Hz, using equation (3). As it is obvious from (2), the permittivity of tissues doesn't affect the results significantly, therefore the value of $\varepsilon_r = 1$ was set for the whole environment to hasten the speed of wave propagation and to reduce the simulation time. On the surface of the simulation, volume absorbing boundary conditions were defined. In this study, Berenger's [3] six perfectly matched layers (PML) boundary condition was used because it is superior to most standard absorbing boundary conditions (ABC) with regard to electromagnetic interferences with human tissues.

In order to validate the low frequency FDTD algorithm a model of disk has been prepared as shown in Fig. 1.

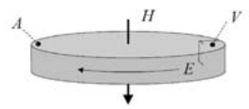

Fig. 1. The model of disk.

The following parameters have been assigned to the disk: r_0 = 15cm, σ = 0.23 S/m, ε_r = 1, ρ =1 g/cm^3, H = 1 A/m, f = 50 Hz. ***H***-field induce circulating CD in the disk i.e.

(4) $$E(r) = \pi f r \mu_0 H$$

(5) $$J(r) = \sigma E(r)$$

(6) $$SAR = \sigma\frac{E^2(r)}{\rho}$$

Taking into account the parameters of the disk (Fig.1) one can calculate:

(7) $$J_{1cm^2} = \max\{\frac{1}{A}\iint_A J(r)dA\} = \frac{1}{1cm}\int_{14cm}^{15cm} J(r)dr = 6.58\frac{\mu A}{m^2}$$

(8) $$SAR_{10_g} = \max\{\frac{1}{V}\iiint_V SAR(r)dV\} = \frac{1}{\sqrt[3]{10}cm}\int_{15-\sqrt[3]{10}}^{15} SAR(r)dr = 0.174\frac{pW}{kg}$$

(9) $$SAR_{wb} = \frac{\sigma(\pi f r_0 H)^2}{2\rho} = 0.1007\frac{pW}{g}$$

where $J_{1cm}{}^2$ is current density averaged to 1cm^2, SAR_{10g} – Specific Absorption Rate averaged to 10 g and SAR_{wb} is whole body SAR.

After that the numerical calculations have been done to validate the algorithm (see Fig. 2 – Fig. 4.)

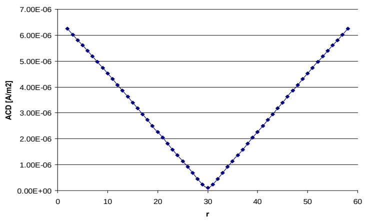

Fig. 2. The variation of ACD over disk radius.

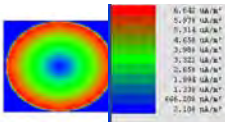

Fig. 3. ACD @ 50 Hz

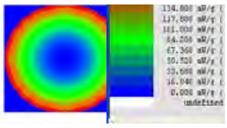

Fig. 4. SAR @ 50 Hz

Model of female breast phantom

The above algorithm has been applied to numerically investigate SAR and ACD distributions in a female breast model as it is shown in Fig. 5.

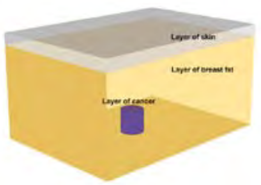

Fig. 5. CAD model of female breast phantom

The details of the phantom preparation and its use in hyperthermia set can be found in [4]. In real low frequency hyperthermia sets, a working frequency of applicator can vary. In our case the frequency was in the range from 140 to 160 kHz. That is why ACD and SAR dependence on frequency have been investigated.

The dielectric parameters of the modeled tissues have been approximated using 4-Cole-Cole [5] with parameters taken from Gabriels [6] and calculated for frequencies: 140, 150 and 160 kHz (see Table 1)

Table 1. The dielectric parameters of the model

Tissue	σ [S/m]	ρ [g/cm^3]
Skin	0.089014 @ 140 kHz 0.093995 @ 150 kHz 0.09869 @ 160 kHz	1.01
Breast fat	0.025111 @ 140 kHz 0.025124 @ 150 kHz 0.025137 @ 160 kHz	0.92
Cancer	0.37043 @ 140 kHz 0.37265 @ 150 kHz 0.37491 @ 160 kHz	1.04

In the pictures (Fig. 6 – Fig. 8) are shown the exemplary SAR and ACD distributions in the model for the frequency of 140 kHz. The results of calculations for different frequencies are gathered in Table 2.

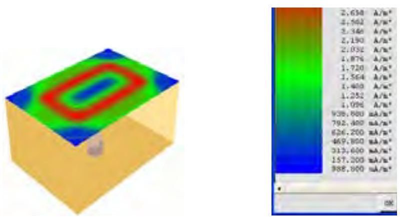

Fig. 6. ACD @ 140kHz – skin layer.

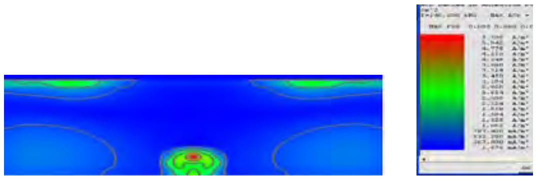

Fig. 7. ACD @ 140kHz – vertical cross section of the phantom.

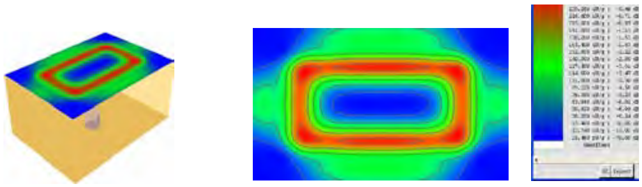

Fig. 8. SAR_{1g} @ 140 kHz

Table 2. Maximum values of ACD and SAR in the skin

f [kHz]	max ACD [A/m^2] skin	SAR_{1g} [μW/g] skin
140	3.126	254.6
150	3.604	337.8
160	4.162	435.6

As it can be seen from Fig. 6 – Fig. 8, the highest value of ADC's and SAR's have occurred in the cancer and skin layers.

Conclusions

The value of magnetic field strength taken to the analysis has been chosen arbitrarily (***H*** = 1 A/m), as the problem is of linear nature. Thus, the results of calculation can be re-scaled to the magnetic field as one wishes. Eddy currents and SAR are of great importance when talking about inductive heating. The maximum ACD and SAR values in the body are determined by the size of body, and so is the distance between the applicator and the skin. Nevertheless, the knowledge of them plays an important role when skin overheating is taken into consideration. The authors hope that the presented results can help to design inductive hyperthermia applicators and avoid the skin overheating problem.

REFERENCES

[1] Taflove A., Computaional Electrodynamics The Finite-Difference Time-Domain Method, Artech House, 1995

[2] Miaskowski A., Krawczyk A., Finite Difference Time Domain Method for High Resolution Modeling of Low Frequency Electric Induction in Humans, *Electrical Review* 2007, No 11, pp. 225-227.

[3] Berenger J., A perfectly matched layer for the absorption of electromagnetic waves, *Journal of Computational Physics* 114: 1994, pp. 185–200

[4] Miaskowski A., Sawicki B., Krawczyk A., Yamada S., The application of magnetic fluid hyperthermia to breast cancer treatment, *Electrical Review* 2010, 12, pp. 99-101

[5] Cole K.S., Cole R.H., *Dispersion and absorption in dielectrics*: *I. Alternating current characteristics*, Journal of Chemical Physics, April 1941, pp.341-351.

[6] Gabriel S., Lau R.W., Gabriel C., The dielectric properties of biological tissues: III. Parametric models for the dielectric spectrum of tissues, *Phys. Med. Biol.* 41,1996, pp. 2271-2293

***Authors**: dr inż. Arkadiusz Miaskowski, University of Life Science in Lublin, Department of Applied Mathematics and Computer Science, Akademicka 13, 20-950 Lublin, E-mail: arek.miaskowski@up.lublin.pl; dr hab. inż. Andrzej Wac-Włodarczyk, Lublin University of Technology, Institute of Electrical Engineering and Electrotechnologies, Nadbystrzycka 38a, 20-618 Lublin, E-mail: a.wac-wlodarczyk@pollub.pl, dr hab. n. med. Grażyna Olchowik, Medical University of Lublin, Department of Biophysics, Jaczewskiego 4, 20-090 Lublin, E-mail: grazyna.olchowik@am.lublin.pl*

Conference ELMECO–7
ELECTROMAGNETIC DEVICES AND PROCESSES IN ENVIRONMENT PROTECTION
joint with 10th Seminar AoS-10 APPLICATIONS OF SUPERCONDUCTORS
28–30.09.2011, Nałęczów, Poland

ANALYSIS ELECTROMAGNETIC FIELD DISTRIBUTION AND SPECIFIC ABSORPTION RATE IN BREAST MODELS

Joanna MICHAŁOWSKA-SAMONek[1] , Arkadiusz MIASKOWSKI[2] , Andrzej WAC-WŁODARCZYK[1]

Lublin University of Technology, Institute of Electrical Engineering and Electrotechnologies (1),
University of Life Sciences in Lublin, Department of Applied Mathematics and Computer Science (2)

Abstract. *The aim of the paper is to introduce numerical analysis of electromagnetic field distribution by FDTD method.*

Streszczenie. *Celem artykułu jest przedstawienie numerycznej analizy rozkładu pola elektromagnetycznego za pomocą metody FDTD dla modelu gruczołu piersiowego.*

Keywords: Breast Cancer, FDTD(finite difference time domain), electromagnetic field distribution SAR(Specific absorption rate)
Słowa kluczowe: nowotwór gruczołu piersiowego, FDTD, rozkład PEM (pola elektromagnetycznego),SAR (współczynnik absorbcji)

Introduction

According to reports based on the data of National Cancer Registry and Polish Committee for Fighting Cancer (Polski Komitet Zwalczania Raka), breast cancer is the most frequent malignant tumor among women between 40 and 60 (in 2008, 14576 cases of breast cancer occurred, and the death toll reached 5368 because of that)[2].

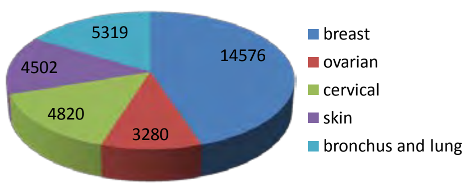

Fig.1 Statistics of incidence for malignant tumors
in women in Poland in 2008.

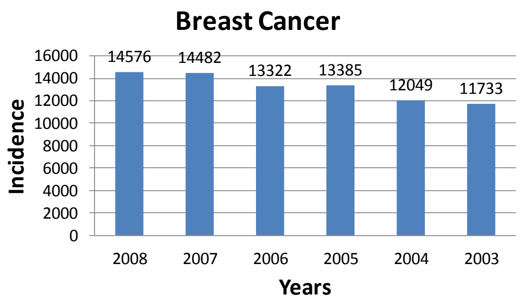

Fig.2 Statistics of incidence for breast cancer .

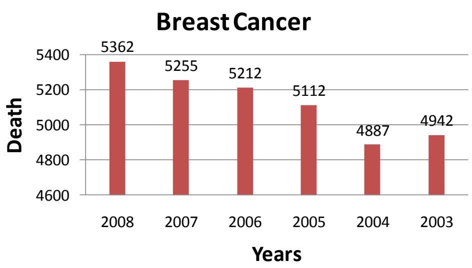

Fig.3 Statistics of death rate for breast cancer.

So far, commonly used methods (mammography and ultrasound) detect tumors with a diameter greater than 5mm

Numerical models

In order to investigate the problem, the authors assumed that the model of breast is homogeneous and its electrical parameters i.e. the dielectric constant (ε_r) and conductivity (σ) are varying with frequency and can be approximated by Cole-Cole formul:

$$\underline{\varepsilon}_{(\omega)} = \varepsilon'_{(\omega)} - j\varepsilon''(\omega) = \varepsilon_\infty + \frac{\Delta\varepsilon}{1+(j\omega\tau)^{1-\alpha}} + \frac{\sigma_s}{j\omega\varepsilon_o} \tag{1}$$

where: ε_s is the static conductivity, ε_∞ is the relative permittivity at infinite frequency, σ_s is the static conductivity , τ is the relaxation time constant, α- parameter of relaxation time.

Electrical parameters comes from C. Gabriel [1,4].

The model, its dimensions and electrical parameters calculated for frequency of 2.45GHZ\z and 5GHz GHz . On the basis of synthetic data recorded at twenty five points (the transmitter – receiver points are marked by Tx/Rx) the authors received twenty five signals. Numerical analysis of electromagnetic field distribution in and out of the model was carried out using FDTD method (Finite Difference Time Domain) using Empire Xccel Software.

Tab.1 Tissue electrical parameters

Tissue name	Conductivity [S/m]	Relative permittivity
	2.45 GHz	
Breast Fat	0.137	5.146
Muscle	1.738	52.729
Skin	1.591	42.853
	5 GHz	
Breast Fat	0.349	4.645
Muscle	4.044	49.54
Skin	0.242	39.61

SAR (Specific absorption Rate)

In breast model was description SAR to aim that method are safe. Specific absorption rate (SAR) is a measure of the rate at which energy is absorbed by the body when exposed to a frequency electromagnetic field. It is defined as the power absorbed per mass of tissue and has units of watts per kilogram (W/kg). SAR is usually averaged either over the whole body, or over a small sample volume (typically 1 g or 10 g of tissue)[3,4].

SAR can be calculated from the electric field within the tissue as:

(2) $$SAR = \frac{dW}{\rho dV}$$

where; *dW* is increment energy, *d*V-is volume element, *ρ* is the density of the volume .

The SAR value is defined in an official EU document prepared on the basis of the document International Commission on Non-Ionizing Radiation Protection - ICNIRP.

In Poland, the protection of the general population and environmental non-ionizing radiation describes Minister of Environment Regulation.

Conclusion

Breast cancer diagnosed early enough, i.e. the diameter of cancer is lower than 5mm, can be treated successfully in 90 percent of cases. In spite of well identified symptoms of the cancer, its detection with the use traditional tomography is still unsatisfactory, as it is proven in numerous research papers. Despite well diagnosed symptoms of the cancer, numerous research reports point the unsatisfactory results of using classical mammography for breast cancer detection. an ideal breast cancer method should: a) detect cancers at the curable stage without false detections, b) have low health risk, c) be noninvasive and relatively simple to perform, d) be low cost.

REFERENCES

[1] Gabriel C. “The dielectric properties of biological tissue: I. Literature survey” Phys. Med. Biol, mvol.41, pp.2231-2249, 1996,

[2] http://epid.coi.waw.pl,

[3] Ciosk K. i inni, On SAR evaluation in the model of human head subjected to radiofrequency electromagnetic field, w: Electromagnetic Fields in Electrical Engineering (ed. A. Krawczyk S. Wiak), IOS Press, Amsterdam 2002,

[4] A. Miaskowski “ Zastosowanie mikrofal do detekcji raka sutka”, Przegląd Elektrotechniczny pp.87-88, 12/2005.

***Authors**: mgr inż.* Joanna Michałowska-Samonek, *Politechnika Lubelska, Instytut Podstaw Elektrotechniki i Elektrotrotechnologii, ul.Nadbystrzycka38a, 20-618 Lublin, Email: joannamichalowska@o2.pl, Dr.hab inż., Prof.PL, Andrzej Wac-Włodarczyk, Politechnika Lubelska, Instytut Podstaw Elektrotechniki i Elektrotrotechnologii, E-mail:a.wac-wlodarczyk@pollub.pl, Dr inż. Arkadiusz Miaskowski, Katedra Zastosowań Matematyki i Informatyki, Uniwersytet Przyrodniczy w Lublinie, 20-950 Lublin, ul. Akademicka 13, E-mail: arek.miaskowski@up.lublin.pl.*

Conference ELMECO–7
ELECTROMAGNETIC DEVICES AND PROCESSES IN ENVIRONMENT PROTECTION
joint with 10th Seminar AoS-10 APPLICATIONS OF SUPERCONDUCTORS
28–30.09.2011, Nałęczów, Poland

APPLICATION OF OPTICAL WAVE MICROPHONE TO GLIDING ARC DISCHARGE

Fumiaki MITSUGI[1], Tomoaki IKEGAMI[1], Shin-ichi AOQUI[2], Yui TASHIMA[3], Hiroharu KAWASAKI[3], Toshiyuki NAKAMIYA[4], Yoshito SONODA[4], and Henryka Danuta STRYCZEWSKA[5]

Kumamoto University (1), Sojo University (2), Sasebo National College of Technology (3),
Tokai University (4), Lublin University of Technology (5)

***Abstract**. In this work, principle and application of a novel method of an optical wave microphone to gliding arc discharge were introduced. The optical wave microphone is based on Fraunhofer diffraction, which can identify slight refractive index change of atmosphere after each discharges. Simultaneous measurement of applied voltage, discharge current and optical wave microphone for an arc discharge was carried out.*

Keywords: Gliding arc discharge, Optical wave microphone, Shock wave, Sound wave

Introduction

Application of gliding arc discharge to gas treatment has been progressed. We focus on evaluation of sound or shock wave emitted after arc discharge from practical and energetic point of view. Conventional condenser microphones have been used to detect sound or ultrasonic wave after discharge however they has limitation for detectable frequency and geometry, which made it impossible to reveal relationship between a discharge and sound caused by the discharge.

In this work, we introduce a new optical method of an optical wave microphone which is expected to substitute for conventional condenser microphones or other optical methods. The optical wave microphone is a unique technique which can detect compressional wave or slight change of density in gas medium or even in liquid medium with a probe laser, a Fourier lens and a detector. Because this technique is based on Fraunhofer diffraction between compressional wave and a probe laser, it is very useful to detect not only audible sound but also ultrasonic wave or shock wave without disturbing propagation of compressional wave and electric field in case of electric discharge. We employed this technique to gliding arc discharge.

Principle of Optical wave microphone

Theoretical explanation of the optical wave microphone is as follows. When a probe laser beam crosses refractive index change such as sound wave at (x_0,y_0), diffracted waves are generated and propagate with and in the penetrating beam through a Fourier optical lens and reach the observing detector which is set at Fraunhofer diffraction region or in the back focal plane (x_f,y_f) of the Fourier lens. The diffracted optical wave is heterodyne-detected by using the penetrating optical wave as a local oscillating power. The optical wave distribution $u_w(x_f,y_f)$ at the detector position is shown in the next equation.

$$u_w(x_f, y_f) = \left\{\frac{i\exp(-2k_i f)}{\lambda_i f}\right\}\int_{-\infty}^{\infty}\int_{-\infty}^{\infty} u_w(x_0, y_0)T(x_0, y_0)\exp\left\{\frac{ik_i(x_0 x_f + y_0 y_f)}{f}\right\}dx_0 dy_0$$

here,

$u_w(x_0,y_0)$: complex amplitude of laser at (x_0,y_0)

$T(x_0,y_0)$: phase modulation component by refractive index change

k_i: wave number of laser

λ_i: wave length of laser

f: focal length of Fourier lens

Spatial Fourier transform is finished at the detecting plane. In this paper, compressional wave of air generated just after one pulsed arc discharge was detected by this method.

Experimental setup

Schematic diagrams of gliding arc discharge system and optical wave microphone setup are shown in Fig. 1. Two electrodes for gliding arc discharge are made of iron and their shortest gap was 2 mm. High voltage (sine wave, 60 Hz) was applied between the two electrodes with a high voltage transformer (VIC international, 120:1). The amplitude was adjusted with a voltage slide autotransformer (TAMABISHI, S-130-39). Applied voltage waveform during discharge was observed with a high voltage probe (IWATSU, HV-P60). Discharge current was measured by clamping a current sensor (HIOKI, 9018-50).

The optical wave microphone system consists of a diode laser, a Fourier lens, a beam expander, optical fibber and the detector. The discharge electrodes should be placed between the diode laser and the Fourier lens. The probe laser beam (w_0=2 mm, 28 mW) was set at 3 mm apart from the electrodes and at the same height as that of the shortest gap along parallel direction to discharge. The two lenses after the Fourier lens play a role of the beam expander. The diffraction signal which was caused by interaction between the laser beam and the discharge sound wave was detected with the detector through the optical fibber. The use of the optical fibber was available to remove discharge noise.

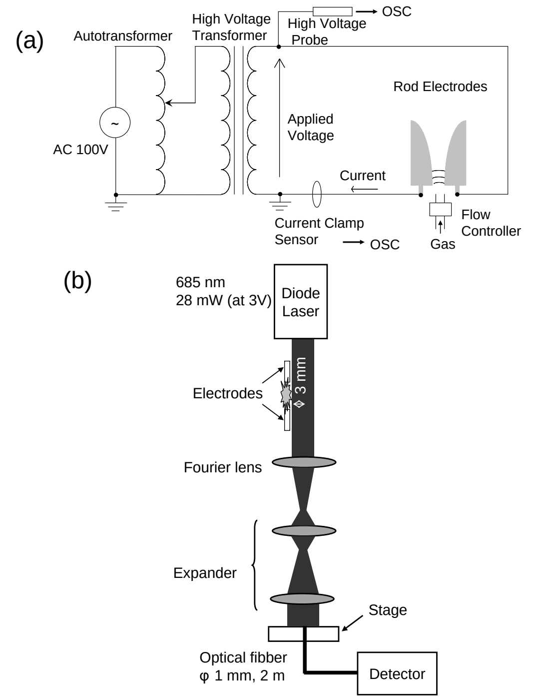

Fig.1. Schematic diagrams of (a) gliding arc discharge system and (b) optical wave microphone setup.

Results and Discussions

High voltage of 8 kV was applied between the electrodes without gas flow to carry out measurement of optical wave microphone. Because the optical wave microphone is very sensitive to density change of atmosphere, no gas flow is desired. The position of the optical fibber was fixed at (x_f,y_f) = (1 mm, 0 mm) where the sensitivity showed maximum. The optimum frequency of this setup which is decided by relationship between wavelength of compressional wave and laser waist is approximately 45 kHz.

Fig.2 shows optical wave microphone waveform captured simultaneously with applied voltage and current waveforms. The generation of one arc discharge started at 0 us when the pulsed current observed and applied voltage decreased drastically due to higher conductivity of arc between the electrodes. It is impossible to observe in the current waveform but slight current flow, which may concern with ionic component, exists after the large pulsed current during the high voltage is applied. It was obvious from the optical wave microphone waveform that a compressional wave emitted by the generation of the arc discharge was detected successfully by this method. The wave arrived approximately 8 us delayed after the generation of the pulsed discharge which means the speed of the wave propagation corresponds to that of sound in air. It is suggested that the wave should be observed as a shock wave near the discharge but it degenerates to sound wave at detecting position as far as 3 mm. The obtained waveform means frequency resolved waveform of the compressional wave. The main frequency component of this optical wave microphone signal analyzed by FFT was about 100 kHz. Such high frequency component can not be detected with mechanical devices like conventional condenser microphones. Moreover, it is impossible to characterize relationship between generation of discharge and sound wave via condenser microphones because it can not be set at close position to high electric field and can not follow a sound wave during high frequent discharges. Therefore, we propose the optical wave microphone as one of potential techniques to evaluate discharge energy as well as sound of arc.

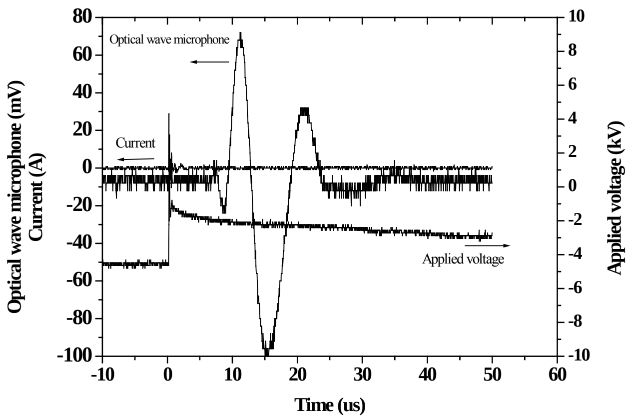

Fig.2 Optical wave microphone waveform after one pulsed arc discharge. The arc discharge is generated at 0 us.

Summary

We applied a novel technique of the optical wave microphone to gliding arc discharge in air.

As the result, a compressional wave, which propagates with sound speed, emitted just after the generation of arc was detected. It was revealed that the wave included the frequency component as high as approximately 100 kHz.

REFERENCES

[1] Toshiyuki NAKAMIYA, Fumiaki MITSUGI, Shota SUYAMA, Tomoaki IKEGAMI, Kenji EBIHARA, Yoshito SONODA, Yoichiro IWASAKI, Shin-ichi AOQUI, Henryka STRYCZEWSKA, Joanna PAWLAT, PRZEGLAD ELEKTROTECHNICZNY (Electrical Review) 1/2011 (2011) 249-253

[2] Toshiyuki Nakamiya, Yoichiro Iwasaki, Fumiaki Mitsugi, Ryosuke Kozai, Tomoaki Ikegami, Yoshito Sonoda, and Ryoichi Tsuda, Journal of Advanced Oxidation Technologies 14(1) (2011) 63-70

***Authors**: Dr. Fumiaki Mitsugi, and Prof. Tomoaki Ikegami, Graduate School of Kumamoto University, Kurokami 2-39-1, Kumamoto city, Kumamoto 860-8555, Japan, E-mail:mitsugi@cs.kumamoto-u.ac.jp.; Mr. Ikuya Muramoto and Prof. Shin-ichi Aoqui, Sojo University, Ikeda 4-22-1, Kumamoto city, Kumamoto 860-0082, Japan, E-mail: aoqui@cis.sojo-u.ac.jp; Prof. Hiroharu Kawasaki, Sasebo National College of Technology, Okisin 1-1, Sasebo, Nagasaki 857-8171, Japan, E-mail: h-kawasa@post.cc.sasebo.ac.jp; Prof. Toshiyuki Nakamiya and Prof. Yoshito Sonoda, Tokai University, Toroku 9-1-1, Kumamoto 862-8652, Japan, E-mail: nakamiya@tokai.ac.jp; Prof. Henryka Stryczewska, Institute of Electrical and Electrotechnologies, Lublin University of Technology, 38A Nadbystrzycka St. 20-618, Lublin, Poland, E-mail: h.stryczewska@pollub.pl*

Conference ELMECO–7
ELECTROMAGNETIC DEVICES AND PROCESSES IN ENVIRONMENT PROTECTION
joint with 10th Seminar AoS-10 APPLICATIONS OF SUPERCONDUCTORS
28–30.09.2011, Nałęczów, Poland

LOW-TEMPERATURE MICROWAVE MICROPLASMA FOR BIO-DECONTAMINATION

Jerzy MIZERACZYK[1, 2], Bartosz HRYCAK[1], Mariusz JASIŃSKI[1], Mirosław DORS[1]

The Szewalski Institute of Fluid Flow Machinery Gdańsk (1), Gdynia Maritime University (2)

***Abstract**. This paper presents results of the investigations of an atmospheric pressure Ar and Ar/O_2 microwave (2.45 GHz) microplasmas which can be used in the biomedical applications. The microplasma in the form of a column was generated using a simple, coaxial microwave microplasma source (MMS). The gas temperature at the microplasma tip was as low as about 300 K. This makes the microwave microplasma suitable for many applications, including bio-medical. Preliminary test with Escherichia coli K-25 indicated antibacterial effect of Ar and Ar/O_2 microplasmas.*

***Streszczenie.** Prezentowana mikrofalowa (2.45 GHz) mikroplazma Ar oraz Ar/O_2 może znaleźć zastosowanie w medycynie, np.: przy dezynfekcji. Mikroplazmę w kształcie kolumny wytwarza prostej konstrukcji, współosiowy mikrofalowy generator mikroplazmy. Temperatura na szczycie kolumny mikroplazmy jest niska, rzędu 300 K. To czyni mikroplazmę użyteczną do zastosowań w medycynie. Wstępne testy z użyciem bakterii Escherichia coli K-25 wskazują na antybakteryjne działanie mikroplazmy Ar i Ar/O_2.*

Keywords: microplasma sources, microwave discharges, decontamination.
Słowa kluczowe: generatory mikroplazmy, wyładowania mikrofalowe, dekontaminacja.

Introduction

The interest in the atmospheric pressure low-temperature microplasmas is growing because of many merits of such a microplasma: small size (from µm to several mm), portability of the source, easy to use, low investment and operation costs. The microplasmas can be used for gas cleaning, in microwelding and surface modification, as light sources, and atomic spectroscopy systems. Also there is interest in the microplasmas used in the biomedical applications such as sterilization of medical instruments, high-precision surgery, cells treatment and deactivation of bacteria and viruses [1-2].

In this paper we report results of the experimental investigation of a simple coaxial microwave microplasma source (MMS). The main advantages of the presented MMS are simplicity and low cost. The paper is focused on low-temperature Ar and Ar/O_2 microwave microplasma.

Microwave microplasma source MMS

The presented MMS (Fig. 1) is a more advanced version of previous MMSs developed by us and described in [3, 4]. The structure of the MMS shown in Fig. 1 is based on a coaxial line, formed by the inner (a brass rod ended with a thinner rod top) and outer (a brass cylinder) conductors. The top of inner conductor was made of tungsten. The inner conductor is fixed inside the outer conductor tightly with a PTFE centring disc. The operating gas was supplied through a void duct between the inner and outer conductors. The MMS was connected to the coaxial cable using N-type connector. The microwave power was supplied through a 50 Ω coaxial cable from a 2.45 GHz microwave magnetron generator.

The MMS could work with various gases like Ar or N_2. Also working with their mixtures with O_2 (up to 5%) was possible.

Optionally, when worked with the Ar, the MMS could be operated with a PTFE or MACOR® ceramic tip. This tip played three functions: it formed a kind of nozzle that increased the velocity of argon in plasma forming zone, it prevented breakdowns between the inner and outer conductors, specially in case operating in the Ar, and it covered the hotter part of the microplasma column, thus exposing only the lowest temperature microplasma (i.e. its tip).

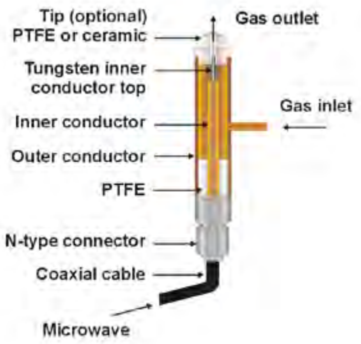

Fig.1. The sketch of coaxial microwave microplasma source

The microplasma was generated by the MMS in the form of a tiny candle-like flame (in Ar, Ar/O_2 at low absorbed powers) or a plasma jet (in Ar/O_2 at high absorbed powers) above the inner conductor top (see Fig. 2). The length and diameter ranged 5-25 mm, 0.5-2 mm, respectively for Ar microplasma and 2-30 mm, 2-16 mm, respectively for Ar/O_2 microplasma. Ar microplasma was relatively

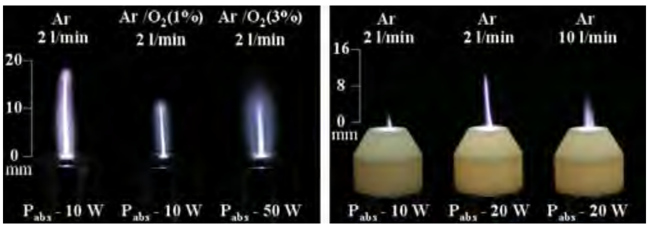

Fig.2. Microwave microplasma. MMS without tip and with MACOR® ceramic tip.

low-temperature. Additive of O_2 to Ar microplasma caused mild increase of temperature for comparable absorbed microwave power levels.

Experiments

The main parts of the experimental setup (see Fig. 3) used in these measurements were the magnetron generator (2.45 GHz), microwave power measuring system, the MMS, gas supplying and flow control system, and spectrometer (CVI DK-480), for emission spectra analysis. The microwave power P_{abs} absorbed by the microplasma was determined from the difference (P_I - P_R), where P_I and P_R are the incident and reflected microwave powers, respectively. The incident P_I and reflected P_R microwave powers were directly measured using directional coupler and dual-channel power meter.

Spectroscopic measurements (Optical Emission Spectroscopy) of the electron density, microplasma temperatures and active species identification, as well as preliminary tests of biocidal effect with *Escherichia coli K-25* bacteria were performed.

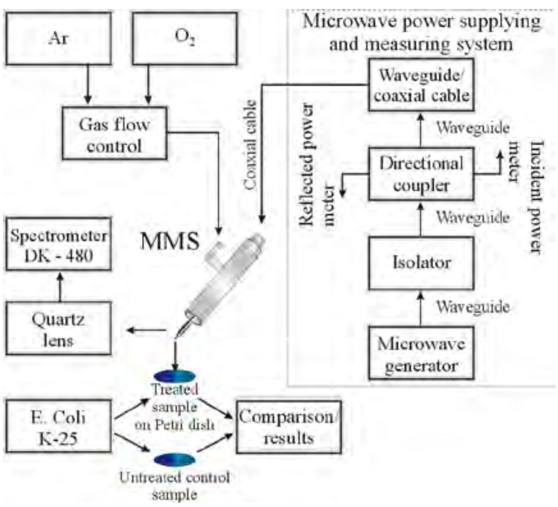

Fig.3. Experimental setup

Results

The operating in Ar and Ar/O_2 (up to 5%) was tested without MMS tip for flow rates from 1 l/min up to 10 l/min. In Fig. 4 required absorbed powers for different O_2 additive are presented. The required absorbed powers were defined by: the minimum power necessary for stable discharge and maximum power, when breakdowns between the inner and outer conductors occurred. The MMS worked stable with Ar and Ar/O_2 for gas flow higher than 2 l/min. Below this value breakdowns between the inner and outer conductors occurred for relatively low absorbed microwave powers in pure Ar microplasma and Ar/O_2 microplasma become very hot due to the fact that the air surrounding it entered into it. As seen in Fig. 4, increasing O_2 additive caused increase of required minimal absorbed power. On the other hand increasing O_2 prevented breakdowns between the inner and outer conductors for higher absorbed powers. The reflection coefficient P_R/P_I for Ar/O_2 as a working gas was less than about 15%.

The measured electron density for Ar microplasma varied from $6{*}10^{14}$ to $1.4{*}10^{15}$ cm^{-3}, depending on operating parameters and location within the microplasma column. Generally, the electron number density increased with increasing absorbed power and no influence of Ar flow rate for it was observed. The presents of O atoms (O I lines

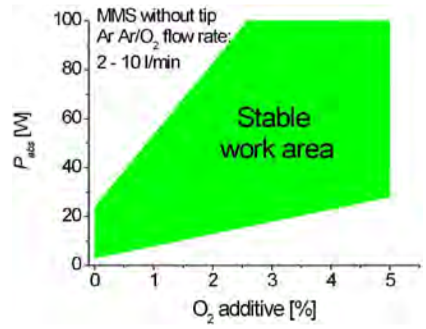

Fig.4. Required absorbed microwave powers for stable microplasma generation for different O_2 additive. MMS without tip. Ar, Ar/O_2 flow rate from 2 l/min up to 10 l/min.

at 615.7 nm) and OH radicals [OH (A-X) rotational band at about 308 nm] in Ar and Ar/O_2 microplasmas were observed. The rotational temperatures were determined to be about 500 K for OH radicals and 800 K for N_2 molecules at the microplasma core of visible part of column, when MMS was operated with MACOR® ceramic tip. These values were measured at an absorbed microwave power of 10 W and Ar flow rate of 10 l/min. Tests with thermocouple showed that at the top of microplasma column gas temperature was from 303 K [3]. The result of biocidal effect test indicated reduction of bacteria population for all samples treated by Ar and Ar/O_2 microplasmas.

Conclusions

The high desity Ar and Ar/O_2 microplasma generated by coaxial microwave microplasma source is presented in this paper. The simplicity of the source, stability of the microplasma and wide range of its parameters allow the conclusion that the MMS can find practical applications in various fields. The relatively low gas temperature (from 303 K [3]) in Ar microwave microplasma allows using it in medicine for treatment of alive tissues without burning them. The presents of active radicals like OH or O indicate that it could be useful in decontamination. Preliminary test with *Escherichia coli K-25* indicated antibacterial effect of Ar and Ar/O_2 microplasma. The quantity investigations are under going.

This research was supported by the The Szewalski Institute of Fluid Flow Machinery, Polish Academy of Sciences.

REFERENCES

[1] Fridman A., Plasma Chemistry, Cambridge University Press, New York, 2008

[2] Kawai Y., Ikegami H., Sato N., Matsuda A., Uchino K., Kuzuya M., Mizuno A., Industrial Plasma Technology, WILEY-VCH Verlag GmbH & Co. KGaA, Weinheim, 2010

[3] Goch M., Jasiński M., Mizeraczyk J., Microwave Microdischarge Generator Based on Coaxial Line, *Przegląd Elektrotechniczny*, 3/2008 (2008), 80-82

[4] Hrycak B., Jasiński M., Mizeraczyk J., Mikrofalowy Generator Mikrowyładowania w Azocie, *Przegląd Elektrotechniczny*, 7/2010 (2010), 115-117

***Authors**: mgr inż. Bartosz Hrycak, dr inż. Mariusz Jasiński, The Szewalski Institute of Fluid-Flow Machinery, Polish Academy of Sciences, ul. Fiszera 14, 80-952 Gdańsk, E-mail: bhrycak@imp.gda.pl; mj@imp.gda.pl;*

prof. dr hab. inż. Jerzy Mizeraczyk, The Szewalski Institute of Fluid-Flow Machinery, Polish Academy of Sciences, ul. Fiszera 14, 80-952 Gdańsk and Gdynia Maritime University, Faculty of Marine Electrical Engineering, Morska 81-87, 81-225 Gdynia, E-mail: jmiz@imp.gda.pl

TOMOGRAPHIC VISUALIZATION OF DISCHARGE SOUND FIELDS USING OPTICAL WAVE MICROPHONE

Toshiyuki NAKAMIYA[1], Fumiaki MITSUGI[2], Ryota IDE[2] , Tomoaki IKEGAMI[2], Yoichiro IWASAKI[1], Ryoichi TSUDA[1], Yoshito SONODA[1]

Tokai University (1), Kumamoto University (2)

***Abstract**. Optical Wave Microphone (OWM) is very useful to detect the sound wave without disturbing the sound field. Moreover, OWM can be used for sound field visualization by computerized tomography (CT) because the ultra small modulation by the sound field is integrated along the laser beam path. Applied voltage, current and the electrical discharge sound of coplanar DBD (Dielectric Barrier Discharge) are measured using CT-OWM, and examined the relationship between the discharge and the acoustic properties.*

Keywords: Optical Wave Microphone, computerized tomography, coplanar DBD, discharge sound

Introduction

To examine the characteristic of coplanar DBD, applied voltage, current signal, and the electrical discharge sound are measured, and investigated the relationship between the coplanar discharge and the acoustic properties. However, it's not easy to detect the sound signal in plasma reactor by the conventional condenser microphone technique [1,2]. A microphone has high sensitivity, but it disturbs the sound field to be measured and averages it over the diaphragm area. In contrast, OWM technique can realize high accuracy measurement without disturbing the sound field. This new method also has potential to diagnose plasma of the discharge during the operation because this measurement system is totally insulated. Therefore, we have continued to develop OWM system, in which sound wave is measured by an optical sensor based on a Fraunhofer diffraction effect between the sound wave and laser beam [3-5]. In addition, OWM system can be applied for the visualization of sound field by CT, because a Fraunhofer diffraction light induced by slight changes of the sound field is integrated along the laser beam path [6].

Experimental setup

Figure 1 shows the experimental setup to detect the sound signal from coplanar DBD using OWM. When the high voltage (7kV: peak to peak voltage, 10 or 30 kHz) is applied to the electrode in atmospheric pressure, the discharge and sound signal is generated. The coplanar DBD is generated ozone with the rate of approximately 15 mg/h and the main atmosphere around the sound detector is air and ozone. The discharge current is measured through a shunt resistance (50 Ω) in series with the grounded electrode. The applied voltage, discharge current and acoustic signal of coplanar discharge are stored in the digital oscilloscope (Tektronix TDS3034). The acoustic signal is measured by using both OWM and condenser microphone (Rion, UC-29, 20-100 kHz). The electrode of DBD is rotated and moved toward the direction to obtain projection data for CT analysis. The rotation step angle was set to 10 degrees and step length was set to 2 mm, respectively.

The top view and cross-section schematic diagrams of the electrodes are shown in Fig. 2. The main part of coplanar DBD is a high-purity Al_2O_3 ceramic substrate (15 mm in width, 37 mm in length, and 1.25 mm in thickness) and is also used as the dielectric. The discharge system consists of two electrodes buried under Al_2O_3 ceramic substrate. The distance between the electrodes is 220 μm. HV electrode (1.25 mm in width, 29.5 mm in length, and 10 μm in thickness) of the surface and a grounded electrode (6 mm in width, 24.5 mm in length, and 10 μm in thickness) inside the substrate are printed by a plasma spray coating method. This type device is used for ozonizer. The discharge plasma is generated on the surface.

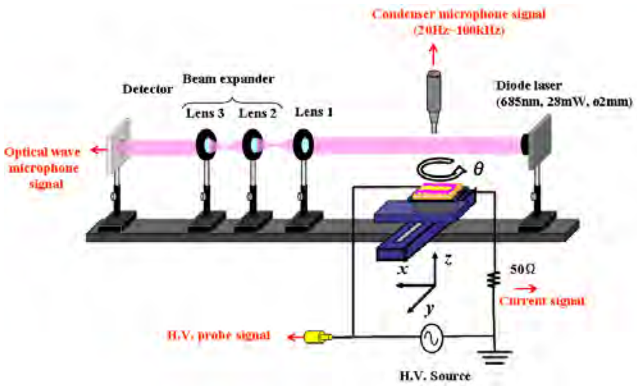

Fig. 1. Experimental setup to detect the sound of coplanar DBD using OWM-CT.

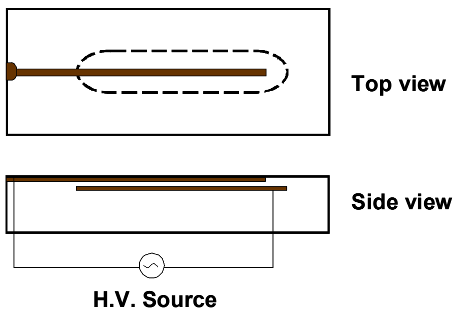

Fig. 2. Top view and cross section of electrodes module.

Results and Discussions

When the high voltage is applied to the electrodes, the discharge current appears and the discharge sound has been generated. The discharge sound is detected by OWM and condenser microphone. The distance of the laser beam and the discharge electrode is set to 2cm. Figure 3 shows the time-resolved waveforms obtained from applied voltage, discharge current that flows in resistance, OWM and condenser microphone in air. When the high voltage of 7kVp-p with the frequency of 10 kHz is applied to the electrodes, the typical DBD current wave form appears. The current of coplanar DBD is composed of two components. The first component is a displacement current due to the dielectric between both electrodes. The second component is glow type discharge current. In micro discharges, it corresponds to the drift of ions between both electrodes. During the positive half-period (or positive-going cycle) of the high voltage, there is a positive micro discharge on the side of the high-voltage electrode when a negative micro discharge occurs on the grounded electrode side. Then current pulses correspond to streamers due to the positive discharge on one side plus Trichel pulses due to the negative discharge on the other side. The signs of both positive and negative discharges are reversed during the negative half-period. It is obvious that the discharge emits the ultrasonic wave because the result obtained by the condenser microphone shows the typical wave form of compressional wave. The waveform of OWM seems to be contained high frequency components. The generation time of the discharge current and the sound signals are fairly in good agreements.

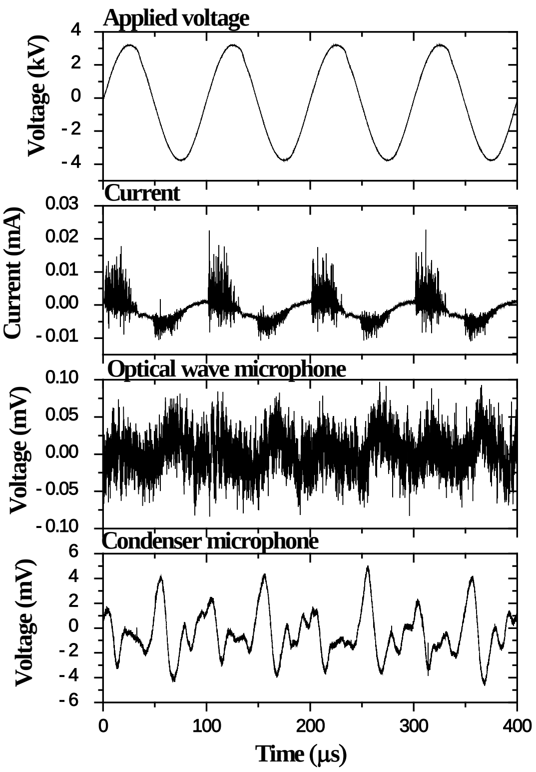

Fig. 3. Voltage waveforms obtained from high voltage probe, shunt resistance, OWM and condenser microphone. The frequency of applied voltage is 10 kHz.

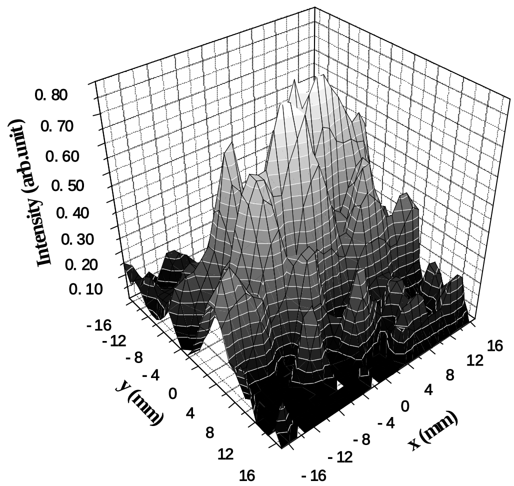

Fig. 4. Reconstructed distribution of the discharge sound in the plane at 10 kHz.

Figure 4 shows a reconstructed distribution of the discharge sound field on the $x-y$ plane. The applied voltage is 7 kVp-p and the frequency of applied voltage is 10 kHz. The proving laser of OWM is 2 cm away from the surface of coplanar electrodes. Therefore, the coordinate of z axes becomes 2cm. The dominant peak is located at $x = 1.21$ mm, $y = -3.33$ mm.

REFERENCES

[1] Nakamiya, T., Ebihara, K., Ikegami, T., Sonoda, Y., Tsuda, R. *Journal of Physics:Conf.* (2008), 100, 062016
[2] Nakamiya, T., Tanaka, T., Ebihara, K., Ikegami, T., Tsuda, R. *IEE Japan* (2004), PST-04-80, 45
[3] Evans, D.E., von Hellermann, M., Holzhauer, E. Plasma Phys. Control Fusion, (1982), 24, 819
[4] Sonoda, Y., Suetsugu, Y., Muraoka, K., Akazaki, M. Plasma Phys. Control Fusion (1983), 25, 1113
[5] Nakamiya, T., Sonoda, Y., Ikegami, T., Mitsugi, F., Ebihara, K., Tsuda, R. PRZEGLĄD ELEKTROTECHNICZNY (Electrical Review) (2009), 5, 143-146
[6] Nakamiya, T., Iwasaki, Y., Mitsugi, F.; Kozai, R.; Ikegami, T.; Sonoda, Y., Tsuda, R. J. Adv. Oxid. Technol. (2011), 14(1), 63-70.

***Authors**: prof. dr Toshiyuki Nakamiya, E-mail:nakamiya@tokai.ac.jp, prof. dr Yoichiro Iwasaki, E-mail: yiwasaki@ktmail.tokai-u.jp, prof. dr Ryoichi Tsuda, E-mail: rtsuda@ktmail.tokai-u.jp, and prof. dr Yoshito Sonoda, E-mail: ysonoda@ktmail.tokai-u.jp, Graduate School of Industrial Engineering, Tokai University, Toroku9-1-1, Kumamoto 862-8652, Japan; dr Fumiaki Mitsugi, E-mail:mitsugi@cs.kumamoto-u.ac.jp, mr Ryota Ide, E-mail: ide.r@st.cs.kumamoto-u.ac.jp,and prof. dr Tomoaki Ikegami, E-mail:ikegami@cs.kumamoto-u.ac.jp, Graduate School of Science and Technology, Kumamoto University, Kurokami 2-39-1, Kumamoto 860-0082, Japan*

Conference ELMECO–7
ELECTROMAGNETIC DEVICES AND PROCESSES IN ENVIRONMENT PROTECTION
joint with 10th Seminar AoS-10 APPLICATIONS OF SUPERCONDUCTORS
28–30.09.2011, Nałęczów, Poland

EHD FLOW MEASURED BY 2D PIV IN A NARROW ELECTROSTATIC PRECIPITATOR WITH LONGITUDINALLY-TO-FLOW WIRE ELECTRODE

Anna NIEWULIS[1], Janusz PODLIŃSKI[1], Jerzy MIZERACZYK[1,2]

Centre for Plasma and Laser Engineering, The Szewalski Institute of Fluid Flow Machinery, Polish Academy of Sciences (1), Department of Marine Electronics, Gdynia Maritime University (2)

Abstract. In this paper, results of the electrohydrodynamic (EHD) flow patterns in two narrow ESPs with longitudinally-to-flow wire electrode are presented. The influence of the ESP geometry on the EHD flow generated in the ESP was investigated. The results obtained from 2-dimensional (2D) Particle Image Velocimetry (PIV) showed similarities and differences of the particle flow in the wire-plate and wire-cylinder type ESP.

Streszczenie. *W niniejszym artykule zaprezentowano wyniki pomiarów struktur przepływu elektrohydrodynamicznego (EHD) wykonanych metodą 2D PIV w dwóch modelach wąskich elektrofiltrów z drutową elektrodą ulotową umieszczoną wzdłuż przepływu. Rezultaty badań wskazują podobieństwa i różnice w strukturach przepływu generowanych w obu typach elektrofiltrów.*

Keywords: ESP, electrostatic precipitator, EHD flow, 2D PIV.
Słowa kluczowe: elektrofiltr, przepływ elektrohydrodynamiczny, 2D PIV.

Introduction

For decades electrostatic precipitators (ESPs) have been used for dust particles collection, and presently are characterized by a high total particle collection efficiency (up to 99.9%) Therefore, several authors proposed electrostatic precipitation as an alternative control of diesel particulate emission [1-3]. However, there is a problem with submicron particles (i.e. in size range up to 1.0 µm) [3], which are less electively collected.

The precipitation of particles in the duct of an ESP depends on the dust-particle properties, electric field, space charge, particle physical parameters, electrode geometry and electrohydrodynamic (EHD) secondary flow. The interaction between the electric field and charge and the flow results in considerable turbulences of the flow [4-5], which seems to lower the fine particle collection efficiency. According to some authors [4-5], the turbulence should be reduced to improve the fine particle collection efficiency. Improving other factors, such as ESP electrode geometry or ESP operating conditions, which influence the flow patterns in ESPs, may also increase the fine particle collection efficiency. Data on the flow patterns in ESPs are essential for studying the performance of ESPs.

In this paper results of 2-dimensional (2D) Particle Image Velocimetry (PIV) measurements of the flow patterns in a narrow ESP for two electrode geometries are presented. The PIV measurements were carried out in the observation plane that is perpendicular to the ESP duct.

Experimental apparatus

The experimental apparatus used in the present work consisted of an ESP, high voltage supply and standard 2D PIV equipment for the measurement of velocity field [6].

The first ESP used in the present work was a wire-cylinder type. The ESP was a glass cylinder (300 mm × 29 mm, Fig. 2) equipped with a wire discharge electrode and two collecting cylinder-electrodes. A 0.23 mm diameter and 100 mm long stainless-steel discharge wire electrode was held in the center of the cylinder, parallel to the main flow direction. The collecting electrodes were made of stainless steel cylinder, each with a length of 100 mm and inner diameter of 25.5 mm.

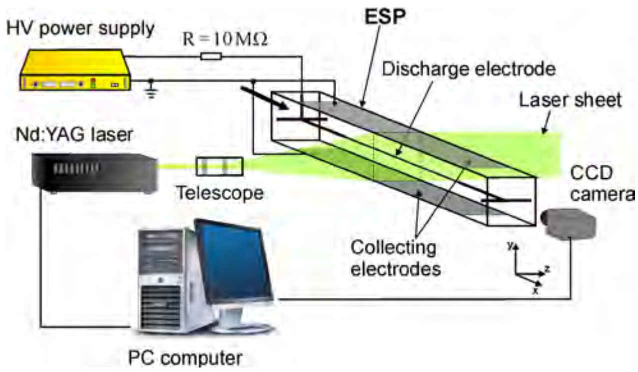

Fig. 1 Experimental set-up

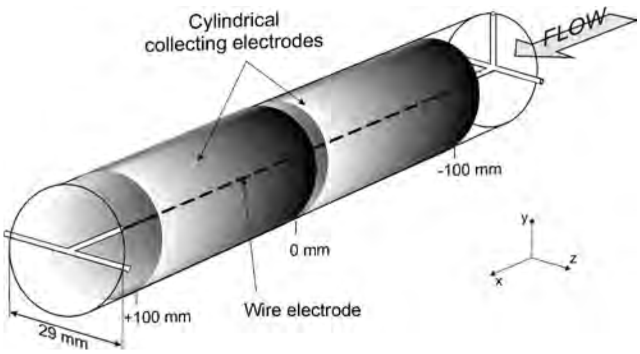

Fig. 2 Wire-cylinder type ESP

The second ESP used in the present work was a wire-plate type. The ESP was a narrow glass parallelepiped (120 mm × 30 mm × 30 mm, Fig. 3) equipped with the wire discharge electrode and four collecting plate-electrodes. The stainless-steel wire electrode (diameter of 0.23 mm, length of 100 mm) was mounted in the middle of the ESP, parallel to the main flow direction. The collecting electrodes were four plates (120 mm long and 27 mm wide, made of aluminium tape of a thickness of 50 µm glued on dielectric supporting plates) placed on all four walls of the ESP.

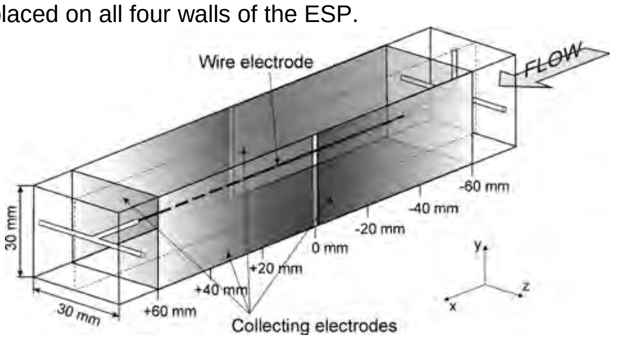

Fig. 3 Wire-plate type ESP

In both ESPs, positive voltage of 10 kV was supplied to the wire electrode through a 10 MΩ resistor. Air flow seeded with cigarette smoke was blown along the ESP duct with an average velocity of about 0.9 m/s.

The PIV measurements were carried out in the wire electrode mid-plane (i.e. at $x = 0$ mm), perpendicularly to the wire and the collecting electrodes. The velocity fields presented in this paper resulted from the averaging of 100 measurements, which means that each velocity map was time-averaged.

Results

Results of the 2D PIV measurements for all electrode geometries are shown in Figs. 4-5. They show averaged flow patterns in the mid-plane (the y-z plane) of the ESP. At the primary flow average velocity of 0.9 m/s, the Reynolds number was Re = 1460 (for the wire-cylinder type ESP) and Re = 1630 (for the wire-plate type ESP).

It is seen from Figs. 4-5 that due to the EHD forces the dust particles flow from the ESP center (i.e. from the discharge wire electrode) towards the collecting electrodes.

In the wire-cylinder type ESP (Fig. 4), the dust particles move radials towards the cylindrical collecting electrodes with migration velocity up to 0.3 m/s. The particle flow is very regular.

In the case of the wire-plate type ESP (Fig. 5), the particle flow is more disturbed. Four strong streams of the dust particles move towards plate electrodes. After reaching the plate electrode, each of four streams meets two oncoming neighboring streams which results in scattering of the streams. Small and irregular double vortex structures are formed in all corners of the ESP cross section. The migration velocity is up to 0.4 m/s, slightly higher than in the wire-cylinder type ESP.

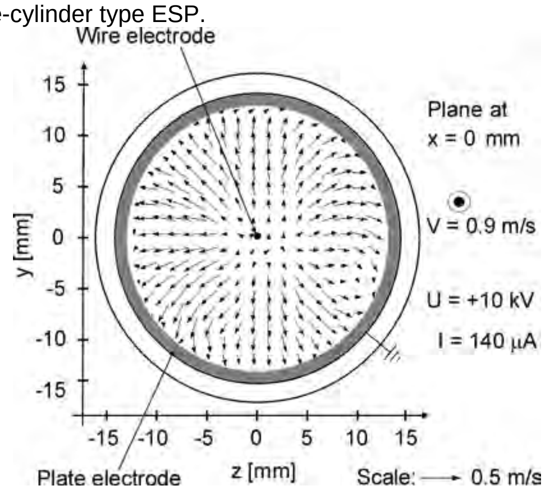

Fig. 4 Averaged flow velocity field in the wire-cylinder type ESP. Average total discharge current 140 μA. Positive voltage of 10 kV. ⦿ - show the direction of the primary flow

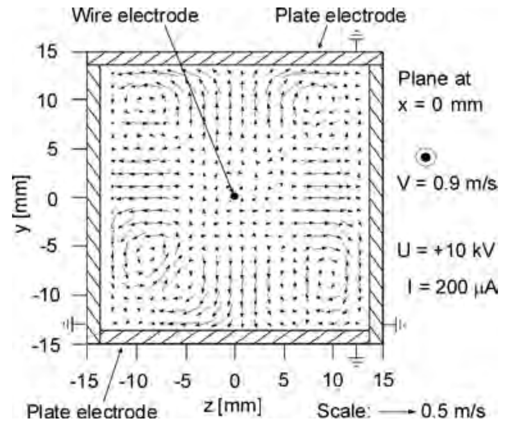

Fig. 5 Averaged flow velocity field in the wire-plate type ESP. Average total discharge current 200 μA. Positive voltage of 10 kV. ⦿ - show the direction of the primary flow

Conclusions

The presented results of 2D PIV measurements of the particle velocity fields in the narrow ESP showed that the electrode geometry significantly change the particle flow patterns. Comparing the results for both ESPs one can see, that flow patterns formed by the EHD forces in the plane perpendicular to the main flow are very different. In the wire-plate type ESP vortex structures were formed, while in the wire-cylinder type ESP instead of forming vortices the particle flow was moved radials towards the collecting electrodes.

The different flow patterns, caused by the different collecting electrode geometry, may result in different particle collection efficiency. The particle collection efficiency for both presented electrode geometries are under investigation.

ACKNOWLEDGMENT

This work was supported by the Ministry of Science and Higher Education (grant PB 281/T02/2010/70, "Iuventus Plus").

REFERENCES

[1] Zukeran A., Ikeda Y., Ehara Y., Matsuyama M., Ito T., Takahashi T., Kawakami H., Takamatsu T., Two-Stage-Type Electrostatic Precipitator Re-Entrainment Phenomena Under Diesel Flue Gases" *IEEE Trans. Ind. App.*, vol. 35, No. 2, (1999), 346-351
[2] Saiyasitpanich Ph., Keenera T. C.,.Khangb S.-J, Lua M., Removal of diesel particulate matter (DPM) in a tubular wet electrostatic precipitator, *J. Electrostatics*, vol. 65, (2007), 618–624
[3] Kittelson D.B., Reinersen J., Michalski J., Further Studies of Electrostatic Collection and Agglomeration of Diesel Particles, *SAE Paper* 910329, (1991), 145-163
[4] Atten P., McCluskey F.M.J., Lahjomri A.C., The Electrohydrodynamic Origin of Turbulence in Electrostatic Precipitators, *IEEE Trans. Ind. Appl.* vol. 23, (1987), 705-711
[5] Yamamoto T., Effects of Turbulence and Electrohydrodynamics on the Performance of Electrostatic Precipitators, *J. Electrostatics*, vol. 22, (1989), 11-22
[6] Westerweel J., Fundamentals of Digital PIV, *Meas. Sci. Tech.* vol. 8, (1997), 1379-1392

***Authors**: M.Sc. Anna Niewulis aniewulis@imp.gda.pl and Dr. Janusz Podliński janusz@imp.gda.pl,* Centre for Plasma and Laser Engineering, The Szewalski Institute of Fluid Flow Machinery, Polish Academy of Sciences, Fiszera 14, 80-952 Gdańsk; Prof. Jerzy Mizeraczyk *jmiz@imp.gda.pl,* Centre for Plasma and Laser Engineering, The Szewalski Institute of Fluid Flow Machinery, Polish Academy of Sciences, Fiszera 14, 80-952 Gdańsk and Department of Marine Electronics, Gdynia Maritime University, Morska 81-87, 81-225 Gdynia

Conference ELMECO–7
ELECTROMAGNETIC DEVICES AND PROCESSES IN ENVIRONMENT PROTECTION
joint with 10th Seminar AoS-10 APPLICATIONS OF SUPERCONDUCTORS
28–30.09.2011, Nałęczów, Poland

SYNTEZA POLA MAGNETYCZNEGO W NADPRZEWODNIKOWYM OGRANICZNIKU PRĄDOWYM

Ryszard PAŁKA

West Pomeranian University of Technology, Szczecin

Streszczenie. *W pracy rozwiązano problem właściwego wykorzystania monolitycznych nadprzewodników wysokotemperaturowych w nadprzewodnikowych ogranicznikach prądu. Dokonano syntezy rozkładu pola magnetycznego w sąsiedztwie pierścieni nadprzewodnikowych uzwojenia wtórnego. Przedyskutowano problemy dokładności i realizowalności otrzymanych rozwiązań.*

Abstract. *This paper deals with the problem of proper use of HTSC bulk material in superconducting current limiters. The task of the magnetic field synthesis in vicinity of superconducting rings of the secondary winding has been solved. The accuracy and the possibility of practical realization of obtained solutions have been discussed (**Synthesis of magnetic field in a superconducting current limiter**).*

Słowa kluczowe: nadprzewodniki wysokotemperaturowe, nadprzewodnikowe ograniczniki prądowe, synteza pola magnetycznego.
Keywords: high temperature superconductors, superconducting current limiters, synthesis of magnetic field.

Wstęp

Zadaniem ogranicznika prądu jest ochrona urządzeń elektrycznych przed skutkami zwarć w instalacji, których skutkiem są udary prądowe w sieci elektroenergetycznej. W ogranicznikach nadprzewodnikowych wykorzystuje się fakt szybkiego przejścia nadprzewodnika wysokotemperaturowego od stanu nadprzewodzącego do stanu rezystywnego na skutek przepływu prądu o natężeniu większym niż natężenie prądu krytycznego. Ze względu na sposób działania rozróżnia się dwa podstawowe typy nadprzewodnikowych ograniczników prądu: rezystancyjne i indukcyjne. W ogranicznikach obu typów można stosować zarówno kable i folie nadprzewodnikowe, polikrystaliczne struktury nadprzewodników wysokotemperaturowych, jak i monolityczne nadprzewodniki wysokotemperaturowe [1-4]. W artykule analizuje się pracę ogranicznika typu indukcyjnego z otwartym rdzeniem magnetycznym.

Synteza rozkładu gęstości prądu w ograniczniku prądowym

Rozkład pola magnetycznego w rozważanym ograniczniku indukcyjnym w stanie pracy normalnej i dla stanu rezystywnego pokazano na rys. 1. Poszczególne pierścienie nadprzewodnikowe ogranicznika znajdują się w polu magnetycznym o znacznie różniących się wartościach, co oznacza ich odmienne obciążenie elektryczne, termiczne i mechaniczne oraz prowadzi do niejednakowego i przedwczesnego ich zużycia. Celem uniknięcia tych niepożądanych efektów należy dokonać ujednorodnienia pola magnetycznego w bezpośrednim sąsiedztwie nadprzewodnika (obszar G_0 na rysunku 1a) tak, aby obie składowe pola magnetycznego miały w nim jednakową wartość. Homogenizacja pola w obszarze pierścieni nadprzewodnikowych może być dokonana przez zasilenie kolejnych sekcji cewki obwodu pierwotnego prądem o odpowiednio dobranym natężeniu (synteza rozkładu gęstości prądu w cewce) lub przez właściwe ukształtowanie formy cewki obwodu pierwotnego przy stałej gęstości prądu w uzwojeniach (synteza kształtu cewki). W pracy rozwiązano problem syntezy rozkładu gęstości prądu umożliwiający otrzymanie jednorodnego pola magnetycznego w sąsiedztwie pierścieni nadprzewodnikowych. Przeprowadzono dyskusję wyników oraz analizę realizowalności otrzymanych rozwiązań.

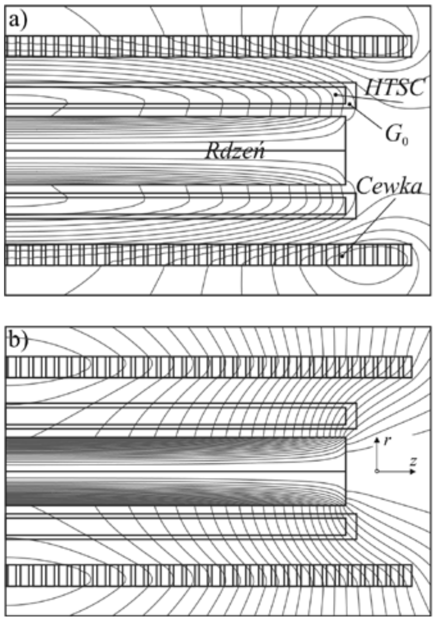

Rys.1. Rozkład pola magnetycznego w indukcyjnym ograniczniku prądowym: a) w stanie zwarcia obwodu wtórnego; b) w stanie rozwarcia obwodu wtórnego

LITERATURA

[1] Krabbes G., Fuchs G., Canders W.-R., May H., Pałka R., High Temperature Superconductor Bulk Materials, Weinheim, WILEY-VCH Verlag GmbH & Co, KGaA 2006
[2] Pałka R., Monolityczne nadprzewodniki wysokotemperaturowe. Modele makroskopowe i zastosowania, *Wydawnictwo Uczelniane Politechniki Szczecińskiej*, Szczecin 2008
[3] Janowski T. et al.: Bi-2223 and Bi-2212 Tubes for Small Fault Current Limiters. IEEE Trans. on Applied Superconductivity, June 2004, Vol. 14, No. 2, 851–854
[4] Surdacki P.: Wpływ warunków propagacji strefy rezystywnej na stabilność pracy cewki nadprzewodnikowej. Przegląd Elektrotechniczny 2004, 11, 1091–1094

Autor*: Prof. dr hab. inż. Ryszard Pałka, Katedra Elektroenergetyki i Napędów Elektrycznych, Zachodniopomorski Uniwersytet Technologiczny w Szczecinie, ul. Sikorskiego 37, 70 313 Szczecin, E-mail: rpalka@zut.edu.pl*

Conference ELMECO–7
ELECTROMAGNETIC DEVICES AND PROCESSES IN ENVIRONMENT PROTECTION
joint with 10th Seminar AoS-10 APPLICATIONS OF SUPERCONDUCTORS
28–30.09.2011, Nałęczów, Poland

NEW BULK – BULK SUPERCONDUCTING BEARING CONCEPT USING ADDITIONAL PERMANENT MAGNETS

Anup PATEL[1], Ryszard PAŁKA[2], Bartłomiej A. GŁOWACKI[1,3]

University of Cambridge (1), West Pomeranian University of Technology, Szczecin (2), Institute of Power Engineering, Warsaw (3)

***Abstract**. The paper deals with an improved concept for the superconducting (HTS) magnetic bearing. This new solution depends on the application of additional permanent magnet rings placed below the bulk superconductors connected with the rotor. Calculations and measurements of the levitation force between the magnetized HTS and a coaxial MgB_2 hollow cylinder are reviewed, proving the validity of the concept of such superconducting bearing.*

***Streszczenie**. W pracy przeanalizowano zmodyfikowaną wersję nadprzewodnikowego (HTS) łożyska magnetycznego. To nowatorskie rozwiązanie polega na zastosowaniu dodatkowych pierścieni z magnesów trwałych umieszczonych poniżej masywnych nadprzewodników wysokotemperaturowych umocowanych do wirnika. Przedstawione w pracy obliczenia oraz wyniki pomiarów sił lewitacji pomiędzy namagnesowanym HTS a cylindrem z MgB_2, potwierdzają poprawność zaproponowanego rozwiązania.*

Keywords: levitation, superconducting magnetic bearings, high temperature bulk superconductors.
Słowa kluczowe: lewitacja, nadprzewodnikowe łożyska magnetyczne, masywne nadprzewodniki wysokotemperaturowe.

Introduction

The paper deals with an improved concept for an HTS magnetic bearing [1]. The main idea of a unique bulk-bulk superconducting rotary bearing design which uses superconducting bulks on both the rotor and the stator has already been reported in [2]. According to [2] cylindrical field source bulks are stacked and magnetized with alternating polarity leading to the magnetic bearing of increased performance. This YBCO-MgB_2 bearing has been shown in Fig. 1.

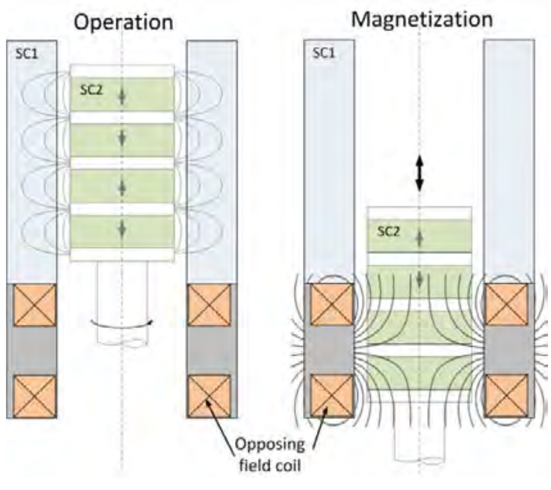

Fig.1. The bulk-bulk superconducting bearing [2]

Problem formulation

The new solution of the HTS bearing depends on the application of additional permanent magnet rings placed below the lower YBCO bulk superconductor. These rings create additional axial and radial forces in the bearing system. PM rings can boost the force for the existing bearing design by providing a 'cushion' of magnetic field for the bottom YBCO bulk. The bottom YBCO bulk can be magnetized and cooled down in the absence of the external magnetic field of the PMs (zero field cooling) and then moved towards the MgB_2-PM system causing repelling forces. This diamagnetic levitation supports the force generation within the bulk-bulk superconducting bearing. The idea of the new HTS bearing has been depicted in Fig. 2.

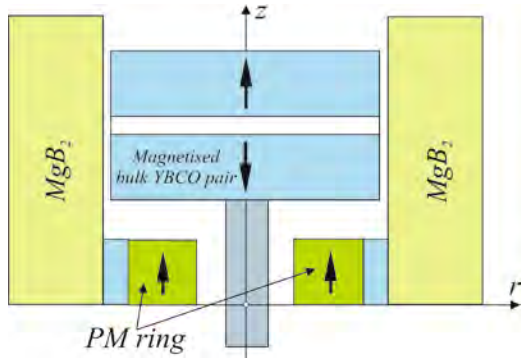

Fig.2. Fundamental structure of the novel bulk-bulk superconducting bearing using additional PM rings

The configuration from Fig. 2 could be experimentally investigated as well as modeled. Measurements of the levitation force between the magnetized HTS and a coaxial MgB_2 hollow cylinder are reviewed, proving the validity of the concept of a magnetized YBCO-MgB_2-PM bearing. The main configuration of the proposed HTS bearing can still be modified in order to obtain higher levitation forces and stiffness.

REFERENCES

[1] Krabbes G., Fuchs G., Canders W.-R., May H., Pałka R., High Temperature Superconductor Bulk Materials: Wiley-VCH, 2006
[2] Patel A., Pałka R., Głowacki B.A.: New fully superconducting bearing concept using the difference in irreversibility field of two superconducting components. *Superconductor Science and Technology* 24 (1) 015009 (2011), 1-8

***Authors**: M.Sc. Anup Patel and Prof. Bartłomiej A. Głowacki, Department of Materials Science and Metallurgy, University of Cambridge, Pembroke Street, Cambridge CB2 3QZ, UK, Email: ap604@cam.ac.uk, bag10@cam.ac.uk; Prof. Ryszard Pałka, Department of Power Systems and Electrical Drives, West Pomeranian University of Technology, Szczecin, ul. Sikorskiego 37, 70-313 Szczecin, Poland, E-mail: rpalka@zut.edu.pl.*

ATMOSPHERIC PRESSURE PLASMA JET FOR STERILIZATION PURPOSES

Joanna PAWŁAT

Institute of Electrical Engineering and Electrotechnologies, Lublin University of Technology, Poland

***Abstract**. The paper presents review of currently applied decontamination methods for medicine, biotechnology and food industry, emphasising the application of non-thermal plasmas, especially the innovative atmospheric pressure plasma jet.*

***Streszczenie.** W artykule omówiono najważniejsze metody sterylizacji dla potrzeb medycyny oraz przemysłu spożywczego i biotechnologicznego ze szczególnym uwzględnieniem metod opartych na plazmie nietermicznej w tym innowacyjną metodę wykorzystującą dysze plazmowe.*

Keywords: atmospheric pressure plasma jet, sterilization, decontamination
Słowa kluczowe: dysza plazmowa, sterylizacja, dekontaminacja

Introduction

Presently many medical wards, biotechnological facilities and food production factories struggle with persistent microbial infections caused by biofilms deposited on various inert and living surfaces e.g.:

-walls of equipment (water supplies, catheters, tubing, masks, dental units, ventilation units)
- linen, fabrics and wound dressing
-living tissues (diabetic ulcers, pressure ulcers, venous leg ulcers, recalcitrant chronic wounds)
- medical prosthetics, implants, stents
-food containers (bottles, boxes, foils)
-food itself

Biofilms are complex communities of microorganisms (bacterias, fungi, protozoa, etc.) embedded in self-secreted matrix of strongly adhesive hydrated polymers. National Institutes of Health have reported that biofilms occur in 80% of all known infections [1] causing worldwide health problem. Some studies have shown that bacteria in biofilms can be 1000-fold more resistant to antimicrobials than are planktonic cells [2].

There are many precautions and treatments implemented to avoid the risk of clinical infections, still thousands of cases appear every year affecting not only patients' and consumers' well-being, but also organizations' budgets. There is an urgent need for development of the time- and cost-effective sterilization tool, which could be safely and flexibly applied to various surfaces and materials.

Methods of decontamination

The idea of plasma sterilization was already proposed in 60-ties [3] as a good, low toxicity method for patients and operating staff. In spite of fact that the number of research papers and devices related to this topic is constantly increasing, most of the solutions were not fully implemented, mostly because of the lack of system optimization, lack of comparability between the proposed reactors and methods, lack of matching between plasma properties and sterilized material, and because of the incomplete sterilization in the case of multi-microorganisms biofilms. Therefore, industrial plasma-based decontamination is still a great challenge.

For medical sterilization several techniques have been implemented so far:

- the most popular thermal sterilization: dry and moist heat. Temperature in the autoclave is about 121°C, which cannot be applied to the heat-sensitive materials.
- membrane filters for liquid heat-sensitive components (problem with filter recycling)
- commercially used ethylene oxide sterilizers (EtO), method with many questions concerning the carcinogenic properties of the EtO residues adsorbed on the materials after processing [4] and worries about the safety of operators when opening the sterilizer before the end of the very long vent time. Because of high toxicity one cycle of EtO operating ranges from 12 to 48 h (sterilization itself- about 60 min).
- liquid formaldehyde and glutaraldehyde, not applicable to the tissues, not environmental-friendly
- costly gamma irradiation process, with many questions about the location of the operation site and damaging of the disinfected materials' surface [5]. Method is sometimes used for sterilizing selected kinds of foods.

Pulsed electric field processing (15-50 kV cm^{-1}, pulse frequency of 200-400 Hz) and high pressure method for food sterilization (300-700 MPa) [6] are currently gaining attention. However, the last one alone seems to be ineffective towards endospores. Sterilizing efficiency of ultrasonic devices is very low.

All above methods cannot be applied to the living tissues and they in the most of the cases, they require closed systems. Except the thermal one, the traditional medical sterilizers involve harmful compounds. Thus, application of plasmas seems to be reasonable solution for biological decontamination. Plasma can inactivate most of pathogens: gram negative and positive bacteria, microbial spores, molds and fungi, viruses and maybe even prions. In perspective, device might help in preventing and fighting pandemic outbreaks.

Presently, low-pressure plasma sterilizers as are commercially offered in the market [7]. However, low-pressure plasma besides the costly vacuum system shares some of the disadvantages of traditional sterilizers- it requires closed reactor and cannot be applied to the living tissues.

Many research groups concentrate on the efforts of designing plasma sterilizing device working in the ambient conditions [8-14] using variety of methods such as barrier discharge, pulsed corona reactors or plasma jets. To maintain the uniform discharge under atmospheric pressure mainly quite expensive gases as helium and argon are used in high concentrations. Plasma disinfection time given in the literature varies from several minutes to even hours.

More and more investigations concern atmospheric-pressure plasma jet (APPJ) as the compact, portable, low-temperature gas discharge plasma device for cold sterilization of various heat-sensitive surfaces and materials.

Atmospheric pressure plasma jet

Typical APPJ for decontamination purposes consists of:
- gas and liquid dosing sub-system,
- electrical discharge generating sub-system
- chemical and biological analyzing sub-system

The main part of the device is usually powered changeable needle/hollow electrode encapsulated in an insulated case. According to the literature data, stainless, acid-proof steel nozzle electrode's diameter range from 1 to 10 mm and gap range between the nozzle and grounded electrode is from 5 to 30 mm. The nozzle electrode is usually powered by a regulated (13-24 MHz) RF supply through an impedance matching network. Temperature of plasma should not exceed 70°C.

Implementing APPJ can ensure the sterile conditions for production, handling and preservation of variety of materials. APPJ device could be broadly applied at the various stages of medical and biochemical procedures, in food factories and restaurants, for various curvatures and surfaces.

Acknowledgements:
Effort sponsored by Marie Curie Grant FP7-PEOPLE-PIRG05-GA-2009-249257

REFERENCES

[1] R. Wolcott, G. Ehrlich, JAMA, 299(22), 2008, 2682-2684.
[2] T. Mah, B. Pitts, B. Pellock, G. Walker, P. Stewart, G. O'Toole, Nature 426, 2003, 306-310.
[3] W. Menashi, Treatment of surfaces, US Patent 3 383 163, 1968.
[4] V. Steelman, Aorn J. 55, 1992, 773–787.
[5] G. Henn, C. Birkinshaw, M. Buggy, E. Jones , J. Mat. Sci.(Mater. Med.) 7, 1996, 591–595.
[6] J. Wan, J. Coventry, P. Swiergon, P. Sanguansri, C. Versteeg, Trends in Food Sci.&Tech. 2009, 1-11.
[7] www.sterrad.com
[8] M. Laroussi, F. Leipold, Int. J. Mass Spectrom. 233, 2004, 81–86.
[9] M. Moisan, J. Barbeau, J. Pelletier, N. Philip, B. Saoudi, 13th CIP, 2001, 12–18.
[10] H. Ohkawa, T. Akitsu, M. Tsuji, H. Kimura, M. Kogoma, K. Fukushima, Surface and Coatings Tech., 200(20-21), 2006, 5829-5835.
[11] T. Montie, K. Kelly-Wintenberg, J.Roth, IEEE Trans Plasma Sci., 28(1), 2000, 41 – 50.
[12] M. Vleugels, G. Shama, X. Deng, E. Greenacre, T. Brocklehurst, M. Kong, IEEE Trans Plasma Sci., 33, 2005, 824–828.
[13] www.cerionx.com
[14] H. Liu, J. Chen, L. Yang, Y. Zhou, Appl.Surface Sci., 254(6), 2008, 815-1821.

***Authors**: Joanna Pawłat, PhD., E-mail: askmik@hotmail.com, Institute of Electrical Engineering and Electrotechnology Faculty of Electrical Engineering and Computer Science Lublin University of Technology, 38A Nadbystrzycka St.,20-618 Lublin, Poland.*

Conference ELMECO–7
ELECTROMAGNETIC DEVICES AND PROCESSES IN ENVIRONMENT PROTECTION
joint with 10th Seminar AoS-10 APPLICATIONS OF SUPERCONDUCTORS
28–30.09.2011, Nałęczów, Poland

REACTANTS STREAMS MIXING IN A CHEMICAL REACTOR EMPLOYING OF GLIDING DISCHARGE PRINCIPLES

Janusz PIECHNA[1], Witold SELEROWICZ[1], Teresa OPALIŃSKA[2], Małgorzata KALCZEWSKA[2]

Warsaw University of Technology (1), Tele & Radio Research Institute (2)

Abstract. *A plasma reactor employing of gliding discharge principles is one of the elements of device for waste utilization. In the reactor a process of oxidation of hydrocarbons formed during thermal decomposition of waste is carried out. An important element of the reactor is a system of nozzles introducing the reactants (oxygen and hydrocarbons) into the reactor. The reagents should be mixed only in the zone of electrical discharge. The goal of the study was designing a simple system of two coaxial nozzles for the introduction of reagents into the reactor using numerical calculations (CFC Fluent program). The nozzles should generate a stream of gases on the stoichiometric composition. The shape of the gas stream should correlate with the shape of an electrical discharge area to ensure maximum efficiency of a chemical reaction in a given experimental conditions.*

Streszczenie. *Reaktor plazmowy działający na zasadzie wyładowania poślizgowego jest jednym z elementów urządzenia do utylizacji odpadów. W reaktorze jest prowadzony proces utleniania węglowodorów powstających podczas rozkładu termicznego odpadów. Istotnym elementem reaktora jest układ dysz służący do wprowadzania reagentów (tlen i węglowodory) do reaktora. Reagenty powinny się mieszać dopiero w strefie wyładowania elektrycznego. W pracy przedstawiono wyniki obliczeń numerycznych, których celem było zaprojektowanie układu dwóch współosiowych prostych dysz dla wprowadzenia reagentów do reaktora. Dysze powinny wytworzyć strumień gazów o składzie stechiometrycznym. Kształt strumienia powinien korelować z kształtem strefy wyładowania elektrycznego dla zapewnienia największej efektywności reakcji chemicznej w danych warunkach doświadczalnych.*

Keywords: gliding discharge visualisation**,** reactants introducing into plasma reactor
Słowa kluczowe: wizualizacja wyładowania poślizgowego, wprowadzenie reagentów do reaktora plazmowego

Introduction

Reactors working on gliding discharge principles are applied to many chemical processes, such as decomposition and partial oxidation of hydrocarbons [1-3]. In a device for thermal and plasma utilization of waste the plasma reactor is applied to oxidation of hydrocarbons that are formed during a thermal decomposition of waste (mainly pyrolysis). Two streams of gases are supplied to the plasma reactor. One of them consists of a mixture of argon and hydrocarbons. This stream is hot because it flows out from a furnace in which the thermal decomposition of waste takes place. The second stream forms oxygen, which has an ambient temperature. The streams cannot be mixed before supplying them into the reactor. They should be mixed only in the plasma reactor, preferably in the moment when they are reached the discharge zone.

It was experimentally proven that in applying system of gases introduction into the plasma reactor utilizing two simple coaxial nozzles is advantageous though possessing some challenges. It is turned out that the nozzles used in experiments should be modified. A computational method was used to limit the number of experiments required to determine the best design of two coaxial nozzles system carrying out the process of hydrocarbons oxidation in plasma reactor. The calculation takes into account the fact that the gases stream entering the zone of discharge should have a stoichiometric composition. Furthermore, the shape of the stream should provide a presence of all the reactants in the zone of discharge. Then the efficiency of chemical reactions should be the highest for the given experimental conditions.

The aim of this study was to numerically determine the coaxial nozzles parameters used in introducing of oxygen and the mixture of hydrocarbons with argon into the plasma reactor.

Assumptions

In the calculations methane was assumed as a standard hydrocarbon. Calculations were performed for the following mass flow rates of gases entering the plasma reactor: methane - $4.9 \cdot 10^{-4}$ kg/s, argon - $9.8 \cdot 10^{-4}$ kg/s; oxygen - $1.9 \cdot 10^{-3}$ kg/s . The temperature of methane with argon mixture was 1100 K and the temperature of oxygen was 273 K. The mass flow rates of gases were calculated for decomposition of 1.5 kilograms of hypothetical waste containing 90% of elemental carbon. The waste completely pyrolyzed into methane. Oxygen mass flow rate was calculated taking into account the stoichiometry of reaction of methane oxidation to carbon dioxide.

On the basis of the assumed mass flow rate of gases, three configurations of nozzles were selected (Fig. 1).For chosen nozzles the numerical analysis of flows was made. Two cases of flows were analyzed. In the first case the mixture of methane and argon flowed through the central nozzle (version A and B). In the second case the oxygen flowed through the central nozzle (version C). Each configuration of flows can be used in the plasma reactor. A computer simulation of gas streams supplying the plasma reactor was performed using computational fluid dynamics commercial program (CFC) FLUENT.

Results

An arc discharge initiating the gliding discharge was formed within 2 mm from the axis of reactor. Therefore an analysis of the distribution of methane and oxygen mass fractions and mass ratio of methane to oxygen in the stream was performed. It includes not only in the axis of the reactor, but also at a distance of 2 mm from the axis of the reactor (Fig. 2 and 3).

In the axis of the reactor there is always an excess of methane for versions of nozzles A and B. In the version of nozzles C the stoichiometric ratio of methane to oxygen is achieved at a distance of 39 mm from the outlet nozzles.

The value of methane to oxygen ratio is fixed at a distance of 95 mm from the outlet nozzle (Fig. 2).

At a distance of 2 mm from the axis of the reactor there is always an excess of methane for the nozzles in versions B and C. The composition of the gas mixture that is closest to the stoichiometric condition occurs at a distance of 16.5 mm from the nozzle exit for version B as well as 38 mm for the nozzle in version C. For version A, the stoichiometric ratio of methane to oxygen occurs at a distance of 18 mm from the nozzle exit (Figure. 3).

Conclusions

Based on the results obtained, a new position of the electrodes in the reactor was designed (Fig. 4). Selecting the location of electrodes should be taken into account both the changes in gas composition and dimensions of the stream. The places where the arc was formed (the smallest electrode-electrode distance) should be placed in the vicinity of the locations where the stoichiometry composition of gases or composition of the nearest stoichiometric condition was achieved.

Based on the results of calculations the optimal version of the simple coaxial nozzles cannot be determined. Gases flowing from the nozzles according to version A form the stream, which is concentrated in a small space of reactor. As a result, significant part of the gas is introduced into the area of electrical discharge between electrodes of the reactor. However the excess of methane with reference to stoichiometric composition is observed in the stream of gases. This is not relevant from the viewpoint of chemical reaction efficiency. Gases flowing from the nozzles according to the version C are much more mixed, but a part of them flowed out the zone of electric discharge and do not react what reduced the efficiency of chemical reactions. Taking into account three versions of simple nozzles, variant A seems to be the most suitable for using it in the reactor.

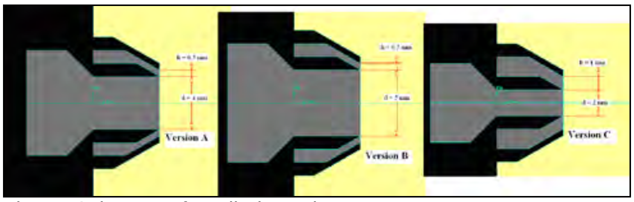

Fig. 1. Schemes of applied nozzles

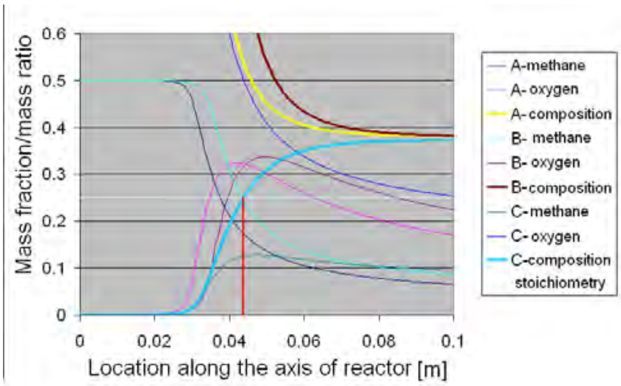

Fig.2. Distribution of oxygen and methane fraction as well as mass ratio of methane to oxygen (in legend – composition) along the axis of the reactor. The red line show the distance in which the stoichiometric composition was obtained.

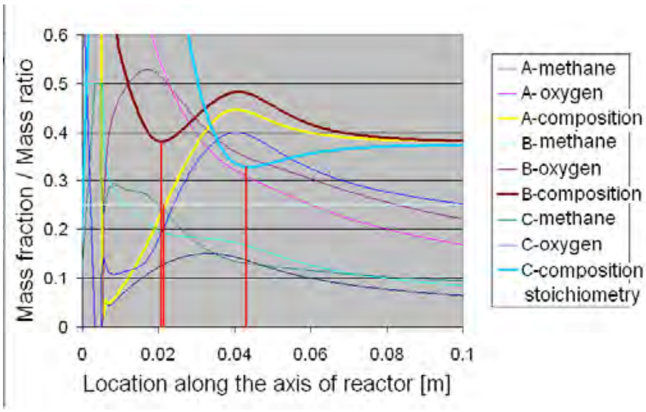

Fig. 3. Distributions of oxygen and methane fraction as well as mass ratio of methane to oxygen (in legend – composition) in the distance of 2 mm from the axis of reactor. The red line show the distance in which the stoichiometric composition was obtained.

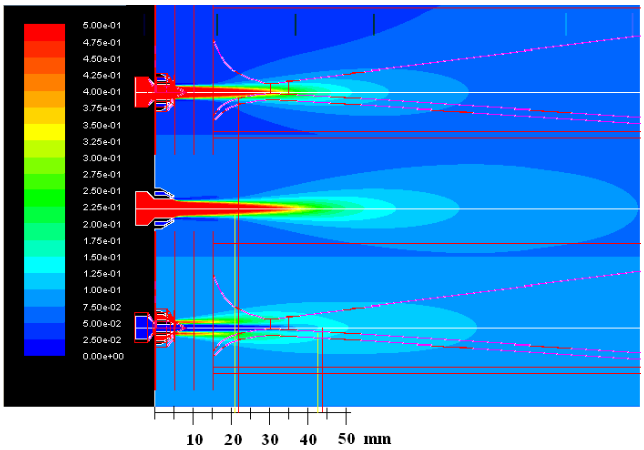

Fig. 4. The mass fraction of methane with marked contour of electrodes for nozzles in version A.B and C (seeing from the top).

Acknowledgments
Scientific work financed by the Ministry of Science and Higher Education and carried out within the frame of project N R14 0023 06/2009.

REFERENCES

[1] Kalra Ch.S., Gustol A.F., Fridman A.A., *IEEE Trans. Plasma Science*, 33 (2005), nr 1, 32-41

[2] Indarto A., Choi J-W., Lee H., Song H.K., *Energy*, 31 (2006) 2986-2995

[3] Krawczyk K., Ulejczyk B., *Plasma Chem. Plasma Process*. 23 (2003), nr 2, 265-280

Authors *dr hab. inż. Janusz Piechna, Politechnika Warszawska, Instytut Techniki Lotniczej i Mechaniki Stosowanej, ul. Nowowiejska 24, 00-665 Warszawa, E-mail: jpie@meil.pw.edu.pl, dr inż. Witold Seferowicz, Politechnika Warszawska, Instytut Techniki Lotniczej i Mechaniki Stosowanej, ul. Nowowiejska 24, 00-665 Warszawa, E-mail: seler@meil.pw.edu.pl, dr Teresa Opalińska, Instytut Tele- i Radiotechniczny, ul. Długa 44/50, 00-241 Warszawa, E-mail: teresa.opalinska@itr.org.pl, mgr inż. Małgorzata Kalczewska, Instytut Tele- i Radiotechniczny, ul. Długa 44/50, 00-241 Warszawa, E-mail: malgorzata.kalczewska@itr.org*

Conference ELMECO–7
ELECTROMAGNETIC DEVICES AND PROCESSES IN ENVIRONMENT PROTECTION
joint with 10th Seminar AoS-10 APPLICATIONS OF SUPERCONDUCTORS
28–30.09.2011, Nałęczów, Poland

THEORETICAL AND EXPERIMENTAL PARAMETERS OF GLIDING DISCHARGE MOVEMENT WITH A STREAM OF REACTANTS FLOWING THROUGH THE DISCHARGE ZONE IN A PLASMA REACTOR FOR A WASTE TREATMENT DEVICE

Janusz PIECHNA[1], Witold SELEROWICZ[1], Teresa OPALIŃSKa[2], Bogdan ULEJCZYK[1], Małgorzata KALCZEWSKA[2]

Warsaw University of Technology (1), Tele & Radio Research Institute (2)

Abstract. *A chemical reactor working on the gliding arc discharge principle is one element of a waste-utilization device. During the thermal decomposition of waste, hydrocarbons are formed. In the plasma reactor the hydrocarbons are oxidized. A set of specially-shaped nozzles is a very important element of the plasma reactor. The nozzles are used to introduce the reactants (hydrocarbons and oxygen) into the plasma reactor. The reactants should be mixed before they leave the discharge zone. The spatial parameters of electric discharge were calculated on the basis of the experimental photography of the discharge movement. The parameters of the reagent streams were calculated theoretically with the use of a commercial program, CFC FLUENT. On the basis of measurements and calculations it was found that the gliding discharge should occur in the entire stream of reactants having stoichiometric composition.*

Streszczenie. *Reaktor plazmowy działający na zasadzie wyładowania poślizgowego jest jednym z elementów urządzenia do utylizacji odpadów. W reaktorze jest prowadzony proces utleniania węglowodorów powstających podczas rozkładu termicznego odpadów. Istotnym elementem reaktora jest układ dysz służący do wprowadzania reagentów (tlen i węglowodory) do reaktora. Reagenty powinny się mieszać dopiero w strefie wyładowania elektrycznego. Parametry przestrzenne wyładowania elektrycznego obliczono na podstawie eksperymentalnej wizualizacji wyładowania poślizgowego. Parametry strumienia reagentów obliczano teoretycznie z zastosowaniem programu komputerowego (CFC) FLUENT. Na podstawie pomiarów i obliczeń stwierdzono, że wyładowanie poślizgowe powinno się generować w całej objętości strumienia reagentów o składzie stechiometrycznym.*

Keywords: gliding discharge, spatial parameters of discharge, parameters of reagent streams CFC FLUENT.
Słowa kluczowe: wyładowanie poślizgowe, przestrzenne parametry wyładowania, parametry strumienia reagentów, CFC FLUENT.

Introduction

Gliding discharge is one technique used to carry out chemical processes, mainly decomposition of contaminants and methane conversion [1-5]. A chemical reactor working on the gliding arc discharge principle is easy to construct. The simplest system contains two knife-shaped electrodes supplied with alternating current or direct current. Gaseous reactants are introduced between electrodes by an injection nozzle. The discharge is ignited where the distance between the electrodes is the shortest. After the arc ignition, the discharge is moved along the electrodes by the flowing gas and the discharge length grows. The arc elongation causes a transition from equilibrium to non-equilibrium plasmas. The equilibrium plasma exists at the initial phase of the discharge, when distance between the electrodes is short. Subsequently the plasma evolves into the non-equilibrium state as the discharge length increases. Existence of non-equilibrium states causes a high electron temperature (~1eV) [6] and a high electron density (10^{11}-10^{12} electrons/cm^3) [7]. In terms of the chemical reaction efficiency it is critical to introduce the entire stream of reactants into the discharge zone. Reactants that flow outside of the discharge zone are unable to react. For this reason, the simple two knife-shaped electrodes system is not optimal. To improve the chemical reaction efficiency other electrode configurations are considered. The following solutions have been proposed: rotary electrodes used to force the growth of the discharge length [4], wire electrodes with reverse vortex flow [6], gas insulation of the space between the reactor wall and the inter-electrode space [2], or application of three electrodes powered by 3-phase current [3].

Recently, a new chemical reactor is under development as part of a system for solid waste utilization. The reactor is used to oxidize hydrocarbons that are formed during the thermal decomposition of waste. The reactants (oxygen and hydrocarbons) are introduced into the reactor by two streams that should be mixed inside the reactor before being introduced into the discharge zone. The stream of mixed gases should have a stoichiometric composition and should flow totally through the discharge zone. To accomplish this aim, a system of two nozzles with a special shape was utilized in the reactor. To assess the correlation between a gaseous stream shape and the discharge area, photographs of the gliding discharge movement with a stream of argon mixed with oxygen were taken. The dimensions of the gliding discharge area were compared with the theoretically obtained shape of a stream of mixed gases to assess the chemical reaction efficiency.

Experimental set up

The reactor consisted of a tube, in which three electrodes of a special shape and a set of two coaxial nozzles with special shapes were placed. The reactor was supplied with high voltage (1.4 kV) at a frequency of 50 Hz. The discharge power amounted to 1.8 kW. The argon flow rate amounted to $1.0*10^{-3}$ kg/s (2.1 Nm^3/h) and the oxygen flow rate amounted to $2.8*10^{-4}$ kg/s (0.7 Nm^3/h). Argon was introduced through the central nozzle and oxygen through the gap between the central and external nozzles. The discharge zone was recorded using a high speed Photron SA 5 camera with frequency of 4000 frames per second and a single exposure time of 2.5 µs. Fig. 1 shows a schematic of the experimental set up. The shortest distance between two consecutive electrodes was 2 mm.

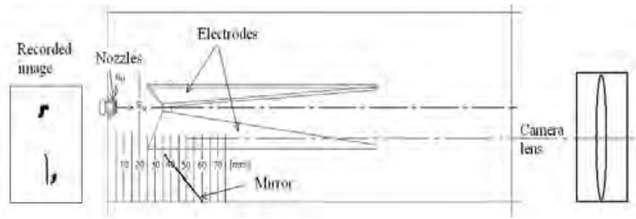

Fig. 1. Scheme of experimental set up

The shape of the electrodes facilitated the formation of the gas jet. The discharge was recorded directly by camera in a plane normal to the axis of symmetry of the reactor. A mirror placed in the reactor also allowed photography of the discharge in the gap between the sides of two neighboring electrodes (the plane parallel to the axis of symmetry of the reactor).

Results

Table 1 shows photographs of consecutive phases of the gliding discharge motion. In frames 1 - 6 the upper halves show the view of the discharge in the plane perpendicular to the axis of the reactor and the lower halves show the view of discharge in the plane parallel to the axis of reactor. In frames 7 – 12 only the plane perpendicular to the axis of reactor is shown since the discharge was too long for the mirror to cover it. The temporal distance was 1.5 ms between frames 1-11 and 0.25 ms between frames 11-12. The maximal discharge diameter occurred 11-12 ms after the discharge ignition. The estimated maximal discharge diameter was 32 mm. This diameter was obtained at a distance of 100 mm from the ignition point.

In addition to experimental results, numerical calculations of the dimensions and composition of the stream of gases leaving the nozzles were made using the computational fluid dynamics commercial program (CFC) FLUENT. In the calculations, methane was assumed as a standard hydrocarbon. Calculations were performed for the following mass flow rates of gases entering the plasma reactor: methane - $4.9*10^{-4}$ kg/s, argon - $9.8*10^{-4}$ kg/s; oxygen - $1.9*10^{-4}$ kg/s. The temperature of the methane and argon mixture was 1100 K and the temperature of the oxygen was 273 K. It was assumed that 1.5 kg of hypothetical waste, composed of 90% elemental carbon, was decomposed in the device for thermal and plasma treatment of waste. During the thermal decomposition of waste, the total quantity of carbon formed into methane. The hot stream of methane and argon was introduced into the plasma reactor by the central, mixing nozzle. The cold stream of oxygen was introduced into the plasma reactor by the external, simple nozzle. The calculations did not take into consideration a presence of electric discharge in the gas stream. Fig. 2 shows a comparison of mass ratio of methane to oxygen at distances of 2, 3 and 4 mm from the axis flow of symmetry of the reactor.

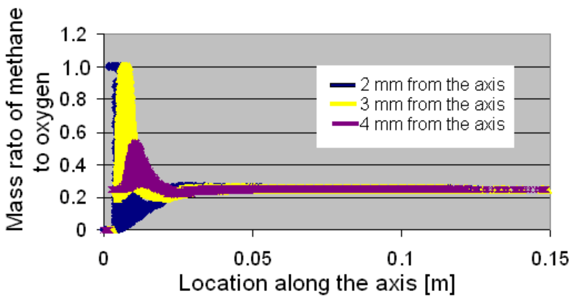

Fig. 2. The mass ratio of methane to oxygen at the distance of 2, 3 and 4 mm from the axis of symmetry of the reactor.

The mass ratio of methane to oxygen for a stoichiometric mixture is 0.26. It should be noted that the stoichiometric composition of gaseous components of the stream is reached at a distance of 15-20 mm from the nozzle outlet regardless of the distance from the axis of symmetry. The distribution of flow velocity in the stream of gases among the electrodes (Fig.3) confirms the existence of a narrow core of flow.

Conclusions

The experimental photography of gliding discharge motion showed that the maximal diameter of the gliding discharge is 32 mm at a distance of 100 mm from the ignition point. The theoretical calculations showed that the stoichiometric composition of the gaseous components of the stream (methane and oxygen) is reached at a distance of 15-20 mm from the nozzle outlet and at a distance of 4 mm from the axis of symmetry of the reactor. Additionally the distribution of flow velocity in the stream of gases among the electrodes confirms the existence of a narrow core of flow. It can be assumed that the gliding discharge should occur in the whole stream of reactants. Thus, the efficiency of the chemical reaction should be optimal for the given experimental conditions. The demonstrated set of nozzles should be useful in plasma chemical reactors for use in a device for thermal and plasma treatment of waste.

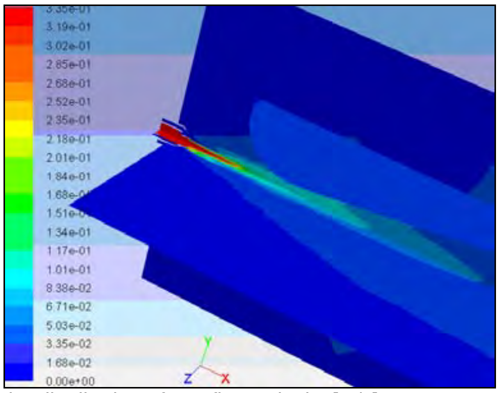
Fig. 3. The distribution of gas flow velocity [m/s].

Table 1. Photographs of consecutive phases of the gliding discharge motion (explanation in the text).

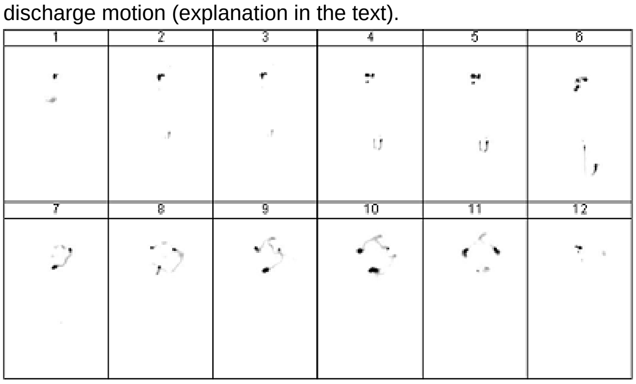

Acknowledgments

Scientific work financed by the Ministry of Science and Higher Education and carried out within the frame of project N R14 0023 06/2009.

REFERENCES

[1] Du C.M., Yan J.H., Cheron B., *Plasma Sources Sci. Technol.* 16 (2007) 791-797

[2] Krawczyk K., Młotek M., Rzepecka K., *Przem. Chem.* 82 1387-1390 (2003)

[3] Kowalska E., Opalińska T., Radomska J., Ulejczyk B., *Vacuum* 82 (2008) 1069-1074

[4] Czernichowski P., Czernichowski A., WO 00/13786 (2000)

[5] Indarto A., Choi J-W., Lee H., Song H.K., *Energy,* 31 (2006) 2986-2995

[6] Chiranjeev S.K., Gutsol A.F. , Fridman A.A., *IEEE Trans. Plasma Sci.* 33 (2005) 32-41

[7] Fridman A., Chirokov A., Gutsol A., *J. Phys. D:Appl. Phys.* 38 (2005) R1-R24

Authors *dr hab. inż. Janusz Piechna, Politechnika Warszawska, Instytut Techniki Lotniczej i Mechaniki Stosowanej, ul. Nowowiejska 24, 00-665 Warszawa, E-mail: jpie@meil.pw.edu.pl, dr inż. Witold Seferowicz, Politechnika Warszawska, Instytut Techniki Lotniczej i Mechaniki Stosowanej, ul. Nowowiejska 24, 00-665 Warszawa, E-mail: seler@meil.pw.edu.pl, dr Teresa Opalińska, Instytut Tele- i Radiotechniczny, ul. Długa 44/50, 00-241 Warszawa, E-mail: teresa.opalinska@itr.org.pl, dr inż. Bogdan Ulejczyk, Politechnika Warszawska, Wydział Chemiczny, ul. Noakowskiego 3, 00-664 Warszawa, E-mail: bulejczyk@ch.pw.edu.pl, mgr inż. Małgorzata Kalczewska, Instytut Tele- i Radiotechniczny, ul. Długa 44/50, 00-241 Warszawa, E-mail: malgorzata.kalczewska@itr.org*

EHD SECONDARY FLOW IN THE ESP WITH SPIKED ELECTRODES

Janusz PODLIŃSKI[1], Artur BERENDT[1], Jerzy MIZERACZYK[1, 2]

Instytut Maszyn Przepływowych im. Roberta Szewalskiego Polskiej Akademii Nauk (1),

Akademia Morska w Gdyni (2)

Abstract. *In this work, the results of electrohydrodynamic (EHD) secondary flow measurements in an electrostatic precipitator (ESP) with one-sided spike electrodes are presented. The EHD secondary flow was measured for one-sided spike electrodes with the spike tips directed either upstream or downstream the primary flow. The results showed different flow patterns for different spike tips positions in respect to the primary flow direction.*

Streszczenie. *W niniejszej pracy zaprezentowano wyniki pomiarów przepływu elektrohydrodynamicznego w elektrofiltrze z elektrodami ostrzowymi z ostrzami po jednej stronie. Pomiary wykonano dla elektrod skierowanych ostrzami w górę oraz w dół przepływu pierwotnego. Uzyskane wyniki prezentują odmienne struktury przepływu w elektrofiltrze dla różnych położeń elektrod ostrzowych.*

Keywords: Electrostatic precipitator, electrohydrodynamic flow, Particle Image Velocimetry method.
Słowa kluczowe: elektrofiltr, przepływ elektrohydrodynamiczny, metoda Particle Image Velocimetry.

Introduction

Electrostatic precipitators (ESPs) are widely used as dust particle collectors. They are characterized by a high total particle collection efficiency (up to 99.9%) with a low pressure drop. However, the collection efficiency of submicron dust particles is much lower [1-4]. Submicron dust particles, which can contain traces of toxic elements, float relatively long in the atmosphere and can easily penetrate into human respiratory system. Therefore, in Europe new standards for emission of fine particles (PM2.5) has been introduced by the European Parliament [5]. The existing ESPs have to be modified to meet those new standards.

One of the proposal to improve the collection efficiency of submicron particles in ESPs was to use spike discharge electrodes. Typically, electrodes with spike tips on two sides of the discharge electrode are used. However, our results of electrohydrodynamic (EHD) secondary flow measurements in an ESP with two-sided spike electrode [6] showed flow structures with pairs of vortices upstream and downstream from the spike electrode. These flow structures may result in a lower dust particle collection efficiency. Therefore we propose to use a discharge electrodes with spike tips only on one side of the discharge electrode.

In this work we present the EHD secondary flow patterns measured in the ESP with two one-sided spike electrodes (OSSEs) directed either upstream or downstream the primary flow.

Experimental set-up

The apparatus used in this experiment to EHD secondary flow measurements consisted of an ESP, a high-voltage supply, and a standard PIV equipment for the measurement of velocity fields.

The ESP housing used in this experiment was a transparent acrylic box, 1600 mm long, 200 mm wide and 100 mm high. At the top and bottom of the ESP two collecting stainless-steel plate electrodes (200 mm $\times$ 1100 mm) were placed. In the middle of the ESP two OSSEs with 12 spike tips each were mounted in the acrylic side-walls. Each OSSE was 200 mm long, 1 mm thick, 25 mm wide, and 15 mm tip-to-tip distance. The spike tips were set parallel to the plate electrodes and transversely to the primary flow direction. The discharge electrodes were mounted so that the spikes were directed either downstream or upstream the primary flow direction. The distance from the OSSEs to the plate electrodes was 50 mm. A flow homogenizer was placed at the ESP inlet.

The air flow, seeded with cigarette smoke particles, was blown along the ESP duct with an average velocity of 0.9 m/s. The high voltage was supplied to the OSSEs through a 10 MΩ resistors. The negative DC voltage applied to the OSSEs was 20 kV and the total discharge current was 135 μA.

The EHD secondary flow measurements were carried out using Particle Image Velocimetry (PIV) equipment [7]. The PIV measurements were carried out in the cross sectional plane placed along the ESP duct, perpendicularly to the plate electrodes. The measurement plane passed through the tips of the spike electrodes be present in the centre of the ESP duct. A 100 instantaneous flow velocity fields were measured, then averaged and presented in this paper, which means that presented velocity maps are time-averaged.

Results

The flow velocity field measurements were carried out in the ESP at a primary flow average velocity of 0.9 m/s. At this velocity the Reynolds number was $Re = V \times L / \nu = 5700$ (the parameters used to calculate Re were: the primary flow velocity V = 0.9 m/s, characteristic length (plate-plate distance) L = 0.1 m, and air kinematic viscosity $\nu = 1.57 \times 10^{-5}$ m^2/s).

When no voltage was applied, the flow measured in the ESP (results not presented in this paper) was laminar (corresponding to the transition region at Re > 2300).

Figures 1 and 2 show the averaged flow velocity fields measured for a negative applied voltage of 20 kV. Figure 1 shows results when the spike tips of the OSSEs were directed upstream the primary flow. At such position, the discharge from the spike tip generates a jet-like flow directed upstream the primary flow. It blocks the dusty air flow in the centre of the ESP duct and causes it to move nearer both plate electrodes.

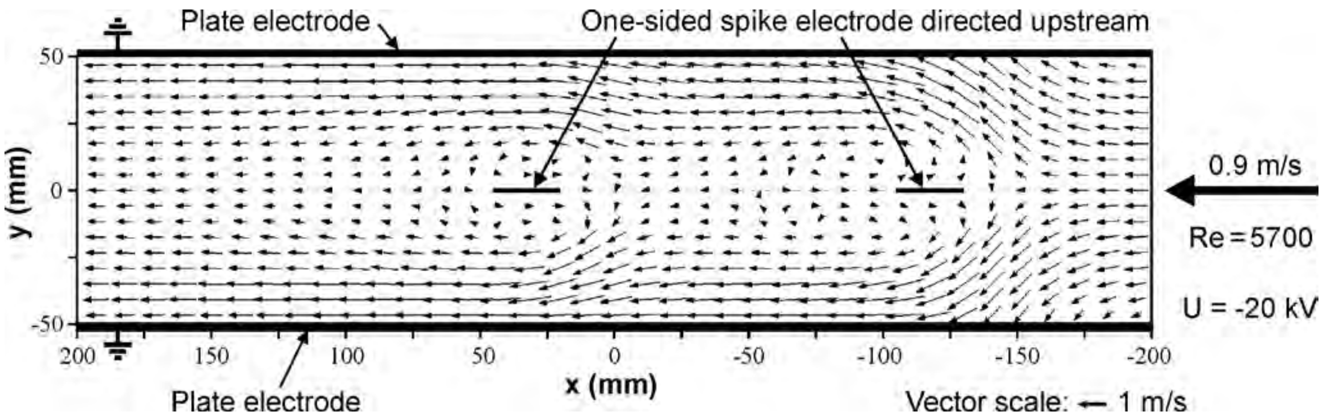

Fig. 1 Averaged flow velocity field measured in the ESP with OSSE directed upstream the primary flow. Negative voltage of 20 kV was applied, discharge current was 135 μA.

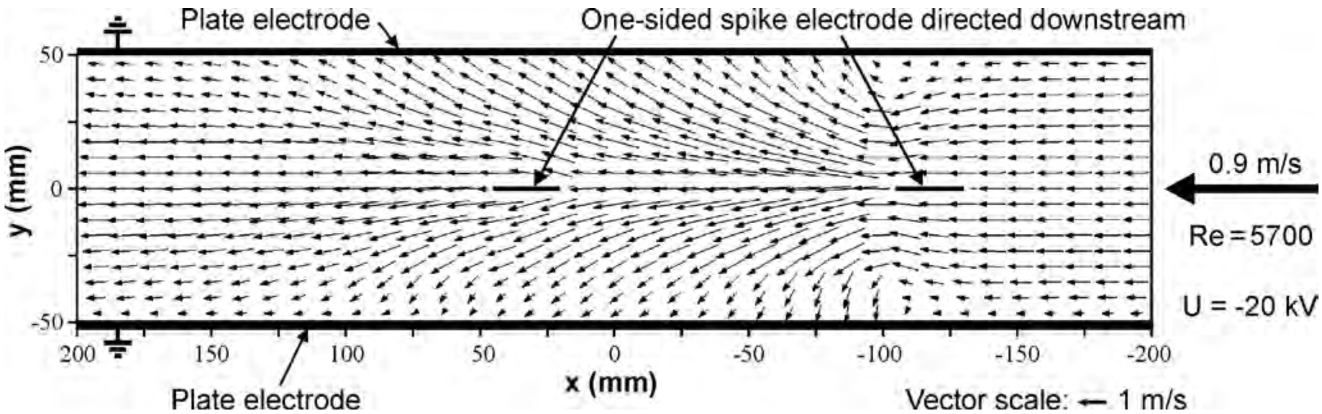

Fig. 2 Averaged flow velocity field measured in the ESP with OSSE directed downstream the primary flow. Negative voltage of 20 kV was applied, discharge current was 135 μA.

When the spike tips of the OSSEs were directed downstream the primary flow the EHD secondary flow in the ESP changed dramatically (Fig. 2). The downstream-directed jet-like flow behind the spike tips was observed. This jet flow causes the dusty air flow mainly along the centre of the ESP duct, far from the collecting plate electrodes.

Conclusions

In this paper the results of the EHD secondary flow measurements in the ESP with two OSSEs are presented. The obtained results clearly show that the EHD secondary flow pattern in the ESP strongly depends on the spike tips direction and, in consequence, on direction of the EHD flow in respect to the primary flow. The particle collection efficiency in the ESP could be dependent on the EHD secondary flow pattern.

REFERENCES

[1] M. Mohr, S. Ylatalo, N. Klippel, E.I. Kauppinen, O. Riccius and H. Burtscher, "Submicron fly ash penetration through electrostatic precipitators at two coal power plants", Aerosol Sci. Technol., Vol. 24, pp. 191-204, 1996.

[2] S.H. Kim and K.W. Lee, "Experimental study of electrostatic precipitator performance and comparison with existing theoretical prediction models", J. Electrostat., Vol. 48, pp. 3-25, 1999.

[3] U. Kogelschatz, W. Egli and E.A. Gerteisen, "Advanced computational tools for electrostatic precipitators", ABB Review, Vol. 4, pp. 33-42, 1999.

[4] A. Mizuno, "Electrostatic precipitation", IEEE Trans. Dielectr. Electr. Insul., Vol. 7, pp. 615-624, 2000.

[5] European Parliament, Council, "Directive 2008/50/EC of the European Parliament and of the council of 21 May 2008 on ambient air quality and cleaner air for Europe", Official Journal of the European Union, L 152, 11.6.2008.

[6] J. Podliński, A. Niewulis and J. Mizeraczyk, "Electrohydrodynamic flow and particle collection efficiency of a spike-plate type electrostatic precipitator", J. Electrostat., Vol. 67, pp. 99-104, 2009.

[7] M. Raffel, Ch.E. Willert and J. Kompenhans, *Particle Image Velocimetry, A practical guide*, Springer-Verlag Berlin Heidelberg, 2007.

Authors: Dr Janusz Podliński janusz@imp.gda.pl and M.Sc. Artur Berendt aberendt@imp.gda.pl, *Centre for Plasma and Laser Engineering, The Szewalski Institute of Fluid Flow Machinery, Polish Academy of Sciences, Fiszera 14, 80-952 Gdańsk; Prof. Jerzy Mizeraczyk jmiz@imp.gda.pl, Centre for Plasma and Laser Engineering, The Szewalski Institute of Fluid Flow Machinery, Polish Academy of Sciences, Fiszera 14, 80-952 Gdańsk and Department of Marine Electronics, Gdynia Maritime University, Morska 81-87, 81-225 Gdynia*

Conference ELMECO–7
ELECTROMAGNETIC DEVICES AND PROCESSES IN ENVIRONMENT PROTECTION
joint with 10th Seminar AoS-10 APPLICATIONS OF SUPERCONDUCTORS
28–30.09.2011, Nałęczów, Poland

PLASMA ARC FOR UTILIZATION OF SOILS

Grzegorz RANISZEWSKI, Zbigniew KOŁACIŃSKI, Łukasz SZYMAŃSKI

Institute of Mechatronics and Information Systems, Technical University of Lodz

***Abstract**. The paper presents the plasma arc method of solid state waste treatment. In this method high temperature of electric arc is used to melt, vaporize and decompose of wastes following to their vitrification. Due to this high temperature harmful elements are converted into a safe and a non-leachable product. The plasma arc utilization process has been described and examples of the end products have been presented. Conditions characteristic for the utilization of soils were determined.*

***Streszczenie.** W artykule przedstawiono metodę utylizacji odpadów stałych przy zastosowaniu plazmy łuku elektrycznego. W metodzie tej temperatura łuku początkowo wykorzystywana jest do stopienia odpadów prowadząc do ich witryfikacji. Dzięki wysokiej temperaturze szkodliwe substancje zamieniane są w bezpieczny produkt. Opisano proces utylizacji plazmowej. Określono warunki niezbędne do utylizacji.*

Keywords: soil treatment, plasma utilization, electric arc plasma, waste treatment
Słowa kluczowe: utylizacja plazmowa, plazma łuku elektrycznego, postępowanie z odpadami

Introduction

Nowadays soil pollution is more common for environment than in the XX century. Contaminants get through the organic matter and surface soil into the subsoil ground waters from intentional or unintentional human activity. The most problematic are contaminants from damaged containers, oil leakage from electrical apparatus or chemical weapons residues. Surrounding environment itself may increase the pollution on a relatively wide area.

The average soil composition depends upon various factors, such as geology, cultivation, or atmospheric deposition. Usually soil consists of about 45% minerals, 25% of water, 25% of air, 5% of organics. The most popular components are iron, silicon, calcium, magnesium, aluminum etc. and their oxides.

Plasma arc for treatment of soils

Due to the diversified composition of wastes there is not only one universal method of waste disposal. The management of solid waste is a major problem in many parts of the world. There are many techniques for waste treatment. One of the most popular method of waste treatment is incineration plant but presence of oxygen and low temperature leads to the formulation of more hazardous forms of wastes such as dioxins and furans.

Thermal plasma is particularly attractive for treatment of solids and liquids containing hydrocarbons. Thus it is possible to convert wastes into valuable fuel. As an effect of plasma pyrolysis at temperature above 2000 K only high-calorific gases and molted inorganic ash fraction and metals appear. Non-leachable solids – vitrificate with structure and strength of basalt - can be used as building materials. Gaseous products which contain hydrogen and oxygen can be used in methanol production or as a fuel for the electric power generator.

One of the most effective methods of soil utilization is thermal plasma waste treatment. The plasma technology offers many benefits. The utilization process can be conducted in a closed system and does not emit harmful chemicals into the environment.

The thermal plasma is a source of high energy density with temperature of a few thousand Kelvin and high ultraviolet radiation. These result in fast reaction rates, and high throughput in smaller reactors. The heat generation is independent of the chemical composition. Avoidance of dioxins and furans is guaranteed due to oxygen free environment. Moreover it is possible to select optimum chemistry for the destruction process, smelting of high melting point inorganic wastes, easy control, rapid start-up and shut down and also the treatment process is relatively flexible.

The main advantages of thermal plasma waste treatment are:

- complete pyrolysis of organic and hazardous wastes without oxygen, vitrification of inorganic toxic leftovers high temperature,
- high calorific value of gas fuel generated,
- smaller size of installation - high energy density
- minimum total gas throughput - no excess gas for combustion required,
- rapid start-up and shutdown - easy automatic control.

The average soil composition is a mixture of minerals such as Si, Al, Fe, Ca, Mg, K, N, P and their oxides. Their temperature of decomposition is much higher than the temperature in classic incinerator. We used thermodynamic program CHEMSAGE to predict variety and amount of different products after heating fly ashes in a plasma arc. Our aim is to determine temperature of total decomposition of ash. The calculation results showed that all compounds are in gas phase when the temperature reaches 4000K [1].

From waste to useful product

In Technical University of Lodz DC plasma furnace has been designed as an Immersed Arc Furnace (IAF) and applied to treat the inorganic wastes (Fig.1) [2]. The furnace is water-cooled and the transferred arc-plasma system has a maximum output power of 250 kW. In axially - symmetrical configuration of an anode - the crucible and a cathode the rod electrode the mineral feed charge files a space between them. Initially (in solid state) the feed does not conduct an electric current. Anode has a hole in its bottom, which enables flowing out of excess of gas as well as tapping of the melt (bath). A DC arc, burning in the environment formed by gaseous mineral substance was named here the gas-mineral-arc (GMA).

The idle current starts to flow following the short-circuiting of the cathode and anode. After electrodes separation to a short gap a stable arc discharge named here the idle arc is initiated using a gas matter (argon, nitrogen or air) from side of the hole. The increase of the feed temperature effects in entering to the arc evaporating mineral compounds. The arc discharge produces a gas sheath from the side of charge which is of mineral origin. The other wall of the gas sheath is a melted mineral material layer. After that the arc is elongated to allow tapping of the full charge. The immersed arc configuration as the heat source within the charge means, that almost whole (up to 98%) of energy is captured by the charge [3].

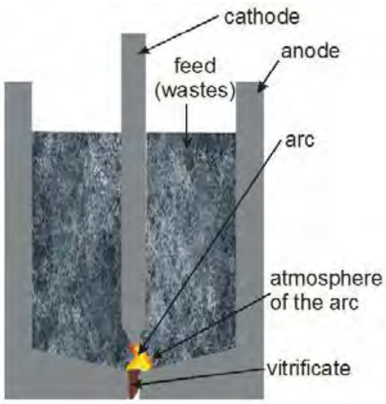

Fig.1. A model of vitrification by immersed arc plasma [4]

In this system it is possible to utilize and recycle mineral wastes in continuous way into vitrificate by electric arc generated inside the utilized material. The safe vitrificate can be formed into the ceramic tiles and can be used as a building material.

Arc-plasma burns between electrode immersed in charge and crucible The arc starts to burn in neutral gas (i.e. argon) and then melts mineral compounds and their oxides followed by their gasification, thermal decomposition, ionization and formation of the mineral arc plasma. In our research a new approach to utilization of mineral wastes using electric arc has been presented. A model of mineral arc-plasma immersed in the furnace feed charge has been elaborated for this purpose. The theory of utilization of materials by electric arc has been verified by experimental tests in the laboratory furnace. To make calculations and measurements of the arc, a small model of a large system has been constructed.

Determination of the mineral feed influence on electric arc for maximal usage of power system is associated with many equilibrium and thermodynamic parameters. In the case of completely immersed arc it burns only in mineral elements vapor and cannot be shunted by the conducting current melt. Metal arc plasma consists of atoms, ions and electrons. Argon has been used as a working gas. It was assumed that unbounded metal occurs in the argon atmosphere and that multiple ionization below 10000 K is negligible. Local thermodynamic equilibrium (LTE) has been assumed to calculate arc plasma composition. To determine electron density, atoms density, ions density system of non-linear equations have been solved. Atomic data for considered elements has been calculated by Drawin [5].

Calculations for Mg, Si, Al, Ca, Fe have been conducted for 0,5 up to 5% mineral ratio in argon plasma. For each examined compound the electron concentration mainly depends of concentration of ions of examined element. Even 1% addition of metal determine electron densities in plasma. In Figure 2 there are results of temperature and resistance measurements for electric arc in plasma arc furnace model. Calculations have been made for graphite and copper 6mm electrodes, current 20A, voltage 60V. Distance between electrodes 3mm. The arc unit volume are computed from Abel's transformation.

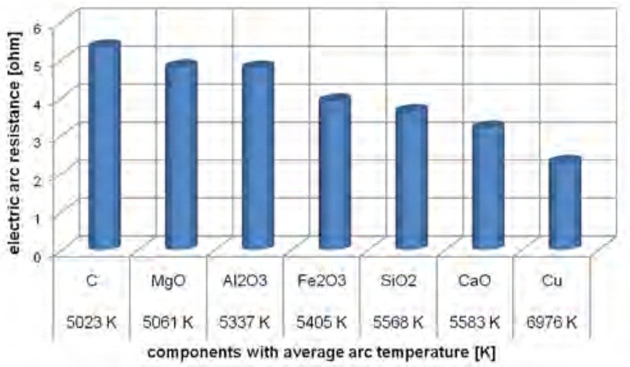

Fig.2. Arc resistance for different plasma composition

Conclusions:

The design and building of arc plasma systems for thermal treatment of materials is economically viable if its thermal efficiency is as high as possible.

The electric arc is able to decompose thermally any organic fraction and to melt an inorganic fraction of the material, what in turns leads to its vitrification in the cooling process. It is possible to utilize and recycle mineral wastes in continuous way into vitryficate by the electric arc generated inside utilized material. Electric arc stability depends on two factors: parameters of source quality and changes of resistance. Minimal addition of mineral (less than 1%) strongly changes plasma composition what results by changing plasma properties such as resistance and electrical conductivity. Electric arc plasma with atmosphere generated by waste vaporization has lower resistance of the arc channel comparing to the nitrogen or argon atmosphere. Continuity of discharge under temporary minerals concentration increase is guaranteed.

This could be a step forward to elaborate and control an effective technological vitrification process of inorganic toxic or hazardous wastes. It should considerably increase the energetic efficiency of waste treatment.

REFERENCES

[1] L. Szymański, Z. Kołaciński, G. Raniszewski: Thermal decomposition of mineral oxides treated by an immersed arc-plasma, *Czechoslovak Journal of Physics*, Vol. 56 (2006), Suppl. B1231-B1236

[2] K. Cedzynska, Z. Kołaciński: Plasma pyrolysis – a novel metod of waste destruction, *Polish Journal of Applied Chemistry*, No XLII,z. 2, (1998), pp.143-149.

[3] L. Szymański: Termiczny rozkład i utylizacja materiałów łukiem elektrycznym, PhD thesis, (2004), Techn. Univ. of Lodz.

[4] Patent nr 207745 "Piec plazmowy"

[5] H. W. Drawin *Data for plasmas in local thermodynamic equilibrium* , Gauthier-Villars, Paris 1965

***Authors**: dr inż. Grzegorz Raniszewski, e-mail: grzegorz.raniszewski@p.lodz.pl, prof. dr hab. inż. Zbigniew Kołaciński, e-mail: zbigniew @p.lodz.pl, dr inż. Łukasz Szymański, Politechnika Łódzka, Instytut Mechatroniki i Systemów Informatycznych, ul. Stefanowskiego 18/22, 90-924 Łódź, e-mail: lusyma@p.lodz.p*

Conference ELMECO–7
ELECTROMAGNETIC DEVICES AND PROCESSES IN ENVIRONMENT PROTECTION
joint with 10th Seminar AoS-10 APPLICATIONS OF SUPERCONDUCTORS
28–30.09.2011, Nałęczów, Poland

WIRELESS RAPID CHARGER OF SUPER CAPACITOR

Eiji SAKAI, Hiroshi SAKAMOTO

Sojo University

***Abstract**. The control technique that can do the wireless rapid charge of a super capacitor without depending on the relative position of the windings of the air-core transformer has been proposed. The rapid charge becomes possible because it can meet the resonance requirement at any time by controlling the switching frequency detecting the current of the switch of the inverter. Because this method can be composed on all the primary side, the circuit configuration is easy.*

Keywords: wireless power transmission, resonant technique, super capacitor, inverter.

Introduction

The energy transmission by the magnetic induction is an important technology, it contributes to making of various electric equipment cordless, it is used for the wireless electric power transmission to IC card and the IC tag, etc. , and it tries to be used for the noncontact charge of the batteries of electric vehicles. Especially, this is thought to be one of the promising technologies as a security precaution to the leak accident at rain in the electric vehicle that charges it in the outdoors. Here, the chemical cell including the lithium-ion battery is a main current as the battery for the electric vehicle. However, the super capacitor (electric double layer capacitor) with an excellent rapid charge and discharge characteristic is examined as an energy storage device. The electrical bus that makes the super capacitor a power source has already been operated in Shanghai in China. The energy density of the super capacitor is lower than that of the chemical cell. Then, when the voltage of the capacitor is decreased, the pantograph is raised and rapidly charged in the bus stop (charge point) that the passenger gets on and off. It is possible to charge rapidly always easily only by parking to the shop front or the garage by the wireless charge technology when a super capacitor is used for the electric vehicle, and it is opened from the trouble with which the plug is connected by the hand. Our group has been researching the wireless power transmission that uses the resonance technology for the half bridge inverter and the noncontact transformer [1]. However, this method has fear that the power cannot be transmitted enough by shifting from the resonance point because the leakage inductance is changed according to a relative position of the windings of the transformer. Then, this paper proposes the control scheme that changes the frequency of the inverter to solve this problem. It becomes possible to always satisfy the resonant condition with this method regardless of the relative position of the windings, and there is a possibility that a rapid charge can be done in any case.

Wireless resonant power transmission circuit

The circuit for charging of a super capacitor that uses the wireless resonant power transmission is shown in Fig. 1. The half bridge inverter is on the primary side. The super-capacitor C_{dl} is charged with the voltage doubler circuit on the secondary side. The feature of the circuit is that the capacitor C_r for the resonance and the secondary winding of the transformer are connected with the series.

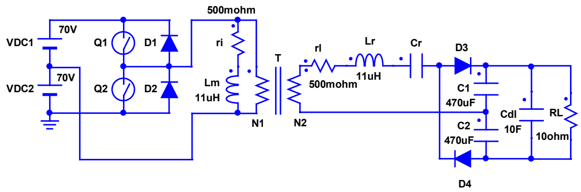

Fig.1. Wireless resonant power transmission circuit

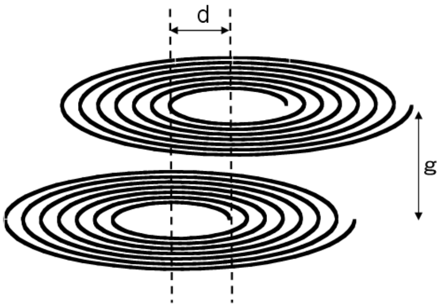

Fig.2. Air-core spiral transformer

The transformer T is expressed by the excitation inductance L_m, the leakage inductance L_r and the ideal transformer of winding N_1 and N_2 as shown in Fig. 1. T is the air-core transformer that is composed of the spiral windings as shown in Fig. 2, and the gap of the windings is g, and the distance from the center of the windings is d, respectively. Here, power transmission can be made by composing the series resonant circuit of L_r and C_r. Moreover, the switching loss can be reduced because the soft switching that uses the exciting current of the transformer can be achieved by installing the deadtime in the drive of the switch Q_1 and Q_2 of the inverter.

Experiment and simulation

In this experiment, the switching frequency of the inverter was 100kHz, the duty ratio was fixed to 50%. The winding of the transformer is N_1=N_2=17, the outer radius of each spiral was 48mm and the self inductance of each winding is 11μH. Fig. 3(a) is the experimental waveform of the current of the windings of the transformer. The upper waveform is the current of the primary winding and the lower one is that of the secondary one. The waveforms simulated by SCAT (Switching Converter Analysis Tool) [2] are shown in Fig. 3(b). Both waveforms are corresponding well. As for the current of the secondary winding, the resonating appearance is understood though the current of the primary winding has changed in most straight lines according to the excitation inductance. Fig. 4 is the experimental result that shows the relation between the resonant capacitor C_r and the time to charge with the voltage of the super capacitor of 10F from 0 to 2V. The parameters are the gap g and the distance d of the windings of the air-core transformer. It is understood from this figure that the charging time shortens extremely for specific C_r. This is because it meets the resonance requirement of the following equation.

$$f = 1/2\pi\sqrt{L_r C_r} \tag{1}$$

where: f – switching frequency of the inverter, L_r – leakage inductance, C_r – resonant capacitance.

Moreover, this figure shows that the resonance point has been shifted slightly by a relative position of the winding. This is because the leakage inductance is changed. Therefore practicably, it is necessary to devise it to satisfy the resonance condition dynamically. There are two methods to satisfy the equation (1); the one is changing C_r and the other is changing f. Here, the latter method is adopted because the former one is not practical. The extra C_r and switches are needed for changing C_r. Here, it is necessary to obtain information whether to satisfy the resonance condition to change switching frequency f. Then, we propose to detect the current of switch Q_2 on the low side of the inverter. Fig. 5 is the simulation of the averaged current of the switch Q_2 when resonant capacitance C_r is changed by SCAT. As for C_r=223nF, when it meets the resonance requirement, it is understood from this figure that the current of the switch grows, too. Therefore, the super capacitor can be charged rapidly at any time if f is changed by detecting the current of the switch of the inverter.

Conclusion

The control technique that can do the wireless rapid charge of a super capacitor without depending on the relative position of the windings of the air-core transformer has been proposed. The rapid charge becomes possible because it can meet the resonance requirement at any time by controlling the switching frequency detecting the current of the switch on the low side of the inverter. Because the control circuit can be composed on all the primary side, the circuit configuration is easy. The validity of the method has been confirmed by the simulation in this paper. The verification by the experiment is the future task.

REFERENCES

[1] H. Sakamoto et al. "Self Oscillated PWM Converter with Impulse Resonant Soft-switching," Proc. of INTELEC'03, pp.340-343, 2003.

[2] http://www.keisoku.co.jp/en/products/pw/soft/scat.html

***Authors**: prof. dr eng. Eiji Sakai, Energy Electronics Lab., Sojo Univ., 4-22-1, Ikeda, Kumamoto 860-0082, Japan, E-mail: sakai@cis.sojo-u.ac.jp; prof. dr eng. Hiroshi Sakamoto, Energy Electronics Lab., Sojo Univ., 4-22-1, Ikeda, Kumamoto 860-0082, Japan, E-mail: hiroshi@cis.sojo-u.ac.jp.*

The Correspondence address is: Eiji Sakai
e-mail: sakai@cis.sojo-u.ac.jp

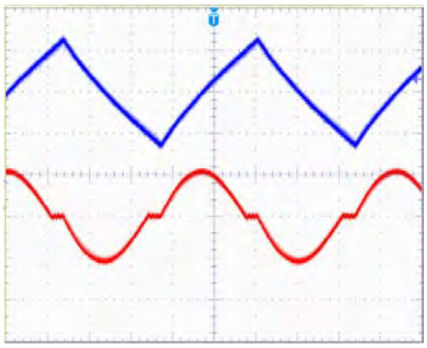

(a)

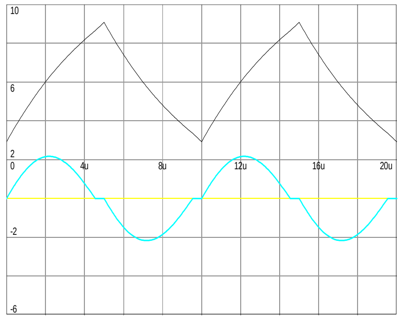

(b)

Fig.3. Waveforms of (a) Experiment and (b) Simulation (Top trace: current of primary winding (10A/div, 2μs/div); bottom trace: current of secondary winding (2A/div, 2μs/div).

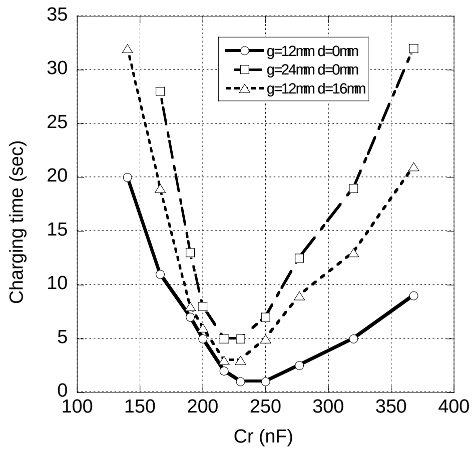

Fig.4. Charging time versus resonant capacitance (C_{dl} = 10F).

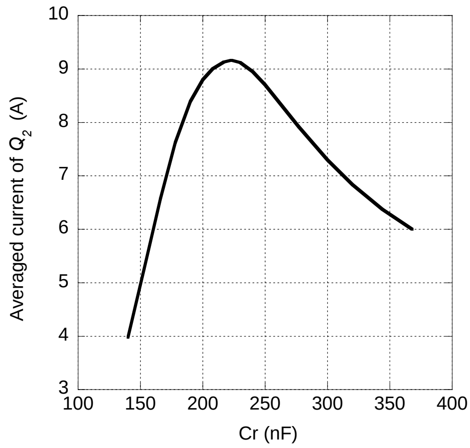

Fig.5. Simulation of the averaged current of the switch Q_2 of the inverter versus resonant capacitance in the secondary side (L_m=11μH, L_r=11μH)

DIAGNOSTICS OF INDUSTRIAL PULVERIZED COAL BURNER USING OPTICAL METHODS AND ARTIFICIAL INTELLIGENCE

Andrzej SMOLARZ, Konrad Gromaszek, Waldemar Wójcik, Piotr Popiel

Lublin University of Technology, *Department of Electronics*

Abstract*. In order to meet very stringent emission standards the modern combustion technologies require advanced diagnostic methods such as optical methods. They provide large amounts of information, but their interpretation requires the use of complex data processing techniques. The article describes a method developed by the authors and the results of the research made using 1:10 scale model.*

***Streszczenie.** Współczesne technologie spalania, aby spełnić bardzo ostre normy emisji zanieczyszczeń wymagają zaawansowanych metod diagnostyki np. z użyciem metod optycznych. Dostarczają one dużej ilości informacji lecz ich interpretacja wymaga zastosowania złożonych technik obróbki danych. W artykule opisana jest metoda opracowywana przez autorów i wyniki badań na modelu w skali 1:10.*

Keywords: diagnostics, combustion, fuzzy modelling, NOx emission.
Słowa kluczowe: diagnostyka, spalanie, modelowanie rozmyte, emisja NOx

Introduction

The premise for the exploration of new methods of diagnostics of the combustion process are the difficulties encountered during the implementation of low emission combustion technology. The combustion process is then run very close to the limit of flammability, which can cause a sharp increase in CO emission, unstable combustion and finally the flame blowout. Measurement of the majority of combustion parameters such as CO, NOx, and oxygen in the exhaust gas can be easily made by using gas analyzers, but the measurement results obtained in this way are significantly delayed and averaged over all the burners in the boiler.

The analysis of the problem let us conclude that there is a lack of method that allows measurement of output parameters of an individual burner like for example NOx or CO emission level. It is therefore necessary to use indirect methods, which could primarily include acoustic, and optical methods [1, 2]. These methods are noninvasive and can be obtained virtually not delayed and additionally spatially selective information about the combustion process. The authors put the thesis that it is also possible to obtain quantitative information on the basis of optical signals originated by a flame. In the article it is demonstrated on the example of nitrogen oxides. Due to the highly nonlinear nature of dependency and lack of an analytical model fuzzy neural networks were used for modelling of emission from turbulent flame. The paper describes the use of methods with a relatively small computational complexity. The work of the research team also includes the use of more complex methods such as Fourier, wavelet and curvelet transforms [3, 4].

Research methodology

Combustion of pulverized coal was examined through optical methods, that were based on analysis of radiation emitted by the flame. The analysis also takes into account spatial features of such radiation source. Estimation of NOx content within the flame of an individual burner based on emission spectrum analysis is possible, yet it can be hardly done in harsh, industrial conditions, especially with presence of high temperature, vibrations and dustiness. It was decided therefore to apply a different approach.

Combustion of pulverized coal in the power burner takes place in a turbulent flow. In its each point local fluctuations of both fuel and gaseous reagents concentrations, as well as temperature occur. It leads to permanent local changes in combustion process intensity, which result in continuous changes in flame luminosity that can be observed as flame flicker. As combustion process affects the turbulent movement of its products and reagents it determines the way the flame flicker parameters such as e.g. mean luminosity and luminosity frequency spectrum. A number of combustion supervision and flame-fault protection systems and use information contained within flame flicker. The multichannel fibre-optic flame monitoring system developed at Lublin University of Technology is an example solution of that kind. Detailed description of the system is presented in [5]. It allows observation of selected areas of the flame and converting the optical signal into an electric one for further processing. The system is designed to operate in industrial environment.

Experimental facility and experiments

Experiments were made on test rig located in the Institute of Power Engineering in Warsaw. It is a combustion chamber with a single pulverized coal swirl burner made in 1:10 scale in relation to a low-emission industrial burner. This object was chosen because of the ability to perform experiments with a single burner, and it's a good instrumentation. All measured and some calculated quantities – relevant to the combustion process operation – are visualized and recorded by the data acquisition system. Sampling period is 1s. The combustion chamber is equipped with a fibre optic probe allows observation of five different areas of the flame.

Voltage signals corresponding to the instantaneous brightness of the flame of the areas observed by the individual optical fibres were sampled at a rate 1KS/s and saved by a dedicated system. After completing the measurements the following parameters of these signals within one second were calculated: the average intensity value, intensity variance, number of mean value crossings and (changes of sign) of the signal derivative. Such choice of parameters was made on the basis of previous studies [6].

The dependence of these parameters on the conditions of combustion of pulverized coal is evident, but this information is not very useful from the standpoint of managing the process of combustion. Then the next step is such processing of these parameters to give information about the important parameter of the combustion process, such as the fuel / air ratio, the content a given compound in flue gases, etc. The nitrogen oxide emission was selected for further analysis.

Analysis of models based on all possible combinations of parameters would be too time-consuming. In order to preliminarily assess the suitability of specific parameters for further study the linear regression analysis was performed in order to find correlations between the parameters of the optical signal from each fibre, and nitrogen oxide emission.

None of the considered signal parameters is correlated with NOx emissions strongly enough to be used alone to determine this quantity. Weak linear correlation with the apparent dependence may also indicate that this relationship is nonlinear. Magnitude of the optical signal intensity, despite a relatively strong correlation with NOx emissions, cannot be used alone for yet another reason. The average intensity may be dependent on the status of the optical path, for example dirt causes a drop in the signal. The possibility of such a factor leads to the conclusion to use signals not dependent on the DC component of intensity, but unfortunately, they are not too strongly correlated with the quantity under consideration. So it seems that the best possible set of data to model NOx emissions is the intensity and the number of zeros of the derivative.

Neuro-fuzzy modelling

The combination of neural networks with fuzzy logic has many benefits, especially where traditional methods and solutions do not give good results or use them for specific tasks would be too time-consuming or costly. Due to the strategy of measurements the data was grouped in distinct centers so the fuzzy rules were generated by subtractive clustering.

Tests carried out using only the parameters that are independent of intensity proved too high model error, even for a large database of rules, more than 25% of the samples was burdened by an error above 10%. According to the linear regression analysis, new models were constructed using only the intensity and the number of zeros of the optical signal derivative. For 32 membership functions, the percentage of errors exceeding 10% was 1.5% and further increasing their number did not result in a significant decrease in error. In order to further reduce the number of inputs we have examined models that use the same signals from fewer fibers, but their error was significantly higher. So the impact of a high correlation of mean intensity with model output quantity is evident. A peculiarity is the fact that in the case of liquid and gaseous fuels variance (or standard deviation) of the optical signal showed a high correlation with the size of the NOx emissions [7, 8], while in the case of pulverized coal, this parameter plays a marginal role.

Conclusions and remarks

Optical signal can be used for diagnostics of an individual burner. The optical signal is the fastest and provides selective way of getting information about the quality of combustion. Its interpretation, however, poses many difficulties.

The results of the use of modern methods of obtaining information about the quality of combustion (e.g. about NOx emissions) appear to be promising. However, the accuracy and repeatability of measurements still requires further research.

The studies, described in the article, confirm that in order to obtain NOx emissions from pulverized coal burner the estimate calculated on the basis of immediate optical signals can be used instead of the delayed signals from the gas analyzers. The use of neuro-fuzzy models allows to determine emissions of nitrogen oxides with satisfactory accuracy and time, what allows application in control systems.

Preliminary research proved the influence of variations in fuel composition on the analyzed parameters. Its quantitative determination requires further studies.

The use of genetic algorithms [9, 10] should assure better exploitation of information contained in the optical signal. Preliminary results of their application indicate that they may improve the control of combustion process.

The experiment technique requires modification. The assumption of the measurement strategy was the constancy of process input and output parameters during each individual measurement. Analysis of the measurements shows that the models have the greatest error in cases where they failed to keep the variability of the emissions on a small level.

REFERENCES

[1] Dowling A.P., Stow S.R., "Acoustic analysis of gas turbine combustors", *Journal of Propulsion and Power*, vol. 19, no. 5: 751–763 (2003)

[2] Docquier N, Candel S., "Combustion control and sensors: a review", *Prog Energy Comb Sci*, 28: 107–50 (2002)

[3] Wójcik W., Kotyra A., Ławicki T., Pilek B., "Application of curvelet transform in accessing of pulverized coal combustion", *Przegląd Elektrotechniczny (Electrical Review)* Vol. 2010, No 7: 247-249, (2010)

[4] Wójcik W., Kotyra A., Komada P., Przyłucki S., Smolarz A., Golec T., "The methods of choosing the proper wavelet for analyzing the signals of the flame monitoring system", *Proceedings of SPIE, Optoelectronic and Electronic Sensor V*, Volume 5124, 2003, pp.226-231

[5] Wójcik W., Surtel W., Smolarz A., Kotyra A., Komada P., "Optical fiber system for combustion quality analysis in power boilers", Optoelectronic Information Technologies, Proceedings of SPIE, vol.4425, pp.517-522, 2001

[6] Smolarz A., Wójcik W., Kotyra A., Wojciechowski C., Komada P., "Fibre optic monitoring system", *Proceedings of SPIE on Lightguides and their applications*, vol. 4239, pp.129-132

[7] Smolarz A., Wójcik W., Ballester J., Hernandez R., Sanz A., Golec T., "Fuzzy controller for a lean premixed burner", *Przegląd Elektrotechniczny (Electrical Review),* Vol. 2010, No7: 287-289 (2010)

[8] Sanz A., Ballester J., Hernandez R., Cerecedo L.M., "Advanced monitoring of industrial burners based on fluctuating flame signals", *Fuel,* 87: 1063–1075 (2008)

[9] Wójcik W., Kalita M., Smolarz A., "The influence of evolutionary niche occurrnce on genetic controller operation in the power boiler", *Przegląd Elektrotechniczny (Electrical Review)* Vol.2008,No 3: 222-224 (2008)

[10] Wójcik W., Kalita M., Smolarz A., "The influence of selection type choice on genetic controller operation in the power boiler", *Przegląd Elektrotechniczny(Electrical Review)* Vol.2008, No 3: 225-227, (2008)

***Authors**: dr inż. Andrzej Smolarz, Lublin University of Technology, Department of Electronics, Nadbystrzycka 38A, 20-618 Lublin, Poland, e-mail: a.smolarz@pollub.pl; dr inż. Konrad Gromaszek, Lublin University of Technology, Department of Electronics, e-mail: k.gromaszek@pollub.pl; prof. dr hab. inż. Waldemar Wójcik, Lublin University of Technology, e-mail: waldemar.wojcik@pollub.pl; mgr inż. Piotr Popiel, Lublin University of Technology, Department of Electronics, e-mail: p.popiel@pollub.pl .*

OPTYMALIZACJA MIKROFALOWEGO GENERATORA PLAZMY O STRUKTURZE WSPÓŁOSIOWEJ ZASILANEGO FALOWODEM

Michał SOBAŃSKI[1], Artur BERENDT[1], Mariusz JASIŃSKI[1], Jerzy MIZERACZYK[1, 2]

Ośrodek Techniki Plazmowej i Laserowej, Instytut Maszyn Przepływowych im. Roberta Szewalskiego, Polskiej Akademii Nauk (1),
Katedra Elektroniki Morskiej, Akademia Morska w Gdyni (2)

***Abstract**. We present optimization process of energy transfer in waveguide-based, coaxial-type microwave plasma source (MPS). The MPS did not work correctly. Comsol Multiphysics software was used to numerical investigate the problem. For shorted coaxial line section length equal to 52 mm the input microwave power reflection coefficient decreased 4 times.*

***Streszczenie.** W niniejszym artykule przedstawiono wyniki optymalizacji transferu energii w mikrofalowym generatorze plazmy o strukturze współosiowej zasilanym falowodem WR 340. Do obliczeń posłużono się programem Comsol Multiphysics. Dla zwartego odcinka linii współosiowej o optymalnej długości 52 mm, minimalny stosunek mocy fali odbitej do mocy fali padającej mierzony w płaszczyźnie wejściowej prezentowanego generatora plazmy zmniejszył się czterokrotnie.*

Keywords: microwaves, microwave plasma source, microwave discharges.
Słowa kluczowe: mikrofale, mikrofalowy generator plazmy, wyładowanie mikrofalowe.

Wprowadzenie

Mikrofalowe generatory plazmy pracujące pod ciśnieniem atmosferycznym znajdują dziś zastosowanie w spektroskopii, oczyszczaniu powierzchni, produkcji nanorurek węglowych oraz sterylizacji. Ponadto znajdują zastosowanie w obróbce gazów zarówno w celu destrukcji szkodliwych dla środowiska freonów [1], jak i w produkcji wodoru poprzez reforming węglowodorów [2].

Omawiany w tym artykule generator plazmy o strukturze współosiowej pracuje na częstotliwości 2,45 GHz i jest zasilany falowodem WR 340. Wyładowanie mikrofalowe w tym generatorze plazmy powstaje pod ciśnieniem atmosferycznym.

Początkowo przedstawiony generator plazmy nie działał prawidłowo, ponieważ nie udało się w nim zainicjować i podtrzymać wyładowania mikrofalowego. Optymalizacja prezentowanego generatora plazmy polega na obliczeniu wymiarów elementów konstrukcyjnych, które zapewnią minimalny stosunek mocy fali odbitej do mocy fali padającej w płaszczyźnie wejściowej.

Aby obliczyć optymalne wymiary kluczowych elementów konstrukcyjnych omawianego generatora plazmy posłużono się modułem RF programu Comsol Multiphysics, który korzysta z metody elementów skończonych [3].

Opis generatora plazmy

Na rysunku 1 przedstawiono szkic omawianego generatora plazmy. Generator składa się z odcinka falowodu prostokątnego WR 340 z wtrąconym prostopadle do szerszego boku falowodu odcinkiem linii współosiowej. Falowód prostokątny zawiera między płaszczyzną 2-2 a płaszczyzną 4-4 metalowy blok o wysokości b - b_1, gdzie b oznacza wysokość falowodu WR 340, a b_1 wysokość szczeliny utworzonej przez blok oraz ściankę falowodu. Zastosowanie bloku zapewnia wzrost natężenia pola elektrycznego w obszarze szczeliny.

Między płaszczyzną 1-1 a płaszczyzną 2-2 wtrącono do falowodu metalowy klin o długości $\lambda_g/2$ (λ_g - długość fali w falowodzie WR 340). Generator plazmy jest zakończony ruchomym zwierakiem.

Przedstawiany generator plazmy jest zmodyfikowaną wersją generatora plazmy, pracującego także w paśmie 2,45 GHz, lecz zasilanego falowodem WR 430 [2,4]. Szerokość i wysokość ścianek falowodu WR 340 jest około 1,26 razy mniejsza niż w falowodzie WR 430. Opisywany w niniejszym artykule generator plazmy o strukturze współosiowej jest zatem mniejszy oraz lżejszy. Ponadto prezentowany generator plazmy w przeciwieństwie do poprzedniej wersji zasilanej falowodem WR 430 nie zawiera rury kwarcowej w torze współosiowym. Zamontowana wzdłuż osi wyładowania rura kwarcowa zapobiegała dostawaniu się gazu do falowodu. Przepływający gaz roboczy o bardzo wysokiej temperaturze często uszkadzał rurę kwarcową. W prezentowanym generatorze plazmy zamiast rury kwarcowej zastosowano wkładkę teflonową z centralnie wyciętym otworem o średnicy zewnętrznego przewodu linii współosiowej.

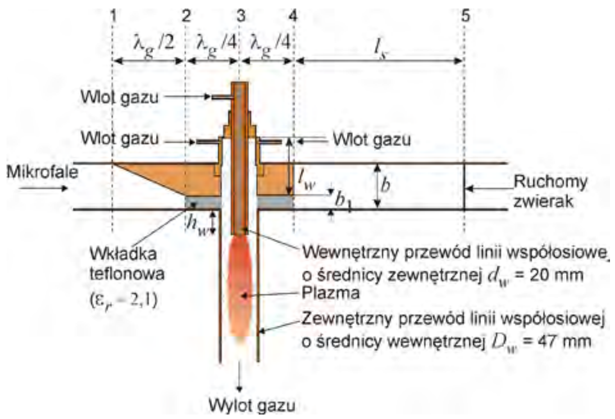

Rys. 1. Generator plazmy o strukturze współosiowej

Główne elementy konstrukcyjne to:

a = 86,4 mm, b = 43,2 mm odpowiednio szerokość oraz wysokość standardowego falowodu prostokątnego WR 340,

b_1 = 9,6 mm – wysokość falowodu o obniżonej wysokości przed optymalizacją,

λ_g = 173,4 mm – długość fali w falowodzie prostokątnym WR 340,

λ = 122,4 mm – długość fali w próżni oraz w linii współosiowej,

l_s – położenie zwieraka falowodowego,

l_w = 27 mm – długość zwartego odcinka linii współosiowej przed optymalizacją,

h_w = 19 mm – długość odcinka linii współosiowej z plazmą przed optymalizacją.

Założenia i kryteria obliczeniowe

W pierwszym etapie optymalizacji przeprowadzono analizę numeryczną układu bez obecności plazmy. Przyjęto kryterium, którym jest maksymalne natężenie pola elektrycznego w obszarze wyładowania dla szerokiego zakresu znormalizowanego położenia zwieraka falowodowego l_S / λ_g. Następnie dla obliczonych wartości parametrów konstrukcyjnych zapewniających wyżej przedstawione kryterium, przeprowadzano analizę numeryczną z plazmą w celu obliczenia charakterystyki strojenia omawianego generatora plazmy. Charakterystyka strojenia jest wskaźnikiem sprawności energetycznej i może być opisana wzorem [4]:

(1) $$\frac{P_R}{P_I}\left(\frac{l_S}{\lambda_g}\right) = \left|\frac{y_{in}-1}{y_{in}+1}\right|^2,$$

gdzie: P_R – moc fali odbitej mierzona w płaszczyźnie wejściowej 1-1 generatora plazmy, P_I – moc fali padającej w płaszczyźnie wejściowej 1-1 generatora plazmy.

Aby określić jakie parametry konstrukcyjne wpływają najbardziej na sprawność prezentowanego generatora plazmy, przeanalizowano schemat zastępczy podobnego generatora plazmy o strukturze współosiowej zasilanego falowodem WR 430 [4]. Stwierdzono, że kluczowymi parametrami konstrukcji omawianego generatora plazmy są: długość zwartego odcinka linii współosiowej l_w, wysokość falowodu o obniżonej wysokości b_1, oraz długość odcinka linii współosiowej z plazmą h_w.

Do obliczeń numerycznych w drugim etapie optymalizacji przyjęto standardowy model jednolitej plazmy zgodnie z [5], w którym znormalizowana do częstości pola ω częstość zderzeń s wynosi 0,1. Znormalizowaną do koncentracji krytycznej n_c koncentrację elektronów n przyjęto z przedziału od 10 do 200. Ponadto przyjęto, że plazma ma kształt walca o średnicy 20 mm i długości 80 mm.

Program Comsol Mulitiphysics wymaga zadeklarowania warunków brzegowych na ściankach analizowanej struktury. Do obliczeń numerycznych przyjęto, że wszystkie ścianki generatora plazmy oraz wszystkie przewody toru współosiowego są doskonale przewodzące. Mikrofale o mocy 2 kW doprowadzono w płaszczyźnie 1-1.

Wyniki optymalizacji

Wyniki analizy numerycznej pokazały, że w przypadku układu bez plazmy dla długości zwartego odcinka linii współosiowej l_w = l_{wopt} = 52 mm, natężenie pola elektrycznego w obszarze wyładowania jest równomiernie wysokie w szerokim zakresie położenia zwieraka falowodowego. W celu weryfikacji obliczeń zmodyfikowano konstrukcję omawianego generatora plazmy, zapewniając wyliczoną długość zwartego odcinka linii współosiowej l_{wopt}. Zoptymalizowany generator plazmy podtrzymywał wyładowanie a minimalny stosunek mocy fali padającej do mocy fali odbitej mierzony w płaszczyźnie wejściowej 1-1 wynosił 25 %. Charakterystykę strojenia omawianego generatora plazmy dla różnych l_w przedstawiono na rysunku 2, na którym wyniki obliczeń numerycznych porównano z wynikami pomiarów.

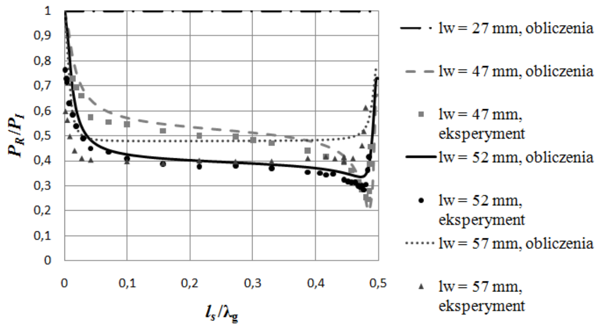

Rys. 2. Charakterystyka strojenia generatora plazmy. Porównanie obliczeń numerycznych dla s =0,1, n = 13,5 z wynikami eksperymentu. Długość linii współosiowej z plazmą h_w = 80 mm. Wysokość falowodu o obniżonej wysokości b_1 wynosi 9,6 mm

Wnioski

Uzyskano dobrą zgodność obliczeń numerycznych z wynikami eksperymentów. Dla początkowej długości zwartego odcinka linii współosiowej l_w = 27 mm, obliczony stosunek P_R / P_I wynosił 100% w całym zakresie znormalizowanego położenia zwieraka falowodowego l_S / λ_g. Potwierdza to fakt, iż początkowo omawiany generator plazmy nie pracował prawidłowo. Obliczona długość l_{wopt} = 52 mm zapewnia równomiernie niski stosunek P_R / P_I w szerokim zakresie znormalizowanego położenia zwieraka falowodowego l_S / λ_g.

Badania zostały zrealizowane w ramach projektu rozwojowego NCBiR NR14-0091-10 /2010.

LITERATURA

[1] Jasiński M., Dors M., Mizeraczyk J., Destruction of Freon HFC-134a Using a Nozzleless Microwave Plasma Source, Plasma Chemistry and Plasma Processing 29,209,pp. 363-372.

[2] Jasiński M., Dors M., Nowakowska H., Mizeraczyk J., Hydrogen Production via Methane Reforming using various Microwave Plasma Sources, *Chem. Listy 99*, 1234-2345 (2008)

[3] Strona internetowa: www.comsol.com

[4] Sobański M., Izdebski T., Lubański M., Jasiński M., Mizeraczyk J., Equivalent Circuit and Electrodynamic Characteristics of Waveguide-Based Coaxial-Type Microwave Plasma Source, 7th International Conference NEET, Zakopane, Poland, 2011.

[5] Nowakowska H., Jasiński M., Mizeraczyk J., Electric Field Distribution and Energy Transfer in Waveguide-Based Axial-Type Microwave Plasma Source, Proceedings of Comsol Conference, Hannover 2008.

***Autorzy**: mgr inż. Michał Sobański, mgr inż. Artur Berendt, dr inż. Mariusz Jasiński, prof. dr hab. inż. Jerzy Mizeraczyk, Polska Akademia Nauk, Instytut Maszyn Przepływowych im. Roberta Szewalskiego, Ośrodek Techniki Plazmowej i Laserowej, ul.Fiszera 14, 80-952 Gdańsk,*
E-mail: msobanski@imp.gda.pl, mj@imp.gda.pl, jmiz@imp.gda.pl

Conference ELMECO–7
ELECTROMAGNETIC DEVICES AND PROCESSES IN ENVIRONMENT PROTECTION
joint with 10th Seminar AoS-10 APPLICATIONS OF SUPERCONDUCTORS
28–30.09.2011, Nałęczów, Poland

REFORMING OF ETHANOL IN PLASMA-LIQUID SYSTEM TORNADO TYPE WITH THE ADDITION OF CO_2

Ol. SOLOMENKO, V. CHERNYAK, O. NEDYBALIUK

Kyiv National Taras Shevchenko University,
Faculty of Radiophysics, department of Fiscal Electronics, Kyiv, Ukraine

Technologies with using syngas are very relevant today. Synthesis gas (or “syngas”), is a mixture of carbon monoxide and hydrogen, it is an important intermediate for various synthesizing chemicals and environmentally clean fuels, such as ammonia, methanol (MeOH), acetic acid, methyl formate, dimethyl ether (DME), synthetic gasoline, and diesel [1] or nanomaterials. Generally, it is required for various H2/CO ratios of syngas to synthesize different products. For example, H2/CO ratio of 2/1 is needed to synthesize methanol, and 1/1 one to synthesize acetic acid or methyl formate. Also, it is known, that the addition of syngas to fuels improves the efficiency of its combustion: less time, triggering the rapid spread of the combustion wave, the stabilization of combustion, more complete combustion of the mixture and decreases the amount of hazardous emissions (NOx).

Synthesis gas can be produced from coal, petroleum coke, natural gas, biomass and even from organic wastes. The most promising is obtaining syngas from renewable hydrocarbon sources nowadays. Various types of discharges for reforming syngas: corona discharge, dielectric barrier discharge (DBD), microwave discharge, atmospheric pressure glow discharge (APGD), gliding arc discharge extensively studied. Of particular interest in reforming of liquid hydrocarbons constitute discharge that does not require an additional gasification, such as tornado discharge with liquid electrode (TD LE) [2] (Fig. 1).

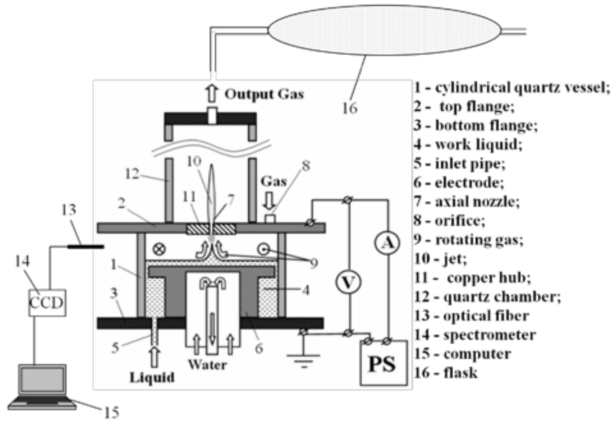

Fig. 1: Plasma-liquid system with reverse vortex gas flow (TORNADO LE)

Adding CO_2 in the reforming system for change and management H_2/CO ratios of syngas is the standard approach. CO_2 was used as a working gas, distillate and ethanol – as a working liquid in this work. The gas flow was changing in range of 110-220 cm^3. The discharge current was changing in the range 260-340 mA. Adding NaOH to the working liquid leads to the stabilization of the discharge. The sign of the differential resistance become negative in these conditions (Fig. 2). Emission spectra of the plasma between the electrodes were investigated. Emission spectra of investigated plasma are multicomponent and contain intensive OH bands, C_2 bands, atomic lines O, H, C, Na (Fig. 3).

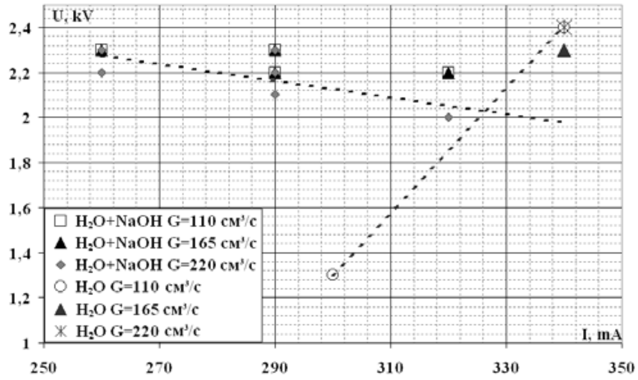

Fig. 2: Current-voltage characteristics

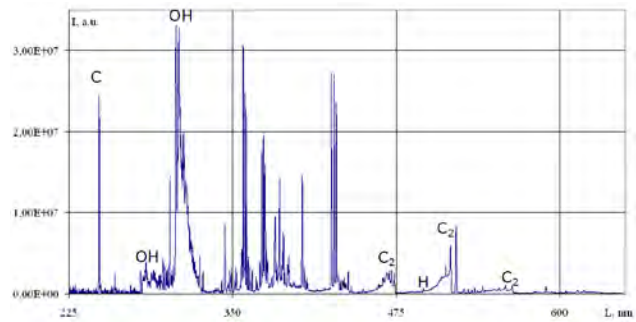

Fig. 3: Typical emission spectrum in case $C_2H_5OH+NaOH+CO_2$

It was found that in case then distillate is a working liquid temperatures T^*_e ~ 3800 K, T^*_r ~ 4000 K, T^*_v ~ 4500 K and it is constant. In case then ethanol is a working liquid temperatures are T^*_r ~ 3000 K, T^*_v ~ 4500 K.

Conclusions

- Adding NaOH ($NaOH/H_2O=1/10^4$) to the working liquid leads to the stabilization of the discharge. The sign of the differential resistance become negative in these conditions.
- Emission spectra of investigated plasma are multicomponent and contain intensive OH bands, C_2 bands, atomic lines O, H, C, Na.
- It was found that in case then distillate is a working liquid temperatures T^*_e ~ 3800 K, T^*_r ~ 4000 K, T^*_v ~ 4500 K and it is constant.
- In case then ethanol is a working liquid temperatures are T^*_r ~ 3000 K, T^*_v ~ 4500 K.

REFERENCES

[1] Xumei Tao, Meigui Bai, Xiang Li, Huali Long, Shuyong Shang, Yongxiang Yin, Xiaoyan Dai, CH_4-CO_2 reforming by plasma – challenges and opportunities, Progressin Energy and Combustion Science XXX. (2010).

[2] O.A. Nedybaliuk, V.Ya. Chernyak, S.V. Olszewski, Plasma-liquid system with reverse vortex flow of “tornado” type (Tornado-LE), Problems of atomic science and technology, № 6. Series: Plasma Physics (16), p. 135-137. (2010).

Authors:

Ol. Solomenko, V. Chernyak, O. Nedybaliuk Kyiv National Taras Shevchenko University, Faculty of Radiophysics, department of Fiscal Electronics, Kyiv, Ukraine *e-mail: elanka@ukr.net*

FEM MODELLING OF QUENCH PROPAGATION IN BISCCO TAPE

Mariusz STĘPIEŃ, Bogusław GRZESIK

Silesian University of Technology

Abstract. *Analysis of quench phenomenon in HTS tape using ANSYS software is aim of the paper. Superconducting tape is supplied by sinusoidal current pulse and voltage response is calculated by FEM. Computational model was constructed based on results of measurements as a part of inverse analysis. Results of calculations are important to determine critical current of superconducting wire in different operational conditions, especially in high power applications like transformers or electrical machines.*

Streszczenie. *Przedmiotem artykułu jest analiza zjawiska quenchu w taśmie nadprzewodnikowej realizowana przy użyciu oprogramowania ANSYS. Taśma nadprzewodnikowa zasilana jest sinusoidalnym pulsem prądu dla której obliczana jest na podstawie analizy MES odpowiedź napięciowa. Model komputerowy jest zbudowany w oparciu o wyniki pomiarów jako element analizy odwrotnej. Wyniki obliczeń są istotne do wyznaczenia prądu krytycznego nadprzewodnika w różnych warunkach pracy, w szczególności w aplikacjach mocy takich jak transformatory lub maszyny elektryczne.*

Keywords: quench modelling, FEM computations, HTS superconductor, inverse analysis.
Słowa kluczowe: modelowanie quenchu, analiza MES, nadprzewodnik HTS, analiza odwrotna.

Introduction

Development of HTS wires needs detailed analysis of superconducting wire structure in respect of multiple criteria. One of the most important criterion is sensitivity of superconducting wire on quench phenomenon. Because of rapid and destructive character of quench it is very important to design wire possibly quench protected. Many works is devoted to quench analysis in both low and high temperature superconductors [1]. Very useful tool to aid wire construction process is analysis based on FEM. Because of nonlinearity and interdisciplinary (electrical and thermal) approach of analysis it needs relatively high computing power. Because of this reason the most often 2D models are developed to carry out calculations [2].

Authors of this paper propose to calculate quench behaviour using 2D planar model of BiSCCO tape in ANSYS software. Assuming, that quench propagation along HTS tape is faster than propagation across cross-section of wire planar model of cross-section of tape is proper to quench analysis. Coupled electrical-thermal model was developed to calculate current distribution in HTS wire due to temperature and temperature. Direct multifield analysis allow to take into account mutual interaction between current and temperature (heat generation). Proposed model is simplified one because of introduced material properties of wire. In practice resistivity of filaments depends on three parameters (critical one), namely current density, temperature and magnetic flux. Calculations carried out in this works takes into account only temperature dependence. Analysis with current density dependence will be taken into account in future works.

Results presented in the paper are calculated using example wire geometry. Geometry of filaments structure in HTS wire changes and detailed and quantitative results should be calculated to given structure. Presented here results are example and qualitative representation of calculations. They are enough portion of information to characterize superconducting wire. The characterization is given by distribution of temperature, distribution of current density and by voltage drop across the wire.

Geometry of wire and model assumptions

Analysis of quench propagation is carried out using 2D model of 1G BiSCCO tape. The High Current Density American Superconductors wire was selected to prepare model geometry. Structure of selected wire is shown in Fig. 1. One can observe cross-section plane to create 2D model (b-c plane). The thickness of the wire is 0.25 mm, width of wire (depth of 2D model) is 4 mm and length of wire is infinite (0.3 mm is modelled). Geometry of computational model is shown in Fig. 2.

Fig.1. Cross-section of HTS tape

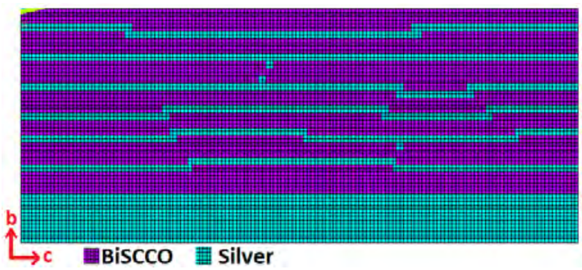

Fig.2. Geometry of computational model with mesh

Direct coupled electrical-thermal model was built using ANSYS PLANE223 finite element and results were calculated using nonlinear material parameters in time range from 0 to 7 minutes with integral step 10 microseconds. Calculations were carried out at given constant DC current applied to the wire in c direction.

Analysis of quench propagation

Presented in this section results are calculated at load current of 180 A. This load is below critical current (Ic=200 A) but it generates quench because of thermal overheating. Wall temperature of wire versus time is shown in Fig. 3. Narrow range of time where quench occurs is shown in Fig.4. It show what happened where temperature exceed safety region. The curve shown in Fig. 3 looks like discontinuous or sharply changed. Zoom shows, that temperature changes smoothly.

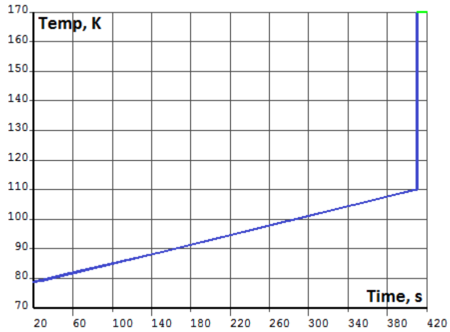

Fig.3. Temperature of wire vs. time in full range of calculations

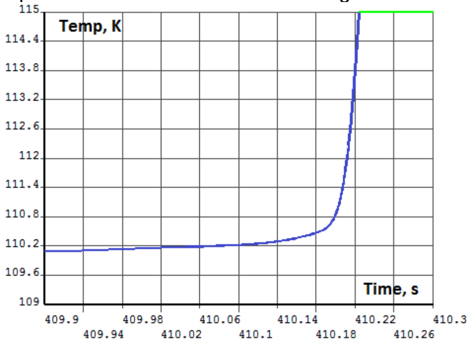

Fig.4. Temperature of wire vs. time during the quench

During the quench current flowing in wire changes its path. It results from huge change of resistivity vs. temperature. Below the quench resistivity of superconductor is significantly lower than resistivity of silver. After the quench resistivity of superconductor increases strongly. Current distribution before the quench, during (mixed state) and after it is shown in Fig. 5.

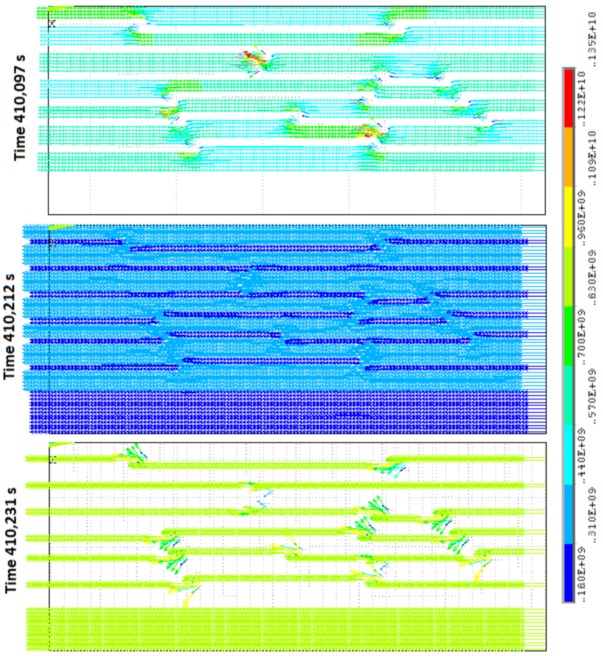

Fig.5. Current distribution before, during and after the quench

Before the quench current flows in the BiSCCO filaments. Because of filament discontinuities power losses are generated in silver matrix. After the quench resistivity of BiSCCO increases and current changes its path to silver. Because of constant value of current power losses increases strongly after the quench. Distribution of power losses (Joule heat) in HTS wire is shown in Fig 6 and Fig 7.

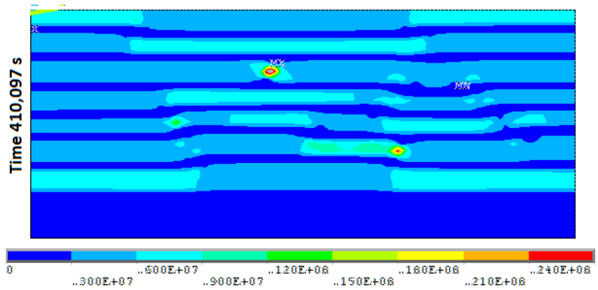

Fig.6. Joule heat distribution before the quench

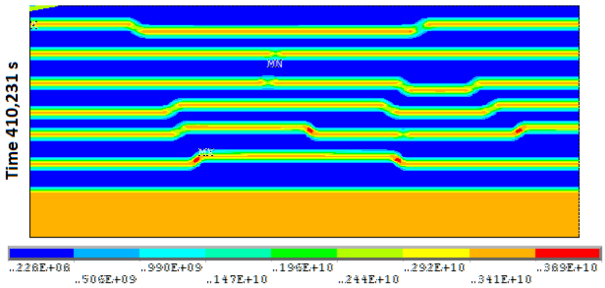

Fig.7. Joule heat generation after the quench

Presented here model of HTS wire during the quench can be verified by measurements. Only one value possible to be measured is voltage drop along the wire. Calculated voltage drop is shown in Fig 8. It will be compared to measured one in future works.

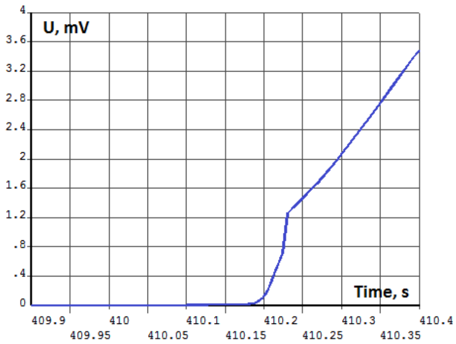

Fig.8. Voltage drop along the wire during the quench

Conclusions

- Presented calculations were carried out to describe in details process of quench generation in BiSCCO tape.
- Nonlinear FEM analysis allows to calculate currents, temperature and voltage drop as a function of time.
- Quench analysis shows its dynamics and energy.
- Proper measurements allows to compare results of calculations with results of laboratory tests.

REFERENCES

[1] Gros D.A., Quench propagation analysis in large solenoidal magnets, *IEEE Transactions on Magnetics*, Vol. 24, No 2, 1988, 1190-1193

[2] Roy F., Dutoit B., Grilli F., Sirois F., Magneto-thermal Finite element modeling of 2nd generation HTS for FCL design purposes, *Journal of Physics, Conf. Ser., 97 (2008) 012286*

Authors: *dr inż. Mariusz Stępień, dr hab. inż. Bogusław Grzesik, prof. Pol. Śl., Politechnika Śląska, Katedra Energoelektroniki, Napędu Elektrycznego i Robotyki, ul. Krzywoustego 2, 44-100 Gliwice,* Mariusz.Stepien@polsl.pl, Boguslaw.Grzesik@polsl.pl

Conference ELMECO–7
ELECTROMAGNETIC DEVICES AND PROCESSES IN ENVIRONMENT PROTECTION
joint with 10th Seminar AoS-10 APPLICATIONS OF SUPERCONDUCTORS
28–30.09.2011, Nałęczów, Poland

WPŁYW IMPULSU ZABURZAJĄCEGO NA PARAMETRY ZANIKANIA NADPRZEWODZENIA W PRZEWODZIE NADPRZEWODNIKOWYM MgB_2/Cu

Paweł SURDACKI

Lublin University of Technology, Institute of Electrical Engineering and Electrotechnologies

Streszczenie. *W pracy wykorzystano model komputerowy termicznych stanów dynamicznych zanikania nadprzewodzenia w kompozytowym przewodzie nadprzewodnikowym z dwuborku magnezu MgB_2/Cu do określenia wpływu parametrów impulsu zaburzającego: energii, czasu trwania i długości wzdłuż przewodu na wybrane parametry procesu zanikania nadprzewodzenia: minimalną energię utraty nadprzewodzenia, temperaturę zaburzenia, temperatury utraty nadprzewodzenia i czas utraty nadprzewodzenia.*

Abstract. *In this paper, the computational model of the thermal dynamic processes of quench in the composite superconducting wire MgB_2/Cu has been adopted to determine the disturbance pulse parameters (energy, pulse duration and pulse length) influence on some parameters of the process: minimum quench energy, disturbance temperature, quench temperature and quench time.*
(Influence of disturbance pulse on the quench parameters in the superconducting wire MgB_2)*.*

Słowa kluczowe: przewód nadprzewodnikowy, dwuborek magnezu, impuls zaburzający, parametry zanikania nadprzewodzenia.
Keywords: superconducting wire, magnesium diboride, disturbance pulse. quench parameters.

Wstęp

Praca przewodów kompozytowych z włókien MgB_2/Cu stabilizowanych miedzią przy gęstościach prądu zbliżonych do gęstości prądu krytycznego wymaga zapewnienia stabilności termicznej wobec lokalnych zaburzeń energetycznych. Mogą one wywołać niekontrolowaną lawinową utratę nadprzewodzenia prowadzącą do przegrzania i zniszczenia przewodu, jak też całego uzwojenia nadprzewodnikowego [1]. W celu zaprojektowania warunków stabilnej i bezpiecznej pracy przewodów nadprzewodnikowych, opracowano model matematyczny termicznych stanów dynamicznych zanikania nadprzewodzenia pod wpływem doprowadzonego impulsu zaburzającego o różnych wartościach energii E_z, czasu trwania zaburzenia t_z i długości zaburzenia x_z [2,3].

W niniejszej pracy, korzystając z opracowanego modelu komputerowego dynamicznego procesu zanikania nadprzewodzenia, przeprowadzono badania wpływu parametrów energetycznego impulsu zaburzającego na wybrane parametry dynamicznego procesu zanikania nadprzewodzenia.

Model matematyczny zanikania nadprzewodzenia

Do analizy stanów dynamicznych zanikania nadprzewodzenia przyjęto kompozytowy przewód nadprzewodnikowy MgB_2/Cu o przekroju kołowym wykonany metodą rurkowo-proszkową (PIT), składający się z 6 włókien nadprzewodnika MgB_2 osłoniętych cienką warstwą buforową z niobu Nb [4]. Włókna te zostały umieszczone w matrycy z miedzi Cu pełniącej rolę stabilizatora, otoczonej wzmacniającą powłoką ze stali nierdzewnej SS.

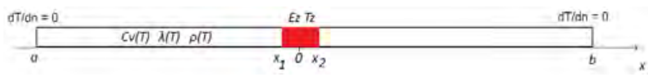

Rys.1. Geometria, parametry materiałowe i wymuszenia oraz warunki brzegowe modelu matematycznego stanów dynamicznych utraty nadprzewodzenia w przewodzie nadprzewodnikowym MgB_2/Cu

Przewód jest poddany zaburzeniu cieplnemu o energii E_z działającemu w czasie t_z na długości x_z odcinka przewodu (rys.1). Niestacjonarne procesy termiczne wywołane zaburzeniem energetycznym, powiązane z modelem podziału prądu, uwzględniające zmienność temperaturową pojemności i przewodności cieplnej, rezystywności oraz gęstości mocy cieplnej stanowiącej wymuszenie zmieniające się w czasie i wzdłuż przewodu opisane zostały modelem matematycznym [3] opartym na jednowymiarowym niestacjonarnym równaniu różniczkowym cząstkowym przewodnictwa cieplnego.

Model ten umożliwia analizę termiczno-elektrycznych procesów zanikania nadprzewodzenia, która jest podstawą do wyznaczenia ich podstawowych parametrów.

Parametry procesu zanikania nadprzewodzenia

Na podstawie przebiegów czasowych temperatury w obszarze zaburzenia cieplnego w przewodzie nadprzewodnikowym można wyznaczyć podstawowe parametry określające dynamikę procesu utraty nadprzewodzenia (rys.2).

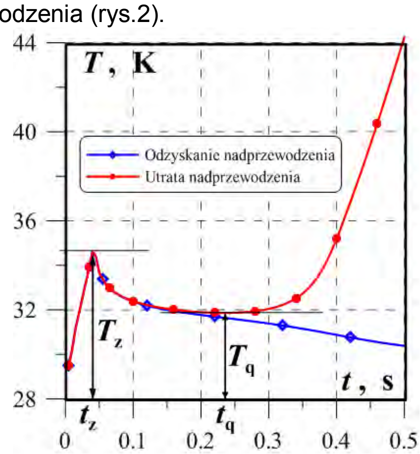

Rys.2. Przebieg temperatury w miejscu poddanym zaburzeniu energetycznemu podczas dynamicznego procesu zanikania nadprzewodzenia dla energii zaburzenia $E_z = E_q$ (niekontrolowana utrata nadprzewodzenia) oraz $E_z < E_q$ (odzyskanie nadprzewodzenia po jego chwilowym zaniku).

Analizowanymi parametrami są: minimalna energia utraty nadprzewodzenia E_q, temperatura zaburzenia T_z, temperatura utraty nadprzewodzenia T_q i czas utraty nadprzewodzenia t_q.

Temperatura $T(t)$ w miejscu zaburzenia po osiągnięciu lokalnego maksimum T_z maleje, a następnie w zależności od wartości dostarczonego impulsu energetycznego w danych warunkach pracy, powraca do wartości początkowej (odzyskanie nadprzewodzenia) albo rośnie w sposób lawinowy i niekontrolowany (całkowita utrata nadprzewodzenia.

Czas utraty nadprzewodzenia t_q oraz temperatura utraty nadprzewodzenia T_q są współrzędnymi lokalnego minimum funkcji $T = f(t)$, w którym przebieg temperatury przewodu w miejscu zaburzenia zaczyna rosnąć po zakończeniu czasu trwania impulsu zaburzającego. Temperatura zaburzenia T_z jest to temperatura do której nagrzewa się przewód w wyniku wydzielenia w nim energii zaburzenia.

Wpływ czasu trwania zaburzenia na parametry zanikania nadprzewodzenia

Badania wpływu czasu trwania zaburzenia t_z na wartość minimalnej energii utraty nadprzewodzenia E_q przeprowadzono dla odcinka przewodu o długości 100 mm, prądu roboczego $I_r = 100$ A, temperatury początkowej $T_0 = 26$ K i długości obszaru zaburzenia $x_z = 4$ mm.

Z zależności minimalnej energii utraty nadprzewodzenia od czasu zaburzenia $E_q(t_z)$ (rys. 3) wynika, że im dłuższy jest czas zaburzenia, tym większa energia może zostać dostarczona do przewodu bez wywołania utraty nadprzewodzenia.

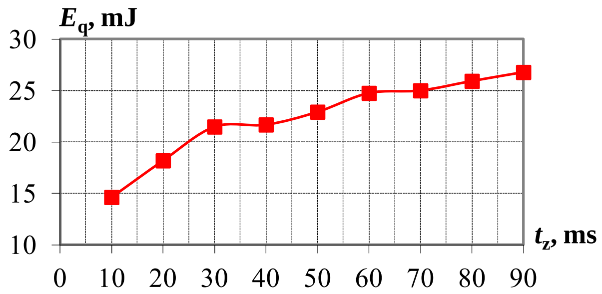

Rys.3. Zależność minimalnej energii utraty nadprzewodzenia E_q od czasu trwania zaburzenia t_z, x_z =4 mm, I_r = 100 A, T_0 = 26 K

Z zależności temperatury utraty nadprzewodzenia T_q oraz temperatury zaburzenia T_z od czasu trwania zaburzenia t_z (rys.4) wynika, że temperatura utraty nadprzewodzenia T_q ma w przybliżeniu stałą wartość. Zatem przy ustalonych parametrach analizy, tj. x_z =4 mm, I_r = 100 A, T_0 = 26 K, wzrost wartości całkowitej energii zaburzenia spowodowany jest tym, że już podczas trwania zaburzenia część jego energii przepływa do obszaru sąsiadującego z obszarem zaburzenia.

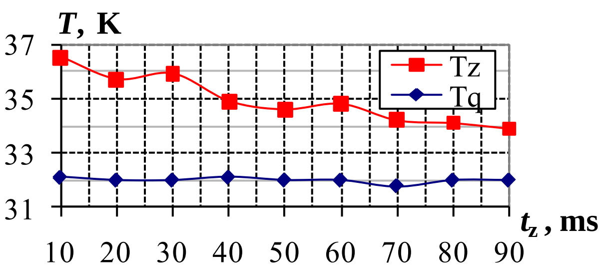

Rys.4. Zależność temperatury zaburzenia T_z oraz temperatury utraty nadprzewodzenia T_q od czasu trwania zaburzenia t_z, x_z =4 mm, I_r = 100 A, T_0 = 26 K

Wpływ długości zaburzenia na parametry zanikania nadprzewodzenia

Wpływ długości obszaru x_z w którym działa impuls zaburzający na minimalną energię utraty nadprzewodzenia (rys.5) zbadano dla wartości $x_z \in$ <2 mm; 40 mm>, przy czasie trwania zaburzenia $t_z = 40$ ms, temperaturze roboczej $T_0 = 26$ K, prądzie roboczym $I_r = 100$ A, długości analizowanego odcinka przewodu $l = 100$ mm.

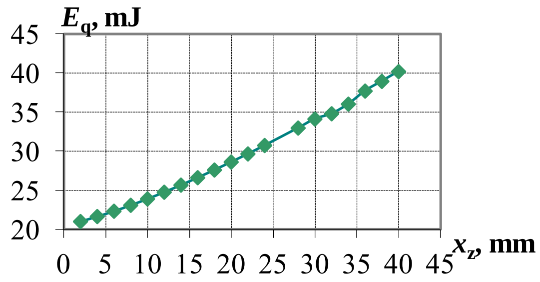

Rys.5. Zależność minimalnej energii utraty nadprzewodzenia $E_q(x_z)$ od długości obszaru zaburzenia x_z przy t_z =40 ms, I_r = 100 A, T_0 = 26 K

Z zależności temperatury utraty nadprzewodzenia T_q oraz temperatury zaburzenia T_z od długości obszaru zaburzenia (rys. 6) wynika, że przy małych długościach zaburzenia x_z temperatura zaburzenia T_z znacznie przewyższa temperaturę utraty nadprzewodzenia T_q. Przy długości zaburzenia rzędu $x_z = 34$ mm temperatury te zbliżają się do siebie. Przy zaburzeniu o długości ok. 37 mm następuje przecięcie tych charakterystyk i wartość temperatury utraty nadprzewodzenia T_q przewyższa wartość temperatury zaburzenia T_z.

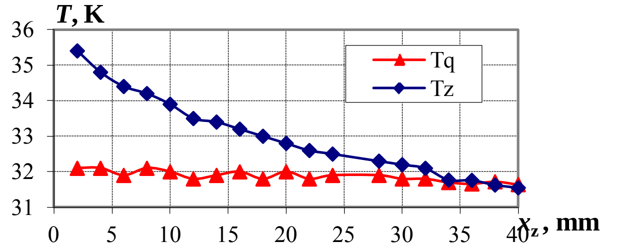

Rys.6. Zależność temperatury zaburzenia $T_z(x_z)$ oraz temperatury utraty nadprzewodzenia $T_q(x_z)$ od długości przedziału zaburzenia x_z, przy t_z =40 ms, I_r = 100 A, T_0 = 26 K

Istotna zmiana charakteru procesu utraty nadprzewodzenia w badanym przewodzie przy zmianie długości obszaru zaburzenia w granicach 30-40 mm pokazuje, że minimalna długość propagacji strefy rezystywnej badanego przewodu (przy t_z =40 ms, I_r = 100 A, T_0 = 26 K) wynosi ok. 37 mm.

LITERATURA

[1] Dresner L., *Stability of superconductors*, Plenum Press, New York, London 1995

[2] Surdacki P., Termiczne stany dynamiczne wysokotemperaturowych przewodów nadprzewodnikowych z dwuborku magnezu, *Przegląd Elektrotechniczny* 86 (2010) 12, 149-152.

[3] Martınez E., Young E.A., Bianchetti M., Munoz O., Schlachter S.I., Yang Y., Quench onset and propagation in Cu-stabilized multifilament MgB_2 conductors, *Supercond. Sci. Technol.* 21 (2008) 025009 (8pp)

***Author**: dr Paweł Surdacki, Lublin University of Technology, Institute of Electrical Engineering and Electrotechnologies Nadbystrzycka 38a, 20-618 Lublin, E-mail: p.surdacki@pollub.pl.*

Conference ELMECO–7
ELECTROMAGNETIC DEVICES AND PROCESSES IN ENVIRONMENT PROTECTION
joint with 10th Seminar AoS-10 APPLICATIONS OF SUPERCONDUCTORS
28–30.09.2011, Nałęczów, Poland

WPŁYW PRĄDU I TEMPERATURY PRACY NA PARAMETRY ZANIKANIA NADPRZEWODZENIA W PRZEWODZIE NADPRZEWODNIKOWYM YBCO

Paweł SURDACKI

Lublin University of Technology, Institute of Electrical Engineering and Electrotechnologies

Streszczenie. *W pracy zbadano wpływ prądu oraz temperatury pracy taśmy warstwowej YBCO II generacji na wybrane parametry procesu zanikania nadprzewodzenia: minimalnej energii utraty nadprzewodzenia, temperatury zaburzenia i temperatury utraty nadprzewodzenia. Do obliczeń wykorzystano makroskopowy model komputerowy termicznych stanów dynamicznych zanikania nadprzewodzenia w kompozytowym przewodzie nadprzewodnikowym.*

Abstract. *In this paper, the YBCO coated conductor working current and temperature influence on the parameters of the superconductivity loss process, i.e. minimum quench energy, disturbance temperature and quench temperature, have been investigated. The macroscopic model of the thermal dynamic processes of quench in the composite superconducting wire has been used in the computations.*
(Influence of the working current and temperature on the quench parameters of the YBCO superconducting tape).

Słowa kluczowe: taśma nadprzewodnikowa YBCO, zanikanie nadprzewodzenia, parametry zanikania nadprzewodzenia.
Keywords: YBCO superconducting tape, superconductivity loss, quench parameters.

Wstęp

Przewody warstwowe II generacji YBCO ($YBa_2Cu_3O_x$), weszły w fazę produkcji przemysłowej i stają się bardzo obiecującym składnikiem nadprzewodnikowych urządzeń elektroenergetycznych. Przewody te wykazują znaczne wartości gęstości prądu w obecności silnych pól magnetycznych przy wysokim poziomie temperatur ok. 77 K, które zapewnione są poprzez chłodzenie ciekłym azotem. Taki sposób chłodzenia eliminuje znaczne rozmiary całego układu i koszty chłodzenia kriochłodziarką mechaniczną. W zakresie temperatur 60 – 80 K właściwości cieplne taśm YBCO powodują jednak bardzo powolną dyfuzję ciepła wzdłuż przewodu. Prowadzi to do nadmiernego lokalnego nagrzewania się przewodu w przypadku wystąpienia zaburzenia nadprzewodzenia. W rezultacie zarówno prędkość propagacji strefy rezystywnej w przewodzie jak i przyrost napięcia są niewielkie, co utrudnia działanie układu zabezpieczającego przed niekontrolowaną utratą nadprzewodzenia.

Mimo prowadzonych ostatnio badań eksperymentalnych nad zanikaniem nadprzewodzenia w taśmach warstwowych YBCO [1,2], wciąż trudny jest do opracowania jego model matematyczny, który uwzględniałby złożone procesy fizyczne, takie jak wpływ rezystancji styków, zjawisko Halla, efekty pojemnościowe oraz szybkie oddziaływania elektrotermiczne pomiędzy warstwami.

W niniejszej pracy do badania procesu zanikania nadprzewodzenia w taśmie warstwowej YBCO przyjęto makroskopowy model matematyczny [3], który uwzględnia silnie nieliniową zależność temperaturową pojemności i przewodności cieplnej oraz rezystywności taśmy. Korzystając z opracowanego modelu komputerowego dokonano określenia wpływu temperatury T_0 przewodu oraz prądu roboczego I_r na wybrane parametry dynamicznego procesu zanikania nadprzewodzenia w taśmie warstwowej YBCO. Otrzymane wyniki porównano z odpowiednimi parametrami stabilności dla przewodu kompozytowego MgB_2.

Model matematyczny zanikania nadprzewodzenia w taśmie warstwowej YBCO

Do analizy stanów dynamicznych zanikania nadprzewodzenia przyjęto kompozytowy przewód nadprzewodnikowy YBCO w kształcie cienkiej taśmy wielowarstwowej II generacji (rys.1) [1]. Taśma ma szerokość 4 mm i grubość zaledwie 130,8 µm, na którą składa się pięć warstw. Podłoże taśmy wykonane ze stopu niklu (grubość 75 µm) oddzielone jest od warstwy nadprzewodnika YBCO (5 µm) warstwą buforową (0,3 µm). Nadprzewodnik jest z kolei oddzielony od warstwy miedzi (50 µm), pełniącej funkcję stabilizatora cieplnego i elektrycznego, cienką warstwą srebra (0,5 µm).

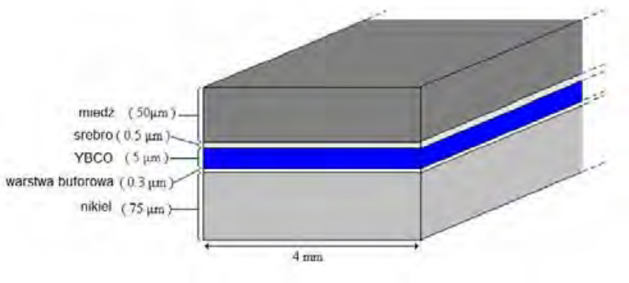

Rys.1. Przekrój taśmy nadprzewodnikowej YBCO II generacji [1]

Parametry taśmy warstwowej YBCO zamieszczono w tab.1. W modelu założono liniowość charakterystyki prądu krytycznego $I_c(T)$ taśmy nadprzewodnikowej YBCO przy braku zewnętrznego pola magnetycznego.

Tab.2. Parametry materiałowe badanej taśmy YBCO

Wykładnik potęgowy n	15
Temperatura krytyczna T_c	92 K
Współczynnik wypełnienia η	3,8 %
Pole przekroju poprzecznego A	0,52 mm^2
Średnia gęstość taśmy γ	8650 kg/m^3
Prąd krytyczny (przy 77 K)	100 A

Ze względu na bardzo niewielki udział w przekroju poprzecznym (tab.2) warstwę srebra oraz buforową pominięto przy obliczaniu średniej gęstości.

Tab.2. Składniki taśmy YBCO wraz z ich gęstością

Materiał	**Zawartość** %	**Gęstość** [kg/m^3]
Ni	57,7%	8350-8900 (8700)
Cu	38,5%	8933
YBCO	3,8%	4400-5300 (5000)

Przewód jest poddany zaburzeniu cieplnemu o energii E_z działającemu w czasie t_z na długości x_z odcinka przewodu (rys.2). Niestacjonarne procesy termiczne wywołane zaburzeniem energetycznym, powiązane z modelem podziału prądu, uwzględniające zmienność temperaturową pojemności i przewodności cieplnej, rezystywności oraz gęstości mocy cieplnej stanowiącej wymuszenie zmieniające się w czasie i wzdłuż przewodu opisane zostały modelem matematycznym [3] opartym na jednowymiarowym niestacjonarnym równaniu różniczkowym cząstkowym przewodnictwa cieplnego.

Rys.2. Geometria, parametry materiałowe i wymuszenia oraz warunki brzegowe modelu matematycznego stanów dynamicznych zanikania nadprzewodzenia w nadprzewodnikowej taśmie warstwowej YBCO

Model ten umożliwia analizę termiczno-elektrycznych procesów zanikania nadprzewodzenia. Na podstawie przebiegów czasowych temperatury w obszarze zaburzenia cieplnego w taśmie nadprzewodnikowej można wyznaczyć podstawowe parametry określające dynamikę procesu utraty nadprzewodzenia. Do analizy przyjęto odcinek taśmy YBCO o długości l = 200 mm, której temperatura robocza T_0 = 77 K (ciekłego azotu) i prąd roboczy I_r = 90 A. Parametry zaburzenia cieplnego: x_z = 4 mm, t_z =10 ms.

Minimalna energia utraty nadprzewodzenia

Obliczenia stanów dynamicznych umożliwiające wyznaczenie minimalnej energii utraty nadprzewodzenia E_q=f(T_0,I_r) taśmy warstwowej YBCO przeprowadzono dla wartości temperatur roboczych $T_0 \in$ <71; 86> K oraz dla wartości prądu roboczego $I_r \in$ <16; 126> A i odpowiadających im wartości względnych prądu roboczego odniesionego do prądu krytycznego w danej temperaturze (rys. 3).

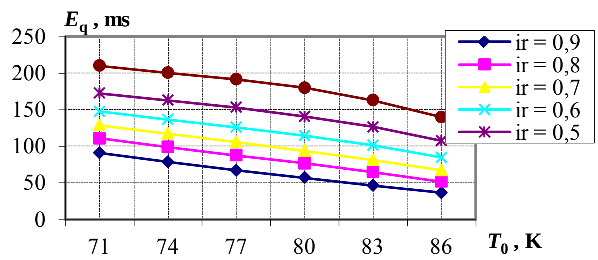

Rys.3. Zależność minimalnej energii utraty nadprzewodzenia $E_q(T_0$, $I_r)$ od temperatury T_0 i prądu roboczego I_r taśmy YBCO

Minimalna energia utraty nadprzewodzenia E_q rośnie wraz ze spadkiem wartości prądu roboczego I_r w przewodzie, natomiast maleje wraz ze wzrostem temperatury pracy T_0. Zatem wraz ze zmniejszaniem się marginesu temperatury zmniejsza się minimalna energia utraty nadprzewodzenia E_q, pogarszając stabilność nadprzewodzenia taśmy YBCO.

Temperatura zaburzenia

Z zależności E_q=f(I_r,T_z) (rys.4) wynika, że im niższa jest wartość prądu roboczego w przewodzie, tym większy musi być lokalny wzrost temperatury, aby wystąpiła nieodwracalna utrata stanu nadprzewodzenia. Jednocześnie przy dużych wartościach prądu roboczego temperatury zaburzenia przyjmują wartości znacznie mniej zbliżone do siebie, niż ma to miejsce w przypadku małych wartości prądu roboczego. Wskazuje to na znacznie większą dynamikę procesu utraty nadprzewodzenia przy prądach bliższych prądowi krytycznemu.

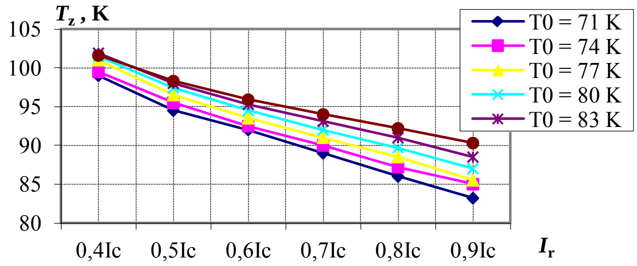

Rys.4. Zależność temperatury zaburzenia T_z=f(I_r ,T_0) od prądu I_r i temperatury T_0

Temperatura utraty nadprzewodzenia

Z zależności T_q = f(I_r,T_0) (rys.5) uzyskanej z obliczeń stanów dynamicznych wynika, że wartość tej temperatury wzrasta wraz ze spadkiem wartości prądu roboczego w przewodzie oraz że temperatury utraty nadprzewodzenia dla różnych temperatur pracy zbliżają się do siebie. Przy dużym prądzie roboczym gwałtowny wzrost temperatury przewodu rozpoczyna się od znacznie niższych wartości niż przy małym prądzie I_r.

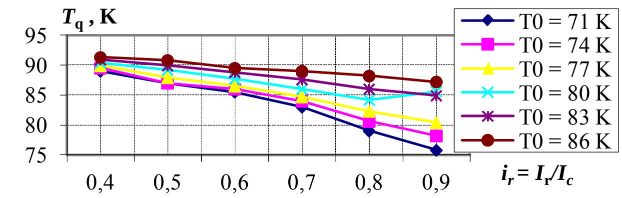

Rys.5. Zależność temperatury utraty nadprzewodzenia od prądu T_q=f(I_r) dla różnych wartości temperatury pracy T_0

Wnioski

Przeprowadzona metoda analizy umożliwia dobranie temperatury pracy i prądu roboczego warstwowej taśmy nadprzewodnikowej YBCO w celu uzyskania pożądanych wartości parametrów procesu przejściowego zanikania nadprzewodzenia oraz zapewnienia stabilnej pracy nadprzewodnika.

LITERATURA

[1] Masson P.J., Rouault V.R., Hoffmann G., Luongo C.A., Development of quench propagation models for coated conductors. *IEEE Trans. Appl. Supercond.*, 18 (2008) (2),1321-4.

[2] Wang X, Caruso AR, Breschi M, et al., Normal zone initiation and propagation in Y-Ba-Cu-O coated conductors with Cu stabilizer. *IEEE Trans. Appl. Supercond.*, 15 (2005), 2, part 3, 2586-2589

[3] Surdacki P., Termiczne stany dynamiczne wysokotemperaturowych przewodów nadprzewodnikowych z dwuborku magnezu, *Przegląd Elektrotechniczny* 86 (2010) no. 12, 149-152.

***Author**: dr Paweł Surdacki, Lublin University of Technology, Institute of Electrical Engineering and Electrotechnologies Nadbystrzycka 38a, 20-618 Lublin, E-mail: p.surdacki@pollub.pl.*

DIAGNOSTICS OF THE LASER GENERATED PLASMA PLUME DYNAMICS USING TIME-RESOLVED IMAGING

Mateusz TAŃSKI [1], Robert BARBUCHA [1], Marek KOCIK [1], Jerzy MIZERACZYK[1,2]

Szewalski Institute of Fluid-Flow Machinery (1), Gdynia Maritime University (2)

***Abstract**. Dynamics of the laser generated ablation plasma plume in the ambient air was investigated. Time-resolved images of forming and expanding ablation plume were captured at few of nanosecond intervals. Using captured images the expansion rate of the plasma was calculated.*

***Streszczenie.** W niniejszym artykule przedstawiono wyniki badań dynamiki plazmy ablacyjnej, generowanej laserowo w powietrzu. Wykonano zdjęcia plazmy ablacyjnej w wysokiej rozdzielczości czasowej, na podstawie tych zdjęć wyznaczono prędkość ekspansji plazmy.*

Keywords: laser ablation, plasma plume, time-resolved imaging
Słowa kluczowe: ablacja laserowa, plazma, zdjęcia w wysokiej rozdzielczości czasowej

Introduction

When a high-energy, nanosecond laser pulse is focused onto the material surface small portion of this material can ablate due to sudden temperature and pressure change. Ablated, highly ionized material creates expanding plasma cloud called plasma plume. But the expansion mechanism of laser generated plasma plume is not fully understood. It involves processes like: deceleration, shock-wave formation, thermal conduction, diffusion, recombination and clustering trough an ambient air [1-6].

Dynamics of the laser generated plasma plume in the ambient air was investigated at the early stage of its expansion (first 100 ns). The ablation plume was generated by focusing UV laser beam onto the surface of thin stainless steel foil. Time-resolved images of forming and expanding ablation plume were captured at few of nanosecond intervals [7-9]. Using captured images the expansion rate of the plasma was calculated.

Experimental setup

The experimental setup used for plasma dynamics measurements is presented in the figure 1. It consisted of laser system for plasma generation and the system for plasma observation applying fast gated ICCD (Intensified CCD) camera.

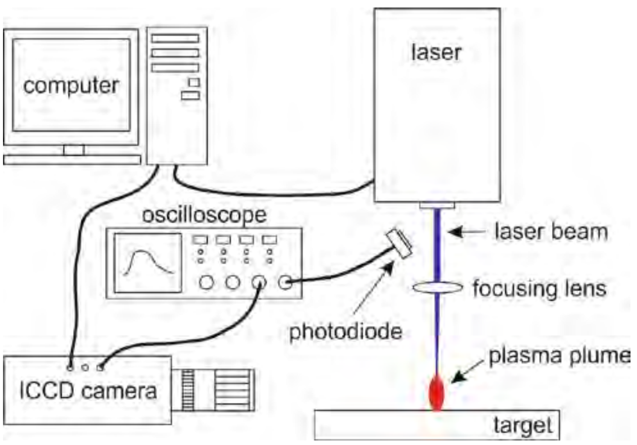

Fig.1. Experimental setup for time-resolved imaging of the laser generated plasma plume.

The main elements of the system for plasma generation were: UV solid state laser with third harmonic generation (wavelength λ = 355 nm, average power P = 2 W, pulse width τ = 55 ns, pulse repetition rate f = 33 kHz), focusing optic (focal length f = 100 mm) and XY table with target made of 304 stainless steel foil of a thickness of 200 μm. The laser spot on the target's surface was d = 30 μm of diameter what corresponds to the energy fluence of 8,5 J/cm^2. Using this system a few hundred micrometers high plasma plume was generated over the surface of the metal target.

System for plasma observation consisted of fast gated ICCD camera (2 ns of minimal exposure time) equipped with macro lens and trigger/delay unit. The field of vision of the ICCD camera was 4 mm × 4 mm and was centered on the area above the metal target. Camera was triggered by the trigger/delay unit and was synchronized with laser pulse trigger signal. This allowed to capture images of the plasma plume in the time intervals after the beginning of the laser pulse. Both laser pulse signal and camera trigger signal were monitored on the oscilloscope. Laser pulse signal was detected using fast photodiode (1 ns rise time) which measured scattered laser light.

The measurements were performed in ambient air under standard conditions (T = 25 °C, P = 1 atm.) in absence of assisting gas jet.

Results

Time-resolved images of forming and expanding ablation plasma plume were captured at few of nanosecond intervals. Typical ICCD images of the plasma plume at the early stage of its expansion (100 ns) are presented in the figure 2.

The formation of the plasma plume starts at the beginning of the laser pulse in the form of high-temperature spot on the surface of the material. In the a few-tens nanoseconds after the beginning of the laser pulse plasma plume starts to detach from the material surface. The laser pulse is being absorbed by the expanding plasma plume in the plasma shielding process. The plasma expands in the vertical and horizontal direction during a mushroom-like explosion. At the end of the laser pulse (around t = 60 ns) the plasma plume is fully developed and the plasma spot on the material surface disappears. After the end of the laser pulse the plasma plume starts to decay.

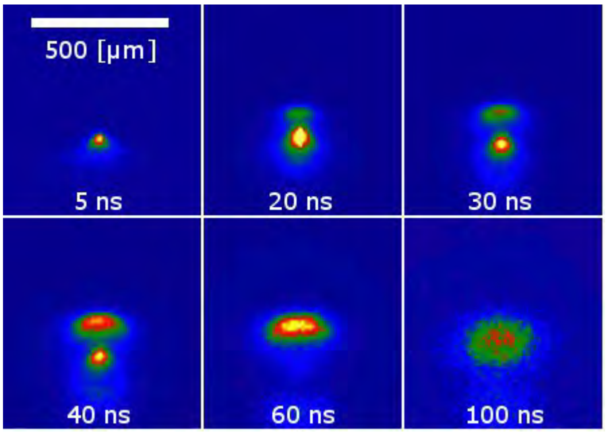

Fig.2. The evolution laser generated plasma plume in the ambient air at the early stage of its expansion (100 ns) recorded using an ICCD camera (gating time 2 ns). All the images are same intensity scale. Laser pulse width τ = 55 ns.

Using captured images of the expanding plasma plume the position of the plasma plume edge in the vertical and horizontal direction was found (figure 3). Next the expansion rate of the plasma plume was calculated. The average expansion velocity of the plasma plume was $V = 4 \cdot 10^3$ m/s in both vertical and horizontal direction.

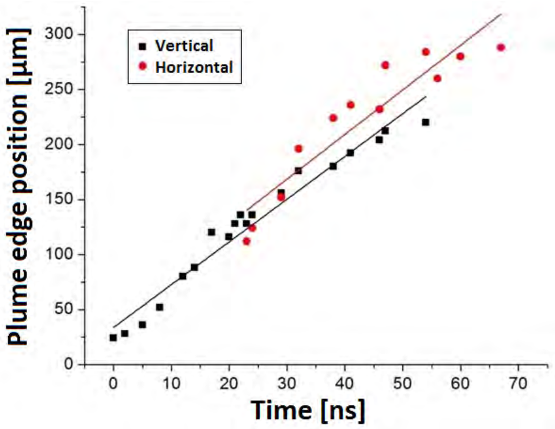

Fig.3. Vertical and horizontal position of the plasma plume edge position in the function of time.

Conclusions

Plasma plume expansion dynamics in its early stage was investigated using timed-resolved imaging. The plasma plume was generated using 55 ns width laser pulse focused on the surface of the metal target.

Three life stages of laser generated plasma plume can be distinguish: creation, expansion and decay. The plasma is created in the form of the spot on the target surface. Next plasma expands in the mushroom like shape absorbing laser pulse energy in shielding process. The expansion rate was calculated to be $V = 4 \cdot 10^3$ m/s. After the end of the laser pulse plasma plume starts to decay.

REFERENCES

[1] Luna H., Kavanagh K.D., Costello J.T. Study of a colliding laser-produced plasma by analysis of time and space-resolved image spectra, J. Appl. Phys., 101 (2007), No. 3, 033302 - 033302-6
[2] Boueri M. Baudelet M., Yu J., Mao X., Mao S., Russo R., Early stage expansion and time-resolved spectral emission of laser-induced plasma from polymer, Applied Surface Science, 255 (2009), 9566-9571
[3] Brygo, F., Dutouquet C., Le Guern F., Oltra R., Semerok A., Weulersse J.M., Laser fluence, repetition rate and pulse duration effects on paint ablation, Applied Surface Science, 252 (2006), 2131-2138
[4] Jedynski M., Hoffman J., Mroz W., Szymanski Z., Plasma plume induced during ArF laser ablation of hydroxyapatite, Applied Surface Science, 255 (2008), 2230-2236
[5] Amoruso S., Sambri A., Wang X., Plume expansion dynamics during laser ablation of manganates in oxygen atmosphere, Applied Surface Science, 253 (2007), 7696-7701
[6] Li P., Lim D., Mazumder J., Diagnostics of nanosecond dynamics of the plasma produced during KrF excimer laser ablation of zirconia in vacuum, J. Appl. Phys., 92 (2002), No. 2, 666-671
[7] Ursu C., Gurliui S., Focsa C., Popa G., Space- and time-resolved optical diagnosis for the study of laser ablation plasma dynamics, Nuclear Instruments and Methods in Physics Research B, 267 (2009), 446-450
[8] Hauer M., Funk D.J., Lippert T., Wokaun A., Time-resolved techniques as probes for the laser ablation process, Optics and Lasers in Engineering, 43 (2005), 545-556
[9] Hong M.H., Lu Y.F., Ho T.M., Lu L.W., Low T.S., Fast ICCD imaging of KrF excimer laser induced titanium plasma plumes for silicon metallization, Appl. Surf. Sci., 139 (1999), 489-493

***Authors**: mgr. inż. Mateusz Tański, Instytut Maszyn Przepływowych PAN, ul. Fiszera 14, 80-231 Gdańsk, E-mail: tanski@imp.gda.pl; dr Marek Kocik, Instytut Maszyn Przepływowych PAN, ul. Fiszera 14, 80-231 Gdańsk, E-mail: kocik@imp.gda.pl; dr inż. Robert Barbucha, Instytut Maszyn Przepływowych PAN, ul. Fiszera 14, 80-231 Gdańsk, E-mail: brobert@imp.gda.pl; prof. dr hab. inż. Jerzy Mizeraczyk, Instytut Maszyn Przepływowych PAN, ul. Fiszera 14, 80-231 Gdańsk, Akademia Morska, ul. ul. Morska 81-87, 81-225 Gdynia, E-mail: jmiz@imp.gda.pl;*

Conference ELMECO–7
ELECTROMAGNETIC DEVICES AND PROCESSES IN ENVIRONMENT PROTECTION
joint with 10th Seminar AoS-10 APPLICATIONS OF SUPERCONDUCTORS
28–30.09.2011, Nałęczów, Poland

ZABURZENIA ELEKTROMAGNETYCZNE NA LINIACH ZASILAJĄCYCH REAKTOR PLAZMOWY TYPU GLIDARC

Andrzej WAC-WŁODARCZYK[1], Andrzej KACZOR[2]

Politechnika Lubelska, Instytut Podstaw Elektrotechniki i Elektrotechnologii (1), Urząd Komunikacji Elektronicznej Delegatura w Lublinie (2)

Streszczenie. *Artykuł przedstawia zagadnienia związane z zaburzeniami elektromagnetycznymi jakie emituje reaktor plazmowy typu GlidArc na liniach zasilania. Na wartości emitowanych zaburzeń elektromagnetycznych mogą mieć wpływ różne parametry pracy reaktora takie jak np. rodzaj gazu roboczego, wartość jego przepływu oraz parametry zasilania reaktora. W pracy zaprezentowano różne pomiary zaburzeń przewodzonych na liniach zasilających reaktor plazmowy.*

Abstract. *The article presents issues related to electromagnetic disturbance a plasma reactor GlidArc power lines. For the emitted electromagnetic disturbances can affect various parameters of the reactor, such as the type of working gas, the value of the flow working gas, and parameters power of the reactor. The paper presents the different measurements of conducted disturbances in the plasma reactor power lines.*
x
x

Keywords: Electromagnetic compatibility, disturbance conducted, plasma reactor, gliding arc.
Słowa kluczowe: Kompatybilność elektromagnetyczna, zaburzenia przewodzone, reaktor plazmowy, wyładowania łukowe.

Wstęp

Jedną z najczęstszych metod wytwarzania plazmy na ziemi są wyładowania elektryczne. Taka też metoda jest wykorzystywana w reaktorach plazmowych ze ślizgającym się wyładowaniem łukowym typu GlidArc. Wytworzony łuk elektryczny w strefie zapłonowej pomiędzy elektrodami roboczymi jest przesuwany wzdłuż elektrod roboczych pomiędzy którymi odległość się zwiększa, a następnie jest gaszony - jeśli moc ze źródła zasilania jest zbyt mała do podtrzymania łuku. Proces zapłonu łuku i jego gaszenia zachodzi automatycznie a częstotliwość jego zmiany jest uzależniona od prędkości przepływu gazu roboczego przez kolumnę, kształtu elektrod roboczych odległości między nimi, mocy z układu zasilania [1].

Urządzenia elektryczne oraz elektroniczne, do jakich można zaliczyć reaktor plazmowy, muszą spełniać wymagania zasadnicze w zakresie kompatybilności elektromagnetycznej. W celu sprawdzenia czy urządzenie spełnia wymagania należy przeprowadzić badania w laboratorium lub w miejscu zainstalowania urządzenia. Wyniki pomiarów można porównać do wartości granicznych określonych przez zharmonizowane normy specjalistyczne, a następnie zgodnie z wymaganiami prawnymi można wystawić odpowiednie dokumenty, które są niezbędne do używania takiego urządzenia [2].

Pomiar zaburzeń na liniach zasilających

Pomiary zaburzeń przewodzonych na liniach zasilających reaktor plazmowy typu GlidArc, były wykonane w miejscu jego zainstalowania, co zostało zaprezentowane na rysunku 1. W kolumnie reaktora zainstalowano trzy elektrody robocze zasilane z układu 3 faz poprzez oddzielne transformatory. Prąd zasilania elektrod roboczych mierzono po stronie pierwotnej transformatorów zasilania. W celu zjonizowania gazu roboczego w strefie zapłonowej zainstalowano elektrody zapłonowe zasilane z oddzielnego elektronicznego układu. Pomiary wykonywano na liniach zasilających elektrody robocze poprzez zastosowanie sieci sztucznej (LISN). Jako gaz roboczy zastosowano powietrze oraz argon.

Rys.1. Układ pomiaru zaburzeń przewodzonych reaktora plazmowego typu GlidArc

Pomiary wykonano w zakresie częstotliwość od 150 kHz do 30 MHz z użyciem detektora szczytowego (PK). Wartość filtra wejściowego odbiornika pomiarowego ustawiona była na 9 kHz, a krok przestrajania na 4,5 kHz. Ze względu na dość dużą liczbę punktów pomiarowych (ponad 6600) czas obserwacji dla jednej częstotliwości wynosił kilkadziesiąt milisekund. Pomiary końcowe powinny być wykonywane z użyciem detektora quasi szczytowego (QP) z czasem pomiaru 1s a następnie porównane z dopuszczalnymi poziomami wskazanymi przez odpowiednie normy. Pomiary takie trwały by jednak długo, z tego też względu przy ocenie zgodności bardzo często wykonuje się pomiary wstępne z detektorem PK i krótkim czasem obserwacji a następnie dokonuje się pomiaru z detektorem QP z długim czasem obserwacji wyłącznie na wybranych częstotliwościach. Z uwagi na krótki czas pomiaru z detektorem PK oraz szybkie zmiany emitowanych zaburzeń na liniach zasilających, wartości te na sąsiednich częstotliwościach bardzo często różnią się znacznie nawet o kilkadziesiąt decybeli, co zaprezentowano na rysunku 2. Ilustracja ta przedstawia wyniki pomiaru napięcia zaburzeń na linii L1 przy prądzie zasilania elektrod roboczych 15 A/fazę. Do kolumny reaktora jako gaz roboczy wdmuchiwano powietrze. Wszystkie zmierzone wartości odniesiono do poziomu określonego w normie zharmonizowanej dla środowiska przemysłowego [3].

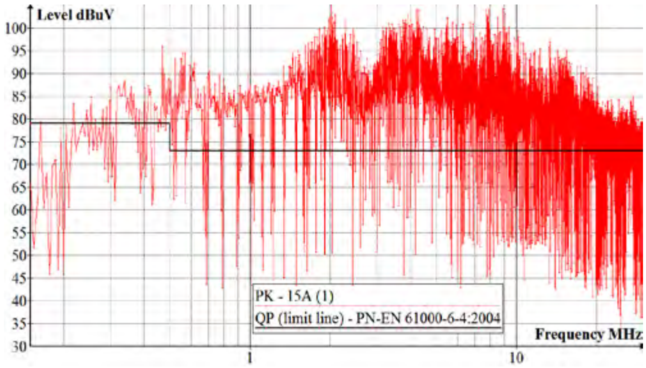

Rys.2. Wartości napięć zaburzeń na linii zasilającej L1 zmierzone detektorem PK

W celu lepszego zaprezentowania wyników oraz możliwości ich porównania zostały one uśrednione dla 25 próbek (rys. 3, 4 i 5). Wykonano serię pomiarów przy użyciu detektora QP z dłuższym czasem obserwacji i porównano je z wartościami zmierzonymi detektorem PK (z krótkim czasem obserwacji). Uzyskane maksymalne różnice osiągnęły poziom kilku decybeli.

Największy wpływ na zmiany wartości zaburzeń przewodzonych powoduje rodzaj użytego gazu roboczego, przepływającego przez kolumnę reaktora. Pomiary wykonano dla powietrza i argonu, a największe różnice osiągnęły poziom nawet kilkudziesięciu decybeli, co zaprezentowano na rysunku 3.

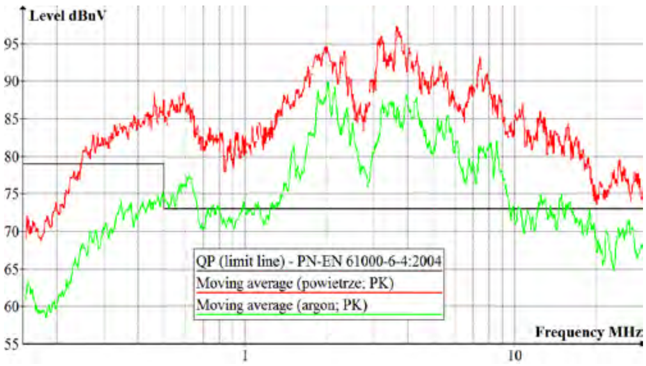

Rys.3. Wartości napięć zaburzeń na linii zasilającej L1 dla różnych gazów roboczych

Wyraźnego wpływu na wartości zaburzeń przewodzonych na liniach zasilających reaktor nie ma przy zmianie prądu zasilania elektrod roboczych. Pomiary wykonano dla prądów od 5 A/fazę do 20 A/fazę. Jako gaz roboczy zastosowano powietrze przy zachowaniu stałej przepływność gazu na poziomie 3,5 m^3/h.

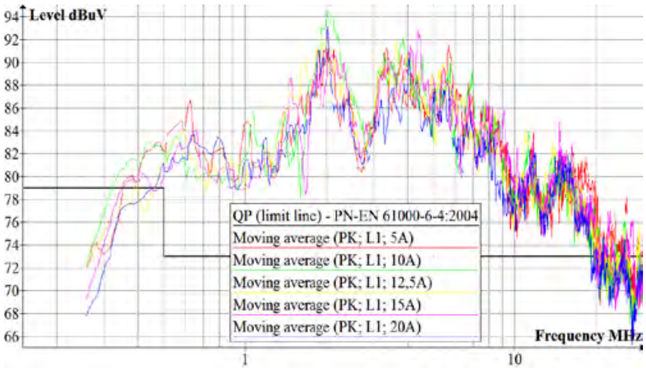

Rys.4. Wartości napięć zaburzeń na linii zasilającej L1 dla różnych prądów elektrod roboczych

W wyniku pomiarów zaburzeń nie stwierdzono również znaczącego wpływu przepływności gazu. W badaniu tym jako gaz roboczy zastosowano powietrze. Prąd zasilania elektrod roboczych utrzymywano na stałym poziomie 15 A/fazę, a przepływność gazu zmieniano od 2,5 m^3/h do 4 m^3/h.

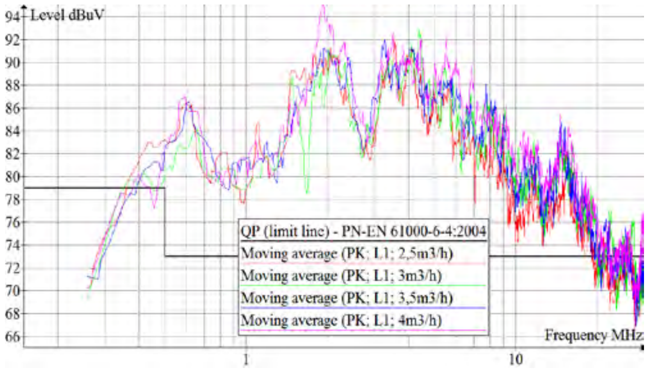

Rys.5. Wartości napięć zaburzeń na linii zasilającej L1 dla różnych przepływności gazów roboczych

Wnioski

Pomiary napięć zaburzeń przewodzonych na liniach zasilających reaktor plazmowy typu GlidArc wskazują, że są znacznie przekroczone poziomy dopuszczalne określone przez normę środowiskową [3]. Ponadto ich wartości uzależnione są od różnych parametrów układu reaktora, jak i jego pracy. Zasadnym zatem jest sprawdzenie, które parametry oraz w jaki sposób wpływają na wartości zaburzeń przewodzonych emitowanych na liniach zasilających. Wiedza taka umożliwi przeprowadzanie oceny zgodności reaktorów tego samego typu w znacznie krótszym czasie. Ponadto w procedurze oceny zgodności można będzie oszacować jak zmiana parametrów pracy reaktora wpłynie na wartości emitowanych zaburzeń na liniach zasilania. Ważnym zagadnieniem jest również określenie jaka część zaburzeń przewodzonych pochodzi z układu zasilania elektrod zapłonowych oraz z wyładowań pomiędzy elektrodami roboczymi.

LITERATURA

[1] Stryczewska H.D., "Technologie plazmowe w energetyce i inżynierii środowiska", Wydawnictwo Politechniki Lubelskiej, Lublin, (2009)

[2] Kaczor A., Wac-Włodarczyk A. *"Ocena zgodności wyrobów z wymaganiami zasadniczymi w zakresie kompatybilności elektromagnetycznej"*, *Przegląd Elektrotechniczny*, 12 (2009), 61-64

[3] PN-EN 61000-6-4:2004 "Kompatybilność elektromagnetyczna (EMC) Część 6-4: Normy Ogólne Norma emisji w środowiskach przemysłowych", Polski Komitet Normalizacyjny, Warszawa (2004)

***Autorzy**: dr hab. inż. Andrzej Wac-Włodarczyk, prof. PL, Politechnika Lubelska, Instytut Podstaw Elektrotechniki i Elektrotechnologii, ul. Nadbystrzycka 38a, 20-618 Lublin, Polska, e-mail: a.wac-wlodarczyk@pollub.pl; mgr inż. Andrzej Kaczor, Urząd Komunikacji Elektronicznej Delegatura w Lublinie, ul. Zana 38c, 20-601 Lublin, Polska, e-mail: a.kaczor@uke.gov.pl*

Conference ELMECO–7
ELECTROMAGNETIC DEVICES AND PROCESSES IN ENVIRONMENT PROTECTION
joint with 10th Seminar AoS-10 APPLICATIONS OF SUPERCONDUCTORS
28–30.09.2011, Nałęczów, Poland

ZASTOSOWANIE KAMER TERMOGRAFICZNYCH W BEZINWAZYJNEJ DIAGNOSTYCE MEDYCZNEJ

Andrzej WAC-WŁODARCZYK, Mateusz WĄSEK

Lublin University of Technology

Abstract*. Thermography is a diagnostic method which is totally non-invasive, painless and safe for both a patient and a diagnostician. It enables to define the physiological condition of the examined tissues or organs basing on the emission of the infrared radiation. The paper described basic problems of thermography measurement and chosen medical application.*

Streszczenie. *Termografia jest całkowicie nieinwazyjną, bezbolesną oraz bezpieczną dla badanego i badającego metodą diagnostyczną umożliwiającą określenie stanu fizjologicznego badanych tkanek czy narządów na podstawie emitowanego promieniowania podczerwonego. W artykule opisano podstawowe zagadnienia problematyki pomiarów termograficznych i zastosowanie w wybranych aplikacjach medycznych.*

Keywords: thermography, medical diagnostics, thermographic camera, infrared.
Słowa kluczowe: termografia, diagnostyka medyczna, kamera termograficzna, podczerwień.

Podstawy termografii

Fala elektromagnetyczna w paśmie podczerwieni, ze względu na swoje właściwości posiada znacznie większą możliwość rozprzestrzeniania się od światła widzialnego. Jej początkowa energia jest w mniejszym stopniu osłabiana przez ośrodki ludzkiego ciała i w ten sposób łatwiej mierzalna. Promieniowanie cieplne to specyficzny rodzaj fali elektromagnetycznej, która rozprzestrzenia się zarówno przez ciągłość, jak i w sposób falowy.

Termografia należy do technik rejestracji i pomiaru emitowanej przez ciało energii promieniowania cieplnego. Promieniowanie to jest emitowane przez wszystkie ciała o temperaturze wyższej od temperatury 0 K (-273,15 ˚C).

Podstawa działania systemów termograficznych jest związana z detekcją i rejestracją promieniowania podczerwonego. Jest ono emitowane przez badany obiekt. Następnie podlega przetwarzaniu na promieniowanie w widzialnym obszarze fal elektromagnetycznych. W ten sposób otrzymuje się obrazy termalne niewidzialnego promieniowania podczerwonego, zwane termogramami. Jest to proces obrazowania w paśmie podczerwieni o długości fali od ok. 0,9 µm do 14 µm. Pomiar taki jest wykonywany bezstykowo i umożliwia wielopunktową, ciągłą obserwacje zmian temperatury. Otrzymywane są termogramy, na których barwa światła widzialnego odpowiada określonym wartościom mocy promieniowania wysyłanego przez badane ciało, co pozwala na zobrazowanie rozkładu temperatury.

U podstaw fizycznych działania kamer termograficznych leży prawo Stefana-Boltzmanna. Przedstawia ono całkowitą egzytancję ciała doskonale czarnego czyli moc promieniowania ciała doskonale czarnego jako funkcję temperatury (1).

(1) $$M_{e,c} = \sigma T^4$$

gdzie: σ – stała Stefana-Boltzmanna.

Jest to wzór Stefana-Boltzmanna, z którego wynika, że całkowita moc promieniowania ciała czarnego jest proporcjonalna do czwartej potęgi jego temperatury bezwzględnej. Dla promieniowania ciała normalnego, z uwagi iż emisyjność jest mniejsza niż (<1) ciała doskonale czarnego, należy otrzymany wynik z powyższego wzoru pomnożyć przez emisyjność danego ciała. Tkanki biologiczne mają współczynnik emisyjności bliski jedności ok. 0,97 – 0,98 w zależności od różnych czynników, wartości te dotyczą zakresu widmowego emisji, (powyżej 2,5 µm w przypadku tkanek biologicznych w temperaturze pokojowej, gdyż dopiero od tej długości promieniowanie jest emitowane).

Urządzenia pomiarowe

Przyrządem niezbędnym do obserwacji rozkładu temperatury na badanej powierzchni jest kamera termograficzna (termowizyjna). Nowoczesna kamera pozwala identyfikować różnicę w gradientach temperatury z bardzo wysoką precyzją na poziomie setnych części stopnia Celsjusza. Kamery termograficzne składają się z bloków optoelektronicznych i mechanicznych o różnej najczęściej bardzo złożonej konstrukcji. Głównymi elementami standardowej kamery termowizyjnej są: detektor podczerwieni (lub zespół detektorów w postaci matrycy) z układem chłodzenia, układ optyczny (filtry i obiektyw), elektroniczne układy rejestracji i analizy sygnału oraz system jego wizualizacji (najczęściej monitor LCD).

Najważniejszym elementem kamery jest zastosowany układ detektorów podczerwieni. Poziom ich doskonałości jest głównym czynnikiem decydującym o jakości uzyskiwanych obrazów, możliwościach zastosowań oraz wymiarach i cenie kamery. Detektor można inaczej zdefiniować jako przetwornik energii promieniowania podczerwonego na inną wielkość fizyczną, np. prąd, napięcie, zmianę ładunku elektrycznego bądź rezystancji. *Detektor* - z łac. znaczy „odkrywca”, zaś *detection* – „wykrywanie”.

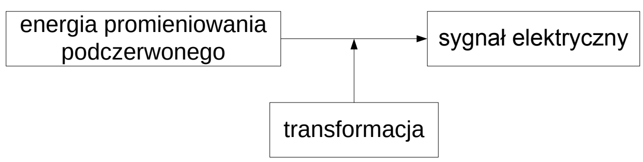

Rys.1. Zasada działania detektora promieniowania

Główny podział detektorów promieniowania podczerwonego wyodrębnia wśród nich dwie klasy: termiczne i fotonowe (matrycowe, liniowe bądź pojedyncze). W przeciwieństwie do detektorów termicznych, czułość widmowa detektorów fotonowych zależy od długości fali (2).

W urządzeniach termograficznych najczęściej spotyka się detektory termiczne bolometryczne bądź piroelektryczne oraz detektory fotonowe półprzewodnikowe. Obecnie stosowane są przede wszystkim matryce niechłodzonych detektorów mikrobolometrycznych.

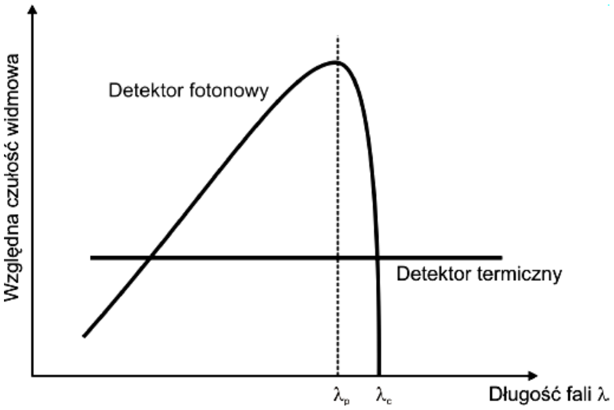

Rys.2. Czułość widmowa detektora termicznego i fotonowego,
λ_p -długość fali, przy której występuje maksimum czułości,
λ_c -długofalowa granica czułości

Równie ważnym elementem kamery jest jej układ optyczny. Zazwyczaj jest to wysokiej jakości soczewka germanowa wyposażona w ultradźwiękowy system automatycznego ogniskowania.

Promieniowanie jakie dociera do kamery nie pochodzi jedynie z badanego obiektu. Sygnał, który generuje kamera jest więc rezultatem pochłaniania przez detektor różnych składników promieniowania.

$$(2)\quad s = A\left[\varepsilon\tau M_{ob} + (1-\varepsilon)\tau M_a + (1-\tau)M_{atm}\right]$$

gdzie: ε - emisyjność badanego obiektu, τ - współczynnik transmisji atmosfery, M_{ob}, M_a, M_{atm} - egzytancje obiektu, otoczenia oraz atmosfery, *A*- stała kamery.

Na podstawie równania (2) można wyznaczyć widmową egzytancję badanego obiektu. Aby określić jego temperaturę należy uzależnić widmową egzytancję obiektu od temperatury ciała doskonale czarnego. Czynność ta wykonywana jest przez producenta danej kamery, który wyznacza krzywą kalibracji.

Do najważniejszych parametrów technicznych kamer termograficznych należą: widmowy zakres pracy, rodzaj i wymiary matrycy detektorów, rodzaje obiektywów, rozdzielczość temperaturowa, rozdzielczość przestrzenna, zakres pomiarowy, temperatura pracy, rodzaj zasilania i pobór mocy, rozdzielczość przetwornika A/C, rodzaj interfejsu, masa i wymiary.

Badania termograficzne w medycynie

Metody termograficzne wynikają z pomiarów emisji fal podczerwieni wysyłanych przez różne okolice ciała. Związane jest to z intensywnością metabolizmu tkanek i ukrwienia, zależnego od układu wegetatywnego i lokalnych mediatorów naczyniokurczących i naczyniorozszerzających. Mają one istotny związek z toczącymi się w badanych tkankach czy narządach procesami chorobowymi, takimi jak różne stadia odczynu zapalnego.

Podstawową zaletą diagnostyki termograficznej jest jej nieinwazyjność, bezbolesność i prostota badania. Może być stosowana niezależnie od wieku i płci pacjenta. Jest ona zupełnie nieszkodliwa dla kobiet w ciąży i płodów, a ponadto umożliwia wielokrotne powtarzanie badań w krótkich odstępach czasu. Możliwość archiwizacji danych w postaci termogramów pozwala na ocenę postępów choroby oraz skuteczności leczenia.

Termografia może być cennym uzupełnieniem innych rutynowo wykonywanych badań np. ultrasonografii, tomografii komputerowej, rezonansu magnetycznego.

Wadą badań termograficznych jest ich mała specyficzność, oznacza to, że w wielu przypadkach badanie takie nie może być podstawą do stawiania ostatecznej diagnozy stanu chorobowego.

Brak popularności termografii w naszym kraju wynika z wysokiego kosztu aparatury badawczej i braku fachowego personelu diagnostycznego.

Do najważniejszych zastosowań termografii w medycynie należy: diagnostyka schorzeń, wspomaganie zabiegów, ocena skuteczności działania leków, wykrywanie chorób związanych z układem krwionośnym.

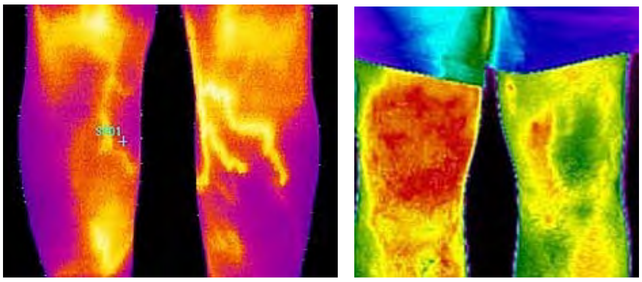

Rys.3. Termogramy kończyn dolnych w stanie zapalnym żył oraz w stanie pourazowym

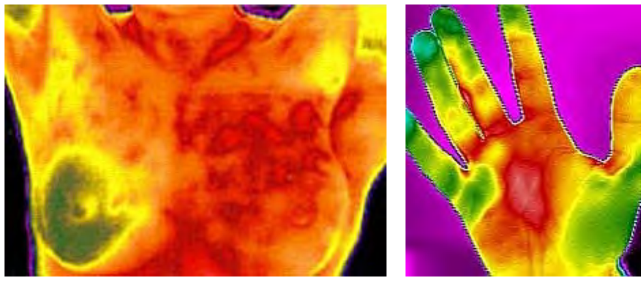

Rys.4. Stan nowotworowy piersi oraz stan zapalny dłoni

Podsumowanie

Szybki rozwój technologiczny oraz wzrost wiedzy na temat właściwości fal elektromagnetycznych w ostatnich latach przyczynia się do coraz to szerszego zastosowania termografii w diagnostyce medycznej.

LITERATURA

[1] Madura H. i inni: Pomiary termowizyjne w praktyce, *Agenda Wydawnicza PAK*, Warszawa 2004.

[2] Bielecki Z., Rogalski A.: Detekcja sygnałów optycznych, *Wydawnictwo Naukowo-Techniczne*, Warszawa 2001.

[3] Więcek B., De Mey G.: Termowizja w podczerwieni: Podstawy i zastosowanie, *Wydawnictwo PAK*, Warszawa 2011.

[4] Vollmer M., Möllmann K.-P.: Infrared Thermal Imaging: Fundamentals, Research and Application, *WILEY-VCH*, Weincheim 2010.

[5] Nowakowski A. i inni: Postępy termografii – aplikacje medyczne, *Wydawnictwo Gdańskie*, Gdańsk 2001.

[6] Materiały reklamowe firmy Termoinspekcja.pl

[7] Fita K. i inni: Przydatność termografii w diagnostyce lekarsko-stomatologicznej – doświadczenia własne, *Pomorska Akademia Medyczna w Szczecinie*, 2007, SUPPL. 3, 34–38.

***Authors**: dr hab. inż. Andrzej Wac-Włodarczyk prof. PL, Instytut Podstaw Elektrotechniki i Elektrotechnologii, ul. Nadbystrzycka 38A, 20-618 Lublin, E-mail: a.wac-wlodarczyk@pollub.pl; Mateusz Wąsek – dyplomant, E-mail: mateusz.wasek@pollub.p*

Conference ELMECO–7
ELECTROMAGNETIC DEVICES AND PROCESSES IN ENVIRONMENT PROTECTION
joint with 10th Seminar AoS-10 APPLICATIONS OF SUPERCONDUCTORS
28–30.09.2011, Nałęczów, Poland

ELECTRICAL MACHINES IN THE MILITARY MORE ELECTRIC AIRCRAFT AND THEIR IMPACT ON THE ENVIRONMENT

Sławomir WIAK[1], Agnieszka PYĆ[2], Marcin PYĆ[3]

Politechnika Łódzka (1, 3), Państwowa Wyższa Szkoła Zawodowa w Kaliszu (2)

Abstract*. This paper describes the impact of the More Electric Aircraft (MEA) on the environment and the main advantages the electrified aircrafts can offer. Because of high demand of the MEA on the electrical energy, a new generator need to be designed. The authors propose a novel homopolar starter-generator which could replace both the starter and the generator and could offer higher efficiency and reliability. The principle of work of the new machine has been explained and the new machine design has been presented.*

Streszczenie. *Niniejszy artykuł opisuje wpływ technologii More Electric Aircraft (MEA) na środowisko oraz prezentuje główne zalety jakie mają samoloty wykonane zgodnie z nową technologią. Z powodu dużego zapotrzebowania MEA na energię, konieczne jest zaprojektowanie nowego generatora. Autorzy proponują generator homopolarny, mający również funkcję rozrusznika.*

Keywords: More Electric Aircraft, Starter-Generator, Homopolar machine.
Słowa kluczowe: More Electric Aircraft, Rozruszniko-Prądnica, Silnik homopolarny.

Within the past several years, there has been a tendency to design the on-board airplane systems according to the More Electric Aircraft (MEA) concept. The main idea is to replace the onboard hydraulics and pneumatics installation and devices with corresponding electrical systems. It is believed that replacing only the pneumatic systems, would extract 35% less power from the engines, and in the case of large airplanes could save hundreds of kilograms of weight [1] and consequently dozens of kilograms of fuel. This results in a higher carbon dioxide production. Honeywell claims that the More Electric Architecture will offer significant cost advantages of approximately 30%, especially due to fewer parts (for example no ducting used to pass pressurized air), the integration of key subsystems and multi-use components [2]. Additionally, electric drives are much less maintenance-intensive and less vulnerable than hydraulic systems with their high temperature flammable liquids. This may be important, especially for aircraft in the case of combat. There is also a risk of the oil leakage from the hydraulic systems which results in environment pollution.

When aeronautical and aircraft systems are considered, the most important factors are low weight, high reliability, high performance and high efficiency as well as a long life cycle [3]. Currently, the main engine produces energy, which is converted into mechanical (for example, thrust), pneumatics (for example, air conditioning), hydraulics (for example, for flap setting) and electric (for example, board electronics supply). Energy conversion produces losses which are mostly emitted as heat. The losses increase the fuel consumption and the heat increases the so called infrared signature, which is one of the crucial parameters of military aircraft.

In order to introduce the so called “Fly-By-Wire” system, which increases the number of onboard ploughs, a generator or generators with more output power are required.

As the development and the test cycle in the aircraft industry last from several to a dozen of years and the existing generators were developed many years ago, there is a large field for improvement. The final aim is to design and produce an “all-electric-aircraft” but as in the case of the automotive industry, hybrid constructions are introduced first in order that experience is gained and all hydraulic parts are gradually replaced with electric drives. This is the reason why the MEA and other similar projects related to the electrification of aircraft around the world have been launched.

As mentioned before, the MEA demand for the electrical energy comparing to standard airplanes, will significantly increase. The currently used electric net system does not allow distributing the required energy without introducing changes. Generators used in military aircraft (usually two pieces) produce independently a 115VAC with a constant frequency of 400Hz and 28VDC. The second voltage is used for safety critical applications. In order to meet the high energy consumption requirements, a new voltage level has been defined. The 115VAC voltage has been replaced with 270VDC voltage whereas the 28VDC has remained unchanged. The replacement of two separate generators with one machine means higher requirements regarding the reliability and durability.

The newly starter-generator will be coupled with the turbine without any gearbox. It allows avoiding complicated and susceptible-to-damage mechanical parts and reduces the weight. As a consequence of the absence of the gear-box with environment polluting oil, the machine has to be capable of reaching the same rotational speed as the turbine does. It implicates a high requirement regarding the robustness of the machine. The high speed machine which could be suitable for the MEA project would need to have neither sliding contact nor magnets in the rotating machine part.

The authors have been involved in the MEA project for over 7 years and developed a novel homopolar machine which was meeting the project requirements [4, 5]. In most currently existing systems, the aircraft engine is started using the so called air-turbine-starter (ATS) also called a pneumatic starter. The air-turbine-starter receives compressed air from an external power source, which can be either mounted on the ground or onboard. These units are usually driven by a small turbine engine. The authors propose a starter which could replace the existing ATS and act as a starter-generator. The homopolar machine has been built and successfully tested at the Military University of Munich [5].

A homopolar machine is an A.C. excited synchronous machine, equipped with an armature and excitation winding on the stator side of the air-gap. The machine is equipped with a rotor divided axially and each of the rotor's salient poles in each rotor part has the same polarity. The homopolar flux produced by a ring-formed excitation winding flows axially through the rotor shaft and closes through the stator teeth and stator yoke. In the figure below the principle of operation of a homopolar machine is presented [6].

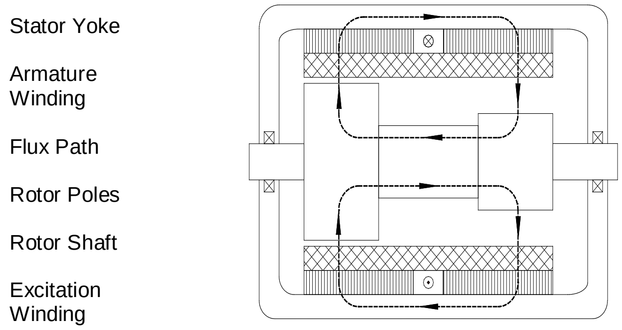

Fig.1. Principle of operation of a homopolar machine

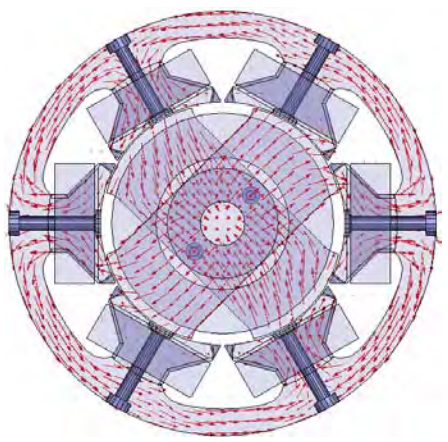

Figure 2. Flux distribution in a homopolar machine

Because of the fact that both excitation and armature windings are on the stator side and do not rotate with the rotor, no sliding contact is required and the total machine can be reduced. It makes the construction very robust and this kind of machine is especially intended for high speed applications. The stator winding carries sine wave currents although there are examples in the literature of homopolar machines with square wave currents [7]. The windings, as in the case of a PM machine, can be realized as a concentrated or lap winding. When using a concentrated winding, the winding can be produced in two different ways. It can go along the whole machine whereas the stator poles have to be mechanically 90° rotated against each other; another possibility is to divide the armature windings axially into two parts, rotate them 90° electrically and keep the rotor poles non-rotated against each other. The second solution would require more copper, increase the reliability but its cost and weight as well. The homopolar machine is rarely discussed in the literature although it combines many advantages of reluctance and PM machines. It has neither an excitation winding nor magnets rotating with the rotor, and compared to a reluctance drive, it has additional excitation. Due to this fact, not only reluctant torque, but also much higher electromagnetic torque can be produced and additionally, the excitation can be freely adjusted. Due to the absence of magnets, there is no risk of demagnetization of magnets. Additional important criteria when choosing the right machine for this project were:

- High temperature resistance – there is hot air from the turbine, which may disqualify some machine types.
- Low production cost – this criterion is important in every industry branch. Although in the aircraft industry the project budget is higher than in almost any other industry branch, the machine has to be cost optimized.
- High failure tolerance – most of the airplane on-board systems are redundant. As the main source of electrical energy, the machine has to be extremely reliable.

The final homopolar machine version meeting all project requirements is presented in the picture below.

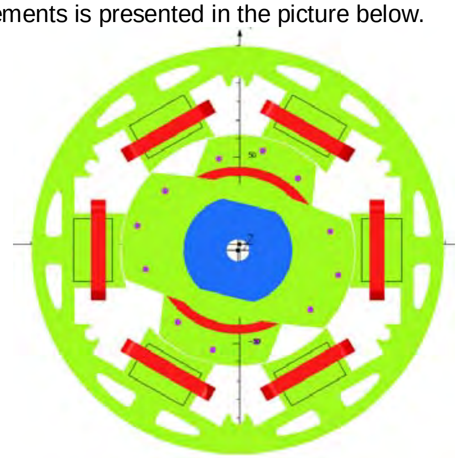

Figure 3. The final version of the homopolar machine designed by the authors

After all, the More Electric Aircrafts are lighter and more energy-efficient than conventional aircrafts, offer a significant fuel reduction and therefore their negative impact on the environment is much lower than in the case of the conventional aircrafts. They seem to be the only way of keeping the humankind flying in a fuel-efficient manner and without further environmental damage. The novel starter-generator presented by the authors is the first step to create an environment friendly aircraft.

REFERENCES

[1] Barchewitz L.P., Seume J.; 787 Special-Electric Dream; Flight International, pp. 58–59; 26/09/06
[2] More Electric Architecture Delivers Next Generation Benefits; http://www.honeywell.com/sites/aero/technology/electricArc.htm Honeywell International Inc., Morristown, USA, 24/03/2009
[3] Advances in more-electric aircraft technologies; Aircraft Engineering and Aerospace Technology; Volume: 73, Issue: 3; Emerald Group Publishing Limited; 2001
[4] Gerling D., Pyc M.; Optimisation of a homopolar machine; 19th International Symposium on Power Electronics, Electrical Drives, Automation and Motion; Italy; Speedam 2008
[5] Pyc M.; Development and Optimization of a Novel Homopolar Starter-Generator, ISBN: 978-3-8322-8910-2, Shaker Verlag, 2010
[6] Kümmel, F.; Elektrische Antriebstechnik; Teil 1. Maschinen, Verlag Springer, Berlin, 1986
[7] Goodier E., Pollock C.; Homopolar Variable Reluctance Machine Incorporating an Axial Field Coil; IEEE Transactions on Industry Applications, Vol. 38, No. 6, November/December 2002

***Authors**: prof. dr hab. inż. Sławomir Wiak, Politechnika Łódzka, Instytut Mechatroniki i Systemów Informatycznych, ul. Stefanowskiego 18/22, 90-924 Łódź, E-mail: swiak@p.lodz.pl;*
dr inż. Agnieszka Pyć, PWSZ Kalisz, Wydział Politechniczny; ul. Poznańska 201-205, 62-800 Kalisz, E-mail: A.Pyc@pwsz.kalisz.pl;
dr inż. Marcin Pyć, Politechnika Łódzka, Instytut Mechatroniki i Systemów Informatycznych, ul. Stefanowskiego 18/22, 90-924 Łódź, E-mail: Marcin.Pyc@p.lodz.pl.

Conference ELMECO–7
ELECTROMAGNETIC DEVICES AND PROCESSES IN ENVIRONMENT PROTECTION
joint with 10th Seminar AoS-10 APPLICATIONS OF SUPERCONDUCTORS
28–30.09.2011, Nałęczów, Poland

CHARACTERISATION OF A MgB_2 WIRE USING DIFFERENT CURRENT PULSE SHAPES IN PULSED MAGNETIC FIELD

Mariusz WOŹNIAK[1], Simon C. HOPKINS[1], Bartłomiej A. GŁOWACKI[1,2]

University of Cambridge (1), Institute of Power Engineering (2)

***Abstract**. A pulse field - pulse current system for critical current measurements has been modified to allow control of the current pulse shape. Regression analysis of the voltage vs. current behaviour has been used to determine critical current and n value using a specified electric field criterion from a single measurement cycle, in place of the previous qualitative approach from a series of pulses. The results for a superconducting magnesium diboride wire agree well with conventional DC measurements in a constant magnetic field.*

***Streszczenie.** System do pomiarów prądu krytycznego przy użyciu impulsowego prądu i pola magnetycznego został zmodyfikowany, aby umożliwić kontrolę kształtu impulsu prądu. Prąd krytyczny i parametr n określono z przebiegu napięcia od prądu używając analizę regresji i kryterium pola elektrycznego z pojedynczego cyklu pomiarowego w zastępstwie poprzednio używanego jakościowego sposobu opartego na serii impulsów. Wyniki otrzymane dla przewodu z dwuborkiem magnezu dobrze zgadzają się z konwencjonalnymi pomiarami stałym prądem i polem magnetycznym.*

Keywords: pulse measurements, magnesium diboride, critical current.
Słowa kluczowe: pomiary impulsowe, dwuborek magnezu, prąd krytyczny.

Introduction

The pulse field – pulse current (PFPC) technique is a promising method for the transport critical current $I_c(B)$ characterisation of short superconductor samples, allowing high fields and high currents to be achieved economically and without excessive sample heating. However, for some samples discrepancies in measured $I_c(B)$ between this and the standard constant field direct current (CFDC) technique arise. The PFPC method often slightly overestimates the CFDC results in higher magnetic fields, as reported recently for an MgB_2/Cu wire [1]. Larger discrepancies, typically an underestimate of I_c at low fields, can occur in some conductor architectures (e.g. those with a large number of filaments) due to flux jumps arising from the non-uniform current distribution resulting from the transient magnetic self-field [2]. A model for the intrinsic stability of a multifilamentary Nb-Ti/Cu-Mn/Cu wire was recently shown to describe quite well the PFPC measurement [3]. The PFPC technique may also underestimate $I_c(B)$ due to difficulties in current transfer from the current leads to the superconducting region through the resistive matrix of short samples, as has been shown by finite element analysis [4].

In all reported measurements [1-4] the critical current $I_c(B)$ was determined by comparing qualitatively the shape of the voltage vs. time response of the sample from a series of approximately sinusoidal current pulses of increasing amplitude, each delivered during a plateau of magnetic field. The qualitative nature of this analysis and the relatively high noise level for high sampling rate data acquisition meant that a low and strictly defined electric field criterion could not be applied. The near-sinusoidal current pulse shape also meant that the rate of change of current, and hence the induced voltage, was time dependent, further complicating analysis. For the measurements reported here, the capacitive discharge current source used previously has been replaced by one capable of delivering accurately sinusoidal, parabolic and linear ramps of current (Fig.1). In this contribution, regression analysis is applied to the voltage vs. current response to allow the critical current to be determined using a 1 μV cm^{-1} criterion for these pulse shapes, and the differences between them and CFDC measurements are discussed.

Experimental methods

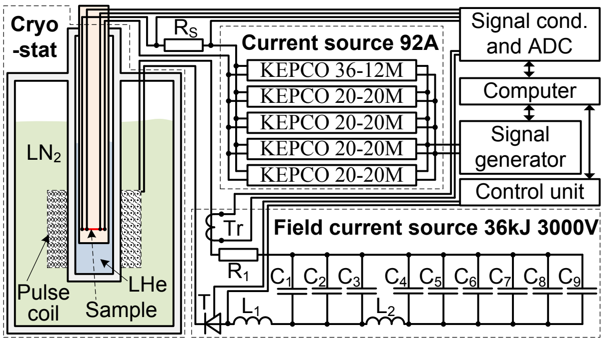

Fig.1. Schematic diagram of the modified Cryo-BI-Pulse system.

A 0.83 mm diameter wire with the MgB_2 core occupying 26.5% of its cross-sectional area was manufactured by Hyper Tech Research, USA using the PIT method with a Monel™ sheath and Fe diffusion barrier. A sample 16 mm long was measured in liquid helium by the CFDC technique in ILHMFLT Wrocław, Poland, with a voltage tap spacing of 4.2 mm and a current ramp rate up to 2 A s^{-1} [1]. An 11 mm long straight sample was measured by the PFPC technique by placing it perpendicular to the magnetic field and in liquid helium (Fig.1). The voltage from taps separated by 3.4 mm was recorded by a high sampling rate ADC system.

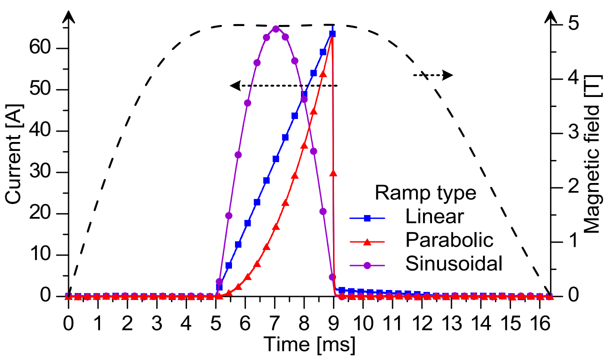

Fig.2. Magnetic field and current pulses used for testing at 4.2 K.

A signal generator was used to control the current delivered by a current source consisting of 5 power supplies in parallel (Fig.1). A current of 92 A (4 × 20 A + 12 A) with a minimum rise or fall time of 35 μs (10%-90% I_{max}) could be achieved. 4 ms long current pulses with sinusoidal, parabolic and linear shapes were delivered during the plateau of pulse magnetic field (Fig.2).

Results and discussion

The measured voltage vs. current response was processed by first subtracting a linear fit to the low-current behaviour, to eliminate any constant resistive contribution, and then scaling by the separation of the voltage taps. An example of the electric field vs. current (E vs. I) behaviour at 5 T is shown in Fig.3. $E=E_c\cdot(I/I_c)^n$ curves were fitted using the Levenberg-Marquardt method in the range of electric field up to 200 μV cm^{-1}, and the resulting I_c and n values are tabulated in Fig.3 based on a E_c=1 μV cm^{-1} criterion.

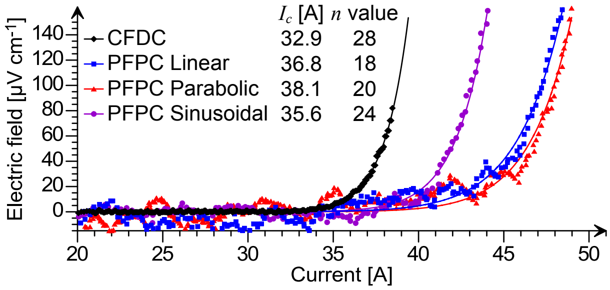

Fig.3. Voltage vs. current at 5 T recorded for different current ramps presented in Fig. 2.

The n values are quite similar between all the pulse shapes and CFDC. The noise level for voltage measurements without software averaging was on the level of 20 μV, so it is likely that the previously-reported qualitative approach would correspond to an electric field criterion at least one order of magnitude higher. Adopting the same criterion may therefore account for ~4 A at 5 T (~12% $I_c(B)$) of the discrepancy between the previously-reported PFDC and CFDC techniques (Fig. 3). Clearly, when using the same criterion, some I_c discrepancy remains.

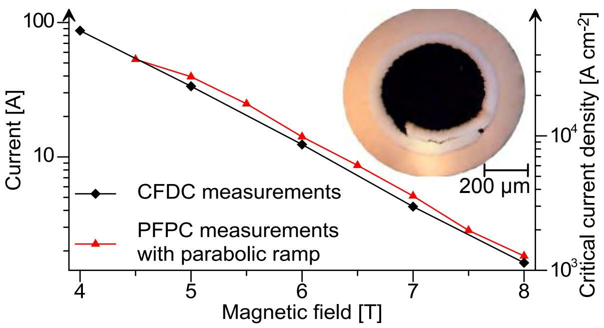

Fig.4. Critical current (density), $I_c(B)$ ($J_c(B)$) vs. magnetic field from constant field - direct current (CFDC) and pulse field–pulse current (PFPC) measurements for MgB_2 wire at 4.2 K.

The most consistent and sharp transitions over the whole investigated field range were observed for a parabolic current shape, which at 5 T also resulted in the largest difference between PFPC and CFDC measurements, so the results for this pulse shape have been used to show the $I_c(B)$ behaviour in Fig.4. The results are in reasonable agreement with the CFDC measurements over the whole field range, within 20% of $I_c(B)$ down to 1.6 A.

As shown in Fig.3 at 5 T, linear and parabolic pulse shapes resulted in very similar estimates of I_c, both systematically higher than the values from the CFDC technique. It is possible that this is due to a small amount of heating during CFDC measurements, which is avoided by the short pulse duration (4 ms) in PFPC measurements. However, this argument does not explain the discrepancy between the results for sinusoidal and linear pulse shapes. It is likely that this is related to the difference in current ramp rate. A sinusoidal current pulse results in a step change in current ramp rate at the start of the pulse; and, for the chosen parameters, that instantaneous ramp rate is higher than for any of the other pulse shapes. A linear dependence of measured critical current on current ramp rate has recently been reported for pulsed current measurements on MgB_2 conductors [5]. For some of the measurements reported here, a feature was also observed in the sample voltage response at the start of a sinusoidal current pulse: the origin of this requires further investigation.

The current source used in the present work restricts the range of currents which can be achieved but provides a very high degree of flexibility in controlling the current pulse shape and duration. This is essential for optimising PFPC $I_c(B)$ characterisation, particularly in the high field region where the previously explained heating and stability effects are less significant [2-4]. A systematic study of the effect of ramp rate, as controlled by pulse duration, is under way.

Conclusions

A refinement of the PFPC technique for $I_c(B)$ measurement has been demonstrated, in which I_c can be determined at a chosen electric field criterion from a single current pulse. I_c and n values are in good agreement with CFDC results, but some dependence on current pulse shape and ramp rate is apparent. A systematic study of this effect is under way.

Acknowledgments

M Woźniak gratefully acknowledges Siemens Magnet Technology for financial support.

REFERENCES

[1] Woźniak M., Hopkins S. C., Glowacki B. A., Study of short duration heat treatments of an *in situ* copper-sheathed MgB_2 wire, *Supercond. Sci. Technol.,* 23 (2010) 105009

[2] Woźniak M., Hopkins S. C., Glowacki B. A., Janowski T., Comparison of DC and pulsed critical current characterisation of NbTi superconducting wires, *Prz. Elektrotech.*, 85 (2009) 198–199

[3] Woźniak M., Hopkins S. C., Glowacki B. A., Intrinsic stability in pulse field – pulse current measurements of critical currents, *Proceedings of Twenty-Third International Cryogenic Engineering Conference - International Cryogenic Materials Conference 2010,* (2011) 1113-1119

[4] Krosny S., Woźniak M., Hopkins S. C., Stępień M. A., Grzesik B., Glowacki B. A., Modelling of transient state phenomena of composite superconducting conductors during pulse $I_c(B)$ measurements, *Journal of Physics: Conference Series,* 234 (2010) 022019

[5] See K. W., Xu X., Horvat J., Cook C. D. Dou S. X., Transport critical current of MgB_2 wires: pulsed current of varying rate compared to direct current method, *Supercond. Sci. Technol.* 24 (2011) 105009.

***Authors**: mgr inż. Mariusz Woźniak, dr Simon C. Hopkins and prof. dr Bartłomiej A. Głowacki, Department of Materials Science and Metallurgy, University of Cambridge, Pembroke Street, Cambridge, CB2 3QZ, UK, prof. dr Głowacki also Institute of Power Engineering, Augustówka 6, 02-981 Warsaw, Poland. E-mails: mw477@cam.ac.uk, sch29@cam.ac.uk and bag10@cam.ac.uk.*

Conference ELMECO–7
ELECTROMAGNETIC DEVICES AND PROCESSES IN ENVIRONMENT PROTECTION
joint with 10th Seminar AoS-10 APPLICATIONS OF SUPERCONDUCTORS
28–30.09.2011, Nałęczów, Poland

ELECTRICAL ELECTRODES of Ni-Me (Me=Ag, Mo, Cu) on $YBa_2Cu_3O_x$ SURFACE

Leszek WOŹNY, Anna KISIEL, Roman F. SZELOCH, Eugeniusz PROCIÓW
Wrocław University of Technology

Abstract. *The quality of metallic electrodes affects the measured critical temperature T_c and critical current I_c of high-temperature ceramic superconductors. It was investigated $YBa_2Cu_3O_x$ system with thin metallic film mono- and bi-layer conductors as current and voltage electrodes. The influence of contact layer systems Ni-Cu, Ni-Ag and Ni-Mo on critical temperature and current density was examined. The simple model of physical phenomena in superconductor-metal interlayer was presented.*

Streszczenie. *Jakość wykonania metalicznych elektrod ma istoty wpływ na mierzone wartości temperatury krytycznej T_c I prądu krytycznego I_c ceramicznych nadprzewodników wysokotemperaturowych. W pracy przedstawiono wyniki badań elektrod dwuwarstwowych. Elektrody te wykonano w celu poprawienia właściwości elektrod niklowych. Zastosowano rozpylanie magnetronowe z odpowiednich targetów w połączeniu z parowaniem próżniowym. (**Kontakty elektryczne z Ni-Me (Me=Ag, Mo, Cu) na powierzchni $YBa_2Cu_3O_x$**).*

Keywords: superconductor; resistivity; metallic electrodes.
Słowa kluczowe: nadprzewodnik; rezystywność; metaliczne elektrody.

Introduction

The main technological problem for high-current applications of ceramic superconductors is to prepare the metallic contacts on the surface of superconducting material. These contacts being the current electrodes have to characterise with very good mechanical properties and low resistance. These requirements allow to avoid a drop of basic superconducting parameters mainly critical temperature T_c and critical current density j_c.

The best materials for electrodes are noble metals: gold, silver or platinum [1-4]. They have very low resistance yet in the form of thin film and are good resistant for environment conditions. Unfortunately, these metals migrate from surface into the porous superconductor very easy. Additionally, platinum can change the chemical, microstructural and superconducting properties [5]. Other metals (copper, aluminium, indium etc.) are usually unstable or react with ceramic substrate and they electrical properties are not good enough for electrical applications. In practice there are several techniques for electrodes forming on ceramic superconductor surface [6-13].

In the previous works we have trying to use nickel for deposition electrical contact on the $YBa_2Cu_3O_x$ surface [14]. Nickel was chosen as electrode material because it is used both in some electronic applications and for superconducting tapes production [15-18]. Unfortunately, nickel layer behavioured as a heater. In presented paper some modifications of Ni-$YBa_2Cu_3O_x$ connection and their properties are described.

Deposition of electrodes

The procedure of electrode deposition was as follow:

1) the substrates ($YBa_2Cu_3O_x$) were mechanical washed in ethyl alcohol with ultrasound washer for ten minutes, dried in furnace at 150°C for one hour, heated in vacuum of $2\text{-}4\times10^{-3}$ Pa at 200°C for a half of hour,

2) the Ni-Ag, Ni-Mo and Ni-cu contacts were formed on superconductor surface by method depending of material:
- Cu-Ni: Cu was vacuum evaporated for 3 min from tungsten boat, Ni was magnetron sputtered for 18 min,
- Ag-Ni: procedure as above,
- Mo-Ni: Mo was magnetron sputtered for 10 min, Ni – for 18 min,

3) current and voltage leads were attached to the metal films prepared on superconductor surfaces by soldering. This process caused a bit of trouble. After many attempts glycerine was used as a proper solder flux.

Results of experiments

Superconducting transport parameters T_c and j_c for $YBa_2Cu_3O_x$ were measured by standard four-probe method. For this aim the low-resistance silver electrode were used. Value of T_c was typical for these materials (above 90 K). The j_c values were like for bulk granular superconductors: tens of mAcm^{-2}. Measurements of magnetic susceptibility showed strong diamagnetic Meissner effect. This indicates that the sample is superconducting on its volume, while the current limit is caused by poor connections between the grains. Such low j_c values were not a problem for contact resistance measurements.

To determine the metal/superconductor contact resistance three- and four-probe geometry was applied. The $U(I)$ characteristics were measured at room temperature and at liquid nitrogen temperature. Then the $R^{3\text{-probe}}(I)$ and $R^{4\text{-probe}}(I)$ dependencies were determined and then contact resistance $R_c(I)=R^{3\text{-probe}}(I)\text{-}R^{4\text{-probe}}(I)$.

The exemplary results of measured electrical resistance for Ni-Ag electrodes are shown in Fig. 1-2. In Table 1 there are collected the values of contact resistance for mono-layer Ni contact sample [14] and for particular bi-layer samples at two points of their $R_c(I)$ characteristics. The values of contact resistance R_c are relatively large for each of the tested samples. This is observed both at room temperature and at the temperature of liquid nitrogen.

In each case the contact resistance is lower at room temperature than at 77 K. This indicates that between the electrode and the superconductor a buffer area with the semiconductor nature is created. This is possible because the $YBa_2Cu_3O_x$ was not cooled during sputtering process.

At room temperature contact resistance R_c of each layer is constant for the current range 0-10 mA. At the temperature of liquid nitrogen the values of R_c rapidly decrease with increasing current values rather in each case. It was also observed for pure Ni layers [14]. This may be caused by high resistance R_c. The heat generated in the area of contact can not be effectively removed by liquid nitrogen. This causes a local temperature increase and decrease resistance of metallic contact.

The resistance of the electrode increases with decreasing temperature and decreases with increasing value of the flowing current for all samples. Reasons for this may be different than those described above. It can not to exclude the existence of more complicated phenomena in the area of contact caused by chemical modification caused by sputtering metallic layers on the superconductor surface.

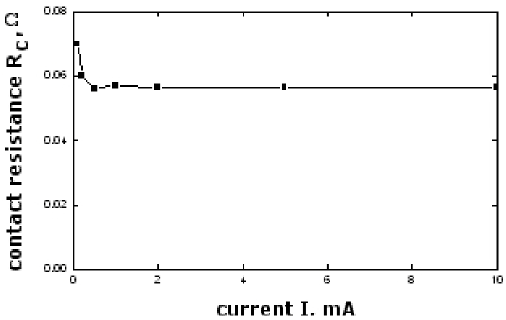

Fig.1. R_c of Ni-Ag interlayer at room temperature

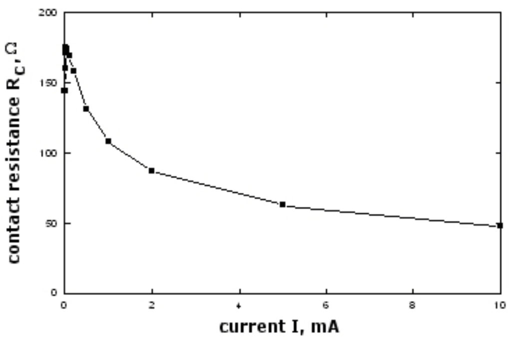

Fig.2. R_c of Ni-Ag interlayer at liquid nitrogen temperature

Table 1. Contact resistance for particular samples

Contact type	R_c [Ω] for I=1 mA	R_c [Ω] for I=10 mA
Ni (T=77 K)	6.50 [14]	6.50 [14]
Ni (T=293 K)	1.10 [14]	1.00 [14]
Ni-Ag (T=77 K)		
Ni-Ag (T=293 K)	0.55	0.55
Ni-Mo (T=77 K)		
Ni-Mo (T=293 K)	3.10	3.05
Ni-Cu (T=77 K)		
Ni-Cu (T=293 K)		

Conclusions

Each of the obtained layers (Ni, Ni-Ag, Ni-Mo, Ni-Cu) was characterized by a relatively high resistance for metal-superconductor contact. The cause of it can be not only electrical properties of electrode material but either chemical reaction in the subtle interlayer between superconductor material and electrode metal.

Any cooling of superconductor material being a substrate for deposited layers was not applied during sputtering process. It could provide better adhesion between deposited metallic film and superconductor surface. Higher temperature could lead to the formation of non-superconducting (semiconducting) interlayer between them and degradation of superconducting properties.

Adding another layer to the layer of Ni did not lead to improve the properties of the contacts. The only positive result was a slight decrease in resistance in some cases. Because of relatively high resistance the Ni, Ni-Ag, Ni-Mo and Ni-Cu thin films deposited on the surface of superconductor can be used as heaters to control the temperature of the material. Thus, the only proper material for low-temperature high-current electrode is still silver.

REFERENCES

[1] Szeloch R., Mazurek B., Woźny L., Dziedzic A., Technology and properties of high temperature superconductors with thick film contact, *Int. J. Electronics*, 70 (1991), 521-525

[2] Woźny L., Szeloch R., Dziedzic A., Wieczorek K., Mazurek B., Thick film contacts in investigations of high T_c superconductors, Proc. European conf. on *High-T_c Thin Films and SIngle Crystals*, Ustroń, Poland (1989), 501-509

[3] Fukuda K. , Fujita H., Ogawa K., Tomita M., Murakami M., Sakai N., Hirabayashi I. and K. Sawa, Quenching characteristics of electrical contacts using YBaCuO bulk superconductor, *Physica C: Superconductivity*, 468 (2008), nr 15-20, 1465-1468

[4] Morán O. and Hott R., On the high-resistivity contacts to $YBa_2Cu_3O_7$ thin films, electrical behavior in the regime of high temperatures and high-bias voltages, *Journal of Physics and Chemistry of Solids*, 71 (2010), nr 3, 253-257

[5] Lewis J. A., Wegmann M., Platt C. E. and Teepe M., Platinum-enhanced densification of grain-aligned $YBa_2Cu_3O_{7-x}$ films, *Appl. Phys. Lett.* 64 (1994), 103-105

[6] Dusoulier L., Denis S., Vanderbemden Ph., Dirickx M., Ausloos M., Cloots R. and Vertruyen B., Preparation of $YBa_2Cu_3O_{7-x}$ superconducting thick films by the electrophoretic deposition method, *Journal of Materials Science*, 41 (2006), nr 24, 8109-8114

[7] Herrmann P.F., Beghin E., Bouthegourt J., Cottevieille C., Duperray G., Grivon F., Leriche A., Winter V. and Verhaege T., Current transfer conditions from a metallic conductor to a high Tc superconductors, *Cryogenics*, 33 (1993), nr 3, 296-301

[8] Kalkur T.S., Kwor R.Y. and Byrne D.P., Contacts to Bi-Sr-Ca-Cu oxide superconducting thin films, *Science and Technology of Thin Film Superconductors 2*, Ed. McConnell R.D. and Noufi R., Plenum Press, New York (1990), 483-489

[9] Chen Y.C., Chong K.K. and Meen T.H., Heat treatment on the metal contacts of high-T_c (Pb, Bi)SrCaCuO superconductor, *Japanese J. of Applied Physics*, 30 (1991), nr 1, 33-37

[10] Elschner S. and Bock J., Electrical contacts with low resistance for melt-processed high-T_c superconductors, *Advanced Materials,* 4 (1992) nr 3, 242-244

[11] Sun Y. and Yang H., Electrical contact to high T_c superconductor, *Cryogenics*, 31 (1991) 760-762

[12] Plecenik A., Benacka S., Darula M., Chromik S., Mikusik P., Grajcar M., The energy gap depression in $YBa_2Cu_3O_{7-x}$/metal contacts, *Solid State Communication*, 78 (1991), nr 9, 809-813

[13] Robertazzi R.P., Kleinsasser A.W., Laibowitz R.B., Koch R.H., and Stawiasz K.G., In situ Ag/$YBa_2Cu_3O_7$ contacts for superconductor–normal metal–superconductor devices, *Physical Review B*, 46 (1992), nr 13, 8456-8471

[14] Szeloch R., Woźny L., Prociów E., Thin film metallic contacts to bulk superconductors, Proc. XXIII Conf. of the International Microelectronics and Packaging Society *IMAPS'99*, Kołobrzeg, Poland (1999), 197-202

[15] Dervos C.T., Kollia C., Psarrou S., Vassiliou, P., Nickel matrix composite electrocoatings as electrical contacts, *IEEE Transactions on Components and Packaging Technologies*, 22 (1999), nr 3, 460-466

[16] Cheggour N., Ekin J.W., Clickner C.C., Verebelyi D.T., Thieme C.L.H., Feenstra R., Goyal A., Paranthaman M., Transverse compressive stress effect in Y-Ba-Cu-O coatings on biaxially textured Ni and Ni-W substrates, *IEEE Transactions on Applied Superconductivity*, 13 (2003), nr 2, 3530-3533

[17] Ekin J.W., Experimental techniques for low-temperature measurements, Oxford University Press, Oxford, (2006), 319

[18] Zhou Y.X., Rizwan T., Salama, K., Growth of cube-textured nickel substrates for HTS coated conductors, *IEEE Transactions on Applied Superconductivity*, 13 (2003), nr 2, 2703-2706

***Authors**: dr inż. Leszek Woźny, Politechnika Wrocławska, Instytut Podstaw Elektrotechniki i Elektrotechnologii, ul. Wybrzeże Wyspiańskiego 27, 50-570 Wrocław, E-mail: leszek.wozny@pwr.wroc.pl; dr inż. Anna Kisiel, Politechnika Wrocławska, Instytut Podstaw Elektrotechniki i Elektrotechnologii, ul. Wybrzeże Wyspiańskiego 27, 50-570 Wrocław, E-mail: anna.kisiel@pwr.wroc.pl; dr hab. inż. Roman F. Szeloch, Politechnika Wrocławska, Wydziałowy Zakład Metrologii Mikro- i Nanostruktur; ul. Wybrzeże Wyspiańskiego 27, 50-570 Wrocław, E-mail: roman.szeloch@pwr.wroc.pl; mgr inż. Eugeniusz Prociów, Politechnika Wrocławska, Wydziałowy Zakład Technologii i Diagnostyki Struktur Mikroelektronicznych; ul. Wybrzeże Wyspiańskiego 27, 50-570 Wrocław, E-mail: eugeniusz.prociow@pwr.wroc.pl.*

Conference ELMECO–7
ELECTROMAGNETIC DEVICES AND PROCESSES IN ENVIRONMENT PROTECTION
joint with 10th Seminar AoS-10 APPLICATIONS OF SUPERCONDUCTORS
28–30.09.2011, Nałęczów, Poland

APPLICATION OF CURVELET TRANSFORM IN THE PROCESSING OF DATA FROM GROUND PENETRATING RADAR

Waldemar WÓJCIK[1], Sławomir CIĘSZCZYK[1], Tomasz ŁAWICKI[1], Arkadiusz MIASKOWSKI[2]
Lublin University of Technology (1), University of Life Sciences in Lublin (2)

***Abstract**. Ground Penetrating Radar (GPR) is used for non-invasive determination of objects and their properties under the surface of a material. The resulting GPR scan contains information useful and a number of distortions that hinder interpretation of results. The article presents the application of curvelet transform as a tool helpful in indicating the location of objects searched.*

***Streszczenie.** Technika GPR (Ground Penetrating Radar) służy do nieinwazyjnego określania obiektów oraz ich właściwości będących pod powierzchnią określonego materiału. Otrzymany obraz GPR zawiera informację użyteczną i szereg zakłóceń utrudniających interpretację wyników. Artykuł prezentuje zastosowanie transformaty curvelet jako narzędzia pomocnego we wskazaniu lokalizacji poszukiwanych obiektów.*

Keywords: GPR, curvelet, image processing
Słowa kluczowe: georadar, GPR, curvelet, przetwarzanie obrazu

Introduction

Ground Penetrating Radar (GPR) is used for non-invasive determination of objects and their properties under the surface in the material. The basic principle of operation is the pulse of electromagnetic wave propagation in a medium with varying properties (time domain impulse radar). If the medium there is step change of dielectric permittivity the electromagnetic wave is reflected to form the characteristic shape received by an antenna on the surface (Fig. 1). Due to the attenuation of electromagnetic wave in the most common uses the tests may be conducted to a depth of several meters. Increasing the frequency of the electromagnetic wave can increase the separation analysis. At the same time, however, decreases the penetration depth of the signal due to its higher attenuation.

GPR applications are:
- archaeological investigations
- identifying the characteristics (parameters) of electrical materials,
- identifying the properties of concrete,
- detection of objects under the surface of the earth (mines)
- test for judicial
- geophysical surveys,
- identifying the location of pipes and cables,
- determining the parameters of sidewalks and roads (thick layer).

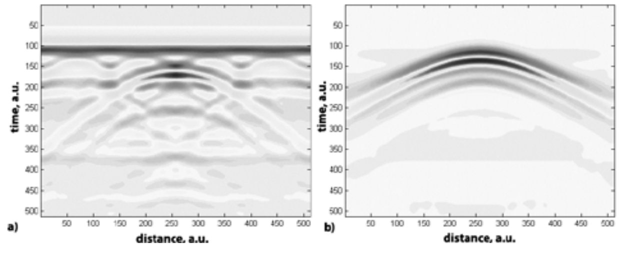

Fig. 1. Typical GPR scan for pipe in concrete with clutter (a) and pipe in ground with added an amendment to remove clutter (b).

During the interpretation of the GPR there are many problems. The first is the large initial reflection from the surface (clutter). Poses a lot of trouble especially on-line analysis. To operate a skilled operator is needed, who will be able based on the GPR images to determine whether under the surface of the object is or is it a distortion. They must then determine what kind it is or what the object has parameters. One of the widely developed issues of GPR imaging is the development issues of signal processing for automatic detection and interpretation of images. With the rapid development of microprocessor technology it is possible to apply more advanced algorithms directly in the GPR equipment.

Due to the non-destructive testing the GPR is often not possible to confirm the radar analysis of alternative strategies. Very aids are modeling techniques. The most popular technique for modeling is fini-difference time-domain (FDTD). Modeling allows you to better understand the phenomena occurring in reality and increases the possibility of interpreting the data. In some cases it is the only method of interpreting the results. The analysis method in time domain does not require knowledge of the frequency dependence of the test medium.

The migration algorithms are the most common methods of creating the shape of objects based on data collected from the surface. However, that algorithms require not noisy and distorted data, a pure reflection from the interesting objects in the absence of interference or, for example a subject close to the reconstructed object. In fact, such situations are rare and most of the register using the GPR technique is highly distorted.

The main objective methods of signal processing is to improve the image quality to highlight the desired characteristics and to facilitate the interpretation by the operator. The operator will be able to better qualify for the observed characteristics of the object. The next step is to replace operator to automatically interpretation the data, e.g. by identifying the type of object or its location and size.
Detection of specific shapes is performed mostly by the correlation with a specific pattern. The most commonly used methods of this type is the moment method, Hough transform. However, they are computationally demanding because of the significant number of calculated parameters. Another recently used algorithm are artificial neural networks and clustering methods. In the case of neural networks due to the high dimensionality of data are used

methods such as PCA to its reduction of [1]. The most widely used algorithm known from the classical image processing is edge detection method allows to detect a specific shape in the B-scan data. Edge detection is a prelude to detect shapes and reinforces the characteristics sought in the GPR image [2].

Wavelet transform is also used for the pipe detection [3]. Wavelet transform is used for analysis at several levels of resolution. The resolution is here understood as both frequency as well as temporarily. Individual sections of the signal is analyzed in terms of frequency. Based on obtained wavelet coefficients (representing the signal) to determine and compare the characteristics of signals. At a certain level of resolution of the GPR signal characteristics are shown [3]. This allows for a better location and identification of objects.

Curvelet transform

An extension of the wavelet analysis are other multi-resolution transform. They are directed towards the identification of signal singularity, such as edges. One of the latest tools of this type is the curvelet transform [4]. As compared to other multi-resolution transforms curvelet are orientation parameter, so that at each level of decomposition is possible to analyze the image in terms of its specific characteristics, that is, edge and shape.

Each level of resolution contains an orientation parameter, so that we get a number of curvelet coefficients matrix, each matrix contains information about other specific characteristics of the image. The article presents the results of the transformation with FDCT via Wrapping algorithm implemented in CurveLab libraries for Matlab. The structure of curvelet coefficients, which is obtained based on the CurveLab library widely discussed in other papers [5].

Tests

Test images were generated in GprMax program [6]. Images were prepare for further processing, they were scaled to the size of 512x512 pixels, and added an amendment to remove clutter. To focused on the problem of the initial rebound, the amendment was not entered for the case of pipes in the concrete. Shown cases of single pipe into the ground in various positions XY, two pipes in the ground, pipes in concrete in the presence of confounding factors (air in concrete). Some results of the analysis are shown in figures 2-3.

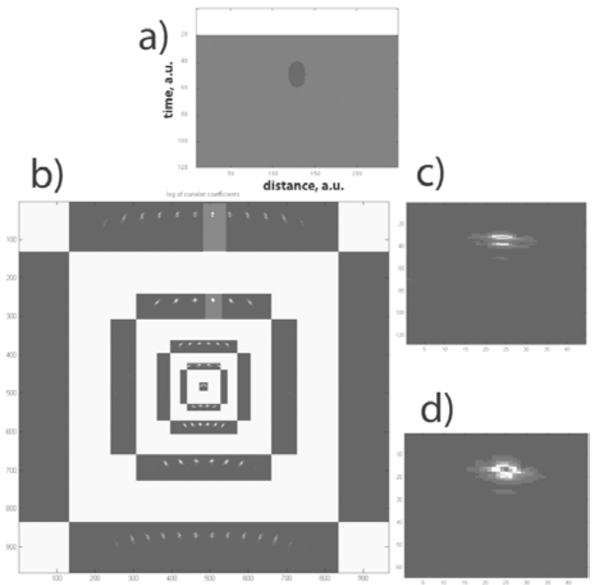

Fig. 2. Analysis case of single pipe in the ground (a) and matrix of curvelet coefficients (b); matrix no. 90 (c) and matrix no. 54 (d).

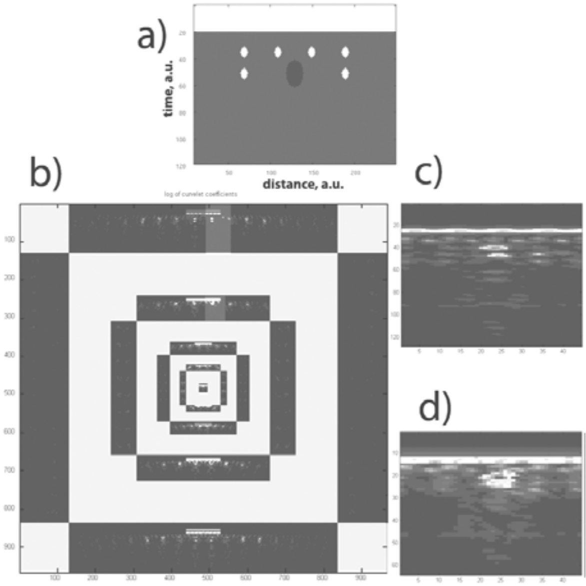

Fig. [illegible] (a) and matrix of curvelet coefficients (b); matrix no. 90 (c) and matrix no. 54 (d).

Conclusions

As shown in Figure 3 and 4, only a small part of the curvelet coefficients contain useful information. They are mainly horizontal components. The values of the mixed and vertical coefficients take very small values. For the detect objects the most useful are the matrices 54 and 90. By using curvelet transform we get a tool with high sensitivity to an object with large difference in dielectric permittivity in relation to the medium. At the same time by selecting the appropriate coefficients we cut from interference and disruption.

REFERENCES

[1]. X. L. Travassos, D.A.G. Vieira, N. Ida, C. Vollaire, A. Nicolas: Characterization of Inclustions in a Nonhomogeneous GPR Problem by Artificial Neural Networks, IEEE Transactions on Magnetics, Vol. 44, 2008

[2]. H. Chenand, A. G. Cohn: Probabilistic robust hiperbola mixture model For interpreting ground penetrating radar data, IEEE World Congress On Computational Intelligence, 2010

[3]. S.H. Ni, Y.H. Huang, K.Feng Lo, D.C. Lin: Buried pipe detection by ground penetrating radar using the discrete wavelet transform, Computer and Geotechnics 37, 2010, p. 440-448

[4]. Candès E.J., Demanet L., Donoho D.L., Ying L.: Fast discrete curvelet transforms. Multiscale Model. Simul., 5, 2005, p. 861-899

[5]. W. Wójcik, A. Kotyra, T. Ławicki, B. Pilek: Zastosowanie transformaty curvelet do analizy procesu spalania, Przegląd Elektrotechniczny, 10, 2010, p. 131-135

[6]. A. Giannopoulos: Modelling ground penetrating radar by GprMax, Construction and Building Materials, Vol. 19, 2005, p. 755-762

Authors: *prof. dr hab. inż. Waldemar Wójcik, dr inż. Sławomir Cięszczyk, mgr inż. Tomasz Ławicki, Lublin University of Technology, Faculty of Electrical Engineering and Computer Science, Nadbystrzycka 38a, 20-618 Lublin, e-mail: t.lawicki@pollub.pl; dr inż. Arkadiusz Miaskowski, University of Life Sciences in Lublin, Faculty of Production Engineering, Akademicka 13, 20-950 Lublin, e-mail: arek.miaskowski@up.lublin.pl*

Contents